

Jose H. Zagal · Fethi Bedioui *Editors*

Electrochemistry of N4 Macrocyclic Metal Complexes

Volume 1: Energy

Second Edition

 Springer

Electrochemistry of N₄ Macrocyclic Metal Complexes

Jose H. Zagal · Fethi Bedioui
Editors

Electrochemistry of N₄ Macrocyclic Metal Complexes

Volume 1: Energy

Second Edition

 Springer

Editors

Jose H. Zagal
Universidad de Santiago de Chile
Santiago
Chile

Fethi Bedioui
CNRS-Chimie ParisTech
Paris
France

ISBN 978-3-319-31170-8

ISBN 978-3-319-31172-2 (eBook)

DOI 10.1007/978-3-319-31172-2

Library of Congress Control Number: 2016934669

© Springer Science + Business Media, LLC 2006

© Springer International Publishing Switzerland 2016

This work is subject to copyright. All rights are reserved by the Publisher, whether the whole or part of the material is concerned, specifically the rights of translation, reprinting, reuse of illustrations, recitation, broadcasting, reproduction on microfilms or in any other physical way, and transmission or information storage and retrieval, electronic adaptation, computer software, or by similar or dissimilar methodology now known or hereafter developed.

The use of general descriptive names, registered names, trademarks, service marks, etc. in this publication does not imply, even in the absence of a specific statement, that such names are exempt from the relevant protective laws and regulations and therefore free for general use.

The publisher, the authors and the editors are safe to assume that the advice and information in this book are believed to be true and accurate at the date of publication. Neither the publisher nor the authors or the editors give a warranty, express or implied, with respect to the material contained herein or for any errors or omissions that may have been made.

Printed on acid-free paper

This Springer imprint is published by Springer Nature

The registered company is Springer International Publishing AG Switzerland

Foreword

Society's mounting concern for the well-being of our environment has given increased impetus to the development of new, efficient, sustainable, and clean industrial processes and energy sources at reasonable cost. Electrochemistry has an important role to play in these developments. Exploring and understanding nature's mechanisms for catalytic reactions gives important indicators towards productive research areas. Such is the case with porphyrins and phthalocyanines, which are the subject of this monograph.

The purpose of this book is to present and discuss the latest advances in the understanding and applications MN₄, or also so-called M-N₄, macrocycles, with a focus on porphyrins and phthalocyanine complexes. Different areas of electrochemistry are examined and linked through the catalytic properties of synthetic and naturally occurring MN₄ complexes. The breadth of the subject is reflected in the contents of the two multiauthor volumes, which include electrocatalysis, energy conversion, biomimetic design, electrochemical monitoring, and electrosynthesis. The editors are to be congratulated for assembling contributions on all these topics by recognized experts in their fields.

I am certain that this two-volume monograph will be valuable to researchers in leading to new ideas and synergies, highlighting state of the art, addressing challenges, and bridging the gap between different areas of research in MN₄ macrocycles. It will aid in driving this important field forward.

Coimbra University, Portugal

Christopher Brett

Preface

Molecules having an MN₄, or also so-called M-N₄, moiety are common in nature and are involved in the catalysis of electron transfer reactions, photosynthesis, and O₂ transport, to name a few instances. For this reason, there has been great interest in both artificial and naturally occurring MN₄ complexes in various fields, including electrochemistry. For example, metalloporphyrins are used as biomimetic models to study several biological redox processes, molecular oxygen transport, and catalytic activation to mimic monooxygenase enzymes of the cytochrome P450 in particular. They are also well known as efficient catalysts for the oxidative degradation of many types of pollutants (such as organohalides and phenols) and residual wastes. The discovery in 1965 by Jasinski that cobalt phthalocyanine presented catalytic activity for the reduction of molecular oxygen in aqueous media triggered the attention of several research groups in the 1970s. They focused their attention on MN₄ complexes as potential catalysts for the reduction of O₂ with the aim of finding a replacement for expensive Pt in the cathode of fuel cells. However, even though some of these complexes are stable under many conditions, they lack the long-term stability required for fuel cell performance. For this reason, attention has been focused on pyrolyzed MN₄ complexes, which are more stable than intact materials. Materials prepared from different ingredients, like nitrogen-containing compounds, ammonia, different carbons, and metal salts, upon pyrolysis at temperatures of 1000 °C or more produce active and stable materials, many of which seem to have M-N₄ centers, with both pyrrolic and pyridinic nitrogens. The MN₄ centers are created during the pyrolysis, but the mechanism for their formation is little understood.

Progress in this area has been considerable in recent years and hopefully some non precious metal catalyst will be used in fuel cells in the near future. On the other hand, the stability of metallophthalocyanines makes them appropriate for applications in various fields such as chemical catalysis (such as the MEROX process for the sweetening of oils), dye stuffs, coloring for plastics and metal surfaces, sensors, chromatographic detectors, photoconducting agents, and so on. These complexes are also used for photobiology and photodynamic cancer therapy, electrochemical

removal of organic wastes, display devices, electrochromism, electroluminescence, molecular metals, and nonlinear optical applications. Further, their versatility for binding extra planar ligands of these complexes confers on them formidable potential uses in electrochemical-sensing devices for several fields of application in analytical, electroanalytical, and spectrophotocchemistry. Metalloporphyrins and metallophthalocyanines and similar MN₄ macrocycles exhibit a reversible and rich redox chemistry which makes them good mediators in many electron transfer reactions when confined to electrode surfaces. For example, they promote the electrooxidation of dopamine, many thiols, H₂S, reduced glutathione, L-cysteine, sulfite, thiocyanate, coenzyme A, penicillin, oxalic acid, NADH, hydroxylamine, hydrazine, nitrite, nitric oxide, cyanide, organic peroxides, hydrogen peroxide, propylgallate, ascorbic acid, hydroquinone, catechol, phenols, chlorophenols, and the reduction of molecular oxygen, hydrogen peroxide, carbon dioxide, L-cystine, disulfides, and thionylchloride. Potentially, they can catalyze many other reactions as well. It is interesting that a large number of the studied reactions involve significantly relevant biological compounds, and the list keeps increasing as more publications appear in the literature. Earlier work involved electrodes made of graphite or carbon electrodes modified with monolayers of these complexes, or graphite powder or carbon pastes mixed with macrocyclic complexes. Recently, many authors have reported electrodes consisting of carbon nanotubes (CNTs) with the complexes grafted to the external walls of CNTs. These hybrid materials exhibit higher activities than the smooth electrodes, as higher surface areas are achieved.

Although the list of studied reactions and processes involving photoassistance is less abundant and fewer systems have been studied in the fields of photoelectrochemistry and photocatalysis, this area of investigation is experiencing intense development due to the potential of these compounds in photobiology and nano-sized semiconductor materials.

It has recently become of great interest to mimic enzymatic or natural systems and design new complex structures that combine well-defined topology and a pronounced chemical flexibility. The idea is to fine-tune the properties of the electron transfer reactions and the expansion of the supramolecular architectures. This is leading to an active area of research, namely "design of intelligent molecular material electrodes" with predetermined reactivity. To do so, highly elaborate synthesis routes have been developed to design chemically modified metalloporphyrins and metallophthalocyanines that can then be strongly adsorbed on conventional materials, electropolymerized on conducting substrates, or incorporated into hybrid organic/inorganic gels or solid matrices, to form single and multi-walled carbon nanotubes to produce catalytic electrodes with long-term stability for new practical analytical applications.

Thus, it is clear that the numerous, varied, and vast possibilities for applications ensure that bio-inspired porphyrins and phthalocyanines and similar compounds will remain of vital importance for many years to come, and that the related fields of investigation will have significant ramifications. The publication since 1997 of *The Journal of Porphyrins and Phthalocyanines*, an international journal of significant impact factor entirely focused on these molecular materials, is a clear indicator, and

the Society of Porphyrins and Phthalocyanines provides a forum for interaction among researchers around the world.

The main objective of this monograph is to provide a general updated view of the vast applications of these materials in electrochemistry by focusing on a few significant topics and examples. It is also aimed at offering future projections and opening new fields of research and the exploration of new applications.

Jose H. Zagal
Fethi Bedioui

Contents

Oxygen Electroreduction on M-N₄ Macrocyclic Complexes	1
Kexi Liu, Yinkai Lei, Rongrong Chen and Guofeng Wang	
Heat-Treated Non-precious Metal Catalysts for Oxygen Reduction	41
Hoon Chung, Gang Wu, Drew Higgins, Pouyan Zamani, Zhongwei Chen and Piotr Zelenay	
Non-noble Metal (NNM) Catalysts for Fuel Cells: Tuning the Activity by a Rational Step-by-Step Single Variable Evolution	69
Alessandro H.A. Monteverde Videla, Luigi Osmieri and Stefania Specchia	
Application of Scanning Electrochemical Microscopy (SECM) to Study Electrocatalysis of Oxygen Reduction by MN₄-Macrocyclic Complexes	103
Justus Masa, Edgar Ventosa and Wolfgang Schuhmann	
Theoretical Aspects of the Reactivity of MN₄ Macrocyclics in Electrochemical Reactions	143
Sebastián Miranda-Rojas, Alvaro Muñoz-Castro, Ramiro Arratia-Pérez and Fernando Mendizábal	
Metalloporphyrins in Solar Energy Conversion	171
Ievgen Obraztsov, Włodzimierz Kutner and Francis D'Souza	
Photoelectrochemical Reactions at Phthalocyanine Electrodes	263
Derck Schlettwein	
Index	315

Editors and Contributors

About the Editors

Jose H. Zagal is Full Professor at the University of Santiago de Chile. He received a degree in Chemistry from the University of Chile and a Ph.D. in Chemistry from Case Western Reserve University. He was postdoctoral fellow at Brookhaven National Laboratory. He was awarded the *Presidential Chair in Science*, The Dr. Alberto Zanlungo Prize is a Fellow of the *International Society of Electrochemistry* and Fellow of *The Electrochemical Society*. He has published over 200 papers, three books, seven book chapters, and three patents. He has served on the Editorial Boards of the following journals: *Journal of Applied Electrochemistry* (1988–2010), *Journal of the Chilean Chemical Society* (1984–2007) *Electrocatalysis*, (2009–2015) and is presently a member of the Editorial Board of: *Journal of Solid State Electrochemistry* (Springer), of the *International Journal of Electrochemistry* (Endawi), *Electrochemistry Communications*, *Journal of the Serbian Chemical Society*, *Electrochemical Energy Technology* and *Chimica Nova*. He has contributed in several areas of electrochemistry including electrocatalysis, conductive polymers, electroanalysis, corrosion, electrochemistry of macrocyclic complexes and is better known for developing reactivity descriptors for the electrocatalytic activity of molecular catalysts.

Fethi Bedioui holds a degree in Chemical Engineering from the Ecole Nationale Supérieure de Chimie de Paris, Diplôme d'Etudes Approfondies de Chimie Analytique, and a Doctorate from the Université Pierre et Marie Curie in Paris. He was a postdoctoral fellow at the Ecole Nationale Supérieure de Chimie de Lille. At present he is a senior researcher in the CNRS in Paris (France) and works in the *Unité de Technologies Chimiques et Biologiques pour la Santé* (Chimie ParisTech/PSL University/CNRS/INSERM/Université Paris Descartes) on the development and implementation of advanced molecular materials for electrocatalysis and electrochemical sensing devices applied to biotechnological issues. In particular, he is actively working in the fields of electrochemical sensors for biological systems, multi sensor arrayed platform for screening biological markers,

porphyrins and phthalocyanines-based molecular materials for electroanalysis and electrocatalysis, microelectrochemical patterning of surfaces using scanning electrochemical microscopy and label-free electrochemical detection of microRNAs. He has published over 250 papers, including books and book chapters. He is currently Chair of the “Analytical Electrochemistry” division of the International Society of Electrochemistry.

Contributors

Ramiro Arratia-Pérez Doctorado en Físicoquímica Molecular, Relativistic Molecular Physics (ReMoPh) Group, Universidad Andres Bello, Santiago, Chile; Center for Applied Nanosciences (CENAP), Universidad Andres Bello, Santiago, Chile

Rongrong Chen Richard G. Lugar Center for Renewable Energy, Indiana University Purdue University Indianapolis, Indianapolis, IN, USA

Zhongwei Chen Department of Chemical Engineering, University of Waterloo, Waterloo, ON, Canada

Hoon Chung Materials Physics and Applications Division, Los Alamos National Laboratory, Los Alamos, NM, USA

Francis D’Souza Department of Chemistry, University of North Texas, Denton, TX, USA; Advanced Materials and Manufacturing Processes Institute (AMMPI), UNT-Discovery Park, Denton, TX, USA

Drew Higgins Department of Chemical Engineering, University of Waterloo, Waterloo, ON, Canada

Włodzimierz Kutner Institute of Physical Chemistry (IPC PAS), Warsaw, Poland; Faculty of Mathematics and Natural Sciences, School of Sciences, Cardinal Stefan Wyszyński University in Warsaw, Warsaw, Poland

Yinkai Lei Department of Mechanical Engineering and Materials Science, University of Pittsburgh, Pittsburgh, PA, USA

Kexi Liu Department of Mechanical Engineering and Materials Science, University of Pittsburgh, Pittsburgh, PA, USA

Justus Masa Analytical Chemistry, Center for Electrochemical Sciences (CES), Ruhr-Universität Bochum, Bochum, Germany

Fernando Mendizábal Faculty of Sciences, Department of Chemistry, Universidad de Chile, Santiago, Chile

Sebastián Miranda-Rojas Facultad de Ciencias Exactas, Departamento de Ciencias Químicas, Universidad Andres Bello, Santiago, Chile; Center for Applied Nanosciences (CENAP), Universidad Andres Bello, Santiago, Chile

Alessandro H.A. Monteverde Videla Politecnico di Torino, Department of Applied Science and Technology, Institute of Chemical Engineering, Gre.En2 Group (Green Energy & Engineering Group), Turin, Italy

Alvaro Muñoz-Castro Grupo de Química Inorgánica y Materiales Moleculares, Universidad Autonoma de Chile, Santiago, Chile

Ievgen Obraztsov Institute of Physical Chemistry (IPC PAS), Warsaw, Poland

Luigi Osmieri Politecnico di Torino, Department of Applied Science and Technology, Institute of Chemical Engineering, Gre.En2 Group (Green Energy & Engineering Group), Turin, Italy

Derek Schlettwein Institute of Applied Physics, Justus-Liebig-University Gießen, Gießen, Germany

Wolfgang Schuhmann Analytical Chemistry, Center for Electrochemical Sciences (CES), Ruhr-Universität Bochum, Bochum, Germany

Stefania Specchia Politecnico di Torino, Department of Applied Science and Technology, Institute of Chemical Engineering, Gre.En2 Group (Green Energy & Engineering Group), Turin, Italy

Edgar Ventosa Analytical Chemistry, Center for Electrochemical Sciences (CES), Ruhr-Universität Bochum, Bochum, Germany

Guofeng Wang Department of Mechanical Engineering and Materials Science, University of Pittsburgh, Pittsburgh, PA, USA

Gang Wu Department of Chemical and Biological Engineering, University at Buffalo, SUNY, Buffalo, NY, USA

Pouyan Zamani Department of Chemical Engineering, University of Waterloo, Waterloo, ON, Canada

Piotr Zelenay Materials Physics and Applications Division, Los Alamos National Laboratory, Los Alamos, NM, USA

Oxygen Electroreduction on M-N₄ Macrocyclic Complexes

Kexi Liu, Yinkai Lei, Rongrong Chen and Guofeng Wang

1 Introduction

There has been tremendous interest to evaluate the performance and acquire fundamental understanding of nitrogen-chelated transition metal (M-N₄) macrocyclic electrocatalysts for oxygen reduction reaction (ORR), which occurs on the cathode of polymeric electrolyte fuel cells, including proton exchange membrane fuel cells (PEMFCs) and alkaline anion exchange membrane fuel cells (AAEMFCs). Both PEMFCs and AAEMFCs can be employed to generate electricity through direct electrochemical conversion of hydrogen and oxygen into water. Switching from current fossil-fuel powered vehicles on road to hydrogen fuel cell vehicles could benefit our society with improved air quality, health, and climate [1]. However, precious metals like platinum (Pt) are normally needed to efficiently catalyze the sluggish ORRs at the cathode of PEMFCs. Currently, the rarity of these precious metals impedes the manufacture and deployment of fuel cells at an industrial scale [2]. Thus, it is crucial to find effective electrocatalysts, containing no precious metals, for ORRs to ensure the sustainable development of the fuel cell technology. In this regard, M-N₄ macrocycles have been demonstrated to have promising potentials to replace Pt as the electrocatalysts in PEMFCs [3].

The family of M-N₄ macrocycles (for instance, metallophthalocyanines (MPc, see Fig. 1a), metalloporphyrins (MP, see Fig. 1b), metallotetraphenylporphyrins (MTPP, see Fig. 1c), as well as the heat treated mixture of nitrogen-containing

K. Liu · Y. Lei · G. Wang (✉)

Department of Mechanical Engineering and Materials Science,
University of Pittsburgh, Pittsburgh, PA 15261, USA
e-mail: guw8@pitt.edu

R. Chen (✉)

Richard G. Lugar Center for Renewable Energy,
Indiana University Purdue University Indianapolis, Indianapolis, IN 46202, USA
e-mail: rochen@iupui.edu

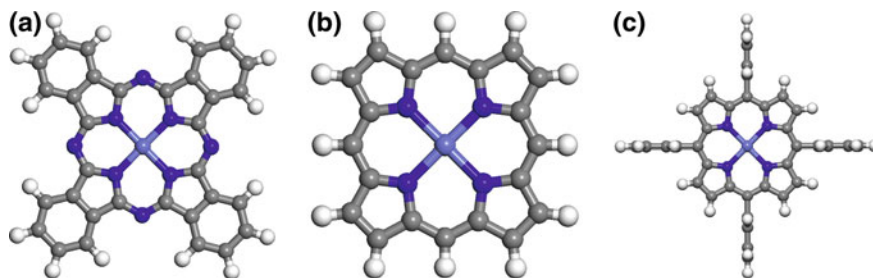


Fig. 1 Atomistic structures of **a** metal phthalocyanine molecule, **b** metal porphyrin molecule, and **c** metal tetraphenylporphyrin molecule. In the figure, the central ball represents non-precious transition metal (for example, Fe or Co) atom. Blue, gray, and white balls represent N, C, and H atoms, respectively

molecules, transition metals, and carbon supports) have a wide range of applications in promoting various electrochemical reactions for energy conversion [4, 5], gas sensor [6, 7], and biological functions [8, 9]. For example, these electrocatalysts have been found to be capable of catalyzing the electrooxidation reactions of carbon monoxide [10], glucose [11], and nitrogen monoxide [12]; as well as the electroreduction reactions of oxygen [4], hydrogen peroxide [13], molecular nitrogen [14], and nitrate [15]. The $M-N_4$ electrocatalysts can also be used to produce hydrogen from water [16] and as photosensitizers for imaging [17]. In addition to their technological significance, these $M-N_4$ electrocatalysts prove to be good example systems to reveal the relation between the molecular (and/or electronic) structure and the activity of catalysts [18].

Specifically for catalyzing oxygen electroreduction, the $M-N_4$ structure has been found in the cytochrome c oxidase (CcO) within bacterial membranes and exhibit capability to convert O_2 into water. Motivated by this discovery, Collman et al. developed a functional model with similar active sites and conducted an extensive study of its electrocatalytic activity for four-electron reduction of O_2 [19–23]. The study on oxygen reduction on $M-N_4$ macrocycles was first performed by Jasinski [4]. In its molecular form (Fig. 1), the $M-N_4$ macrocycles most often contain a central transition metal atom and some surrounding N-containing ligand groups. The central metal atom is linked to the ligands through metal-nitrogen bond formation, so that the ligand groups can modulate the electronic structure of the central transition metal atoms. Therefore, the catalytic activity of the $M-N_4$ macrocycles could be tuned by varying the central transition metal and modifying the peripheral ligands [24–26].

Furthermore, it has been found that heat treatment processing to the mixture of metal macrocyclic molecules and carbon materials can improve both the activity and durability of the attained $M-N_4/C$ electrocatalysts. Jahnke et al. [27] showed that heat treatment had a significant effect on the catalytic activity of carbon-supported CoTAA (cobalt-dihydrodibenotetraazaannulene) for ORR. They found that all the heat-treated CoTAA samples had better catalytic performance than those untreated

ones. The catalysts heat treated at 600 °C showed the best ORR activity while the catalysts heat treated at 800–900 °C showed the best stability. Moreover, Chu et al. prepared their catalysts by heat treating a series of single transition metalloporphyrins (metals: V, Mn, Fe, Co, Ni, Cu, and Zn) and the combination of two transition metalloporphyrins (systems: V/Fe, Co/Fe, Ni/De, and Cu/Fe). They found that the heat-treated FeTPP/CoTPP was the best catalyst for ORR and methanol-tolerant [28].

Some recent advances in studying the O₂ electroreduction on the M-N₄ macrocyclic complexes are particularly notable and encouraging. First, many novel M-N₄ macrocyclic complexes with different functional groups and various spatial structures have been found to exhibit enhanced catalytic performance. For example, Chen et al. introduced diphenyl thiophenol groups onto FePc and observed a significant enhancement in the durability of the catalysts [29, 30]; Ward et al. synthesized a series of first row transition metal tris(2-pyridylmethyl)amine M-N₄ complexes that have three-dimensional structures and possess good selectivity for four-electron O₂ reduction over two-electron reduction [31]; Honda found enhanced catalytic two-electron reduction of O₂ on a saddle-distorted CoPc which has eight phenyl groups on the peripheral carbon rings [32]; Kakuda found that the catalytic four-electron reduction of O₂ by a copper complex could be enhanced by introducing a pendant ligand pivalamido group [33]; and he also found that using scandium triflate could change reduction of O₂ from four-electron to two-electron process [34].

Secondly, more and more research studies are devoted to compounding M-N₄ macrocyclic complexes with other materials or regularly assembling them on various substrates to enhance their catalytic performance. For example, McClure et al. produced M-N₄ imbedded carbon nanofibers through heat treatment of as-electrospun FePc-doped polyacrylonitrile and reported remarkable oxygen reduction catalytic activity [35]. They also coated the fibers with TiO₂ to improve their durability. Sedona et al. tuned the oxygen reduction catalytic activity of Ag (110)-supported FePc through precisely adjusting the long-range supramolecular arrangement and the local adsorption geometry of FePc molecules on the Ag(110) surface [36]. In contrast, Ponce et al. linked FePc to Au(111) by conjugated self-assembled monolayers of aromatic thiols as axial ligands which significantly improved the catalytic activity compared with directly laying FePc onto Au(111) [37, 38].

In a third trend, functional carbon nanostructures (such as, graphene and nanotube) have been used as the substrates for M-N₄ macrocyclic complexes to improve their catalytic performance. In particular, different graphene supported macrocyclic complex composites through forceful π - π interaction have been fabricated and characterized [39–42]. Moreover, a family of high-performance nitrogen-derived non-precious transition metal (M-N_x) electrocatalysts for ORR was fabricated through heat treating the mixture of carbon particle, polyaniline, iron, and cobalt in the temperature range of 400–1000 °C under a N₂ atmosphere [3, 43]. Experimental characterizations revealed that these catalysts had the feature structures of Fe-N_x and/or Co-N_x clusters. The acquired best catalyst could catalyze

the ORR at potentials within 60 mV of that of carbon support Pt and retain its performance stability up to 700 h at a fuel cell voltage of 0.4 V [3]. In a recent study, the $\text{FeN}_4\text{C}_{12}$ moiety which contain M-N_4 feature group has been identified as the catalytic active sites for oxygen reduction on these pyrolyzed catalysts [44].

In summary, the M-N_4 macrocyclic electrocatalysts have shown promising potentials to replace precious Pt catalysts in many applications related to renewable energy technology (in particular, PEMFCs). However, there still exists a large performance gap in activity and durability between the M-N_4 electrocatalysts and Pt-based catalysts. Bridging such a performance gap demands an in-depth understanding about the nature of active sites, the pathway of reaction mechanism, and the function of heat treatment processing on these non-precious metal electrocatalysts. In this review, we focus on a survey of the published knowledge pertinent to the experimental and theoretical aspects of the catalytic electroreduction of oxygen on M-N_4 macrocycles.

2 ORRs on Carbon-Supported M-N_4 Macrocyclic Molecules

In 1964, Jasinski first reported the catalytic activity of cobalt phthalocyanine (CoPc) for ORRs in alkaline medium [45]. Following this work, extensive studies on various metallophthalocyanine (MPc) and metalloporphyrin (MP) derivatives containing different central transition metals and different substitutes on the peripheral organic skeleton in both acid and alkaline electrolyte has been conducted [27, 46–64]. In these M-N_4 macrocyclic complexes, the central transition metals could be Fe, Co, Ni, Cu, Ru, Mn, Zn, Pd, or Pt atoms. It has been found that Fe- and Co- N_4 macrocycles show better ORR activity than the others. Moreover, various functional substitutes were added to the organic skeleton of metallophthalocyanine and metalloporphyrin, for purpose of tuning the catalytic activity of M-N_4 macrocyclic complexes. Some of the most promising and widely studied derivatives include metallo-tetrasulfonated-phthalocyanine (MTsPc) [48, 58, 61, 64–66], metallo-tetraphenyl-porphyrin (MTPP) [27, 67–70], metallo-tetraazaannulene (MTAA) [27, 62, 71–73] and metallo-tetramethoxyphenyl-porphyrin (MTMPP) [67, 74–78]. We summarize the observed catalytic performance of various M-N_4 macrocyclic complexes for ORRs in Table 1. It has been recognized that the type of the central transition metal mainly determines the catalytic activity of these macrocyclic complexes while the chelates and peripheral substitutes help further fine-tune their activity [27, 47, 79, 80]. In addition, the catalytic activity of M-N_4 macrocycles for ORR is affected by the polymerization degree, approach of electrode preparation, the nature of substrate materials, the pH of the electrolyte, and heat treatment processing [27, 47, 79, 81]. In below, we review in details these effects on the ORR activity on M-N_4 macrocycles.

Table 1 Summary of experimental measurements on the activity of M-N₄ macrocyclic complexes for ORR

Complex	Electrode/Substrate	E_{onset} (V vs. RHE)	$E_{1/2}$ (V vs. RHE)	Electron transfer	Medium	References
CoPc	Pyrolytic graphite	~0.88 (pH 14)	~0.74 (pH 14)	–	pH 0–14	[62]
		~0.37 (pH 0)	~0.17 (pH 0)	–		
CoP	Graphite	–	0.77/0.44 ^a	~3.8/4.0 ^a	1 M HClO ₄	[82]
CoP	Pyrolytic graphite	~0.58	–	2.7 (at low E)	1 M HClO ₄	[83]
CoTsPc	Pyrolytic graphite	~0.2 (acid); ~0.1 (alkaline)	–	2	0.05 M H ₂ SO ₄ ; 0.1 M NaOH	[48]
CoTsPc	PVP modified pyrolytic graphite	~0.4	~0.16	2	0.05 M H ₂ SO ₄	[84]
CoTAA	Pyrolytic graphite	~0.87 (pH 14)	~0.82 (pH 14)	–	pH 0–14	[62]
		~0.72 (pH 0)	~0.56 (pH 0)	–		
CoTrNPc	Pyrolytic graphite	–	–	2	pH 1–13	[63]
CoTMP	Graphite	–	0.65/0.44 ^a	3.3/4.0 ^a	1 M HClO ₄	[82]
CoOEP	Graphite	–	0.69/0.39 ^a	2.8/2.8 ^a	1 M HClO ₄	[82]
CoPPIX	Graphite	–	0.69/0.44 ^a	2.6/2.6 ^a	1 M HClO ₄	[82]
CoTPP	Graphite	–	0.44	2.0	1 M HClO ₄	[82]
CoTPyP	Graphite	–	0.44	2.0	1 M HClO ₄	[82]
FePc	Pyrolytic graphite	~0.94 (pH 14)	~0.83 (pH 14)	–	pH 0–14	[62]
		~0.6 (pH 0)	~0.31 (pH 0)	–		
FePc	Vulcan XC72	~0.8	~0.75	3.9	0.5 M H ₂ SO ₄	[85]
FePc	Pyrolytic graphite	0.75	–	3 (20 °C)	0.1 M H ₂ SO ₄	[86]
FePcTA, poly-FePcTA	–	~0.1 (poly, pH 13)	–	2	pH 13, 5.85	[87]
FeTPPPP	Pyrolytic graphite	~0.53	–	4	0.5 M H ₂ SO ₄	[88]

(continued)

Table 1 (continued)

Complex	Electrode/Substrate	E_{onset} (V vs. RHE)	$E_{1/2}$ (V vs. RHE)	Electron transfer	Medium	References
$\text{FePc}(\text{SO}_3\text{H})_4$	Pyrolytic graphite	–	–	2 (20 °C)	0.1 M H_2SO_4	[86]
FePcCl_{16}	Pyrolytic graphite	–	–	2 (20 °C)	0.1 M H_2SO_4	[86]
$\text{FeNpPc}(\text{tBu})_4$	Pyrolytic graphite	–	–	3 (20 °C)	0.1 M H_2SO_4	[86]
MnPc	Glassy carbon	–	–	2.6	pH 5	[89]
MnTAPc	Glassy carbon	–	–	2.0	pH 5	[89]
MnTPePyPc	Glassy carbon	–	–	2.2	pH 5	[89]
MnTPPyPc	Glassy carbon	–	–	2.8	pH 5	[89]
MnTMPyrPc	Glassy carbon	–	–	2.1	pH 5	[89]
MnTETPc	Glassy carbon	–	–	1.8	pH 5	[89]
MnP	Graphite	–	0.62	–	0.1 M KOH	[90]
MnTPhP	Graphite	–	0.74	–	0.1 M KOH	[90]
MnTTP	Graphite	–	0.72	–	0.1 M KOH	[90]
MnTAPhP	Graphite	–	0.77	–	0.1 M KOH	[90]
MnTcPhP	Graphite	–	0.69	–	0.1 M KOH	[90]
Mn4HIPhTTP	Graphite	–	0.70	–	0.1 M KOH	[90]
MnTrT-AphP	Graphite	–	0.73	–	0.1 M KOH	[90]
MnTrT-CPhP	Graphite	–	0.70	–	0.1 M KOH	[90]
MnTrMPPhPyP	Graphite	–	0.76	–	0.1 M KOH	[90]
MnTrTPyP	Graphite	–	0.71	–	0.1 M KOH	[90]
MnTPyP	Graphite	–	0.78	–	0.1 M KOH	[90]
MnTPhP	Graphite	–	0.74	–	0.1 M KOH	[90]

E_{onset} is the onset potential for ORR. $E_{1/2}$ is the potential where the half-maximum current is reached. The approximate values of E_{onset} and $E_{1/2}$ are read from the polarization curves in corresponding literature. The standard electrode potential of SCE is set as 0.241 V if the SCE is used as reference

^aDouble current limit plateaus appear on the polarization curve

2.1 Effect of Central Transition Metal Atom

The type of the central metal atom is a dominant factor influencing the catalytic activity of the M-N₄ macrocyclic complexes for ORR. At early time, it had been known that the ORR activity in acid electrolyte would decrease in the order of Fe > Co > Ni > Cu > Mn for the MPc, while in the order of Co > Mn > Fe > Ni > Cu for the MTAA macrocycle complexes [27, 47]. Figure 2 shows an example electrochemical measurement result systematically examining the ORR activity on various metal tetra-sulfonated-phthalocyanines (MTsPc) in alkaline electrolytes. It can be observed in Fig. 2 that the ORR activity decreases in the order of Fe > Mn > Co > Cr > Ni ≈ Zn > Cu for the MTsPc macrocycles. Importantly, the results in Fig. 2b revealed a correlation between the observed ORR activity and the number of the *d* electrons in the central transition metal of the M-N₄ macrocycles. It appears that the MTsPc macrocycles could possess superior ORR catalytic activity when their central transition metal atoms, such as Fe, Mn, and Co, have nearly half-filled *d* orbitals. Such a correlation had also been confirmed for the ORR on the MPc macrocycles in alkaline medium, namely the ORR activity of the MPc were found to decrease following the sequence of Fe > Co > Mn, Pd, Pt > Zn [79]. It notes that Mn-N₄ macrocycle complexes exhibit low stability in both acid

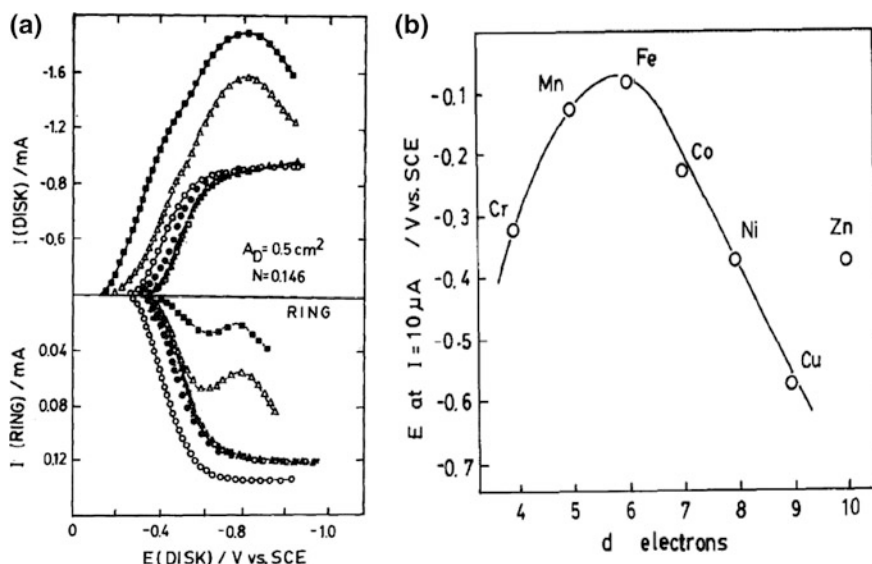


Fig. 2 a Rotating ring-disk polarization curves for O₂ reduction in 0.1 M NaOH on different transition metal phthalocyanines adsorbed on the ordinary pyrolytic graphite disk ($f = 1000$ rpm; $v = 2$ mV/s; $A_D = 0.5$ cm²; $N = 0.146$) ■ FeTsPc; MnTsPc; ○ CoTsPc; ● CrTsPc; Δ NiTsPc; □ ZnTsPc; x VOTsPc; and b Electrocatalytic activity of MeTsPc for O₂ reduction in 0.1 M NaOH as a function of the number of *d* electrons. Adapted with permission from [91]. Copyright 1992 Elsevier

and alkaline electrolytes [92]. Consequently, most of the current literature focuses on studying the ORRs on the Fe- and/or Co- N_4 macrocyclic complexes [46, 91, 92].

More importantly, extensive studies have shown that the central transition metals would dictate the oxygen reduction pathways on these M- N_4 macrocyclic complexes. It has been found that most Co- N_4 macrocyclic complexes promote only $2e^-$ reduction of oxygen to produce hydrogen peroxide as final products [18, 50, 81, 92, 93]. In contrast, Fe- N_4 macrocyclic complexes are found to likely promote $4e^-$ reduction of oxygen to produce water with cleavage of O-O bond [18, 50, 81, 92, 93].

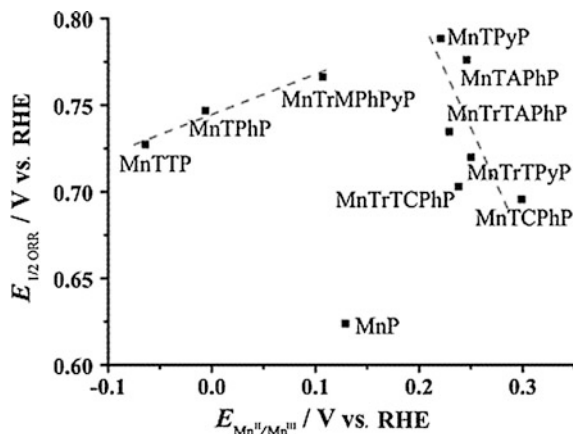
2.2 Effect of Chelates and Peripheral Substitutes

In addition to M- N_4 chelates, some other metal chelates, including M- N_2O_2 , M- N_2S_2 , M- O_4 , and M- S_4 , have demonstrated the catalytic activities for ORRs [27]. Previous studies showed that ORR activity varied in a decreasing order of $N_4 > N_2O_2 > N_2S_2 > O_4 \approx S_4$ in the Fe-macrocyclic complexes, whereas in the decreasing order of $N_2O_2 > N_4 > N_2S_2 > O_4 \approx S_4$ in the Co-macrocyclic complexes [27]. In most cases, M- N_4 chelates exhibit higher catalytic activity and relatively better stability than other chelates [92]. Hence, M- N_4 macrocycles have been extensively investigated. In particular, it is of interest to study how their ORR activity could be tuned by replacing the peripheral functional groups on the organic skeleton of M- N_4 chelates, i.e., porphyrins and phthalocyanines [82, 86, 89–91]. For example, Zhang et al. reported that the substituted FePcs (i.e., FePcCl₁₆, FePc(SO₃H)₄ and FeNpPc(tBu)₄) could exhibit considerably lower diffusion-limited current density in acid electrolyte than the FePc [86]. Further kinetic Koutecky–Levich analysis showed that, as compared to that on FePc, the ORR on these substituted FePcs would proceed with lower number of the overall electron transfer, indicating lower ORR catalytic efficiency on these substituted FePcs [86]. Sehlotho et al. measured the overpotentials for ORR on the MnPc and its five derivatives in alkaline or weak acid (pH = 5) medium and found that the ORR catalytic activity decreased in the order of MnPc \approx MnTPePyPc \approx MnTMPyrPc $>$ MnTAPc $>$ MnTETPc $>$ MnTPPyPc [89]. In Fig. 3, we show the result of the measured half-wave potentials of the Mn macrocyclic complexes with different peripheral substitutes. It could be observed that peripheral substitutes indeed could tune the half-wave potentials of ORR on the M- N_4 macrocyclic complexes to a modest extent.

2.3 Effect of Polymerization

It has been reported that polymerization of M- N_4 macrocyclic complexes could enhance the catalytic activity for ORR [87, 92, 94]. It is believed that the

Fig. 3 Plot of ORR activity measured as the potential at half-maximum oxygen reduction current against the formal potential for the Mn^{II}/Mn^{III} transition. Adapted with permission from [90]. Copyright 2013 John Wiley and Sons



polymerization of M-N₄ macrocycles could improve the electronic conductivity and hence enhance the electrocatalytic activity of the catalysts [94]. In this regard, Ramírez et al. compared the ORR catalytic activity of the monomeric and polymeric FePcTA in electrolyte with different pH values [87]. The result showed that the poly-FePcTA was more active and stable than the monomer one [87].

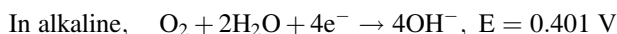
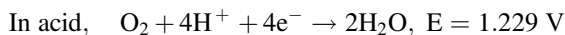
2.4 Effect of Substrate Materials and Electrode Preparation

High specific area carbon is usually used as support materials for M-N₄ macrocyclic complexes due to its large surface area, high conductivity, and beneficial surface groups [81, 94]. Pretreatment on the carbon support materials affects the catalytic activity of the M-N₄ macrocycles on the supports. It was found that the carbon substrates covered with basic surface groups helped the M-N₄ macrocycles to have better ORR catalytic performance than the substrates covered with neutral or acidic surface groups [92].

Elzing et al. studied the influence of electrode preparation on the ORR electrocatalysis on CoPc [95]. They prepared the electrodes using five different methods, including (a) irreversible adsorption, adsorbing a monolayer of complexes; (b) vacuum deposition, yielding a large amount of complexes loading; (c) incorporation in polypyrrole, catalysts thickness under control; (d) impregnation of porous carbon, using carbon as substrate; and (e) evaporation of the solvent, catalysts thickness under control [95]. Their results indicated that the different electrode preparation methods could lead to different number of active sites, as a result of varying catalyst loading and surface area, and thus appreciably affect the ORR activity on the M-N₄ macrocycles [95].

2.5 Effect of pH Value of Electrolyte

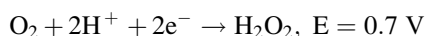
The ORR has different reaction pathways in acid and alkaline electrolytes as follows.



The M-N₄ macrocyclic complexes are usually more efficient and stable ORR catalysts in alkaline electrolyte than in acid media. Hence, the pH value of the electrolyte is also an important factor affecting the ORR activity on M-N₄ macrocycles [51, 62, 63, 96–98]. It is known that the ORR activity is strongly correlated with the redox potential of central transition metal atom, which varies with the pH value of the electrolytes [62]. For example, as shown in Fig. 4, both the redox potential of CoTAA and the half-wave potential for the ORR on CoTAA were found to decrease at a rate of 60 mV per pH value of the electrolyte from pH 14 to pH 10 whereas to remain unchanged with pH value below 10 [62]. Similar trend could also be observed for the ORR on CoPc in Fig. 4 [62].

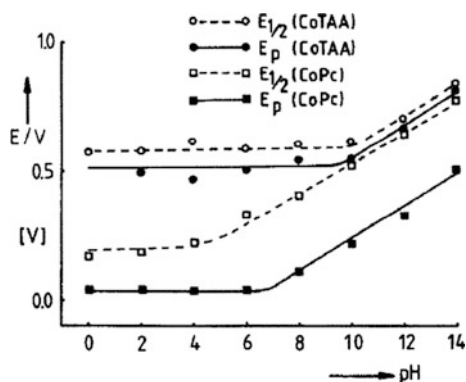
2.6 Mechanism of ORR on M-N₄ Macrocyclic Complexes

On M-N₄ macrocyclic complexes, oxygen could be completely reduced to water through a 4-electron pathway or be incompletely reduced through a 2-electron pathway, producing hydrogen peroxide.



Since the 2-electron pathway has a much lower efficient for energy generation, the M-N₄ complex catalysts which promote the complete reduction of oxygen

Fig. 4 pH dependence of the redox potentials E_p of CoPc and CoTAA, and $E_{1/2}$ of the O₂ reduction to H₂O₂. Adapted with permission from [62]. Copyright 1987 Elsevier



(4-electron pathway) are normally preferred. Most studies indicate that Fe-N₄ macrocyclic complexes could promote the reduction of oxygen to water whereas Co-N₄ macrocyclic complexes could catalyze only hydrogen peroxide pathway for ORR [18, 51, 81, 99, 100]. In 2009, Chen et al. conducted a detailed study on the mechanism pathway of the ORR on CoPc and FePc in alkaline electrolyte through Koutecky–Levich approach and rotating ring-disk electrode (RRDE) method [99]. A nearly 4-electron reduction of oxygen on FePc and around 2-electron reduction of oxygen on CoPc have been revealed from the Koutecky–Levich plot [99].

However, the reaction mechanism of the ORR on the M-N₄ macrocycle catalysts is still not fully understood. Several ORR mechanisms have been proposed so far [50, 100–104]. The main distinction between the 4-electron pathway and 2-electron pathway of ORR is whether the O–O bond in the O₂ molecule can be broken during the reaction. A successful scission of the O–O bond would lead to the reduction of oxygen to water on the surface of catalysts. It has been proposed as shown in Fig. 5 that, for the M-N₄ macrocycles such as dimeric metalloporphyrin molecules which have a face-to-face structure [49, 53, 100, 103, 105, 106], the O₂ molecule could be adsorbed on an active site bridging between two transition metal centers. As proposed by Yeager et al., the formation of the M–O–O–M configuration could facilitate the cleavage of the O–O bond [103]. Liu et al. further elaborated that the *cis* configuration rather than the *trans* configuration of the O₂ adsorption on such a

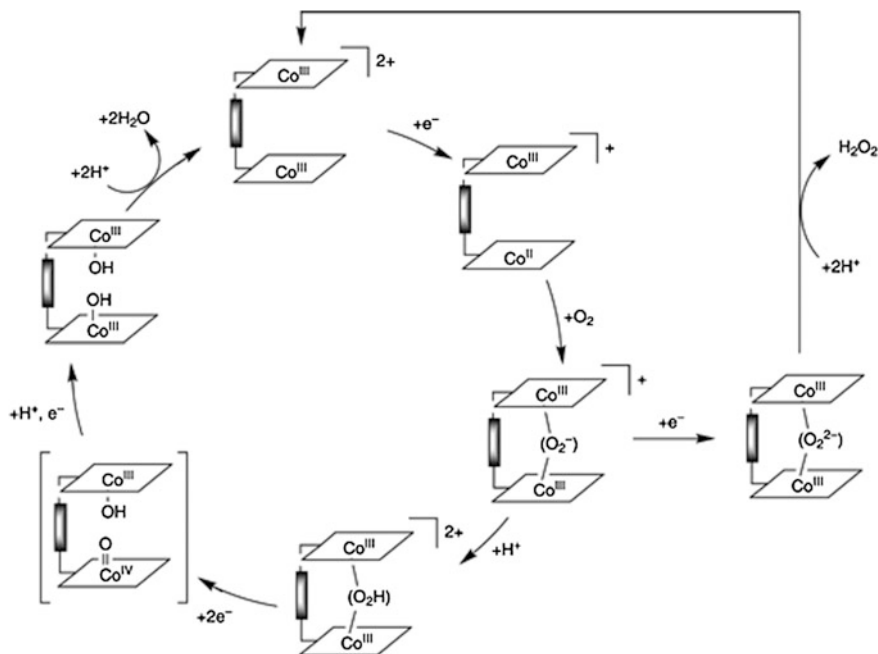


Fig. 5 Proposed ORR mechanism on a dicobalt cofacial diporphyrin. Adapted with permission from [106]. Copyright 2004 American Chemical Society

bridging sites would favor the rupture of the O–O bond and promote the 4-electron pathway of ORR [53]. A more recent study by Tsuda showed that the heme interacts with O₂ adopting the side-on configuration could lower the activation energy for the O–O bond breaking, compared with the end-on configuration [107].

3 ORRs on Carbon-Supported Heat-Treated M-N₄ Macrocyclic Molecules

Jahnke et al. reported that heat treatment processing could not only improve the catalytic activity of CoTAA for ORR but also enhance the stability of the catalysts in an electrochemical environment [27]. Ever since, the heat treatment of M-N₄ macrocyclic complexes on carbon support in inert gas has been employed as an effective method to promote the ORR catalytic activity of the M-N₄ macrocycles

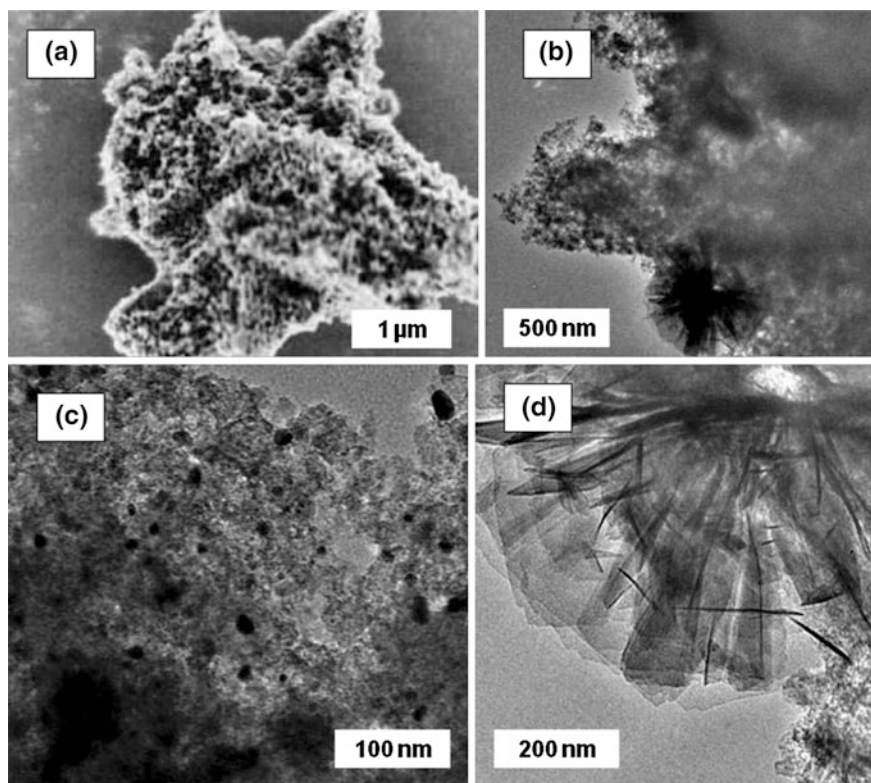


Fig. 6 a Scanning electron microscopy (SEM) image of pyrolyzed H₂TMPP materials and b–d Tunneling electron microscopy (TEM) images of pyrolyzed CoTMPP materials. Adapted with permission from [124]. Copyright 2009 The Electrochemical Society

[28, 66–75, 77, 78, 94, 103, 108–123]. Figure 6 shows the typical morphology of the attained carbon-supported heat-treated (pyrolyzed) M-N₄ macrocylic molecules. We summarize processing procedures and parameters on the synthesis of heat-treated (pyrolyzed) M-N₄ macrocylic complexes as ORR electrocatalysts in Table 2. It has been recognized that the heat treatment temperature, atmosphere, and duration are important parameters determining the final catalytic activity of the attained pyrolyzed M-N₄ macrocylic complexes.

3.1 Effect of Heat Treatment Temperature and Duration

Survey on the current literature (Table 2) indicates that the heat treatment processing employed in the synthesis of pyrolyzed M-N₄ macrocylic complexes typically uses annealing temperature ranging from 300 to 1100 °C and heat treatment duration ranging from 1 to 2 h. It has been reported that the catalytic activity of the attained pyrolyzed M-N₄ macrocylic complexes would increase with an increase in annealing temperature and reach an optimal value at annealing temperature of 700–800 °C. The ORR activity of the pyrolyzed M-N₄ macrocylic complexes heat-treated above 800 °C was found to have low values. On the other hand, the long-term stability of the pyrolyzed M-N₄ macrocylic complexes under the electrochemical conditions was found to be acquired only through heat treating at relatively high temperature (≥ 900 °C) [66, 112]. Moreover, our survey suggests that the duration of heat treatment processing has little effect on the catalytic activity of the pyrolyzed M-N₄ macrocylic complexes.

3.2 Effect of Pyrolysis Gas Atmosphere

The N₂, Ar and NH₃ gases are usually used as pyrolysis gas atmosphere. The N₂ and Ar are inert gases which can prevent the M-N₄ catalysts from oxidation. The NH₃ gas may not only protect the M-N₄ catalysts from oxidation, but also be used as nitrogen resources which could increase the nitrogen content in the final heat-treated catalysts. Dodelet et al. compared the ORR activity on the pyrolyzed FeTMPPCl (mixed with non-microporous carbon black) heat-treated in either Ar/H₂ or NH₃ gas atmosphere at 950 °C for 100 min [119]. They found that the pyrolyzed catalysts attained in NH₃ gas atmosphere was more active for ORR but less stable than the pyrolyzed catalysts heat-treated in Ar gas atmosphere [119]. Further characterization showed that the catalysts pyrolyzed in NH₃ gas a higher surface nitrogen concentration as well as more than a hundred times of micropore specific area than the catalyst pyrolyzed in Ar gas [119]. Hence, it was inferred that the NH₃ gas might be helpful in etching the carbon surface to produce large surface area.

Table 2 Summary of processing procedures on the synthesis of heat-treated (pyrolyzed) M-N₄ macrocyclic complexes as ORR electrocatalysts

Complex	Substrate	Temperature range (°C)	Duration	Atmosphere	Optimum temperature (°C)	Medium	References
CoPc, CoTBP, CoTMPhP, CoTPhP	AG-3 Active carbon	400–1000	20–30 min	Inert gas	800–900	2.25 M H ₂ SO ₄	[67]
MePc (Me = Fe, Co, Zn, Mn, Ru, Pt)	Norit BRX Active carbon	300–800	1 h	N ₂ , Ar	700	4 M H ₂ SO ₄	[79]
MePc, MeTPP, MeOEP (Me = Fe, Co, Rh, Ru, Os, Ir)	Norit BRX Active carbon HSA graphite, PVDC carbon	–	20 min–4 h	Inert gas	600–800	Acid	[108]
CoTMPP	XC-72 carbon	450–900	2 h	N ₂	850	4 M NaOH	[74]
FeTAA, CoTAA	P33 Active carbon	150–1100	Short term	Ar	600–700	2.25 M H ₂ SO ₄	[71]
FeTPPCL	–	450–850	10–260 min	N ₂ , Ar	470	2.3 M H ₂ SO ₄	[68]
CoTPP, FeTPPCL	Carbon black (acetylene)	470–900	30 min	N ₂ , Ar	500–600	2.3 M H ₂ SO ₄	[69]
CoPc	Vulcan XC-72 carbon black	300–1150	2 h	Ar	700–950	H ₂ SO ₄ (pH 0.5)	[111]

(continued)

Table 2 (continued)

Complex	Substrate	Temperature range (°C)	Duration	Atmosphere	Optimum temperature (°C)	Medium	References
TpOCH ₃ PPCo, TpCF ₃ PPCo, CoTAA	Printex XE2 carbon black	500–800	2 h	N ₂ , Ar	800	PEMFC	[72]
	Norit SX ultra active charcoal						
FeTPP, CoTPP	Vulcan XC-72R carbon black	100–1100	–	Ar	500–700 (high a, unstable); ≥ 900 (active and stable)	H ₂ SO ₄ (pH 0.5), PEMFC	[112]
FePc, FePcTc	Vulcan XC-72R carbon black	100–1100	2 h	Ar	Unpyrolyzed (high a, unstable); ≥ 900 (active and stable)	H ₂ SO ₄ (pH 0.5), PEMFC	[66]
FeTMPP-Cl	Black Pearl 2000 carbon black	800	2 h	Ar	–	1 M H ₃ PO ₄	[113]
FeTPP	Vulcan XC-72R carbon black	1000	2 h	Ar	–	H ₂ SO ₄ (pH 0.5)	[114]
FeTMPP-Cl	Black Pearl 2000 carbon black	200–1000	2 h	Ar	–	1 M or 0.1 M NaOH, 0.1 M H ₂ SO ₄ , 0.1 M H ₃ PO ₄ , 0.1 M HClO ₄	[75]

(continued)

Table 2 (continued)

Complex	Substrate	Temperature range (°C)	Duration	Atmosphere	Optimum temperature (°C)	Medium	References
CoTCPP, CoTMPyP	Graphite powder	200–1000	–	Ar	800	0.05 M H ₂ SO ₄	[115]
FeTMPP-Cl	Un-deashed RB carbon	800	2 h	Ar	–	PEMFC	[76]
FeTPP-Cl, CoTPP, CoTSPc, RuTPP-CO	Vulcan XC-72R carbon black	700	2 h	Ar	–	0.5 M H ₂ SO ₄	[116]
FeTMPP-Cl	Black Pearl 2000 carbon black	200–1000	2 h	Ar	700–1000	0.1 M NaOH, 0.1 M H ₂ SO ₄ , 0.1 M H ₃ PO ₄ , 0.1 M HClO ₄	[77]
CoTAA	Norit SX Ultra active charcoal	500–900	2 h	Ar	800	0.25 M H ₂ SO ₄	[73]
FePc, CoPc, FeCy, CoCy	Vulcan XC-72 carbon black	–	2 h	Ar	600–800	1 M H ₂ SO ₄	[117]
MeTPP (Me = Fe, Co, Cu, Mn, V, Ni, Zn)	–	600	–	Ar	–	0.5 M H ₂ SO ₄	[28]
FeTMPP-Cl	Black Pearl carbon black	900	1 h	Ar	–	0.5 M H ₂ SO ₄	[125]
CoTPP, FeTPP, Co/FeTPP	amorphous fumed silica	500–800	–	N ₂	600	0.5 M H ₂ SO ₄ , PEMFC	[118]

(continued)

Table 2 (continued)

Complex	Substrate	Temperature range (°C)	Duration	Atmosphere	Optimum temperature (°C)	Medium	References
FeTMPP-Cl	N330 carbon black	950	100 min	Ar/H ₂ , NH ₃	–	H ₂ SO ₄ (pH 1), PEMFC	[119]
CoTMPP	FeC ₂ O ₄	450 (2 h), then 850 (1 h)	–	Ar	–	0.5 M H ₂ SO ₄	[120]
CoTPTZ	Black Pearl 2000 carbon black	600–900	2 h	N ₂	700	0.5 M H ₂ SO ₄	[122]

3.3 *Effect of Additives*

It was also found that adding additives into the catalysts during heat treatment processing could enhance the ORR catalytic activity of the pyrolyzed M-N₄ macrocyclic complexes. For example, Herrmann et al. added metal oxalate (FeC₂O₄ or SnC₂O₄), as a structure forming agent, to CoTMPP catalysts during heat treatment, and observed an enhanced ORR current densities as compared to the pyrolyzed CoTMPP [120]. The enhanced ORR activity on the heat-treated metal oxalate-CoTMPP catalysts was attributed to the formation of high-area meso-porous structure from etching out metal oxalate by acid after heat treatment [120]. In another study, Herrmann et al. further doping sulfur to the mixture of FeC₂O₄-CoTMPP during the heat treatment and found that additive sulfur had a beneficial effect for ORR on the acquired pyrolyzed catalysts with increased catalytic activity and lowered H₂O₂ production [121].

3.4 *Proposed Mechanisms for Heat Treatment*

The mechanisms of heat treatment underlying the enhanced ORR activity of the pyrolyzed M-N₄ macrocyclic complexes have not been fully understood yet. Complicated physical and chemical processes could take place in the catalysts during the heat treatment processing. Some of such processes have been identified as (1) chelates migration over the carbon support surface; (2) reaction of the peripheral organic skeleton of the macrocyclic complexes with the carbon support with the M-N₄ center remaining intact; (3) decomposition of the complexes producing single metal or metal oxide [109]. Correspondingly, several assumed enhancement mechanisms of heat treatment have been proposed and are stated as follows: (1) Chelate dispersion improvement. For example, porphyrins and phthalocyanines as large molecules could possibly block micropores of the carbon support. During heat treatment, the excessive chelates could be removed, making those micropores accessible [110]. (2) Formation of highly active carbon [94] which is a catalyst without the metal involved. However, this assumption proves to be highly implausible based on experiment observations [110]. (3) M-N_x cluster, rather than M-N₄, serves as active site for ORR [126]. According to van Veen et al., this is still an untenable explanation since extended X-ray absorption fine structure (EXAFS) study showed a strong correlation between the ORR activity and the M-N₄ moiety [110]. (4) Modification of the electronic structure of the M-N₄ center by reaction between the peripheral ligands and carbon substrates [108]. This explanation has been regarded as the most tenable mechanism of the beneficial effect of heat treatment [110]. However, how such modification happens need further study.

4 ORRs on M-N₄ Macrocyclic Modified Carbon Nanostructures (Nanotubes and Graphene)

Carbon nanostructures, i.e., carbon nanotube (CNT) and graphene, draw a lot of attention due to outstanding mechanical, electrical, and thermal properties. They have been investigated for potential applications in structural, electrical and many other areas since they were discovered. In recent years, M-N₄ macrocycle modified CNT [127–144] (Fig. 7) and M-N₄ Macrocycle modified graphene [140, 143, 145–152] have been synthesized and evaluated for ORR electrocatalysis.

4.1 M-N₄ Macrocycle Modified CNT

Several methods have been developed for synthesizing the M-N₄ macrocycle modified CNTs. The method most widely employed is the impregnation method [129, 134–142, 144], in which the Me-N₄ macrocyclic complexes are first impregnated into CNTs in a solution and subsequently the M-N₄ macrocycle modified CNT composites are obtained by evaporation of solvent. In some studies, the acquired composites are further heat-treated in inert gas atmosphere [138, 141, 144]. The other synthesis methods to produce the M-N₄ macrocycle modified CNTs include electrochemical deposition [128, 133] direct deposition [131, 132] and chemical vapor deposition [130].

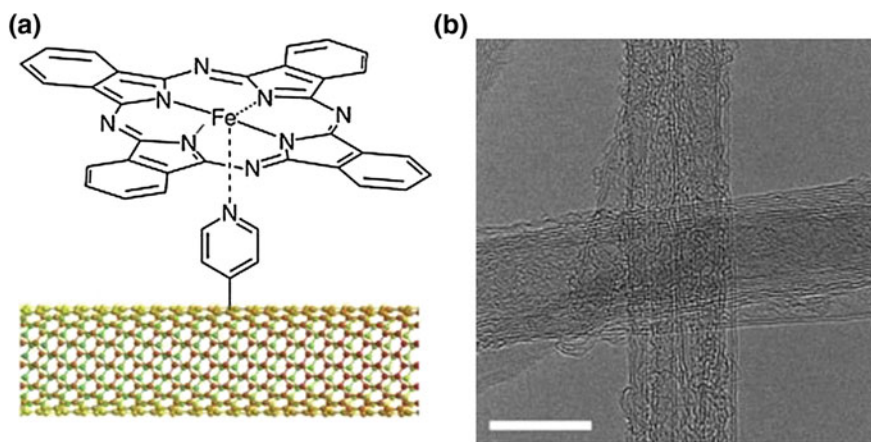


Fig. 7 **a** Schematic diagram of the structure of FePc-Py-CNTs composite; **b** HR-TEM image of FePc-Py-CNTs composite; scale bar, 10 nm. Adapted with permission from [127]. Copyright 2013 Nature Publishing Group

It has been shown that using CNTs as the substrate of M-N₄ macrocycle catalysts could improve the activity and stability for ORR in alkaline/neutral medium [128, 131, 132, 135, 136]. However, CNTs supported M-N₄ macrocycle composites are unstable in acid medium [134]. It was reported that FePc modified CNTs exhibit higher activity than CoPc complexes modified CNTs [134]. Moreover, the FePc modified CNTs can promote 4e⁻ pathway [127, 131, 134–137] in alkaline medium. In contrast, the CoPc modified CNTs can only partially promote 4e⁻ pathway with a portion of H₂O₂ production [134, 139].

The influence of different types of the CNTs, i.e., single-wall nanotubes (SWCNT), double-wall nanotubes (DWCNT) and multiwall nanotubes (MWCNT) on the ORR catalytic activity of the M-N₄ macrocycle modified CNT composites has been studied by Morozan et al. [134]. Their results show that the oxidized MWCNT supported MPc catalysts exhibit higher current density, lower onset potential and more electron transfer for ORR in alkaline and acid medium than the catalysts prepared with other types of CNTs [134].

The catalytic activity and stability of the M-N₄ macrocycle modified CNTs, especially in acid electrolyte, can also be enhanced by heat treatment processing [138, 141, 145]. Most heat treatment studies reported a continuous enhancement effect on the catalytic performance of the M-N₄ macrocycle modified CNTs with the increase of annealing temperature up to 800 °C [138, 141, 144]. Kruusenberg et al. compared heat treatment effects on CoPc, FePc, CoP, and FeP modified multi-walled carbon nanotubes [141]. It was shown that the MP modified CNTs heat-treated at 800 °C exhibited higher ORR activity than the MPc modified CNTs [141].

4.2 *M-N₄ Macrocycle Modified Graphene*

The M-N₄ macrocycle modified graphene composites are mainly prepared through solvothermal synthesis method [140, 145, 146, 149–152] in which the M-N₄ macrocyclic complexes are dispersed on graphene by thermal evaporation of solvent in the solution of macrocycle and graphene mixture (Fig. 8). The SEM and TEM images of the FeTsPc dispersed on graphene nanosheets are shown in Fig. 9. The synthesized FePc or CoPc modified graphene composites exhibit promising improvement of the catalytic activity for ORR in alkaline and acid medium [145, 147, 152]. It is worth noting that the 4e⁻ pathway has been demonstrated feasible on the CoPc modified graphene [145, 151, 152], which is unachievable if other carbon materials (carbon black, CNTs) are used as substrates.

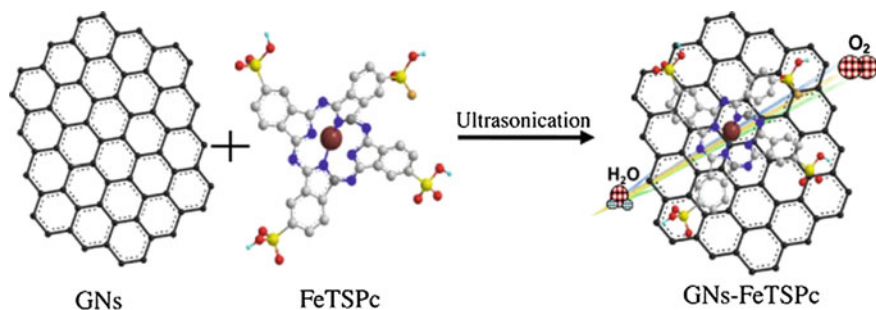


Fig. 8 Schematic diagram of noncovalently functionalized GNs with FeTsPc via a π - π stacking interaction. Adapted with permission from [150]. Copyright 2014 Elsevier

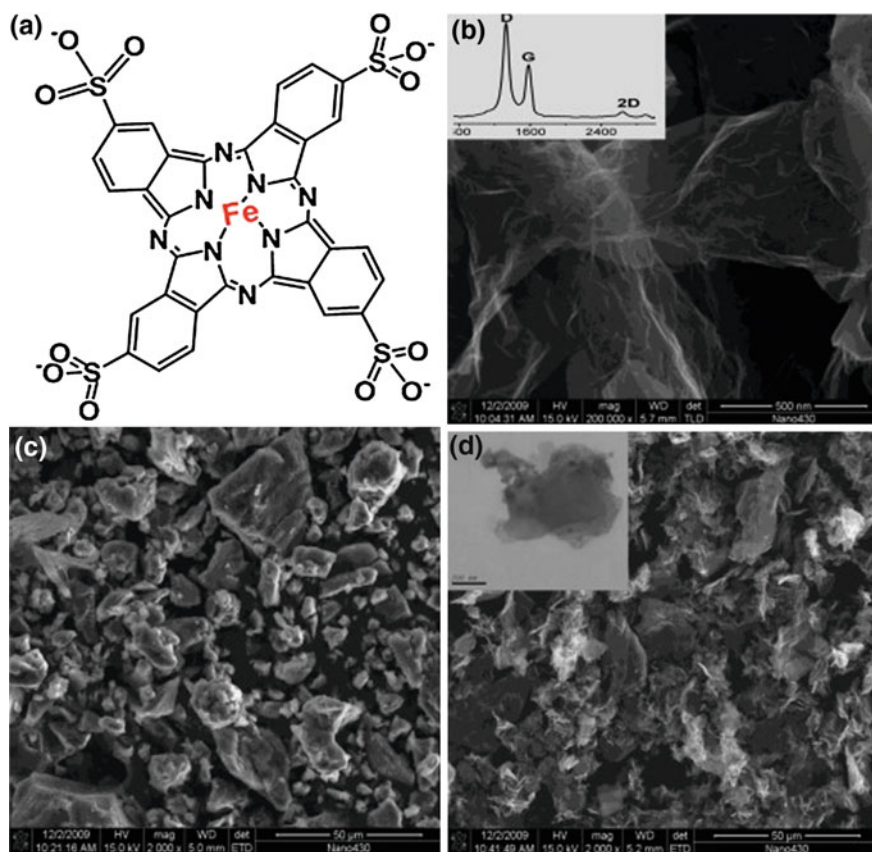


Fig. 9 a Structure of FeTsPc; b SEM image of graphene nanosheets (GNs), *inset* Raman spectra of GNs; c FeTsPc; d GNs-FeTsPc, *inset* TEM image of GNs-FeTsPc. Adapted with permission from [150]. Copyright 2014 Elsevier

5 Application of DFT to Understand ORRs on M-N₄ Macrocycles

Density functional theory (DFT) calculation method is a powerful tool for directly calculating the energy and electronic structure of catalysts from the principles of quantum mechanics. Utilizing electron density of ground state as the variable which uniquely defines the energy of the system, Kohn, Hohenberg, and Sham [153, 154] proved that the ground state of a many electron system can be determined by self-consistently solving the Kohn–Sham (KS) equations, i.e., [155]

$$\left\{ -\frac{\hbar^2}{2m} \nabla^2 + V_{\text{ext}}(\vec{r}) + \int \frac{n(\vec{r}')}{|\vec{r} - \vec{r}'|} d\vec{r}' + V_{xc}[n(\vec{r})] \right\} \psi_i(\vec{r}) = \varepsilon_i \psi_i(\vec{r})$$

and

$$n(\vec{r}) = \sum_i |\psi_i(\vec{r})|^2$$

The KS equations reduce the problem of solving an N-electron Schrodinger equation into the problem of solving a single electron Schrodinger equation and thus make the calculation of the ground state properties of catalyst practical. With the rapid development of digital computers in the last two decades, the DFT calculation method becomes one of the most popular simulation methods in condensed matter physics, chemistry and materials sciences owing to its relatively low computational costs and reasonable accuracy. Moreover, the quantum mechanical origin of the DFT makes it a useful predictive tool in investigating the mechanism of catalytic reactions on the surface of catalysts. The example applications of the DFT method to catalyst study include atom segregations [156, 157], atom/molecule adsorptions [158, 159] and diffusions [160, 161] and chemical reactions [162–164] on catalyst surfaces. These studies improved our understanding in catalysts and provided us an opportunity to rational design catalysts from fundamental principles [165–167].

5.1 DFT Study of O₂ Adsorption on M-N₄ Macrocyclic Complexes

The ORR on M-N₄ macrocyclic complexes always starts with the O₂ adsorption on the central metal atom and then the electron transfer between the central metal atom and the adsorbed O₂ molecule [93]. Consequently, the configuration and the resulting electronic structure of the O₂ adsorption on M-N₄ macrocyclic complexes

are crucial for us to understand their catalytic mechanism. The DFT calculation methods have been used to find the most stable adsorption configurations of O₂ on M-N₄ macrocyclic complexes [93, 99, 168, 169].

Two fashions of stable O₂ adsorption on M-N₄ macrocyclic complexes (as shown in Fig. 10) have been predicted from DFT calculations. Figure 10a, b show the end-on adsorption configurations in which one oxygen atom in the O₂ molecule is adsorbed on the top of central metal atom while the other one tilted away. Figure 12c, d show the side-on adsorption configurations in which the axis of the O₂ molecule is parallel to the molecule plane of the M-N₄ macrocyclic complexes and the distances between the central metal atom and the two oxygen atoms in the O₂ molecule are equal.

Analysis of the molecular orbitals obtained by the DFT calculations reveals that these two types of O₂ adsorption correspond to different bonding formed between the adsorbed O₂ molecule and the central metal atom of the M-N₄ macrocyclic complexes.

In the end-on configurations, the axis of the O₂ molecule is neither perpendicular nor parallel to the plane of the M-N₄ macrocyclic molecule. In this configuration, one of the π^* orbital of the O₂ molecule lies in a vertical plane perpendicular to the M-N₄ molecule plane. This π^* orbital can overlap with the a_{1g} (d_{z^2}) orbital of the transition metal and form a σ -type bond. The other π^* orbital can form a π -type bond by overlapping with a, e_g (d_{xz} or d_{yz}) orbital of the transition metal [168].

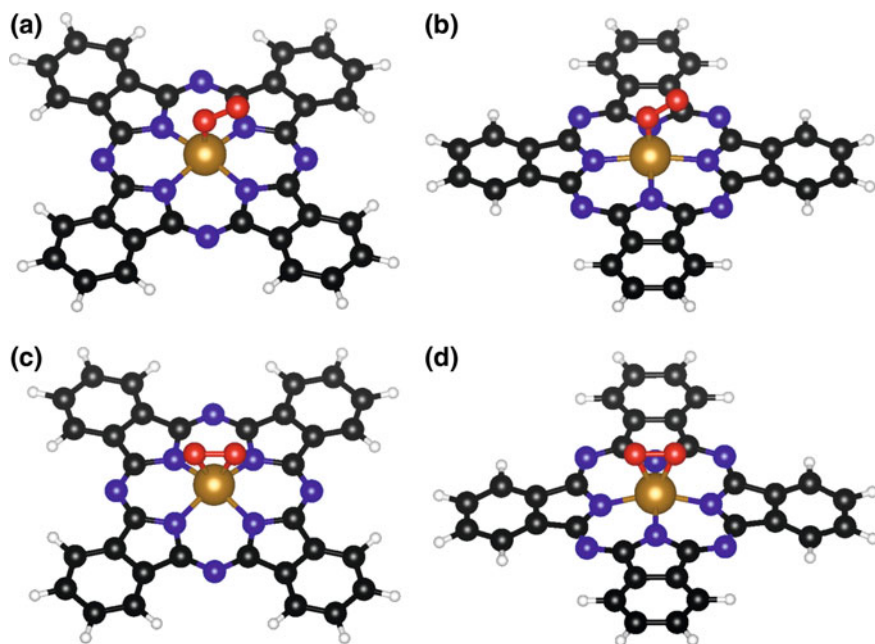


Fig. 10 Four possible configurations of O₂ adsorption on M-N₄ macrocyclic complexes. **a** and **b** are end-on configurations, **c** and **d** are side-on configurations

Table 3 The most stable adsorption configuration, spin multiplicity and the calculated adsorption energy (ΔE_{ad}), distance ($D_{\text{TM}-\text{O}_1}$) between the central metal atom and the nearest neighboring O atom (O_1), length ($D_{\text{O}_1-\text{O}_2}$) of the O–O bond, and angle formed by the central metal atom with the two oxygen atoms of O_2 adsorption on MnPc, FePc and CoPc [169]

	MnPc	FePc	CoPc
Configurations	Figure 10d	Figure 10a	Figure 10b
Multiplicity	Quartet	Singlet	Doublet
ΔE_{ad} (eV)	−0.837	−0.818	−0.496
$D_{\text{TM}-\text{O}_1}$ (Å)	1.883	1.758	1.912
$D_{\text{O}_1-\text{O}_2}$ (Å)	1.361	1.279	1.268
$\angle \text{O}_2\text{O}_1\text{TM}$ (°)	68.81	120.13	117.11

In the side-on configurations, similar to that of the end-on adsorption configuration, a σ -type bond can be formed between the σ - π hybrid orbital of the O_2 molecule and the a_{1g} (d_{z^2}) orbital of the transition metal and a π -type bond can be formed by overlapping a π^* orbital of the O_2 with a, e_g (d_{xz} or d_{yz}) orbital of the transition metal. Moreover, the other π^* orbital can form a δ -type bond by overlapping with a b_{2g} (d_{xy}) orbital of the transition metal [169].

Furthermore, the DFT study revealed that the adsorption energy of O_2 molecule on M- N_4 macrocyclic complexes were related to the energy level of the nonbonded $3d$ -orbitals and their occupation numbers of the central metal atom. In Table 3, we listed the calculated adsorption energy and structural properties of O_2 adsorption on MnPc, FePc, and CoPc [169]. Liu et al. have established a linear correlation between the O_2 adsorption energy and the nonbonding d -orbital center of metalloporphyrins and phthalocyanines macrocyclic complexes [169]. It was found that for the M- N_4 macrocyclic complexes with central metal atom varying from Cr to Ni, the interaction between the M- N_4 macrocyclic complexes and the adsorbed O_2 molecule became weaker as the number of electrons on the d -orbitals of the metal atom increases.

5.2 DFT Study of ORR on M- N_4 Macrocyclic Complexes

The first-principles DFT calculations of ORR on various M- N_4 macrocyclic complexes have been carried out by several research groups [93, 168–173]. Through comparative study of O_2 dissociation on different metalloporphyrins (MnP, FeP, CoP, NiP), the trends of the activation barriers for the O_2 dissociation with respect to LUMO-HOMO characters of these metalloporphyrins have been discussed by Tsuda et al. [172]. FeP is demonstrated to be the best one due to the large d electrons contribution to the LUMO-HOMO level of the FeP and the stable Fe–O bond [172]. Shi and Zhang performed the DFT calculation on the O_2 adsorption on various iron and cobalt porphyrins and phthalocyanines [171]. The catalytic activities of the transition metal macrocyclic complexes were positively related with

the ionization potential and the O₂ binding ability [171]. The ORR pathways on FePc and CoPc were also investigated using DFT calculations [170]. The 4e⁻ pathway of ORR on FeP/FePc and the 2e⁻ pathway of ORR on CoP/CoPc were attributed to the higher, e_g , orbital of the FeP/FePc than the CoP/CoPc [170].

Systematic studies of ORR on various iron and cobalt porphyrins and phthalocyanines have also been conducted by Wang et al. [93, 168, 169]. They performed the DFT calculations to determine the adsorption configurations and energies of chemical species O₂, H₂O, OH, and H₂O₂ on the iron and cobalt porphyrins (FeP and CoP), iron and cobalt tetraphenylporphyrins (FeTPP and CoTPP), iron and cobalt phthalocyanines (FePc and CoPc), iron and cobalt fluorinated phthalocyanines (FePcF₁₆ and CoPcF₁₆), and iron and cobalt chlorinated phthalocyanines (FePcCl₁₆ and CoPcCl₁₆). Through such a systematic, comparative DFT study, Wang et al. gained much insight about how the molecular structures of the M-N₄ catalysts affect the catalytic behavior of these catalysts for promoting ORR.

Figure 11 shows the lowest-energy adsorption configurations of the chemical species relevant to the ORR on the FePc and CoPc molecules [93, 168]. In Table 4, the corresponding adsorption energies from the DFT calculations are listed [93, 168]. It is inferred from these DFT calculations that (1) The O–O bond in H₂O₂ molecule can be split on the Fe-N₄ catalyst as shown in Fig. 11d. The O–O bond

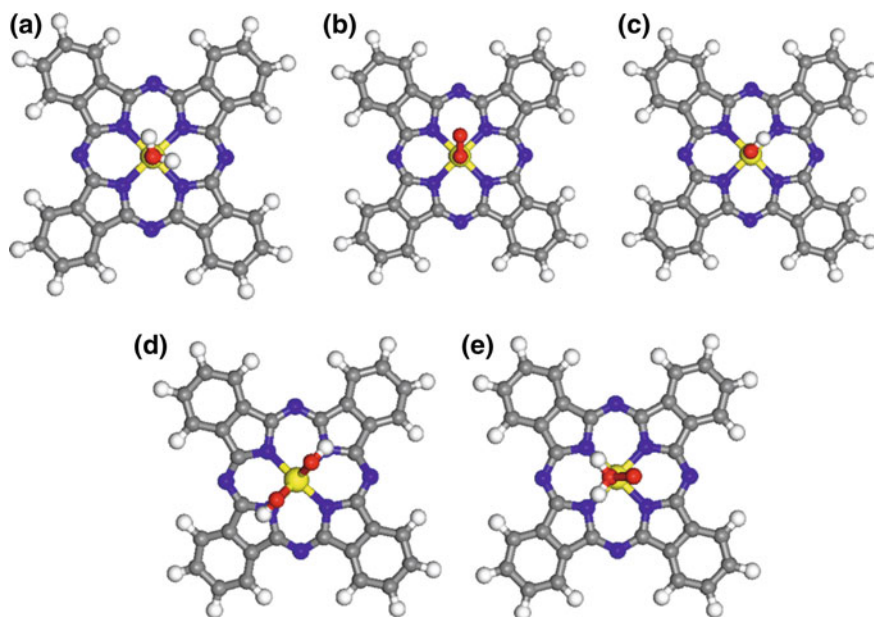


Fig. 11 Optimized adsorption configurations of **a** O₂, **b** H₂O, and **c** OH on FePc or CoPc, **d** H₂O₂ on FePc, and **e** H₂O₂ on CoPc. In the figure, the central yellow balls represent Fe or Co atoms, the blue balls represent N atoms, the gray balls represent C atoms, the white balls represent H atoms, and the red balls represent O atoms

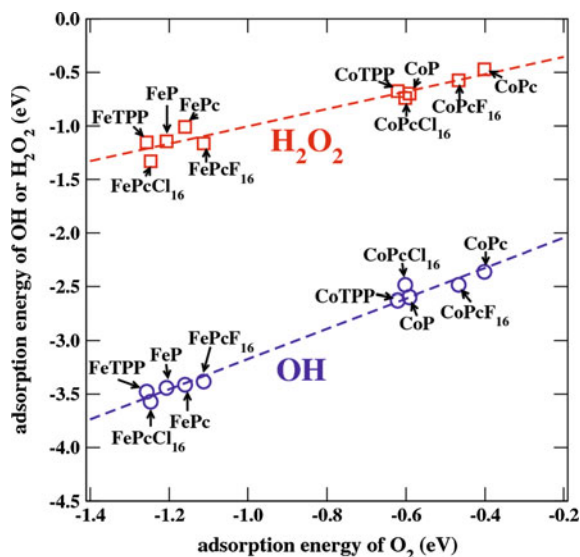
Table 4 Calculated adsorption energy (in eV) of O₂, H₂O, OH, and H₂O₂ on FePc, CoPc, and (111) surface of metal Pt using the DFT method

	O ₂	H ₂ O	OH	H ₂ O ₂
FePc	1.16	1.05	3.41	1.05
CoPc	0.40	0.32	2.36	0.47
Pt (111) surface	0.69	0.35	2.23	0.37

splitting process involves the central Fe atom attracting the two O atoms and the two adjacent N atoms attracting the two H atoms. Consequently, the N-Fe-N feature in the stable Fe-N₄ cluster is essential for the four-electron ORR on the FePc catalysts. (2) In contrast, the O–O bond in H₂O₂ molecule cannot be split on the Co-N₄ catalysts. This explains why only two-electron ORR was found to occur on the planar CoPc molecule catalysts [168]. (3) As compared to that on Pt (111) surface, O₂ molecule is found to adsorb more strongly on the FePc catalyst and more weakly on the CoPc catalyst. Since O₂ adsorption is the first elementary step of ORR on electrocatalysts, FePc could have even higher rate for ORR than pure Pt due to faster O₂ adsorption [168]. (4) However, FePc also binds OH molecule (one of the intermediate of ORR) more strongly than other catalysts (see Table 4). These OH (or radical O•) might oxidize the central Fe atom and cause the FePc lose its catalytic activity [168].

Furthermore, a linear relation between the adsorption energy of OH or H₂O₂ and the adsorption energy of O₂ on the ten studied macrocyclic M-N₄ complexes has been observed (Fig. 12) [168]. It is noticeable in Fig. 12 that the adsorptions of the involved species (O₂, OH, and H₂O₂) are always distinguishably stronger on the

Fig. 12 Correlation plot showing the variation of the calculated adsorption energy of OH (blue circles) and H₂O₂ (red squares) as a function of the calculated adsorption energy of O₂ on the iron and cobalt macrocyclic molecules. Adapted with permission from [168]. Copyright 2012 American Chemical Society



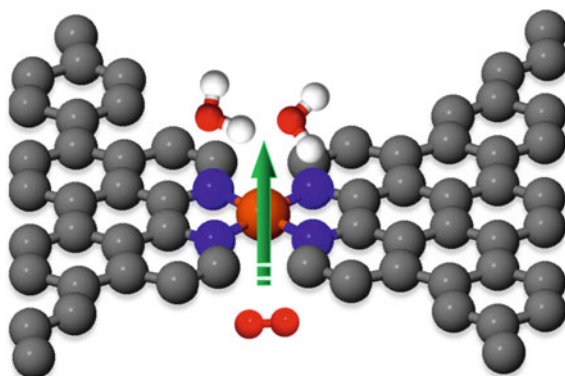
Fe-N₄ complexes than on the Co-N₄ complexes. An ideal catalyst for ORR should keep an optimal balance between retaining O₂ on its surface and removing OH from its surface [174–178]. Since the adsorption energies of O₂ and OH on these M-N₄ complexes have a linear relation, a volcano plot is expected when plotting the catalytic activity for ORR as a function of the calculated O₂ adsorption energy. Consequently, the results in Table 4 and Fig. 12 suggested that increasing the O₂ adsorption energy on Co-N₄ complexes or decreasing the OH adsorption energy on Fe-N₄ complexes could lead to a catalyst for ORR with a good combination of activity and durability.

5.3 DFT Study of ORR on M-N₄ Clusters Between Graphitic Pores

To understand the ORR activity on heat-treated M-N₄ macrocycles, the reaction pathway of ORR on the M-N₄ (M = Fe, Co, and Ni) macrocyclic complexes which are embedded between graphitic pores and bridge two edges of graphenes has been modeled using the first-principles DFT calculation method [51]. It was found that the assumed M-N₄-C structure (Fig. 13) was thermodynamically more stable as compared to isolated Fe ion, N₂ gas, and carbon graphite [178]. Furthermore, the binding energies of ORR intermediates O₂, O, OH, OOH, H₂O₂, and H₂O on these macrocyclic complexes have been calculated [178]. It was found that the involved ORR intermediates favor to bind with the central transition metal M atoms with the configurations shown in Fig. 14. In particular, it could be observed in Fig. 14c that the O–O bond will be split in the lowest-energy adsorption configuration of H₂O₂ on the Fe-N₄-C or Co-N₄-C clusters.

Based on calculated binding energies, it was proposed that the ORR on the Fe-N₄ and Co-N₄ macrocyclic complexes would adopt a pathway which follows the

Fig. 13 Atomistic structures of M-N₄ (M = Fe, Co, or Ni) macrocyclic complex embedded between graphitic pores. In the figure, *gray, blue, brown, red, and white balls* represent C, N, TM, O, and H atoms, respectively. Adapted with permission from [178]. Copyright 2014 Royal Society of Chemistry



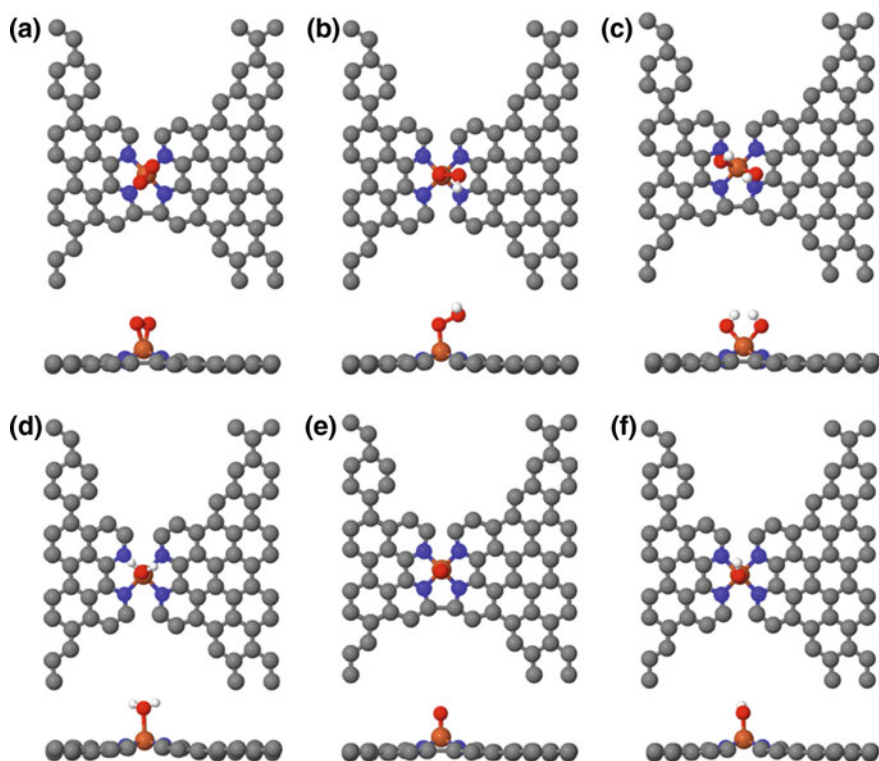


Fig. 14 Optimized geometries of various ORR species adsorbed on M-N₄ macrocyclic complexes embedded near graphitic pores: **a** O₂, **b** OOH, **c** H₂O₂, **d** H₂O, **e** O, and **f** OH. *Top and bottom panels* show the projection and lateral views of the adsorption configurations. In the figure, *gray, blue, brown, red, and white balls* represent C, N, TM, O, and H atoms, respectively. Adapted with permission from [178]. Copyright 2013 Royal Society of Chemistry

chemical reactions: (1) $\text{O}_2 \rightarrow * \text{O}_2$ (adsorption); (2) $* \text{O}_2 + (\text{H}^+ + \text{e}^-) \rightarrow * \text{OOH}$; (3) $* \text{OOH} + (\text{H}^+ + \text{e}^-) \rightarrow 2 * \text{OH}$; and (4) $2 * \text{OH} + 2(\text{H}^+ + \text{e}^-) \rightarrow 2 \text{H}_2\text{O}$. In this pathway, the O–O bond in the reactant O₂ will be split during the interaction of intermediate HOOH with the Fe-N₄ and Co-N₄ macrocyclic complexes. Hence, it was predicted from the DFT calculations that the Fe-N₄ or Co-N₄ macrocyclic complexes near graphitic pores could promote the 4e⁻ ORR with a single active site, which contains a central transition metal M atom and four surrounding chelated N atoms. Furthermore, a linear correlation between the calculated O₂ adsorption energy on the M-N₄ (Me = Fe, Co, or Ni) macrocyclic complexes and the calculated nonbonding *d*-orbital center (i.e., excluding $d_{x^2-y^2}$ orbital) of the central M atom have been identified [178].

5.4 DFT Study of ORR on M-N₄ Clusters Embedded in Graphene

The ORR on the M-N₄ clusters embedded in graphene layer has also been studied to provide insight on the catalytic activity of heat-treated M-N₄ macrocycles [179–183]. Limited by the local structure of extended graphene layer, only two configurations (Fig. 15) of the M-N₄ clusters embedded in a graphene layer are quite possible. Active site A (Fig. 15a) is the most used model in literatures [179–183] while active site B (Fig. 15b) is also studied in Ref. [180].

Calle-Vallejo et al. studied the adsorption of *O, *OH, and *OOH on M-N₄ cluster embedded in graphene using both models [180]. They found that the adsorption energy of these chemical species on M-N₄ clusters follow the same trend with respect to the change of central metal atom. As same as on M-N₄ macrocyclic molecules, increasing the number of electrons in the *d*-orbital of the central metal atom would weaken the interaction between the M-N₄ cluster and the adsorbates. Based on the DFT calculated volcano plots for ORR and oxygen evolution reaction (OER), they predicted that Ir-N₄ cluster embedded in graphene might be most active for both ORR and OER.

Kattel et al. investigated the detailed reaction pathway for ORR on Fe-N₄ clusters embedded in graphene (Active site A) using the DFT method [179]. Specifically, they calculated the activation energies for all the elementary reaction steps relevant to ORR, which include the O₂ dissociation, O₂ hydrogenation, OOH dissociation, OOH hydrogenation, O hydrogenation, and OH hydrogenation reactions on the FeN₄ embedded graphene. From their DFT results, Kattel et al. proposed that the ORR would follow the OOH dissociation pathway on the Fe-N₄ clusters. Namely, O₂ molecule first adsorbs on the Fe atom of the Fe-N₄ cluster, the adsorbed O₂ undergoes a hydrogenation reaction to form an adsorbed OOH molecule, then the O–O bond of the OOH is split to produce an O atom and an OH molecule, subsequently the O and OH will undergoes sequential hydrogenation reactions to form two H₂O molecules. Along this ORR pathway, the DFT calculations indicate that the

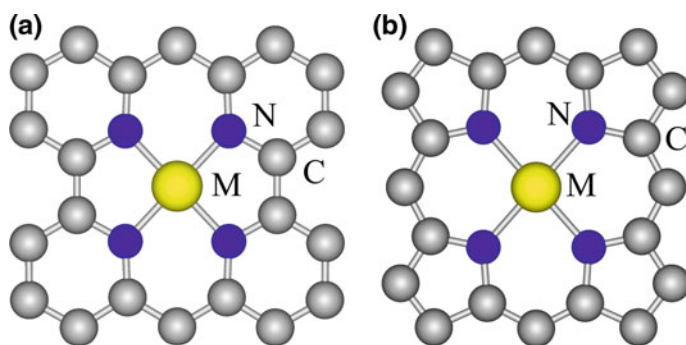


Fig. 15 Two model structures of M-N₄ cluster embedded in graphene

rate-determining step for the ORR on the FeN₄ embedded graphene is the OOH dissociation step in which *OOH dissociates to form *O and *OH and has activation energy of 0.56 eV. This low activation energy is comparable to the 0.79 eV on Pt (111) surface, which indicates that the embedded Fe-N₄ cluster could have similar catalytic activity as compared to that of Pt catalysts.

6 Concluding Remarks

In this contribution, we reviewed the current knowledge on the experimental and theoretical aspects of ORRs on M-N₄ macrocyclic complexes. It has been well-established that M-N₄ macrocyclic complexes possess promising catalytic activity for ORR. In theory, the central transition metal (M) atom (chelated by surrounding N atoms) is widely believed to be the main active site for ORR. Consequently, clear elucidation of the relation between the electronic structure, geometric structure, and ORR activity is highly desired for the rational design of M-N₄ macrocycle catalysts. In this regard, the first-principles density functional theory computational method proves to be a predictive theoretical technique useful for gaining insights into the mechanisms underlying the ORR on M-N₄ macrocyclic complexes.

References

1. Jacobson MZ, Colella WG, Golden DM (2005) Cleaning the air and improving health with hydrogen fuel-cell vehicles. *Science* 308:1901–1905
2. Materials Research Society/American Physical Society (2011) Energy critical elements: securing materials for emerging technologies. Washington, DC
3. Wu G, Moore KL, Johnston CN, Zelenay P (2011) High-performance electrocatalysts for oxygen reduction derived from polyaniline, iron, and cobalt. *Science* 332:443–447
4. Jasinski R (1964) A new fuel cell cathode catalyst. *Nature* 201:1212–1213
5. Wiesener K, Ohms D, Neumann V, Franke R (1989) N₄ macrocycles as electrocatalysts for the cathodic reduction of oxygen. *Mater Chem Phys* 22:457–475
6. Pontie M, Gobin C, Pauporte T, Bedioui F, Devynck J (2000) Electrochemical nitric oxide microsensors: sensitivity and selectivity characterization. *Anal Chim Acta* 411:175–185
7. Nguyen TQ, Escano MCS, Kasai H (2010) Nitric oxide adsorption effects on metal phthalocyanines. *J Phys Chem B* 114:10017–10021
8. Liu KJ, Gast P, Moussavi M, Norby SW, Vahidi N, Walczak T, Wu M, Swartz HM (1993) Lithium phthalocyanine: a probe for electron paramagnetic resonance oximetry in viable biological systems. *P Natl Acad Sci USA* 90:5438–5442
9. Medina WS, Dos Santos NA, Curti C, Tedesco AC, dos Santos AC (2009) Effects of zinc phthalocyanine tetrasulfonate-based photodynamic therapy on rat brain isolated mitochondria. *Chem-biol Interact* 179:402–406
10. Van Baar JF, Van Veen JAR, De Wit N (1982) Selective eletro-oxidation of carbon monoxide with carbon-supported Rh- and Ir-porphyrins at low potentials in acid electrolyte. *Electrochim Acta* 27:57–59

11. Villagra E, Bedioui F, Nyokong T, Carlos Canales J, Sancy M, Paez MA, Costamagna J, Zagal JH (2008) Tuning the redox properties of Co-N₄ macrocyclic complexes for the catalytic electrooxidation of glucose. *Electrochim Acta* 53:4883–4888
12. Vilakazi SL, Nyokong T (2001) Voltammetric determination of nitric oxide on cobalt phthalocynine modified microelectrodes. *J Electroanal Chem* 512:56–63
13. Jiang R, Dong S (1990) Study on the electrocatalytic reduction of H₂O₂ at iron protoporphyrin modified electrode with a rapid rotation-scan method. *Electrochim Acta* 35:1227–1232
14. Furuya N, Yoshiba H (1989) Electroreduction of nitrogen to ammonia on gas-diffusion electrodes modified by Fe-phthalocyanine. *J Electroanal Chem Interfacial Electrochem* 263:171–174
15. Yoshiba H, Furuya N (2003) Simultaneous reduction of carbon dioxide and nitrate ions at gas diffusion electrodes with various metalophthalocynine catalysts. *Electrochim Acta* 48:3953–3958
16. Osmanbas OA, Koca A, Kandaz M, Karaca F (2008) Electrocatalytic activity of phthalocynines bearing thiophenes for hydrogen production from water. *Int J Hydrogen Energ* 33:3281–3288
17. Kato M, Nishioka Y, Kaifu K, Kawamura K, Ohno S (1985) Nearinfrared sensitive electrophotographic photoconductors using chloroindium chlorophthalocynine. *Appl Phys Lett* 46:196–197
18. Zagal JH, Griveau S, Silva JF, Nyokong T, Bedioui F (2010) Metallophthalocynine-based molecular materials as catalysts for electrochemical reactions. *Coordin Chem Rev* 254:2755–2791
19. Collman JP, Fu L, Herrman PC, Zhang X (1977) A functional model related to cytochrome c oxidase and its electrocatalytic four-electron reduction of O₂. *Science* 275:949–951
20. Boulatov R, Collman JP, Shiryaeva IM, Sunderland CJ (2002) Functional analogues of the dioxygen reduction site in cytochrome oxidase: mechanistic aspects and possible effects of CuB. *J Am Chem Soc* 124:11923–11935
21. Collman JP, Boulatov R, Sunderland CJ, Fu L (2004) Functional analogues of cytochrome c oxidase, myoglobin, and hemoglobin. *Chem Rev* 104:561–588
22. Coliman JP, Devaraj NK, Decreau RA, Yang Y, Yan YL, Ebina W, Eberspacher TA, Chidsey CED (2007) Cytochrome c oxidase model catalyzes oxygen to water reduction under rate-limiting electron flux. *Science* 315:1565–1568
23. Collman JP, Ghosh S (2010) Recent applications of a synthetic model of cytochrome c oxidase: beyond functional modeling. *Inorg Chem* 49:5798–5810
24. Masa J, Ozoemenab K, Schuhmanna W, Zagal JH (2012) Oxygen reduction reaction using N₄-metallomacrocyclic catalysts: fundamentals on rational catalyst design. *J Porphyrins Phthalocyanines* 16:761–784
25. Richards G, Swavey S (2009) Electrooxidation of Fe Co, Ni and Cu metalloporphyrins on edge-plane pyrolytic graphite electrodes and their electrocatalytic ability towards the reduction of molecular oxygen in acidic media. *Eur J Inorg Chem* 2009:5367–5376
26. Yuasa M, Nishihara R, Shi C, Anson FC (2001) A comparison of several meso-tetraalkyl cobalt porphyrins as catalysts for the electroreduction of dioxygen. *Polym Adv Technol* 12:266–270
27. Jahnke H, Schonborn M, Zimmermann G (1976) Organic dyestuffs as catalysts for fuel cells. *Top Curr Chem* 61:133–181
28. Chu D, Jiang R (2002) Novel electrocatalysts for direct methanol fuel cells. *Solid State Ionics* 148:591–599
29. Li W, Yu A, Higgins DC, Llanos BG, Chen Z (2010) Biologically inspired highly durable iron phthalocyanine catalysts for oxygen reduction reaction in polymer electrolyte membrane fuel cells. *J Am Chem Soc* 132:17056–17058
30. Seo MH, Higgins D, Jiang G, Choi SM, Han B, Chen Z (2014) Theoretical insight into highly durable iron phthalocyanine derived non-precious catalysts for oxygen reduction reactions. *J Mater Chem A* 2:19707–19716

31. Ward AL, Elbaz L, Kerr JB, Arnold J (2012) Nonprecious metal catalysts for fuel cell applications: electrochemical dioxygen activation by a series of first row transition metal tris (2-pyridylmethyl)amine complexes. *Inorg Chem* 51:4694–4706
32. Honda T, Kojima T, Fukuzumi S (2012) Proton-coupled electron-transfer reduction of dioxygen catalyzed by a saddle-distorted cobalt phthalocyanine. *J Am Chem Soc* 134: 4196–4206
33. Kakuda S, Peterson RL, Ohkubo K, Karlin KD, Fukuzumi S (2013) Enhanced catalytic four-electron dioxygen (O_2) and two-electron hydrogen peroxide (H_2O_2) reduction with a copper(II) complex possessing a pendant ligand pivalamido group. *J Am Chem Soc* 135:6513–6522
34. Kakuda S, Rolle CJ, Ohkubo K, Siegler MA, Karlin KD, Fukuzumi S (2015) Lewis acid-induced change from four- to two-electron reduction of dioxygen catalyzed by copper complexes using scandium triflate. *J Am Chem Soc* 137:3330–3337
35. McClure JP, Devine CK, Jiang R, Chu D, Cuomo JJ, Parsons GN, Fedkiw PS (2013) Oxygen electroreduction on Ti- and Fe-containing carbon fibers. *J Electrochem Soc* 160:F769–F778
36. Sedona F, Marino MD, Forrer D, Vittadini A, Casarin M, Cossaro A, Floreano L, Verdini A, Sambri M (2012) Tuning the catalytic activity of Ag(110)-supported Fe phthalocyanine in the oxygen reduction reaction. *Nat Mater* 11:970–977
37. Ponce I, Silva JF, Oñate R, Rezende MC, Páez MA, Zagal JH (2011) Enhanced catalytic activity of Fe phthalocyanines linked to Au(111) via conjugated self-assembled monolayers of aromatic thiols for O_2 reduction. *Electrochem Commun* 13:1182–1185
38. Ponce I, Silva JF, Oñate R, Rezende MC, Paez MA, Zagal JH, Pavez J (2012) Enhancement of the catalytic activity of Fe phthalocyanine for the reduction of O_2 anchored to Au(111) via conjugated self-assembled monolayers of aromatic thiols as compared to Cu phthalocyanine. *J Phys Chem C* 116:15329–15341
39. Jiang Y, Lu Y, Lv X, Han D, Zhang Q, Niu L, Chen W (2013) Enhanced catalytic performance of Pt-free iron phthalocyanine by graphene support for efficient oxygen reduction reaction. *ACS Catal* 3:1263–1271
40. Cui L, Liu Y, He X (2014) Iron(II) tetraaminophthalocyanine functionalized graphene: synthesis, characterization and their application in direct methanol fuel cell. *J Electroanal Chem* 727:91–98
41. Li T, Peng Y, Li K, Zhang R, Zheng L, Xia D, Zuo X (2015) Enhanced activity and stability of binuclear iron (III) phthalocyanine on graphene nanosheets for electrocatalytic oxygen reduction in acid. *J Power Sources* 293:511–518
42. Xi YT, Wei PJ, Wang RC, Liu JG (2015) Bio-inspired multinuclear copper complexes covalently immobilized on reduced graphene oxide as efficient electrocatalysts for the oxygen reduction reaction. *Chem Commun* 51:7455–7458
43. Wu G, Johnston CM, Mack NH, Artyushkova K, Ferrandon M, Nelson M, Lezama-Pacheco JS, Conradson SD, Moore KL, Myers DJ, Zelenay P (2011) Synthesis-structure-performance correlation for polyaniline-Me-C non-precious metal cathode catalysts for oxygen reduction in fuel cells. *J Mater Chem* 21:11392–11405
44. Zitolo A, Goellner V, Armel V, Sougrati MT, Mineva T, Stievano L, Fonda E, Jaouen F (2015) Identification of catalytic sites for oxygen reduction in iron- and nitrogen-doped graphene materials. *Nat Mater* 14:937–942
45. Jasinski R (1964) A new fuel cell cathode catalyst. *Nature* 201:1212–1213
46. Jasinski R (1965) Cobalt phthalocyanine as a fuel cell cathode. *J Electrochem Soc* 112: 526–528
47. Randin JP (1974) Interpretation of the relative electrochemical activity of various metal phthalocyanines for the oxygen reduction reaction. *Electrochim Acta* 19:83–85
48. Zagal JH, Sen RK, Yeager E (1977) Oxygen reduction by Co(II) tetrasulfonatephthalocyanine irreversibly adsorbed on a stress-annealed pyrolytic graphite electrode surface. *J Electroanal Chem* 83:207–213

49. Collman JP, Denisevich P, Konai Y, Marrocco M, Koval C, Anson FC (1980) Electrode catalysis of the four-electron reduction of oxygen to water by dicobalt face-to-face porphyrins. *J Am Chem Soc* 102:6027–6036
50. Zagal J, Bindra P, Yeager E (1980) A mechanistic study of O₂ reduction on water soluble phthalocyanines adsorbed on graphite electrodes. *J Electrochem Soc* 127:1506–1517
51. Durand R Jr, Anson FC (1982) Catalysis of dioxygen reduction at graphite electrodes by an adsorbed cobalt(II) porphyrin. *J Electroanal Chem* 134:273–289
52. Shigehara K, Anson FC (1982) Catalysis of the reduction of dioxygen to water at graphite electrodes coated with two transition metal catalysts acting in series. *J Electroanal Chem* 132:107–118
53. Liu HY, Weaver MJ, Wang CB, Chang CK (1983) dependence of electrocatalysis for oxygen reduction by adsorbed dicobalt cofacial porphyrins upon catalyst structure. *J Electroanal Chem* 145:439–447
54. van den Brink F, Visscher W, Barendrecht E (1983) Electrode catalysis of cathodic oxygen reduction by metal phthalocyanines—Part I. Introduction, cobalt phthalocyanine as electrocatalyst: experimental part. *J Electroanal Chem* 157:283–304
55. van den Brink F, Visscher W, Barendrecht E (1984) Electrode catalysis of cathodic oxygen reduction by metal phthalocyanines—Part III. Iron phthalocyanine as electrocatalyst: experimental part. *J Electroanal Chem* 172:301–325
56. Zagal JH, Paez M, Sturm J, Ureta-zanartu S (1984) Electroreduction of oxygen on mixtures of phthalocyanines co-adsorbed on a graphite electrode. *J Electroanal Chem* 181:295–300
57. Collman JP, Kim K (1986) Electrocatalytic four-electron reduction of dioxygen by iridium porphyrins adsorbed on graphite. *J Am Chem Soc* 108:7847–7849
58. Elzing A, van der Putten A, Visscher W, Barendrecht E (1986) The cathodic reduction of oxygen at cobalt phthalocyanine—influence of electrode preparation on electrode catalysis. *J Electroanal Chem* 200:313–322
59. Nevin WA, Hempstead MR, Liu W, Leznoff CC, Lever ABP (1987) Electrochemistry and spectroelectrochemistry of mononuclear and binuclear cobalt phthalocyanines. *Inorg Chem* 26:570–577
60. van der Putten A, Elzing A, Visscher W, Barendrecht E (1986) Oxygen reduction on vacuum-deposited and adsorbed transition-metal phthalocyanine films. *J Electroanal Chem* 214:523–533
61. Elzing A, van der Putten A, Visscher W, Barendrecht E (1987) The mechanism of oxygen reduction at iron tetrasulfonato-phthalocyanine incorporated in polypyrrole. *J Electroanal Chem* 233:113–123
62. van der Putten A, Elzing A, Visscher W, Barendrecht E (1987) Redox potential and electrocatalysis of O₂ reduction on transition metal chelates. *J Electroanal Chem* 221:95–104
63. Janda P, Kobayashi N, Auburn PR, Lam H, Leznoff CC, Lever ABP (1989) Dioxygen reduction at a graphite electrode modified by mononuclear tetraneopentoxyphtalocyaninatocobalt(II) and related polynuclear species. *Can J Chem* 67:1109–1119
64. Jiang R, Dong S (1988) Research on chemically modified electrodes—catalytic reduction of dioxygen at a cobalt phthalocyanine-doped polyaniline film electrode. *J Electroanal Chem* 246:101–117
65. Coutanceau C, el Hourch A, Crouigneau P, Leger JM, Lamy C (1995) Conducting polymer electrodes modified by metal trtrasulfonated phthalocyanines: preparation and electrocatalytic behavior towards dioxygen reduction in acid medium. *Electrochim Acta* 40:2739–2748
66. Lalande G, Faubert G, Cote R, Guay D, Dodelet JP, Weng LT, Bertrand P (1996) Catalytic activity and stability of heat-treated iron phthalocyanines for the electroreduction of oxygen in polymer electrolyte fuel cells. *J Power Sources* 61:227–237
67. Bagotzky VS, Tarasevich MR, Radyushkina KA, Levina OA, Andrusyova SI (1977/78) Electrocatalysis of the oxygen reduction process on metal chelates in acid electrolyte. *J Power Sources* 2:233–240

68. Blomquist J, Lang H, Larsson R, Widelov A (1992) Pyrolysis behavior of metalloporphyrins Part 2—A mossbauer study of pyrolysed Fe tetraphenylporphyrin chloride. *J Chem Soc, Faraday Trans* 88:2007–2011
69. Widelov A, Larsson R (1992) ESCA and electrochemical studies on pyrolyzed iron and cobalt tetraphenylporphyrins. *Electrochim Acta* 37:187–197
70. Widelov A (1993) Pyrolysis of iron and cobalt porphyrins sublimated onto the surface of carbon black as a method to prepare catalysts for O₂ reduction. *Electrochim Acta* 38: 2493–2502
71. Franke R, Ohms D, Wiesener K (1989) Investigation of the influence of thermal treatment on the properties of carbon materials modified by N₄-chelates for the reduction of oxygen in acidic media. *J Electroanal Chem* 260:63–73
72. Biloul A, Gouerec P, Savy M, Scarbeck G, Besse S, Riga J (1996) Oxygen electrocatalysis under fuel cell conditions: behavior of cobalt porphyrins and tetraazaannulene analogues. *J Appl Electrochem* 26:1139–1146
73. Gouerec P, Savy M (1999) Oxygen reduction electrocatalysis: ageing of pyrolyzed cobalt macrocycles dispersed on an active carbon. *Electrochim Acta* 44:2653–2661
74. Scherson DA, Gupta SL, Fterro C, Yeager EB, Kordesch ME, Eldkidge J, Hoffman RW, Blue J (1983) Cobalt tetramethoxyphenyl porphyrin—emission mossbauer spectroscopy and O₂ reduction electrochemical studies. *Electrochim Acta* 28:1205–1209
75. Gojković SL, Gupta S, Savinell RF (1998) Heat-treated iron(III) tetramethoxyphenyl porphyrin supported on high-area carbon as an electrocatalyst for oxygen reduction—I. Characterization of the electrocatalyst. *J Electrochem Soc* 145:3493–3499
76. Sun GQ, Wang JT, Savinell RF (1998) Iron(III) tetramethoxyphenylporphyrin (FeTMPP) as methanol tolerant electrocatalyst for oxygen reduction in direct methanol fuel cells. *J Appl Electrochem* 28:1087–1093
77. Gojković SL, Gupta S, Savinell RF (1999) Heat-treated iron(III) tetramethoxyphenyl porphyrin chloride supported on high-area carbon as an electrocatalyst for oxygen reduction —Part II. Kinetics of oxygen reduction. *J Electroanal Chem* 462:63–72
78. Gojković SL, Gupta S, Savinell RF (1999) Heat-treated iron(III) tetramethoxyphenyl porphyrin chloride supported on high-area carbon as an electrocatalyst for oxygen reduction: Part III. Detection of hydrogen-peroxide during oxygen reduction. *Electrochim Acta* 45: 889–897
79. van Veen JAR, Visser C (1979) Oxygen reduction on monomeric transition metal phthalocyanines in acid electrolyte. *Electrochim Acta* 24:921–928
80. Steiger B, Anson FC (1997) 5,10,15,20-Tetrakis(4-((pentaammineruthenio)-cyano)phenyl)porphyrinato]cobalt(II) immobilized on graphite electrodes catalyzes the electroreduction of O₂ to H₂O, but the corresponding 4-cyano-2,6-dimethylphenyl derivative catalyzes the reduction only to H₂O₂. *Inorg Chem* 36:4138–4140
81. Vasudevan P, Santosh Mann N, Tyagi S (1990) Transition metal complexes of porphyrins and phthalocyanines as electrocatalysts for dioxygen reduction. *Transition Met Chem* 15: 81–90
82. Song E, Shi C, Anson F (1998) Comparison of the behavior of several cobalt porphyrins as electrocatalysts for the reduction of O₂ at graphite electrodes. *Langmuir* 14:4315–4321
83. Shi C, Steiger B, Yuasa M, Anson FC (1997) Electroreduction of O₂ to H₂O at unusually positive potentials catalyzed by the simplest of the cobalt porphyrins. *Inorg Chem* 36: 4294–4295
84. Zeng ZY, Gupta SL, Huang H, Yeager EB (1991) Oxygen reduction on poly (4-vinylpyridine)-modified ordinary pyrolytic graphite electrodes with adsorbed cobalt tetra-sulphonated phthalocyanine in acid solutions. *J Appl Electrochem* 21:973–981
85. Baranton S, Coutanceau C, Roux C, Hahn F, Leger JM (2005) Oxygen reduction reaction in acid medium at iron phthalocyanine dispersed on high surface area carbon substrate: tolerance to methanol, stability and kinetics. *J Electroanal Chem* 577:223–234

86. Baker R, Wilkinson DP, Zhang J (2008) Electrocatalytic activity and stability of substituted iron phthalocyanines towards oxygen reduction evaluated at different temperatures. *Electrochim Acta* 53:6906–6919
87. Ramírez G, Trollund E, Isaacs M, Armijo F, Zagal J, Costamagna J, Aguirre MJ (2002) Electroreduction of molecular oxygen on poly-iron-tetraaminophthalocyanine modified electrodes. *Electroanalysis* 14:540–545
88. Zhang L, Song C, Zhang J, Wang H, Wilkinson DP (2005) Temperature and pH dependence of oxygen reduction catalyzed by iron fluoroporphyrin adsorbed on a graphite electrode. *J Electrochem Soc* 152:A2421–A2426
89. Sehlotho N, Nyokong T (2006) Effects of ring substituents on electrocatalytic activity of manganese phthalocyanines towards the reduction of molecular oxygen. *J Electroanal Chem* 595:161–167
90. Masa J, Schuhmann W (2013) Systematic selection of metalloporphyrin-based catalysts for oxygen reduction by modulation of the donor-acceptor intermolecular hardness. *Chem Eur J* 19:9644–9654
91. Zagal J, Paez M, Tanaka AA, dos Santos JR, Linkous CA (1992) Electrocatalytic activity of metal phthalocyanines for oxygen reduction. *J Electroanal Chem* 339:13–30
92. van den Brink F, Barendrecht E, Visscher W (1980) The cathodic reduction of oxygen—a review with emphasis on macrocyclic organic metal complexes as electrocatalysts. *Recl Trav Chim Pay B* 99:253–262
93. Wang G, Ramesh N, Hsu A, Chu D, Chen R (2008) Density functional theory study of the adsorption of oxygen molecule on iron phthalocyanine and cobalt phthalocyanine. *Mol Simulat* 34:1051–1056
94. Wiesener K (1986) N₄-chelates as electrocatalyst for cathodic oxygen reduction. *Electrochim Acta* 31:1073–1078
95. Elzing A, van der Putten A, Visscher W, Barendrecht E (1986) The cathodic reduction of oxygen at cobalt phthalocyanine—influence of electrode preparation on electrocatalysis. *J Electroanal Chem* 200:313–322
96. Zhang J, Anson FC (1993) Complexes of Cu(II) with electroactive chelating ligands adsorbed on graphite electrodes: surface coordination chemistry and electrocatalysis. *J Electroanal Chem* 348:81–97
97. Zhang J, Anson FC (1993) Electrocatalysts for the reduction of O₂ and H₂O₂ based on complexes of Cu(II) with the strongly adsorbing 2,9-dimethyl-1,10-phenanthroline ligand. *Electrochim Acta* 38:2423–2429
98. Liu H, Zhang L, Zhang J, Ghosh D, Jung J, Downing BW, Whittemore E (2006) Electrocatalytic reduction of O₂ and H₂O₂ by adsorbed cobalt tetramethoxyphenyl porphyrin and its application for fuel cell cathodes. *J Power Sources* 161:743–752
99. Chen R, Li H, Chu D, Wang G (2009) Unraveling oxygen reduction reaction mechanisms on carbon-supported Fe-phthalocyanine and Co-phthalocyanine catalysts in alkaline solutions. *J Phys Chem C* 113:20689–20697
100. Yeager E (1981) Recent advances in the science of electrocatalysis. *J Electrochem Soc* 128:160C–171C
101. Beck F (1977) The redox mechanism of the chelate-catalysed oxygen cathode. *J Appl Electrochem* 7:239–245
102. van den Brink F, Visscher W, Barendrecht E (1983) Electrocatalysis of cathodic oxygen reduction by metal phthalocyanines: Part II. Cobalt phthalocyanine as electrocatalyst: a mechanism of oxygen reduction. *J Electroanal Chem* 157:305–318
103. Yeager E (1984) Electrocatalysts for O₂ reduction. *Electrochim Acta* 29:1527–1537
104. Shi C, Anson FC (1990) Catalytic pathways for the electroreduction of O₂ by iron Tetrakis (4-N-methylpyridyl)porphyrin or iron tetraphenylporphyrin adsorbed on edge plane pyrolytic graphite electrodes. *Inorg Chem* 29:4298–4305
105. Nikolic BZ, Adzic RR, Yeager EB (1979) Reflectance spectra of monolayers of tetrasulfonated transition metal phthalocyanines adsorbed on electrode surfaces. *J Electroanal Chem* 103:281–287

106. Chang CJ, Loh ZH, Shi C, Anson FC, Nocera DG (2004) Targeted proton delivery in the catalyzed reduction of oxygen to water by bimetallic pacman porphyrins. *J Am Chem Soc* 126:10013–10020
107. Tsuda M, Dino AW, Nakanishi H, Kasai H (2005) Orientation dependence of O₂ dissociation from heme–O₂ adduct. *Chem Phys Lett* 402:71–74
108. van Veen JAR, van Baar JF, Kroese KJ (1981) Effect of heat treatment on the performance of carbon-supported transition-metal chelates in the electrochemical reduction of oxygen. *J Chem Soc, Faraday Trans 1* (77):2827–2843
109. van der Putten A, Elzing A, Visscher W, Barendrecht E (1986) Oxygen reduction on pyrolyzed carbon-supported transition metal chelates. *J Electroanal Chem* 205:233–244
110. van Veen JAR, Colijn HA, van Baar JF (1988) On the effect of a heat treatment on the structure of carbon-supported metalloporphyrins and phthalocyanines. *Electrochim Acta* 33:801–804
111. Ladouceur M, Lalande G, Guay D, Dodelet JP, Dignard-Bailey L, Trudeau ML, Schulz R (1993) Pyrolyzed cobalt phthalocyanine as electrocatalyst for oxygen reduction. *J Electrochem Soc* 140:1974–1981
112. Faubert G, Lalande G, Cote R, Guay D, Dodelet JP, Weng LT, Bertrand P, Denes G (1996) Heat-treated iron and cobalt tetraphenylporphyrins adsorbed on carbon black: physical characterization and catalytic properties of these materials for the reduction of oxygen in polymer electrolyte fuel cells. *Electrochim Acta* 41:1689–1701
113. Bae IT, Tryk DA, Scherson DA (1998) Effect of heat treatment on the redox properties of iron porphyrins adsorbed on high area carbon in acid electrolytes: an in situ Fe K-edge X-ray absorption near-edge structure study. *J Phys Chem B* 102:4114–4117
114. Faubert G, Cote R, Guay D, Dodelet JP, Denes G, Bertrand P (1998) Iron catalysts prepared by high-temperature pyrolysis of tetraphenylporphyrins adsorbed on carbon black for oxygen reduction in polymer electrolyte fuel cells. *Electrochim Acta* 43:341–353
115. Okada T, Gokita M, Yuasa M, Sekine I (1998) Oxygen reduction characteristics of heat-treated catalysts based on cobalt-porphyrin ion complexes. *J Electrochem Soc* 145:815–822
116. Bouwkamp-Wijnoltz AL, Visscher W, van Veen JAR (1998) The selectivity of oxygen reduction by pyrolyzed iron porphyrin supported on carbon. *Electrochim Acta* 43:3141–3152
117. Kalvelage H, Mecklenburg A, Kunz U, Hoffmann U (2000) Electrochemical reduction of oxygen at pyrolyzed iron and cobalt N₄-chelates on carbon black supports. *Chem Eng Technol* 23:803–807
118. Pylypenko S, Mukherjee S, Olson TS, Atanassov P (2008) Non-platinum oxygen reduction electrocatalysts based on pyrolyzed transition metal macrocycles. *Electrochim Acta* 53:7875–7883
119. Charretier F, Jaouen F, Dodelet JP (2009) Iron porphyrin-based cathode catalysts for PEM fuel cells: influence of pyrolysis gas on activity and stability. *Electrochim Acta* 54:6622–6630
120. Herrmann I, Kramm UI, Fiechter S, Bogdanoff P (2009) Oxalate supported pyrolysis of CoTMPP as electrocatalysts for the oxygen reduction reaction. *Electrochim Acta* 54:4275–4287
121. Herrmann I, Kramm UI, Radnik J, Fiechter S, Bogdanoff P (2009) Influence of sulfur on the pyrolysis of CoTMPP as electrocatalyst for the oxygen reduction reaction. *J Electrochem Soc* 156:B1283–B1292
122. Li S, Zhanga L, Liu H, Pan M, Zan L, Zhang J (2010) Heat-treated cobalt–tripyrindyl triazine (Co–TPTZ) electrocatalysts for oxygen reduction reaction in acidic medium. *Electrochim Acta* 55:4403–4411
123. Kramm UI, Abs-Wurmbach I, Herrmann-Geppert I, Radnik J, Fiechter S, Bogdanoff P (2011) Influence of the electron-density of FeN₄-centers towards the catalytic activity of pyrolyzed FeTMPPCl-based ORR-electrocatalysts. *J Electrochem Soc* 158:B69–B78
124. Olson TS, Pylypenko S, Fulghum JE, Atanassov P (2010) Bifunctional oxygen reduction reaction mechanism on non-platinum catalysts derived from pyrolyzed porphyrins. *J Electrochem Soc* 157:B54–B63

125. Schulenburg H, Stankov S, Schunemann V, Radnik J, Dorbandt I, Fiechter S, Bogdanoff P, Tributsch H (2003) Catalysts for the oxygen reduction from heat-treated iron(III) tetramethoxyphenylporphyrin chloride: structure and stability of active sites. *J Phys Chem B* 107:9034–9041
126. Scherson D, Tanaka AA, Gupta SL, Tryk D, Fierro C, Holze R, Yeager EB, Lattimer RP (1986) Transition metal macrocycles supported on high area carbon: pyrolysis—mass spectrometry studies. *Electrochim Acta* 31:1247–1258
127. Cao R, Thapa R, Kim H, Xu X, Kim MG, Li Q, Park N, Liu M, Cho J (2013) Promotion of oxygen reduction by a bio-inspired tethered iron phthalocyanine carbon nanotube-based catalyst. *Nat Commun* 4:2076
128. Okunola A, Kowalewska B, Bron M, Kulesza PJ, Schuhmann W (2009) Electrocatalytic reduction of oxygen at electropolymerized films of metalloporphyrins deposited onto multi-walled carbon nanotubes. *Electrochim Acta* 54:1954–1960
129. Zhang W, Shaikh AU, Tsui EY, Swager TM (2009) Cobalt porphyrin functionalized carbon nanotubes for oxygen reduction. *Chem Mater* 21:3234–3241
130. Chen Z, Higgins D, Chen Z (2010) Electrocatalytic activity of nitrogen doped carbon nanotubes with different morphologies for oxygen reduction reaction. *Electrochim Acta* 55:4799–4804
131. Mamuru SA, Ozoemena KI, Fukuda T, Kobayashi N, Nyokong T (2010) Studies on the heterogeneous electron transport and oxygen reduction reaction at metal (Co, Fe) octabutylsulphonylphthalocyanines supported on multi-walled carbon nanotube modified graphite electrode. *Electrochim Acta* 55:6367–6375
132. Mamuru SA, Ozoemena KI (2010) Heterogeneous electron transfer and oxygen reduction reaction at nanostructured iron(II) phthalocyanine and its MWCNTs nanocomposites. *Electroanalysis* 22:985–994
133. Schilling T, Okunola A, Masa J, Schuhmann W, Bron M (2010) Carbon nanotubes modified with electrodeposited metal porphyrins and phenanthrolines for electrocatalytic applications. *Electrochim Acta* 55:7597–7602
134. Morozan A, Campidelli S, Filoramo A, Jusselme B, Palacin S (2011) Catalytic activity of cobalt and iron phthalocyanines or porphyrins supported on different carbon nanotubes towards oxygen reduction reaction. *Carbon* 49:4839–4847
135. Dong G, Huang M, Guan L (2011) Iron phthalocyanine coated on single-walled carbon nanotubes composite for the oxygen reduction reaction in alkaline media. *Phys Chem Chem Phys* 14:2557–2559
136. Yuan Y, Zhao B, Jeon Y, Zhong S, Zhou S, Kim S (2011) Iron phthalocyanine supported on amino-functionalized multi-walled carbon nanotube as an alternative cathodic oxygen catalyst in microbial fuel cells. *Bioresour Technol* 102:5849–5854
137. Moa G, Liao S, Zhang Y, Zhang W, Ye J (2012) Synthesis of active iron-based electrocatalyst for the oxygen reduction reaction and its unique electrochemical response in alkaline medium. *Electrochim Acta* 76:430–439
138. Ramavathu LN, Maniam KK, Gopalram K, Chetty R (2012) Effect of pyrolysis temperature on cobalt phthalocyanine supported on carbon nanotubes for oxygen reduction reaction. *J Appl Electrochem* 42:945–951
139. Dobrzaniecka A, Zeradjanin A, Masa J, Puschhof A, Stroka J, Kulesza PJ, Schuhmann W (2013) Application of SECM in tracing of hydrogen peroxide at multicomponent non-noble electrocatalyst films for the oxygen reduction reaction. *Catal Today* 202:55–62
140. Yoo E, Zhou H (2013) Fe phthalocyanine supported by graphene nanosheet as catalyst in Lie-air battery with the hybrid electrolyte. *J Power Sources* 244:429–434
141. Kruusenberg I, Matisen L, Tammeveski K (2013) Oxygen electroreduction on multi-walled carbon nanotube supported metal phthalocyanines and porphyrins in acid media. *Int J Electrochem Sci* 8:1057–1066
142. Elouarzaki K, Haddad R, Holzinger M, Goff AL, They J, Cosnier S (2014) MWCNT-supported phthalocyanine cobalt as air-breathing cathodic catalyst in glucose/O₂ fuel cells. *J Power Sources* 255:24–28

143. Zhou J, Duchesne PN, Hu Y, Wang J, Zhang P, Li Y, Regier T, Dai H (2014) Fe–N bonding in a carbon nanotube–graphene complex for oxygen reduction: an XAS study. *Phys Chem Chem Phys* 16:15787–15791
144. Zhang R, Peng Y, Li Z, Li K, Ma J, Liao Y, Zheng L, Zuo X, Xia D (2014) Oxygen electroreduction on heat-treated multi-walled carbon nanotubes supported iron polyphthalocyanine in acid media. *Electrochim Acta* 147:343–351
145. Lv G, Cui L, Wu Y, Liu Y, Pu T, He X (2013) A novel cobalt tetranitrophthalocyanine/graphene composite assembled by an in situ solvothermal synthesis method as a highly efficient electrocatalyst for the oxygen reduction reaction in alkaline medium. *Phys Chem Chem Phys* 15:13093–13100
146. Cui L, Lv G, Dou Z, He X (2013) Fabrication of iron phthalocyanine/graphene micro/nanocomposite by solvothermally assisted π - π assembling method and its application for oxygen reduction reaction. *Electrochim Acta* 106:272–278
147. Jiang Y, Lu Y, Lv X, Han D, Zhang Q, Niu L, Chen W (2013) Enhanced catalytic performance of Pt-free iron phthalocyanine by graphene support for efficient oxygen reduction reaction. *ACS Catal* 3:1263–1271
148. Xu Z, Li H, Yin B, Shu Y, Zhao X, Zhang D, Zhang L, Li K, Hou X, Lu J (2013) N-doped graphene analogue synthesized by pyrolysis of metal tetrapyrroline porphyrine with high and stable catalytic activity for oxygen reduction. *RSC Adv* 3:9344–9351
149. Cui L, Liu Y, He X (2014) Iron(II) tetraaminophthalocyanine functionalized graphene: synthesis, characterization and their application in direct methanol fuel cell. *J Electroanal Chem* 727:91–98
150. Gao X, Wang J, Ma Z, Ye J (2014) Iron tetrasulfophthalocyanine functionalized graphene nanosheets for oxygen reduction reaction in alkaline media. *Electrochim Acta* 130:543–550
151. Jiang L, Li M, Lin L, Li Y, He X, Cui L (2014) Electrocatalytic activity of metalloporphyrins grown in situ on graphene sheets toward oxygen reduction reaction in an alkaline medium. *RSC Adv* 4:26653–26661
152. Li M, Jiang LQ, Lin L, Li YF, Yu DL, Cui LL, He XQ (2014) Fabrication of graphene-supported tetraferrocenylporphyrin electrocatalyst for oxygen reduction and its unique electrochemical response in both alkaline and acid media. *J Solid State Electrochem* 18:2743–2753
153. Hohenberg P, Kohn W (1964) Inhomogeneous electron gas. *Phys Rev* 136:B864
154. Kohn W, Sham LJ (1965) Self-consistent equation including exchange and correlation effects. *Phys Rev* 140:A1133
155. Kohn W (1999) Nobel lecture: electronic structure of matter—wave functions and density functionals. *Rev Mod Phys* 71:1253
156. Ruban AV, Skriver HL, Nørskov JK (1999) Surface segregation energies in transition-metal alloys. *Phys Rev B* 59:15990
157. Zhang Y, Duan Z, Xiao C, Wang G (2011) Density functional theory calculation of platinum surface segregation energy in Pt₃Ni (111) surface doped with a third transition metal. *Surf Sci* 605:1577–1582
158. Xu Y, Ruban AV, Mavrikakis M (2004) Adsorption and dissociation of O₂ on Pt-Co and Pt-Fe alloys. *J Am Chem Soc* 126:4717–4725
159. Abild-Pedersen F, Greeley J, Studt F, Rossmeisl J, Munter TR, Moses PG, Skulason E, Bligaard T, Nørskov JK (2007) Scaling properties of adsorption energies for hydrogen-containing molecules on transition-metal surfaces. *Phys Rev Lett* 99:016105
160. Li S-C, Zhang Z, Sheppard D, Kay BD, White JM, Du Y, Lyubinsky I, Henkelman G, Dohnalek Z (2008) Intrinsic diffusion of hydrogen on rutile TiO₂ (110). *J Am Chem Soc* 130:9080–9088
161. Ferrin P, Kandoi S, Nilekar AU, Mavrikakis M (2012) Hydrogen adsorption, absorption and diffusion on and in transition metal surfaces: a DFT study. *Surf Sci* 606:679–689
162. Grabow LC, Gokhale AA, Evans ST, Dumesic JA, Mavrikakis M (2008) Mechanism of the water gas shift reaction of Pt: first principles, experiments and microkinetic modelling. *J Phys Chem C* 112:4608–4617

163. Duan Z, Henkelman G (2014) CO oxidation on the Pd (111) surface. *ACS Catal* 4: 3435–3443
164. Shi C, O'grady CP, Peterson AA, Hansen HA, Nørskov JK (2013) Modeling CO₂ reduction on Pt (111). *Phys Chem Chem Phys* 15:7114–7122
165. Greeley J, Mavrikakis M (2004) Alloy catalysts designed from first principles. *Nat Mater* 3:810–815
166. Wang C, Li D, Chi M, Pearson J, Rankin RB, Greeley J, Duan Z, Wang G, Van der Vliet D, More KL, Markovic NM, Stamenkovic VR (2012) Rational development of ternary alloy electrocatalysts. *J Phys Chem Lett* 3:1668–1673
167. Nørskov JK, Bligaard T, Rossmeisl J, Christensen CH (2009) Towards the computational design of solid catalysts. *Nat Chem* 1:37
168. He H, Lei Y, Xiao C, Chu D, Chen R, Wang G (2012) Molecular and electronic structures of transition-metal macrocyclic complexes as related to catalyzing oxygen reduction reactions: a density functional theory study. *J Phys Chem C* 116:16038–16046
169. Liu K, Lei Y, Wang G (2013) Correlation between oxygen adsorption energy and electronic structure of transition metal macrocyclic complexes. *J Chem Phys* 139:204306
170. Sun S, Jiang N, Xia D (2011) Density functional theory study of the oxygen reduction reaction on metalloporphyrins and metallophthalocyanines. *J Phys Chem C* 115:9511–9517
171. Shi Z, Zhang J (2007) Density functional theory study of transition metal macrocyclic complexes' dioxygen-binding abilities and their catalytic activities toward oxygen reduction reaction. *J Phys Chem C* 111:7084–7090
172. Tsuda M, Dy ES, Kasai H (2005) Comparative study of O₂ dissociation on various metalloporphyrins. *J Chem Phys* 122:244719
173. Trojánek A, Langmaier J, Kvapilová H, Zálíš S, Samec Z (2014) Inhibitory effect of water on the oxygen reduction catalyzed by cobalt(II) tetraphenylporphyrin. *J Phys Chem A* 118:2018–2028
174. Duan Z, Wang G (2011) First-principles study of oxygen reduction reaction on Pt (111) surface modified by subsurface transition metal M (M = Ni Co, or Fe). *Phys Chem Chem Phys* 13:20178–20187
175. Stamenkovic V, Fowler B, Mun BS, Wang G, Ross PN, Lucas CA, Markovic NM (2007) Improved oxygen reduction activity on Pt₃Ni(111) via increased surface site availability. *Science* 315:493–497
176. Nørskov JK, Rossmeisl J, Logadottir A, Lindqvist L, Kitchin JR, Bligaard T, Jonsson H (2004) Origin of the overpotential for oxygen reduction at a fuel-cell cathode. *J Phys Chem B* 108:17886–17892
177. Stamenkovic V, Mun BS, Mayrhofer KJJ, Ross PN, Markovic NM, Rossmeisl J, Greeley J, Nørskov JK (2006) Changing the activity of electrocatalysts for oxygen reduction by tuning the surface electronic structure. *Angew Chem Int Ed* 45:2897–2901
178. Kattel S, Wang G (2013) A density functional theory study of oxygen reduction reaction on Me-N₄ (Me = Fe Co, or Ni) clusters between graphitic pores. *J Mater Chem A* 1: 10790–10797
179. Kattel S, Wang G (2014) Reaction pathway for oxygen reduction reaction on FeN₄ embedded graphene. *J Phys Chem Lett* 5:452–456
180. Calle-Vallejo F, Martinez JI, Rossmeisl J (2011) Density functional studies of functionalized graphitic materials with late transition metals for oxygen reduction reactions. *Phys Chem Chem Phys* 13:15639–15643
181. Kattel S, Atanassov P, Kiefer B (2014) A density functional theory study of oxygen reduction reaction on non-PGM Fe-N_x-C electrocatalysts. *Phys Chem Chem Phys* 16: 13800–13806
182. Saputro AG, Hideaki Kasai (2014) Oxygen reduction reaction on neighboring Fe-N₄ and quaternary-N sites of pyrolyzed Fe/N/C catalyst. *Phys Chem Chem Phys* 17:3059
183. Kattel S, Plamen A, Kiefer B (2013) Catalytic activity of Co-N_x/C electrocatalyst for oxygen reduction: a density functional theory study. *Phys Chem Chem Phys* 15:148–153

Heat-Treated Non-precious Metal Catalysts for Oxygen Reduction

Hoon Chung, Gang Wu, Drew Higgins, Pouyan Zamani,
Zhongwei Chen and Piotr Zelenay

1 Introduction

1.1 *Polymer Electrolyte Fuel Cells—The Cathode Challenge*

Polymer electrolyte fuel cells (PEFCs) are touted as a green alternative to the internal combustion engine, yet commercial penetration of PEFCs into the automotive sector remains hindered by cost and durability issues. Under projected conditions of mass production, almost half of the overall fuel cell stack cost is due to the expensive platinum-based catalysts [1]. Current cost targets are unattainable unless the extensive reliance on this precious metal is alleviated. This can only be accomplished by developing alternative cathode catalysts for the oxygen reduction reaction (ORR). Research on new platinum catalyst supports or nanostructured platinum alloys to increase ORR activity on a precious metal mass basis have been largely successful [2–6]. This approach is not ideal, however, due to the volatile pricing and geopolitical instabilities that can likely affect the supply of platinum. For these reasons, the development of entirely non-platinum group metal (non-PGM) catalysts for the oxygen reduction reaction (ORR) is highly desirable [7–9].

H. Chung · P. Zelenay (✉)

Materials Physics and Applications Division, Los Alamos National Laboratory,
Los Alamos, New Mexico 87545, USA
e-mail: zelenay@lanl.gov

G. Wu

Department of Chemical and Biological Engineering, University at Buffalo,
SUNY, Buffalo, New York 14260, USA

D. Higgins · P. Zamani · Z. Chen

Department of Chemical Engineering, University of Waterloo, Waterloo,
Ontario N2L 3G1, Canada

Several different non-PGM catalysts have been investigated in the scientific community. Among them, the most promising systems in terms of activity and stability are made by heat-treating a mixture of transition metal nitrogen, and carbon species (M–N–C) at temperatures in excess of 700 °C [10]. Different synthesis approaches, precursor selection, and fabrication parameters are known to result in catalyst variations, with iron-based catalysts showing the highest activity. By applying rational design strategies, numerous research teams have achieved success in improving the ORR activity, electrochemical durability, and membrane electrode assembly (MEA) performance of M–N–C catalysts [11–19]. This chapter will give a synopsis on the current state of knowledge of heat-treated non-PGM catalysts and recent progress in this important area of research.

1.2 Performance Requirements

Traditional non-PGM catalyst performance evaluation in an MEA has been done on a volumetric-activity basis, with the U.S. Department of Energy (U.S. DOE) 2020 target set at 300 A cm⁻³ at a cell voltage of 0.8 V (*iR*-corrected) [20]. To be technologically viable in PEFCs for automotive applications, the performance capabilities of non-PGM catalysts must ultimately meet targets that have also been established for platinum catalysts. For MEAs, these are generally specified on an areal basis and include achieving a current density of 0.3 A cm⁻² at 0.8 V and a power density of 1.0 W cm⁻² at rated power. The durability must also be sufficient enough to compete with the capabilities of internal combustion engines. The DOE 2020 target requires that less than 10 % of performance loss (voltage at rated power) after 5000 h of cycling is achieved. While the cycling conditions used are often assumed to be equivalent to 150,000 miles of driving, the ultimate stability testing must also be done under practical conditions (i.e., ambient environments, dynamic loads, and start-up/shutdown) in order to be technologically viable.

In spite of dramatic progress achieved over the past two decades, to the point that non-PGM catalysts have advanced past being considered basic research, [21] the above targets are still very ambitious for non-PGM catalysts. While rotating disc electrode (RDE) and rotating ring disc electrode (RRDE) experiments are very useful for catalyst screening and electrochemical kinetic investigations, MEA integration and performance evaluation in fuel cells have become a priority. Performance improvement investigations need to continue, along with studies to understand the catalyst properties and phenomena that govern performance and stability of electrocatalysts. Only through the application of this knowledge will non-PGM catalysts be capable of achieving established technical targets. If successful, such catalysts will play a key role in reaching the \$40 per kW cost targets in place for the automotive-scale PEFC systems [20].

2 Synthesis Path

Jahnke et al. [22] pioneered the use of transition metal macrocycle compounds that contain $M-N_4$ structures as ORR catalysts. Their research inspired efforts to develop active oxygen reduction catalysts by heat-treating macrocyclic precursors. It was later shown that new synthesis routes for heat-treated transition metal catalysts were successful using less complex ligands, such as sulfates, chlorides, and nitrates. Since that time, several research groups have focused on novel catalyst synthesis and performance improvement [3, 13, 14, 18, 19, 23–36]. Meanwhile, at Los Alamos National Laboratory, Zelenay et al. have been able to increase the activity of Fe–N–C compounds using two heat treatment steps and with proper selection of nitrogen–carbon precursors (e.g., polyaniline and cyanamide) [15, 37]. It is also worth noting that the nature of the non-precious active sites in such heat-treated catalysts is still under debate. This derives from the fact that the function of the transition metal during the catalyst synthesis remains unresolved. Regardless, the catalytic activity was found strongly dependent on the synthesis chemistry, including the structure of the nitrogen precursor transition metals heat treatment temperatures, and inclusion of support materials (i.e., carbon black). On the basis of recent breakthroughs in this field, we will provide a brief outline of the synthesis pathways for such heat-treated M–N–C catalysts. This will be followed by a discussion of the current ORR activity as well as fuel cell performance.

2.1 Precursors

The heat treatment of virtually any mixture of nitrogen, metal, and carbon species can yield a material that displays some ORR activity. To achieve well-performing catalysts, the selection of precursors, supports, and synthesis conditions is much more important. These factors play a major role toward obtaining materials with the high activity and long-term durability required for practical catalysts [38, 39].

2.1.1 Nitrogen–Carbon Precursors

Heat-treated transition metal–nitrogen–carbon catalysts are currently derived from various nitrogen precursors which can be divided into three categories: (i) $C\equiv N$ -based; (ii) C–N-based; and (iii) aromatic-compound-based precursors. According to the available experimental data, the $C\equiv N$ and aromatic nitrogen precursors appear to be advantageous over the C–N-based ones in terms of resulting catalyst activity and durability. For example, catalysts derived from heteroatomic polymers show higher activity than catalysts obtained from simple amines, such as ethylenediamine [40]. Two types of polymer-based catalysts were systematically compared using either polyaniline (PANI) or polypyrrole (PPy) as nitrogen

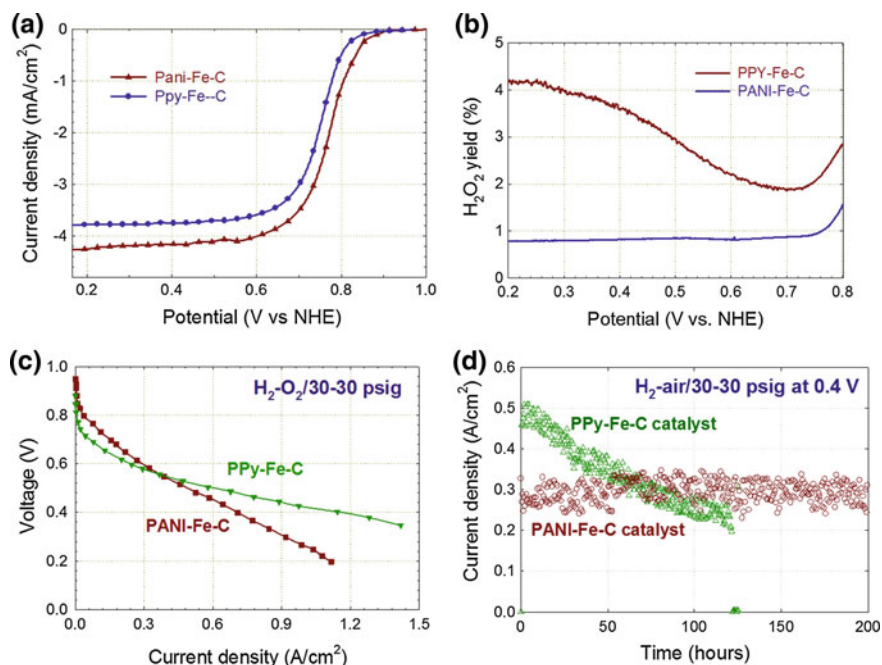


Fig. 1 a RDE and b RRDE tests for PANI- and PPy-based catalysts. Fuel cell performance of PANI- and PPy-derived catalysts: c polarization plots, d life tests. Cell temperature 80 °C; anode—0.25 mg cm⁻² Pt on a woven-web GDL (E-TEK), 30 psig H₂; cathode—catalyst loading 4 mg cm⁻²; membrane—Nafion® 1135. Reproduced with permission from Ref. [41], copyright (2009) The Electrochemical Society

precursors for catalyst synthesis. As shown in Fig. 1, [41] electrochemical data obtained using RDE shows a lower onset potential (higher overpotential) for oxygen reduction with the PPy-Fe-C (~0.85 V vs. RHE) than with PANI-Fe-C (~0.91 V vs. RHE). RRDE results further indicate better selectivity of the PANI-derived catalyst for the four-electron oxygen reduction. The H₂O₂ yield at 0.4 V remains below 1 % for the best performing PANI-derived catalysts.

In good agreement with electrochemical experiments, fuel cell polarization data shown in Fig. 1c confirms higher performance of the PANI-Fe-C catalyst at high cell voltages (>0.55 V). On the other hand, more porous structures of the PPy-derived catalyst benefits performance at lower voltages, where oxygen mass transfer becomes the limited step. Long-term fuel cell performance of both catalysts at a constant voltage of 0.4 V is depicted in Fig. 1d. While PPy-Fe-C shows significantly better activity early in the life test, its performance drops below that of PANI-Fe-C in less than 100 h. On the other hand, PANI-Fe-C exhibits very good stability during the 200-h life test. The difference in the two catalysts' durability may be caused by differences in the nature of the active ORR sites, water tolerance, and/or other factors. There are some indications that precursors with an aromatic

structure may stabilize interactions between the metal and nitrogen species that become embedded into the graphitic structure of the catalyst during heat treatment. This can lead to improved stability of the active reaction sites. This is one possible reason for the much better stability of PANI-derived catalysts.

During the high-temperature catalyst synthesis, one morphological property worth mentioning is that the catalyst structures are dominated by in situ formed graphitized carbon nanostructures, derived from the carbon/nitrogen precursors. The appearance of these nanostructures can be correlated to the oxygen reduction activity, providing critical clues in the identification of active sites. Figure 2 shows different carbon nanostructures that result from using various nitrogen/carbon and transition metal precursors during synthesis [42]. Noteworthy, no graphitized carbon structure was formed when polyaniline was heat-treated in the absence of transition metals. This indicates the crucial role of the transition metal in the formation of highly graphitized carbon during heat treatment. The use of ethylenediamine and Co yields an abundance of onion-like carbon nanostructures formed during heat treatment (Fig. 2, top). When cyanamide is used with Fe, bamboo-like carbon nanotubes tend to appear (Fig. 2, mid part). Among the other extensively investigated precursors, polyaniline-derived catalysts are the only ones to demonstrate substantial graphene content following the heat treatment (Fig. 2, bottom). This shows that the aromatic structure of PANI may be a factor in forming graphene, possibly arising due to their structural similarities.

2.1.2 Transition Metal Precursors

Metal-free nitrogen-doped carbon materials exhibit some ORR activity in alkaline media. In the more challenging acidic media, they suffer from inactivity and poor durability. The addition of transition metal(s) is necessary for achieving good catalytic activity and improved durability [43, 44]. Some studies have shown the important effect of the type of transition metal ions used during synthesis on the oxygen reduction activity. Among other approaches, this effect was demonstrated with polyacrylonitrile-derived catalysts and studied in both acidic and alkaline solutions [45]. The nature of the metallic center in the precursors played a governing role on the resultant ORR catalysis. It has become well established that the most active catalysts in acidic electrolyte are formed using either iron or cobalt. Iron-derived catalysts especially have more positive onset potentials than cobalt-derived catalysts, indicating higher intrinsic activity. The iron-containing catalysts also exhibit the highest four-electron selectivity among several other transition metals [45]. In alkaline media, iron- and cobalt-based electrocatalysts often show similar activity [45].

In a recent report, [46] Liao and coworkers systematically studied the effects of the addition of transition metals (Mn, Fe, Co, Ni, Cu) on the structure and performance of doped carbon catalysts derived from PANI and melamine. The results show that the doping of various transition metals significantly affects the structures and performance of the catalysts. Doping with Fe or Mn led to a catalyst with a

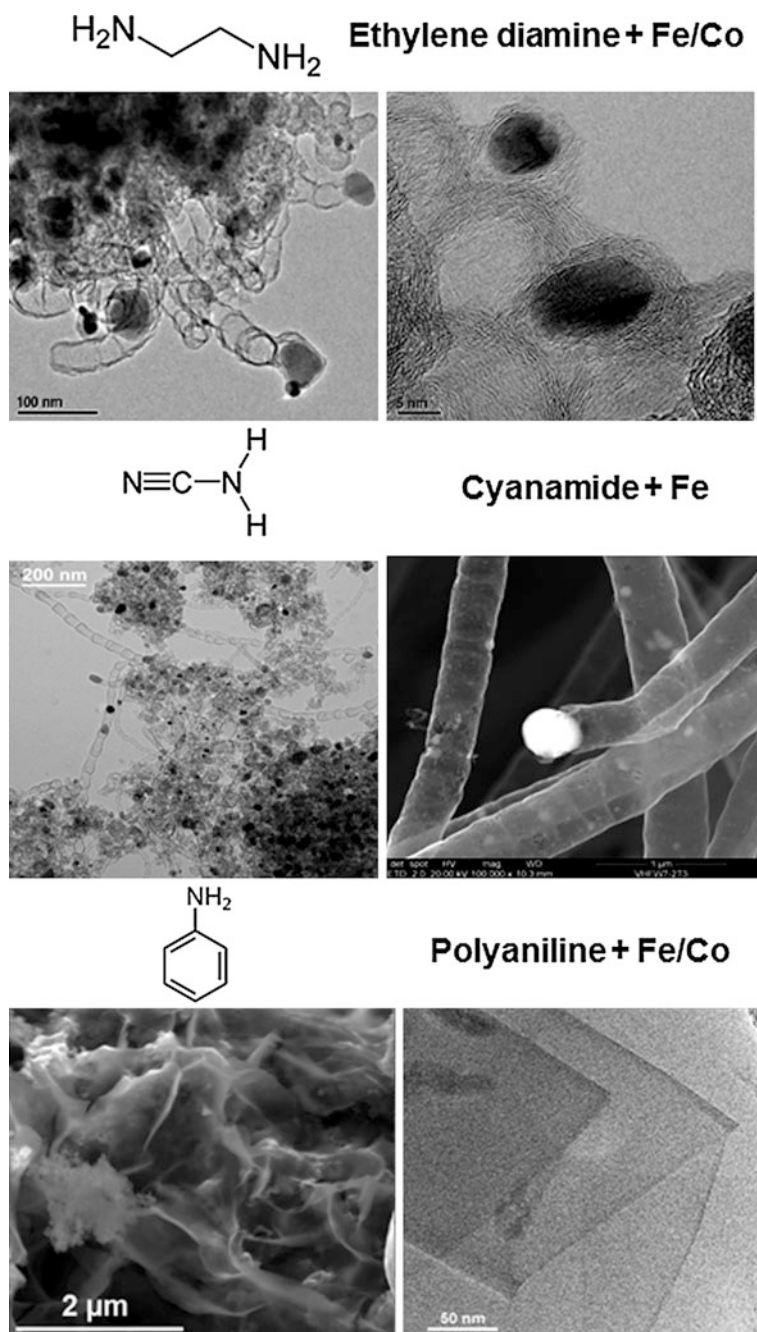
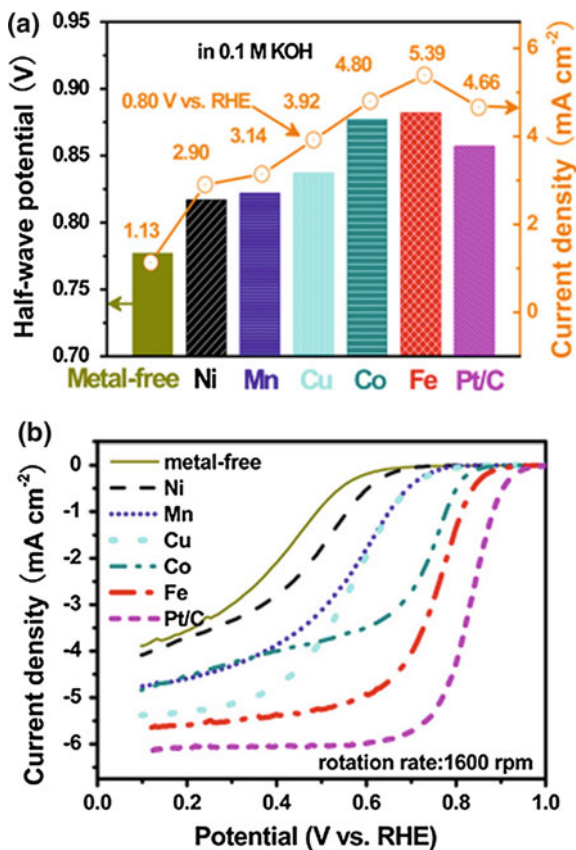


Fig. 2 The various carbon nanostructures observed from the catalysts derived from different nitrogen precursors and transition metal species. Reprinted with permission from Ref. [42], copyright (2012) American Chemical Society

Fig. 3 ORR polarization for catalysts derived from different transition metal precursors in **a** 0.1 M KOH and **b** 0.1 M HClO₄ at 298 K. Reprinted with permission from Ref. [46]. Copyright (2014) American Chemical Society



graphene-like structure, whereby doping with Co, Ni, or Cu yielded a disordered or nanosheet structures. As shown in Fig. 3, the doping of transition metals can enhance the performance of the catalysts. The ORR activity of thus doped catalysts in alkaline solution (another order is often observed in acidic electrolytes) decreases in the following order: Fe > Co > Cu > Mn > Ni. It is suggested that this trend is the result of the impact the transition metal has on three properties: (i) the N content of the catalyst, (ii) the amount and type of residual metal species, and (iii) the resulting catalyst surface area and pore structure.

Transition metals can be used for tuning both the morphology of nanostructured carbon and incorporation of nitrogen dopants [10, 37, 38, 42]. As shown in Fig. 4, the carbon nanotube size and doped nitrogen functionalities can be well controlled using different transition metals, such as Ni, Co, and Fe. For example, compared to other metals, Ni-catalyzed carbon nanotubes have the highest pyridinic nitrogen content. On the other hand, Fe is able to yield largest size of carbon nanotubes with relatively high graphitic nitrogen doping. Given the commonly accepted hypothesis that ORR active sites are embedded into the graphitized carbon structures, the

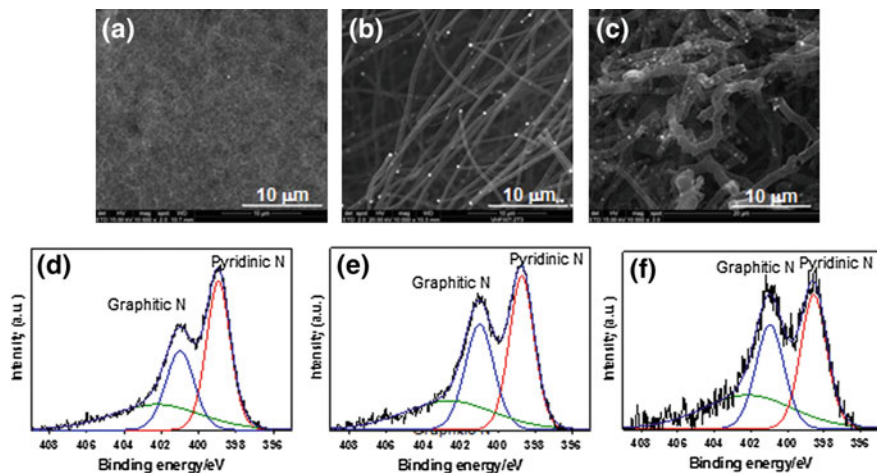


Fig. 4 Nitrogen-doped carbon micro- and nanotubes with the diameter and nitrogen functionalities controlled by the transition metal used in the synthesis: (a, d) Ni; (b, e) Co, and (c, f) Fe. *Top* scanning electron microscopy images; *bottom* corresponding N1s X-ray photoelectron spectroscopy data. Reproduced from Ref. [47] with permission from the Royal Society of Chemistry

highly graphitic nanotubes can offer a potentially attractive host for ORR active sites in these catalysts. By strategically controlling the morphology and N-dopant types/concentrations, improvements to the catalyst performance, durability, and even mass transfer properties are possible.

It was also determined that, in some special cases, the Fe content used for non-PGM catalyst synthesis can play an important role in morphology optimization and activity enhancement [48]. For example, following synthesis involving a nominal iron loading of 30 wt%, the final catalyst had only 2 wt% Fe remaining after acid leach and a second heat treatment. The BET surface area was $845 \text{ m}^2 \text{ g}^{-1}$, a high value for a non-PGM catalyst supported on Ketjenblack[®] (KJ) carbon. On the other hand, when using a nominal metal loading of 30 wt% to prepare polyaniline–cobalt–carbon (PANI–Co–C) catalysts, the Co content in the resulting catalyst was 8 wt% and a significantly lower BET surface area was achieved. In good agreement with BET results, the morphology of the catalysts as determined by scanning electron microscopy (SEM) Fig. 4 shows more porosity when higher nominal iron loadings were used for synthesis (Fig. 5) [48]. The highest nominal Fe loading used during synthesis leads to the lowest bulk Fe content in the final catalyst and to the highest BET surface area. This indicates that the in situ formed FeS (with sulfur originating from the ammonium persulfate used as oxidant to polymerize polyaniline) acts as an effective sacrificial pore-forming “template” that is removed during the acid leaching step. It is possible that a higher portion of FeS particles formed with lower Fe loadings of 3 and 10 wt% is fully encapsulated within carbon agglomerates, protecting them during the acid leach step.

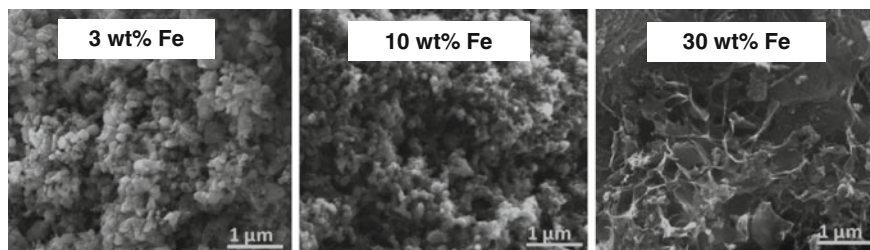


Fig. 5 SEM images of PANI-Fe-C catalysts as a function of Fe loading used during the synthesis. Adapted from Ref. [48]. Reproduced by permission of the American Chemical Society

2.1.3 Effect of Carbon Support

Thanks to their high electronic conductivity, good corrosion resistance, high specific surface area, and falling price, carbon nanotubes have been considered as a replacement for traditional carbon-black supports in fuel cell electrocatalysts. A number of earlier studies have shown that Pt loaded on multi- and single-walled carbon nanotubes exhibits high activity for methanol electro-oxidation and oxygen reduction. Four types of carbon were systematically studied at Los Alamos as supports in non-PGM catalyst synthesis: Vulcan[®] XC-72, Ketjenblack[®] 300 J, Black Pearls[®] 2000, and multi-walled carbon nanotube (MWNTs). Fuel cell polarization plots and life test data for polyaniline-iron (PANI-Fe) catalysts obtained using different carbon supports during synthesis are shown in Fig. 6 [49]. Almost identical polarization plots were observed above 0.35 V, above which MWNT-supported catalysts were found to assure the highest current density, likely thanks to the more open structure of the nanotube-based electrode. MWNTs also benefit the catalyst stability, with virtually no performance degradation after more than 500 h of operation at a cell voltage of 0.40 V. This represents an improvement over the Ketjenblack-supported catalyst that exhibits performance loss already after 200 h of operation.

In general, carbon nanotube (CNT) supports promise improved fuel cell performance over that of traditional carbon blacks. In addition to the excellent electron conductivity, CNTs possess dominant mesoporosity (>2 nm), thus offering better gas permeability and catalytic-site accessibility. Also, water removal within the electrode is facilitated by the hydrophobic nature of the CNT surface, which is of important advantage, especially in the case of non-PGM cathode layers that reach 100 μm in thickness. Higher durability of the MWNT-supported PANI-Fe catalyst may also be related to the higher degree of graphitization of MWNTs, leading to enhanced corrosion resistance and improved stability of the ORR active site(s) [50, 51].

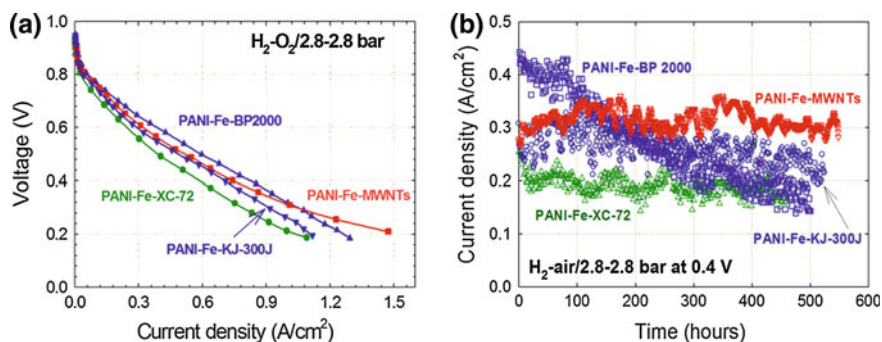


Fig. 6 Fuel cell performance of PANI-Fe catalyst obtained using MWNTs and Ketjenblack as supports: **a** initial polarization plots, **b** life tests. Cell temperature 80°C ; anode— 0.25 mg cm^{-2} Pt on a woven-web GDL (E-TEK), 30 psig H_2 ; cathode—catalyst loading 4.0 mg cm^{-2} ; membrane—Nafion[®] 1135. Adapted from Ref. [49]. Reproduced by permission of The Royal Society of Chemistry

2.2 Effect of Heating Temperature

The activity of ORR sites formed in the heat treatment step strongly depends on the temperature used. In research shown in Fig. 7, [15] the ORR activity of the PANI-Fe-C catalyst was studied as a function of temperature ranging from 400 to 1000°C . The poor activity at 400°C is very similar to the behavior shown for regular carbons, indicating that no new active sites are formed at low heat treatment temperatures. At temperatures above 600°C , a significant shift of the ORR onset potential in the positive direction takes place. 900°C was found to be the optimal temperature in terms of the most positive onset and half-wave potentials.

Elemental analysis of the catalysts heat-treated at different temperatures was determined using X-ray photoelectron spectroscopy (XPS) [38]. It was found that the final Fe content of the catalysts likely increases with the heat treatment

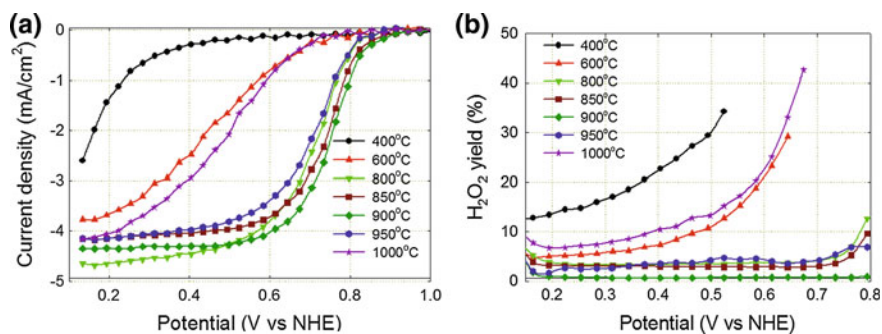


Fig. 7 Effect of heating temperatures on the **a** oxygen reduction activity and **b** four-electron selectivity. Adapted from Ref. [15]. Reproduced by permission of the AAAS

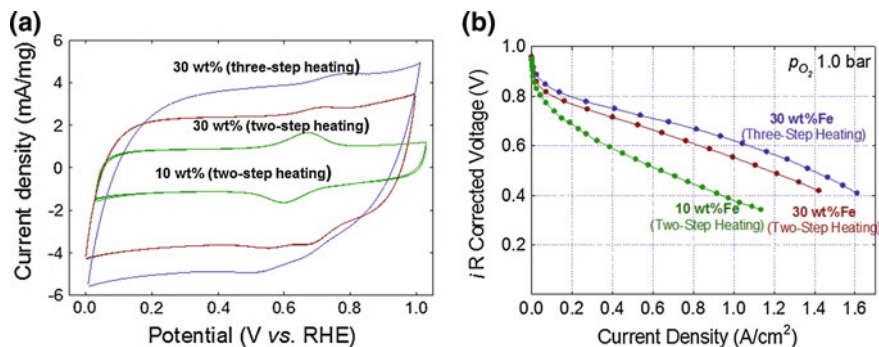


Fig. 8 **a** Cyclic voltammety and **b** fuel cell performance for various PANI–Fe–C non-PGM catalyst. Cyclic voltammety: 20 mV s^{-1} in $0.5 \text{ M H}_2\text{SO}_4$ solution. Fuel cell tests: Anode: 0.5 mg cm^{-2} Pt (E-TEK) 1.0 bar (partial pressure), H_2 , 200 sccm; cathode: $\sim 4.0 \text{ mg cm}^{-2}$ 1.0 bar (partial pressure), O_2 , 200 sccm; Membrane: Nafion[®] 211; Cell: $80 \text{ }^\circ\text{C}$; 100 % RH

temperature. This is probably due to the enhanced formation of graphitized carbon shells that tend to form around and protect Fe-rich phases at high temperatures. High-resolution transmission electronic microscopy (HRTEM) imaging has repeatedly provided an evidence for that interpretation [48]. An increase in the heat treatment temperature also leads to an increase in the carbon formed in PANI carbonization. Interestingly, the nitrogen content decreases with an increase in the heating temperature from 600 to $900 \text{ }^\circ\text{C}$, which is not accompanied by a drop in ORR activity. This suggests that catalyst activity is not entirely dependent on the total amount of doped nitrogen, as claimed by some researchers, [38] but is strongly related to the doping position and local atomic environment.

Beside the heat treatment temperature, the number of heating steps has been found to affect the ORR activity of non-PGM catalysts. Recently, a novel three-step heating strategy to prepare high-surface-area Fe catalysts was developed at Los Alamos [48]. The new cathode catalysts were found to have much increased electrochemically accessible surface area relative to the traditional two-step synthesis (Fig. 8a). A current density of 190 mA cm^{-2} at a voltage of 0.80 V (iR -free) was achieved in fuel cell testing using this strategy (Fig. 8b).

3 Performance Evaluation and Catalyst Characterization Techniques

3.1 Electrochemical Cell Testing

Electrochemical cell testing is a simple and convenient approach to measuring the ORR activity and H_2O_2 yield. Among numerous electrochemical techniques, the most important and widely used are the RDE and RRDE methods.

3.1.1 Electrochemical Cell Set-up

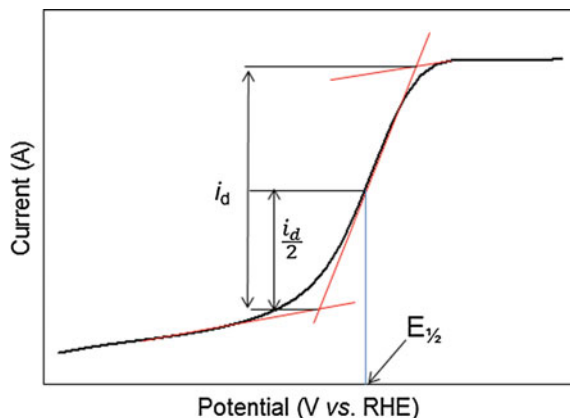
Glass cells equipped with three electrodes are usually used in electrochemical testing. A thorough cleaning of the glassware is essential to eliminate impurities that negatively affect ORR activity of catalysts. A typical cleaning procedure involves soaking the glassware in a mixture of concentrated sulfuric acid and an inorganic oxidizer, such as Nochromix (GODAX Laboratories, Inc.), and then rinsing them with deionized (DI) water (18 M Ω cm). Acid electrolyte (e.g., 0.5 M H₂SO₄, 0.1 M HClO₄) or alkaline electrolyte, (e.g., 0.1 M KOH) is chosen depending on the application of interest. In selecting a reference electrode, it is most appropriate to choose a reference electrode that shares the same anion as the electrolyte, such as the mercury–mercurous sulfate electrode (MSE, 0.68 V vs. NHE) when using sulfuric acid electrolyte. All potentials measured versus a reference electrode should be converted into the reversible hydrogen electrode (RHE) scale to facilitate comparison of results from different laboratories. In order to avoid any potential contamination of the non-PGM catalyst with platinum or other precious metals, the use of a graphite rod as a counter electrode is suggested. RDE using a glassy carbon disk and RRDE made up of a glassy carbon disk surrounded by a platinum ring are typically used as working electrodes. The non-PGM catalysts are ultrasonically dispersed in an alcoholic solution containing suspended Nafion[®] ionomer to form a catalyst “ink” that is applied to the glassy carbon disk surface. At Los Alamos National Laboratory, the catalyst ink is usually prepared by ultrasonically blending for 1 h 10 mg of the non-PGM catalysts and 40 μ l of 5 wt% Nafion[®] suspension in alcohol (Solution Technology, Inc.) in 2.0 mL isopropanol. Homogeneous catalyst deposition onto the glassy carbon electrode is very important for obtaining reliable and reproducible electrochemical data.

3.1.2 RDE/RRDE Measurements

RDE and RRDE measurements are usually performed using a computer-controlled potentiostat and a rotator. RDE is a simple and convenient screening tool for assessing ORR activity of newly developed non-PGM catalysts. One way of evaluating the ORR activity is to measure the half-wave potential ($E_{1/2}$). This is the potential at which the current density is equal to one-half of the mass-transport limited current density (Fig. 9). A higher $E_{1/2}$ corresponds to higher ORR activity (for a given catalyst loading). The other way of estimating ORR activity is to measure the current density in the kinetic region, such as at an electrode potential of 0.90 V versus RHE.

Linear sweep voltammetry (LSV) is usually conducted with the electrode immersed in deoxygenated electrolyte prior to carrying out LSV in oxygen-saturated electrolyte. The ORR polarization curve is obtained by subtracting the LSV measured in deoxygenated electrolyte from the LSV measured in oxygen-saturated electrolyte, whereby capacitive currents can be eliminated. As higher LSV

Fig. 9 Half-wave potential ($E_{1/2}$) determination in RDE testing



scan rates lead to higher $E_{1/2}$ and higher current densities in the kinetic region, the scan rate is important in reporting ORR performance and needs to be specified. Slow scan rates ($5\text{--}10\text{ mV s}^{-1}$) are recommended for recording ORR polarization plots with non-PGM catalysts. At Los Alamos National Laboratory, steady-state measurements have been adopted to obtain ORR polarization plots. These are recorded in oxygen-saturated electrolytes, starting at the open cell potential (OCP) and decreasing it stepwise, typically by 20 or 30 mV, with a hold time of 30–60 s, down to 0.0 V versus RHE. A 120-s potential hold at the open-circuit potential precedes every ORR polarization experiment.

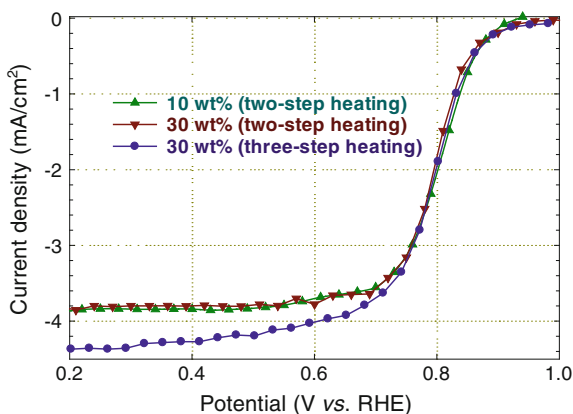
The kinetic current (i_k) and average number of electrons transferred per oxygen molecule (n) can be obtained through RDE experiments using the Koutecky–Levich equation (Eq. 1):

$$\frac{1}{i} = \frac{1}{i_k} + \frac{1}{i_D} = \frac{1}{i_k} + \left(\frac{1}{0.62nFD^{3/2}\nu^{-1/6}C_O} \right) \omega^{-1/2} \quad (1)$$

Here, i is the measured current density, i_k is the kinetic current density, i_D is the diffusion limited current density, n is the number of electrons transferred per oxygen molecule, F is the Faraday constant (96485 C mol^{-1}), D is the diffusion coefficient of the molecular O_2 , C_O is the concentration of molecular O_2 in the electrolyte, ν is the kinematic viscosity of electrolyte, and ω is the angular rotation rate (rad s^{-1}). Plotting $\frac{1}{i}$ versus $\omega^{-1/2}$ yields n from the slope and i_k from the intercept on the $\frac{1}{i}$ axis. The i_k obtained from the Koutecky–Levich plot can also be utilized to obtain the Tafel plot, $\log i_k$ versus E , to determine the Tafel slope and exchange current density (i_0).

The theoretical limiting current density in RDE experiments can be calculated using Levich Eq. 2:

Fig. 10 RDE performance with three different Fe–PANI–C catalysts



$$i_L = 0.62nFAD^{2/3}\omega^{1/2}\nu^{-1/6}C_O \quad (2)$$

Here, i_L is the limiting current and A is the electrode area.

Using RRDE, H_2O_2 yield can be measured based on Eq. 3 by setting the ring potential for H_2O_2 oxidation to ca. 1.4 V versus RHE:

$$H_2O_2(\%) = 200 \times \frac{i_R/N}{(i_R/N) + i_D} \quad (3)$$

Here, i_D and i_R are the disk and ring current densities, respectively, and N is the ring collection efficiency $\left(N = \left|\frac{i_R}{i_D}\right| \left(\frac{n_D}{n_R}\right)\right)$. The peroxide yield can be directly correlated to the average number of electrons transferred per O_2 molecule (n) through the following:

$$n = 4 - (\%H_2O_2)/50\% \quad (4)$$

One should keep in mind though that RDE ORR performance of a catalyst does not always reflect its fuel cell performance. This consideration holds true for non-PGM catalysts in particular. For example, test data shown for three PANI–Fe–C catalysts in Fig. 8b above attest to a major performance differences in the fuel cell, which is not at all reflected in the RDE testing (Fig. 10). Among possible reasons for the observed discrepancy between the RDE and fuel cell performance, water generation may be of particular importance. While obviously having no impact on RDE performance of catalysts, it can significantly influence the fuel cell performance by affecting the oxygen access to the active sites in the fuel cell cathode.

3.2 Fuel Cell Testing

Testing of non-PGM catalysts in the fuel cell cathode is of utmost significance for the evaluation of their activity and durability under PEFC operating conditions. MEA fabrication is thus an important element of a non-PGM catalyst evaluation. Typically, a catalyst “ink” is first prepared by ultrasonically mixing the catalyst powder with a Nafion[®] suspension for 3–4 h. One commonly used ink composition at Los Alamos National Laboratory to obtain a catalyst layer containing 35 wt% of Nafion[®] involves mixing of a non-PGM catalyst, water, isopropanol, and a 5 wt% of Nafion[®] suspension in a weight ratio of 1:12:12:11, respectively. The ink is then applied to the membrane or gas diffusion layer by successive brush painting (or spraying) until a target cathode catalyst loading is reached on a vacuum hot plate maintained at 80 °C. Commercial Pt-catalyzed carbon paper ($0.2 \text{ mg}_{\text{Pt}} \text{ cm}^{-2}$) is normally used at the anode. The gasket thickness is chosen to be *ca.* 80 % of the uncompressed (gas diffusion layer + catalyst layer) thickness. The cathode and anode are hot-pressed at 80–120 °C for 5 min onto a piece of a Nafion[®] membrane. In some cases, two membranes are used. This approach minimizes the risk of a possible cross-contamination of the cathode with Pt from the anode during MEA preparation and also facilitates postmortem characterization of the individual fuel cell electrodes. Figure 11 shows the comparison of fuel cell performance of single- and two-membrane MEAs with non-PGM catalysts. As shown in Fig. 11a, the double membrane MEA exhibits a higher high-frequency resistance (HFR) and lower performance at the mass-transport limited region. However, comparison of the iR -corrected polarization plots reveals identical performance of both MEAs (Fig. 11b).

Recommended fuel cell test conditions include the use of pure hydrogen and air/oxygen, humidified at 80 °C to assure 100 % relative humidity at an anode stoichiometry of 2 and cathode stoichiometry of 9.5. Both electrodes should be maintained at a backpressure that results in a 1.0 bar partial pressure of the gases. Testing is typically carried out a cell temperature of 80 °C.

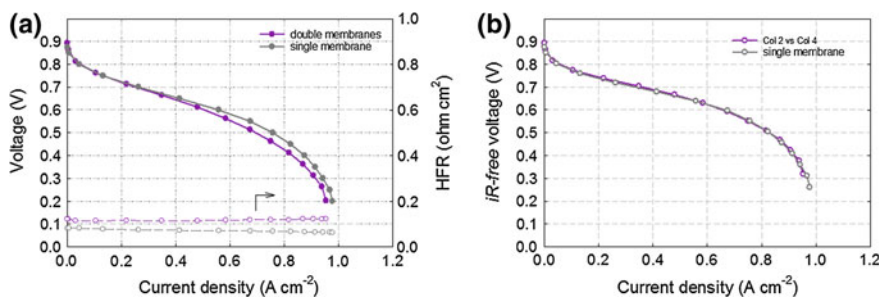


Fig. 11 Fuel cell performance of MEAs single and double MEAs: **a** before and **b** after iR -correction

3.3 Physicochemical Characterization Techniques

Heat-treated non-PGM catalysts have a complex structure, usually consisting of carbon (*ca.* 90 at.%), nitrogen (*ca.*, 5 at.%), metal (most commonly Fe or Co, *ca.* 2 at.%), and other elements (e.g., O, *ca.* 3 at.%). A systematic study of catalysts prepared by various synthesis paths is of importance for gaining insight into the structure and for improving ORR performance and stability of the catalysts. Since nitrogen, iron, and carbon are the main elements in non-PGM ORR catalysts, we will concentrate below on techniques that particularly useful in the analysis of these elements.

XPS is the most common technique to determine elemental composition of non-PGM catalysts. In particular, XPS is an excellent tool to ascertain the type and relative amount of nitrogen functionalities doped into carbon through deconvolution of high-resolution N1s spectra (Detailed analysis of C1s spectra is difficult due to the lack of distinct spectral features.). The valence state of metals in catalysts can be established by the deconvolution of metal spectra. XPS is often referred to as a surface-sensitive technique but in reality the information obtained is not limited to the catalyst surface. Since ORR is strictly a surface reaction, it is important to know the sampling depth of XPS for non-PGM catalysts to conclude how relevant XPS signatures are to the catalyst surface. Universal curves of electron inelastic mean free path curve for either Mg K α X-ray (1253.6 eV) or Al K α X-ray (1486.6 eV) sources, typically used in XPS, reveal the sampling (escape) depth for carbon, i.e., the depth from which 95 % of all photoelectrons are absorbed by the time they reach the surface is *ca.* 6 nm. In the case of carbon, the distance between graphene planes is *ca.* 0.34 nm. Thus, the XPS information from carbon-based non-PGM catalysts originates from *ca.* 20 atomic layers of carbon. By lowering the angle between the X-ray source and the sample, more surface-specific information can be obtained.

X-ray absorption spectroscopy (XAS) is another widely used tool for analyzing the structure of non-PGM catalysts. Depending on the X-ray energy range, carbon (280–300 eV), nitrogen (390–420 eV), and iron (7100–7200 eV) spectra can be obtained. An X-ray absorption spectrum is generally divided into four sections: (i) pre-edge, $E < E_0$ (binding energy); (ii) X-ray absorption near-edge structure (XANES), $E = E_0$ up to $E_0 + ca. 10$ eV; (iii) near-edge X-ray absorption fine structure (NEXAFS), $E = E_0 + ca. 10$ eV to $E_0 + ca. 50$ eV; and (iv) extended X-ray absorption fine structure (EXAFS), $E = E_0 + ca. 50$ eV to $E_0 + ca. 1000$ eV. In carbon NEXAFS, the relative amount of unsaturated carbon bonds (sp or sp^2) and saturated carbon bonds (sp^3) can be assessed by comparing $1s \rightarrow \pi^*$ carbon spectra (284–288 eV) and $1s \rightarrow \sigma^*$ carbon spectra (*ca.* 290 eV). The presence of a π^* resonance in the low-energy range of the carbon spectra is characteristic of unsaturated (sp or sp^2) carbon bonds. However, for diamond which is purely sp^3 -bonded, no π^* resonance is observed, only $1s \rightarrow \sigma^*$ transition at *ca.* 290 eV. Nitrogen analysis for non-PGM catalysts with NEXAFS is difficult due to the low doping level of nitrogen in the catalysts. The oxidation state of iron can be

measured by XANES, while the coordination number of the iron center and type of direct neighboring atoms can be identified by EXAFS.

Raman spectroscopy is also useful tool for structural analysis of non-PGM catalysts. However, the complexity of the carbon phase in such catalysts makes interpretation of Raman spectra very difficult. Raman spectra are affected by the ratio of sp^2/sp^3 bonds, crystallite size, bond-angle disorder, bond-length disorder, heteroatoms, etc. [52]. Generally, the spectra around 1580 cm^{-1} (G band) and 1350 cm^{-1} (D band) are known to correspond to the planar motion of sp^2 -hybridized carbon atoms in an ideal graphene layer and carbon atoms close to the edge of a graphene sheet, respectively [53]. The D band is inversely proportional to the crystallite size. The ratio of $I(D)/I(G)$ (where I denotes the band intensity) is often used to measure the degree of disorder in the graphene layer. The relative concentration of amorphous carbon could be assessed from G and D bands in the Raman spectra.

The morphology of non-PGM catalysts can be studied by SEM and TEM. Combining these techniques with energy-dispersive X-ray spectroscopy (EDS) makes elemental mapping possible. The specific surface area, total pore volume, and pore-size distribution are important parameters that play a key role in the ORR performance of non-PGM catalysts. The Brunauer–Emmett–Teller (BET) method is widely used to determine the surface area of solid materials. Before measurements the samples are degassed under a nitrogen flow at *ca.* $250\text{ }^\circ\text{C}$ for approximately 5 h to ensure the removal of adsorbed water. The W_m , the weight of adsorbate (mostly N_2) constituting a monolayer of surface coverage, is obtained from the BET isotherm using the following equation:

$$\frac{1}{W(P_0/P - 1)} = \frac{1}{W_m C} + \frac{C - 1}{W_m C} \left(\frac{P}{P_0} \right) \quad (5)$$

Here, W is the weight of gas adsorbed at a relative pressure P/P_0 . The total surface area S_t of the sample is calculated from W_m :

$$S_t = \frac{W_m N A_{cs}}{M} \quad (6)$$

Here, N is the Avogadro's constant (6.022×10^{23}), M is the molar mass of the adsorbate (14 for N_2), and A_{cs} is the cross-sectional area of the adsorbate (16.2 \AA^2 for nitrogen). The total pore volume is derived from the amount of vapor adsorbed (V_{ads}) at a relative pressure close to unity by assuming that the pores are then filled with liquid adsorbate (V_{liq}) as follows:

$$V_{liq} = \frac{P_a V_{ads} V_m}{RT} \quad (7)$$

Here, P_a and T are ambient pressure and absolute temperature, respectively, and V_m is the molar volume of the liquid adsorbate ($34.7\text{ cm}^3\text{ mol}^{-1}$ for nitrogen). The

pore-size distribution is calculated based on the pore-size dependence of adsorbate condensation (evaporation) a specific P/P_0 , using several available models in the calculation. The pores are classified as macro-, meso-, and microporos for the diameter greater than 500 Å, between 20 and 500 Å, and smaller than 20 Å, respectively.

4 Catalyst Structure

4.1 The Active Site Debate

In the synthesis of M–N–C catalysts, significant structural and chemical changes occur during the heat treatment. For this reason, a complex mixture of various species results, including both graphitic and amorphous carbon structures, along with the presence of doped nitrogen species, as well as metal oxides, sulfides, and carbides [54]. Because of the highly heterogeneous structure of these catalysts, elucidating the exact identity of the active site structure(s) has been a difficult endeavor and subject of contention in the scientific community. This has been further complicated by the fact that not only the atomic identity of the active site can govern M–N–C activity, but the surrounding environment can play a role owing to induced electronic and geometric effects [55–57]. Establishing this fundamental understanding regarding the active site identity (identities) is, however, highly desirable as it will provide a missing piece of information that can be used to guide improved catalyst designs and mechanistic studies.

An intense debate remains on whether or not metal species are an integral component of the ORR active site, [8] with iron-based catalysts being the most extensively investigated. Some researchers assert that metal species are actually not present in the active site structures, although transition metals, Fe in particular, play a crucial role in facilitating the formation of highly active nitrogen–carbon moieties [58, 59]. This can be used to explain the dramatic performance enhancement achieved upon the addition of even small amounts of transition metal precursors [58, 60]. This activity remains following an acid leach performed to remove metal-based species, as confirmed by surface-specific characterization, such as XPS. Other research teams strongly believe that the active site involves metal ions, e.g., $\text{Fe}^{2+/3+}$, directly coordinated to nitrogen species [57, 61, 62]. Nitrogen coordination is viewed as providing a relatively stable configuration that is not prone to removal during acid leaching or under the electrochemical conditions encountered during ORR activity evaluation. This Fe–N₄/C arrangement also implies a commonality between transition metal macrocycle complexes that have been shown to be ORR active, albeit with limited activity and electrochemical stability [63, 64]. The most common notion for a metal-based active site is that Fe ions are coordinated by four nitrogen species. This for example includes the FeN₄/C (Fig. 12a) or FeN₂₊₂/C (Fig. 12b, c) structures. Of these different species, it is the FeN₄/C

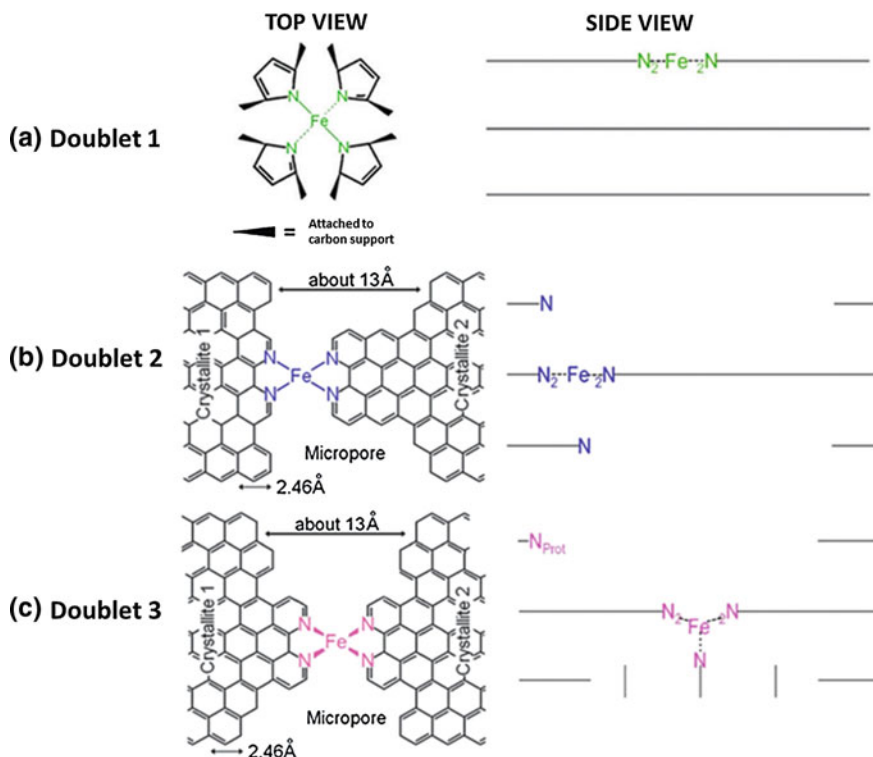


Fig. 12 Schematic representation of the iron–nitrogen coordinated sites observed using Mössbauer spectroscopy for catalysts prepared by heat-treating a mixture of iron acetate and carbon black in ammonia. Depicted are **a** FeN_4/C , **b** $\text{FeN}_{2+2}/\text{C}$, and **c** five-nitrogen coordinated $\text{N}-\text{FeN}_{2+2}/\text{C}$. The majority of ORR activity is attributed to sites **(a)** and **(c)**. Adapted from Ref. [57] with permission of the PCCP Owner Societies

(Fig. 12a) and $\text{N}-\text{FeN}_{2+2}/\text{C}$ structure with a fifth coordinated nitrogen (Fig. 12c) that were found to be responsible for ORR activity in catalysts prepared by heat-treating a mixture of iron acetate and carbon black in ammonia [57]. Particularly, the $\text{N}-\text{FeN}_{2+2}/\text{C}$ structure was unique to catalysts that were subjected to a heat treatment in ammonia. MEA performance variations of ammonia-treated catalysts were also later ascribed to increased reactant accessibility induced by ammonia treatment [12].

The other debate in the non-PGM catalyst community is whether or not there is a second active site species at play. Hydrogen peroxide is commonly produced as an intermediate or ORR by-product. Serov et al. [29] based on an observed loading dependence on RDE activity showed that the ORR occurs by a 2×2 electron reduction mechanism on catalysts prepared by heat-treating a mixture of iron chloride, polyethyleneimine, and carbon black. This unveils the rather complicated mechanism of oxygen reduction, as the generated hydrogen peroxide could very

likely undergo chemical decomposition (forming oxygen and hydrogen) or be electrochemically reduced to water. The extent of each of these occurrences is unknown and difficult to differentiate through experimentation. Based on results from in situ XAS experiments, Mukerjee et al. [25] claimed that the first 2-electron reduction of oxygen to hydrogen peroxide occurs on the aforementioned FeN_4/C moieties. These hydrogen peroxide species then migrate to a secondary active site where they are electrochemically reduced, resulting in an overall four-electron process.

The theories and hypotheses proposed are traditionally based on results from an array of surface and structural characterization techniques that are linked to catalyst performance evaluation (discussed in Sect. 3). It is also very likely that the real identity and behavior of the active site structure(s) in non-PGM catalysts is material-dependent and relates to the particular synthesis procedures and conditions selected. It is therefore important to gain a fundamental understanding into each particular system of M–N–C catalysts. Along with overlying trends, established in the field of non-PGM catalysis, this progress is essential toward achieving an established PEFC performance metrics.

4.2 *Mass Transport Facilitation*

As non-PGM catalysts are only a fraction of the cost of conventionally used precious metals, it is economically possible to use significantly higher loadings in the catalyst layer to achieve performance targets. The non-PGM catalyst layers in fuel cells are as much as 100 μm in thickness. At this length scale, mass transport through both the electrode and catalyst structures becomes an important technological challenge that must be addressed [14, 65]. If the developed catalysts have poor intrinsic mass-transport properties, electrode utilization will be very poor and PEFC performance will suffer accordingly. It has become well established that a high content of meso- and macropores is important for the efficient transport of ORR species [12, 57]. This includes the access of oxygen and proton to the catalytically active sites, along with the removal of the product water. To capitalize on the many recent advances, which have dramatically increased the intrinsic ORR activity of heat-treated M–N–C catalysts, rational meso- and macrostructure design strategies must be applied to facilitate effective mass transport. To accomplish this, a few different catalyst preparation strategies have been employed with varying degrees of success.

Serov et al. [66–68] have incorporated silica templates into the reaction mixture that consists of iron, nitrogen, and carbon precursors. The overall synthesis procedure is depicted in Fig. 13a. After a high-temperature heat treatment, the silica template particles are removed using an etching reagent, such as hydrofluoric acid. What remains are highly porous structures that are inverse replicas of the initial silica templates. By this approach, pore size and property tuning can be made by deliberate selection of the silica templates being employed. This not only allows for

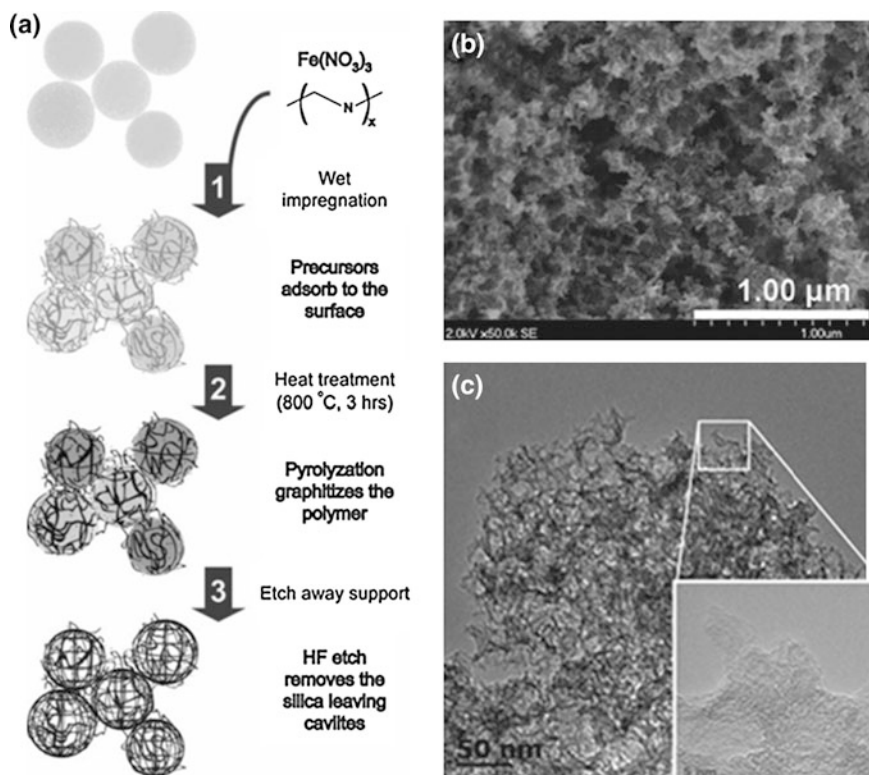
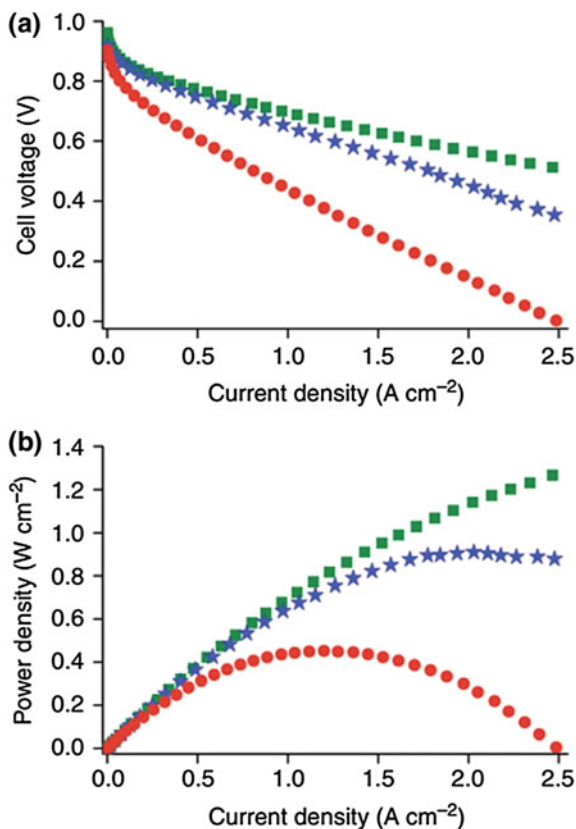


Fig. 13 **a** Schematic representation of the sacrificial support method to prepare catalysts, in which iron, nitrogen, and carbon precursors are mixed with silica templates. After heat treatment, the silica templates are removed by hydrofluoric acid. Reprinted from Ref. [66] Copyright (2012), with permission from Elsevier. **b, c** Transmission and scanning electron microscopy images, respectively, of high-surface-area M–N–C catalysts prepared by the sacrificial support method using 30-nm silica templating particles. Reprinted with permission from Ref. [18], copyright Wiley

practical performance gains realized using this technique, but also provides valuable opportunity to generate fundamental information regarding the effect of pore sizes and structures on catalyst activity and MEA performance. Using 30-nm silica particles mixed with iron nitrate and carbendazim [18] these authors prepared highly mesoporous catalysts using a heat treatment and successive hydrofluoric acid etching (Fig. 13b, c). Upon integration into electrode structures for $\text{H}_2\text{--O}_2$ MEA evaluation, areal current densities of 120 and 700 mA cm^{-2} were achieved at cell voltages of 0.8 and 0.6 V, respectively (no iR -correction).

Another interesting approach taken to structurally control M–N–C catalysts was first pioneered by Ma et al. [69] and involves metal-organic framework (MOF)-derived catalysts. In this work they heat-treated an in-house prepared cobalt imidazolate MOF to prepare a catalyst that showed promising half-cell electrochemical activity toward oxygen reduction. Proietti et al. [14] advanced on this work, instead

Fig. 14 **a** Polarization curves ($\text{H}_2\text{-O}_2$) and **b** corresponding power density curves for (green squares) state-of-the-art platinum-based cathode with $0.3 \text{ mg}_{\text{Pt}} \text{ cm}^{-2}$ loading, (blue stars) best performing zinc imidazolate framework-derived catalyst [14] and (red dots) the author's previously reported most active iron-based catalyst. Adapted from Ref. [13]. Reprinted by permission from Macmillan Publishers Ltd: [14] copyright (2011)



using a commercial zinc imidazolate framework mixed with 1,10-phenanthroline and iron acetate. These were chosen as iron and nitrogen precursors owing to the authors' previous investigations [13]. Interestingly, after an initial heat treatment in argon and subsequent heat treatment in ammonia, a highly porous catalyst resulted with a high content of both mesopores and micropores [14]. By combining high activity of the optimized catalyst technology with the excellent mass-transport properties arising from the structure, a current density of 1.25 A cm^{-2} at 0.6 V under $\text{H}_2\text{-O}_2$ conditions was achieved, corresponding to a power density of 750 mW cm^{-2} (Fig. 14). This MOF approach is relatively straightforward and feasible; however, only a limited number of MOFs are commercially available. The other alternative is to synthesize the templates in house, where tailoring the structure of the nitrogen ligands in zinc-based MOFs was demonstrated by Zhao et al. [16]. This resulted in different structures of the resulting heat-treated M-N-C catalysts, with the optimal formulation developed by these authors providing a peak power density of 620 mW cm^{-2} at 0.43 V .

Recently, a new method has been developed at Los Alamos National Laboratory to generate highly porous structures using a combined nitrogen precursor approach

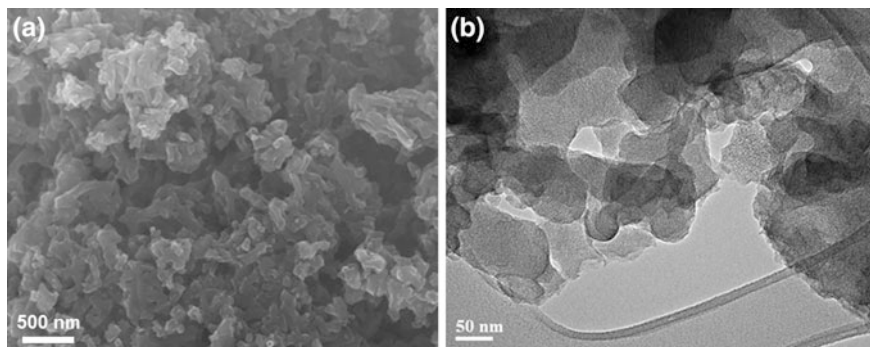


Fig. 15 **a** Scanning and **b** transmission electron microscopy images of highly porous M–N–C derived from the mixed nitrogen precursor approach, using both cyanamide and polyaniline in tandem

[21]. In the method, cyanamide and iron chloride are mixed together, followed by the addition of aniline and subsequent polymerization. Both cyanamide and polyaniline have been previously shown as highly effective precursors [15, 40, 41, 70, 71]. In this work, cyanamide plays an additional role of acting as a pore-forming agent. This technique thereby alleviates the reliance on hazardous etching reagents to remove templates (i.e., hydrofluoric acid) and does not require the inclusion of precursor species that are not involved in active site formation (i.e., zinc). After the addition of carbon black, the precursor mixture is subject to a first heat treatment in argon. The materials are then acid-leached to remove surface inactive species, and a second heat treatment is done in argon. The resulting catalyst is highly porous, including a microporous surface area of more than $1500 \text{ m}^2 \text{ g}^{-1}$ and a large content of mesopores observed through electron microscopy (Fig. 15). This structural arrangement translates to high performance in an H_2 – O_2 and H_2 –air tested MEA, including a power density of 870 mW cm^{-2} at 0.4 V and 380 mW cm^{-2} at 0.50 V, respectively.

It is important that the mass-transport properties of heat-treated M–N–C catalysts be taken into consideration when attempting to translate excellent ORR kinetics into practical fuel cell performance. Strategies must continue to be developed that are effective at simultaneously providing electrokinetic improvements, along with excellent active site accessibility throughout the relatively thick non-PGM catalyst layers.

5 Summary

Although the fuel cell performance of heat-treated non-PGM catalysts has been dramatically improved over the past two decades, further improvements are still required to compete with state-of-the-art Pt catalysts. Due to the fact that an

essential heat treatment of a combination of nitrogen precursors metal precursors, and carbon supports produces catalysts with varying degrees of ORR activity, researchers have been led to adopt a variety of precursors and synthetic approaches to advance non-PGM catalyst development. Though indispensable, the heat treatment destroys the initial structure of precursors, producing a highly heterogeneous, complicated structure that makes it very difficult to elucidate and understand the active site(s) of the resulting non-PGM catalysts. For this reason, the development of non-PGM catalysts depends more on a trial-and-error type approach, rather than scientific studies that are rationally guided by fundamental knowledge surrounding the active site structure(s) and their formation. It is therefore becoming increasingly clear that active site understanding is required in order to propel non-PGM catalyst development to new levels of achievement. According to published papers about non-PGM catalysts, the nitrogen precursor selection plays one of the most important roles in governing ORR activity when comparing a variety of different non-PGM catalysts. Therefore, understanding how the structure and properties of the different nitrogen precursors influence the nanostructure, surface properties, and activity of the resultant catalysts after heat treatment is an important starting point.

Another important issue related to this type of non-PGM catalysts is durability. Until now, no non-PGM catalyst has been demonstrated to be durable under practical PEFC operating conditions. From the practical application viewpoint, durability is as important as performance. Therefore, understanding the cause of performance loss of this type of non-PGM catalysts and developing durable alternatives are also an urgent research field. Applying a host of diverse physico-chemical analysis tools in conjunction with electrochemical and fuel cell tests is crucial in this endeavor, and has been the focus of a large number of investigations. Considering the complex structure of non-PGM catalysts, thorough investigations must be carried out that provide fundamental insight, exceeding these now “routine” studies. Sophisticated techniques, including a host of both microscopy and spectroscopy experiments are required in tandem, with the ability to investigate catalysts in situ (either in “half-cell” or MEA), potentially providing the key to breakthroughs in terms of elucidating the active site structure(s) of the most active non-PGM catalysts prepared to date.

References

1. U.S. Department of Energy’s 2014 Annual Merit Review and Peer Evaluation Meeting Presentation (2014) Fuel cell transportation cost analysis. http://www.hydrogen.energy.gov/pdfs/review14/fc018_james_2014_o.pdf
2. Bing Y, Liu H, Zhang L, Ghosh D, Zhang J (2010) Nanostructured Pt-alloy electrocatalysts for PEM fuel cell oxygen reduction reaction. *Chem Soc Rev* 39:2184–2202
3. Higgins D, Hoque MA, Seo MH, Wang R, Hassan F, Choi JY, Pritzker M, Yu A, Zhang JJ, Chen Z (2014) Development and simulation of sulfur-doped graphene supported platinum with exemplary stability and activity towards oxygen reduction. *Adv Funct Mater* 24: 4325–4336

4. Higgins DC, Wang R, Hoque MA, Zamani P, Abureden S, Chen Z (2014) Morphology and composition controlled platinum-cobalt alloy nanowires prepared by electrospinning as oxygen reduction catalyst. *Nano Energy* 10:135–143
5. Shao Y, Liu J, Wang Y, Lin Y (2009) Novel catalyst support materials for PEM fuel cells: current status and future prospects. *J Mater Chem* 19:46–59
6. Hoque MA, Hassan FM, Higgins D, Choi JY, Pritzker M, Knights S, Ye S, Chen Z (2014) Multigrain platinum nanowires consisting of oriented nanoparticles anchored on sulfur-doped graphene as a highly active and durable oxygen reduction electrocatalyst. *Adv Mater* 27:1229–1234
7. Higgins DC, Chen Z (2013) Recent progress in non-precious metal catalysts for PEM fuel cell applications. *Can J Chem Eng* 91:1881–1895
8. Chen Z, Higgins D, Yu A, Zhang L, Zhang J (2011) A review on non-precious metal electrocatalysts for PEM fuel cells. *Energy Environ Sci* 4:3167–3192
9. Jaouen F, Proietti E, Lefèvre M, Chenitz R, Dodelet JP, Wu G, Chung HT, Johnston CM, Zelenay P (2010) Recent advances in non-precious metal catalysis for oxygen-reduction reaction in polymer electrolyte fuel cells. *Energy Environ Sci* 4:114–130
10. Wu G, Zelenay P (2013) Nanostructured nonprecious metal catalysts for oxygen reduction reaction. *Acc Chem Res* 46:1878–1889
11. Jaouen F, Herranz J, Lefèvre M, Dodelet JP, Kramm UI, Herrmann I, Bogdanoff P, Maruyama J, Nagaoka T, Garsuch A, Dahn JR, Olson T, Pylypenko S, Atanassov P, Ustinov EA (2009) Cross-laboratory experimental study of non-noble-metal electrocatalysts for the oxygen reduction reaction. *ACS Appl Mater Interfaces* 1:1623–1639
12. Kramm UI, Lefèvre M, Larouche N, Schmeisser D, Dodelet J-P (2013) Correlations between mass activity and physicochemical properties of Fe/N/C Catalysts for the ORR in PEM fuel cell via Fe Mössbauer spectroscopy and other techniques. *J Am Chem Soc* 136:978–985
13. Lefevre M, Proietti E, Jaouen F, Dodelet JP (2009) Iron-based catalysts with improved oxygen reduction activity in polymer electrolyte fuel cells. *Science* 324:71–74
14. Proietti E, Jaouen F, Lefevre M, Larouche N, Tian J, Herranz J, Dodelet JP (2011) Iron-based cathode catalyst with enhanced power density in polymer electrolyte membrane fuel cells. *Nat Commun* 2:416
15. Wu G, More KL, Johnston CM, Zelenay P (2011) High-performance electrocatalysts for oxygen reduction derived from polyaniline, iron, and cobalt. *Science* 332:443–447
16. Zhao D, Shui JL, Grabstanowicz LR, Chen C, Commet SM, Xu T, Lu J, Liu DJ (2014) Highly efficient non-precious metal electrocatalysts prepared from one-pot synthesized zeolitic imidazolate frameworks. *Adv Mater* 26:1093–1097
17. Choi J, Hsu R, Chen Z (2010) Highly active porous carbon-supported nonprecious metal-N electrocatalyst for oxygen reduction reaction in PEM fuel cells. *J Phys Chem C* 114:8048–8053
18. Serov A, Artyushkova K, Atanassov P (2014) Fe-N-C oxygen reduction fuel cell catalyst derived from carbendazim: synthesis, structure, and reactivity. *Adv Energy Mater* 4:1301735
19. Zitolo A, Goellner V, Armel V, Sougrati MT, Mineva T, Stievano L, Fonda E, Jaouen F (2015) Identification of catalytic sites for oxygen reduction in iron- and nitrogen-doped graphene materials. *Nat Mater* 14:937–942
20. U. S. Drive (2013) Fuel cell technical team roadmap. http://energy.gov/sites/prod/files/2014/02/f8/fctt_roadmap_june2013.pdf
21. U.S. Department of Energy's 2014 Annual Merit Review and Peer Evaluation Meeting Presentation (2014) Non-precious metal fuel cell cathodes: catalyst development and electrode structure design. http://www.hydrogen.energy.gov/pdfs/review14/fc107_zelenay_2014_o.pdf
22. Jahnke H, Schoenborn M, Zimmermann G *Electrochem Soc* 303–318
23. Biddinger EJ, von Deak D, Ozkan US (2009) Nitrogen-containing carbon nanostructures as oxygen-reduction catalysts. *Top Catal* 52:1566–1574
24. Mamtani K, Ozkan US (2015) Heteroatom-doped carbon nanostructures as oxygen reduction reaction catalysts in acidic media: an overview. *Catal Lett* 145:436–450

25. Tylus U, Jia Q, Strickland K, Ramaswamy N, Serov A, Atanassov P, Mukerjee S (2014) Elucidating oxygen reduction active sites in pyrolyzed metal–nitrogen coordinated non-precious-metal electrocatalyst systems. *J Phys Chem C* 118:8999–9008
26. Ramaswamy N, Tylus U, Jia Q, Mukerjee S (2013) Activity descriptor identification for oxygen reduction on nonprecious electrocatalysts: linking surface science to coordination chemistry. *J Am Chem Soc* 135:15443–15449
27. Nallathambi V, Lee JW, Kumaraguru SP, Wu G, Popov BN (2008) Development of high performance carbon composite catalyst for oxygen reduction reaction in PEM proton exchange membrane fuel cells. *J Power Sources* 183:34–42
28. Olson TS, Pylypenko S, Fulghum JE, Atanassov P (2010) Bifunctional oxygen reduction reaction mechanism on non-platinum catalysts derived from pyrolyzed porphyrins. *J Electrochem Soc* 157:B54–B63
29. Serov A, Tylus U, Artyushkova K, Mukerjee S, Atanassov P (2014) Mechanistic studies of oxygen reduction on Fe-PEI derived non-PGM electrocatalysts. *Appl Catal B* 150–151:179–186
30. Hudak NS, Galloway JW, Barton SC (2009) Mediated biocatalytic cathodes operating on gas-phase air and oxygen in fuel cells. *J Electrochem Soc* 156:B9–B15
31. Parvez K, Yang S, Hernandez Y, Winter A, Turchanin A, Feng X, Müllen K (2012) Nitrogen-doped graphene and its iron-based composite as efficient electrocatalysts for oxygen reduction reaction. *ACS Nano* 6:9541–9550
32. Matter PH, Wang E, Arias M, Biddinger EJ, Ozkan US (2006) Oxygen reduction reaction catalysts prepared from acetonitrile pyrolysis over alumina-supported metal particles. *J Phys Chem B* 110:18374–18384
33. Matter PH, Zhang L, Ozkan US (2006) The role of nanostructure in nitrogen-containing carbon catalysts for the oxygen reduction reaction. *J Catal* 239:83–96
34. Garsuch A, MacIntyre K, Michaud X, Stevens DA, Dahn JR (2008) Fuel cell studies on a non-noble metal catalyst prepared by a template-assisted synthesis route. *J Electrochem Soc* 155:B953–B957
35. Kim JH, Ishihara A, Mitsushima S, Kamiya N, Ota KI (2007) Catalytic activity of titanium oxide for oxygen reduction reaction as a non-platinum catalyst for PEFC. *Electrochim Acta* 52:2492–2497
36. Maldonado S, Stevenson KJ (2005) Influence of nitrogen doping on oxygen reduction electrocatalysis at carbon nanofiber electrodes. *J Phys Chem B* 109:4707–4716
37. Chung HT, Won JH, Zelenay P (2013) Active and stable carbon nanotube/nanoparticle composite electrocatalyst for oxygen reduction. *Nat Commun* 4:1922
38. Wu G, Johnston CM, More KL, Mack NH, Artyushkova K, Ferrandon M, Nelson M, Pacheco JSL, Conradson SD, More KL, Myers DJ, Zelenay P (2011) Synthesis-structure-performance correlation for polyaniline–Me–C non-precious metal cathode catalysts for oxygen reduction in fuel cells. *J Mater Chem* 21:11392–11405
39. Jaouen F, Herranz J, Lefèvre M, Dodelet JP, Kramm UI, Herrmann I, Bogdanoff P, Maruyama J, Nagaoka T, Garsuch A, Dahn JR, Olson T, Pylypenko S, Atanassov P, Ustinov EA (2009) Cross-laboratory experimental study of non-noble-metal electrocatalysts for the oxygen reduction reaction. *ACS Appl Mater Interfaces* 1:1623–1639
40. Wu G, Chen Z, Artyushkova K, Garzon FH, Zelenay P (2009) Polyaniline-derived non-precious catalyst for the polymer electrolyte fuel cell cathode. *ECS Trans* 16:159–170
41. Wu G, Artyushkova K, Ferrandon M, Kropf AJ, Myers DJ, Zelenay P (2009) Performance durability of polyaniline-derived non-precious cathode catalysts. *ECS Trans* 25:1299–1311
42. Wu G, Mack NH, Gao W, Ma S, Zhong R, Han J, Baldwin JK, Zelenay P (2012) Nitrogen-doped graphene-rich catalysts derived from heteroatom polymers for oxygen reduction in nonaqueous lithium–O₂ battery cathodes. *ACS Nano* 6:9764–9776
43. Bezerra CWB, Zhang L, Liu H, Lee K, Marques ALB, Marques EP, Wang H, Zhang J (2007) A review of heat-treatment effects on activity and stability of PEM fuel cell catalysts for oxygen reduction reaction. *J Power Sources* 173:891–908

44. Bezerra CWB, Zhang L, Lee K, Liu H, Marques AL, Marques EP, Wang H, Zhang J (2008) A review of Fe–N/C and Co–N/C catalysts for the oxygen reduction reaction. *Electrochim Acta* (53):4937–4951
45. Ohms D, Herzog S, Franke R, Neumann V, Wiesener K, Gamburcev S, Kaisheva A, Liev L (1992) Influence of metal ions on the electrocatalytic oxygen reduction of carbon materials prepared from pyrolyzed polyacrylonitrile. *J Power Sources* 38:327–334
46. Peng H, Liu F, Liu X, Liao S, You C, Tian X, Nan H, Luo F, Song H, Fu Z, Huang P (2014) Effect of transition metals on the structure and performance of the doped carbon catalysts derived from polyaniline and melamine for ORR application. *ACS Catal* 4:3797–3805
47. Chung HT, Zelenay P (2015) A simple synthesis of nitrogen-doped carbon micro- and nanotubes. *Chem Commun* 51:13546–13549
48. Li Q, Wu G, Cullen DA, More KL, Mack NH, Chung HT, Zelenay P (2014) Phosphate-tolerant oxygen reduction catalysts. *ACS Catal* 4:3193–3200
49. Wu G, More KL, Xu P, Wang HL, Ferrandon M, Kropf AJ, Myers DJ, Ma S, Johnston CM, Zelenay P (2013) Carbon-nanotube-supported graphene-rich non-precious metal oxygen reduction catalyst with enhanced performance durability. *Chem Commun* 49:3291–3293
50. Wu G, Chen Y-S, Xu B-Q (2005) Remarkable support effect of SWNTs in Pt catalyst for methanol electrooxidation. *Electrochem Commun* 7:1237–1243
51. Wu G, Xu B-Q (2007) Carbon nanotube supported Pt electrodes for methanol oxidation: A comparison between multi- and single-walled carbon nanotubes. *J Power Sources* 174:148–158
52. Ferrari AC, Robertson J (2000) Interpretation of Raman spectra of disordered and amorphous carbon. *Phys Rev B* 61:14095–14107
53. Tuinstra F, Koenig JL (1970) Raman spectrum of graphite. *J Chem Phys* 53:1126–1130
54. Ferrandon M, Kropf AJ, Myers DJ, Artyushkova K, Kramm U, Bogdanoff P, Wu G, Johnston CM, Zelenay P (2012) Multitechnique characterization of a polyaniline–iron–carbon oxygen reduction catalyst. *J Phys Chem C* 116:16001–16013
55. Kramm U, Wurmbach IA, Geppert H, Radnik J, Fiechter S, Bogdanoff P (2011) Influence of the electron-density of FeN-centers towards the catalytic activity of pyrolyzed FeTMPPCl-based ORR-electrocatalysts. *J Electrochem Soc* 158:B69–B78
56. Herranz J, Jaouen F, Lefevre M, Kramm UI, Proietti E, Dodelet JP, Bogdanoff P, Fiechter S, Wurmbach IA, Bertrand P, Arruda TM, Mukerjee S (2011) Unveiling N-protonation and anion-binding effects on Fe/N/C catalysts for O₂ reduction in proton-exchange-membrane fuel cells. *J Phys Chem C* 115:16087–16097
57. Kramm UI, Herranz J, Larouche N, Arruda TM, Lefevre M, Jaouen F, Bogdanoff P, Fiechter S, Wurmbach IA, Mukerjee S, Dodelet JP (2012) Structure of the catalytic sites in Fe/N/C-catalysts for O₂-reduction in PEM fuel cells. *Phys Chem Chem Phys* 14:11673–11688
58. Matter PH, Wang E, Arias M, Biddinger EJ, Ozkan US (2007) Oxygen reduction reaction activity and surface properties of nanostructured nitrogen-containing carbon. *J Mol Catal A Chem* 264:73–81
59. Matter PH, Wang E, Millet JMM, Ozkan US (2007) Characterization of the iron phase in CN_x-based oxygen reduction reaction catalysts. *J Phys Chem C* 111:1444–1450
60. Liu G, Li XG, Ganesan P, Popov BN (2009) Development of non-precious metal oxygen-reduction catalysts for PEM fuel cells based on N-doped ordered porous carbon. *Appl Catal B* 93:156–165
61. Jaouen F, Lefevre M, Dodelet JP, Cai M (2006) Heat-treated Fe/N/C catalysts for O₂ electroreduction: Are active sites hosted in micropores? *J Phys Chem B* 110:5553–5558
62. Jaouen F, Marcotte S, Dodelet JP, Lindbergh G (2003) Oxygen reduction catalysts for polymer electrolyte fuel cells from the pyrolysis of iron acetate adsorbed on various carbon supports. *J Phys Chem B* 107:1376–1386
63. Li W, Yu A, Higgins DC, Llanos BG, Chen Z (2010) Biologically inspired highly durable iron phthalocyanine catalysts for oxygen reduction reaction in polymer electrolyte membrane fuel cells. *J Am Chem Soc* 132:17056–17058
64. Zagal JH, Griveau S, Silva F, Nyokong T, Bedioui F (1992) Metallophthalocyanines as catalysts in electrochemical reactions. *Coord Chem Rev* 119:89–136

65. Higgins D, Chen Z (2013) Electrocatalysis in fuel cells. In: Shao M (ed) *Lecture Notes in Energy Ch. 9*, vol 9. Springer, London, pp 247–269
66. Serov A, Robson MH, Artyushkova K, Atanassov P (2012) Templated non-PGM cathode catalysts derived from iron and poly(ethyleneimine) precursors. *Appl Catal B* 127:300–306
67. Robson MH, Serov A, Artyushkova K, Atanassov P (2013) A mechanistic study of 4-aminoantipyrine and iron derived non-platinum group metal catalyst on the oxygen reduction reaction. *Electrochim Acta* 90:656–665
68. Serov A, Robson MH, Smolnik M, Atanassov P (2012) Templated bi-metallic non-PGM catalysts for oxygen reduction. *Electrochim Acta* 80:213–218
69. Ma S, Goenaga GA, Call AV, Liu D-J (2011) Cobalt imidazolate framework as precursor for oxygen reduction reaction electrocatalysts. *Chem Eur J* 17:2063–2067
70. Zamani P, Higgins D, Hassan F, Jiang G, Wu J, Abureden S, Chen Z (2014) Electrospun iron–polyaniline–polyacrylonitrile derived nanofibers as non-precious oxygen reduction reaction catalysts for PEM fuel cells. *Electrochim Acta* 139:111–116
71. Chung HT, Johnston CM, Artyushkova K, Ferrandon M, Myers DJ, Zelenay P (2010) Cyanamide-derived non-precious metal catalyst for oxygen reduction. *Electrochem Commun* 12:1792–1795

Non-noble Metal (NNM) Catalysts for Fuel Cells: Tuning the Activity by a Rational Step-by-Step Single Variable Evolution

Alessandro H.A. Monteverde Videla, Luigi Osmieri
and Stefania Specchia

1 Introduction

A sustainable high quality of life cannot be kept apart from the worldwide supply of a clean, safe, reliable and secure energy, taking into account that the energy demand is growing more and more every year. The European “World Energy Technology and Climate Policy Outlook” (WETO) predicted, for primary energy, an average growth rate worldwide of 1.8 % per year for the period 2000–2030 [1]. Recently, the Annual Energy Outlook 2015 (AEO2015) [2] illustrated the projection of the primary fuel consumption forecast for the period 2013–2040, where renewable energy consumed is expected to increase by 10 % compared to the 2015 (Fig. 1).

Renewable energies are assumed as biomass, hydro power, geothermal energy, solar energy, wind energy, and wave power. It is forecasted that wind-powered generation, the second largest category of renewable electricity generation in 2013 after hydro power, will become the largest contributor in 2040 (including wind generation by utilities and end-users onsite). However, solar photovoltaic (6.8 %/year), geothermal (5.5 %/year), and biomass (3.1 %/year) will increase at faster average annual rates than the wind (2.4 %/year) [2]. Depending on weather conditions and day/night cycles, solar, wind and wave power energy produce intermittent energy. When energy production exceeds energy consumption, the excess of energy can be stored, to exploit it when production is not enough (peaks of electricity consume). Different approaches for energy storage can be used: i. mechanical energy storage (pumped hydro energy storage, or compressed air energy storage);

A.H.A. Monteverde Videla (✉) · L. Osmieri · S. Specchia
Politecnico Di Torino, Department of Applied Science and Technology, Institute of Chemical Engineering, Gre.En2 Group (Green Energy & Engineering Group), Corso Duca degli Abruzzi 24, 10129 Turin, Italy
e-mail: alessandro.monteverdevidela@polito.it

S. Specchia
e-mail: stefania.specchia@polito.it

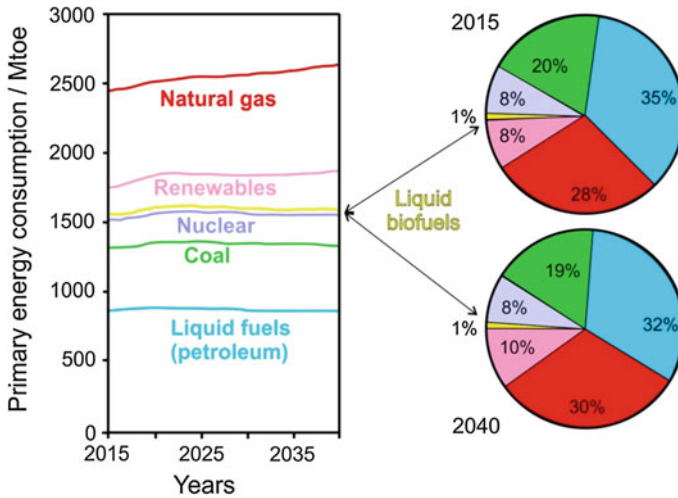


Fig. 1 Projections of the world primary energy consumption in million tons of oil equivalent (Mtoe) by fuel type from today to 2040. Data from [2]

ii. electrical storage through batteries (Lead acid battery, nickel battery, sodium-sulfur battery, lithium battery, metal-air battery, and redox flow battery); iii. chemical storage via fuel cells (FCs), where hydrogen can be used as energy vector [3]. In particular, molten carbonate fuel cell (MCFC), proton exchange membrane fuel cell (PEMFC), alkaline fuel cell (AFC), solid oxide fuel cell (SOFC), and phosphoric acid fuel cell (PAFC) are used as hydrogen technology, with electric conversion varying from 50 to 80 % [4, 5].

Specifically, low-temperature fuel cells (LTFCs) based on PEM and fed with hydrogen (direct hydrogen fuel cells, DHFCs) or methanol produced by biomass (direct methanol fuel cells, DMFCs) are being recognized to be among the best candidates as pollution-free and energy-saving power sources for electric or hybrid vehicles or portable apparatuses because of their high-energy conversion efficiency ($\sim 58\%$) and zero or nearly zero emissions [4-6].

1.1 Technical Challenges

Currently, cost and durability are the main limitations of FC technology to be commercialized. Development of low-cost FC components allows being competitive compared to other technologies now on the market [6, 7]. Compared to gasoline internal combustion engines (ICEs) that currently cost about 25-35 U.S./kW, FC current cost must be reduced by 30-35 U.S./kW to be competitive on the market [8]. A significant percentage of the cost of PEMFCs comes from precious group metal (PGM) based catalysts that are used for oxidation and reduction

reactions. Other significant costs are membrane, cell hardware, and balance-of-plant (BoP) components [4–8]. In particular, the oxygen reduction reaction (ORR) is one of the key factors that determines FC cost and performance. Currently, the use of PGM catalysts contributes to a large portion of the cost of a state-of-the-art PEMFC stack [5–9]. A recent technical report from the United States Department of Energy [8] forecasted a cost of 55 U.S.\$/kW for a 80 kW stack based on PGM (Platinum-based) catalyst, produced as 500,000 units per year (Fig. 2a). In the cost breakdown of the stack, with platinum commodity price accounted as 1,500 U.S.\$ per troy ounce [8], the cost of the catalyst plus its application accounts for 49 % (20 % only for purchasing Pt) of the total price of the stack itself (Fig. 2a). Considering the highly variable price of the Pt commodity at the stock exchange (Fig. 2b) [9], the development of alternative cheaper catalysts is currently driving the research efforts worldwide.

Durability is an additional key factor affecting the PEMFC performance. In fact, platinum dissolution/coalescence phenomena and carbon support corrosion are mainly responsible for PEMFC degradation. It is clear that the current catalysis technology cannot satisfy both cost and durability requirements for a widespread PEMFC commercialization. Therefore, a breakthrough in the development of cost-effective, highly performant, and durable catalysts has been identified as the determining factor for success toward PEMFC commercialization [10–12]. Thus, the formulation of a new generation of ORR electrocatalysts to overcome the existing bottlenecks is now the focus of many research teams around the world. In past years, two critical electrocatalyst research directions have been identified and carried out: one focused on low PMG loading cathodic electrocatalyst development [13–25], the other focused on non-noble metal (NNM) cathodic electrocatalyst exploration [26–32]. For long-term strategy toward commercialization, NNM catalysts would be the everlasting solution [12]. As a matter of fact, preliminary new cost breakdown analyses estimate the cost of a NNM-based 80 kW PEMFC stack as 30 U.S.\$/kW, with a cost of 0.35 U.S.\$/kW for the NNM catalyst (Fig. 2a) [33].

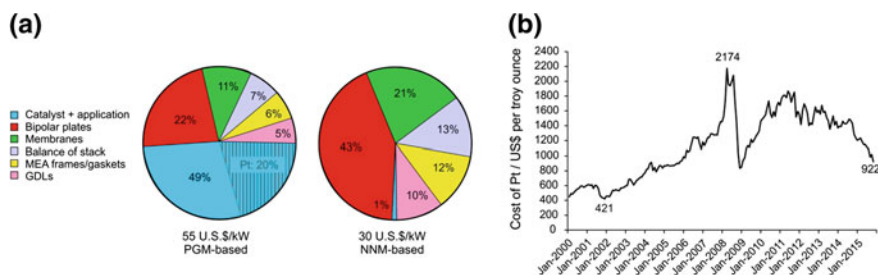


Fig. 2 **a** Cost breakdown of a 80 kW PGM-based stack (assumptions done in 2013: Pt loading $0.153 \text{ mg}_{\text{Pt}} \text{ cm}^{-2}$; power density 692 mW cm^{-2} ; Pt price assumed as 1,500 U.S.\$ per troy ounce; 500,000 units per year production [8]) and of a 80 kW NNM-based stack (assumptions done on 2015: NNM loading $4 \text{ mg}_{\text{cat}} \text{ cm}^{-2}$; power density 370 mW cm^{-2} ; catalyst cost 0.35 U.S.\$/kW; 500,000 units per year production [33]). **b** Oscillations of the Pt commodity price from January 2000 to October 2015 [9]

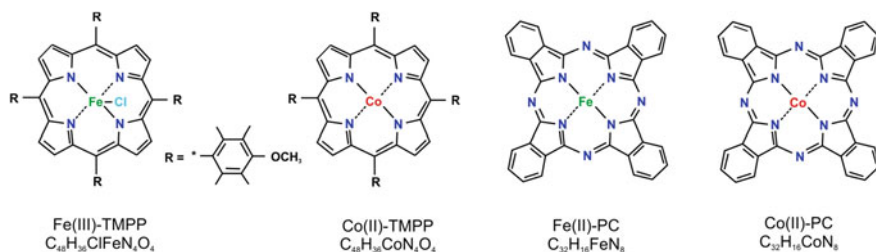


Fig. 3 Structural formula of typical NNM catalysts precursors used for ORR

Considering the current average state-of-the-art level of specific power density ranging from 300 to 400 mW cm^{-2} reached for NNM catalysts [33], the improvement of this parameter to levels close to the specific power density of PGM catalysts (more than 700 mW cm^{-2} [8]) is crucial on the point of view of the stack size and dimensioning.

Among the available precursors, NNM macrocycles such as iron(III) 5,10,15,20-tetrakis(4-methoxyphenyl)-21H,23H-porphine ($C_{44}H_{36}ClFeN_4O_4$, Fe-TMPP), cobalt(II) 5,10,15,20-tetrakis(4-methoxyphenyl)-21H,23H-porphine ($C_{44}H_{36}CoN_4O_4$, Co-TMPP), iron(II) phthalocyanine ($C_{32}H_{16}FeN_8$, Fe-PC), cobalt(II) phthalocyanine ($C_{32}H_{16}CoN_8$, Co-PC), and chalcogenides have been considered so far to replace PGM-based catalysts for ORR (Fig. 3) [34–39].

Within the various NNM electrocatalysts, the most promising ones seem to be heat-treated Fe(II) and/or Co(II) chelates and macrocycles supported on carbon particles [12, 40–56]. The formation of metal–nitrogen ($M-N_X/C$) and metal–carbon (M/C) active ensembles after the heat treatment is necessary for ORR (Fig. 4), as emphasized by the groups of Yeager [48–50], Zelenay [12, 52, 53] and Dodelet [44, 51, 52, 57].

“Active ensembles” represent a specific arrangement of surface atoms that favors the ORR reaction in this case [58]. According to the literature, in fact, two types of active ensembles are considered the most active: $M-N_2/C$ and $M-N_4/C$, produced by heat treatment (500–1000 °C) normally under inert or reducing atmospheres [12, 57]. Van Veen et al. [56] concluded that the continuing existence of the $M-N_4$ moiety of the chelate is the structural feature associated with the high activity of

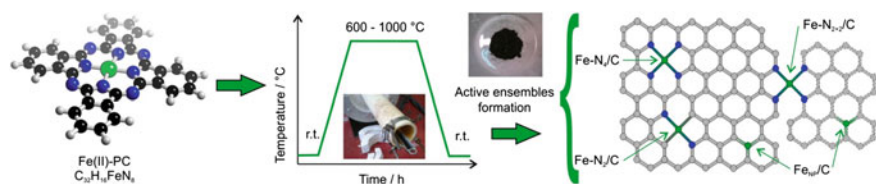


Fig. 4 Formation of active ensembles from the heat treatment of a macrocycle (iron-phthalocyanine Fe-PC) containing Fe (green), N (blue), and C (gray) atoms: $Fe-N_4/C$, $Fe-N_2/C$, and Fe_{N_2}/C on the same carbon sheet, $Fe-N_{2+2}/C$ linking two separate carbon sheets

heat-treated materials. Also, metal nanoparticles embedded in the carbon structure, M_{NP}/C , are considered active ensembles, especially when used in acidic environment to complete the reduction of H_2O_2 to H_2O : together with $M-N_X/C$ active ensembles, they act as a dual-site ORR catalyst [59].

As summarized by Dodelet [57], to form ORR active ensembles, three conditions are necessary contemporarily: (i) nitrogen/metal (or nitrogen/metal/carbon) sources, (ii) carbon support, and (iii) heat treatment. Regarding the carbon support, various types of carbons, such as active carbon, Black Pearls BP2000 with pore filler, and Vulcan XC-72 have been explored in recent years [57]. Jaouen et al. [51, 52] suggested that the porosity plays an important role in forming ORR active ensembles. Specifically, only micropores formed during pyrolyzation host catalytic sites. In fact, the use of highly microporous carbon supports did not improve the activity relative to catalysts made with non-microporous carbon supports [60]. The reason lies mainly in the low disordered carbon content of the starting carbon materials, which is not favoring the anchoring of surface nitrogen [60]. In this regard, only micro- and mesopores formed during pyrolyzation may be more efficient in hosting active ensembles [57]. Therefore, exploring new carbon supports which possess highly disordered carbon structure, whose surface can be easily doped by nitrogen, should be one of the approaches in improving the ORR catalytic activity of NNM catalysts through the increase of micro- and mesoporosity [51].

The role of the transition metal used to form active ensembles is still debated. The question is if transition metals participate directly into the oxygen reduction mechanism or if they only help as catalyst or promoter for fixing nitrogen into the carbon framework [50–55]. Unfortunately, most of the explored heat-treated NNM catalysts up to now show relatively low activity and stability compared to PGM catalysts in the acidic operating environment of a real PEMFC [51, 54]. Considering that transition metals usually have a very low concentration in the catalysts (less than 0.5 wt% [57]), the concentration of active ensembles is expected to be low as well. This means that to distinguish the real active ensembles taking part to the reaction is a very difficult task. Conventional physicochemical characterizations are not anymore sufficient, that is, specific in situ techniques under operating conditions as extended X-ray absorption spectroscopy fine structure (EXAFS), X-ray absorption near-edge spectroscopy (XANES), for example, become necessary to understand ORR reaction mechanisms [59] for elucidating electrocatalytic pathways in complex reaction centers. Until now the maximum FC performance using NNM catalysts available in the literature are listed in Table 1.

Different approaches have been adopted to synthesize the active NNM catalysts listed in Table 1. For the first one, ammonia was used as nitrogen source fluxing it into a hot tubular furnace containing the mixture of carbon and transition metal [60]. For the second one, aniline was polymerized in the presence of a transition metal, then two consecutive pyrolyzations were performed [12]. For the third one, a dry macrocyclic molecule was mixed with a porous silica template and then pyrolyzed in

Table 1 Performance of NNM catalysts available in the literature measured in single cell PEMFC at 80 °C, fully humidified H₂ and O₂

Research group	Starting precursors of Fe-N _x -C catalysts developed, and pyrolyzation conditions	Max power density (mW cm ⁻²)	Specific power density (mW mg _{NNM} ⁻¹)	PEMFC conditions used
Lefèvre et al. [60]	Black Pearls 2000 mixed with iron acetate, ball milling. Pyrolyzation @ 1050 °C in NH ₃	280	280	5 cm ² MEA Nafion 117, cathode: 5 mg _{NNM} cm ⁻² ; anode: 0.5 mg _{Pt} cm ⁻² (Pt/C 20 wt %), 1 bar gauge, 0.5 bar attributed to water vapor
Wu et al. [12]	Ketjen black EC 300 J mixed with aniline, ammonium peroxydisulfate, iron chloride, and cobalt nitrate. Two pyrolyzations in N ₂ from 400 to 1000 °C with intermediate acid leaching	550	138	5 cm ² , MEA Nafion 1135, cathode: 4 mg _{NNM} cm ⁻² ; anode: 0.25 mg _{Pt} cm ⁻² , 2.8 bar gauge
Cheon et al. [61]	FeTMPPCl, CoTMPP and SBA15. Pyrolyzation @ 800 °C in N ₂	700	460	25 cm ² MEA Nafion 212, cathode: 1.52 mg _{NNM} cm ⁻² ; anode: 0.425 mg _{Pt} cm ⁻² (Pt/C 60 wt %), 2 bar, gauge, 0.47 attributed to water vapor
Zitolo et al. [62]	ZIF-8, 1,10-phenanthroline and iron acetate. Pyrolyzation @ 1050 °C in Ar and 5 min @ 950 °C in NH ₃	528	132	5 cm ² MEA Nafion 211, cathode: 4 mg _{NNM} cm ⁻² ; anode: 0.5 mg _{Pt} cm ⁻² , 1 bar gauge
Strickland et al. [63]	2-methylimidazole, zinc nitrate, 1,10 phenanthroline, iron acetate. Pyrolyzation @ 1050 °C in Ar and 18 min @ 1050 °C in NH ₃	380	127	5 cm ² MEA Nafion 211, cathode: 3 mg _{NNM} cm ⁻² ; anode: 0.25 mg _{Pt} cm ⁻² (Pt/C 20 wt %), 1.5 bar gauge
Zhao et al. [64]	Imidazole, ZnO, f tris-1,10-phenanthroline, iron(II) perchlorate (TPI). Pyrolyzation @ 1050 °C in Ar, acid leaching, pyrolyzation 15 min @ 950 °C in NH ₃	620	282	5 cm ² MEA Nafion 211, cathode: 2.2 mg _{NNM} cm ⁻² ; anode: 0.25 mg _{Pt} cm ⁻² (Pt/C 20 wt %), 1.5 bar gauge

order to obtain a porous catalyst [61]. For the fourth one a commercial metal organic framework, zeolitic imidazolate framework (MOF ZIF-8), 1,10-phenanthroline and Fe(II) acetate were dry mixed together in a ball mill, and pyrolyzed first under argon for 1 h and then under ammonia at 950 °C for 5 min. No intermediate acid leaching was performed [62]. For the fifth one, 1,10 phenanthroline, Fe(II) acetate, 2-methylimidazole and Zn(II) nitrate were mixed together to obtain a complex used to impregnate an in-house synthesized MOF. Two pyrolysis steps followed, first under argon at 1050 °C for 1 h, then under ammonia for 18 min, without intermediate acid leaching [63]. For the sixth catalyst, 5 % of tris-1,10-phenanthroline Fe(II) perchlorate was mixed with ZnO and imidazole, ground and sealed in an autoclave for 18 h at 180 °C. The product was first pyrolyzed at 1050 °C for 1 h under argon, and then under ammonia for 15 min at 950 °C, with an intermediate acid leaching [64]. In these six different syntheses, high temperature and porosity of the support play an important role in the production of highly active electrocatalyst as well as the pyrolysis atmosphere and the transition metals used.

In this chapter, we will describe an enhancement of the electrochemical activity toward ORR through a step-by-step understanding of the variables involved during the formation of active NNM catalysts. As we understood during these years [65–76], active ensembles formation during the pyrolyzation is affected by a multiple variables process that involves, respectively: (i) the carbon source (mesoporous carbon MPC, carbon nanonetworks CNN, reduced graphene oxide rGO), (ii) the nitrogen source (macrocycles, polymers) coordinated with iron, and (iii) the temperature of the pyrolysis. The synthesis of NNM catalysts results through the decomposition of reagents (release of gases), and the consequent formation of new solid phases whose rearrangement forms new compounds, the active ensembles [76, 77]. The real understanding of this multivariable process is still not clear. The ideal situation should be a synthesis process, based on the use of reagents containing a transition metal, nitrogen, and carbon, whose parameters should be controlled to produce a homogenous catalyst. Unfortunately, according to the current state of the art, the synthesis process is still a difficult task.

We adopted different approaches, described in this chapter and summarized in Fig. 5, in order to understand the formation of active ensembles and to increase the activity by a rational step-by-step progression.

First, three different in-house made porous carbons structures were used as a support, specifically: a hollow core mesoporous shell carbon (MPC), a carbon nanonetwork (CNN), and a reduced graphene oxide (rGO). For all of these carbon structures, iron as Fe(II) acetate was coordinated with the TPTZ as ligand in acid conditions, and the formed complex was impregnated on the carbon-based supports. Then, pyrolyzation in nitrogen atmosphere followed, with a final acid leaching to remove all iron-containing moieties not linked with the support. Second, an in-house made mesoporous carbon (MPC) was functionalized with polypyrrole (PPY), as an alternative source of nitrogen, and impregnated with Fe(II) acetate.

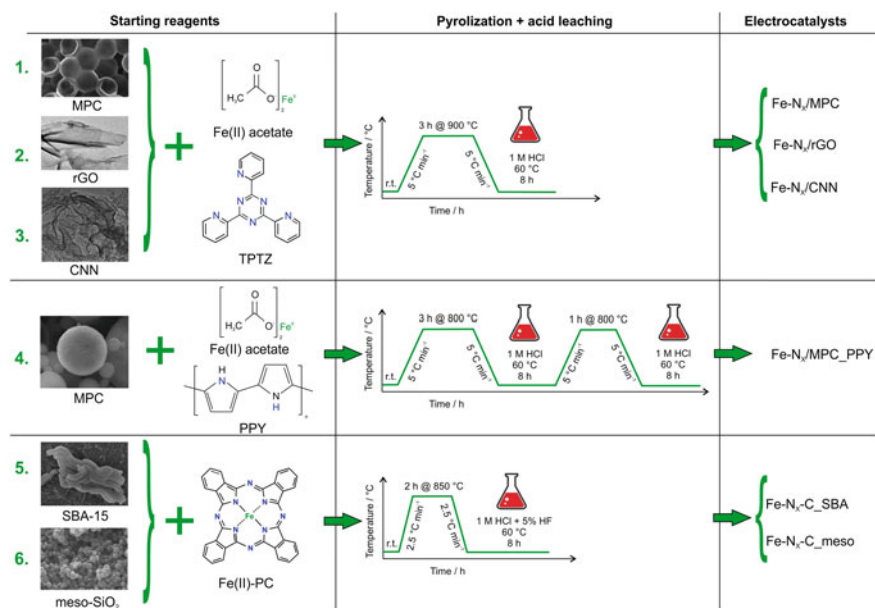


Fig. 5 Rational scheme of the in-house made NNM catalysts prepared

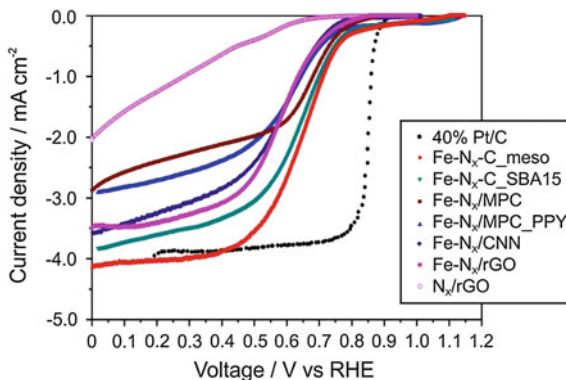
Pyrolyzation was performed in two steps, with intermediate and final acid leaching. Third, the carbon support was no longer used. Iron phthalocyanine (Fe-PC) was used as a unique source of iron, nitrogen, and carbon to synthesize the catalyst. The porosity of the catalyst was obtained by mixing the Fe-PC molecule with two different templating agents, an in-house made SBA15 silica, and a commercial mesoporous silica (meso-SiO₂). A single pyrolyzation was performed, faster compared to previous catalysts, followed by final etching with HF to remove the templating agent, and acid leaching with HCl.

All of the catalysts synthesized are listed in Table 2, and the performance in rotating disk electrode (RDE) in acid conditions are depicted in Fig. 6 [65, 67, 70–72]. In RDE tests (RRDE-3A ALS coupled with a Bio-Logic SP-150 multi-potentiostat), a conventional three-electrode electrochemical cell configuration, equipped with a glassy carbon disk working electrode (0.1256 cm² geometric area), a Pt helical wire counter electrode, and a saturated calomel (SCE) reference electrode, was used. The activity of a commercial 40 % Pt/C (Hyspec 6000 from Johnson Matthey) catalyst was assessed as well, as reference catalyst toward ORR.

Table 2 Electrochemical (from RDE measurements, Fig. 6), chemical (from XPS and EDX analyses), and physical (from BET/BJH analyses) characterization of in-house made NNM catalysts [65, 67, 70–72] (n.a.: not available)

NNM catalysts	Half wave potential (V)	Activity @ 0.8 V (mA cm ⁻²)	Total Fe (at.%)	Total N (at.%)	Pyridinic N (at.%)	Pyrolic N (at.%)	BET s.s. a. (m ² g ⁻¹)	Pore volume (cm ³ g ⁻¹)	Micropore volume (cm ³ g ⁻¹)
Fe-N _x /MPC [65]	0.64	-0.128	n.a.	11.7	50.4	37.9	n.a.	n.a.	n.a.
Fe-N _x /rGO [67]	0.58	-0.032	0.35	4.6	40.0	52.3	n.a.	n.a.	n.a.
N _x /rGO [67]	0.27	-0.004	–	1.3	n.a.	n.a.	n.a.	n.a.	n.a.
Fe-N _x /CNN [70]	0.57	-0.053	0.38	5.7	36.0	28.0	61	0.54	0.01
Fe-N _x /MPC_PPY [72]	0.60	-0.198	0.1	0.4	43.9	39.7	426	0.354	0.115
Fe-N _x -C_SBA [71]	0.63	-0.240	0.2	0.9	33.9	50.3	221	0.2	0.06
Fe-N _x -C_meso [71]	0.64	-0.303	0.1	2.0	23.5	53.3	601	0.8	0.18
Pt/C	0.85	-3.450	–	–	–	–	n.a.	n.a.	n.a.

Fig. 6 ORR performance of in-house made NNM catalysts tested in RDE (conditions: O_2 -saturated 0.5 M H_2SO_4 solution at a rotational speed of 900 rpm; potential scan rate 5 mV s^{-1} ; 40 % Pt/C tested in 0.1 M $HClO_4$; Pt loading: $17 \mu\text{g cm}^{-2}$) [rearranged from 65, 67, 70–72]



2 Influence of the Carbon Support in Forming Active Ensembles

Macrocycles not exposed to any kind of heat treatment have been reported to have electrochemical activity in reducing molecular oxygen [42, 48]. Unfortunately, these macromolecules are not stable under acid conditions, which is one of major issues for application on FCs technology [51, 57, 78].

The electrochemical ability to break the oxygen–oxygen bond is related to the formation of a complex with appropriate coordination between the metal and nitrogen of various nature ($M-N_2/C$, $M-N_4/C$, M_2-N_5/C) [57, 62], or between the metal encapsulated and/or covered by carbon sheets $M-C$ [79–83], or either nitrogen-doped carbon $N-C$ [84], which represent the active ensembles. A natural question comes out: do these compounds exist in nature in order to be used? The answer is yes, i.e., heme derivate, metal carbides, etc. [85, 86]. The problem of these compounds is that they are not totally stable in acid conditions, or they do not have sufficient oxygen vacancy defects. Moreover, they suffer from low electric conductivity, and they are not porous enough to favor the diffusion of reactants to the active ensembles, as is needed for the ORR [13, 87]. In fact, the reduction of oxygen needs an absorber site, which splits the oxygen molecule by bridge mode or on-edge mode, by tuning the electronic surface depending on the electron density [88–90]. Then, a recombination with ions and further formation of products occurs. Generally speaking, for ORR, accessible active ensembles are needed, able to adsorb and desorb reagents and products in a fast way. The combination of accessibility and active ensembles of different nature needs to coexist to boost the ORR. For example, in PGM-based catalysts, Pt adsorbs oxygen strongly enough so that dissociation is favorable, but not so strongly enough to oxidize its surface [91].

It is necessary to underline that mixing a carbonaceous support with a precursor containing carbon, oxygen, nitrogen, and hydrogen with appropriate coordination to the transition metal, two parallel reaction steps coexist during the pyrolysis treatment. The first one is the graphitization of the support until the structure collapses

because of the high temperature. Normally, graphitic carbons are resistant to the thermal process, but their porosity decreases by long exposition time or very high temperatures, losing their conductivity [40, 92, 93]. The second step is the formation of active ensembles because of the decomposition of the precursors from their external and more exposed functional groups. Normally, the decomposition of precursors goes through four major steps: adsorbed water evaporation, sublimation of fragments of the precursor, formation of the active ensembles, graphitization of the carbon structure up to its collapse.

The first variable we faced was the influence of different carbon supports (Fig. 5, catalysts 1, 2, and 3). In these several studies [65, 67, 70, 72] various types of carbons, MPC, rGO, and CNN, respectively, were used as support and impregnated with 2,4,6-Tris(2-pyridyl)-s-triazine (TPTZ) ligand molecule as nitrogen source and Fe(II) acetate as iron source. After an initial drying process, the formed complexes impregnated on the carbon based materials were pyrolyzed and acid leached to remove all iron moieties not anchored to the carbon-based structure.

2.1 *The Use of Mesoporous Carbon (MPC) Hosting the Nitrogen–Iron Active Ensembles*

In this study, three different porous carbons were used as support, specifically: a home-made ultrasonic spray pyrolyzed MPC (MPC_USS), a home-made hollow core shell MPC (MPC_HCS), and a commercial MPC (Ketjen Black CJ600), having BET specific surface areas of 2124, 1187, and 1400 m² g⁻¹, respectively [65]. Iron as Fe(II) acetate was coordinated with the TPTZ ligand molecule in acid conditions. The Fe–TPTZ complex was further impregnated on the three different MPCs, followed by pyrolyzation in nitrogen for 3 h in a tubular furnace with a heating ramp rate of 5 °C min⁻¹ until 900 °C (Fig. 5).

Using the same pyrolysis conditions for the three catalysts, different final nitrogen contents were obtained for each catalyst, varying from 5.4 to 11.7 at.% [65], with the presence of both pyridinic and pyrrolic nitrogen, in different amounts. The most active catalyst, the Fe–N_x on the MPC_HCS (Fe–N_x/MPC in Fig. 6), showed a half-wave potential of 0.64 V versus RHE (Table 2), which is 210 mV less compared to the half-wave potential of the standard Pt/C-based catalyst (Fig. 6 and Table 2). This catalyst was synthesized starting from the carbon support with the lowest BET specific surface area, with the simultaneous presence of both micro- and mesopores (micropore volume of 0.2 cm³ g⁻¹, Fig. 7, Table 2 [65]), compared to the other MPC_USS which, instead had only mesopores. The XPS analysis conducted on the narrow nitrogen spectra enlightened that the higher activity of the Fe–N_x/MPC catalyst, with the MPC_HCS support, can be linked with the higher content of pyridinic nitrogen (more than 50 % of the total N, Fig. 7, Table 2). In fact, the pyridinic nitrogen is known to favor the formation of the most active Fe–N₄ or Fe–N₂ ensembles [57]. Fe(II) ions and four pyrrolic-like nitrogen should be the preferential

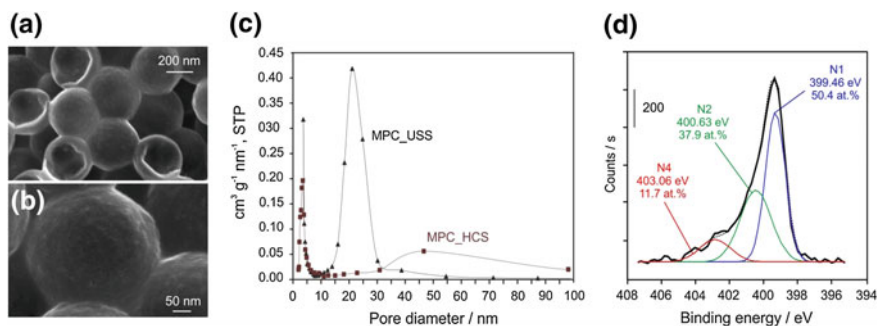


Fig. 7 Fe-N_x/MPC catalyst: FESEM (a, b), pore diameter distribution of the two different MPC used as precursors (c), and XPS (d) analyses. Data from [65]

actors forming active ensembles. In this situation, we assume that carbon pores from the support act as a “microreactor” for the formation of active ensembles (M–N, N–C, or M–C). Moreover, the presence of mesopores should allow the accessibility of the reactants to the active ensembles. The simultaneous presence of both micro- and mesopores explains the activity of this catalyst.

2.2 The Use of Reduced Graphene Oxide (rGO) Hosting the Nitrogen–Iron Active Ensembles

In a second study, rGO was used as support for the impregnation of TPTZ coordinated with iron to synthesize Fe–N_x-based electrocatalysts (Fe–N_x/rGO, Fig. 6) for the ORR. rGO was synthesized via microwave exfoliation method from graphite oxide (GO) obtained by oxidizing graphite flakes. TPTZ was used as a ligand for the Fe–N_x complex, in an analogous way for the preparation of the MPC-based catalysts [67]. The pyrolyzation was conducted for 2 h at 900 °C in a nitrogen atmosphere, with a ramp temperature of 5 °C min⁻¹. Furthermore, to verify the influence of the transition metal on the ORR, a second catalyst, N_x/rGO, was synthesized by following the same procedure, by impregnating the rGO with the starting TPTZ molecule, without using iron(II) acetate. The same heat treatment was performed.

The main idea was to take advantage of the unique properties of planar graphene sheets in order to enhance the electrical conductivity of the final catalyst, compared to the use of other types of carbon supports [94, 95]. Moreover, the use of graphene gained a lot of attention recently due to its outstanding thermal properties and mechanical resistance [96, 97]. In fact, rGO is known for its ability to reduce the molecular oxygen better than other types of carbons [98]. The main problem lies in the accessibility of the reactants to each graphene sheet, in order to really take advantage of its good electric conductivity on the plane [99, 100]. The exfoliation

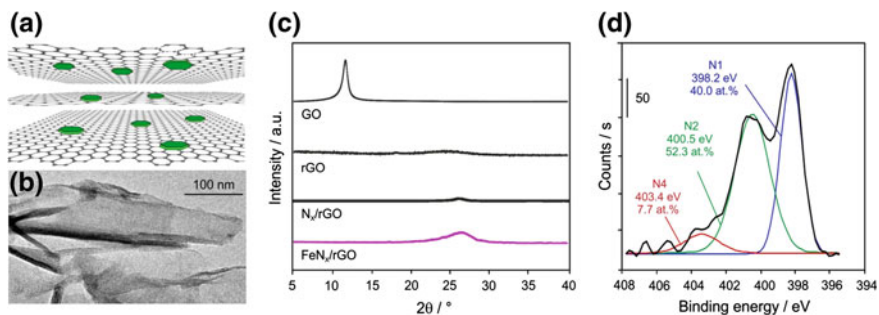


Fig. 8 Fe- N_x /rGO catalyst: scheme of the ideal structure (a); TEM (b), XRD (c: together with graphene oxide GO, rGO and the catalyst without iron, N_x /rGO), and XPS (d) analyses. Data from [67, 101]

process adopted to synthesize rGO should increase the interspace between the sheets, to favor the formation of “surface” active ensembles on both sides of each graphene sheet (Fig. 8a).

Thus, we tried to synthesize a rGO-based catalyst by preserving the characteristic planar structure of the graphene sheets, to maintain the same electric properties of the starting support, and by incorporating surface active ensembles between the sheets, to favor the catalytic activity, as in the ideal scheme of Fig. 5a. The RDE measured ORR activity of the Fe- N_x /rGO catalyst was not as good as expected: with an half-wave potential of 0.58 V versus RHE, its performance was 60 mV lower compared to the Fe- N_x /MPC catalyst previously developed (Fig. 6, Table 2). Interestingly, the N_x /rGO, produced without iron, showed a very limited activity toward the ORR, 0.27 V versus RHE, much lower compared to the Fe- N_x /rGO catalyst, sign that probably also N/C ensembles show activity toward ORR.

According to TEM and XRD analyses (Fig. 8b, c), the amorphous planar structure of the rGO support remained almost unchanged on the Fe- N_x /rGO catalyst: compared to the starting rGO, the sheets appeared to be only slightly agglomerated. It is clear that it was difficult to favor the formation of surface active ensemble between graphene sheets. Apparently, during the pyrolyzation active ensemble were formed preferentially only on the external surface of graphene sheets not facing to other graphene sheets, limiting thus the formation of a higher number of active ensemble between the sheets.

This hypothesis can be linked with the low nitrogen content (4.6 at.%, of which 40 % pyridinic N, and 52.3 % pyrrolic N, from XPS analysis in Fig. 5d and Table 2) fixed to the rGO support and the relatively low electrochemical activity. In fact, the N_x /rGO catalyst, which had lower activity compared to the Fe- N_x /rGO, had lower nitrogen content (1.3 at.%) compared to the Fe- N_x /rGO catalyst [67]. Interestingly, the Fe- N_x /rGO had a lower overall pyridinic N content in comparison to the more active Fe- N_x /MPC catalyst. The formation of more pyrrolic-like N on Fe- N_x /rGO suggests less iron–nitrogen interactions on the catalyst, thus explaining the lower activity toward ORR.

2.3 The Use of Graphitic Interconnected Carbon Nano-Networks (CNN) Hosting the Nitrogen–Iron Active Ensembles

In this section, graphitic CNN was used as support to host active ensembles. The most outstanding properties of CNN are good thermal stability, good electric conductivity, and the interconnection between each single carbon framework, which can lead to a higher overall electric conductivity compared to other graphitic structures [102–104].

Normally in porous carbon materials, active ensembles are bonded or incorporated on the support, which is usually constituted by frameworks not totally connected among them. This causes a decrease of electrical conductivity, with consequent energy dissipation (cut bridges: Fig. 9a) [104–107]. The interconnection among various “frameworks” hosting active ensemble is crucial to have a good overall current density, or electron percolation, and to exploit each active ensemble as a “generator” of electricity.

Several approaches have been pursued recently to connect frameworks of the carbon support among them to increase the electronic percolation [108–110]. One option is to simply mix (mechanically or chemically) a carbon support with the same support already hosting the active ensembles in order to increase the bridging and to favor the interconnections among various frameworks. Another option is to mix carbon structures of different morphology, or, alternatively, to add conductive metals (Cu, Au) to increase the electrical conductivity [111–113].

The main idea of this study was to favor the formation of active ensembles on CNNs, by maintaining the connections among the frameworks (Fig. 9b). Three different CNN supports were synthesized by chemical vapor deposition (CVD) of ethene over nanoparticles of cobalt in different amounts (0.1 to 1.7 wt% [70]).

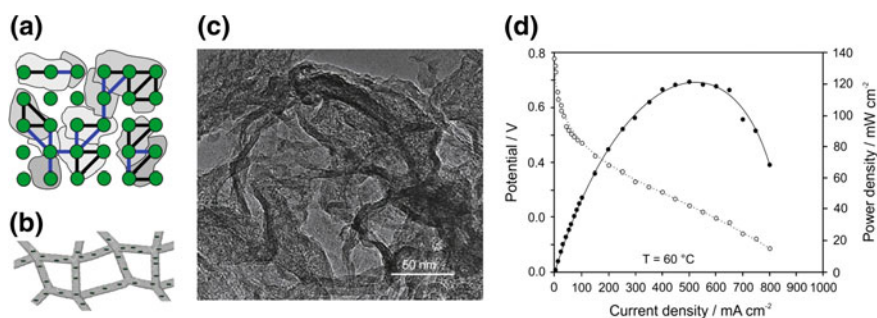


Fig. 9 Fe-N_x/CNN catalyst: scheme of the inter- and intra-framework selectrical conductivity (blue and black bridges, respectively) in porous carbon materials hosting active ensembles: the concept of the cut bridges (a); scheme of the ideal structure of CNN (b); TEM image of CNN (c); polarization and performance in FC single cell at 60 °C (d: conditions used: fully humidified 0.1 NL min⁻¹ H₂ and 0.2 NL min⁻¹ O₂; Fe-N_x/CNN cathode loading = 2.6 mg cm⁻²; commercial PtRu 1:1 at.% anode loading = 2.6 mg cm⁻²; Nafion® 115 membrane). Data from [70]

The BET specific surface areas of these supports were approximately $72 \text{ m}^2 \text{ g}^{-1}$, regardless of the amount of Co used as growing seed. The catalysts were then synthesized by impregnating Fe(II) acetate coordinated with TPTZ under acid conditions and by pyrolyzing the precursors at $900 \text{ }^\circ\text{C}$ for 3 h in nitrogen. After the pyrolyzation, Fe- N_x /CNN catalysts had slightly lower BET specific surface areas, of approx. $62 \text{ m}^2 \text{ g}^{-1}$, with a total pore volume of $0.54 \text{ cm}^3 \text{ g}^{-1}$ and a micropore volume of $0.01 \text{ cm}^3 \text{ g}^{-1}$ (Table 2), suggesting some blockage or diffusion limitation in the accessibility of the active ensembles because of the pyrolysis step, as mentioned in the literature as well [114].

The most active catalyst among the three prepared CNN-based ones (Fe- N_x /CNN in Fig. 6) showed a half-wave potential of 0.57 V versus RHE, lower compared to the Fe- N_x /rGO and Fe- N_x /MPC previously described. HRTEM analyses (Fig. 9c) showed that the starting structure of the CNN was preserved during the synthesis of the catalyst. This result could be due to a less effective incorporation or formation of active ensembles on CNN supports, linked to the low BET specific surface area values (less area available to host active ensembles), much lower compared to the Fe- N_x /rGO and Fe- N_x /MPC catalysts (Table 2). Moreover, the lower micro- and mesopore volumes of the CNN structures compared to those of the rGO and MPC supports, played a role in limiting the accessibility of the reactants to active ensembles. Therefore, the activity could be mainly linked with the good electrical conductivity due to the interconnected frameworks, which remained preserved on the Fe- N_x /CNN.

The activity of the best Fe- N_x /CNN was tested on a single cell MEA, reaching a performance of 121 mW cm^{-2} corresponding to a power density of $47 \text{ mW mg}_{\text{cat}}^{-1}$ at $60 \text{ }^\circ\text{C}$, using fully humidified oxygen and hydrogen (Fig. 9d). The 5 cm^2 MEA (Nafion® 115 membrane) was prepared by loading 2.6 mg cm^{-2} of NNM catalyst at the cathode, and 2.6 mg cm^{-2} of commercial PtRu 1:1 at.% at the anode. This value is almost 10 times less compared to the most active NNM catalyst reported in the literature until nowadays (Table 1 [61, 64]).

2.4 The Use of Polymerized Mesoporous Carbon (MPC_PPY) Hosting the Nitrogen–Iron Active Ensembles

In this work, we investigated the use of home-made MPC together with polypyrrole (PPY) as a source of nitrogen and Fe(II) acetate trying to create more active catalysts. The use of N-containing polymers like PPY has been proved to be an effective and cheap way to functionalize the surface of a carbon support with nitrogen atoms [12]. In fact, nitrogen-containing electroconductive polymers (i.e., PPY and polyaniline) were found to be active toward ORR even without performing any heat treatment [115–117]. However, after pyrolyzation at high temperature under an inert atmosphere, the ORR electroactivity improves significantly, as well as the stability.

In this study, MPC and pyrrole monomer were mixed together. Afterward, ammonium persulfate (APS) was used as an oxidant for the polymerization of pyrrole [72]. After the reaction, the suspension was filtered, washed, and dried in air at room temperature overnight. The resulting composite was mixed with Fe(II) acetate in water/ethanol solution. From this powder, two catalysts were then obtained: the first one pyrolyzed for 3 h at 800 °C under nitrogen, and acid leached; the second pyrolyzed twice at 800 °C under nitrogen flow, first for 3 h and then for 1 h, with intermediate and final acid leaching (Fig. 5).

The most active catalyst between the two was the Fe-N_x/MPC_PPY synthesized with two pyrolyzation steps, which reached a half-wave potential of 0.60 V versus RHE (Fig. 6). The second pyrolysis step allowed gaining 100 mV in half-wave potential [69]. Interestingly, from TEM analyses, the catalyst had different types of carbon structures (Fig. 10a): the starting mesoporous carbon structure evolved to filamentous particles, similar to carbon nanotubes, and to 2-D flat structures, similar to graphene-like flakes. We suppose that part of the new carbon frameworks present in the catalyst came from the decomposition of the starting polypyrrole macromolecule. In fact, iron can act as “catalyst” for the growth of nanotubes. The catalyst displayed a BET specific surface area of 426 m² g⁻¹, with a total pore volume of 0.354 cm³ g⁻¹ (microporosity: 0.115 cm³ g⁻¹, Fig. 10b). The BET specific surface area and both the total porosity and the microporosity increased of +30 % with the second pyrolyzation, compared to the twin catalyst pyrolyzed only once. Such a gaining went in parallel with the gaining in activity, equal to +20 %. We suppose that the increase in porosity is linked with the formation of new carbon frameworks, both nanotubes and graphene sheets, able to host a higher number of active ensembles, which, in turn, gave rise to the increase of activity. The XPS analysis showed an increase of the pyridinic nitrogen content of approximately 30 % because of the second heat treatment, which is correspondent to the gaining in activity toward the ORR.

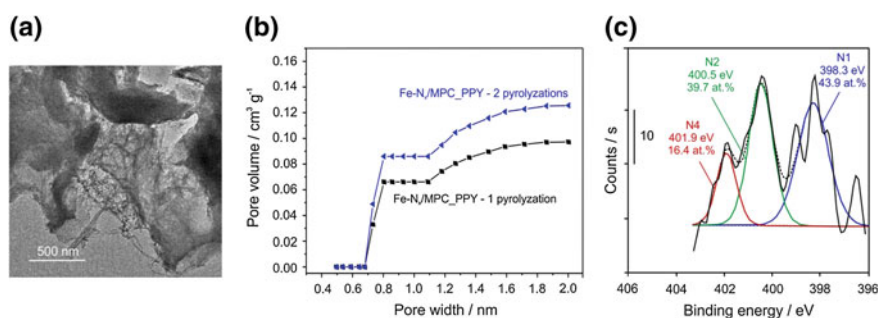


Fig. 10 Fe-N_x/MPC_PPY catalyst: TEM (a); BJH pore distribution for the catalyst pyrolyzed one or two times (b), and XPS analysis (c). Data from [72]

2.5 *The Lesson Learned from the Use of Different Types of Carbon Hosting the Nitrogen–Iron Active Ensembles*

We learned that to form a potentially high number of active ensembles, the M–N–C catalyst must deploy microporosity. And mesoporosity is necessary as well to assure the accessibility of reactants to the active ensembles. The nature of the carbon support and the conditions of the pyrolysis treatment play crucial roles in affecting the micro-/mesoporosity content of a NNM catalyst. But these conditions are not enough. The nature of the active ensembles is another crucial point.

In effect, one of the main disadvantages of using carbonaceous materials is linked to their loss in conductivity because of carbon corrosion during operation in fuel cell due to radicals attack [118–120]. Also unstable nitrogen fixation can lead to loose conductivity. According to the literature, in fact, pyridinic and pyrrolic nitrogen can be protonated in acidic medium [29, 121–123], leading to loss of stability with time. On the contrary, stability could be attributed to the presence of more stable graphitic-like nitrogen groups [60, 124] and a higher degree of graphitization of the carbon support [125, 126].

Another reason for the loss of stability during operation in fuel cell is attributed to the water flooding of the electrode because of its water-absorbing ability [127], which in turn affects the gas transport and cell performance. In fact, the presence of micropores and the formation of excessive oxygenated functional groups at the carbon surface can increase the hydrophilicity of the support and thus enhance flooding effects [128].

As mentioned previously, during the synthesis of catalysts because of the pyrolysis, two parallel reaction steps coexist. The first one being the graphitization of the support. The second step being the formation of active ensembles because of the decomposition of the precursors from their external and more exposed functional groups. If the pyrolysis step is not performed under strict control, the carbonaceous structure can start to collapse, by losing its initial properties as conductivity [129]. Such a phenomenon can lead to a partial hindering of active ensembles formed during the pyrolyzation process because of the “cut bridges,” with consequent loss of conductivity and electrocatalytic activity.

This is what we observed, indeed! According to a series of stability tests based on chronoamperometries performed with the RDE, at a fixed potential in O₂-saturated 0.5 M H₂SO₄, the NNM catalysts we developed partially lost their activities (Fig. 11). In particular, the more or less accentuated loss can be linked with the content of graphitic nitrogen. In fact, according to XPS analyses (Figs. 7 and 8), the lower the current density loss, the higher the content of graphitic nitrogen, in agreement with the literature: the loss of activity of Fe–N_x/rGO and Fe–N_x/MPC could be attributed to the relatively high content of both pyridinic and pyrrolic nitrogen, and absence of graphitic-like nitrogen. Thus, the pyrolysis conditions

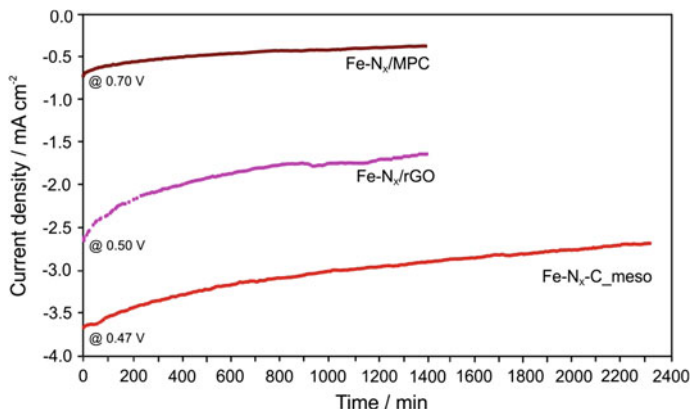


Fig. 11 Chronoamperometric *curves* and related percentage loss of current density of NNM catalysts for ORR activity at different voltages (conditions applied: O₂-saturated 0.5 M H₂SO₄ solution in RDE at a rotational speed of 900 rpm at fixed potential) [rearranged from 65, 67, 71]

during the catalysts synthesis must be tuned to favor the contemporary growth of micro- and mesopores, and to promote the presence of high content of pyridinic and graphitic-like nitrogen, to enhance both the activity and the stability.

These conditions are indeed difficult to be controlled, mainly because of the presence of the carbon itself used as support. According to the literature, the most active catalysts prepared so far require double or even triple pyrolyzation to see an effective increase of the ORR activity [12, 33, 69], making difficult to tune effectively the parameters to increase both the porosity and the density of active ensembles. As we noticed (Fig. 9), a mesoporous carbon, that is an ordered and highly porous carbon structure, used as support and exposed to several pyrolyzations, rearranged its structure into a mix of different carbons as graphene sheets, nanotubes, and nanorods because of the exposition to a high temperature for a prolonged time. Since it is difficult to imagine nanotubes' formation from a pure mesoporous carbon, we believe that these nanotubes are formed because of the presence of transition metal, which is acting as a seed for the growth of nanotubes. The intensive use of pyrolyzation suggests that the starting carbons used as supports undergo to a deep rearrangement or either partial destruction, depending on the temperature and time of exposure, to give origin to new types of carbon structures, not all of them being able to host active ensembles [64, 130]. Controlling the pyrolyzation to favor a selective and homogeneous growth of these new forming carbon structures able to host active ensembles is very difficult. Consequently, an idea to have a catalyst densely populated of active ensembles is to remove the carbon support and use a starting molecule that already contains a sufficient number of carbon, nitrogen, and transition metal atoms to form active ensembles.

3 The Use of a Non-carbonaceous Support in Forming Active Ensembles

To avoid the disadvantages of carbon-based supports previously mentioned, several efforts have been made recently to synthesize new NNM catalysts without using a carbonaceous support [56, 59, 61, 64, 130]. The basic idea lies in the use of sacrificial supports, to be mixed with precursor macrocycles containing nitrogen, carbon, and the transition metal together. The template is removed after the pyrolyzation step, resulting in a self-supported M–N–C catalyst with high pore volume and, consequently, high density of active ensembles.

The porosity can be tuned by using sacrificial supports (silica, alumina, zirconia, etc.) as templating agents [131, 132], with an approach similar to that used when producing mesoporous carbon by hard templating method [133]. In general, the templating agent hosts N–C, or M–N–C precursors, inside its structure (Fig. 12). The templating agent, SBA15 silica as an example, can be imagined as a series of ordered packed tubular (or hexagonal) open “microreactors”, which is hosting the precursors. When pyrolyzation starts, the decomposition process of the precursors takes place inside each SBA15 “microreactor”: the temperature raises favoring the graphitization of the carbon, decomposition gases are released, and contemporarily pressure increases locally as well, forming a very porous carbon structure and favoring its nitrogen–iron doping (Fig. 12). The templating agent is then removed by strong acid leaching. The resulting NNM catalyst is self-supported, highly porous and homogeneous, with better accessibility to reactants, and densely populated of active ensembles.

3.1 The Use of Non-carbonaceous Supports (SBA15 And commercial Mesoporous SiO₂) Hosting the Carbon–Nitrogen–Iron Active Ensembles

In this study, Iron phthalocyanine (Fe–PC) is used as iron/nitrogen/carbon source to synthesize Fe–N_x–C electrocatalysts for ORR by pyrolyzation in an inert atmosphere [71]. Considering the high carbon content of the Fe–PC molecule, the

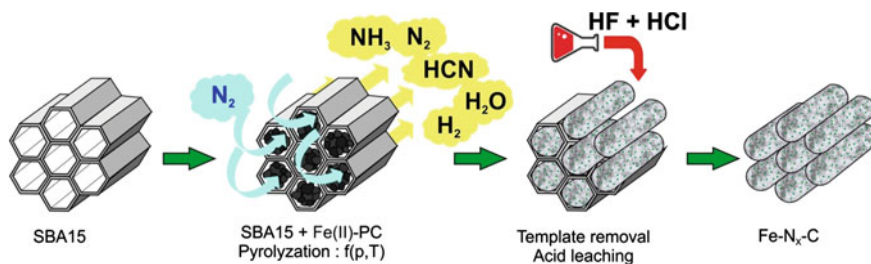


Fig. 12 Schematic representation of the formation of self-supported NNM catalysts by hard templating method using SBA15 as sacrificial agent, and Fe–PC as unique Fe–N–C source

electrocatalysts are prepared without using any other external carbonaceous support to favor an homogeneous graphitization during the thermal treatment [134, 135]. Here the morphology of the electrocatalysts is varied by means of different mesoporous silica templating agents to evaluate the effects on the porosity, electrocatalytic activity, and stability [61]. Two different porous silica were used as a sacrificial support during synthesis (SBA15 in-house prepared and commercial mesoporous $mSiO_2$ from Aldrich).

Specifically, $mSiO_2$ and SBA15 were used in a 30 wt% respect to the Fe-PC, followed by a mixing process in a ball milling apparatus for 1 h at 10 Hz. The precursors were pyrolyzed at 850 °C for 2 h, with a heating ramp of 2.5 °C min^{-1} . After pyrolysis, 5 wt% HF and 1 M HCl solutions were used to remove the templating agent.

The use of the templating agent as sacrificial support allows drastically increasing the BET specific surface area and the microporosity of the catalysts, especially with the use of the commercial mesoporous $mSiO_2$, compared to the same catalyst prepared by pyrolyzation of Fe-PC not templated with silica, as shown in Fig. 13. The best catalyst, Fe-N_x-C_meso in Fig. 6, prepared by templating with commercial mesoporous silica, reached a half wave potential of 0.64 V versus RHE, better than our previous reported catalysts so far (Table 2), and 10 mV better compared to the Fe-N_x-C_SBA prepared by templating with in-house prepared SBA15. The use of the in-house prepared SBA15, which has a typical rod-shaped morphology, caused the modification in the shape of the Fe-N_x-C_SBA15 catalyst to a worm-like structure that favored a good distribution of iron, without formation of agglomerates (Fig. 13a). Instead, the commercial $mSiO_2$, which has a typical spherical-shaped structure, favored the formation of a globular shape mixed with root-like filament structure on the Fe-N_x-C_meso catalyst (Fig. 13b). According to the BET/BJH analysis, the Fe-N_x-C_meso catalyst has a higher specific surface area (601 $m^2 g^{-1}$), and a higher pore volume (0.8 $cm^3 g^{-1}$), compared to the Fe-N_x-C_SBA15 catalyst (221 $m^2 g^{-1}$ and 0.2 $cm^3 g^{-1}$ respectively) (Table 2). Therefore on the Fe-N_x-C_meso catalyst the presence of high micropores content and a uniform distribution of iron (Fig. 13a, b), not only

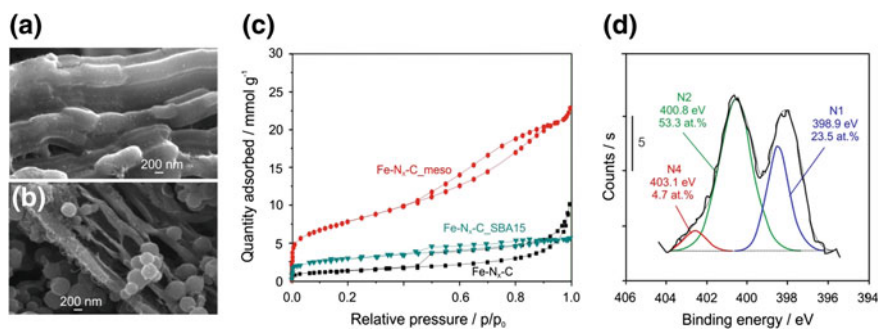


Fig. 13 Fe-N_x-C catalysts: FESEM images of Fe-N_x-C_SBA15 (a) and Fe-N_x-C_meso (b); BET adsorbed volumes, included also the non-templated Fe-N_x-C catalyst (c), and XPS analysis of the Fe-N_x-C_meso catalyst (d). Data from [71]

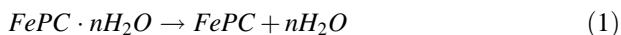
significantly improved the catalytic activity for ORR, but also reduced the overall percentage of hydrogen peroxide production, leading to better electrochemical activity [71]. According to XPS analysis, the Fe-N_x-C_meso catalyst has an overall pyridinic nitrogen content higher than the other Fe-N_x-C_SBA15 catalyst (Fig. 13d and Table 2).

The Fe-N_x-C_meso catalyst resulted more stable compared to the other Fe-N_x/C catalysts home-made previously mentioned (Fig. 11).

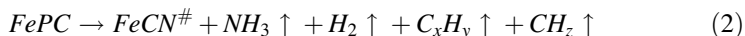
3.2 Considerations On the Pyrolyzation Process and the Decomposition of Iron–Nitrogen–Carbon Macrocyces used as Precursor

To produce active NNM catalysts, it is crucial to have a clear understanding of the process forming active ensembles during pyrolyzation (decomposing of the macrocycles). The macrocycle can contain atoms of transition metal (Fe, Co, etc.), nitrogen, hydrogen, carbon, and oxygen. During the decomposition of a macrocycle, Fe-PC for example, different reactions occur in the presence of an inert gas [76–79].

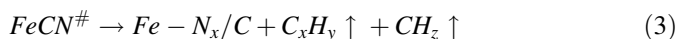
T : 20–150 °C \Rightarrow



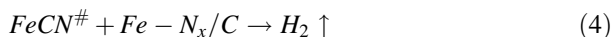
T : 120–700 °C \Rightarrow



T : 400–600 °C \Rightarrow



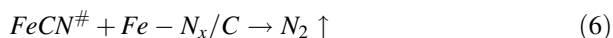
T : 430–700 °C \Rightarrow



T : 650–730 °C \Rightarrow



T : 700–720 °C \Rightarrow



In a first step, reaction (1), the water adsorbed by the macrocycle is released by evaporation in the temperature range of 20–150 °C. After water evaporation, sublimation of the macrocycle occurs, in a temperature range depending on the nature of the macrocycle itself. Contemporarily to the sublimation, the macrocycle undergoes to a partial decomposition of its structure in the range of 120–700 °C, reaction (2), with the release of gases as ammonia, hydrogen, volatile short hydrocarbons C_XH_Y and CH_X -like compounds (CH_3^+ and CH_4). In parallel to reaction (2), various recombinations of carbon and nitrogen (and oxygen if present in the starting macrocycle) give raise to different nitrogen-doped carbon structures, generally indicated as $FeCN^\#$.

According to the literature [79, 136], the formation of $Fe-N_X/C$ active ensembles require the coordination of iron (II) with pyridinic nitrogen over a π - π type carbon sheet in the range of 400–600 °C, reaction (3). The decomposition of the $FeCN^\#$ nitrogen-doped carbon structures continues even at higher temperatures, with the release of hydrogen in the range of 430–700 °C, reaction (4), of HCN in the range of 650–730 °C, reaction (5), of nitrogen in the range 700–720 °C, reaction (6). These steps are experimentally visible by differential thermo-gravimetric coupled with mass spectroscopy analysis (DTGA-MS) of a $Fe-PC$ macrocycle pyrolyzed in nitrogen up to 800 °C (Fig. 14).

The structural rearrangement of the catalyst at high temperature as per reactions (4) to (6) involves the partial loss of active ensembles already formed. Since forming active ensembles is the major task in the synthesis of NNM catalysts, a natural question arises: why do not stop the pyrolyzation in the range of 400–600 °C, as per reaction (3)? The answer is not obvious. The forthcoming processes in the temperature range of 450–750 °C, reactions (4) to (6), release gases that actually can perforate the nitrogen-doped carbon matrix of the forming catalyst, by further increasing porosity on the catalyst itself. This is a crucial step to increase accessibility of the reactants for ORR. Thus, the compromise between increasing accessibility through the raise of the porosity, and destroying part of the already formed active ensembles is a key factor to have good electrochemical activity. In an ideal

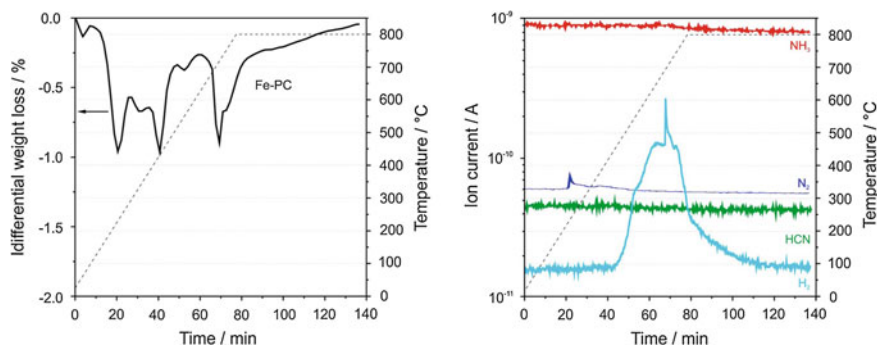


Fig. 14 DTGA-MS of $Fe-PC$ pyrolyzed in nitrogen atmosphere up to 800 °C (temperature ramp 10 °C min^{-1}). Data from [76]

situation, the formation of active ensembles should be concurrent with porosity formation. A good approach to preserve as much as possible active ensembles should be the use of already porous precursors to reduce the temperature of the pyrolyzation process.

Considering the morphology of the catalyst, a variety of carbon structures/configurations can be obtained during the pyrolyzation, because of the action of the gases released. The carbon growing mechanism depends upon to the graphitization process, the metal used, and the pyrolyzation temperature as well, as shown in the literature [57]. The use of various metals (Fe, Co, Zn, Cu, etc.) influences the formation of the active ensembles, as well. Each metal can act as a “catalyst” itself to enhance or depress the release of gases during the pyrolyzation [73, 76]. This leads to a final NNM catalyst structure with higher or lower porosity, and in turn more or less active toward ORR.

Another process that can happen during the pyrolyzation is the metal carbide formation, together with metal encapsulation into carbon sheets, as reported by [79–83, 136]. This process takes place in the temperature range of 520–650 °C, as shown in reaction (7), if oxygen atoms are already available in the starting macromolecule used to synthesize the catalyst:

$T: 520\text{--}650\text{ }^{\circ}\text{C} \Rightarrow$



Metal carbides do not play an active role in the ORR reaction mechanisms, whereas encapsulated metal nanoparticles Fe_{NP}/C can be considered as active ensembles as well, together with $Fe-N_4/C$ active ensembles, in an acid environment. Specifically, according to the most recent literature on $Fe-N_x-C$ catalysts, the $Fe(II)-N_4/C$ active ensemble is involved in the starting process of oxygen adsorption [42, 43, 59], and consequent reduction to H_2O_2 with 2 electrons involved. The intermediate H_2O_2 requires a second active ensemble, encapsulated Fe_{NP}/C , which must be adjacent to a $Fe(II)-N_4/C$ active ensemble, to ensure the subsequent reduction of H_2O_2 to the 4 electrons product H_2O . Otherwise H_2O_2 desorbs directly [59].

Furthermore, the particle size of the Fe_{NP} metal in the catalyst can be controlled by tuning the heating rate during the pyrolyzation [137]. In fact, the iron particle size results smaller if fast heating rate is applied (usually more than $10\text{ }^{\circ}\text{C min}^{-1}$), as reported by several groups [12, 59–64].

4 Alternative Perspectives

Scientists are now focusing the attention on alternative methods for synthesizing active NNM catalysts. According to the literature, one way to enhance the activity of NNM catalysts for ORR consists of performing a supplementary pyrolyzation in

ammonia atmosphere [60–64, 137, 138], in addition to the pyrolyzation in a inert atmosphere, which is not a totally controllable process. In fact, it is believed that ammonia “activates” the catalyst produced during the inert pyrolysis. Ammonia acts on the catalyst inducing a rearrangement of iron, nitrogen, and carbon to more electrochemically active Fe–N_x/C ensembles. A detailed and interesting work of Tüysüz et al. [137] reports the influence of ammonia decomposition up to 700 °C on Fe–PC, previously heat-treated under argon and vacuum atmosphere. The main crystallographic phases change after an exposure time of 20 min to ammonia, with an increase of the Fe and N at.%, and the increase of Fe–N, Fe₂–N, Fe₄–N ensembles, which are the preferential active ensembles for ORR.

Moreover, some elements as sulfur, added to the precursors during the synthesis, can suppress the formation of metal carbides during the pyrolyzation. Metal carbides, in fact, lead to the disintegration of Fe–N₄ active ensembles, thus decreasing the number of ORR active ensembles on the final catalyst [77].

5 Conclusions

This chapter summarizes several approaches adopted to synthesize non-noble metal catalysts for ORR containing active ensembles based on iron, nitrogen, carbon, and oxygen. These catalysts were synthesized by using various carbon structures, two different iron sources, and by pyrolyzing under inert gas atmosphere.

In the first part of this investigation, the influence of carbon supports such as mesoporous carbon (MPC), carbon nano-network (CNN), and reduced graphene oxide (rGO), was investigated in terms of hosting active ensembles. The performance of the Fe–N_x/C catalysts synthesized was evaluated by means of several *ex situ* techniques. Independent on the carbon support used, the activity toward ORR was similar for the three catalysts prepared. Noticeably, better results were obtained when pyridinic nitrogen and both micro- and mesoporosity were available. The main problem, in fact, lies in the synthesis of the catalyst. In particular, the Fe–N_x/C catalysts prepared were analyzed and correlated with their electrochemical performance. The decomposition of the starting macrocycle containing iron, nitrogen, and carbon is a difficult step to be controlled. In fact, considering the various reactions occurring during the pyrolyzation (degradation of the starting compounds, recombination of atoms to form active ensembles, release of gases, graphitization of the carbon structure), it is difficult to control and maximize the formation of active ensembles. The microporosity plays also a crucial role: the better catalytic activity appears to be linked with higher values of the microporosity of the catalyst, whose presence seems to be necessary to obtain catalysts with an increased population of active ensembles.

In the second part of this investigation, ORR catalysts were developed by avoiding the direct use of carbon-based supports. That is, a macrocycle containing iron, nitrogen, and carbon was used as starting precursor. Its porosity was

controlled by templating the macrocycle with silica, through the so-called “sacrificial support method.” After the pyrolyzation the templating agent was removed, leading to a final Fe–N_X–C catalyst with a high value of microporosity. The influence of the silica as templating agent leads to the formation of very porous materials as a negative replica of the silica itself, forming a self-supporting catalyst. The starting macrocycle, in fact, penetrates each pore of the silica, using it as a “microreactor” during the decomposition because of the pyrolyzation process. Thus, the final catalyst results to be highly homogeneous, rich of active ensembles. By using templates with different morphologies, the specific surface area can be tuned, and pore size distribution can be tailored over a wide range of micro- and mesopores. This is demonstrated by the superior electrochemical activity of Fe–N_X–C catalysts toward ORR, more than one order of magnitude as current density at 0.8 V versus RHE compared to Fe–N_X/C catalysts. With self-supported Fe–N_X–C catalysts, four electrons pathway reaction was achieved by “simply” tuning the structure of the catalyst during the synthesis.

Thus, the synthesis of highly active NNM catalysts toward ORR requires materials with well-developed pore structures and high density of Fe–N_X active ensembles, whose formation depends on many different variables: the choice of the starting precursors (macrocycles containing transition metal, carbon, and nitrogen), the conditions of the pyrolyzation process (temperature, time, inert or reactive atmosphere). During precursors decomposition because of the pyrolyzation, many different reactions occur, with several intermediate decomposition steps.

According to the state of the art, Fe–N_X active ensembles are of various nature: Fe–N₂, Fe–N₄, Fe–N₂₊₂, Fe₂–N₅, as well as iron encapsulated on carbon, each of them linked to a specific temperature range, that is decomposition step, during the pyrolyzation. All of them coexist to boost the ORR activity. The ability to control the decomposition of the starting precursors by choosing the hosting support, and by tuning the conditions of the reactions represent the key to synthesizing highly active NNM catalysts. To better understand how active ensembles are formed, quantum chemistry can be used to tune in detail the macrocycles needed during the preparation of NNM catalysts, and consequently, achieve a rational design the final product.

Acknowledgments Authors gratefully acknowledge all colleagues that stimulated the review process of the obtained results to accomplish this chapter. In particular: Dr. G. Ercolino, Dr. R. Alipour Moghadam Esfahani, Dr. N.S. Vasile, and Prof. A. Kotarba (Jagiellonian University in Krakow). The research leading to these results has received funding from the European Community’s Seventh Framework Programme (FP7/2011-2014) for the Fuel Cells and Hydrogen Joint Technology Initiative under grant agreement DURAMET n° 278054 (Improved durability and cost-effective components for new generation solid polymer electrolyte direct methanol fuel cells), and from the Italian Ministry of Education, Universities and Research (MIUR, PRIN 2010–2011) under grant agreement NAMEDPEM n° 2010CYTAW (Advanced nanocomposite membranes and innovative electrocatalysts for durable polymer electrolyte membrane fuel cells).

References

1. EU Commission, Hydrogen Energy and Fuel Cells, A vision of our future. Special Report, EUR 20719 EN (2003) https://ec.europa.eu/research/energy/pdf/hlg_vision_report_en.pdf. Accessed on Sep 2015
2. U.S. Energy Information Administration, Annual Energy Outlook 2015 with projections to 2040, DOE/EIA-0383 (2015). [www.eia.gov/forecasts/aeo/pdf/0383\(2015\).pdf](http://www.eia.gov/forecasts/aeo/pdf/0383(2015).pdf). Accessed on Sep 2015
3. Mahlia TMI, Saktisahdan TJ, Jannifar A, Hasan MH, Matseelar HSC (2014) A review of available methods and development on energy storage; technology update. *Renew Sustain Energy Rev* 33:532–545
4. Van Mierlo J, Maggetto G, Lataire Ph (2006) Which energy source for road transport in the future? A comparison of battery, hybrid and fuel cell vehicles. *Energy Conv Manag* 47:2748–2760
5. Garcia P, Torreglosa JP, Fernández LM, Jurado F (2013) Control strategies for high-power electric vehicles powered by hydrogen fuel cell, battery and supercapacitor. *Expert Syst Appl* 40:4791–4804
6. Specchia S, Francia C, Spinelli P (2011) Polymer electrolyte membrane fuel cells. In: Liu R-S, Zhang L, Sun X, Liu H, Zhang J (eds) *Electrochemical technologies for energy storage and conversion*. Wiley-VCH Verlag GmbH & Co., KGaA, Weinheim (Germany), pp 601–670, ISBN: 978-3-527-328679
7. Pollet BG, Staffell I, Shang JL (2012) Current status of hybrid, battery and fuel cell electric vehicles: From electrochemistry to market prospects. *Electrochim Acta* 84:235–249
8. DOE Fuel Cell Technologies Office Record # 13012, (2013). http://energy.gov/sites/prod/files/2014/03/f11/13012_fuel_cell_system_cost_2013.pdf. Accessed on Sep 2015
9. <http://www.platinum.matthey.com/prices/price-charts>. Accessed on Oct 2015
10. Gasteiger H, Kocha SS, Sompalli B, Wagner FT (2005) Activity benchmarks and requirements for Pt, Pt-alloy, and non-Pt oxygen reduction catalysts for PEMFCs. *Appl Catal B Environ* 56:9–35
11. Ishihara A, Ohgi Y, Matsuzawa K, Mitsushima S, Ota K-I (2010) Progress in non-precious metal oxide-based cathode for polymer electrolyte fuel cells. *Electrochim Acta* 55:8005–8012
12. Wu G, More KL, Johnston CM, Zelenay P (2011) High-performance electrocatalysts for oxygen reduction derived from polyaniline, iron, and cobalt. *Science* 332:443–447
13. Stamenković VR, Fowler B, Mun BS, Wang G, Ross PN, Lucas CA, Marković NM (2007) Improved oxygen reduction activity on Pt₃Ni(111) via increased surface site availability. *Science* 315:493–497
14. Long NV, Yang Y, Thi CM, Minh NV, Cao Y, Nogami M (2013) The development of mixture, alloy, and core-shell nanocatalysts with nanomaterial supports for energy conversion in low-temperature fuel cells. *Nano Energy* 2:636–676
15. Shao M, Odell JH, Peles A, Su D (2014) The role of transition metals in the catalytic activity of Pt alloys: quantification of strain and ligand effects. *Chem Commun* 50:2173–2176
16. Cui C, Gan L, Li HH, Yu SH, Heggen M, Strasser P (2012) Octahedral PtNi nanoparticle catalysts: exceptional oxygen reduction activity by tuning the alloy particle surface composition. *Nano Lett* 12:5885–5889
17. Kitchin JR, Nørskov JK, Barteau MA, Chen JG (2004) Modification of the surface electronic and chemical properties of Pt(111) by subsurface 3d transition metals. *J Chem Phys* 120:10240–10246
18. Stamenkovic V, Stamenković V, Schmidt TJ, Ross PN, Marković NM (2002) Surface composition effects in electrocatalysis: Kinetics of oxygen reduction on well-defined Pt₃Ni and Pt₃Co alloy surfaces. *J Phys Chem B* 106:11970–11979

19. Yang W, Wang X, Yang F, Yang C, Yang X (2008) Carbon nanotubes decorated with Pt nanocubes by a noncovalent functionalization method and their role in oxygen reduction. *Adv Mater* 20:2579–2587
20. Lim B, Jiang M, Camargo PH, Cho EC, Tao J, Lu X, Zhu Y, Xia Y (2009) Pd-Pt bimetallic nanodendrites with high activity for oxygen reduction. *Science* 324:1302–1305
21. Choi S-I, Xie S, Shao M, Odell JH, Lu N, Pen H-C, Protsailo L, Guerrero S, Park J, Xia X, Wang J, Kim MJ, Xia Y (2013) Synthesis and characterization of 9 nm Pt–Ni octahedra with a record high activity of 3.3 A/mg_{Pt} for the oxygen reduction reaction. *Nano Lett* 13:3420–3425
22. Wu J, Zhang J, Peng Z, Yang S, Wagner FT, Yang H (2010) Truncated octahedral Pt₃Ni oxygen reduction reaction electrocatalysts. *J Am Chem Soc* 132:4984–4985
23. Wang D, Xin HL, Hovden R, Wang H, Yu Y, Muller DA, Di Salvo FJ, Abruña HD (2013) Structurally ordered intermetallic platinum–cobalt core–shell nanoparticles with enhanced activity and stability as oxygen reduction electrocatalysts. *Nature Mater* 12:81–87
24. Kang Y, Murray CB (2010) Synthesis and electrocatalytic properties of cubic Mn – Pt Nanocrystals (Nanocubes). *J Am Chem Soc* 132:7568–7569
25. Liu L, Samjeské G, Takao S, Nagasawa K, Iwasawa Y (2014) Fabrication of PtCu and PtNiCu multi-nanorods with enhanced catalytic oxygen reduction activities. *J Power Sources* 253:1–8
26. Chen Z, Higgins D, Yu A, Zhang L, Zhang J (2011) A review on non-precious metal electrocatalysts for PEM fuel cells. *Energy Environ Sci* 4:3167–3195
27. Jaouen F, Herranz J, Lefèvre M, Dodelet J-P, Kramm UI, Herrmann I, Bogdanoff P, Maruyama J, Nagaoka T, Garsuch A, Dahn JR, Olson T, Pylypenko S, Atanassov P, Ustinov EA (2009) Cross-laboratory experimental study of non-noble-metal electrocatalysts for the oxygen reduction reaction. *ACS Appl Mater Interfaces* 1:1623–1639
28. Ramaswamy N, Tylus U, Jia Q, Mukerjee S (2013) Activity descriptor identification for oxygen reduction on nonprecious electrocatalysts: linking surface science to coordination chemistry. *J Am Chem Soc* 135:15443–15449
29. Liu G, Li X, Ganesan P, Popov BN (2010) Studies of oxygen reduction reaction active sites and stability of nitrogen-modified carbon composite catalysts for PEM fuel cells. *Electrochim Acta* 55:2853–2858
30. Stamenković VR, Mun BS, Arenz M, Mayrhofer KJJ, Lucas CA, Wang G, Ross PN, Marković NM (2007) Trends in electrocatalysis on extended and nanoscale Pt-bimetallic alloy surfaces. *Nat Mater* 6:241–247
31. Chen C, Kang Y, Huo Z, Zhu Z, Huang W, Xin HL, Snyder JD, Li D, Herron JA, Mavrikakis M, Chi M, More KL, Li Y, Marković NM, Somorjai GA, Yang P, Stamenković VR (2014) Highly crystalline multimetallic nanoframes with three-dimensional electrocatalytic surfaces. *Science* 343:1339–1343
32. Gasteiger HA, Marković NM (2009) Chemistry: Just a dream—or future reality? *Science* 324:48–49
33. P. Zelenay. Non-precious metal fuel cell cathodes: Catalyst development and electrode structure design. http://www.hydrogen.energy.gov/pdfs/review15/fc107_zelenay_2015_o.pdf. Accessed on Oct 2015
34. Chung HT, Johnston CM, Zelenay P (2009) Synthesis and evaluation of heat-treated, cyanamide-derived non-precious catalysts for oxygen reduction. *ECS Trans* 25:485–492
35. Chung HT, Johnston CM, Artyushkova K, Ferrandon M, Myers DJ, Zelenay P (2010) Cyanamide-derived non-precious metal catalyst for oxygen reduction. *Electrochem Comm* 12:1792–1795
36. Wu G, Artyushkova K, Ferrandon M, Kropf AJ, Myers DJ, Zelenay P (2009) Performance durability of polyaniline-derived non-precious cathode catalysts. *ECS Trans* 25:1299–1311
37. Nekooi P, Akbari M, Amini MK (2010) CoSe nanoparticles prepared by the microwave-assisted polyol method as an alcohol and formic acid tolerant oxygen reduction catalyst. *Int J Hydrogen Energy* 35:6392–6398

38. Ziegelbauer JM, Olson TS, Pylypenko S, Alamgir F, Jaye C, Atanassov P, Mukerjee S (2008) Direct spectroscopic observation of the structural origin of peroxide generation from Co-based pyrolyzed porphyrins for ORR applications. *J Phys Chem C* 112:8839–8849
39. Lee KR, Lee KU, Lee JW, Ahn BT, Woo SI (2010) Electrochemical oxygen reduction on nitrogen doped graphene sheets in acid media. *Electrochem Commun* 12:1052–1056
40. Herranz J, Lefèvre M, Larouche N, Stansfield B, Dodelet J-P (2007) Step-by-step synthesis of non-noble metal electrocatalysts for O₂ reduction under proton exchange membrane fuel cell conditions. *J Phys Chem C* 111:19033–19042
41. Biddinger EJ, Knapke DS, von Deak D, Ozkan US (2010) Effect of sulfur as a growth promoter for CN_x nanostructures as PEM and DMFC ORR catalysts. *Appl Catal B Environ* 96:72–82
42. Zagal JH, Griveau S, Silva JF, Nyokong T, Bedioui F (2010) Metallophthalocyanine-based molecular materials as catalysts for electrochemical reactions. *Coord Chem Rev* 23–24:2755–2791
43. Masa J, Ozoemena K, Schuhmann W, Zagal JH (2012) Oxygen reduction reaction using N₄-metallomacrocyclic catalysts: fundamentals on rational catalyst design. *J Porphyrins Phthalocyanines* 16:761–784
44. Charreteur F, Jaouen F, Dodelet J-P (2009) Iron porphyrin-based cathode catalysts for PEM fuel cells: Influence of pyrolysis gas on activity and stability. *Electrochim Acta* 54:6622–6630
45. Collman JP, Marrocco M, Denisevich P, Koval C, Anson FC (1979) Potent catalysis of the electroreduction of oxygen to water by dicobalt porphyrin dimers adsorbed on graphite electrodes. *J Electroanal Chem Interfacial Electrochem* 101:117–122
46. Collman JP, Denisevich P, Konai Y, Marrocco M, Koval C, Anson FC (1980) Electrode catalysis of the four-electron reduction of oxygen to water by dicobalt face-to-face porphyrins. *J Am Chem Soc* 102:6027–6036
47. Liu HY, Weaver MJ, Wang C-B, Chang CK (1983) Dependence of electrocatalysis for oxygen reduction by adsorbed dicobalt cofacial porphyrins upon catalyst structure. *J Electroanal Chem Interfacial Electrochem* 145:439–457
48. Yeager EB (1984) Electrocatalysts for O₂ reduction. *Electrochim Acta* 29:1527–1537
49. Scherson D, Tanaka AA, Gupta SL, Tryk D, Fierro C, Holze R, Yeager EB (1986) Transition metal macrocycles supported on high area carbon: Pyrolysis—mass spectrometry studies. *Electrochim Acta* 31:1247–1390
50. Morcos I, Yeager EB (1970) Transition metal macrocycles supported on high area carbon: pyrolysis—mass spectrometry studies. *Electrochim Acta* 15:953–975
51. Jaouen F, Lefèvre M, Dodelet J-P, Cai M (2006) Heat-treated Fe/N/C catalysts for O₂ electroreduction: are active sites hosted in micropores? *J Phys Chem B* 110:5553–5558
52. Jaouen F, Proietti E, Lefèvre M, Chenitz R, Dodelet J-P, Wu G, Chung HT, Johnston CM, Zelenay P (2011) Recent advances in non-precious metal catalysis for oxygen-reduction reaction in polymer electrolyte fuel cells. *Energy Environ Sci* 4:114–130
53. Chung HT, Won JH, Zelenay P (2013) Active and stable carbon nanotube/nanoparticle composite electrocatalyst for oxygen reduction. *Nat Commun* 4:1922
54. Velázquez-Palenzuela A, Zhang L, Wang L, Cabot PL, Brillas E, Tsay K, Zhang J (2011) Fe–Nx/C electrocatalysts synthesized by pyrolysis of Fe(II)–2,3,5,6-tetra(2-pyridyl)pyrazine complex for PEM fuel cell oxygen reduction reaction. *Electrochim Acta* 56:4744–4752
55. Li S, Zhang L, Liu H, Pan M, Zan L, Zhang J (2010) Heat-treated cobalt–tripyrindyl triazine (Co–TPTZ) electrocatalysts for oxygen reduction reaction in acidic medium. *Electrochim Acta* 55:4403–4411
56. van Veen JAR, Colijn HA, van Baar JF (2008) On the effect of a heat treatment on the structure of carbon-supported metalloporphyrins and phthalocyanines. *Electrochim Acta* 33:801–804

57. Dodelet JP (2013) The controversial role of the metal in Fe- or Co-based electrocatalysts for the oxygen reduction reaction in acid medium. In: Shao M (ed) *Electrocatalysis in fuel cells: a non- and low-platinum approach*. Springer London, United Kingdom, pp. 271–338, ISBN: 978-1-4471-4910-1
58. Li H, Li Y, Koper MTM, Calle-Vallejo F (2014) Bond-making and breaking between carbon, nitrogen, and oxygen in electrocatalysis. *J Am Chem Soc* 136:15694–15701
59. Tylus U, Jia Q, Strickland K, Ramaswamy N, Serov A, Atanassov P, Mukerjee S (2014) Elucidating oxygen reduction active sites in pyrolyzed metal–nitrogen coordinated non-precious-metal electrocatalyst systems. *J Phys Chem C* 118:8999–9008
60. Lefèvre M, Proietti E, Jaouen F, Dodelet J-P (2009) Iron-based catalysts with improved oxygen reduction activity in polymer electrolyte fuel cells. *Science* 324:71–74
61. Cheon JY, Kim TY, Choi YM, Jeong HY, Kim MG, Sa YJ, Kim J, Lee ZH, Yang TH, Kwon KJ, Terasaki O, Park G-G, Adzic RR, Joo SH (2013) Ordered mesoporous porphyrinic carbons with very high electrocatalytic activity for the oxygen reduction reaction. *Sci Rep* 3:2715
62. Zitolo A, Goellner V, Armel V, Sougrati M-T, Mineva T, Stievano L, Fonda E, Jaouen F (2015) Identification of catalytic sites for oxygen reduction in iron- and nitrogen-doped graphene materials. *Nature Mater* 14:937–942
63. Strickland K, Miner E, Jia Q, Tylus U, Ramaswamy N, Liang W, Sougrati M-T, Jaouen F, Mukerjee S (2015) Highly active oxygen reduction non-platinum group metal electrocatalyst without direct metal–nitrogen coordination. *Nat Commun* 6:7343
64. Zhao D, Shui J-L, Grabstanowicz LR, Chen C, Commet SM, Xu T, Lu J, Liu D-J (2014) Highly efficient non-precious metal electrocatalyst prepared from one-pot synthesized zeolitic imidazolate. *Adv Mater* 26:1093–1097
65. Monteverde Videla AHA, Zhang L, Kim J, Zeng J, Francia C, Zhang J, Specchia S (2013) Mesoporous carbons supported non-noble metal Fe–N_x electrocatalysts for PEM fuel cell oxygen reduction reaction. *J Appl Electrochem* 43:159–169
66. Monteverde Videla AHA, Osmieri L, Specchia S (2014) The use of different types of reduced graphene oxide (rGO) on the reduction oxygen reaction (ORR) under alkaline conditions. Electronic abstract FA-4:L13. In: 6th Forum on New Materials, CIMTEC2014, Montecatini Terme (Italy) 15–19/06/2014. http://2014.cimteccongress.org/abstracts_symposium_fa. Accessed on Oct 2015
67. Monteverde Videla AHA, Ban S, Specchia S, Zhang L, Zhang J (2014) Non-noble Fe–N_x electrocatalysts supported on the reduced graphene oxide for oxygen reduction reaction. *Carbon* 76:386–400
68. Zeng J, Francia C, Monteverde Videla AHA, Bodoardo S, Specchia S, Penazzi N (2014) Reduced graphene oxide as cathode materials for rechargeable Li–O₂ cells. In: 65th annual meeting of the international society of electrochemistry, Lausanne (Switzerland), 31/08-05/09/2014. pp 1317
69. Osmieri L, Monteverde Videla AHA, Specchia S (2015) Activity of Co–N multi walled carbon nanotubes electrocatalysts for oxygen reduction reaction in acid conditions. *J Power Sources* 278:296–307
70. Negro E, Monteverde Videla AHA, Baglio V, Aricò AS, Specchia S, Koper GJM (2015) Fe–N supported on graphitic carbon nano-networks grown from cobalt as oxygen reduction catalysts for low-temperature fuel cells. *Appl Catal B Environ* 166–167:75–83
71. Monteverde Videla AHA, Osmieri L, Armandi M, Specchia S (2015) Varying the morphology of Fe–N–C electrocatalysts by templating iron phthalocyanine precursor with different porous SiO₂ to promote the oxygen reduction reaction. *Electrochim Acta* 177:43–50
72. Osmieri L, Monteverde Videla AHA, Specchia S (2015) Optimization of a Fe–N–C electrocatalyst supported on ordered mesoporous carbon functionalized with polypyrrole for oxygen reduction reaction. E-book of Abstracts, V Iberian Symposium on Hydrogen, Fuel Cells and Advanced Batteries, Tenerife (Spain) 5–8/07/2015, pp. 36–39, ISBN: 978-84-606-8621-7

73. Osmieri L, Monteverde Videla AHA, Alipour Moghadam Esfahani R, Vankova S, Armandi M, Specchia S (2015) Zinc(II)-phthalocyanine as precursor for preparation of extremely high surface area N-doped carbon for potential applications in electrochemical devices. In: Abstract book the italian meeting on porphyrins and phthalocyanines, Rome (Italy) 6–8/07/2015. pp 51. ISBN 978–88–7959–879–8
74. Osmieri L, Alipour Moghadam Esfahani R, Monteverde Videla AHA, Vasile NS, Specchia S (2015) Kinetic analysis of oxygen reduction reaction on different self-supported C-N-Me (Me = Fe, Co, Cu) catalysts in acidic medium. In: ECS conference on electrochemical energy conversion & storage with SOFC-XIV. Glasgow (United Kingdom) 26–31/07/2015. <http://ma.ecsdl.org/content/MA2015-03/3/622.abstract>. Accessed on Oct 2015
75. Vasile NS, Doherty R, Monteverde Videla AHA, Specchia S (2015) 3D multi-physic modeling and validation of a gas diffusion electrode for analyzing transport and kinetic phenomena of noble and non-noble based catalysts for PEMFC. In: international conference on electrochemical energy science and technology (EEST2015). Vancouver (Canada) 16–22/08/2015
76. Osmieri L, Videla AHAM, Armandi M, Specchia S (2015) A micro-silica reactor (μSiO_2 -R) able to produce highly porous non-noble catalysts for oxygen reduction reaction under alkaline conditions. In: challenges towards zero platinum for oxygen reduction. La Grande Motte (France) 14–16/09/2015
77. Kramm UI, Herrmann-Geppert I, Fiechter S, Zehl G, Zizak I, Dorbandt I, Schmeißer D, Bogdanoff P (2014) Effect of iron-carbide formation on the number of active sites in Fe–N–C catalysts for the oxygen reduction reaction in acidic media. *J Mater Chem A* 2:2663–2670
78. Bezerra CWB, Zhang L, Lee K, Liu H, Marques ALB, Marques EP, Wang H, Zhang J (2008) A review of Fe–N/C and Co–N/C catalysts for the oxygen reduction reaction. *Electrochim Acta* 53:4937–4951
79. Kramm UI, Lefèvre M, Larouche N, Schmeisser D, Dodelet J-P (2013) Correlations between mass activity and physicochemical properties of Fe/N/C catalysts for the ORR in PEM fuel cell via ^{57}Fe Mössbauer spectroscopy and other techniques. *J Am Chem Soc* 136:978–985
80. Hu Y, Jensen JO, Zhang W, Cleemann LN, Xing W, Bjerrum NJ, Li Q (2014) Hollow spheres of iron carbide nanoparticles encased in graphitic layers as oxygen reduction catalysts. *Angew Chem Int Ed* 53:3675–3679
81. Dodelet J-P, Chenitz R, Yang L, Lefèvre M (2014) A new catalytic site for the electroreduction of Oxygen? *Chem Cat Chem* 7:1866–1867
82. Hu Y, Jensen JO, Zhang W, Huang Y, Cleemann LN, Xing W, Bjerrum NJ, Li Q (2014) Direct synthesis of Fe_3C -functionalized graphene by high temperature autoclave pyrolysis for oxygen reduction. *Chem Sus Chem* 7:2099–2105
83. Hu Y, Jensen JO, Zhang W, Martin S, Chenitz R, Pan C, Xing W, Bjerrum NJ, Li Q (2015) Fe_3C -based oxygen reduction catalysts: synthesis, hollow spherical structures and applications in fuel cells. *J Mater Chem A* 3:1752–1760
84. Strickland K, Miner E, Jia Q, Tylus U, Ramaswamy N, Liang W, Sougrati M-T, Jaouen F, Mukerjee S (2015) Highly active oxygen reduction non-platinum group metal electrocatalyst without direct metal–nitrogen coordination. *Nat Commun* 6:7343–7357
85. Wikström M (2012) Active site intermediates in the reduction of O_2 by cytochrome oxidase, and their derivatives. *Biochim Biophys Acta* 1817:468–475
86. Ishihara A, Tamura M, Ohgi Y, Matsumoto M, Matsuzawa K, Mitsushima S, Imai H, Ota K-I (2013) Emergence of oxygen reduction activity in partially oxidized tantalum carbonitrides: roles of deposited carbon for oxygen reduction-reaction-site creation and surface electron conduction. *J Phys Chem C* 117:18837–18844
87. Nørskov JK, Rossmeisl J, Logadottir A, Lindqvist L (2004) Origin of the overpotential for oxygen reduction at a fuel-cell cathode. *J Phys Chem B* 108:17886–17892
88. Suntivich J, Gasteiger HA, Yabuuchi N, Nakanishi H, Goodenough JB, Shao-Horn Y (2011) Design principles for oxygen-reduction activity on perovskite oxide catalysts for fuel cells and metal–air batteries. *Nat Chem* 3:546–550

89. Zagal JH, Bindra P, Yeager E (1980) A mechanistic study of O₂ reduction on water soluble phthalocyanines adsorbed on graphite electrodes. *J Electrochem Soc* 127:1506–1517
90. Stamenkovic VR, Mun BS, Mayrhofer KJJ, Ross PN, Markovic NM, Rossmeisl J, Greeley J, Nørskov JK (2006) Changing the activity of electrocatalysts for oxygen reduction by tuning the surface electronic structure. *Angew Chem Int Ed* 45:2897–2901
91. Hyman MP, Medlin JW (2007) Effects of electronic structure modifications on the adsorption of oxygen reduction reaction intermediates on model Pt(111)-alloy surfaces. *J Phys Chem C* 111:17052–17060
92. Lalande G, Côté R, Tamizhmani G, Guay D, Dodelet J-P, Dignard-Bailey L, Weng LT, Bertrand P (1995) Physical, chemical and electrochemical characterization of heat-treated tetracarboxylic cobalt phthalocyanine adsorbed on carbon black as electrocatalyst for oxygen reduction in polymer electrolyte fuel cells. *Electrochim Acta* 40:2635–2646
93. Li ZP, Liu ZX, Zhu KN, Li Z, Liu BH (2012) Synergy among transition element, nitrogen, and carbon for oxygen reduction reaction in alkaline medium. *J Power Sources* 219:163–171
94. Han MY, Özyilmaz B, Zhang Y, Kim P (2007) Document energy band-gap engineering of graphene nanoribbons. *Phys Rev Lett* 98:206805-1–206805-4
95. Neto AHC, Guinea F, Peres NMR, Novoselov KS, Geim AK (2009) The electronic properties of graphene. *Rev Mod Phys* 81(2009):109–162
96. Xu C, Xu B, Gu Y, Xiong Z, Sunb J, Zhao XS (2015) Graphene-based electrodes for electrochemical energy storage. *Energy Environ Sci* 8:790–823
97. Bonaccorso F, Colombo L, Yu G, Stoller M, Tozzini V, Ferrari AC, Ruoff RS, Pellegrini V (2015) Graphene, related two-dimensional crystals, and hybrid systems for energy conversion and storage. *Science* 347:6217
98. Dai L, Xue Y, Qu L, Choi H-J, Baek J-B (2015) Metal-free catalysts for oxygen reduction reaction. *Chem Rev* 115:4823–4892
99. Lee KR, Lee KU, Lee JW, Ahn BT, Woo S (2010) Electrochemical oxygen reduction on nitrogen doped graphene sheets in acid media. *Electrochem Commun* 12:1052–1055
100. Wang S, Yu D, Dai L, Chang DW, Baek J-B (2011) Polyelectrolyte-functionalized graphene as metal-free electrocatalysts for oxygen reduction. *ACS Nano* 8:6202–6209
101. Gartia Y, Parnell CM, Watanabe F, Szwedko P, Biris AS, Peddi N, Nima ZA, Ghosh A (2015) Graphene-enhanced oxygen reduction by MN₄ type Cobalt(III) catalyst. *ACS Sustain Chem Eng* 3:97–102
102. Borup R, Meyers J, Pivovar B, Kim YS, Mukundan R, Garland N, Myers D, Wilson M, Garzon F, Wood D, Zelenay P, More K, Stroh K, Zawodzinski T, Boncella J, McGrath JE, Inaba M, Miyatake K, Hori M, Ota K-I, Ogumi Z, Miyata S, Nishikata A, Siroma Z, Uchimoto Y, Yasuda K, Kimijima K-I, Iwashita N (2007) Scientific aspects of polymer electrolyte fuel cell durability and degradation. *Chem Rev* 107:3904–3951
103. Kowłgi K, Lafont U, Rappolt M, Koper GJM (2012) Uniform metal nanoparticles produced at high yield in dense microemulsions. *J Colloid Interf Sci* 372:16–23
104. Negro E, Latsuzbaia R, Dieci M, Boshuizen I, Koper GJM (2015) Pt electrodeposited over carbon nano-networks grown on carbon paper as durable catalyst for PEM fuel cell. *Appl Catal B Environ* 166:155–165
105. Wu D, Lv Q, Feng S, Chen J, Chen Y, Qiu Y, Yao X (2015) Polylactide composite foams containing carbon nanotubes and carbon black: Synergistic effect of filler on electrical conductivity. *Carbon* 95:380–387
106. Yang H, Gong J, Wen X, Xue J, Chen Q, Jiang Z, Tian N, Tang T (2015) Effect of carbon black on improving thermal stability, flame retardancy and electrical conductivity of polypropylene/carbon fiber composites. *Compos Sci Technol* 113:31–37
107. Negro E, Dieci M, Sordi D, Kowłgi K, Makkee M, Koper GJM (2014) High yield, controlled synthesis of graphitic networks from dense micro emulsions. *Chem Commun* 50:11848–11851
108. Woo S, Lee J, Park S-K, Kim H, Chung TD, Piao Y (2013) Enhanced electrocatalysis of PtRu onto graphene separated by Vulcan carbon spacer. *J Power Sources* 222:261–266

109. Barroso-Bogeat A, Alexandre-Franco M, Fernández-González C, Sánchez-González J, Gómez-Serrano V (2015) Temperature dependence of DC electrical conductivity of activated carbon–metal oxide nanocomposites. Some insight into conduction mechanisms. *J Phys Chem Solids* 87:259–270
110. Wang S-C, Yang J, Zhou X-Y, Xie J, Ma L-L, Huang B (2014) Electrochemical properties of carbon nanotube/graphene oxide hybrid electrodes fabricated via layer-by-layer self-assembly. *J Electroanal Chem* 722:141–147
111. Jin S, Li N, Cuia H, Wang C (2013) Growth of the vertically aligned graphene@ amorphous GeOx sandwich nanoflakes and excellent Li storage properties. *Nano Energy* 2:1128–1136
112. Na HG, Cho HY, Kwon YJ, Kang SY, Lee C, Jung TK, Lee H-S, Kim HW (2015) Reduced graphene oxide functionalized with Cu nanoparticles: Fabrication, structure, and sensing properties. *Thin Solid Films* 588:11–18
113. Ku K, Kim B, Chung H, Kim W (2010) Characterization of graphene-based supercapacitors fabricated on Al foils using Au or Pd thin films as interlayers. *Synth Met* 160:2613–2617
114. Yu Z, Carter RN (2010) Measurement of effective oxygen diffusivity in electrodes for proton exchange membrane fuel cells. *J Power Sources* 195:1079–1084
115. Khomenko VG, Barsukov VZ, Katashinskii AS (2005) The catalytic activity of conducting polymers toward oxygen reduction. *Electrochim Acta* 50:1675–1683
116. Sulub SR, Martínez-Millán W, Smit MA (2009) Study of the catalytic activity for oxygen reduction of polythiophene modified with Cobalt or Nickel. *Int J Electrochem Sci* 4:1015–1027
117. Martínez-Millán W, Smit MA (2009) Study of electrocatalysts for oxygen reduction based on electroconducting polymer and nickel. *J Appl Polym Sci* 112:2959–2967
118. Zhang HJ, Yuan X, Sun L, Zeng X, Jiang QZ, Shao Z, Ma ZF (2010) Pyrolyzed CoN₄-chelate as an electrocatalyst for oxygen reduction reaction in acid media. *Int J Hydrogen Energy* 35:2900–2903
119. Choi YJ, Higgins D, Chen Z (2012) Highly durable graphene nanosheet supported iron catalyst for oxygen reduction reaction in PEM fuel cells. *J Electrochem Soc* 159:B86–B89
120. Shao Y, Zhang S, Wang C, Nie Z, Liu J, Wang Y, Lin Y (2010) Highly durable graphene nanoplatelets supported Pt nanocatalysts for oxygen reduction. *J Power Sources* 195:4600–4605
121. Liu G, Li X, Ganesan P, Popov BN (2009) Development of nonprecious metal oxygen-reduction catalysts for PEM fuel cells based on N-doped ordered porous carbon. *Appl Catal B Environ* 96:156–165
122. Merzougui B, Hachimi A, Akinpelu A, Bukola S, Shao M (2013) A Pt free catalyst for oxygen reduction reaction based on Fe–N multiwalled carbon nanotube composites. *Electrochim Acta* 107:126–132
123. Byon HR, Suntivich J, Shao-Horn Y (2011) Graphene-based non noble-metal catalysts for oxygen reduction reaction in acid. *Chem Mater* 23:3421–3428
124. Charretier F, Jaouen F, Ruggeri S, Dodelet J-P (2008) Fe/N/C nonprecious catalysts for PEM fuel cells: influence of the structural parameters of pristine commercial carbon blacks on their activity for oxygen reduction. *Electrochim Acta* 53:2925–2938
125. Byon HR, Suntivich J, Crumlin EJ, Shao-Horn Y (2011) Fe–N modified multi-walled carbon nanotubes for oxygen reduction reaction in acid. *Phys Chem Chem Phys* 13:21437–21445
126. Oh HS, Oh JG, Roh B, Hwang I, Kim H (2011) Development of highly active and stable non-precious oxygen reduction catalysts for PEM fuel cell using polypyrrole and a chelating agent. *Electrochem Commun* 13:879–881
127. Babu SK, Chung HT, Wu G, Zelenay P, Litster S (2014) Modeling hierarchical non-precious metal catalyst cathodes for PEFCs using multi-scale X-ray CT imaging. *ECS Trans* 64:281–292
128. Artyushkova K, Atanassov P, Dutta M, Wessel S, Colbow V (2015) Structural correlations: design levers for performance and durability of catalyst layers. *J Power Sources* 284:631–641

129. Banham D, Ye S, Pei K, Ozaki J-I, Kishimoto T, Imashiro Y (2015) A review of the stability and durability of non-precious metal catalysts for the oxygen reduction reaction in proton exchange membrane fuel cells. *J Power Sources* 285:334–348
130. Yuan S, Shui J-L, Grabstanowicz L, Chen C, Commet S, Reprogie B, Xu T, Yu L, Liu D-J (2013) A highly active and support-free oxygen reduction catalyst prepared from ultrahigh-surface-area porous polyporphyrin. *Angew Chem Int Ed* 52:8349–8353
131. Wu W, Wan Z, Chen W, Zhu M, Zhang D (2015) Synthesis of mesoporous alumina with tunable structural properties. *Microporous Mesoporous Mater* 217:12–20
132. Badoga S, Sharma RV, Dalai AK, Adjaye J (2015) Synthesis and characterization of mesoporous aluminas with different pore sizes: application in NiMo supported catalyst for hydrotreating of heavy gas oil. *Appl Catal A Gen* 489:86–97
133. Zeng J, Francia C, Dumitrescu MA, Monteverde Videla AHA, Ijeri VS, Specchia S, Spinelli P (2012) Electrochemical performance of Pt-based catalysts supported on different ordered mesoporous carbons (Pt/OMCs) for oxygen reduction reaction. *Ind Eng Chem Res* 51:7500–7509
134. Qin Y, Li J, Yuan J, Kong Y, Tao Y, Lin F, Li S (2014) Hollow mesoporous carbon nitride nanosphere/three-dimensional graphene composite as high efficient electrocatalyst for oxygen reduction reaction. *J Power Sources* 272:696–702
135. Hung C-T, Yu N, Chen C-T, Wu P-H, Han X, Kao Y-S, Liu T-C, Chu Y, Deng F, Zheng A, Liu S-B (2014) Highly nitrogen-doped mesoscopic carbons as efficient metal-free electrocatalysts for oxygen reduction reactions. *J Mater. Chem A* 2:20030–20037
136. Kramm UI, Herranz J, Larouche N, Arruda TM, Lefèvre M, Jaouen F, Bogdanoff P, Fiechter S, Abs-Wurbach I, Mukerjee S, Dodelet J-P (2012) Structure of the catalytic sites in Fe/N/C-catalysts for O₂-reduction in PEM fuel cells. *Phys Chem Chem Phys* 14:11673–11688
137. Tüysüz H, Schüth F, Zhi L, Müllen K, Comotto M (2015) Ammonia decomposition over iron phthalocyanine-based materials. *Chem Cat Chem* 7:1453–1459
138. Kramm UI, Herrmann-Geppert I, Bogdanoff P, Fiechter S (2011) Effect of an ammonia treatment on structure, composition, and oxygen reduction reaction activity of Fe-N-C catalysts. *J Phys Chem C* 115:23417–23427

Application of Scanning Electrochemical Microscopy (SECM) to Study Electrocatalysis of Oxygen Reduction by MN_4 -Macrocyclic Complexes

Justus Masa, Edgar Ventosa and Wolfgang Schuhmann

1 Introduction

1.1 Scanning Electrochemical Microscopy (SECM)

Scanning electrochemical microscopy (SECM) is a scanning probe technique using a micro- or nanoelectrode which is scanned in very close proximity to a solid/liquid, liquid/liquid, or gas/liquid interface to investigate its chemical or electrochemical properties [1–6]. A simple graphic representation of the basic working principle of the SECM technique is presented in Fig. 1. The unique feature of SECM, as opposed to conventional electrochemical techniques, is its ability to probe the local properties of a selected region on a surface, or to map the electrochemical reactivity of the surface if suitable electrochemical perturbation is applied to the tip, or to both the tip and the probed surface. By recording the currents due to electrochemical reactions occurring at a nano- or microelectrode (also referred to as the SECM tip), as the tip is scanned in close proximity to a surface, SECM can be used to acquire among others, chemical reactivity images of surfaces, including interfacial rates of heterogeneous electron transfer and the diffusion profiles of redox species.

The development of SECM, which began in the late 1980s, is mainly credited to A. Bard and his coworkers who first described the technique, coined its name, and also developed the early modes of its operation, namely the feedback and the generation–collection modes, which will be described later. In the course of its nearly 30 years of existence, SECM has established itself as the tool of choice for studying spatially resolved local electrochemical reactivity of surfaces, including the quantitative study of the kinetics of both electrochemical and chemical reactions from microscopic to submicroscopic scales [2, 7]. Indeed, the ability of SECM to

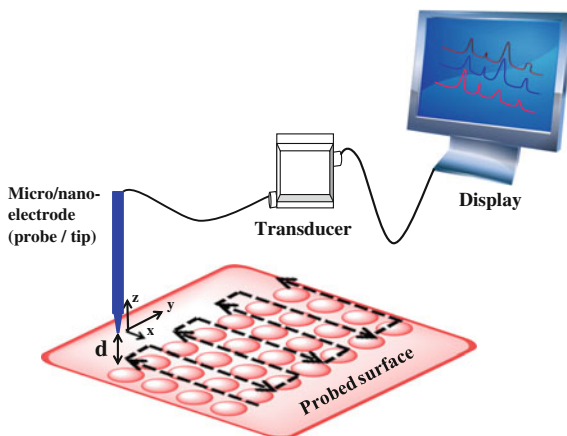
J. Masa · E. Ventosa · W. Schuhmann (✉)

Analytical Chemistry - Center for Electrochemical Sciences (CES),

Ruhr-Universität Bochum, Universitätsstr. 150, 44780 Bochum, Germany

e-mail: wolfgang.schuhmann@rub.de

Fig. 1 Representation of the basic working principle of an SECM



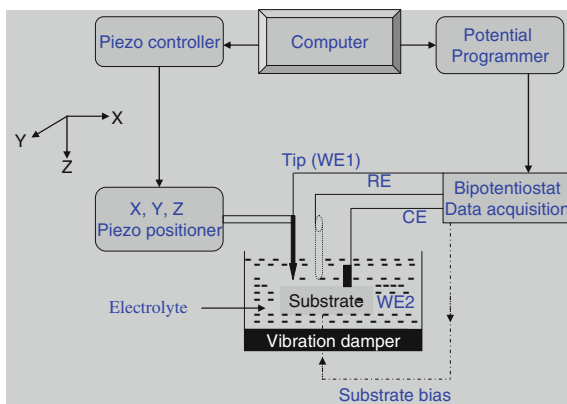
acquire spatially resolved electrochemical information at and beyond the microlevel has been exploited for localized corrosion investigation [8, 9], the study of the electrocatalytic behavior of individual nanoparticles [10–12], enzyme catalyzed reactions [13], charge-transfer mechanisms [14], adsorption and desorption phenomena, diffusion processes across membranes, real-time determination of hydrogen peroxide release from bacterial films [15], and for monitoring the physiological activity of single living cells [16, 17]. The versatility of SECM has been made possible by the complimentary development of micro- and nanoelectrodes [18] along with more precise positioning systems thus enabling high-resolution imaging, advancement in the theoretical understanding of the diffusion properties at ultra-microelectrodes, and the development and/or improvement of experimental methods and procedures. SECM also finds application as a tool for microfabrication and micropatterning of surfaces [19, 20], and new fields of application are expected in future [21].

1.2 Instrumentation

The essential components of a basic SECM setup are shown in Fig. 2. As with other scanning probe techniques, an SECM is equipped with a positioning system to allow for lateral scanning as well the vertical approach of the tip as close as possible to the surface to be probed.

The positioning system is comprised of micro- to nanoscale precision stepper motors and piezo elements with integrated encoders of a few nm resolution to facilitate precise positioning of the tip at x-, y-grid points at a very close distance above the sample surface. SECM instruments are equipped with a potentiostat if an electrochemical signal is to be applied or monitored at only the tip (WE1), or specifically, a bipotentiostat if a second electrochemical signal is to be applied or

Fig. 2 Schematic representation of the essential components of an SECM including a potentiostat, positioning systems, an electrochemical cell, and a computer. *WE1* working electrode 1, *WE2* work electrode 2, *CE* counter electrode, *RE* reference electrode



monitored at the sample which serves as a second working electrode (WE2). In a typical setup, an electrochemical cell is assembled using the sample as a working electrode, a counter electrode (CE), and a reference electrode (RE). Specially designed electrochemical cells are necessary for SECM measurements. Since very low currents, typically from nanoamperes to sub-picoamperes are measured, the whole system is set up in a Faraday cage and on a vibration-damping table. The lateral resolution of the SECM is primarily limited by the size and nature of the SECM tip, which can therefore be considered as the heart of the SECM. In the following Sect. 1.3, we discuss the important features of microelectrodes including their mass transport and diffusion properties.

1.3 Microelectrodes

A microelectrode is an essential element in an SECM. Precisely, the microelectrode is the probe with which the surface of the sample is scanned. The lateral resolution of the SECM is determined by the size of the scanning probe. Therefore, microelectrodes of small dimensions are necessary to obtain laterally highly resolved images. Decreasing the size of the electrode from macro- to micro-scale brings additional features to the electrode behavior. The special properties of microelectrodes are very important not only to their application in SECM. The small size of a microelectrode influences two key parameters: (i) the mass transport of species and (ii) the current line distribution.

1.3.1 Mass Transport at Microelectrodes

When an electrochemical reaction is limited by diffusion at a flat macroelectrode, the electroactive species only diffuse perpendicular (planar or axial) to/from the surface

sample (Fig. 3a). If the dimensions of the electrode (at least one dimension) are decreased to the microscale, the flux of species is not only perpendicular to the sample surface, but additionally a radial flux (parallel diffusion) originates from the sides of the microelectrode (Fig. 3b). Therefore, the mass transport of species at microelectrodes is enhanced due to the additional flux (non-perpendicular diffusion).

The flux of species to an electrode is described by Fick's laws, which varies according to the electrode geometry: flat electrode, cylindrical electrode, disk electrode, spherical electrode, etc. Applying electrochemical boundary conditions, the solution of the diffusion equation is obtained. Considering a chronoamperometry experiment at a disk microelectrode where a potential step is applied to the electrode and the reaction proceeds under diffusion control without convection or migration, the following equations are obtained:

$$i = \frac{nFAD^{0.5}C^*}{\pi^{0.5}t^{0.5}} + 4nFDC^*r_0 \quad (1)$$

$$i_{ss} = 4nFDC^*r_0 \quad (2)$$

where i is the current intensity, i_{ss} is the current intensity under steady-state conditions, n is the number of transferred electrons, F is the Faraday constant, A is the electrode area, D is the diffusion coefficient, C^* is the concentration of the redox species in the bulk of the solution, t is time, and r_0 is the radius of the microelectrode.

The current response contains two terms: a time-dependent and a time-independent one. Note that the former is the current–time response (known as Cottrell equation) obtained for axial diffusion at macroelectrodes. The additional

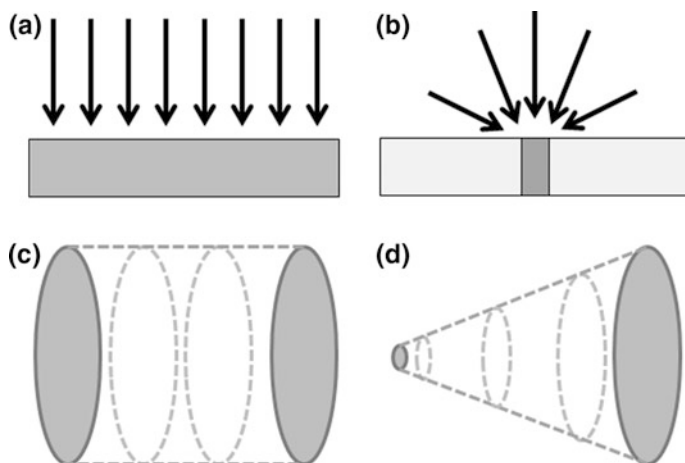


Fig. 3 Schematic representation of diffusion field (a, b) and current lines (c, d) for a macroelectrode (a, c) and a microelectrode (b, d)

radial diffusion results in the time-independent term. Since the axial diffusion term is dependent on the inverse of the square root of time, axial diffusion dominates at very short timescales and it diminishes for longer times. After a given time, the contribution of the time-dependent term is negligible and the current response reaches a stationary steady state (Eq. 2). How long it takes for the current response to reach the steady state is determined by the radius of the microelectrode. The current response is proportional to the square of the radius of the electrode (area) for the axial diffusion term, while it is proportional to the radius for the radial diffusion term. Therefore, the axial diffusion term decreases faster with decreased radius than the radial diffusion term. As a consequence, the timescale over which the axial diffusion term dominates the current response shortens as the radius of the electrode decreases. For example, when the diameter of a disk electrode is decreased from 10 to 1 μm , the necessary time to reach steady state shortens from 1.3 to 0.01 s, assuming a diffusion coefficient of $10^{-9} \text{ m}^2 \text{ s}^{-1}$.

1.3.2 Current Line Distribution and Ionic Resistance of the Electrolyte

The polarization of an electrode triggers the movement of ionic species in the solution. The current lines represent the path of the ionic species which are perpendicular to the equipotential lines. When two macroelectrodes of comparable size are used, the equipotential lines are parallel to the electrode and the current lines are perpendicular to the electrodes. The current lines are confined within the volume defined by the area of the electrodes and the distance between them (Fig. 3c).

The ionic resistance of the electrolyte solution is determined by the specific ionic conductance of the solution, the area of the electrode, and the distance between them, as shown in Eq. 3

$$R_i = \frac{1 L}{k A} \quad (3)$$

$$R_i = \frac{1}{4k} \left(\frac{1}{r} - \frac{1}{L} \right) \quad (4)$$

$$R_i = \frac{1}{4k r} \quad (5)$$

where R_i is the ionic resistance, k is the specific conductance of the electrolyte solution, L is the distance between the electrodes, A is the area of the electrode, and r is the radius of the electrode.

Equation 3 is no longer valid when one of the two electrodes becomes significantly smaller than the other one. Assuming disk electrodes, the ionic resistance of a small electrode surrounded by a much larger electrode is defined by Eq. 4 [22]. Now, the volume in which the current lines are confined is no longer a cylinder, but it becomes a cone (Fig. 3d). The parallel sections to the electrode which are near to

the smaller electrode contribute more to the overall ionic resistance since the area of those sections is much smaller. Indeed, the contribution of the sections far away from the small electrode becomes negligible. Mathematically, when the radius of the small electrode is much smaller than the distance between the electrodes, Eq. 5 is obtained. Two major differences are observed between Eq. 5 (microelectrode) and Eq. 3 (macroelectrode). The ionic resistance for a microelectrode becomes (i) independent of the distance between the electrodes and (ii) proportional to the inverse of the radius of the electrode, instead of being proportional to the inverse of the square of the radius. The new features in the ionic resistance when using a microelectrode in an electrochemical cell strongly affect (i) the iR drop and (ii) the time constant of the cell.

The potential drop across the electrolyte solution is determined by the product of current intensity and ionic resistance. In a microelectrode, the ionic resistance is independent of the distance to the other electrode, which allows working in solutions with low ionic conductivity. In addition, the ionic resistance is proportional to the inverse of the radius of the electrode. Since the intensity is proportional to the radius for steady-state conditions, the iR drop is not dependent on the size of the microelectrode. However, at nonsteady-state conditions, that is, e.g., in ultrafast cyclic voltammetry, the intensity is proportional to the area, and thus the iR drop is proportional to the radius of the microelectrode. In other words, the iR drop decreases as the size of the microelectrode decreases under nonsteady-state conditions.

A simple electrochemical cell consists of a minimum of two elements in series, that is, a double-layer capacitance and an ionic resistance. The time constant of a cell is the product of capacitance and the resistance, and it represents the required timescale for building the double layer when polarizing an electrode. The time constant of a cell is very important because it determines the timescale over which an electrochemical process cannot be studied. The double-layer capacitance is proportional to the surface area of the electrode, regardless of its dimensions. At a macroelectrode, the ionic resistance of the solution is proportional to the inverse of the area. As a result, the time constant is not dependent on the size of the electrode for flat macroelectrodes. At microelectrodes, the ionic resistance is proportional to the inverse of the electrode radius. Therefore, the time constant is proportional to the electrode radius for microelectrodes. In practice, it means that one is able to study faster reactions by decreasing the size of the microelectrode.

In conclusion, microelectrodes possess unique electrochemical properties, namely, steady-state current response within short timescales, increased faradaic-to-capacitive ratio of the current intensity, independence of the ionic resistance from the distance between electrodes, and short time constants (fast response).

1.4 Modes of Operation in SECM

An SECM is a versatile analytical tool since it can operate in a variety of modes depending on the targeted systems and pursued information. Indeed, the number of

operating modes increases every year, and so do the applications of SECM. In this section, only a selection of the most representative modes are discussed, including feedback, generation/collection (SG-TC and TG-SC), redox competition, and surface patterning mode.

1.4.1 Feedback Mode

The feedback mode of operation provides information about the electron transfer kinetics at the surface of a sample. To this end, a freely diffusing redox mediator is added into the electrolyte solution. The microelectrode (tip) is polarized to a potential at which a steady-state diffusion-limited current value is measured at the tip (Fig. 4a). When the tip is made to approach the surface of a nonreactive or insulating sample, the diffusion of the redox mediator is hindered leading to decreased current intensity at the tip (negative feedback), as shown in Fig. 4b, d. On the contrary, when the tip approaches the surface of a reactive and/or conductive sample, the redox mediator is regenerated at the sample surface with a certain rate leading to an increased current intensity (positive feedback), as illustrated in Fig. 4c, d. An important feature of the feedback mode is that the sample does not need to be polarized, although a potential may be applied in the case of a conducting sample.

Approach curves (current vs. distance curves) are employed to estimate the electron transfer rate constants at the sample surface by fitting experimental data to

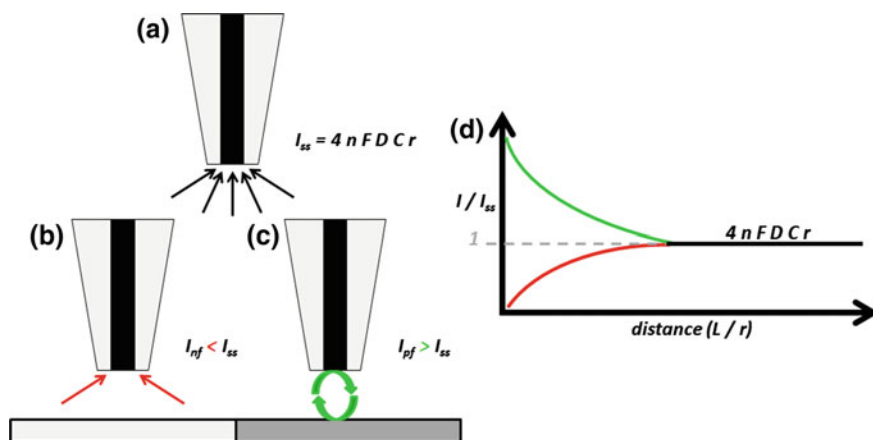


Fig. 4 Feedback mode. **a** Steady-state diffusion-limited current at the tip when it is located far from the sample surface. **b** Negative feedback due to hindered diffusion of the redox mediator toward the tip when approaching a nonreactive or insulating sample. **c** Positive feedback due to the regeneration of the redox mediator at the sample surface when approaching a reactive and/or conductive sample. **d** Normalized intensity measured at the tip as a function of the normalized tip-to-sample distance (normalized by the radius of the tip)

simulated curves. For this propose, only z-direction motion of the tip is required. Images of the surface reactivity are obtained when a selected tip-to-sample distance is kept constant while scanning in the x- and y-directions. For example, a relatively higher current intensity is recorded at the tip as it is scanned over a sample area with fast electron transfer kinetics for the regeneration of the redox mediator.

1.4.2 Generation/Collection Mode

There are two modes for generation/collection, depending on whether the tip or the sample generates or collects the species of interest.

(i) *Tip generation/sample collection mode (TG-SC)*

In the tip generation/sample collection mode of SECM, the concentration of a given species (R) is locally perturbed near the sample surface by generating it at the tip (Fig. 5a). In TG-SG, both the tip and the sample are connected to a bipotentiostat since the current responses of both electrodes are measured. If the tip-to-sample distance is small, most of the species generated at the tip are collected at the sample in case of a simple one-step heterogeneous electron transfer reaction. For processes with a coupled homogeneous chemical reaction, the current measured at the tip and sample may differ largely since electrochemically inactive species may be generated in the coupled chemical reaction. Information about the kinetics of the coupled homogeneous chemical reaction is obtained from the analysis of the current intensity at the tip and sample.

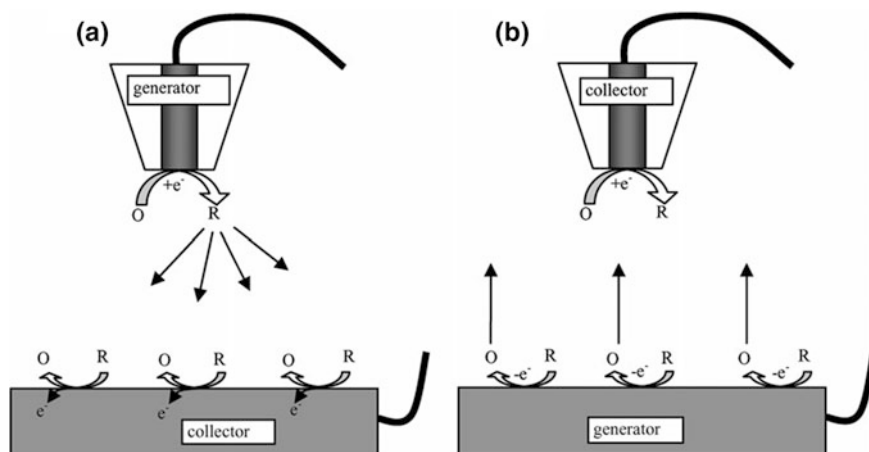


Fig. 5 Generation/collection mode. **a** Tip generation/sample collection mode. A species is generated at the tip and collected at the sample. **b** Sample generation/tip collection mode. A species is generated at the sample and collected at the tip. Reproduced from [3] with permission of the Royal Society of Chemistry

(ii) *Sample generation/tip collection mode (SG-TC)*

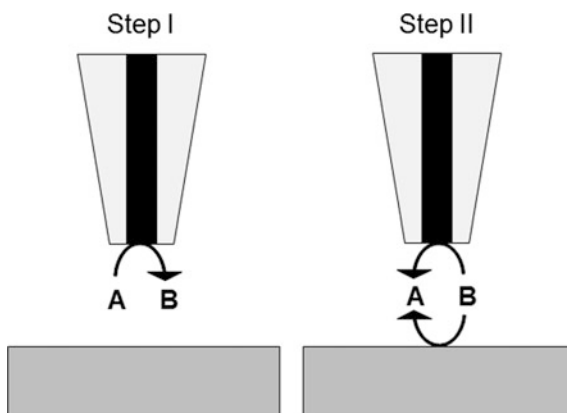
In the sample generation/tip collection (SG-TC) mode, a redox species is generated at the sample and collected at the tip (Fig. 5b). Again, the current intensities of both tip and sample are measured. Initially, this mode of operation was designed to determine concentration profiles in the diffusion layer generated at the sample [23, 24]. However, in principle, any electrochemically active species generated at the sample can potentially be studied in the SG-TC mode. Ideally, a small microelectrode should not perturb much the free diffusion of species generated at the sample.

1.4.3 Redox Competition Mode

The redox competition mode consists of two subsequent steps (Fig. 6). In the first step, the species of interest is electrochemically generated at the tip increasing the concentration of this species in the gap between tip and sample surface. In the subsequent step, the generated species is collected at the tip. Simultaneously, the generated species is also collected at the sample, which means that both tip and sample compete in the second step for the species generated at the tip in the first step.

The current intensity recorded at the tip in the second step is dependent on how active the sample surface is toward the conversion of the generated species. If the sample is not reactive or exhibits a slow kinetics toward the electrochemical reaction of the generated species, the tip is able to recollect a large portion of the initially generated species. On the other hand, if the sample surface is very reactive showing a fast kinetics toward the electrochemical reaction of the generated species, the current intensity at the tip in the second step decreases significantly since a large portion of the generated species are collected at the sample.

Fig. 6 Redox competition mode. *Left* the species of interest is generated at the tip in the first step. *Right* Both the tip and sample compete to collect the generated species



1.5 Influence of the Sample Surface Topography

The tip response is not only dependent on the chemical and electrochemical properties of the sample surface, but also on the distance between tip and sample surface. In a simple SECM experiment, three z-approach curves are performed to calculate the tilt of the sample with respect to the scanning plane of the tip. After correcting the sample tilt, a distance between the tip and the sample surface is selected for scanning in x- and y-directions at the selected “constant height” (constant z-position). In these measurements, one assumes that the sample surface is relatively smooth, so that the constant height translates to a constant distance between tip and sample surface. However, this assumption is not always correct. The evaluation of samples with rough surfaces (in the order of micrometers) or the use of very small microelectrodes or nanoelectrodes (the necessary tip-to-sample surface distance is proportional to the electrode radius) requires correcting the tip-to-sample distance (Fig. 8). In these cases, scanning at constant height is not sufficient, and additional methods must be implemented in the SECM system to maintain a constant tip-to-sample surface distance to deconvolute electrochemical and topographic contributions to the tip current.

1.5.1 Intermittent Contact in SECM

In the intermittent contact mode, the tip vertically oscillates at a given amplitude and frequency [25]. When the tip comes in contact with the sample (tapping), the amplitude of the vertical oscillation changes and this change is used as a feedback signal to control the tip-to-sample distance (Fig. 9a). As a result, the intermittent contact mode allows operating at a constant distance as well as obtaining the topography of the surface. In addition, the hopping mode can also be implemented and SECM images at several tip-to-sample surface distances are obtained leading to 4D representations of the local electrochemical activity of a sample surface [26].

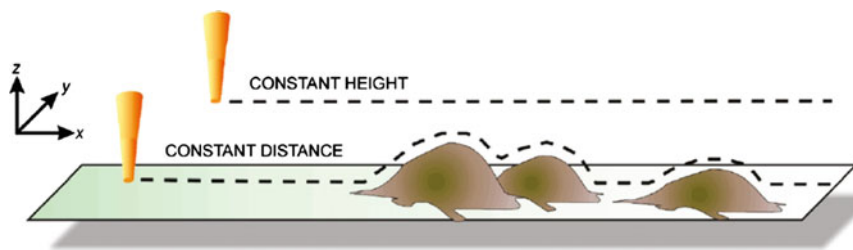


Fig. 8 Schematic illustration of the difference between scanning at constant height and at constant distance in SECM. Reproduced from [16] with permission of the American Chemical Society

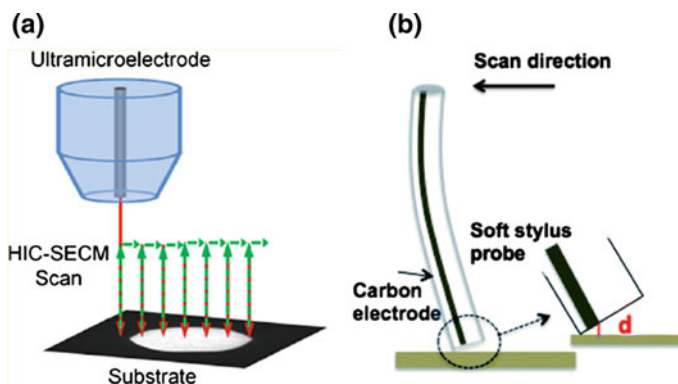


Fig. 9 **a** Schematic representation of intermittent contact SECM. Reproduced from [25] with permission of the American Chemical Society. **b** Schematic illustration of a soft microelectrode. Reproduced from [18] with permission of the Royal Society of Chemistry

1.5.2 Soft Microelectrodes in SECM

Instead of using a glass sheath or a rigid microelectrode like in the majority of SECM experiments, flexible and soft electrodes are employed in this approach [27]. When the soft electrode is brought in contact with the scanned surface, it bends creating a small gap between the tip and surface (Fig. 9b). Since the microelectrode is flexible, it will adopt the topography of the surface, maintaining a relatively constant distance between tip and sample surface.

1.5.3 Combination of Atomic Force Microscopy with Scanning Electrochemical Microscopy (AFM-SECM)

Atomic force microscopy (AFM) is a scanning probe technique that provides topographical information of a surface at the nanoscale. The main limitation of combining AFM (topography) with SECM (electrochemistry) is to implement a nano- or microelectrode into an AFM probe to create a bifunctional tip (Fig. 10). The implemented nanoelectrode can be (i) located below the apex of the AFM cantilever tip [28], or (ii) separated from the apex of the tip [29]. The former approach allows simpler fabrication at Si-wafer level. On the other hand, the location of the nanoelectrode below the apex of the tip leads to electrical short-circuiting problems when scanning in contact mode (Fig. 10b). This issue is amended by scanning in the so-called lift mode which requires first recording the topography of a line and then performing a second pass following sample topography after retraction of the tip to a predefined distance for the electrochemical measurement (Fig. 10c). When the nanoelectrode is separated from the tip apex by positioning the electrode at a certain distance above the AFM tip, so-called recessed electrodes, topography, and electrochemistry data are acquired simultaneously in

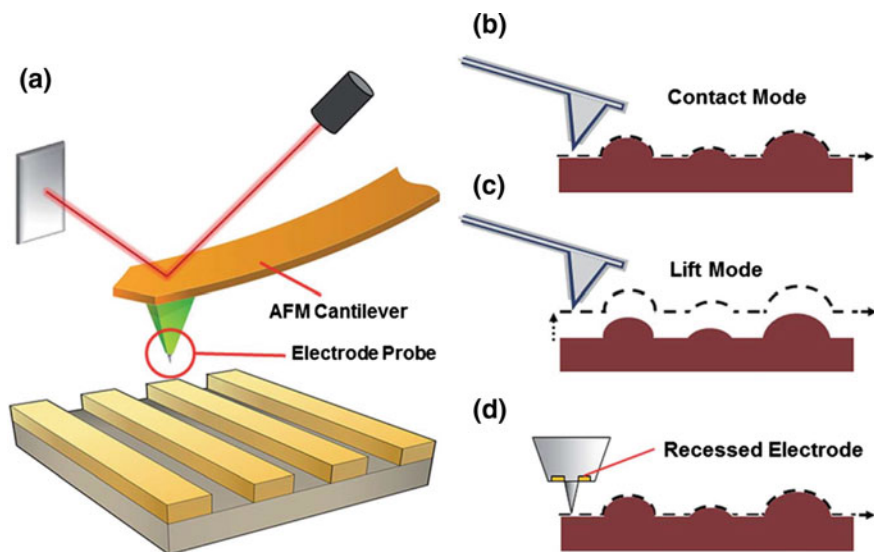


Fig. 10 Combination of AFM with SECM. **a** Schematic illustration of the AFM—SECM setup. AFM—SECM in **b** contact mode, **c** lift mode, and **d** recessed electrode mode. Reproduced from [30] with permission of the Royal Society of Chemistry

the contact mode (Fig. 10d), since the nanoelectrode and the sample are not in direct contact but separated by a constant distance.

1.5.4 Shear force in SECM

In the shear force mode, a microelectrode is horizontally vibrated at its resonance frequency using a piezoelectric positioner (Fig. 11a) [31, 32]. The detection and monitoring of the amplitude of the oscillation can be carried out via optical, piezo, or tuning fork methods (Fig. 11b–d).

Increase in the shear force in close proximity to the sample surface leads to damping of the amplitude of oscillation. Using the amplitude of the oscillations as feedback signal, the tip-to-sample surface distance is maintained constant during the SECM measurements.

1.5.5 Combination of Scanning Ion-Conductance Microscopy with Scanning Electrochemical Microscopy (SICM–SECM)

Scanning ion-conductance microscopy (SICM) was initially developed to obtain topographical information on delicate and fragile samples, typically biological samples, immersed in liquid solution in a noncontact and noninvasive way [33]. SICM employs a hollow capillary as scanning probe instead of a microelectrode.

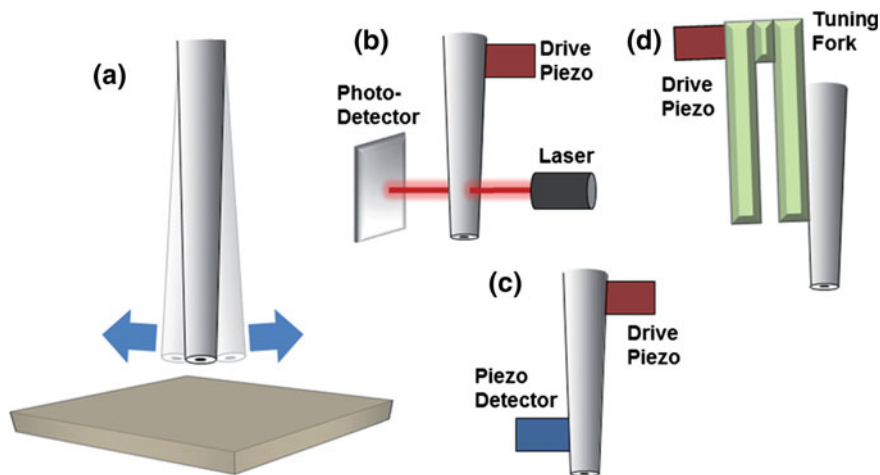


Fig. 11 Shear force in SECM. **a** Illustration of a microelectrode horizontally vibrating at its resonance frequency. Detection of the vibration by **b** optical, **c** piezo, and **d** tuning fork methods. Reproduced from [30] with permission of the Royal Society of Chemistry

The capillary is immersed into solution. Two electrodes, one inside the capillary and the other one outside are employed. When applying a voltage between the two electrodes, the faradaic current depends on the ionic resistance of the solution which is dominated by the small area of the opening of the capillary. In close proximity to the sample surface, the current lines passing through the opening are disturbed and the ionic resistance increases, which in turn decreases the current intensity between the two electrodes (Fig. 12a). Therefore, using the current intensity between the two electrodes as a feedback signal, the distance between the tip of the capillary and the sample surface is maintained constant while scanning in *x*- and *y*-directions.

The microelectrode can be implemented in the SICM system following either of the following two approaches. (i) Depositing a thin layer of conducting metal, which is then coated with a second layer of insulator onto the outer wall of the capillary to obtain a capillary (SICM) with a ring microelectrode (SECM) at the end of the capillary [34]. (ii) Splitting the inner volume of the capillary into two compartments. One compartment remains hollow (SICM), while the other one is filled with a conducting agent to convert it into a microelectrode (SECM) [35].

1.5.6 Scanning Electrochemical Cell Microscopy (SECCM)

Scanning electrochemical cell microscopy (SECCM) uses a capillary with double compartment (dual barrel capillary) pulled to a sharp opening (Fig. 13b) as scanning probe [36]. Both compartments of the capillary are filled with the electrolyte solution, and a quasi-reference counter electrode (QRCE) is inserted in each compartment (Fig. 13a).

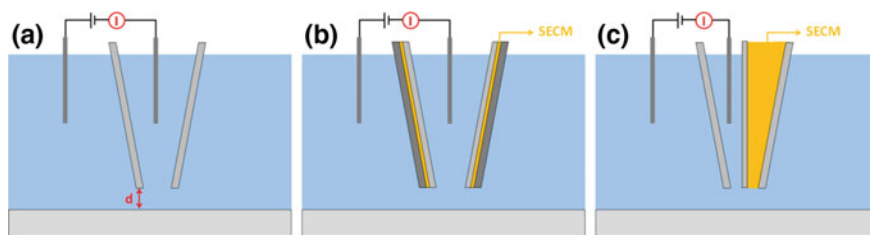


Fig. 12 SICM–SECM. **a** Illustration of the cross section of an SICM system. **b** Ring microelectrode implemented into the capillary wall. **c** Microelectrode included in the second compartment of the capillary (dual barrel capillary)

The electrolyte solution is only located inside the capillary and the sample is not immersed in solution. When the capillary is located far from the sample surface, the small meniscus hanging at the tip of the capillary ionically connects both compartments, which allows ion migration between the two compartments when a voltage is applied between the two QRCEs. The ionic connection is maintained when the meniscus makes contact with the sample surface. Further approach of the meniscus to the surface results in an increased ionic resistance which is employed as a feedback signal to maintain the distance between the tip of the capillary and the sample surface constant while scanning across the sample in x - and y -directions. At each x -, y -grid point, the electrochemical properties of the small area of the sample surface, defined by the area of the capillary opening, are evaluated using classic electrochemical methods, e.g., cyclic voltammetry or potentiostatic chronoamperometry. One of the QRCE acts both as reference and counter electrode of the minuscule cell (Fig. 13a).

2 Study of the Oxygen Reduction Reaction (ORR) Using SECM

2.1 Electrocatalysis of Oxygen Reduction

The oxygen reduction reaction (ORR) is of vital importance in numerous electrochemical energy conversion and storage technologies, including fuel cells, metal–air batteries, and in the chlor-alkali industry [38–40]. The electrochemical reduction of oxygen is however kinetically slow and occurs at rather high overpotentials, thus drastically lowering the overall energy output from galvanic cells. The search for stable catalysts which can improve the kinetics and thermodynamic efficiency of the ORR is a major goal of many investigations on the ORR.

The electrochemical reduction of oxygen is generally considered to proceed via a mechanism involving one, or both of two possible reaction pathways outlined in reaction equations [i] to [iv] [41]. In the first pathway [i], oxygen is reduced by the

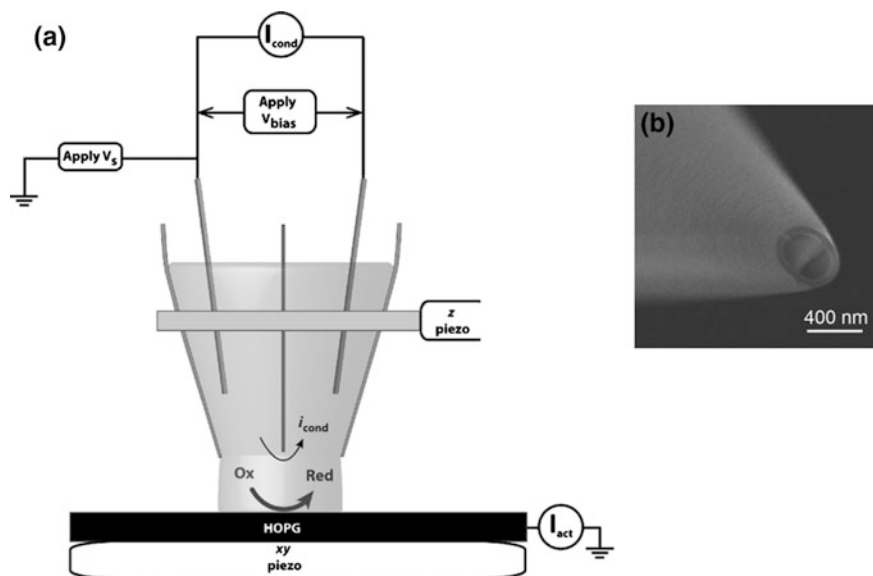
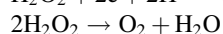
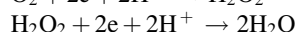
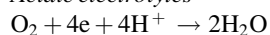


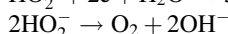
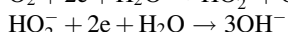
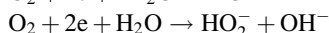
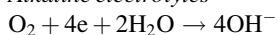
Fig. 13 **a** Scanning Electrochemical Cell Microscopy (SECCM). **b** SEM image of the tip of a double barrel capillary. Reproduced from [37] with the permission of Wiley

transfer of four electrons to form H_2O or OH^- , depending on the pH value of the electrolyte, the catalyst used, and the reaction conditions. In an alternative pathway, oxygen is reduced by the transfer of two electrons to form H_2O_2 , reaction [ii], either as the end product, or the primarily formed H_2O_2 may undergo a further 2-electron reduction to form H_2O (or OH^-), reaction [iii] or chemical decomposition [iv] to regenerate oxygen and form H_2O (or OH^-).

Acidic electrolytes



Alkaline electrolytes



$$E^\circ = 1.23 \text{ V}_{\text{RHE}} \quad [\text{i}]$$

$$E^\circ = 0.67 \text{ V}_{\text{RHE}} \quad [\text{ii}]$$

$$E^\circ = 1.77 \text{ V}_{\text{RHE}} \quad [\text{iii}]$$

$$[\text{iv}]$$

For electrochemical energy conversion processes, reaction [i] is desirable since a maximum free energy ($\Delta G = -nFE^\circ$) is harnessed from the reaction, where E° is the standard theoretical equilibrium potential, n is the number of electrons transferred, F the Faraday constant, ΔG the Gibbs free energy. Besides the formation of H_2O_2 , reaction [iii] being less energy efficient, the formed H_2O_2 tends to destroy cell components due to its oxidizing nature [42, 43].

Characterization of electrocatalysts for the ORR therefore routinely involves determination of their selectivity, which essentially requires the determination of the number of electrons transferred, the percentage of H_2O_2 generated, and the rate of decomposition of H_2O_2 . Rotating disk electrode (RDE) voltammetry and

rotating-ring disk electrode voltammetry (RRDE) are the routine techniques of choice for investigating potential ORR catalysts [44–47]. These techniques owe their popularity to their simplicity and relatively simple mathematical treatment of experimental data. However, both RDE and RRDE suffer from the disadvantage that only one catalyst can be investigated at a time which makes it cumbersome if many samples are to be investigated. Second, both RDE and RRDE perform well when they are used to investigate smooth and thin uniform catalyst films where diffusion of the analyte inside the film is negligible. Significant shortcomings arise when RDE and RRDE are used to investigate ORR on highly porous materials, and when thick catalyst films are to be investigated, since diffusion of the analyte through the film cannot be neglected [47]. Some of the shortcomings of RDE and RRDE can be overcome using SECM for quantitative study of the ORR [48–50]. Additionally, SECM can be employed as a semi-combinatorial or high-throughput technique to screen the ORR activity of catalyst libraries of variable nature, properties, or composition [51–53]. In Sects. 2.1.1 through 2.1.3 we discuss the application of SECM as a tool for qualitative and quantitative study of the ORR, as well as for high-throughput screening of catalyst libraries.

2.1.1 Visualization of Oxygen Reduction Using SECM

By recording an electrochemical response, typically the current at the SECM tip, sample, or both, as the tip is scanned in close proximity to a surface, micro- to nano-spatially resolved chemical reactivity images of the surface, and quantitative data for analyzing heterogeneous electron transfer rates [3, 4, 13, 54, 55], as well as diffusion profiles [56] and adsorption/desorption phenomena [57] can be acquired. For visualization of the ORR activity of catalysts, various operation modes of SECM including SG-TC [48, 49, 58], TG-SC [59, 60], and the oxygen competition mode may be used [61].

In the TG-SC mode, a constant current or potential applied to the tip is used to produce oxygen by water oxidation while a suitable potential is applied to the sample to induce oxygen reduction. In this way, the steady-state current measured at the sample is a direct measure of its local ORR activity [59, 62]. This method has the advantage that the measured signal is less sensitive to the tip-to-sample distance, which is crucial in the feedback mode. Fernández and Bard [59] employed the TG-SC mode of SECM to visualize the ORR activity on a disk-shaped Pt micro-electrode (127 μm diameter) at different tip-to-sample distances. To avoid interference by oxygen from air, the electrolyte was purged with argon and maintained under an argon atmosphere during measurements, so that only oxygen generated by the tip diffuses to the sample. Figure 14 shows the steady-state currents (i_s) measured at the Pt disk (sample) as a function of the x-y position of the SECM tip. i_s increases sharply as the tip is scanned from the insulating glass sheath over the Pt disk and decreases back to zero (or background) when the tip is again located over the insulating sheath. The resulting SECM image reproduces the size and form of

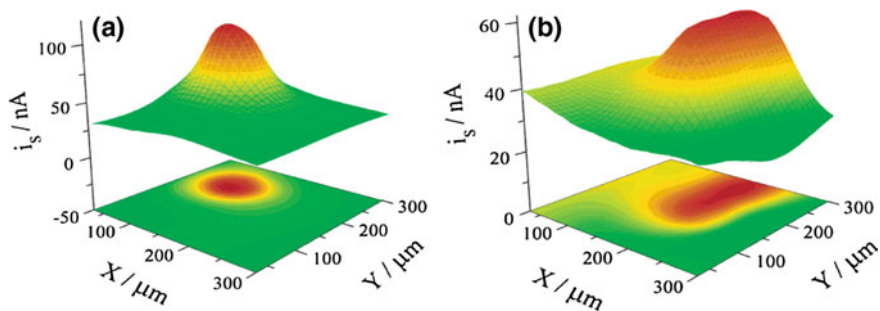
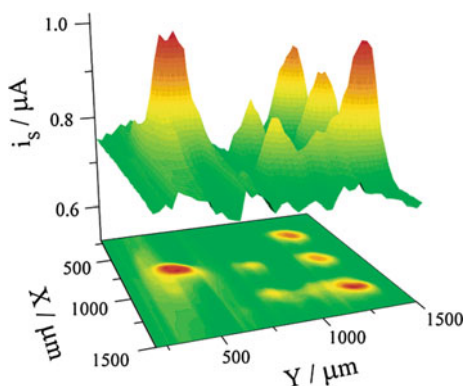


Fig. 14 SECM images showing oxygen reduction on a smooth Pt disk microelectrode ($127\ \mu\text{m}$ diameter) embedded in glass, recorded in the TG-SG mode of SECM: Scan rate = $300\ \mu\text{m}\ \text{s}^{-1}$, sample potential (E_s) = $0.1\ \text{V}$ **a** $d = 30\ \mu\text{m}$; $i_T = 76\ \text{nA}$. **b** $d = 5\ \mu\text{m}$; $i_T = 36\ \text{nA}$. In both **(a)** and **(b)**, the lower figure is a false color image where the current is represented by the color, and the upper is an actual representation of steady-state current i_s as a function of the x - y position

the disk with good resolution. The resolution of the SECM image is sensitive to the tip-to-sample distance. For example, when the tip is very close to the sample ($5\ \mu\text{m}$), a distorted image results (Fig. 14b). The spread of the current was attributed to traces of oxygen remaining between the sheath and the tip when the tip was already a few μm away from the active catalyst. The intensity of the sample current is dependent on the ORR activity of the sample, the tip-to-sample distance, and the potential applied to the sample, which makes it possible to visualize differences in the intrinsic ORR activity of material libraries under appropriate experimental conditions.

In Fig. 15, the TG-SC mode was used to visualize the ORR activity of a small array of spatially resolved Pt and Ru spots (size range $200\text{--}300\ \mu\text{m}$) deposited on a glassy carbon disk by means of a micropipette [59]. Higher sample currents indicate higher ORR activity of the underlying region or catalyst spot. Intrinsic differences in the ORR activity of Pt and Ru deposits could be clearly visualized, with Pt

Fig. 15 SECM images obtained with the TG-SC mode of an array of Pt (*left spot and right row*) and Ru (*middle row*) spots on a glassy carbon surface. Scan rate $600\ \mu\text{m}\ \text{s}^{-1}$; $d = 30\ \mu\text{m}$; $i_T = 210\ \text{nA}$; $E_s = 0.1\ \text{V}$. Taken from reference [59] with the permission of the American Chemical Society



exhibiting a significantly higher ORR activity than Ru, as expected [63]. However, it has to be noted that the height of the individual catalyst spots can have a significant impact on the measured steady-state current values. Nevertheless, this effect is less severe than in the feedback mode. One drawback of the TG-SC mode for screening the ORR activity of material arrays on a conductive support is the nonnegligible contribution of the background current to the measured sample current. Actually, the larger the area of the sample on which the catalyst spots are located, the higher is the background current. Low background currents are necessary to enable a high contrast in the activity of materials with almost similar activity.

In the redox competition mode (RC-SECM), the tip is scanned over a sample surface while both the sample and the tip are polarized at potentials where they both reduce oxygen [61, 64]. In this case, a decline in tip current proportional to the activity of the underlying sample is observed when the tip is scanned over an oxygen consuming spot or site. To maintain the concentration of oxygen in the gap between tip and sample at each grid point during scanning, a potential pulse profile is implemented where oxygen production by water oxidation at the tip precedes the oxygen reduction process. Several authors have deployed the RC-SECM mode to map the ORR activity of small catalyst arrays [65–72], and to monitor oxygen consumption by living cells [73, 74]. Quantitative determination of ORR kinetic parameters, including the average number of electrons transferred and the percentage of H_2O_2 is possible through sequential implementation of the oxygen competition mode and the SG-TC mode by means of a suitable pulse profile [50, 64].

2.1.2 High-Throughput Screening of ORR Catalysts Using SECM

The development of new catalysts is either guided by theoretical predictions or derived from material properties based on experimental observations. However, experimentalists are often faced with the need to investigate the electrochemical properties of a large collection of materials with variable chemical composition or structure in order to identify the most optimal catalyst [52, 75–79].

A unique feature of SECM is the possibility to use it as a semi-combinatorial or high-throughput tool to screen the electrocatalytic activity of material libraries [52, 80, 81]. For example, Bard's group formulated a thermodynamic criterion for the design of bimetallic catalysts for ORR based on the combination of a metal which readily cleaves the O–O bond of the oxygen molecule, and one which readily reduces the adsorbed oxygen atom. They tested their theory by screening the ORR activity of combinations of Pd and Co in H_2SO_4 (0.5 M) using SECM in the TG-SC mode. Figure 16 shows SEM images of bimetallic Pd–Co (i) and trimetallic Pd–Co–Au (ii) catalyst spots with variable Pd:Co and Pd:Co:Co:Au atomic ratios, respectively, prepared on glassy carbon plates using a piezo-based microarray dispenser, followed by reduction with hydrogen at 350 °C.

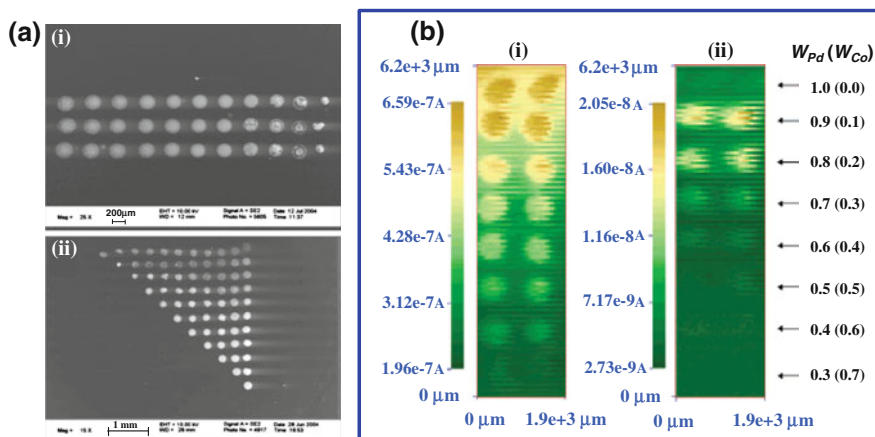


Fig. 16 **a** SEM images of bimetallic Pd–Co catalyst spots with variable Pd:Co atomic ratios (i), and trimetallic Pd–Co–Au catalyst spots with variable Pd:Co:Au atomic ratios (ii) prepared on a glassy carbon plate using a piezo-based microarray dispenser. **b** SECM images showing the ORR activity of Pd–Co binary arrays in 0.5 M H_2SO_4 . Tip-to-sample distance = 30 μm , tip current = -160 nA. Scan rate = 50 μm each 0.2 s, sample potential $E_s = 0.4$ V (i) and 0.7 V (ii). The potential is reported against the normal hydrogen reference electrode (HRE)

The atomic composition of Co in the bimetallic mixture was varied from 10–70 %. Results of the ORR activity of the bimetallic Pd–Co array at different sample potentials, 0.4 V (HRE) (i) and 0.7 V (HRE) (ii) at a constant tip current of -160 nA in the TG-SC mode are presented in Fig. 16b. At a sample potential of 0.4 V all catalyst compositions were able to reduce oxygen. Pd exhibited the highest activity, and a decrease in activity with Co content was observed. However, at a sample polarization potential of 0.7 V, the catalyst combination with 10 % Co was found to be the most active while pure Pd showed no activity at all. The activity decreased with increasing Co content >20 %. After the rapid screening procedure, more careful quantitative investigation using current–potential curves of the most promising compositions revealed that Pd–Co (80–20 %) had the highest activity with a positive shift in potential of about 150 mV compared to the results for pure Pd. To validate the performance of the catalysts, catalysts with a similar composition were prepared on high-surface area carbon with a combined metal of 20 wt %, and investigated for ORR using RDE. RDE studies revealed that Pd–Co (80–20 %) indeed had the highest activity which was consistent with the SECM studies.

The ORR activity of Pd–Co (80–20 %) was observed to readily decay after 3 h of continuous operation. To investigate the possibility for stabilization of the catalyst, and for further improvement of the activity, trimetallic combinations of Pd–Co and Au with variable compositions were investigated by a similar SECM rapid screening procedure. SEM images of the Pd–Co–Au catalyst spots of variable composition prepared on glassy carbon surfaces are shown in Fig. 16a (ii). SECM

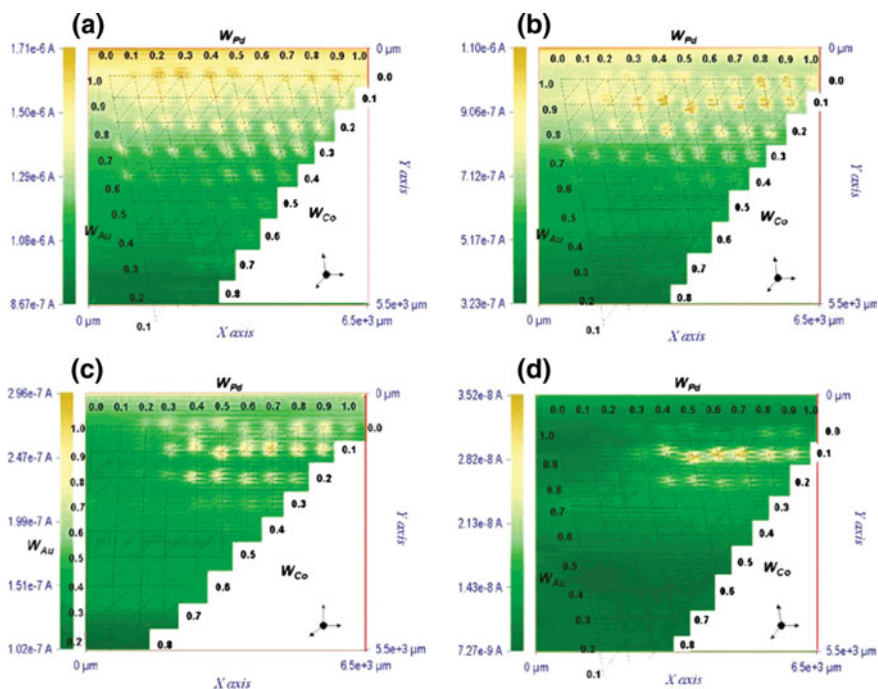


Fig. 17 SECM TG-SC images of ORR activity measured on Pd–Au–Co arrays in 0.5 M H_2SO_4 . Tip-to-sample distance = 30 μm , tip current = -160 nA, scan rate = 50 μm each 0.2 s, sample potential, $E_S = 0.2$ V (a), 0.4 V (b), 0.6 V (c) and 0.75 V versus the hydrogen reference electrode (HRE). W_M is the atomic ratio of metal M in the spot. Taken from [80] with permission of the American Chemical Society

screening of the trimetallic catalyst combinations at four different sample potentials at a constant tip current (-160 nA) in the TG-SC mode are shown in Fig. 17. The highest ORR activity was observed for the combination with Pd (70 %), Co (20 %), and Au (10 %). Interestingly, this combination also exhibited much better stability than the bimetallic catalyst Pd (80 %) and Co (20 %). The Pd (70 %)–Co(20 %)–Au (10 %) catalyst was further prepared on carbon by a reverse microemulsion method heated in a reducing atmosphere (H_2 (10 %) in Ar) and assembled into a membrane electrode assembly (MEA). Steady-state polarization curves under fuel cell test conditions established that the optimized Pd–Co–Au was as active as Pt (20 %) on carbon (Johnson Matthey).

Smaller catalyst libraries have been investigated by several other research groups. For example, Chen et al. electrodeposited a small library of noble metals (Pt, Ru, Rh, and Au) by means of a capillary-based droplet cell onto carbon nanotubes predeposited on glassy carbon by electrophoretic accumulation, and screened their ORR activity in a 0.1 M phosphate solution using the oxygen competition mode ($\text{pH} = 6.7$) [68, 82]. Our group employed RC-SECM to map the ORR activity of Pt, and Pt-based alloy nanoparticles, including core–shell structures

deposited on glassy carbon [69, 83]. Moreover, enzyme libraries have been screened with respect to their biocatalytic activity using SECM [13, 84, 85].

2.1.3 Quantification of Hydrogen Peroxide

The SG-TC mode is the most commonly used technique for visualization and quantification of the amount of H_2O_2 produced during ORR [15, 48–50, 64, 86–88]. In the SG-TC mode, the SECM is essentially similar to the RRDE technique, as depicted in Fig. 18. In SG-TC SECM, the H_2O_2 formed at the sample is transported to the collector (SECM tip) purely by diffusion, while in RRDE, transport of the H_2O_2 formed at the disk to the ring is both by diffusion and forced convection. In both methods, only a fraction of the H_2O_2 generated is able to reach the sensing electrode. The collection efficiency (CE), also commonly denoted as N , can be computed from Eq. 6, using a suitable redox mediator such as ferrocenemethanol, in the SG-TC mode of SECM, where i_{tip} is the tip current and i_{sample} is the sample current.

$$N = \left| \frac{i_{\text{tip}}}{i_{\text{sample}}} \right| \quad (6)$$

The CE in SECM depends on the RG value of the SECM tip (ratio of the radius of the tip including the sheath to the radius of the electrode excluding the sheath), the tip-to-sample distance (d), and the size of the sample surface in relation to the tip electrode and RG value, among other factors.

The influence of the tip-to-sample distance on the CE in SECM measurements were investigated by Bard et al. [49], both by simulation and experimentally in a deaerated solution of ferrocenemethanol (1 mM) in 0.1 M K_2SO_4 . Ferrocenemethanol was oxidized at the sample by applying a linear potential scan from 0.3 to 0.7 V versus RHE, while ferrocenemethanol was reduced at the tip, which was kept at a constant potential of 0.3 V versus RHE. Figure 19

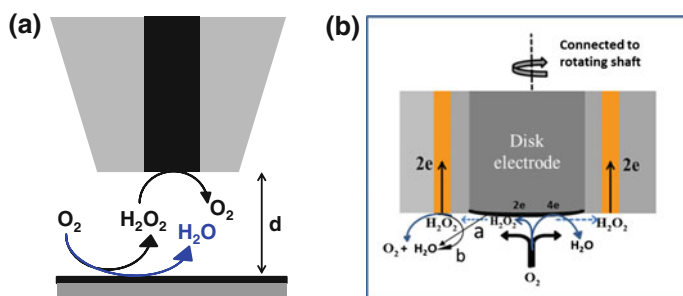


Fig. 18 Schematic illustration of the detection of H_2O_2 formed during the ORR using SECM in the SG-TC mode (a), and detection of H_2O_2 using the RRDE. Figure 18b was adopted from [89] with the permission of World Scientific

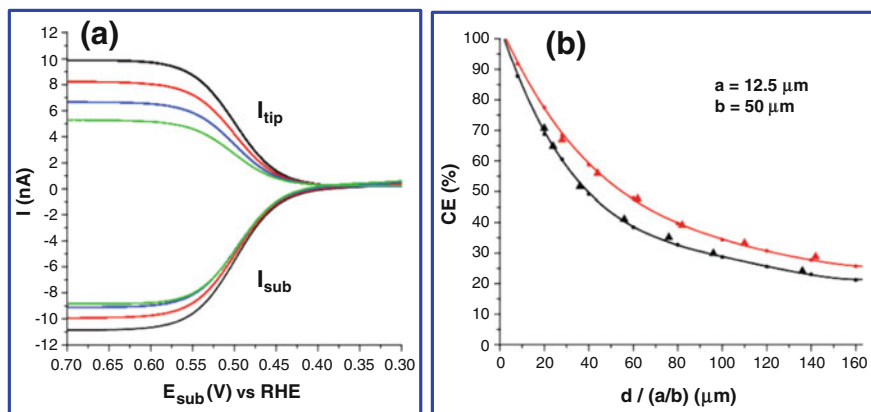


Fig. 19 **a** Experimental results of SG-TC SECM using ferrocenemethanol oxidation at the sample (Au, 100 μm diameter) and ferrocenemethanol reduction at the tip (Pt, 25 μm diameter). The electrolyte solution was ferrocenemethanol (1 mM) in 0.1 M K_2SO_4 . The sample potential was scanned from 0.3 to 0.7 V at a rate of 2 mV s^{-1} while the tip potential was held constant at 0.3 V. All the potentials are reported against the reversible hydrogen electrode (RHE). The different curves correspond to different tip-to-sample distances as follows, *black* (5 μm), *red* (10 μm), *blue* (15 μm), and *green* (25 μm). **b** Collection efficiency values calculated for a 25 μm diameter tip, and a sample with a diameter of 100 μm . The *red line* and symbols correspond to a tip with $\text{RG} = 10$, and the *black line* and symbols correspond to a tip with $\text{RG} = 6$. *Circles* correspond to CE values obtained from simulation and *triangles* correspond to CE values obtained from experimental data using ferrocenemethanol (1 mM) in K_2SO_4 (0.1 M) as the redox mediator. *Continuous lines* correspond to the polynomial regression line for the simulated values. Reproduced from [49] with permission of the American Chemical Society

shows the results of this experiment. The experimental values of the CE obtained from Fig. 19 were found to be in good agreement with simulated data. In principle, the CE in SG-TC SECM measurements should approach 100 % when the tip-to-sample distance (d) is very small. However, a CE of 100 % is experimentally very difficult to achieve due to the challenge to precisely approach the sample surface to within $<5 \mu\text{m}$, especially when using tips with large RG values. At large values of d , it is unavoidable that some of the redox species generated at the sample is lost into the bulk. The situation becomes complicated if homogeneous or heterogeneous chemical reactions are involved. For example, in the case of the ORR, H_2O_2 may disproportionate, either at the sample where it is generated, or at the tip, thus affecting the CE. To maximize the CE in SG-TC SECM experiments, as well as to minimize the contribution of capacitive currents, Sánchez-Sánchez et al. proposed the use of small sample surfaces, $<100 \mu\text{m}$ in diameter for SECM tips with a diameter of 25–50 μm [49]. Typically, the sample is also a microelectrode with RG values in the range of 15–20, or cavity (or recessed) microelectrodes [72, 88, 90] with a diameter of about 100 μm and a depth of a few μm for filling with the sample material. A specific advantage of using cavity microelectrodes is that catalysts can be conveniently investigated without the use of a binder.

For quantification of the average number of electrons (n) transferred and the amount of H_2O_2 produced during the ORR, Eqs. 7 and 8, respectively, have been proposed [48, 49], analogous to the RRDE technique.

$$n = \frac{4I_{\text{O}_2}}{\left[I_{\text{O}_2} + \left| \frac{I_{\text{H}_2\text{O}_2}}{N} \right| \right]} \quad (7)$$

$$\text{H}_2\text{O}_2(\%) = \frac{\frac{I_{\text{H}_2\text{O}_2}}{N}}{\left[I_{\text{O}_2} + \left| \frac{I_{\text{H}_2\text{O}_2}}{N} \right| \right]} \times 200 \quad (8)$$

where I_{O_2} is the net catalytic oxygen reduction current, $I_{\text{H}_2\text{O}_2}$ is net H_2O_2 oxidation current, and N is the collection efficiency of the tip. Applying this methodology, [48, 49], the selectivity of ORR in H_2SO_4 (0.5 M) at a mercury electrode supported on a gold sample was investigated. Results of the SG-TC measurements, showing oxygen reduction at the mercury electrode (generator), and the amperometric response of the tip due to oxidation of H_2O_2 are presented in Fig. 20a.

The number of electrons transferred during ORR on Hg was found to be 2.19, very close to 2 (Fig. 20b), and the percentage of H_2O_2 generated was over 90 %. These results are in agreement with theoretical predictions [63]. The slight discrepancy between the experimental data and theoretical value of $n = 2$ for two electron reduction of oxygen is attributed to chemical decomposition of H_2O_2 at the tip, which leads to a lower value of the CE, which is actually also a challenge for the RRDE technique [44, 50, 89].

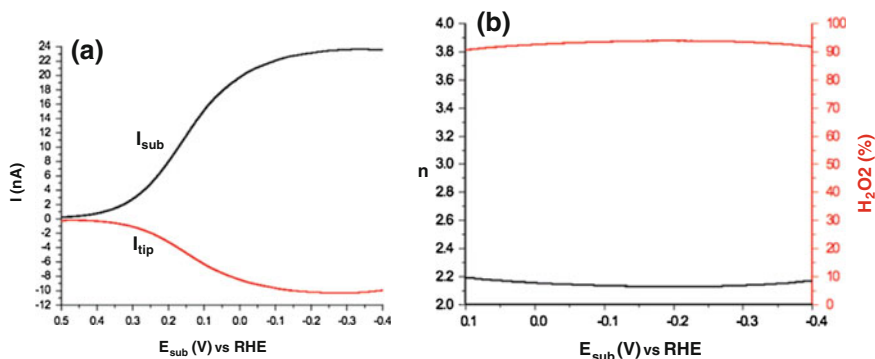


Fig. 20 **a** Experimental results of the SG-TC mode of SECM for H_2O_2 collection during ORR in H_2SO_4 (0.5 M) at a Hg on gold electrode. The sample potential was scanned from 0.5 to -0.4 V versus RHE at 2 mV s^{-1} while the tip potential was held constant at 1.2 V versus RHE. **b** The number of electrons transferred (n , black line) and the percentage of H_2O_2 generated (red line) during ORR at a mercury (Hg) on gold electrode measured in the SG-TC mode of SECM. Reproduced from [49] with permission of the American Chemical Society

2.2 Evaluation of the Electrocatalytic Activity of Single Particles

There are many parameters of a catalyst, such as particle size or shape, affecting its electrocatalytic properties. In the majority of the studies, the properties of electrocatalysts are evaluated from ensembles of nanoparticles, obtaining the averaged information of large numbers of particles. It is unlikely that all particles forming the ensemble possess identical particle shape and size. Even if they do, the diffusion field of neighboring particles would overlap, so that the behavior of the group hinders the evaluation of the intrinsic properties of the individuals. Therefore, the study of single particles is highly desired for obtaining structure–function relationships of the electrocatalysts. There are three major approaches to study the electrocatalytic properties of a single particle (Fig. 21): (i) single particle attached to a nanoelectrode, (ii) electrocatalytic current amplification via single nanoparticle collisions, and (iii) scheme for evaluation of a single particle supported on a noncatalytic macroelectrode using SECM.

2.2.1 Single Particle Attached to a Nanoelectrode

The low mass transport coefficient of oxygen in solution limits the evaluation of the ORR kinetics of electrocatalysts. The use of rotating disk electrodes (RDEs) amends this issue since the mass transport is greatly increased, making RDEs a commonly used tool in ORR studies. Attaching a single particle to a nanoelectrode not only enables the evaluation of the properties of an individual well-defined catalyst, but also enhances drastically the mass transport due to the unique properties of micro- or nanoelectrodes. Chen and Kucernak were pioneers in using this approach to study the ORR at electrocatalysts [91]. They deposited single Pt nanoparticles of a selected size, tunable from the range of several micrometers to

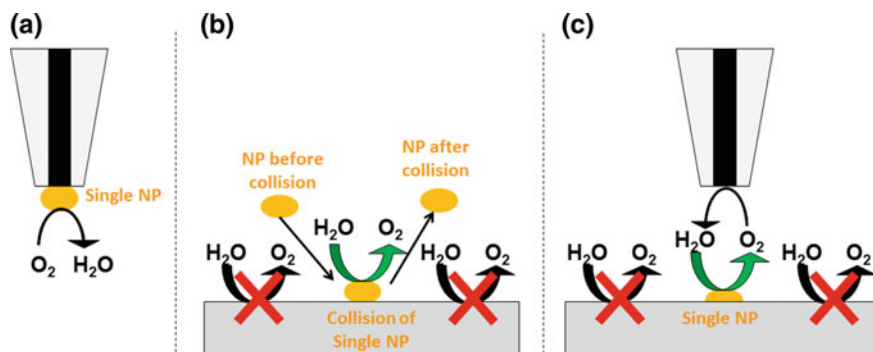


Fig. 21 Evaluation of ORR catalyzed at a single particle. **a** Single nanoparticle attached to a nanoelectrode, **b** electrocatalytic current amplification via single nanoparticle collisions, and **c** a single particle supported on a noncatalytic macroelectrode evaluated by SECM. Adapted from [10]

several tens of nanometers, to a carbon nanoelectrode. Since mass transport is directly related to the size of the single particle, they were able to study ORR at single Pt nanoparticles under several mass transport conditions; the smaller the particle size, the higher the mass transport. While an expected four-electron reduction of oxygen to water was observed at the Pt nanoparticles under low mass transport condition (equivalent to 10^4 rpm in RDEs), only 75 % of oxygen reduction proceeded via four-electron reduction at high mass transport conditions (equivalent to 10^8 rpm) resulting in the production H_2O_2 . While the Pt nanoparticles were electrochemically grown at the nanoelectrode, this approach is not limited to electrodeposited metals and other nanoparticles attached to the nanoelectrodes via covalent bonds as later studied [92].

2.2.2 Electrocatalytic Current Amplification via Single Nanoparticle Collisions

The evaluation of single particle collisions at a microelectrode is another strategy used for studying electrocatalysis at single particles. In a diluted suspension of freely diffusing catalytic particles, a single particle eventually lands on a microelectrode and leaves few moments after (residence time). Considering that a kinetically slow electrochemical reaction does not occur at a noncatalytic microelectrode when a small overpotential is applied, the collision of the catalytic particle at the microelectrode establishes electrical contact and allows the single particle to catalyze a reaction of interest during the residence time. Due to the low concentration of particles in the suspension, the collision of multiple particles is unlikely, enabling the evaluation of single particle collision events.

Xiao and Bard first followed this approach to study the collision of single Pt nanoparticles at a carbon microelectrode for the reduction of protons and the reduction of H_2O_2 [93]. Although many electrocatalytic reactions, such as water oxidation, NaBH_4 oxidation, hydrazine oxidation, or nitrothiophenol oxidation [94–97] were studied since the initial work of Xiao and Bard, it is surprising, that to the best of our knowledge the ORR has not been investigated yet using this approach. It is expected that single particle collision events could be applied for the study of the ORR in the near future.

2.2.3 Evaluation of ORR at Single Particles Using SECM

The electrocatalytic properties of an electrode surface can be mapped via the generation/collection or the redox competition mode of SECM. However, evaluation of the properties of a single nanoparticle supported on a noncatalytic macroelectrode requires rather high spatial resolution of the SECM, below a few hundreds of nanometers which is highly challenging. Two approaches have shown the potential to resolve the electrocatalytic properties of single nanoparticles toward ORR, namely SICM–SECM and SECCM.

(a) *ORR at single particles using SICM–SECM*

The combination of scanning ion-conductance microscopy (SICM) and scanning electrochemical microscopy (SECM) allows precise control of the tip-to-sample distance, which is necessary for the use of nanoelectrodes in SECM. Therefore, highly spatially resolved images of the electrochemical properties of a sample are obtained using SICM–SECM. O’Connell and Wain first demonstrated that SICM–SECM in the redox competition mode can be used to map the electroactivity of surfaces decorated with individual features (Pt nanoparticles) toward the ORR at the 100–150 nm scale (Fig. 22) [98]. More recently, the same authors employed SICM–SECM in the substrate generation/tip collection mode to map localized H_2O_2 generation during the ORR at individual gold nanoparticles [99]. Different amounts of H_2O_2 were observed to be generated at different individual nanoparticles of comparable size which was attributed to differences in crystalline facets or morphologies of gold nanoparticles.

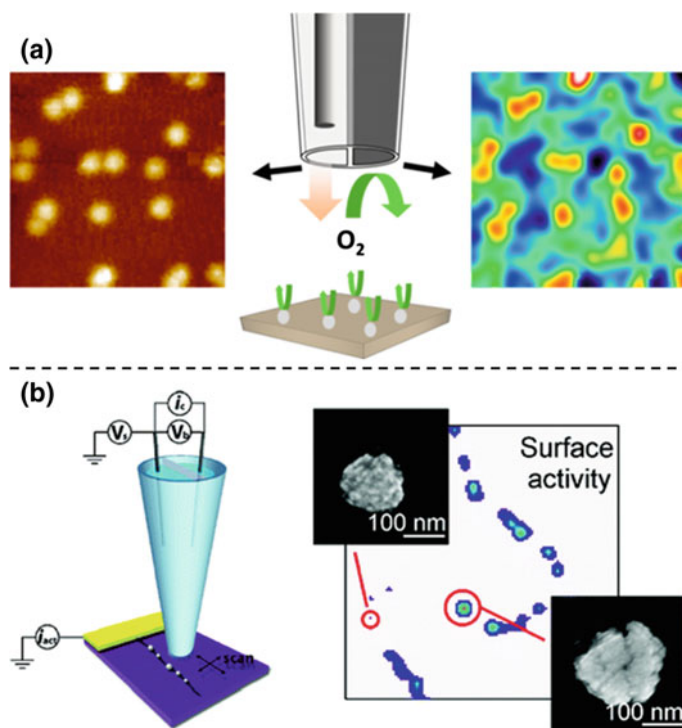


Fig. 22 (a) Images ($5 \times 5 \mu\text{m}$) of oxygen reduction at Pt nanospheres using platinized probes in 0.1 M NaOH: *Left* SICM topography, *middle*: representation of SICM–SECM for the study of the ORR, and *Right* SECM image of the competitive oxygen reduction signal during which the substrate is held at -0.3 V versus Ag/AgCl/3 M KCl and the tip at -0.6 V versus Ag/AgCl/3 M KCl. **b** *Left* SECCM setup, and *Right* SECCM images of Pt particles deposited on a carbon nanotube. Reproduced from [98, 100] with permission of the American Chemistry Society

(b) *ORR at single particle using SECCM*

Scanning electrochemical cell microscopy (SECCM) also allows acquisition of high-resolution images of the reactivity of an electrode surface.

The principle of operation of SECCM was explained in Sect. 1.5.6. Unwin's group demonstrated that the reactivity toward ORR of individual nanoparticles with a size in the order of 100 nm can be resolved using SECCM (Fig. 22b) [100]. Their study showed that subtle variations in the morphology of nanoparticles lead to dramatic changes in (potential-dependent) reactivity, which has important implications for the design and assessment of nanoparticle catalysts.

2.3 *Variable Temperature SECM*

Chemical reactions are temperature sensitive, and indeed, chemical rate constants and reactions mechanism are expected to vary considerably with temperature. Most investigations on the electrocatalysis of the ORR are usually performed at ambient conditions, which do not necessarily represent the behavior of the materials and the reaction at the conditions of practical interest. For example, in proton exchange membrane fuel cells, the temperature of operation is between 80 and 100 °C. Significant discrepancy in behavior may arise if reactions and materials are tested at ambient conditions and their behavior at high temperatures is merely deduced from extrapolation. Schäfer et al. introduced variable temperature SECM, with an operational range of 0–100 °C, by integrating a temperature control unit (Peltier element) into an SECM setup, as shown in the schematic of Fig. 23 [66]. At the heart of the temperature control unit is the Peltier element, which is housed in a stainless steel block.

The steel block serves as the heat reservoir from which the Peltier element draws heat to supply to the sample (heating mode), or to which the Peltier element delivers heat from the sample (cooling mode). The fine details of the temperature control system can be found in the original work [66].

The feasibility of the system was tested on a model Pt/C catalyst, which was deposited on a 1-mm-thick glassy carbon plate using a microdispenser head mounted on a translation stage. The catalyst spots had diameters of about 500 μm. Figure 24 shows the ORR activity of the Pt/C catalyst with different loadings, one droplet (left) and two droplets (right) at 15, 25, and 45 °C, imaged using the RC-SECM mode. The ORR activity of Pt/C increased with temperature and was dependent on the catalyst loading. The line scans in the figure show the change in the tip current as the tip was scanned over the catalyst spots.

It is intriguing to note that at 15 °C, the ORR activity of the two spots with different catalyst loadings was indistinguishable. On the other hand, the activity of the spot with a higher loading did not significantly change when the temperature was increased from 25 to 45 °C whereas a substantial change in activity was observed for the spot with a lower loading upon increasing the temperature from 25 to 45 °C.

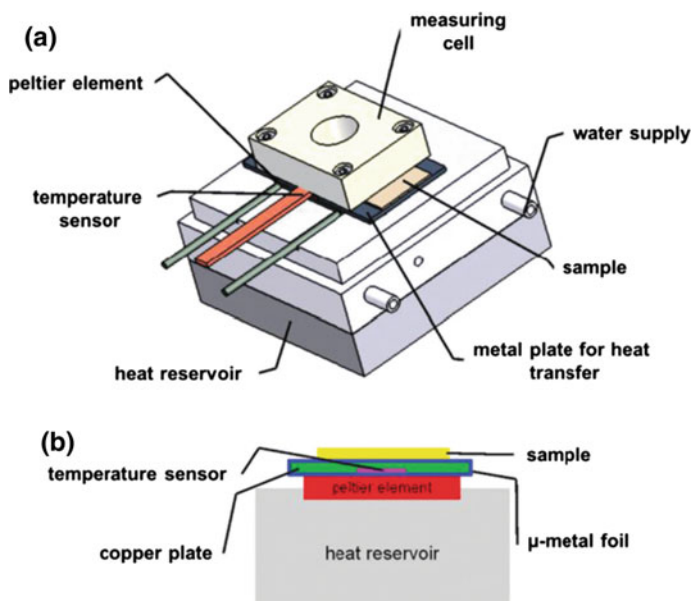
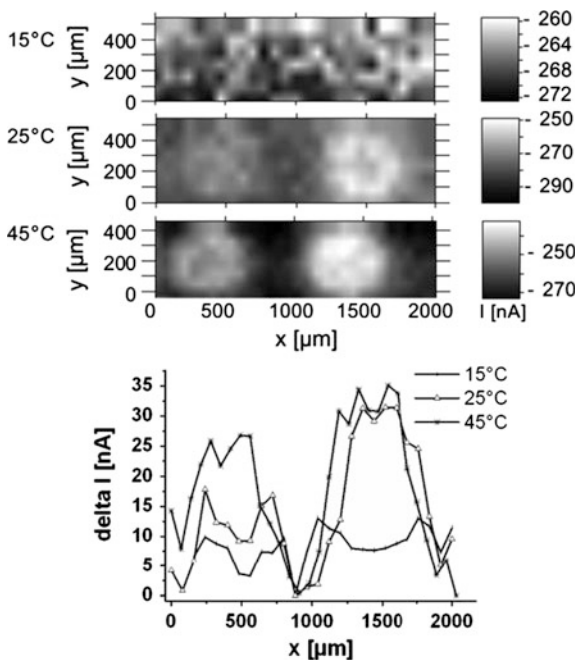


Fig. 23 Schematic view of the temperature-controlled measuring cell (a), and its cross section (b). Reproduced from [66] with permission of the Royal Society of Chemistry

Fig. 24 SECM images of local electrocatalytic activity of Pt/C spots with different catalyst loading, 1 droplet (left); 2 droplets (right) showing the local O_2 consumption obtained using the redox competition mode of SECM. Sample potential = 200 mV versus Ag/AgCl/3 M KCl; electrolyte = H_2SO_4 (200 mM); tip potential = 0 mV (5 s) and -600 mV (0.5 s)



Temperature is therefore a very important factor which needs to be controlled when investigating reactions and materials. Data acquired at room temperature may not always necessarily hold true at higher temperatures and vice versa.

3 Application of SECM to Study Oxygen Reduction by MN_4 -Macrocyclic Complexes

SECM has generally been less applied to investigate the ORR by MN_4 -macrocycles than it has been for Pt-based catalysts, which is quite understandable due to the dominance of Pt-based catalysts for the ORR. We highlight examples from the literature where SECM has been used to investigate the ORR by MN_4 -macrocyclic complexes and related complexes. The central metal ion and nature of substitution groups have a strong influence on the electrocatalytic properties of MN_4 -macrocyclic complexes [89, 101–103]. In Fig. 25, the influence of the central metal ion on the electrocatalytic activity of *meso*-tetratolylporphyrin (TTP) electrodeposited on glassy carbon plates was investigated by RC-SECM [67]. The thickness of the catalyst films was controlled by the number of potential pulses during electrochemical deposition. An electrochemical droplet cell with a narrow orifice, a $Ag/AgCl/3\text{ M KCl}$ reference electrode, and a Pt counter electrode were used to confine the size of the electrodeposited complexes (Fig. 25a). For the ORR

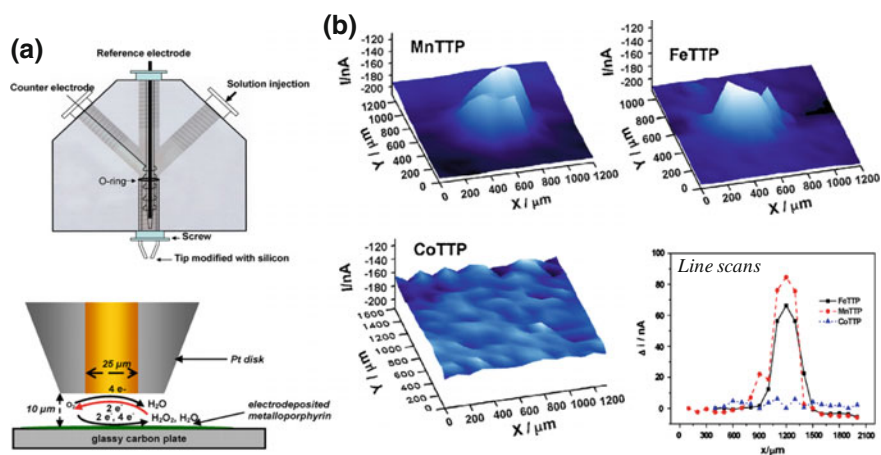


Fig. 25 a Depiction of the electrochemical droplet cell used for electrodeposition of the metalloporphyrins (top), schematic representation of the reactions taking place at the SECM tip and at the metalloporphyrin film during oxygen reduction (bottom), b RC-SECM images recorded in phosphate buffer (pH 7) showing the influence of the central metal ion on the ORR of *meso*-tetratolylporphyrins electrodeposited on glassy carbon plates. The background corrected line scans show the change in tip current which is directly proportional to the activity of the samples. Images reproduced from [67] with the permission of Elsevier

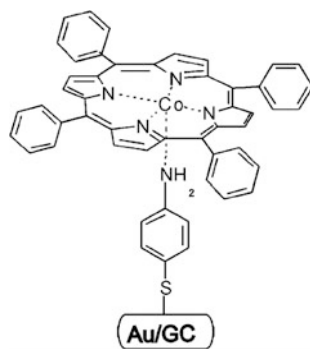
measurements, the tip was positioned at 10 μm above the sample by means of z-approach curves in the feedback mode. The electrocatalytic activity of CoTTP, FeTTP, and MnTTP and their selectivities during the ORR in phosphate buffer (pH = 7) were acquired in a single scan by applying a measurement sequence involving TG-SC, SG-TC, and RC-SECM. During the measurements, the sample potential was maintained at -600 mV while the following pulse profile was applied to the SECM tip: $+50$ mV for 500 ms (no-effect potential), $+1200$ mV for 200 ms (O_2 production), -600 mV for 500 ms (O_2 reduction and data acquisition), $+1200$ mV for 200 ms (O_2 production), and $+600$ mV for 500 ms (H_2O_2 oxidation and data acquisition). The 3D activity maps shown in Fig. 25b enabled the differences in the electrocatalytic activity of the complexes to be visualized. In RC-SECM, a decline in the tip current as the tip is scanned over an oxygen consuming spot is proportional to the activity of the underlying catalyst spot. The line scans in Fig. 25b reflect these changes more clearly. MnTTP was found to be the most active catalyst, followed by FeTTP with CoTTP being the least active. Qualitative comparison of the H_2O_2 generation by SECM visualization also indicated that MnTTP reduced oxygen more selectively toward water compared to CoTTP and FeTTP.

One of the greatest challenges hindering the practical application of MN_4 -macrocyclic complexes is their low stability due to lack of suitable methods to immobilize them on electrode supports. New strategies that enhance the adhesion of N_4 -macrocyclic complexes on electrode supports are therefore needed.

Mezour et al. successfully attached cobalt (II) 5,10,15,20-tetraphenyl-21 H, 23 h-porphine (CoTTP) onto gold and glassy carbon surfaces via its coordination with 4-aminothiophenol (ATP) self-assembled monolayers as depicted in the scheme of Fig. 26 [104]. The electrocatalytic activity of the resulting film, Au-ATP-CoTTP was investigated for oxygen reduction in H_2SO_4 (0.5 M) using SECM in the SG-TC mode. The tip was a Pt nanoelectrode with a diameter of 460 nm. The measurements were recorded at a constant distance of 6 μm which was achieved by means of shear force-based constant distance SECM [105].

Figure 27 shows line scans at different sample potentials, 0, 200 and 700 mV (vs. Ag/AgCl/3 M KCl). During the measurements, the tip potential was maintained

Fig. 26 Scheme of 4-aminothiophenol (4-ATP)-cobalt (II) 5,10,15,20-tetraphenyl-21 H, 23 h-porphine (CoTTP) deposited on Au and glassy carbon (GC) surfaces. Reproduced from [104] with permission of the American Chemical Society



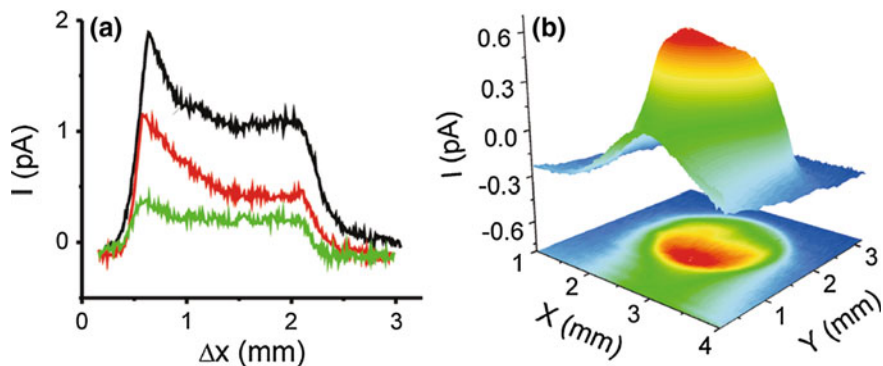


Fig. 27 Line scans above a Au-4-ATP-CoTPP sample recorded at 0 mV (*black line*), 100 mV (*red line*), and 200 mV (*green line*). **b** SECM image of a Au-4-ATP-CoTPP sample recorded at a potential of 0 mV. A 460 nm-diameter microelectrode with RG 8 was biased at 900 mV and positioned 6 μm from the sample surface. The measurements were recorded in O_2 -saturated 0.5 M H_2SO_4 at a scan rate of $90 \mu\text{m s}^{-1}$. The potentials are reported against the Ag/AgCl/3 M KCl electrode. Reproduced from [104] with permission of the American Chemical Society

constant at 700 mV (Ag/AgCl/3 M KCl) to oxidize any H_2O_2 formed at the catalyst layer. The amount of H_2O_2 detected at the tip increased with the sample overpotential. Therefore, for the reported data in Fig. 27a, the highest amount of H_2O_2 produced was observed at a sample potential of 0 V. The concentration of H_2O_2 increased with time eventually reaching a steady state. The rate constant for decomposition of H_2O_2 was independent of the potentials applied to the sample. The main product of oxygen reduction on Au-ATP-CoTPP was H_2O_2 .

In other studies, SECM was used to investigate the kinetics of the ORR on three nonprecious metal catalysts, namely multiwalled carbon nanotubes (MWCNTs), cobalt protoporphyrin (CoP), and a composite of the MWCNTs and CoP (CoP/MWCNTs) in phosphate buffer (pH 7.4) [50]. The investigation involved combination of RC-SECM and SG-TC in the measurement sequence in order to fully characterize the ORR on the catalysts. The average number of electrons and the percentage of H_2O_2 generated were estimated by assuming an analogy between SECM and RRDE and a tip collection efficiency of 100 %.

To distinguish whether H_2O_2 , if formed, undergoes further electrochemical reduction or chemical disproportionation, the SECM tip was used to determine the rate of chemical disproportionation of H_2O_2 on CoP, MWCNTs and on CoP/MWCNTs. The possibility for further electrochemical reduction of H_2O_2 to H_2O was investigated using RDE. The electrochemical reduction of oxygen was observed to follow a 2-electron transfer pathway on MWCNTs and on CoP with H_2O_2 being formed as the main product. There was a good agreement between the SECM results and the RDE results with respect to the number of electrons transferred. In contrast, it was revealed by SECM that H_2O_2 was formed as an intermediate during O_2 reduction on CoP/MWCNTs, with chemical disproportionation of the formed H_2O_2 being facilitated with respect of its further electrochemical

reduction. In RDE/RRDE voltammetry, this would manifest as an apparent 4-electron transfer process as the oxygen regenerated through the disproportionation reaction is cyclically re-reduced to form H_2O_2 which undergoes disproportionation to form O_2 , continually until all the oxygen is ultimately converted to H_2O .

Oxygen reduction on MWCNTs at neutral pH values proceeds predominantly via the 2-electron transfer pathway forming H_2O_2 as the main product [50, 106]. On the other hand, horseradish peroxidase (HRP) and Prussian blue derivatives (PBs) efficiently catalyze both the chemical decomposition and the electrochemical reduction of H_2O_2 . Upon this background, Dobrzaniecka et al. proposed the incorporation of cobalt protoporphyrin (CoP) and HRP or PBs into MWCNTs in order to realize the complete reduction of O_2 to water [106]. A measurement sequence combining RC-SECM and SG-TC was employed to investigate the selectivity and kinetics of oxygen reduction on the multicomponent catalysts. Additionally, the SECM tip probed the rate of decomposition of H_2O_2 on the composite catalysts, and their individual components [107]. The reduction of oxygen on MWCNTs/CoP and on the individual components, MWCNTs, and CoP was observed to proceed predominantly through the 2-electron transfer to form H_2O_2 as the main product. In contrast, the amount of H_2O_2 drastically diminished in the composites containing HR or the PBs.

4 Conclusions and Outlook

SECM offers unique capabilities for probing interfacial chemical phenomena both in fundamental and applied research, and the scope and significance of its applications keep broadening. Recent advances of SECM or SECM coupled to other auxiliary techniques, such as scanning ion-conductance microscopy (SICM) and scanning electrochemical cell microscopy (SECCM), and the design of robust small SECM tips, including new tip concepts such as soft microelectrodes, have led to investigation of local interfacial electrochemical phenomena at unprecedented spatial resolutions. It is now possible to use SECM, or variants of it, to observe, or to quantitatively study electrocatalytic phenomena at single submicron particles. Mapping of the chemical reactivity of surfaces, from a few millimeters to submicrometers dimensions, including observation of heterogeneities within a single particle are possible with SECM.

The use of SECM for combinatorial and high-throughput applications is a very promising means to accelerate the discovery of new functional materials and for optimization of material properties. A recent development in the field of SECM is its adaptability to study reactions at variable temperatures, including temperatures of relevance for industrial applications. This new application means that reactions and materials can now be investigated using SECM at the conditions of their intended application.

Although SECM has become a common tool for studying the ORR activity of catalysts, including enzymes, very few reports exist of its application to study electrocatalysis of oxygen reduction by MN_4 -macrocyclic complexes. Considering the unique capabilities and advantages that SECM offers, it will be interesting to see more frequent use of SECM to probe oxygen reduction on these materials.

The use of SECM as an alternative to RRDE, for both qualitative and quantitative study of the selectivity of the ORR is very promising. The use of special electrodes as SECM tips, and advances in new imaging techniques, including the coupling of SECM to other techniques, will evidently unlock new and fascinating analytical applications of SECM.

References

1. Bard AJ, Fan FRF, Kwak J, Lev O (1989) Scanning electrochemical microscopy. *Introductory principles Anal Chem* 61(2):132–138
2. Wittstock G, Burchardt M, Pust SE, Shen Y, Zhao C (2007) Scanning electrochemical microscopy for direct imaging of reaction rates. *Angew Chem Int Ed* 46(10):1584–1617
3. Sun P, Laforge FO, Mirkin MV (2007) Scanning electrochemical microscopy in the 21st century. *Phys Chem Chem Phys* 9(7):802–823
4. Mirkin MV (2011) Scanning electrochemical microscopy in the 21st century. Update 1: five years after. *Phys Chem Chem Phys* 13:21196–21212
5. Bard AJ, Mirkin MV (2012) Scanning electrochemical microscopy, 2nd edn. CRC Press, Boca Raton
6. Edwards MA, Martin S, Whitworth AL, Macpherson JV, Unwin PR (2006) Scanning electrochemical microscopy: principles and applications to biophysical systems. *Physiol Meas* 27(12):R63–108
7. Fernández JL, Bard AJ (2004) Scanning electrochemical microscopy 50. Kinetic study of electrode reactions by the tip generation-substrate collection mode. *Anal Chem* 76(8):2281–2289
8. Izquierdo J, Nagy L, González S, Santana JJ, Nagy G, Souto RM (2013) Resolution of the apparent experimental discrepancies observed between SVET and SECM for the characterization of galvanic corrosion reactions. *Electrochem Commun* 27:50–53
9. Simões AM, Bastos AC, Ferreira MG, González-García Y, González S, Souto RM (2007) Use of SVET and SECM to study the galvanic corrosion of an iron–zinc cell. *Corros Sci* 49(2):726–739
10. Sambur JB, Chen P (2014) Approaches to single-nanoparticle catalysis. *Annu Rev Phys Chem* 65:395–422
11. Buurmans ILC, Weckhuysen BM (2012) Heterogeneities of individual catalyst particles in space and time as monitored by spectroscopy. *Nat Chem* 4(11):873–886
12. Sun T, Yu Y, Zacher BJ, Mirkin MV (2014) Scanning electrochemical microscopy of individual catalytic nanoparticles. *Angew Chem Int Ed* 53(51):14120–14123
13. Wittstock G (2001) Modification and characterization of artificially patterned enzymatically active surfaces by scanning electrochemical microscopy. *Fresenius J Anal Chem* 370(4):303–315
14. Wei C, Bard AJ, Mirkin MV (1995) Scanning electrochemical microscopy. 31. Application of SECM to the study of charge transfer processes at the liquid/liquid interface. *J Phys Chem* 99(43):16033–16042

15. Liu X, Ramsey MM, Chen X, Koley D, Whiteley M, Bard AJ (2011) Real-time mapping of a hydrogen peroxide concentration profile across a polymicrobial bacterial biofilm using scanning electrochemical microscopy. *Proc Natl Acad Sci USA* 108(7):2668–2673
16. Beaulieu I, Kuss S, Mauzeroll J, Geissler M (2011) Biological scanning electrochemical microscopy and its application to live cell studies. *Anal Chem* 83(5):1485–1492
17. Bergner S, Vatsyayan P, Matysik F (2013) Recent advances in high resolution scanning electrochemical microscopy of living cells—a review. *Anal Chim Acta* 775:1–13
18. Kranz C (2014) Recent advancements in nanoelectrodes and nanopipettes used in combined scanning electrochemical microscopy techniques. *Analyst* 139(2):336–352
19. Hussien EM, Schuhmann W, Schulte A (2010) Shearforce-based constant-distance scanning electrochemical microscopy as fabrication tool for needle-type carbon-fiber nanoelectrodes. *Anal Chem* 82(13):5900–5905
20. Mandler D Micro- and nanopatterning using scanning electrochemical microscopy. In: Bard JA, Mirken MV (eds) *Scanning electrochemical microscopy*, 2nd edn. CRC Press, pp 489–524
21. Behm RJ (2015) Electrocatalysis on the nm scale. *Beilstein J Nanotechnol* 6:1008–1009
22. Kasper C (1940) The theory of the potential and the technical practice of electrodeposition. *Trans Electrochem Soc* 78(1):147
23. Engstrom RC, Weber M, Wunder DJ, Burgess R, Winquist S (1986) Measurements within the diffusion layer using a microelectrode probe. *Anal Chem* 58(4):844–848
24. Engstrom RC, Meaney T, Tople R, Wightman RM (1987) Spatiotemporal description of the diffusion layer with a microelectrode probe. *Anal Chem* 59(15):2005–2010
25. McKelvey K, Edwards MA, Unwin PR (2010) Intermittent contact-scanning electrochemical microscopy (IC-SECM): a new approach for tip positioning and simultaneous imaging of interfacial topography and activity. *Anal Chem* 82(15):6334–6337
26. Lazenby RA, McKelvey K, Unwin PR (2013) Hopping intermittent contact-scanning electrochemical microscopy (HIC-SECM): visualizing interfacial reactions and fluxes from surfaces to bulk solution. *Anal Chem* 85(5):2937–2944
27. Cortés-Salazar F, Träuble M, Li F, Busnel J, Gassner A, Hojeij M, Wittstock G, Girault HH (2009) Soft stylus probes for scanning electrochemical microscopy. *Anal Chem* 81(16):6889–6896
28. Macpherson JV, Unwin PR (2000) Combined scanning electrochemical—atomic force microscopy. *Anal Chem* 72(2):276–285
29. Kranz C, Friedbacher G, Mizaikoff B, Lugstein A, Smoliner J, Bertagnolli E (2001) Integrating an ultramicroelectrode in an AFM cantilever. Combined technology for enhanced information. *Anal Chem* 73(11):2491–2500
30. O’Connell MA, Wain AJ (2015) Combined electrochemical-topographical imaging. A critical review. *Anal Methods*. doi:[10.1039/c5ay00557d](https://doi.org/10.1039/c5ay00557d)
31. Hengstenberg A, Kranz C, Schuhmann W (2000) Facilitated tip-positioning and applications of non-electrode tips in scanning electrochemical microscopy using a shear force based constant-distance mode. *Chem Eur J* 6(9):1547–1554
32. Nebel M, Eckhard K, Erichsen T, Schulte A, Schuhmann W (2010) 4D shearforce-based constant-distance mode scanning electrochemical microscopy. *Anal Chem* 82(18):7842–7848
33. Hansma P, Drake B, Marti O, Gould S, Prater C (1989) The scanning ion-conductance microscope. *Science* 243(4891):641–643
34. Comstock DJ, Elam JW, Pellin MJ, Hersam MC (2010) Integrated ultramicroelectrode-nanopipet probe for concurrent scanning electrochemical microscopy and scanning ion conductance microscopy. *Anal Chem* 82(4):1270–1276
35. Takahashi Y, Shevchuk AI, Novak P, Zhang Y, Ebejer N, Macpherson JV, Unwin PR, Pollard AJ, Roy D, Clifford CA, Shiku H, Matsue T, Klenerman D, Korchev YE (2011) Multifunctional nanopipettes for nanoscale chemical imaging and localized chemical delivery at surfaces and interfaces. *Angew Chem Int Ed* 50(41):9638–9642

36. Snowden ME, Güell AG, Lai SCS, McKelvey K, Ebejer N, O'Connell MA, Colburn AW, Unwin PR (2012) Scanning electrochemical cell microscopy: theory and experiment for quantitative high resolution spatially-resolved voltammetry and simultaneous ion-conductance measurements. *Anal Chem* 84(5):2483–2491
37. Lai SCS, Patel AN, McKelvey K, Unwin PR (2012) Definitive evidence for fast electron transfer at pristine basal plane graphite from high-resolution electrochemical imaging. *Angew Chem Int Ed* 51(22):5405–5408
38. Katsounaros I, Cherevko S, Zeradjanin AR, Mayrhofer KJJ (2014) Oxygen electrochemistry as a cornerstone for sustainable energy conversion. *Angew Chem Int Ed* 53(1):102–121
39. Gasteiger HA, Kocha SS, Sompalli B, Wagner FT (2005) Activity benchmarks and requirements for Pt, Pt-alloy, and non-Pt oxygen reduction catalysts for PEMFCs. *Appl Catal B* 56(1–2):9–35
40. Spendelow JS, Wieckowski A (2007) Electrocatalysis of oxygen reduction and small alcohol oxidation in alkaline media. *Phys Chem Chem Phys* 9(21):2654–2675
41. Yeager E (1984) Electrocatalysts for O₂ reduction. *Electrochim Acta* 29(11):1527–1537
42. de Bruijn FA, Dam VAT, Janssen GJM (2008) Durability and degradation issues of PEM fuel cell components. *Fuel Cells* 8(1):3–22
43. Wu J, Yuan XZ, Martin JJ, Wang H, Zhang J, Shen J, Wu S, Merida W (2008) A review of PEM fuel cell durability: degradation mechanisms and mitigation strategies. *J Power Sources* 184(1):104–119
44. Paulus UA, Schmidt TJ, Gasteiger HA, Behm RJ (2001) Oxygen reduction on a high-surface area Pt/Vulcan carbon catalyst: a thin-film rotating ring-disk electrode study. *J Electroanal Chem* 495(2):134–145
45. Garsany Y, Baturina OA, Swider-Lyons KE, Kocha SS (2010) Experimental methods for quantifying the activity of platinum electrocatalysts for the oxygen reduction reaction. *Anal Chem* 82(15):6321–6328
46. Mayrhofer KJJ, Strmcnik D, Blizanac BB, Stamenkovic V, Arenz M, Markovic NM (2008) Measurement of oxygen reduction activities via the rotating disc electrode method: from Pt model surfaces to carbon-supported high surface area catalysts. *Electrochim Acta* 53(7):3181–3188
47. Masa J, Batchelor-McAuley C, Schuhmann W, Compton RG (2014) Koutecky-Levich analysis applied to nanoparticle modified rotating disk electrodes: electrocatalysis or misinterpretation. *Nano Res* 7(1):71–78
48. Sánchez-Sánchez CM, Bard AJ (2009) Hydrogen peroxide production in the oxygen reduction reaction at different electrocatalysts as quantified by scanning electrochemical microscopy. *Anal Chem* 81(19):8094–8100
49. Sánchez-Sánchez CM, Rodríguez-López J, Bard AJ (2008) Scanning electrochemical microscopy. 60. Quantitative calibration of the SECM substrate generation/tip collection mode and its use for the study of the oxygen reduction mechanism. *Anal Chem* 80(9):3254–3260
50. Dobrzeniecka A, Zeradjanin AR, Masa J, Puschhof A, Stroka J, Kulesza PJ, Schuhmann W (2013) Application of SECM in tracing of hydrogen peroxide at multicomponent non-noble electrocatalyst films for the oxygen reduction reaction. *Catal Today* 202:55–62
51. Walsh DA, Fernández JL, Bard AJ (2006) Rapid screening of bimetallic electrocatalysts for oxygen reduction in acidic media by scanning electrochemical microscopy. *J Electrochem Soc* 153(6):E99
52. Wain AJ (2014) Scanning electrochemical microscopy for combinatorial screening applications. A mini-review. *Electrochem. Commun* 46:9–12
53. Black M, Cooper J, McGinn P (2004) Scanning electrochemical microscope characterization of thin film Pt-Ru alloys for fuel cell applications. *Chem Eng Sci* 59(22–23):4839–4845
54. Liu B, Bard AJ, Mirkin MV, Creager SE (2004) Electron transfer at self-assembled monolayers measured by scanning electrochemical microscopy. *J Am Chem Soc* 126(5):1485–1492

55. Martin RD, Unwin PR (1998) Scanning electrochemical microscopy kinetics of chemical reactions following electron-transfer measured with the substrate-generation–tip-collection mode. *Faraday Trans.* 94(6):753–759
56. Nugues S, Denuault G (1996) Scanning electrochemical microscopy. amperometric probing of diffusional ion fluxes through porous membranes and human dentine. *J Electroanal Chem* 408(1–2):125–140
57. Yang Y, Denuault G (1996) Scanning electrochemical microscopy (SECM). Study of the adsorption and desorption of hydrogen on platinum electrodes in Na₂SO₄ solution (pH = 7). *J Electroanal Chem* 418(1–2):99–107
58. Shen Y, Trauble M, Wittstock G (2008) Detection of hydrogen peroxide produced during electrochemical oxygen reduction using scanning electrochemical microscopy. *Anal Chem* 80(3):750–759
59. Fernández JL, Bard AJ (2003) Scanning electrochemical microscopy. 47. Imaging electrocatalytic activity for oxygen reduction in an acidic medium by the tip generation—substrate collection mode. *Anal Chem* 75(13):2967–2974
60. Lu G, Cooper JS, McGinn PJ (2007) SECM imaging of electrocatalytic activity for oxygen reduction reaction on thin film materials. *Electrochim Acta* 52(16):5172–5181
61. Eckhard K, Chen X, Turcu F, Schuhmann W (2006) Redox competition mode of scanning electrochemical microscopy (RC-SECM) for visualisation of local catalytic activity. *Phys Chem Chem Phys* 8(45):5359–5365
62. Johnson L, Walsh DA (2012) Tip generation–substrate collection–tip collection mode scanning electrochemical microscopy of oxygen reduction electrocatalysts. *J Electroanal Chem* 682:45–52
63. Nørskov JK, Rossmeisl J, Logadottir A, Lindqvist L, Kitchin JR, Bligaard T, Jónsson H (2004) Origin of the overpotential for oxygen reduction at a fuel-cell cathode. *J Phys Chem B* 108(46):17886–17892
64. Eckhard K, Schuhmann W (2007) Localised visualisation of O₂ consumption and H₂O₂ formation by means of SECM for the characterisation of fuel cell catalyst activity. *Electrochim Acta* 53(3):1164–1169
65. Sztot K, Nogala W, Niedziolka-Jönsson J, Jönsson-Niedziolka M, Marken F, Rogalski J, Kirchner CN, Wittstock G, Opallo M (2009) Hydrophilic carbon nanoparticle-laccase thin film electrode for mediatorless dioxygen reduction. *Electrochim Acta* 54(20):4620–4625
66. Schäfer D, Puschhof A, Schuhmann W (2013) Scanning electrochemical microscopy at variable temperatures. *Phys Chem Chem Phys* 15(14):5215–5223
67. Okunola AO, Nagaiah TC, Chen X, Eckhard K, Schuhmann W, Bron M (2009) Visualization of local electrocatalytic activity of metalloporphyrins towards oxygen reduction by means of redox competition scanning electrochemical microscopy (RC-SECM). *Electrochim Acta* 54(22):4971–4978
68. Chen X, Eckhard K, Zhou M, Bron M, Schuhmann W (2009) Electrocatalytic activity of spots of electrodeposited noble-metal catalysts on carbon nanotubes modified glassy carbon. *Anal Chem* 81(18):7597–7603
69. Schwamborn S, Stoica L, Chen X, Xia W, Kundu S, Muhler M, Schuhmann W (2010) Patterned CNT arrays for the evaluation of oxygen reduction activity by SECM. *Chem Phys Chem* 11(1):74–78
70. Maljusch A, Nagaiah TC, Schwamborn S, Bron M, Schuhmann W (2010) Pt-Ag catalysts as cathode material for oxygen-depolarized electrodes in hydrochloric acid electrolysis. *Anal Chem* 82(5):1890–1896
71. Nagaiah TC, Maljusch A, Chen X, Bron M, Schuhmann W (2009) Visualization of the local catalytic activity of electrodeposited Pt-Ag catalysts for oxygen reduction by means of SECM. *Chem Phys Chem* 10(15):2711–2718
72. Nebel M, Erichsen T, Schuhmann W (2014) Constant-distance mode SECM as a tool to visualize local electrocatalytic activity of oxygen reduction catalysts. *Beilstein J Nanotechnol* 5:141–151

73. Nebel M, Grütze S, Diab N, Schulte A, Schuhmann W (2013) Visualization of oxygen consumption of single living cells by scanning electrochemical microscopy: the influence of the faradaic tip reaction. *Angew Chem Int Ed* 52(24):6335–6338
74. Nebel M, Grütze S, Diab N, Schulte A, Schuhmann W (2013) Microelectrochemical visualization of oxygen consumption of single living cells. *Faraday Discuss* 164:19
75. Mallouk TE, Smotkin ES Combinatorial catalyst development methods
76. Senkan SM (1998) High-throughput screening of solid-state catalyst libraries. *Nature* 394(6691):350–353
77. Hagemeyer A, Jandeleit B, Liu Y, Poojary DM, Turner HW, Volpe AF, Henry Weinberg W (2001) Applications of combinatorial methods in catalysis. *Appl Catal A* 221(1–2):23–43
78. Reddington E (1998) Combinatorial electrochemistry: a highly parallel, optical screening method for discovery of better electrocatalysts. *Science* 280(5370):1735–1737
79. Schäfer D, Mardare C, Savan A, Sanchez MD, Mei B, Xia W, Muhler M, Ludwig A, Schuhmann W (2011) High-throughput characterization of Pt supported on thin film oxide material libraries applied in the oxygen reduction reaction. *Anal Chem* 83(6):1916–1923
80. Fernández JL, Walsh DA, Bard AJ (2005) Thermodynamic guidelines for the design of bimetallic catalysts for oxygen electroreduction and rapid screening by scanning electrochemical microscopy. M–Co (M: Pd, Ag, Au). *J Am Chem Soc* 127(1):357–365
81. Lu G, Cooper JS, McGinn PJ (2006) SECM characterization of Pt–Ru–WC and Pt–Ru–Co ternary thin film combinatorial libraries as anode electrocatalysts for PEMFC. *J Power Sources* 161(1):106–114
82. Chen X, Li N, Eckhard K, Stoica L, Xia W, Assmann J, Muhler M, Schuhmann W (2007) Pulsed electrodeposition of Pt nanoclusters on carbon nanotubes modified carbon materials using diffusion restricting viscous electrolytes. *Electrochem Commun* 9(6):1348–1354
83. Kulp C, Chen X, Puschhof A, Schwamborn S, Somsen C, Schuhmann W, Bron M (2010) Electrochemical synthesis of core-shell catalysts for electrocatalytic applications. *Chem Phys Chem* 11(13):2854–2861
84. Wilhelm T, Wittstock G (2003) Analysis of interaction in patterned multienzyme layers by using scanning electrochemical microscopy. *Angew Chem Int Ed* 42(20):2248–2250
85. Fernández JL, Mano N, Heller A, Bard AJ (2004) Optimization of “wired” enzyme O₂-electroreduction catalyst compositions by scanning electrochemical microscopy. *Angew Chem Int Ed* 43(46):6355–6357
86. Shen Y, Träuble M, Wittstock G (2008) Electrodeposited noble metal particles in polyelectrolyte multilayer matrix as electrocatalyst for oxygen reduction studied using SECM. *Phys Chem Chem Phys* 10(25):3635
87. Kishi A, Shironita S, Umeda M (2012) H₂O₂ detection analysis of oxygen reduction reaction on cathode and anode catalysts for polymer electrolyte fuel cells. *J Power Sources* 197:88–92
88. Kishi A, Inoue M, Umeda M (2010) Scanning electrochemical microscopy study of H₂ O₂ byproduct during O₂ reduction at Pt/C-Nafion composite cathode. *J Phys Chem C* 114(2):1110–1116
89. Masa J, Ozoemena KI, Schuhmann W, Zagal JH (2012) Oxygen reduction reaction using N₄. *J. Porphyrins Phthalocyanines* 16(07n08):761–784
90. Guilminot E, Corcella A, Chatenet M, Maillard F (2007) Comparing the thin-film rotating disk electrode and the ultramicroelectrode with cavity techniques to study carbon-supported platinum for proton exchange membrane fuel cell applications. *J Electroanal Chem* 599(1):111–120
91. Chen S, Kucernak A (2004) electrocatalysis under conditions of high mass transport rate. oxygen reduction on single submicrometer-sized pt particles supported on carbon. *J Phys Chem B* 108(10):3262–3276
92. Li Y, Cox JT, Zhang B (2010) Electrochemical responses and electrocatalysis at single au nanoparticles. *J Am Chem Soc* 132(9):3047–3054
93. Xiao X, Bard AJ (2007) Observing single nanoparticle collisions at an ultramicroelectrode by electrocatalytic amplification. *J Am Chem Soc* 129(31):9610–9612

94. Kwon SJ, Fan FF, Bard AJ (2010) Observing iridium oxide (IrO(x)) single nanoparticle collisions at ultramicroelectrodes. *J Am Chem Soc* 132(38):13165–13167
95. Zhou H, Fan FF, Bard AJ (2010) Observation of discrete Au nanoparticle collisions by electrocatalytic amplification using Pt ultramicroelectrode surface modification. *J Phys Chem Lett* 1(18):2671–2674
96. Xiao X, Fan FF, Zhou J, Bard AJ (2008) Current transients in single nanoparticle collision events. *J Am Chem Soc* 130(49):16669–16677
97. Zhou Y, Rees NV, Compton RG (2012) The electrochemical detection of tagged nanoparticles via particle-electrode collisions: nanoelectroanalysis beyond immobilisation. *Chem Commun* 48(19):2510–2512
98. O'Connell MA, Wain AJ (2014) Mapping electroactivity at individual catalytic nanostructures using high-resolution scanning electrochemical-scanning ion conductance microscopy. *Anal Chem* 86(24):12100–12107
99. O'Connell MA, Lewis JR, Wain AJ (2015) Electrochemical imaging of hydrogen peroxide generation at individual gold nanoparticles. *Chem Commun* 51(51):10314–10317
100. Lai SCS, Dudin PV, Macpherson JV, Unwin PR (2011) Visualizing zeptomole (electro) catalysis at single nanoparticles within an ensemble. *J Am Chem Soc* 133(28):10744–10747
101. Masa J, Schuhmann W (2013) Systematic selection of metalloporphyrin-based catalysts for oxygen reduction by modulation of the donor-acceptor intermolecular hardness. *Chem Eur J* 19(29):9644–9654
102. Zagal JH, Páez M, Tanaka A, dos Santos J, Linkous C (1992) Electrocatalytic activity of metal phthalocyanines for oxygen reduction. *J Electroanal Chem* 339(1–2):13–30
103. Zagal JH, Bedioui F, Dodelet JP (eds) (2006) *N₄-macrocyclic metal complexes*. Springer, New York
104. Mezour MA, Cornut R, Hussien EM, Morin M, Mauzeroll J (2010) Detection of hydrogen peroxide produced during the oxygen reduction reaction at self-assembled thiol—porphyrin monolayers on gold using SECM and nanoelectrodes. *Langmuir* 26(15):13000–13006
105. Ballesteros Katemann B, Schulte A, Schuhmann W (2003) Constant-distance mode scanning electrochemical microscopy (SECM)—Part I: adaptation of a non-optical shear-force-based positioning mode for SECM tips. *Chem Eur J* 9(9):2025–2033
106. Dobrzeniecka A, Zeradjanin AR, Masa J, Stroka J, Goral M, Schuhmann W, Kulesza PJ (2011) *ECS Trans* 35:33–44
107. Dobrzeniecka A, Zeradjanin AR, Masa J, Blicharska M, Wintrich D, Kulesza PJ, Schuhmann W Evaluation of kinetic constants on porous, non-noble catalyst layers for oxygen reduction—a comparative study between SECM and hydrodynamic methods. *Catal Today*. doi:10.1016/j.cattod.2015.07.043

Theoretical Aspects of the Reactivity of MN₄ Macrocyclics in Electrochemical Reactions

Sebastián Miranda-Rojas, Alvaro Muñoz-Castro,
Ramiro Arratia-Pérez and Fernando Mendizábal

1 Introduction

In the last 130 years, chemistry has focused its attention on the behavior of molecules and their construction from the atoms. Atoms are held together in molecules by chemical bonds [1]. This is within the framework of the theoretical of atoms-in-molecules. From a modern point of view, the chemical bond has been designed using theoretical methods based on the quantum mechanical *ab initio* for molecules isolated with high accuracy by comparing the results with high-resolution spectroscopies [2, 3]. The basic and fundamental unit that we call molecule is interpreted with some detail. However, in the last three decades chemists have moved beyond the atomic and molecular chemistry towards the area of supramolecular chemistry [4–6]. This new area is in the central part of the bottom-up approaches to

S. Miranda-Rojas

Departamento de Ciencias Químicas, Facultad de Ciencias Exactas,
Universidad Andres Bello, República 275, Santiago, Chile

R. Arratia-Pérez (✉)

Doctorado en Físicoquímica Molecular, Relativistic Molecular Physics (ReMoPh) Group,
Universidad Andres Bello, República 275, Santiago, Chile

e-mail: rarratia@unab.cl

A. Muñoz-Castro

Grupo de Química Inorgánica y Materiales Moleculares, Universidad Autónoma de Chile,
El Llano Subercaseaux 2801, Santiago, Chile

S. Miranda-Rojas · R. Arratia-Pérez

Center for Applied Nanosciences (CENAP), Universidad Andres Bello,
República 275, Santiago, Chile

F. Mendizábal (✉)

Department of Chemistry, Faculty of Sciences, Universidad de Chile,
Las Palmeras 3425, Ñuñoa, P.O. Box 653, Santiago, Chile

e-mail: hagua@uchile.cl

nanoscience and nanotechnology. The supramolecular chemistry is often pursuing the development of new functions that do not appear in a single molecule.

Supramolecular chemistry has been defined by the winner of Nobel Prize in Chemistry J.M. Lehn as “Intermolecular chemistry, focusing on the structure and function of the entities formed by the association of two or more chemical species” [7]. Supramolecular chemistry has provoked a substantial shift in chemistry from its interest in the molecule (atoms and bonds that form them) to focus on the association between the molecule and bonds between molecules. This conceptual change impacted all areas of chemistry. The intermolecular term is a synonym of non-covalent, which is explained by interactions of the type: electrostatic, hydrogen bonding, and van der Waals [8, 9]. The expression “non-covalent” implies that the association type between two or more molecules is not explained by the traditional chemical bond concept, e.g., sigma bond with two electrons.

Non-covalent intermolecular interactions are characterized by acting in long distances, between 200 and 400 pm. Thus, orbital overlapping is not necessary [10]. The reason for the attraction among the subsystems is the electrical properties of the molecules that are associated. Non-covalent interactions originate from interactions among permanent multipoles, between a permanent multipole and an induced multipole, and finally an instant multipole and an induced multipole. The respective terms of energy are called electrostatic, inductive, and dispersion [11, 12]. The total stabilization energy when molecules associated themselves to form a supramolecular structure is between 1 and 100 kJ/mol, considerably less than a covalent bond energy (400 kJ/mol) [8, 9]. Thus, the description and study of the non-covalent interactions requires very precise methods of quantum chemistry that includes the correlation and dispersion energies.

From this point of view, supramolecular systems can be designed and built with any specific functionality, such as for light conversion, nonlinear optics, molecular wires, self-assembly molecular channels, chemical sensors, etc. [13]. Non-covalent interactions present in these processes are hydrogen bonding, π - π stacking, electrostatic, hydrophobic, charge transfer, metal coordination, and metallophilic interactions [14, 15]. This has led to the synthesis of supramolecular structures of different sizes, shapes, and functionalities. Supramolecular chemistry offers applications in different fields such as medical chemistry and host-guest chemistry, catalysis, molecular electronics, etc. [16]. Within this broad field, we are interested in evaluating the effects of complexes of transition metal such as metallophthalocyanine (MPc) and metalloporphyrines (MP), since they are important components in the supramolecular organization. This is due to the ability to generate potential interactions and direct the structural organization [17–19]. These complexes have unique structural properties leading to novel functions and applications, such as catalysts over noble metals (e.g., gold) self-assembly [20, 21].

In order to incorporate these attributes in the design and rational manufacture of supramolecular entities, it is necessary to understand the supramolecular forces and energies for inorganic compounds of interest. The understanding of these systems comes from the observation of structures and patterns, coupled with the theory and

calculation of the energies of the intermolecular interactions [22, 23]. Data on molecular structures and their interactions come from their crystalline phase. In this regard, our goal is to advance in the understanding of the supramolecular interactions of inorganic compounds at a theoretical level in systems that deployed such arrangements.

The organic–inorganic hybrid materials may be formed via self-assembly of organic and inorganic components [24, 25]. Surfactant-coated gold, silver, copper, etc., electrodes have attracted significant attention in the past decades, and their interesting optical, electronic, and catalytic properties have led to technology applications [26]. Currently, gold electrode has numerous applications in, for example, advanced elements for optoelectronics and information storage devices. A key element in the rational design of gold nanoparticles is the role of ligand conformation and adsorption onto the inorganic surface in order to influence particle growth and assembly. At a molecular level, the control of the organic–inorganic interface is required for any application that couples organic material with metal or semiconductor substrates for integrated nanoelectronics [17–19]. Understanding and ultimately harnessing the driving forces underlying this ligand-mediated metallic nanoparticle synthesis requires detailed nanoscale experiments and simulations. In the literature it is possible to find complementing experimental synthesis and microscopy characterization, using atomic and molecular resolution computer simulations [27, 28].

We focus here on the more promising complexes comprised of metallophthalocyanines and metalloporphyrins that represent a design of supramolecular structures anchored to a gold surface via thiol groups, which potentially allow very precise control of both covalent and non-covalent ligand stabilization effects in the gold systems [23, 29–35]. The theoretical calculations in the present work will allow the quantification of the forces underlying the assembly of metallophthalocyanines and metalloporphyrins on gold electrode, namely, the multiple (individually weak, reversible) binding interactions that act collectively to give self-assemblies. These systems show transfers reactions and the catalytic activity of the metallomacrocycles [36–42]. Also, we will investigate the electrocatalytic activity of metal macrocycles for the above-described reactions using self-assembled monolayers of thiols on gold surfaces in electrode, modified in the external layers with macrocycle complexes (see Fig. 1).

Metallomacrocycles forming supramolecular structures and interactions with electrode are called “metallomacrocycle-based molecular electrodes” [21]. Inorganic complexes can be attached to an electrode surface by chemical and physical methods [29–35]. Figure 1 shows the different approaches for immobilizing MPC and MP on electrode surfaces. In the different methods, the use of self-assembled monolayers (SAMs) of alkylthio-arylthio- and thiol-derivatized MPC and MP is very convenient for immobilizing these metallomacrocycles on gold surfaces [43]. SAMs consist of molecules having a head group and a tail group with functionality, where the head group has special affinity for a substrate, and the tail exhibits a functional group whose terminal end provides the functionality of the SAMs. Usually, the functional group is a redox center or a molecule that can

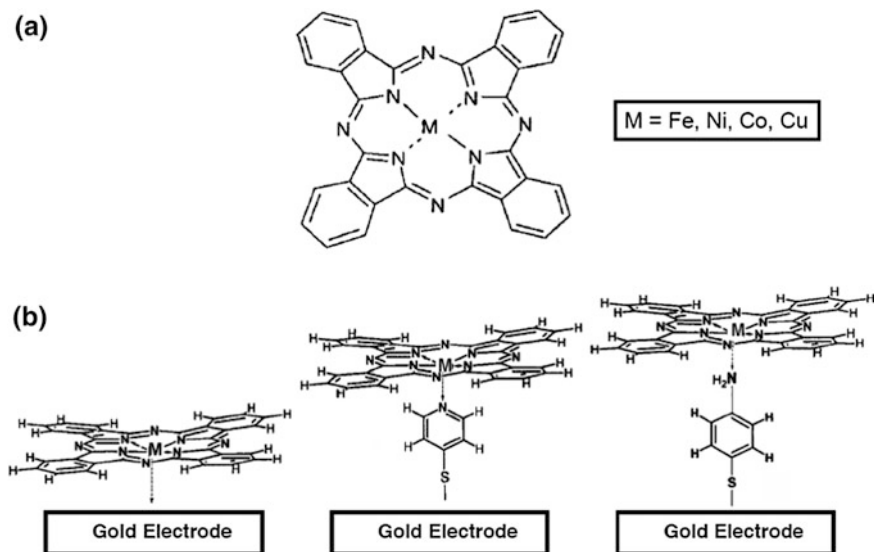


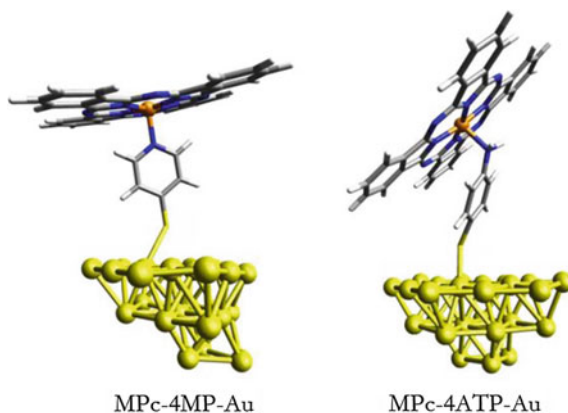
Fig. 1 Scheme of self-assembled monolayers of MetalloPhthalocyanines (MPc) (a) and b adsorbed on gold

undergo fast electron-transfer (ET) processes. In general, the head group of the SAM film promotes the spontaneous adsorption of the appropriated molecules from the solution onto a metal substrate. In this respect, the chemisorption of thiolates on gold represents the most important class of SAMs in electrochemical studies [44], leading to interesting modified electrodes [29–35] which continues to be a focus for research interest due to their importance in supramolecular nanotechnology, fundamentals studies of electron-transfer (ET) reactions, etc. [35–42].

Gold exhibits a strong affinity to sulfur leading to the formation of Au-S bonds, involving an energy of 35–45 kcal/mol [28, 35, 36], where thiols can serve as effective “molecular anchors” in order to immobilize molecules that act as catalyst for ET reactions. Thus, these assemblies can be used as electrochemical sensors for several target molecules, among other applications. In particular, the advantages of SAM-gold electrodes using different metallophthalocyanine complexes have been reported by Nyokong, Zagal, and other researchers for the electrochemical detection of several analytes [29–42]. To immobilize metallophthalocyanine molecules on gold surfaces, among the ligands used are 4-aminothiophenol (4-ATP), 4-mercaptopyridine (4-MP) and 1-(4-mercaptophenyl)-2, 6-diphenyl-4-(4-pyridyl) pyridinium tetrafluoroborate (MDPP) [35, 36], shown in Fig. 2.

Other interesting systems that show catalytic activity is a variety of molecules that contain thiol groups [39–41]. Studies of the electrooxidation of thiols to give disulfides have shown that the catalytic activity of the molecular electrodes of gold. In this case, the metallomacrocycles of Co and Fe have exhibited the high activity. A very interesting case corresponds to the oxidation of L-cysteine and

Fig. 2 MPc-L (M = Fe, Co, Ni; L = 4-MP, 4-ATP) adsorbed on the Au₂₆ modeling gold electrode



2-mercaptoethanol (2-ME) on MPc-4-MPy-SAM(gold) (M = Fe, Mn, Co; 4-MPy = 4-mercaptopyridine). In the literature the same mechanisms have been proposed in the oxidation of thiols, which involves the formation of a bond between the metal center (Fe, Mn, Co) in the metallomacrocycle (MM = MPc and MP) and sulfur in the thiolate [21].

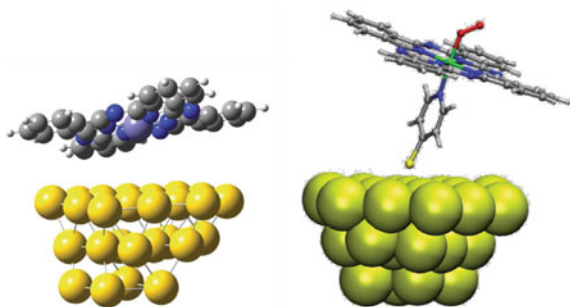
There are a variety of experimental results with phthalocyanines and substituted. There are theoretical studies [42], but they have not yet proposed theoretical models or the evaluation of gold electrode. In the literature the importance of the surface of gold in the above-described processes has been demonstrated [35, 36].

We will further investigate the adsorption of macrocycles on a gold electrode and how the interactions with this surface influence the catalytic properties at the macrocycle. The electrochemical properties of these compounds will be studied as a function of the nanocluster size and the adsorption sites on the surface. In general, the catalytic activity of the attached macrocycles on the above-mentioned structures can be studied directly by the reaction of the active site of the metal complexes with the incoming molecular species, by means of quantum chemistry [43–51]. The information that can be extracted from the reactions is the potential energy surface, the activation energy, and the charge transfers [35, 36].

2 Theoretical and Computational Details

The set of factors affecting these interactions have not been fully clarified and generalized for some fundamental properties. Thus, it is necessary to go more deeply into the problem by developing theoretical models. This will allow us to identify the different factors that allow the existence of the interactions described above. Naturally, we think that the results of these theoretical studies will help to understand the supramolecular inorganic chemistry, where the description of metal–metal interactions via ligands and metal–ligand interactions may provide answers to

Fig. 3 Structure of the complexes studied theoretically, MPC-Au₂₆ and MPC-L-Au₂₆ (M = Fe, Cu; L = 4-ATP, 4-MP, MDPP)



interesting properties, such as optical, electric, and catalysis observed in these systems. Based on the literature discussion, we propose the density functional theory (DFT) modeling approach.

Different MPC configurations (where M = Fe, Co, Ni, Cu) will be examined: directly adsorbed and deposited or anchored with thiol groups on gold via SAM (see Fig. 3). Theoretical calculations of the binding energies and frontier orbitals of different macrocycle complexes anchored on gold surfaces will be conducted, by studying the adsorption of these macrocycles on gold and how the interactions with this surface influence the catalytic properties of the macrocycle. In particular, it has been observed for the O₂ reduction and thiocyanate oxidation processes.

The interaction of the metallophthalocyanine-L, MPC, (M = Fe, Co, Ni); L = 4-aminothiophenol(4-ATP), 4-mercaptopyridine(4-MP) and 1-(4-mercaptophenyl)-2, 6-diphenyl-4-(4-pyridyl) pyridinium tetrafluoroborate (MDPP) moiety with the Au(111) surface is modeled by using a closed shell Au₂₆ cluster, according to the literature [35, 36]. The Au₂₆ cluster has been built and optimized by having three layers containing 14, 8, and 4 gold atoms (Fig. 1), respectively. The geometry of the MPC-L is fully optimized in all calculations, leaving the Au₂₆ atoms at fixed positions, depicting Au–Au distances of 2.87 Å. We use this model to study the mechanism of reduction of O₂. Moreover, we have used two models clusters representing the gold electrode: Au₂₆ and Au₅₈. With these models, we intend to study the form as the MPCs deposit and interact directly with gold. Finally, we have included CoPc models used to study the effect of oxidative catalysis of thiocyanate [52, 53].

The B3LYP, PBE (Perdew–Burke–Ernzerhof) and TPSS nonlocal exchange–correlation functional were employed in all the calculations, by using the Turbomole and ADF programs [54, 55]. We used the PBE and TPSS functionals to be consistent with our previous publication and also for its improved description of long-range interactions [56]. Moreover, we are interested in studying the formation of supramolecular systems, where the weak and coordination interactions are important. Due to this reason, Grimme’s dispersion correction is used for those functionals for which are available, and its use is indicated by appending “DFT-D3” to the acronym of the density functional [57–59].

For heavy elements Au, Fe, Co, Ni, and Cu, the Stuttgart small-core pseudorelativistic effective core potentials (ECPs) were used: 19 valence-electrons (VE) for Au, 16 for Fe, 17 for Co, 18 for Ni, and 19 for Cu [60]. The orbitals associated with the ECP are all Gaussian-type 31*G or 31**G; in addition, two f-type polarization functions were added Au ($\alpha_f = 0.20, 1.19$). The C, N, O, and S atoms were also treated with pseudopotentials, using a double-zeta basis set and adding one d-type polarization function [61]. For hydrogen, a valence-double-zeta basis set with one p-polarization function used [62]. Spin unrestricted method is used for all open shell systems. The counterpoise correction has been employed in order to avoid the basis set superposition errors (BSSEs) in the calculated interaction energies defined in each step described above. The excitation energies were obtained using the time-dependent perturbation theory approach (TD) [63, 64], which is based on the random-phase approximation (RPA) method [65] using Turbomole program [54].

In addition, the Ziegler–Rauk partitioning scheme was employed [66, 67] as implemented in the ADF code [56] by using the optimized geometries obtained from the Turbomole calculations. According to this scheme, the interaction energy is partitioned as follows: $\Delta E_{\text{int}} = \Delta E_{\text{pauli}} + \Delta V_{\text{elstat}} + \Delta E_{\text{orb}}$, where the ΔV_{elstat} term accounts for the stabilizing electrostatic interaction, and ΔE_{orb} stands for the stabilizing covalent character of the fragment interaction. Triple-zeta STOs plus polarization function were employed as a basis set, where the scalar relativistic effects were taken into account through a two-component zero-order regular approximation (ZORA) Hamiltonian in conjunction with the PBE functional (TZP-ZORA/PBE) in the ADF calculation.

We will use these theoretical models to address the following three important questions concerning the design of inorganic supramolecular systems: (1) How stable is a fully bound metallomacrocyclic configuration on the surface of the electrode? (2) How is the binding and dynamics of metallomacrocyclic with different central units on the surface? (3) How are the relative stabilities of the metallomacrocyclic with regard to the transfer of charge and energy, and the catalysis activity on the surface of the electrode?

3 Results and Discussion

3.1 *Self-assembled Metallophthalocyanines Complexes on a Gold Clusters*

These inorganic systems have attracted much attention due to their potential applications in the design of electronic devices and catalytic process, among other fields [68–70]. Metal phthalocyanine (MPc) represents one of the most promising classes owing to its unique electronic properties and chemical stability. In the literature it is possible to find the MPc (M = Fe, Co and Cu) adsorption behavior on

a Au(111) surface [71–75]. For some applications, these molecular systems need to be deposited on supporting surfaces with the subsequent interaction with the molecules to affect the properties of the isolated molecules [76, 77]. Therefore, understanding and controlling the growth of molecular films on the gold surface are of fundamental importance in improving their performance. Many important investigations about structural and electronic properties of metallophthalocyanines have been achieved by using various surface science techniques, such as scanning tunneling microscopy (STM) [78, 79]. STM has been extensively used to explore the structural and electronic features of these systems at the molecular level in real space [70, 78, 79].

We have studied directly MPc (where M = Fe, Co and Cu) adsorbed on gold cluster (Au₂₆) which represents the Au(111) surface (see Fig. 3). Theoretical calculations of the binding energies on gold surfaces will be conducted, by studying the adsorption of these macrocycles on gold and how the interactions with this surface influence the catalytic properties of macrocycle. We have used the PBE and TPSS functional without and with dispersion correction at the Grimme (D3) level. FePc has been modeled in a triplet electronic state, while for CuPc and CoPc are modeled in a doublet electronic state. Such electronic states are maintained when MPcs are deposited on the cluster gold.

Selected geometric parameters are summarized in Table 1. The complete systems show the MPc quasi plane parallel orientation of the complexes onto the cluster Au₂₆ surface. To be more precise, the MPc molecules adsorb on the gold acquire top angle configuration. This geometry is in agreement with experimental results based on STM and theoretical models [80–83]. The obtained M–Au distances are close to the bond length experimental reported. The transition metal in all molecules MPc adopts a bridge-like structure with two of the closest gold. This is

Table 1 Some geometric parameters of the systems (distances in angstroms and angles in degrees) denoting the two closest M–Au distance, M–N distance, the Au–M–Au angle and N–M–Au

System	Method	M–Au ^a	M–Au ^b	M–N	Au–M–Au	N–M–Au ^c
FePc-Au ₂₆	PBE	3.14	3.56	1.94	47.2	87.7
	PBE-D3	3.06	3.34	1.93	49.8	93.8
	TPSS	3.00	3.30	1.94	50.7	94.9
	TPSS-D3	2.97	3.23	1.93	51.6	94.1
CuPc-Au ₂₆	PBE	4.00	4.18	1.96	38.6	107.1
	PBE-D3	3.44	3.68	1.96	44.6	93.2
	TPSS	4.37	4.46	1.96	35.7	105.1
	TPSS-D3	3.32	3.39	1.97	47.6	92.9
CoPc-Au ₂₆	PBE	3.32	3.86	1.94	43.5	97.4
	PBE-D3	3.23	3.45	1.93	47.7	97.5
	TPSS	3.15	3.72	1.94	45.5	98.1
	TPSS-D3	3.13	3.31	1.94	49.6	96.3

^aClosest M–Au distance. ^bSecond closest M–Au distance. ^cNitrogen ring pyrrole

Table 2 Adsorption energies (ΔE_{int}) in Kcal/mol between MPc and Au₂₆ with counterpoise correction (CP)

System	Method	ΔE_{int}
FePc-Au ₂₆	PBE	-13.30 (-31.20)
	PBE-D3	-76.23 (-95.08)
	TPSS	-15.52 (-31.77)
	TPSS-D3	-106.29 (-123.86)
CuPc-Au ₂₆	PBE	-3.97 (-19.90)
	PBE-D3	-58.20 (-77.70)
	TPSS	-3.01 (-16.91)
	TPSS-D3	-83.25 (-102.80)
CoPc-Au ₂₆	PBE	-3.96 (-37.31)
	PBE-D3	-62.23 (-98.77)
	TPSS	-0.01 (-33.68)
	TPSS-D3	-86.57 (-123.27)

In parentheses adsorption energies without CP

shown in the angle Au–M–Au. The distance between the axial nitrogen and the Pc metal center ($N_{\text{ax}}\text{--M}$ distance) denotes typical coordination bond length for Fe, Co, and Cu. The N–M–Au angle, denoting the parallel between the MPc and the gold cluster surface, shows values around 90°. For all the MPc adsorption on gold can see the same behavior: once included the dispersion via the term -D3, M–Au distances are reduced and closer to the experimental values. The TPSS functional shows M–Au distances slightly shorter than using PBE.

An analysis of the adsorption energies between MPc and gold surface is given in Table 2. The strength of interaction energies follows as: Fe > Co > Cu, which correlates with the M–Au₂₆ bond distances described above. From the data presented in Table 2 we can see that the inclusion of dispersion term is relevant and justified most of the adsorption energy. For example the FePc-Au₂₆ system with the DFT-D3 method generates 85 and 82 % of the dispersion using TPSS-D3 and PBE-D3, respectively. Previous calculations of FePc on Au(111) using PW91 functional produce an adsorption energy and Fe–Au at a magnitude of -10.1 kcal/mol and 3.76 Å, respectively [82]. These results are similar when we have used TPSS or PBE with dispersion. This situation is repeated for the CoPc and CuPc molecules. At the TPSS-D3 and PBE-D3 levels, the adsorption energies are defined by the term dispersion. At PW91 level reported in the literature, the adsorption energies are of magnitudes -9.91 and -7.68 kcal/mol for CuPc and CoPc, respectively. Moreover, Table 2 shows that the use of counterpoise correction is important, since some results without counterpoise correction overestimate the magnitude of the interaction energies.

In order to get a deeper insight into the electronic charge rearrangement caused by the interaction of MPc moiety with the gold substrate, the natural population atomic (NPA) analysis based on the TPSS-D3 density was performed for all the series studied here (Table 3). We can see a different behavior for the FePc system in comparison to the other two (CuPc and CoPc). It is possible to observe a charge

Table 3 Natural population atomic (NPA) analysis of the systems at the TPSS-D3 level

System	Au ₂₆	Au ^a	Au ^b	M	Pc
FePc-Au ₂₆	0.184	-0.037	-0.038	0.947	-1.130
FePc				1.055	-1.055
CuPc-Au ₂₆	-0.017	-0.070	-0.066	1.261	-1.244
CuPc				1.216	-1.216
CoPc-Au ₂₆	0.057	-0.057	-0.046	1.147	-1.204
CoPc				1.219	-1.219

^aGold more closest at M–Au distance. ^bGold second more closest at M–Au distance

transfer from Au₂₆ towards the FePc. The charge on Fe and Pc decreases, so there is a transfer of such charge density centers. On the other hand, in the CuPc and CoPc the metal centers (Cu and Co) show a small change in their charges when the complexes are formed on the gold cluster. The Pc ring increases its withdrawing capability when the complexes interact with Au₂₆. Gold cluster acquires a slight negative and positive charge when CuPc and CoPc are deposited, respectively. The biggest changes are observed for the FePc-Au₂₆ system, for which it shows higher adsorption energies at the different levels of calculation. The effect of a low charge on the cluster of gold may be an explanation for the poor catalysis experimentally observed in these systems.

The experimental and theoretical studies about the adsorption of MPc on Au (111) have estimated that the energy involved in the process is about 10–105 kcal/mol [80–83]. Our calculated adsorption energies are between 58 and 107 kcal/mol depending on the method used (PBE-D3 or TPSS-D3), which is in quite good agreement with the values reported in the literature [83]. First-principles calculations for MPc (M = Co, Cu, Fe) absorbed on Au(111) surfaces with LDA, PW91 and opt-B86b-vdW functionals have been previously reported. Zhang and coworkers have used the PW91 functional to study MPc/Au(111) systems in the bands theoretical scheme [82]. The results obtained are underestimated because molecule–substrate distances are between 3.4 and 4.0 Å, while the interaction energies are around 10 kcal/mol [82]. The experimental value molecule–substrate distances are around 3.0 Å from the STM [70, 80, 81]. On the other hand, LDA and optB86b-vdW functionals give more reliable results. It must be present that LDA gives good results because the errors in exchange and correlation tend to cancel each other in LDA. Also, as well-known, the LDA functional is derived from the homogeneous electron gas model. In addition, LDA and PW91 calculations do not include the van der Waals (vdW) interactions, which seemed to play an important role in these systems.

For system-specific FePc/Au(111) with vdW-DF method reported reasonable results, where the molecule–substrate distance is 3.10 Å and the adsorption energy is 105.1 kcal/mol. In the same systems, the DFT-D3, DFT-TS, and OptB86b-vdW methods given out adsorption energies of 110, 102, and 105 kcal/mol and the molecule–substrate distance of 3.13, 3.19 and 3.10 Å, respectively [83]. The difference between those results is small, so the van der Waals interactions should

work. These results are in accordance with the data reported above by us. It indicates the calculations including van der Waals interactions may be a good reference and lead to an agreement of the theoretical calculations. For CuPc/Au(111) and CoPc/Au(111) systems is obtained the same trend with regard to FePc/Au(111).

3.2 *Self-assembled Metallophthalocyanines Complexes Anchored on a Gold Clusters for O₂ Reduction*

The extensive use of metallophthalocyanines as electrocatalysts for the O₂ reduction (ORR) [21, 84–103] is a suitable alternative for replacing expensive Pt-based catalysts in the cathode of fuel cells. In aqueous media, O₂ reduction can undergo a 2-electron reduction to give peroxide, or via 4-electron to give finally water [21, 85–87, 102], where the 4-electron reduction releases more energy than the 2-e reduction process [85]. In this context, Fe phthalocyanines catalyze the reduction of O₂ directly to water via 4-electrons, with cleavage of the O–O bond in contrast to what is observed with Co phthalocyanines [21, 85–87, 90].

With the purpose of gaining more insights into the ORR process involving supported metallophthalocyanines, the analysis of the first step of the ORR processes, which involves the adsorption of O₂ on the metal center of the MPc molecules, has been studied employing MPc-L-Au₂₆ and MPc-L models [36]. In such processes, the adsorption energy (ΔE_{ad}) can be evaluated by considering the energy of the optimized structure of O₂ adsorbed on MPc-L-Au₂₆ ($E_{\text{O}_2\text{-MPc}}$) and the energy of each separated fragment is given as follows:

$$\Delta E_{\text{ad}} = E_{\text{O}_2\text{-MPc}} - (E_{\text{O}_2} + E_{\text{MPc}}) \quad (1)$$

Then, the following two steps model involves the reduction of the oxygen molecule (ΔE_2) and the formation of a HO₂-intermediate (ΔE_3),

$$\Delta E_2 = E_{\text{-O}_2\text{-MPc}} - E_{\text{O}_2\text{-MPc}} \quad (2)$$

$$\Delta E_3 = E_{\text{HO}_2\text{-MPc}} - (E_{\text{-O}_2\text{-MPc}} + E_{\text{H}^+}) \quad (3)$$

Furthermore, the nature of the respective interaction energy can be decomposed according to the Morokuma–Ziegler partitioning scheme, which describes the overall energy in terms of chemically intuitive quantities. According to this scheme, the interaction energy is given by several terms as follows: $\Delta E_{\text{int}} = \Delta E_{\text{pauli}} + \Delta V_{\text{elstat}} + \Delta E_{\text{orb}}$, where the ΔV_{elstat} quantity accounts for the stabilizing electrostatic interaction, and ΔE_{orb} stands for the stabilizing covalent character of the fragment interaction. The theoretical evaluation was done by using Triple-zeta STOs plus polarization function, including scalar relativistic effects through a two-component zero-order regular approximation (ZORA) Hamiltonian in conjunction with the PBE functional (TZP-ZORA/PBE).

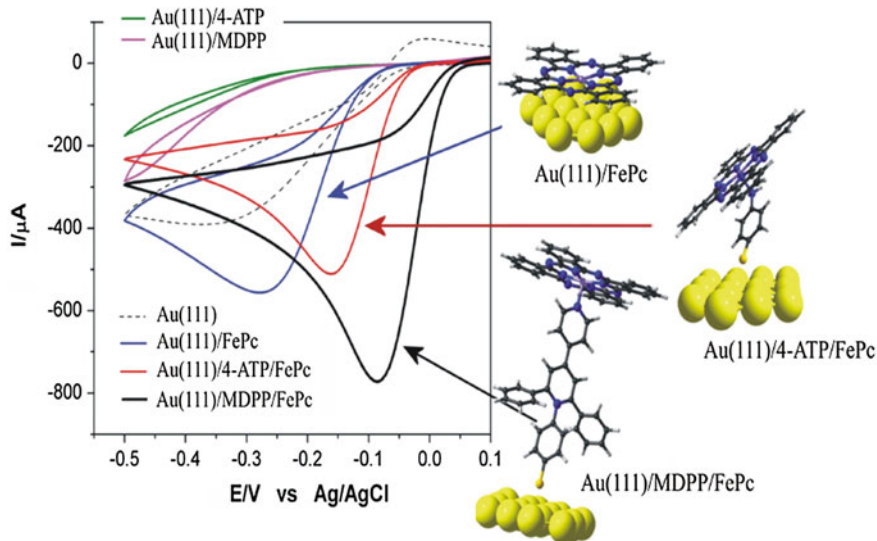
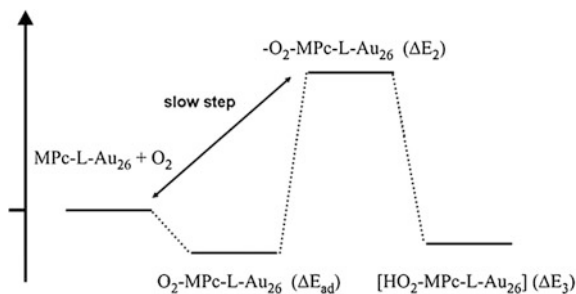


Fig. 4 Electroreduction of O_2 on a clean Au(111) surface and modified with FePc, with and without 4-ATP and MDPP SAMs. Measurements conducted in O_2 saturated 0.1 M NaOH, $dE/dt = 0.05$ V/s. Data from Ref. [36]

Electrochemical measurements depicted in Fig. 4 compare the potentiodynamic response of the Au(111) electrode in the presence of oxygen before and after modification using different molecular configurations containing SAMs with and without FePc. The intensity of the currents for all systems varied linearly with the potential scan rate which corroborates that the ORR is under mass-transport control, i.e., controlled by the diffusion of O_2 from the bulk of the electrolyte to the electrode surface. For comparison, the dashed line shows the response of the bare Au (111). ORR on gold is known to proceed up to 2-electrons to give peroxide [104, 105], thus the voltammetric waves correspond to a total transfer of 2-electrons. After modification of the Au(111) with SAMs of MDPP, the ORR currents are severely suppressed, indicating that most of the surface of Au(111) is coated with these SAMs, probably leaving very few open spots or pinholes for the direct reduction of O_2 on the Au sites (see purple line). When the Au(111) is modified with a SAM of 4-ATP, the O_2 reduction currents are suppressed even to much lower values compared to those obtained when MDPP (see green line) showing that in this case the SAM layers are probably more compact, leaving practically no free Au sites when O_2 reduction can take place.

It is important to point out that FePc in alkaline media catalyzes the ORR preferentially via 4 electrons [85–87, 89, 90, 100], so the enhancement of the catalytic currents in the presence of FePc can be attributed in part to a change in the overall mechanism of the reaction. A generally accepted mechanism for O_2 reduction by Fe phthalocyanines confined to graphite or carbon surfaces [21, 85–87, 89, 90, 101, 106, 107] and seems to operate for FePc anchored to Au(111) is the following:

Fig. 5 Schematic energy profile of O₂ reduction on FePc-L (L = 4-ATP, MDPP). Adapted from Ref. [36]



$[\text{Fe(III)PcOH}]_{\text{ads}} + e^-$	\rightleftharpoons	$[\text{Fe(II)Pc}]_{\text{ads}} + \text{OH}^-$	<i>fast</i>	(I)
$[\text{Fe(II)Pc}]_{\text{ads}} + \text{O}_2$	\rightleftharpoons	$[\text{Fe III-O}_2]_{\text{ads}}$	<i>fast</i>	(II)
$[\text{Fe III-O}_2^-]_{\text{ads}} + e^-$	\rightarrow	intermediates	<i>rds</i>	(III)

However, according to the theoretically calculated energy profile in Fig. 5, the formation of the adduct in step (II) will slow down the reaction instead of catalyzing it since the energy barrier is larger compared to that where the initial reactants proceed directly to the formation of the adduct, concerted with the transfer of one-electron. So, the following mechanism seems to be more plausible and still agrees with the kinetic data:

$[\text{Fe(II)Pc}]_{\text{ads}} + \text{O}_2 + e^-$	\rightarrow	$[\text{Fe III-O}_2^-]_{\text{ads}}$	<i>r.d.s.</i>	(IV)
---	---------------	--------------------------------------	---------------	------

Under this new scheme, the rate-determining step (IV) proceeds immediately after step (I), so again, the fast electron-transfer steps is followed by a slow step. In this case, O₂ adsorption on the Fe sites takes place in a concerted fashion with an electron-transfer process.

Selected calculated geometric parameters are summarized in Table 4 for the first step, which corresponds to the adsorption of O₂ on the central metal atoms of the MPc molecules. The obtained S–Au distances are close to the typical bond length, depicting a stabilization of the S–Au interaction of ~ 40 kcal/mol [36, 37]. The distance between the axial nitrogen and the metal center in the phthalocyanine (N_{ax}–M distance) denotes a typical coordination bond length for Fe. When the 4-ATP is employed as anchor ligand, the results showed that O₂ adsorption energy on FePc/4-ATP is about 23.0 and 22.5 kcal/mol when the complex is free and when it is attached to the gold surface, respectively. On the other hand, when the ligand is MDPP, O₂ adsorption energy on FePc is about 13.0 and 13.1 kcal/mol when the complex is free and when it is attached to the gold surface, respectively. Such energy magnitudes are all weak. This is evident from the O–O bond distance which is still short at this stage and it is associated to a double bond. The O–M distance corresponds to a bond length for complex formation as previously described in the literature [108–111]. It is interesting to observe the effect of interaction of O₂

Table 4 Selected geometric parameters of the systems (distances in Å and angles degrees) and adsorption energy (ΔE_{ad} kcal/mol), when the complex is formed with and without the gold cluster: $\text{O}_2\text{-FePc-L-Au}_{26}$, $\text{O}_2\text{-FePc-L}$, $\text{O}_2\text{-FePc-Au}_{26}$ and $\text{O}_2\text{-FePc}$, respectively (L = 4-ATP and MDPP)

Systems	S–Au	M–Au	O–M	O–O	ΔE_{ad}
O_2				1.21	
$\text{O}_2\text{-FePc-4ATP-Au}_{26}$	2.60		1.88	1.27	-22.5
$\text{O}_2\text{-FePc-MDPP-Au}_{26}$	2.79		1.96	1.25	-13.1
$\text{O}_2\text{-FePc-4ATP}$			1.94	1.27	-23.0
$\text{O}_2\text{-FePc-MDPP}$			1.95	1.26	-13.0
$\text{O}_2\text{-FePc-Au}_{26}$		3.96	1.74	1.26	-32.8
$\text{O}_2\text{-FePc}$			1.92	1.26	-43.2

Data from [36]

Table 5 Selected some geometric parameters of the systems (distances in Å and angles in degrees) and reduction energy (ΔE_2 , kcal/mol), when the complex is formed and reduction with and without the gold cluster: $\text{O}_2\text{-FePc-L-Au}_{26}$, $\text{O}_2\text{-FePc-L}$, $\text{O}_2\text{-FePc-Au}_{26}$ and $\text{O}_2\text{-FePc}$, respectively (L = 4-ATP and MDPP)

Systems	S–Au	M–Au	O–M	O–O	ΔE_2
$\text{O}_2\text{-FePc-4ATP-Au}_{26}$	2.62		1.89	1.27	71.1
$\text{O}_2\text{-FePc-MDPP-Au}_{26}$	2.78		1.96	1.27	24.9
$\text{O}_2\text{-FePc-4ATP}$			1.96	1.28	109.0
$\text{O}_2\text{-FePc-MDPP}$			1.96	1.28	38.8
$\text{O}_2\text{-FePc-Au}_{26}$		4.03	1.88	1.26	23.4
$\text{O}_2\text{-FePc}$			1.88	1.28	42.1

Data from [36]

without ligand spacer and gold cluster in the systems $\text{Au}_{26}\text{-MPc-O}_2$ and MPc-O_2 . For FePc a higher interaction energy is obtained compared with the same system with ligands spacers.

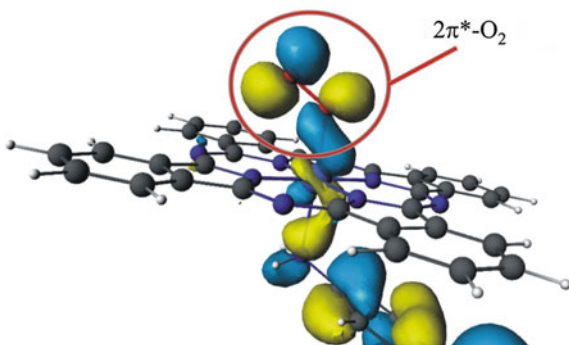
The results of the study of the second step which involves the reduction of the systems are described in Table 5. It is possible to appreciate that most of the geometric parameters do not change, with exception of the O–O and O–M distances. The energy of the reduction reaction, which we have called $\otimes E_2$, shows that it is an endergonic process. The complexes without the gold surface have a higher barrier. For complexes with MDPP, the energetic barriers are about one half of the obtained with 4-ATP. For the reduced models MPc-Au_{26} and $\text{O}_2\text{-MPc}$, there is a noticeable decrease of the energy barrier.

The third step describes the formation of the HO_2 intermediate. This species is formed from the protonation reaction of the previous step involving the adduct. The geometric parameters and reaction energies are shown in Table 6, where it is possible to notice that the O–O bond distance is associated to a single bond, leading to exergonic reactions. As indicated above, the three steps are described in Fig. 5. The energy barrier is located between the first and second step, and the barrier heights are summarized in Table 6. Moreover, when complexes are linked to gold

Table 6 Some geometric parameters of the systems (distances in Å and angles in degrees) and energy intermediate species HO₂ (ΔE_3 , kcal/mol), when the complex is formed and reduction with and without the gold cluster: H₂O-FePc-L-Au₂₆, H₂O-FePc-L, H₂O-FePc-Au₂₆, and H₂O-FePc respectively (L = 4-ATP and MDPP)

Systems	S-Au	M-Au	O-M	O-O	ΔE_3	ΔE
HO ₂ -FePc-4ATP-Au ₂₆	2.64	2.64	1.81	1.44	-70.3	48.6
HO ₂ -FePc-MDPP-Au ₂₆	2.77	2.77	1.83	1.43	-27.8	11.8
HO ₂ -FePc-4ATP			1.85	1.45	-101.8	86.0
HO ₂ -FePc-MDPP			1.82	1.43	-41.3	25.8
HO ₂ -FePc-Au ₂₆		4.01	1.76	1.46	-23.3	-9.4
HO ₂ -FePc			1.76	1.46	-40.9	-1.1

Fig. 6 Molecular orbital comprising the back-donation towards the $2\pi^*$ molecular orbital of O₂, denoting the participation from the anchoring ligand



via the MDPP axial ligand, the barriers are lower, thus enhancing their catalytic activity. For the reduced models MPC-Au₂₆ and O₂-MPc, Fe systems show a trend almost without an energy barrier. These latest results demonstrate the importance of the ligand spacer and the cluster of gold.

The nature of the O₂-FePc bond has been rationalized by using the Ziegler–Rauk energy decomposition scheme [56] focusing into the O₂ interaction and its variation through the three catalytic steps considered in Eqs. 1, 2 and 3.

The 4-ATP/FePc-O₂ interaction with a calculated strength of -23.0 kcal/mol, exhibits a covalent character (70.2 % [112]) as a consequence of the backbonding towards the partially filled $2\pi^*$ molecular orbital of O₂ (Fig. 6). In contrast, the O₂-FePc(MDPP) interaction is only -13.0 kcal/mol, mainly due to a decrease in the backbonding, thus decreasing the orbital stabilizing term to a 60.3 % of the overall stabilizing terms (i.e., electrostatic and covalent interactions). For the 4-ATP systems the inclusion of the gold surface slightly decreases the strength of the O₂ adsorption, whereas for the MDPP counterpart the catalytic site remains almost unchanged. This can be attributed to the length of the MDPP ligand, which decreases the influence from the gold surface at this stage (Eq. 1). As comparison, the related copper-based system exhibits a weaker O₂ adsorption due to almost

negligible backbonding, which accounts for its low capability to promote the catalytic reduction of O_2 [36].

We also focused our analysis on the results provided by the 4-ATP/FePc and its interaction between the adsorbed O_2 and the catalyst, since MDPP and its gold surface models exhibit a similar behavior along the steps of the catalysis. The reduction of the system (Eq. 2), leads to an increase in the population of the $2\sigma^*$ molecular orbital of O_2 (initially of 2 e) from about 2.49 e for 4-ATP/FePc- O_2 to 2.71 e, for 4-ATP/FePc- O_2 destabilizing the system (Fig. 6) and thus promoting the formation of 4-ATP/FePc- HO_2 . In 4-ATP/FePc- O_2 , the orbital stabilizing contribution to the stabilizing energy increase from 70.2 to 75.8 %, for the 4-ATP/FePc- O_2 interaction. However, as a consequence of the destabilization of the system (Fig. 5), the 4-ATP/FePc- O_2 interaction strength decreases to -16.3 kcal/mol mainly due to an increase in the destabilizing Pauli repulsion term [113], within the EDA scheme. Next, the formation of 4-ATP/FePc- HO_2 stabilizes the system leading to an adsorbate-catalyst interaction of about 20.3 kcal/mol, with similar character to that of the initial 4-ATP/FePc- O_2 adduct (71.3 % orbitalary character). Such system can undergo similar steps to promote the O_2 conversion to H_2O_2 or $2H_2O$. For the MDPP case, the studied reaction steps are quite similar, showing a minor energy of the rate-determining step (slow step) because of a lesser destabilization of the MDPP/FePc- O_2 adduct, due to that ligand stabilize the extra charge.

The inclusion of the gold surface greatly decreases the calculated energies for the slow step (Table 6), due to its influence over the interaction of the adsorbate-catalyst due to a modulation of the catalyst center, decreasing the destabilization of the reduced system, due to an electron-withdrawing effect over the FePc moiety favoring such interaction [36]. As can be seen, in the overall catalysis steps, the gold surface, in addition to its electron-source role, decreases the energy barrier of the processes because of its influence over the M- O_2 interaction.

3.3 *Electrocatalytic Activity MetalloN4-Macrocyclic Complexes of Thiocyanate*

Thiocyanate is a small molecule known to have similar reactivity to halide ions, thus defined as a pseudohalide. Thiocyanate has been found in human saliva as a key component of antibacterial system and also as a result of tobacco smoking [114–116]. A distinction between smokers and nonsmokers is essential in many epidemiologic studies, thus the use of thiocyanate as a “smokers impicator” appears to be a good strategy. This is supported by the fact that in samples such as saliva and urine, the presence of high levels of thiocyanate in the range of ca. 10^{-5} – 10^{-3} mol dm $^{-3}$ correlates with excessive cigarette smoking [117–120]. On the other hand, the operation of gold recovery plant results in the formation and accumulation of

solutions containing impurities such as cyanides and thiocyanates [121], which generates species that are harmful to aquatic life. Therefore, the design of simple and easy-to-make sensors for thiocyanate is of high potential value for quick detection and quantification of this compound in real samples [122].

Electrochemical methods have some advantages over other methods because they are of low cost and rapid to use, but the nature of the electrode surface employed as a sensor is of key importance. Thus, it is relevant to develop electrodes that are very reactive towards the target molecule, and this implies that the electrode needs to be a good catalyst for the reaction involving the analyte. Several authors have reported that electrodes modified with metal complexes of N_4 -ligands, such as metallophthalocyanines (MPc), can serve as electrochemical sensors for a great variety of analytes such as thiocyanate [21, 85, 89, 123]. In this regard, MPcs have been reported as important complexes for the design of new technological devices such as, electrochemical sensors, molecular electronics and photovoltaic devices, from which Fe, Mn and Co have good electrocatalytical properties in Pc [124].

For the analysis of thiocyanate, cobaltphthalocyanines (CoPc) has been reported to exhibit the best catalytic activity than all transition metals towards thiol oxidation [124]. This is attributed to good match of the d_{xz} and d_z^2 orbital energies of the metal with that of the sp-orbital enabling transfer of electron density.

Thiol and thiocyanate oxidation reactions occur at high overpotentials on conventional electrodes, hence electrocatalysts should be able to reduce the overpotentials, lower the current densities and accelerate electron-transfer mechanisms [125–128]. For example, on bare gold electrode in pH 4 thiocyanate oxidation occurred at 0.70 V (vs Ag|AgCl), while with a CoPc-SAM modified electrode the process occurred at 0.64 V (vs Ag|AgCl), showing also a large increase in current confirming the electrocatalytic behavior. In addition, it indicates that the CoPc is able to enhance the communication between the gold electrode and the thiocyanate. It should be noticed that the oxidation of thiocyanate resulted in an irreversible process under this conditions.

It has been found that between pH 1 and 4 the oxidation of thiocyanate electrocatalyzed by MPcs involves two one-electron steps, complemented by Tafel plots that have shown the participation of one electron transfer as the rate-determining step with an unsymmetrical energy barrier [129, 130]. According to this, it has been suggested that the first electron transfer corresponds to the rate-determining step.

Experimental evidence has proven that thiocyanate binds to the MPc through the metal center [131], thus pointing out that this interaction is the main responsible of the electrocatalytic power observed for the oxidation of thiocyanate. Also, there is a 1:1 stoichiometry between thiocyanate and MPcs [132], which reduces the number of possible binding conformations of thiocyanate with the metal center. In agreement with this, the bond formed between the catalyst and the target molecule involves an inner sphere process, in which the observed reactivity of the catalysts is much higher than that predicted by its redox potential [130]. It has been also stated that it is even more complicated if the mediator is confined on the electrode surface,

as it is the case when MPc is immobilized in a SAM-electrode as a support, process described by the following mechanism:

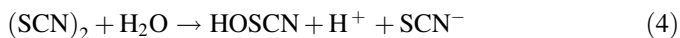
$[\text{MPc}]_{\text{sol}}$	\rightleftharpoons	$[\text{MPc}]_{\text{ad}}$	(I)
$[\text{MPc}]_{\text{ad}}$	\rightarrow	$[\text{MPc}]_{\text{ad}}^+ + \bar{e}$	(II)
$[\text{MPc}]_{\text{ad}}^+ + \text{SCN}^-$	\rightleftharpoons	$[\text{MPc-SCN}^-]_{\text{ad}}^+$	(III)
$[\text{MPcSCN}^-]_{\text{ad}}^+$	\rightarrow	$[\text{MPc}]_{\text{ad}} + \text{oxidation products}$	(IV)

The peak currents (I_p) were found to increase linearly with the square root of the scan rates, (for scan rates ranging from 10–800 mVs^{-1}) indicating that the electrode process are diffusion-controlled [133].

There is consensus on the fact that oxidation reaction of thiocyanate occurs within the (III)/(II) redox couple. According to this, the mechanism first involves the coordination of the M(II)Pc system to the linker distributed as a SAM over the gold electrode. Then it follows the initial oxidation of the metal, from M(II)Pc to M(III)Pc activating the catalyst to finally oxidize the analyte to its products via M(III)Pc with the subsequent regeneration of the M(II) species.

It has been widely reported that electrooxidation of the thiocyanate ion at pH 4 yields hydrogen cyanide and (or) cyanide and sulfate ions as main products [134]. However, there is a huge gap in terms of the mechanism that takes place between the binding of thiocyanate to the catalyst and the products experimentally found. In order to get insight about the elemental reactions between these processes, it is proposed based on experimental evidence that the oxidation of thiocyanate particularly catalyzed by MPc and MPc like systems, leads to the production of thiocyanate radicals that dimerize to form the pseudohalogen molecule thiocyanogen ($\text{SCN})_2$ [132, 135–139].

Interestingly, at fast scan rates on a gold electrode modified with FePc SAM, there appeared a return peak revealing the existence of a major oxidation product that disappear without detection at low scan rates. This peak could be related to the appearance of an unstable major oxidation product of SCN^- as ($\text{SCN})_2$ [140], which at fast scan rates is possible to reduce it before the chemical transformation caused by its instability at pH 4.0, in which it is supposed to rapidly hydrolyze according to the following equation [132, 135–139].



The attractiveness regarding this proposal is that HOSCN is the perfect precursor for the formation of hydrogen cyanide and sulfate ions after sequential oxidation. Thus, according to all the information gathered and discussed above, the proposed reaction mechanism for thiocyanate oxidation in pH 4 using CoPc as catalyst should look like the following:

$[\text{Co(II)Pc}]_{\text{sol}}$	\rightleftharpoons	$[\text{Co(II)Pc}]_{\text{ad}}$	(I)
$[\text{Co(II)Pc}]_{\text{ad}}$	\rightarrow	$[\text{Co(III)Pc}]_{\text{ad}} + \bar{e}$	(II)
$[\text{Co(III)Pc}]_{\text{ad}} + \text{SCN}^-$	\rightleftharpoons	$[\text{Co(III)Pc-SCN}^-]_{\text{ad}}$	(III)
$[\text{Co(III)Pc-SCN}^-]_{\text{ad}}$	\rightarrow	$[\text{Co(III)Pc-SCN}]_{\text{ad}} + \bar{e}$	(III-a)
$[\text{Co(III)Pc-SCN}^-]_{\text{ad}} + \text{SCN}^-$	\rightleftharpoons	$[\text{Co(III)Pc-(SCN)}_2]_{\text{ad}}$	(III-b)
$[\text{Co(III)Pc-(SCN)}_2]_{\text{ad}}$	\rightarrow	$[\text{Co(II)Pc-(SCN)}_2]_{\text{ad}}$	(III-c)
$[\text{Co(II)Pc-(SCN)}_2]_{\text{ad}}$	\rightarrow	$[\text{Co(II)Pc-(SCN)}_2]_{\text{ad}}$	(III-d)
$[\text{Co(II)Pc-(SCN)}_2]_{\text{ad}}$	\rightleftharpoons	$[\text{Co(II)Pc}]_{\text{ad}} + (\text{SCN})_2$	(III-e)
$(\text{SCN})_2 + \text{H}_2\text{O}$	\rightarrow	$\text{HOSCN} + \text{H}^+ + \text{SCN}^-$	(III-f)
$\text{HOSCN} + 3\text{H}_2\text{O}$	\rightarrow	$\text{SO}_4^{2-} + \text{CN}^- + 7\text{H}^+$	(IV)

This mechanism ends with the hydrolysis of $(\text{SCN})_2$ and the oxidation of HOSCN to cyanide and sulfate ions. Evidently, this mechanism raises several questions such as if the dimerization really occurs while the thiocyanate radical is still bonded to Co(III)Pc, in which case how would it change the hydrolysis of the dimer if it is still in complex with CoPc, or if it is only feasible when it is dissociated. Also, understanding how it changes the affinity of the different intermediates towards the cobalt center at the different stages of the reaction mechanism, may provide relevant information on how to modulate it. This is accompanied by the question about if thiocyanate is bonded to cobalt through its sulfur or nitrogen atom along the reaction. Most of these open questions aim to reveal at which extent the CoPc is involved in the process of generating the products experimentally found.

It has been also suggested that there may take place an early oxidation process involving the macrocyclic ring of cobalt tetraethoxy thiophene phthalocyanine (CoTETHpc) [129]. This was suggested because of a weak anodic peak in the potential range for ring oxidation $(\text{Co(III)Pc}^{-1}/\text{Co(III)Pc}^{-2})$ [141]. According to this data, the following mechanism has been additionally proposed as a previous stage to the oxidation of thiocyanate:

$[\text{Co(II)TETHpc}^{-2}]_{\text{sol}}$	\rightleftharpoons	$[\text{Co(II)TETHpc}^{-2}]_{\text{ad}}$	(I)
$[\text{Co(II)TETHpc}^{-2}]_{\text{ad}}$	\rightarrow	$[\text{Co(III)TETHpc}^{-2}]_{\text{ad}} + \bar{e}$	(II)
$[\text{Co(III)TETHpc}^{-2}]_{\text{ad}}$	\rightarrow	$[\text{Co(III)TETHpc}^{-1}]_{\text{ad}} + \bar{e}$	(III)

The question about if the catalytic properties of CoPc are increased or decreased because of the ring oxidation and more important if it really takes place for thiocyanate oxidation are still to be answered.

Thoroughly experimental and theoretical exploration of the role of the chemical bonding between thiocyanate and the catalyst, together with the tuning of the electroactivity associated to its oxidation have provided interesting findings [130, 142]

In this regard, it was experimentally demonstrated that the reactivity of the metal macrocyclic complexes confined on electrode surfaces by SAMs can be controlled by manipulating the redox potential for maximum activity. This in turn was tested by

modifying several CoPc with suitable substituents to withdraw or donate electron density to the metal center, thus providing relevant insights into the modulation of the catalytic activity of these systems. Among these it was possible to find $4\beta(\text{NH}_2)\text{CoPc}$, $8\beta(\text{SC}_2\text{H}_4\text{OH})\text{CoPc}$, $4\beta(\text{PenPyr})\text{CoPc}$, $4\beta(\text{Pyr})\text{CoPc}$, $8\beta\text{-(EH)CoPc}$, $8\beta(\text{OCH}_3)\text{-CoPc}$, and $16(\text{F})\text{CoPc}$. For the CoPcs in which the electron density from the metal center is reduced by withdrawing groups, the redox potential is shifted towards more positive values [143, 144].

Theoretical calculations involving the series listed above exposed a linear correlation between the energy of the LUMO of the adduct with the Co(III)/Co(II) redox potential of the catalyst, where the solvent effects resulted to be important in order to obtain a good correlation [130, 142]. In addition to that, the maximum catalytic activity was attributed to an 'optimum' interaction between the LUMO of the CoPc complex and the HOMO of the thiocyanate anion, finally concluding that the interaction of thiocyanate ions with Co active sites need to be not too weak, not too strong for maximum activity [130]. From a thermodynamic point of view, for an oxidation reaction mediated by MPc, it is expected that more positive the formal potential of the mediator, meaning a more powerful oxidant, higher its reactivity for the oxidation of the target. Some of the most active systems were $4\beta(\text{NH}_2)\text{CoPc}$ and $4\beta(\text{MeO})\text{Pc}$ corresponding to catalysts with electron-donating groups.

The interaction geometries for the adduct showed a Co–S–C angle near to 110° in all cases. The lineal Co–S–C angle was evaluated, but resulted to be less stable. This preference was due to the interaction between the LUMO of the CoPc ($89\% 3d_z^2$) and the HOMO of thiocyanate (S $74\% p_x$, N $26\% p_x$).

The CoPcs which have a LUMO near in energy to the $\text{HOMO}_{\text{SCN}^-}$ are prone to form a covalent interaction that according to the previous statements, will result in a very stable adduct with a slow rate of reaction. Conversely, the CoPcs that have a LUMO far in energy from the $\text{HOMO}_{\text{SCN}^-}$ will make difficult the formation of a covalent bond, thus increasing the catalytic activity of the complexes to some extent (remember, not too weak and not too strong). Then, it is possible to remark that an optimal stability of the adduct for the catalyst effectiveness should exist. Covalent bond between thiocyanate and Co becomes stronger moving down to $16(\text{F})\text{CoPc}$ (that should have the lowest HOMO–LUMO gap) so that $16(\text{F})\text{CoPc}$ shows low activity as expected. The same and inverse is true for $8\beta(\text{EH})\text{CoPc}$ that is too far high so the gap is very large and the strength will be too weak. So the highest activity should be shown by some $\text{N}(\text{R})\text{CoPc}$ having intermediate bond strength and intermediate gap values.

Regarding the adduct formation, further information concerning the formation of the $\text{Co(II)Pc-SCN}^-/\text{NCS}^-$ and $[\text{Co(III)Pc-SCN}^-/\text{NCS}^-]^+$ complexes at different oxidation states can be gained through the study of the Co–S or Co–N bond, within the Morokuma–Ziegler partitioning scheme, which provided a detailed description of the interaction energy. After comparing both oxidation states of the redox center namely, Co(II) and Co(III), the latter exhibited a higher stabilization of the adduct than the complex with Co(II) (see Table 7), thus supporting the idea of the initial formation of $[\text{Co(III)Pc}]^+$ leading to a favored interaction between the thiocyanate moiety and the metal center. Additionally, the formation of the isothiocyanate

Table 7 Energy decomposition analysis according to the Morokuma Ziegler scheme

Complex	ΔE_{pauli}	ΔV_{elstat}	ΔE_{orb}	ΔE_{int}
Isothiocyanate				
SCN^- -Co(II)Pc	72.98	-25.00 (22 %) ^a	-89.09 (78 %)	-41.10
SCN^- -Co(III)Pc	91.69	-99.87 (39 %)	-153.75 (61 %)	-161.93
Thiocyanate				
NCS^- -Co(II)Pc	95.33	-62.90 (50 %)	-63.05 (50 %)	-30.63
NCS^- -Co(III)Pc	124.04	-128.54 (56 %)	-100.61 (44 %)	-105.11

Both SCN^- -CoPc or NCS^- -CoPc complexes were evaluated considering the Co(II) and Co(III) oxidation states. All the energies are in kcal mol⁻¹. Data from [142]

^aNumber in parenthesis indicate the contribution of each term in the overall interaction energy. Calculated as $(\Delta E_{\text{orb}}/(\Delta V_{\text{elstat}} + \Delta E_{\text{orb}}))\%$, where $\Delta E_{\text{int}} = \Delta E_{\text{pauli}} + \Delta V_{\text{elstat}} + \Delta E_{\text{orb}}$

adduct involved a stronger interaction than the observed for the thiocyanate coordination mode. This was because of a larger covalent contribution for the isothiocyanate complex (78 and 61 %, the stabilizing terms, namely ΔV_{elstat} and ΔE_{orb}).

4 Summary and Outlook

These results indicate a promising route for the realization of supramolecular structures, such as molecular chains, based on the well-controlled anchoring of specially designed molecular building blocks on the regularly ordered and stepped gold electrode surfaces. The formation of SAM on a gold substrate and a thiolate ligand as an “anchoring” fragment of metallophthalocyanine leads to an interesting charge donation from the 4-ATP or A-MP towards both gold substrate and phthalocyanine, denoting an effective gold-MPc interaction mediated by the titled anchor ligands. The thiolate-gold substrate interaction is favored by about 40 kcal/mol, which decreases when the MPc moiety is included, denoting the influence of the active center into the SAM structure. The MPc-ligand interaction also varies when the modified SAM is formed, showing a slight destabilization with regards to the isolated MPc-ligand fragment. The results revealed the influence of the MPc and gold substrate towards the formation of the overall structure, showing that the MPc is connected to the surface effectively by the anchor ligand.

In summary, theoretical calculations indicate the importance of the backbonding mechanism into the adduct formation, showing the catalytic role of the supporting gold surface mediated by anchoring ligands. It also shown that the formation of an adduct between FePc and O₂ before the electron-transfer process will slow down the reaction, so it is likely that adduct formation occurs in a concerted fashion at the rate-determining step and involving the transfer of one-electron. This agrees with the kinetic parameters obtained from experiments.

Acknowledgments This work has been supported by Millennium Nucleus RC120001, NC120082 and Fondecyt Projects 1140503, 1110758, 1150629, 3130383 and 1140359.

References

1. Bader RFW (1990) *Atoms in molecules. A quantum theory*. Clarendon Press, Oxford
2. Herzberg G (1991) *Spectra and molecular structure. Electronic spectra and electronic structure of polyatomic molecules, vol III*. Krieger, Malabar, FL
3. Bunker PR, Jensen P (2000) *Computational molecular spectroscopy*. Wiley
4. Lehn J-M (2007) From supramolecular chemistry towards constitutional dynamic chemistry and adaptive chemistry. *Chem Soc Rev* 36:151–160
5. Scheider H-J (2009) Binding mechanisms in supramolecular complexes. *Angew Chem Int Ed* 48:3924–3977
6. Smulders M, Riddell I, Browne C, Nitschke JR (2013) Building on architectural principles for three-dimensional metallosupramolecular construction. *J Chem Soc Rev* 42:1728–1735
7. Lehn J-M (2004) Supramolecular chemistry: from molecular information towards self-organization and complex. *Rep Prog Phys* 64:249–265
8. Chalasinski G, Szczesniak MM (2000) State of the art and challenges of the ab initio theory of intermolecular interactions. *Chem Rev* 100:4227–4252
9. Braga D, Grepioni F (2000) Intermolecular interactions in nonorganic crystal engineering. *Acc Chem Res* 33:601–608
10. Buckingham AD (1978) Basic theory of intermolecular forces: applications to small molecules. In: Pullman B (ed) *Intermolecular interactions: from diatomics to biopolymers*. Wiley, Chichester, pp 1–67
11. Hoeben FJM, Jonkheijm P, Meijer EW, Schenning APH (2005) About supramolecular assemblies of π -conjugated systems. *Chem Rev* 105:1491–1546
12. Stone AJ (1996) *The theory of intermolecular forces*. Clarendon Press, Oxford
13. Lehn J-M, Atwood JL, Davies JED, MacNicol DD, Vögtle G (1996) *Comprehensive supramolecular chemistry*. Pergamon, Oxford
14. Desiraju GR (2010) Crystal engineering: a brief overview. *J Chem Sci* 122:667–680
15. Mati IK, Cockroft SL (2010) Molecular balances for quantifying non-covalent interactions. *Chem Soc Rev* 39:4195–4202
16. Oshovsky G, Reinhoudt D, Verboom W (2007) Supramolecular chemistry in water. *Angew Chem Int Ed* 46:2366–2393
17. Kinge S, Crego-Calama M, Reinhoudt DN (2008) Self-assembling nanoparticles at surfaces and interfaces. *Chem Phys Chem* 9:20–42
18. Otero R, Gallego J, Vázquez de Parda A, Marín N, Miranda R (2011) Molecular self-assembly at solid surfaces. *Adv Mater* 23:5148–5176
19. Bonifazi D, Mohnani S, Llanes-Pallas A (2009) Supramolecular chemistry at interfaces: molecular recognition on nanopatterned porous surfaces. *Chem Eur J* 15:7004–7025
20. Grätzel M (2009) Recent advances in sensitized mesoscopic solar cells. *Acc Chem Res* 42:1788–1798
21. Zagal JH, Griveau S, Silva JF, Nyokong T, Bedioui F (2010) Metallophthalocyanine-based molecular materials as catalysts for electrochemical reactions. *Coord Chem Rev* 254:2755–2791
22. Aakeröy CB, Champness NR, Janiak C (2010) Recent advances in crystal engineering. *Cryst Eng Comm* 12:22–35
23. Braga D, Grepioni F (2005) Making crystals from crystals: a green route to crystal engineering and polymorphism. *Chem Commun* 41:3635–3645
24. Pensa E, Cortés E, Corthey G, Carro P, Vericat C, Salvarezza R (2012) The chemistry of the sulfur-gold interface. in search of a unified model. *Acc Chem Res* 45:1183–1192
25. Mandler D, Krauss-Ophir S (2011) Self-assembled monolayers (SAMs) for electrochemical sensing. *J Solid State Electrochem* 15:1535–1558
26. Yamanoi Y, Nishihara N (2007) Assembly of nanosize metallic particles and molecular wires on electrode surfaces. *Chem Commun* 43:3983–3989

27. Thompson D, Hermes JP, Quinn AJ, Mayor M (2012) Scanning the potential energy surface for synthesis of dendrimer-wrapped gold clusters: design rules for true single-molecule nanostructures. *ACSNano* 6:3007–3017
28. Häkkinen H (2012) The gold-sulfur interface at the nanoscale. *Nat Chem* 4:443–455
29. Katiuce S, Codorin S, Pacheco T, Neves A, Cruz I (2009) Self-assembled monolayer of nickel (II) complex and thiol on gold electrode for the determination of catechin. *Talanta* 78:1063–1068
30. Agboola BO, Ozoemena KI (2008) Self-assembly and heterogeneous electron transfer properties of metallo-octacarboxyphthalocyanine complexes on gold electrode. *Phys Chem Chem Phys* 10:2399–2408
31. Silvanesan A, John SA (2008) Amino group positions dependent morphology and coverage of electropolymerized metallophthalocyanine (M = Ni and Co) films on electrode surfaces. *Electrochim Acta* 53:6629–6635
32. Agboola B, Nyokong T (2007) Comparative electrooxidation of nitrite by electrodeposited Co(II), Fe(II) and Mn(III) tetrakis (benzylmercapto) and tetrakis (dodecylmercapto) phthalocyanines on gold electrodes. *Anal Chim Acta* 587:116–123
33. Agboola B, Nyokong T (2007) Comparative electrooxidation of sulphite by self-assembled monolayers (SAMs) of Co(II), Fe(II), Ni(II) and Mn(III) tetrakis benzylmercapto and dodecylmercapto metallophthalocyanines complexes on gold electrodes. *Talanta* 72:691–698
34. Mashazi P, Westbroek P, Ozoemena K, Nyokong T (2007) Surface chemistry and electrocatalytic behaviour of tetra-carboxy substituted iron, cobalt and manganese phthalocyanine monolayers on gold electrode. *Electrochim Acta* 53:2007–2015
35. Ponce I, Silva JF, Oñate R, Miranda-Rojas S, Muñoz-Castro A, Arratia-Pérez R, Mendizabal F, Zagal JH (2011) Theoretical and experimental study of bonding and optical properties of self-assembly metallophthalocyanines complexes on a gold surface. A survey of the substrate-surface interaction. *J Phys Chem C* 115:23512–23518
36. Ponce I, Silva J, Oñate R, Rezende M, Paez M, Pavez J, Zagal JH (2011) Enhanced catalytic activity of Fe phthalocyanines linked to Au(111) via conjugated self-assembled monolayers of aromatic thiols for O₂ reduction. *Electrochem Commun* 13:1182–1185
37. Erdogmus A, Booyens I, Nyokong T (2011) Synthesis and electrochemical properties of new tetra substituted cobalt phthalocyanine complexes, and their application in electrode modification for the electrocatalysis of l-cysteine. *Synth Met* 161:241–250
38. Silva C, Pavez J, Silva JF, Sancy M, Guerrero J, Paez M, Zagal JH (2010) Electrochemical transducer based on nanostructured polyaniline films obtained on functionalized self assembled monolayers of 4-aminothiophenol. *Mol Cryst Liq Cryst* 522:112–124
39. Bedioui F, Nyokong T, Appleby A, Caro C, Gulppi M, Zagal JH (2007) Tuning the redox properties of metalloporphyrin- and metallophthalocyanine-based molecular electrodes for the highest electrocatalytic activity in the oxidation of thiols. *Phys Chem Chem Phys* 9:3383–3396
40. Ciofini I, Bedioui F, Zagal J, Adamo C (2003) Environment effects on the oxidation of thiols: cobalt phthalocyanine as a test case. *Chem Phys Lett* 376:690–696
41. Love J, Estroff L, Kriebel JK, Nuzzo RG, Whitesides GM (2005) Self-assembled monolayers of thiolates on metals as a form of nanotechnology. *Chem Rev* 105:1103–1170
42. Cão R, Díaz-García AM, Cão R (2009) Coordination compounds built on metal surfaces. *Coord Chem Rev* 253:1262–1275
43. Hättig C, Weigend F (2000) CC2 excitation energy calculations on large molecules using the resolution of the identity approximation. *J Chem Phys* 113:5154–5164
44. Christiansen C, Koch H, Jørgensen P (1995) The second-order approximate coupled cluster singles and doubles model CC2. *Chem Phys Letter* 243:409–418
45. Send R, Sundholm D (2007) Coupled-cluster studies of the lowest excited states of the 11-cis-retinal chromophore. *Phys Chem Chem Phys* 9:2862–2867
46. Winter NOC, Hättig C (2012) Benchmarks for 0–0 transitions of aromatic organic molecules: DFT/B3LYP, ADC (2), CC2, SOS-CC2 and SCS-CC2 compared to high-resolution gas-phase data. *Chem Phys* 401:217–224

47. Grimme S (2006) Semiempirical GGA-type density functional constructed with a long-range dispersion correction. *J Comput Chem* 27:1787–1799
48. Casida M (1995) Recent advances in density functional methods (I). Ed Chong D, World Scientific, pp 155–170
49. Bauernschmitt R, Ahlrichs R (1996) Treatment of electronic excitations within the adiabatic approximation of time dependent density functional theory. *Chem Phys Lett* 256:454–464
50. Ozoemena K, Nyokong T (2006) Comparative electrochemistry and electrocatalytic activities of cobalt, iron and manganese phthalocyanine complexes axially co-ordinated to mercaptopyrindine self-assembled monolayer at gold electrodes. *Electrochim Acta* 51:2669–2677
51. Ponce I, Silva JF, Oñate R, Rezende MC, Paez MA, Zagal JH, Pavez J, Mendizabal F, Miranda-Rojas S, Muñoz-Castro A, Arratia-Pérez R (2012) Enhancement of the catalytic activity of Fe Phthalocyanine for the reduction of O₂ anchored to Au(111) via conjugated self-assembled monolayers of aromatic thiols As compared to Cu Phthalocyanine. *J Phys Chem C* 116:15329–15341
52. Sancy M, Pavez J, Gulppi MA, de Mattos IL, Arratia-Pérez R, Linares-Flores C, Paez M, Nyokong T, Zagal JH (2011) Optimizing the electrocatalytic activity of surface confined Co macrocyclics for the electrooxidation of thiocyanate at pH 4. *Electroanalysis* 23:711–718
53. Linares-Flores C, Mac-LeadCarey D, Muñoz-Castro A, Zagal JH, Pavez J, Pino-Riffo D, Arratia-Pérez R (2012) Reinterpreting the role of the catalyst formal potential. The case of thiocyanate electrooxidation catalyzed by CoN₄-macrocyclic complexes. *J Phys Chem C* 116:7091–7098
54. Ahlrichs R, Bär M, Häser M, Horn H, Kölmel C (1989) Electronic structure calculations on workstation computers: the program system turbomole. *Chem Phys Lett* 162:165–169
55. Amsterdam Density Functional (ADF) Code (2010) Vrije Universiteit, Amsterdam, The Netherlands
56. Johansson MP, Lechtken A, Schooss Kappes MM, Furche F (2008) 2D-3D transition of gold cluster anions resolved. *Phys Rev A* 77:053202–053208
57. Grimme S, Antony J, Ehrlich S, Krieg H (2010) *J Chem Phys* 132:154104(1)–154104(10)
58. Hujo W, Grimme S (2011) Performance of the van der Waals density functional VV10 and (hybrid) GGA variants for thermochemistry and noncovalent interactions. *J Chem Theory Comput* 7:3866–3871
59. Grimme S (2012) On the accuracy of DFT methods in reproducing ligand substitution energies for transition metal complexes in solution: the role of dispersive interactions. *Chem Phys Chem* 13:1407–1409
60. Andrae D, Häusserman M, Dolg H, Stoll H, Preuss H (1990) Energy-adjusted ab initio pseudopotentials for the second and third row transition elements. *Theor Chim Acta* 77:12–25
61. Bergner A, Dolg M, Küchle W, Stoll H, Preuss H (1993) Ab initio energy-adjusted pseudopotentials for elements of groups 13–17. *Mol Phys* 80:1431–1441
62. Dunning T, Hay P (1997) *Modern theoretical chemistry*, vol 3. Ed. H. Schaefer, Plenum Press, pp 1–28
63. Bauernschmitt R, Ahlrichs R (1996) Treatment of electronic excitations within the adiabatic approximation of time dependent density functional theory. *Chem Phys Lett* 256:454–464
64. Casida ME, Jamorski C, Casida KC, Salahub DR (1998) Molecular excitation energies to high-lying bound states from time-dependent density-functional response theory: characterization and correction of the time-dependent local density approximation ionization threshold. *J Chem Phys* 108:4439–4449
65. Olsen L, Jørgensen P (1995) *In modern electronic structure theory*, vol 2. Ed. D.R. Yarkony, World Scientific, River Edge, NJ
66. te Velde G, Bickelhaupt FM, Baerends EJ, Fonseca-Guerra C, van Gisbergen JA, Snijders JG, Ziegler T (2001) *Chemistry with ADF*. *J Comput Chem* 22:931–967
67. Ziegler T, Rauk A (1977) On the calculation of bonding energies by the Hartree Fock Slater method. *Theor Chim Acta* 46:1–10

68. Eremtchenko M, Schaefer JA, Tautz FS (2003) Understanding and tuning the epitaxy of large aromatic adsorbates by molecular design. *Nature* 425:602–605
69. Li ZY, Li B, Yang JL, Hou JG (2010) Single-molecule chemistry of metal phthalocyanine on noble metal surfaces. *Acc Chem Res* 43:954–962
70. Wang Y, Wu K, Kröger J, Berndt R (2012) Structures of phthalocyanine molecules on surfaces studied by STM. *Advances* 2:041402–041412
71. Lu X, Hipps KW, Wang XD, Mazur U (1996) Scanning tunneling microscopy of metal Phthalocyanines: d7 and d9 cases. *J Am Chem Soc* 118:7197–7202
72. Gao L, Ji W, Hu YB, Cheng ZH, Deng ZT, Liu Q, Lin X, Guo W, Du SX (2007) Site-specific Kondo effect at ambient temperatures in iron-based molecules. *Phys Rev Lett* 99:106402–106406
73. Betti MG, Gargiani P, Frisenda R, Biagi R, Cossaro A, Verdini A, Floreano L, Mariani C (2010) Localized and dispersive electronic states at ordered FePc and CoPc chains on Au (110). *J Phys Chem C* 114:21638–21644
74. Kroger L, Stadtmuller B, Kleimann C, Pajpnt P, Kumpf C (2011) Normal-incidence x-ray standing-wave study of copper phthalocyanine submonolayers on Cu(111) and Au(111). *Phys Rev B* 83:195414–195422
75. Stepanow S, Rizzini AL, Krull C, Kavich J, Cezar JC, Yakhov-Harris F, Sheverdyayeva PM, Moras P, Carbone C, Ceballos G (2014) Spin tuning of electron-doped metal-Phthalocyanine layers. *J Am Chem Soc* 136:5451–5459
76. Tsukahara N, Shiraki S, Itou S, Ohta N, Takagi N, Kawai M (2011) Evolution of Kondo resonance from a single impurity molecule to the two-dimensional lattice. *Phys Rev Lett* 106:187201–187205
77. Minamitani E, Tsukahara N, Matdunaka D, Kim Y, Takagi N, Kawai M (2012) Symmetry-driven novel Kondo effect in a molecule. *Phys Rev Lett* 109:086602–086606
78. Zhang L, Cheng Z, Huan Z, He X, Lin X, Gao L, Deng Z, Jiang N, Liu Q, Du S, Guo H, Gao H-J (2011) Site- and configuration-selective anchoring of iron-Phthalocyanine on the Step Edges of Au(111) surface. *J Phys Chem C* 115:10791–10796
79. Jiang YH, Xiao WD, Liu LW, Zhang LZ, Lian JC, Yang K, Du SX, Gao H-J (2015) Self-assembly of metal Phthalocyanines on Pb(111) and Au(111) surfaces at submonolayer coverage. *J Phys Chem C* 115:21750–21754
80. Jiang N, Zhang YY, Liu Q, Deng ZH, Deng ZT, Du S, Gao HJ, Beck M, Pantelides ST (2010) Diffusivity control in molecule-on-metal systems using electric fields. *Nano Lett* 10:1184–1188
81. Liu Q, Zhang YY, Jiang N, Zhang HG, Gao L, Du SS, Gao HJ (2010) Identifying multiple configurations of complex molecules in dynamical processes: time resolved tunneling spectroscopy and density functional theory calculation. *Phys Rev Lett* 104:166101–166105
82. Zhang YY, Du SX, Gao H-J (2011) Binding configuration, electronic structure, and magnetic properties of metal phthalocyanines on a Au(111) surface studied with ab initio calculations. *Phys Rev B* 84:125446–125454
83. Li S, Hao J, Li F, Niu Z, Hu Z, Zhang L (2014) The key role of van der Waals interactions in MPc/Au(111) (M = Co, Fe, H₂) systems based on first-principles calculations. *J Phys Chem C* 118:27843–27849
84. Vasudevan P, Santosh N, Mann N, Tyagi S (1990) Transition metal complexes of porphyrins and phthalocyanines as electrocatalysts for dioxygen reduction. *Transit Met Chem* 15:81–90
85. Zagal JH (1992) Metallophthalocyanines as catalysts in electrochemical reactions. *Coord Chem Rev* 119:89–136
86. Lipkowsky J, Ross PN (1998) *Electrocatalysis*. Wiley
87. Zagal JH (2010) *Macrocycles in handbook of fuel cells*. Wiley, pp 1–12
88. Li Z, Liu B (2010) The use of macrocyclic compounds as electrocatalysts in fuel cells. *J Appl Electrochem* 40:475–483
89. Zagal JH, Silva JF (2006) Páez M. In: Zagal JH, Bedioui F, Dodelet JP (eds) *N4-macrocyclic metal complexes*. New York, Springer, pp 41–82

90. Alkire RC, Kolb DM, Lipkowsky J, Ross P (2008) Electrochemical surface modification: thin films, functionalization and characterization. Wiley
91. Dodelet JP, Zagal JH, Bedioui F, Dodelet JP (eds) (2006) N4-macrocyclic metal complexes. Springer, New York, pp 83–147
92. Bezerra CWB, Zhang L, Lee K, Liu H, Marques ALB, Marques EP, Wang H, Zhang J (2008) A review of Fe–N/C and Co–N/C catalysts for the oxygen reduction reaction. *Electrochim Acta* 53:4937–4951
93. Bashuam R, Zelenay P (2006) A class of non-precious metal composite catalysts for fuel cells. *Nature* 443:63–66
94. Wu G, More KL, Johnston CM, Zelenay P (2011) High-performance electrocatalysts for oxygen reduction derived from polyaniline, iron, and cobalt. *Science* 22:443–447
95. Chlistunoff J (2011) RRDE and voltammetric study of ORR on pyrolyzed Fe/Polyaniline catalyst. on the origins of variable Tafel Slopes. *J Phys Chem C* 115:6496–6507
96. Othman R, Dicks AL, Zhu Z (2012) Non precious metal catalysts for the PEM fuel cell cathode. *Int J Hydrogen Energy* 37:357–372
97. Wood TE, Tan Z, Schmoeckel AK, O’Neill D, Atanasoski R (2008) Non-precious metal oxygen reduction catalyst for PEM fuel cells based on nitroaniline precursor. *J Power Sources* 178:510–516
98. Jaouen F, Herranz J, Lefevre JM, Dodelet J-P, Kramm UI, Herrmann I, Bogdanoff P, Maruyama J, Nagaoka T, Garsuch A, Dahn JR, Olson T, Pylypenko S, Atanassov P, Ustinov EA (2009) Efficient metal-free oxygen reduction in alkaline medium on high-surface-area mesoporous nitrogen-doped carbons made from ionic liquids and nucleobases. *Appl Mater Interfaces* 1:1623–1639
99. Zagal JH, Ponce I, Baez D, Venegas R, Pavez J, Paez M, Gulppi M (2012) A possible interpretation for the high catalytic activity of heat-treated non-precious metal Nx/C catalysts for O₂ reduction in terms of their formal potentials. *Electrochem Solid-State Lett* 15:B90–B92
100. Baker R, Wilkinson DP, Zhang J (2009) Facile synthesis, spectroscopy and electrochemical activity of two substituted iron phthalocyanines as oxygen reduction catalysts in an acidic environment. *Electrochim Acta* 54:3098–3102
101. van den Brink F, Barendrecht E, Visscher W (1980) The cathodic reduction of oxygen: A review with emphasis on macrocyclic organic metal complexes as electrocatalysts. *Recl Trav Chim Pays-Bas* 99:253–262
102. Tarasevich KAR (1986) Electrocatalytic properties of pyrolytic polymers produced from N-4-complexes. *Elektrokhimiya* 22:1155–1170
103. Yeager E (1984) Electrocatalysts for O₂ reduction. *Electrochim Acta* 29:1527–1537
104. Zurilla RW, Sen RK, Yeager E (1978) The kinetics of the oxygen reduction reaction on gold in alkaline solution. *J Electrochem Soc* 125:1103–1109
105. Damjanovic A, Genshaw MA, Bockris JOM (1967) The role of electrochemistry in environmental control. *J Electroanal Chem Int Electrochem* 15:173–180
106. Zagal J, Bindra P, Yeager E (1980) A mechanistic study of O₂ reduction on water soluble phthalocyanines adsorbed on graphite electrodes. *J Electrochem Soc* 127:1506–1517
107. Zagal JH, Páez M, Tanaka AA, dos Santos JR, Linkous C (1992) Electrocatalytic activity of metal phthalocyanines for oxygen reduction. *J Electroanal Chem* 339:13–30
108. Shi Z, Zhang J (2007) Density functional theory study of transitional metal macrocyclic complexes’ dioxygen-binding abilities and their catalytic activities toward oxygen reduction reaction. *J Phys Chem C* 111:7084–7090
109. Wang G, Ramesh N, Hsu A, Chu D, Chen R (2008) Density functional theory study of the adsorption of oxygen molecule on iron phthalocyanine and cobalt phthalocyanine. *Mol Simulat* 34:1051–1056
110. Chen R, Li H, Chu D, Wang G (2009) Unraveling oxygen reduction reaction mechanisms on carbon-supported Fe-phthalocyanine and Co-phthalocyanine catalysts in alkaline solutions. *J Phys Chem C* 113:20689–20697

111. Sun S, Jiang N, Xia D (2011) Density functional theory study of the oxygen reduction reaction on metalloporphyrins and metallophthalocyanines. *J Phys Chem C* 115:9511–9517
112. Within the Morokuma-Zigler scheme, the ΔE_{orb} represent 70.2% of the total stabilizing energy (calculated as $\Delta E_{orb}/(\Delta V_{elstat} + \Delta E_{orb})\%$)
113. Jakobsche CE, Choudhary A, Miller SJ, Raines RT (2010) $n \rightarrow \pi^*$ interaction and $n(\pi)$ pauli repulsion are antagonistic for protein stability. *J Am Chem Soc* 132:6651–6653
114. Bendtsen AB, Hansen EH (1991) Spectrophotometric flow injection determination of trace amounts of thiocyanate based on its reaction with 2-(5-Bromo-2-pyridylazo)-5-diethylaminophenol and dichromate: assay of the Thiocyanate level in saliva from smokers and non-smokers. *Analyst* 116:647–651
115. Michigami Y, Fujii K, Ueda K, Yamamoto Y (1992) Determination of thiocyanate in human saliva and urine by ion chromatography. *Analyst* 117:1855–1858
116. Tamosiunas V, Padaruskas A, Pranaitytė B (2006) Convenient synthesis of novel tetrahydro-1, 5-benzodiazepine amide oximes. *Chemija* 17:21–24
117. Cox JA, Gray T, Kulkarni KR (1988) Stable modified electrodes for flow-injection amperometry: application to the determination of thiocyanate. *Anal Chem* 60:1710–1713
118. Gao D, Li J-Z, Yu R-Q, Zheng G-D (1994) Metalloporphyrin derivatives as neutral carriers for PVC membrane electrodes. *Anal Chem* 66:2245–2249
119. Amini MK, Shahrokhian S, Tangestaninejad S (1999) PVC-based cobalt and manganese phthalocyanine coated graphite electrodes for determination of thiocyanate. *Anal Lett* 32:2737–2750
120. Amini MK, Shahrokhian S, Tangestaninejad S (1999) Thiocyanate-selective electrodes based on nickel and iron phthalocyanines. *Anal Chim Acta* 402:137–143
121. Kenova TA, Kormienko VL, Drozdov SV (2010) On electrochemical oxidation of thiocyanates in solutions for cyanidation of gold-containing ores and concentrates. *Russ J Appl Chem* 83:1589–1592
122. Ozoemena KI, Nyokong T (2005) Surface electrochemistry of iron phthalocyanine axially ligated to 4-mercaptopyridine self-assembled monolayers at gold electrode: applications to electrocatalytic oxidation and detection of thiocyanate. *J Electroanal Chem* 579:283–289
123. Vasudevan P, Phougat N, Shukla AK (1996) Metal phthalocyanines as electrocatalysts for redox reactions. *Appl Organomet Chem* 10:591–604
124. Ozoemena KI, Nyokong T (2006) Comparative electrochemistry and electrocatalytic activities of cobalt, iron and manganese phthalocyanine complexes axially co-ordinated to mercaptopyridine self-assembled monolayer at gold electrodes. *Electrochim Acta* 51:2669–2677
125. Zagal JH, Páez C (1989) Catalytic electrooxidation of 2-mercaptoethanol on a graphite electrode modified with metal—phthalocyanines. *Electrochim Acta* 34:243–247
126. Griveau S, Pavez J, Zagal JH, Bedioui F. *J Electroanal Chem* 497:75–83
127. Griveau S, Bedioui F (2001) Electro-oxidation of 2-mercaptoethanol on adsorbed monomeric and electropolymerized cobalt tetra-aminophthalocyanine films. Effect of film thickness. *Electroanal* 13:253–256
128. Griveau S, Albin V, Pauporté T, Zagal JH, Bedioui F (2002) Comparative study of electropolymerized cobalt porphyrin and phthalocyanine based films for the electrochemical activation of thiols. *J Mater Chem* 12:225–232
129. Sehlotho N, Nyokong T (2006) Electrocatalytic oxidation of thiocyanate, L-cysteine and 2-mercaptoethanol by self-assembled monolayer of cobalt tetraethoxy thiophene phthalocyanine. *Electrochim Acta* 51:4463–4470
130. Sancy M, Pavez J, Gulppi MA, Mattos IL, Arratia-Pérez R, Linares-Flores C, Paez M, Nyokong T, Zagal JH (2011) Optimizing the electrocatalytic activity of surface confined Co macrocyclics for the electrooxidation of thiocyanate at pH 4. *Electroanal* 23:711–718
131. Ozoemena KI, Nyokong T, Westbroek P (2003) Self-assembled monolayers of cobalt and iron phthalocyanine complexes on gold electrodes: comparative surface electrochemistry and electrocatalytic interaction with thiols and thiocyanate. *Electroanal* 15:1762–1770

132. Figlar JN, Stanbury DM (2000) Thiocyanogen as an intermediate in the oxidation of thiocyanate by hydrogen peroxide in acidic aqueous solution. *Inorg Chem* 39:5089–5094
133. Liu L, Feng J, Wu G, Lü X, Gao Q (2009) Dynamical complexity in electrochemical oxidations of thiocyanate. *Chin J Chem* 27:649–654
134. Gauguin R (1951) Oxydation électrochimique de l'ion thiocyanique. Application aux dosages et à l'étude des réactions. *Anal Chim Acta* 5:200–214
135. Wilson IR, Harris GM (1961) The oxidation of thiocyanate ion by hydrogen peroxide. II. The acid-catalyzed reaction. *J Am Chem Soc* 83:286–289
136. Stedman G, Whincup PA (1969) Acidic aqueous decomposition of thiocyanogen. *J Chem Soc* 25:1145–1148
137. Itabashi E (1985) Spectroelectrochemical characterization of iron(III)-thiocyanate complexes in acidic thiocyanate solutions at an optically transparent thin-layer-electrode cell. *Inorg Chem* 24:4024–4027
138. Modi S, Deodhar SS, Behere DV, Mitra S (1991) Horseradish peroxidase catalyzed oxidation of thiocyanate by hydrogen peroxide: comparison with lactoperoxidase-catalysed oxidation and role of distal histidine. *Biochem* 30:118–124
139. Adak S, Mazumdar A, Banerjee K (1997) Low catalytic turnover of horseradish peroxidase in thiocyanate oxidation evidence for concurrent inactivation by cyanide generated through one-electron oxidation of thiocyanate. *J Biol Chem* 272:11049–11056
140. Ozoemena KI, Nyokong T (2005) Surface electrochemistry of iron phthalocyanine axially ligated to 4-mercaptopyridine self-assembled monolayers at gold electrode: applications to electrocatalytic oxid. *Electroanal Chem* 579:283–289
141. Obirai J, Nyokong T (2005) Synthesis, electrochemical and electrocatalytic behaviour of thiophene-appended cobalt, manganese and zinc phthalocyanine complexes. *Electrochim Acta* 50:5427–5434
142. Linares-Flores C, Mac-Leod D, Muñoz-Castro A, Zagal JH, Pavez J, Pino-Riffo D, Arratia-Pérez R (2012) Reinterpreting the role of the catalyst formal potential. the case of thiocyanate electrooxidation catalyzed by CoN4-macrocyclic complexes. *J Phys Chem C* 116:7091–7098
143. Lever AB (1999) Palladium-catalyzed hydrogen reduction and decolorization of reactive phthalocyanine dyes. *J Porphyr Phthal* 3:488–499
144. Alexiou C, Lever AB (2001) Tuning metalloporphyrin and metallophthalocyanine redox potentials using ligand electrochemical (EL) and Hammett (σ) parametrization. *Coord Chem Rev* 216:45–54

Metalloporphyrins in Solar Energy Conversion

Ievgen Obraztsov, Włodzimierz Kutner and Francis D'Souza

Abbreviation

APCE	Absorbed photon-to-current conversion efficiency
ATR-FTIR	Attenuated total reflection Fourier transform infrared (spectroscopy)
BHJ	Bulk heterojunction
BODIPY	Boradiazaindacene
CAA	Cyanoacrylic acid
CB	Conduction band
CI	Charge injection
CNT	Carbon nanotube
CR	Charge recombination
D	Electron-donor molecule
D*	Excited electron-donor molecule
D-B-A	Donor-(porphyrin bridge)-acceptor
D- π -A	“Push-pull”, donor-(π -bridged chromophore)-acceptor
<i>FF</i>	Fill factor of a photovoltaic cell
FHJ	Flat heterojunction
FTO	Fluorine-doped tin oxide
HOMO	Highest occupied molecular orbital
IPCE	Incident photon-to-current efficiency
ITO	Tin-doped indium oxide

I. Obraztsov · W. Kutner (✉)

Institute of Physical Chemistry (IPC PAS), Kasprzaka 44/52, 01-224 Warsaw, Poland
e-mail: wkutner@ichf.edu.pl

W. Kutner

Faculty of Mathematics and Natural Sciences, School of Sciences, Cardinal Stefan Wyszyński University in Warsaw, Woycieckiego 1/3, 01-938 Warsaw, Poland

F. D'Souza (✉)

Department of Chemistry, University of North Texas, 1155, Union Circle, #305070, Denton, TX 76203-5017, USA
e-mail: francis.dsouza@unt.edu

F. D'Souza

Advanced Materials and Manufacturing Processes Institute (AMMPI),
UNT-Discovery Park, 3940 N. Elm St., #E132, Denton, TX 76207-7102, USA

LB	Langmuir–Blodgett
LUMO	Lowest unoccupied molecular orbital
MO	Metal oxide
MP	Metalloporphyrin
NIR	Near-infrared
NHE	Normal hydrogen electrode
OPV	Organic photovoltaics
PCE	Power conversion efficiency (of a photovoltaic cell)
PV	Photovoltaics
PVC	Photovoltaic cell
RCP	Redox-conducting polymer
SC	Solar cell
SQ	Squaraine
SMSC	Supramolecular solar cell
SWCNT	Single-wall carbon nanotube
TPP	Tetraphenyl porphyrin
TPPZn	Tetraphenyl zinc porphyrin
TLSC	Thin-layer solar cell
TCO	Transparent conductive oxide
UV–vis	Ultraviolet–visible (light)
ZnP	Zinc porphyrin

Symbols

i_{mp}	photocurrent corresponding to maximum power of a photovoltaic cell (A)
i_{sc}	short-circuit current (A)
j	current density ($A\ cm^{-2}$)
P	power (W)
P_{in}	incident light power ($W\ m^{-2}$)
P_{ir}	light irradiation power (W)
$P_{max,ideal}^{PVC}$	maximum power of an ideal photovoltaic cell (W)
$P_{max,ideal}^{PVC}$	maximum power of a photovoltaic cell (W)
P_{out}	output power of a photovoltaic cell (W)
V	voltage (V)
V_{mp}	voltage corresponding to maximum power (of a photovoltaic cell) (V)
V_{oc}	open-circuit voltage (V)
Γ	surface concentration ($nmol\ cm^{-2}$)
ΔG_{inj}	Gibbs free energy change resulting from electron injection (from D^* to the CB of TiO_2)
η	overall power conversion efficiency of a photovoltaic cell (%)
ϕ	solar energy conversion efficiency, i.e., quantum yield

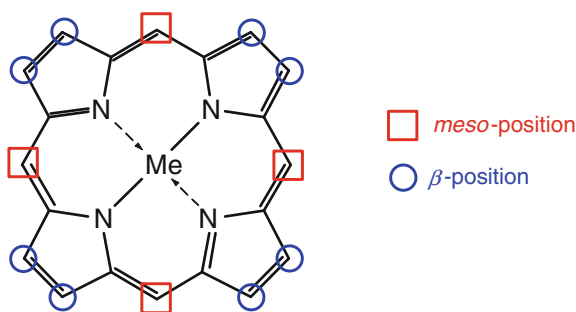
1 Introduction

Solar cells (SCs) with the organic or hybrid (combined organic and inorganic) photoactive electrode materials are the emerging types of SCs. Despite their adolescence, progress in the development of these SCs brought their efficiency close to the level, which allows their commercialization. However, this remains as a great challenge [1, 2]. Metalloporphyrins (MPs) are important electro- and photoactive components of these SCs. The present book chapter briefly describes operating principles of different MP-based SCs and critically overviews the progress in the MP application to organic photovoltaics (OPV) and dye-sensitized solar cells (DSSCs) that have been made since 2009.

1.1 Metalloporphyrins in Photovoltaics

Being still one of the most-studied redox dyes, MPs continuously attract attention because of their functional universality, chemical stability, ease of chemical modification, and great potential of tuning their chemical and electronic properties. MPs have intensively been studied with respect to their promising application for conversion of solar energy into electric energy in SCs. MPs are mostly used in three types of SCs. These include DSSCs, supramolecular SCs (SMSCs), and bulk heterojunction solar cells (BHJ SCs).

A unique ease of chemical derivatization of MPs is due to their structure. In a typical porphyrin, there are four *meso*- and eight β -positions available for substitution (Scheme 1). Moreover, a metal atom can be introduced in the center of the macrocycle to form a metalloporphyrin. This atom may axially coordinate a ligand or ligands depending upon the metal nature.



Scheme 1 General structural formula of a metalloporphyrin macrocycle with indicated positions available for peripheral substitution

1.2 Solar Cell Fundamentals

Evaluation of an SC photovoltaic performance is usually accomplished with a set of tests. Those involve measurements of the current–voltage (I – V) curves for the cell in the dark and under light illumination, fluorescent decay upon photoexcitation, determination of the incident photon-to-electron-conversion efficiency (IPCE), etc.

In order to obtain mutually comparable results, light sources imitating solar radiation are used. Gases and water vapor in atmosphere partially absorb solar energy. The sunlight passes one atmospheric thickness in tropical regions only. However, the effective atmosphere thickness is larger for all other latitudes. A widely applied air mass (AM) 1.5 is the solar radiation spectrum obtained after passing the 1.5 Earth atmosphere thicknesses (curve 3 in Fig. 1).

Figure 2 shows parameters of an SC, which can be determined from an I – V curve. The direction of current and curvature of the current–voltage curves depend upon the SC architecture and properties of the electrode materials applied.

Noteworthy, the IUPAC definition of an anode and cathode is herein quoted because erroneous definitions in literature on SC schemes are frequently encountered. An anode is the electrode where redox species are oxidized, i.e., the complete removal of one or more electrons from a molecular entity or an increase in the oxidation number of any atom within any substrate or gain of oxygen and/or loss of hydrogen of an organic substrate takes place [3]. The cathode, respectively, is the electrode where redox species are reduced. These definitions apply to electrodes of both an electrochemical cell and a galvanic or voltaic cell.

Solar energy conversion efficiency, ϕ , represents the number of electron/hole pairs generated per an *absorbed* photon, called the quantum yield or the internal

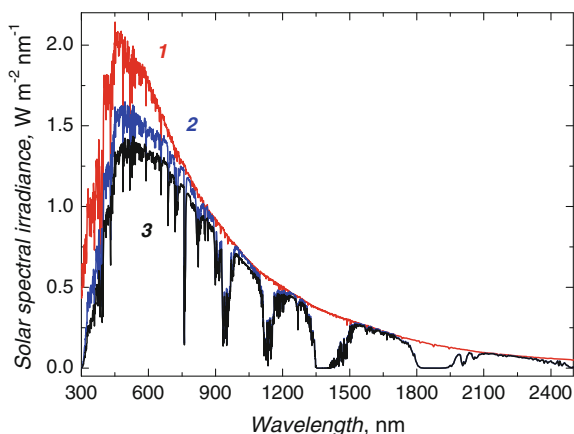


Fig. 1 Reference solar spectral irradiance, (1) the AM 0 standard, i.e., the solar spectrum outside the Earth atmosphere, (2) the AM 1.0, i.e., direct solar irradiance on the ground level, and (3) the AM 1.5 standard, i.e., solar light that passed 1.5 atmosphere thicknesses. Adapted from <http://redc.nrel.gov/solar/spectra/am1.5>, U.S. Department of Energy (DOE)/NREL/ALLIANCE

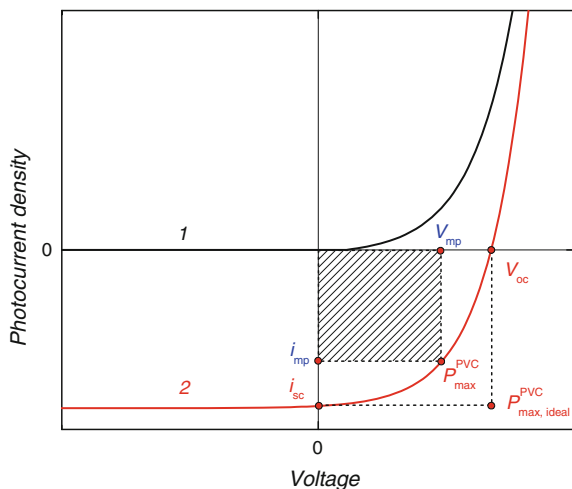


Fig. 2 Illustrative photocurrent–voltage curves for a solar cell (SC) (1) in the dark and (2) under light illumination. V_{oc} open-circuit voltage, V_{mp} and j_{mp} voltage and photocurrent corresponding to maximum power of the SC, respectively, j_{sc} short-circuit current, P_{max}^{PVC} maximum power of the SC, $P_{max,ideal}^{PVC}$ maximum power of an “ideal” SC, i.e., which converts all photogenerated charge to energy and passes it into an external circuit

quantum efficiency. Further, the number of electron/hole pairs generated per *incident* photon, IPCE, or the external quantum efficiency is expressed by Eq. 1:

$$IPCE(\lambda) = \frac{n_{\text{electrons}}}{n_{\text{photons}}} = \frac{j/e}{P_{in}/h\nu} = \frac{j}{P_{in}} \times \frac{h\nu}{e\lambda} = \frac{j}{P_{in}} \times \frac{1240}{\lambda(\text{nm})} \quad (1)$$

where j is the photocurrent density ($A\ m^{-2}$), and P_{in} is the incident light power ($W\ m^{-2}$). The IPCE parameter provides a detail insight into the performance of a photovoltaic cell because it informs about efficiency of the light absorption by a photoactive material, efficiency of charge separation between the electron donor (D) and the acceptor (A), and efficiency of the charge collection by external electrodes.

The most complex parameter describing the SC efficiency is the overall power conversion efficiency (PCE), η . The ratio of the output power of a photovoltaic cell, P_{out} , to the irradiation power, P_{in} , describes this parameter (Eq. 2).

$$\eta = \frac{P_{out}}{P_{in}} = FF \times \frac{V_{oc}I_{sc}}{P_{in}} \quad (2)$$

Here, FF is the so-called fill factor. It represents efficiency of electron withdrawal from the photoexcited donor molecule (D^*) or D^* -A dyad into external circuit, i.e., the ratio of photogenerated electrons withdrawn by the external circuit to those recombined inside the cell (Eq. 3):

$$FF = \frac{j_{\text{mp}} V_{\text{mp}}}{j_{\text{sc}} V_{\text{oc}}} \quad (3)$$

where j_{mp} and V_{mp} stand for current and voltage, respectively, which corresponds to the maximum cell power, whereas j_{sc} and V_{oc} represent short-circuit current and open-circuit voltage, respectively.

2 Mechanism of Organic Photovoltaics Operation

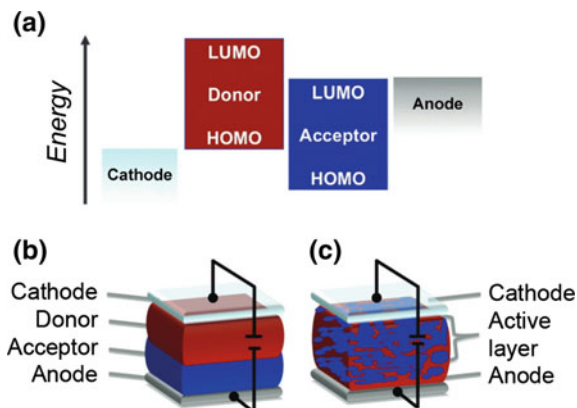
With respect to the material used, SCs with MPs can be divided into three main categories, including those using supramolecular electron donor–acceptor dyads, thin films of a small-molecule or polymer semiconductor, and a hybrid combining an organic dye and a metal oxide semiconductor, TiO_2 , prevalingly. Despite different terminologies used for naming species and processes in mechanisms of photocurrent generation, there is no difference in chemical meaning between these events. There are fundamental steps of organic and hybrid SC operation, common for these types involving (i) absorption of light by a photoactive electrode material resulting in photoexcitation of this material, (ii) photoinduced charge separation between the D and A materials, (iii) collection or release of electrons by electrodes, and (iv) reduction of photo-oxidized D. In a photoelectrochemical reaction, photocathode is the electrode where photo-electroactive material is reduced, i.e., it accepts an electron, and a photoanode is the electrode where photo-electroactive material is oxidized, i.e., an electron is abstracted from this material. One should keep these definitions in mind when discussing the mechanisms, operation schemes of electrochemical, galvanic, and voltaic cells in order to escape from misinterpretation of experimental data.

2.1 *Thin-Film Small-Molecule and Polymer Solar Cells*

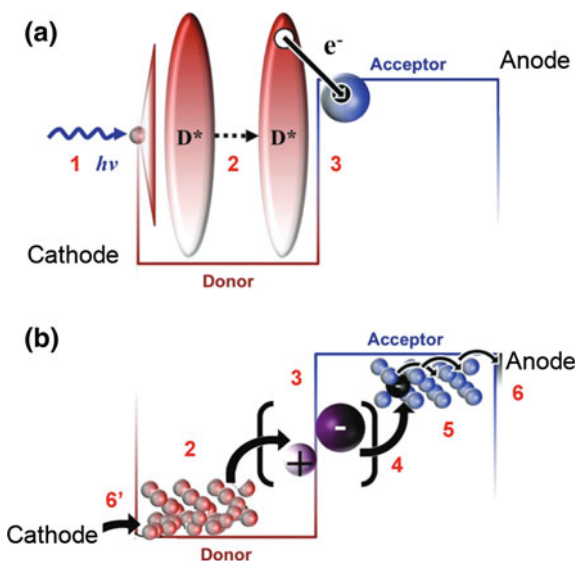
The first small-molecule SC was devised as early as three decades ago [4]. Depending on the nature of the interface between the electron-donor and electron-acceptor films in this SC, one can distinguish flat (or planar) heterojunction (FHJ) and bulk heterojunction (BHJ) SCs (Scheme 2).

That is, there are the layer-by-layer deposited electron donor (n-type organic semiconductor) layer and the acceptor (p-type organic semiconductor) layer or a blend of polymers, respectively. The operation principle of a small-molecule or polymer SC is relatively simple and close to that of the inorganic semiconductor SC. For an FHJ organic SC with the one D and one A layer, six steps in the mechanism of energy conversion can be distinguished (Scheme 3). That is, (1) initially, light is

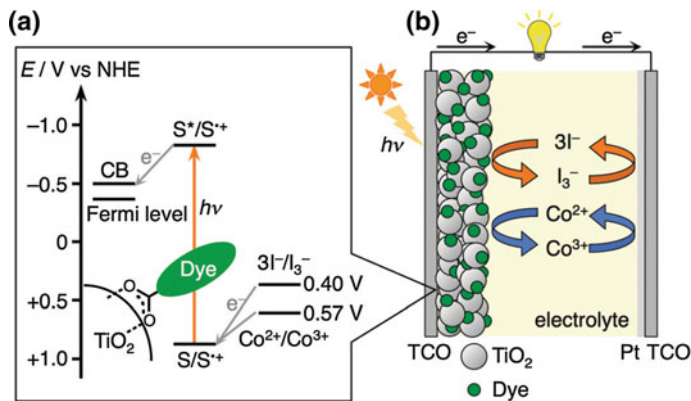
Scheme 2 A simplified view of **a** the solar cell energy diagram as well as the solar cell with **b** flat heterojunction (FHJ) and **c** bulk heterojunction (BHJ). Adapted from Ref. [5] with permission from The Royal Society of Chemistry



Scheme 3 **a** A simplified energy diagram and **b** principle of operation of a flat heterojunction solar cell. The numbered cell operation steps are explained in text. Adapted from Ref. [5] with permission from The Royal Society of Chemistry



absorbed by the D to generate an exciton (D^*). Subsequently, (2) the D^* diffuses (by electron hopping) to the donor-acceptor interface where (3) a D^+A^- complex is formed. Formation of an exciton of electron acceptor (A^*) is also possible, thus corresponding stages 1–3 for an A may also occur. Next, (4) charge is separated at the D–A interface when electron is transferred from the excited donor (D^*) to A molecule. Further, (5) electron is transported to the anode and, finally (6) it is collected at the anode, and, (6') simultaneously, it is injected at the cathode, via an external electric current, to reduce the oxidized D.



Scheme 4 A simplified **a** energy diagram and **b** principle of operation of a DSSC. CB stands for the conduction band and TCO for the transparent conductive oxide. Reproduced from Ref. [7] with permission from The Royal Society of Chemistry

2.2 Dye-Sensitized Solar Cells

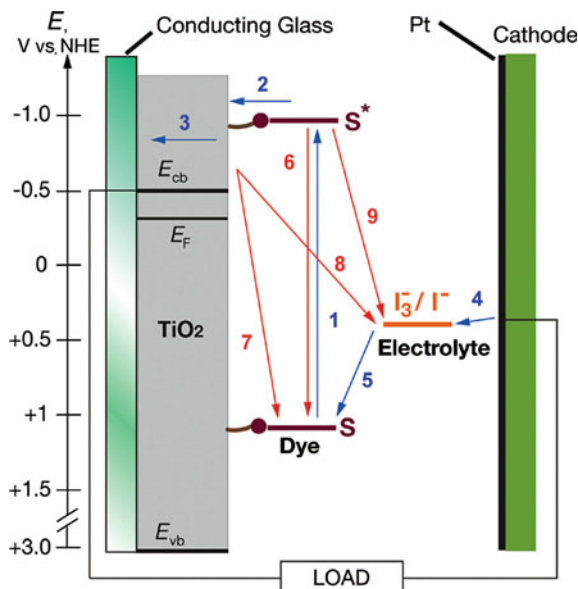
A hybrid SC, i.e., the dye-sensitized solar cell (DSSC), usually uses an organic electron donor to inject electron into a conduction band (CB) of an inorganic semiconductor, usually TiO₂, proposed by Grätzel et al. in 1991 (Scheme 4) [6].

The DSSC is one of the most-studied types of emerging SCs. Initially, ruthenium dyes were used. Then, porphyrin dyes found widespread application in DSSCs because of their favorable optical properties and chemical bond flexibility. Efficiency of these DSSCs was not much impressive until mid-2000. Progress in a molecular design and synthesis of new porphyrins as well as preparation of new more efficient charge mediators allowed improving this efficiency dramatically. This improvement was mostly due to introduction of the “push–pull” structured and π -extended peripheral substituents. The recent research focuses on enriching absorbance spectra of MPs. It resulted in efficiency of DSSCs with MPs equal to those with the ruthenium dyes.

Many components of this cell appear in many different other cells, including TiO₂, electrodes, electron mediators; the principle of DSSC operation is thoroughly studied (Scheme 5). Moreover, it is relatively easy to compare and to draw conclusions on the effect of different MPs on the cell performance because these cells are very similar.

2.3 Supramolecular Solar Cells

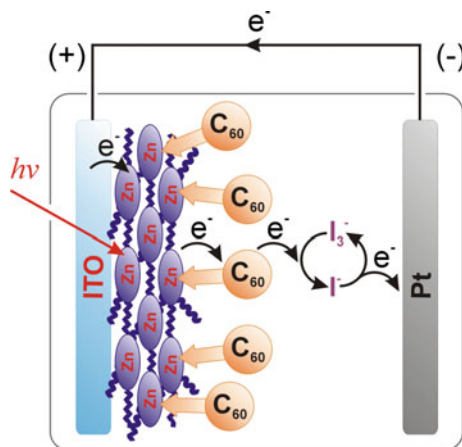
Supramolecular SCs share features of both BHJ SCs and DSSCs. Unlike DSSC, however, they use organic materials as both the electron donors and acceptors.



Scheme 5 A simplified energy diagram and operation principle of DSSC. (1–5) Favorable processes of current generation in the DSSC (blue arrows and numbers); (6–9) unfavorable recombination processes (red arrows and numbers). (1) Photoexcitation of D molecules, (2) D^* -to- TiO_2 electron transfer, (3) electron transfer from TiO_2 to the transparent conductive oxide (TCO) electrode, (4) heterogeneous reduction of the I_3^- electron mediator, (5) regeneration of the oxidized dye to its reduced form by the reduced, I^- , electron mediator, (6) radiative or non-radiative decay of energy of the photoexcited dye, (7) reduction of the photo-oxidized dye by electron of the TiO_2 electron conduction band (E_{cb}) energy, (8) the reverse electron flow because of reduction of the I_3^- electron mediator in solution, (9) reduction of the electrolyte species by the photoexcited dye. Reproduced from Ref. [8] with permission from The Royal Society of Chemistry

In contrast to the thin film or polymer SCs, though, supramolecular SCs use photoelectrochemical cell construct where D and A are placed in close proximity and bound together to form a supramolecular electron donor–acceptor dyad. This binding may be afforded with the covalent bond, hydrogen bond, metal–ligand coordination, or π – π stacking. Therefore, exciton does not travel upon D excitation, within a bulk donor layer to find the D–A interface, but rather through a charge-separated state of the D–A dyad. This charge-separated state can move by electron hopping in the film. In order to increase the performance of these SCs, electron mediators are used, similarly as in DSSCs.

MPs are widely applied to supramolecular SCs as electron-donating moieties because of their outstanding convenience of use as “building blocks”. That is, they can be used in the form of single molecules, dimers, oligomers, liquid crystals, or polymers. The acceptor moieties most commonly used in supramolecular SCs include carbon nanomaterials, such as fullerenes and carbon nanotubes (CNTs).



Scheme 6 Operation mechanism of a supramolecular solar cell with a ZnP-C₆₀ donor-acceptor dyad assembled by axial metal-ligand coordination of the C₆₀-imidazole adduct to a ZnP polymer film. Reprinted with permission from Subbaiyan NK, Obraztsov I, Wijesinghe CA, Tran K, Kutner W, D'Souza F (2009) Supramolecular donor-acceptor hybrid of electropolymerized zinc porphyrin with axially coordinated fullerene: formation, characterization, and photoelectrochemical properties. *J Phys Chem C* 113(20):8982–8989. Copyright (2009) American Chemical Society

Scheme 6 shows a simplified view of the mechanism of operation of a supramolecular SC.

Advantageously, electronic properties of both the D and A species in supramolecular SCs can easily be tuned, unlike DSSCs where TiO₂ with fixed energy levels is used. Prospectively, this tuning possibility gives more freedom to increase efficiency of SCs using D–A dyads. Mechanisms of unfavorable charge recombination in supramolecular SCs are similar to those in DSSCs.

In the supramolecular SC operation mechanism, the order of organization of the D–A dyads on the electrodes plays the crucial role.

3 Effects of Peripheral Substituents of the Metalloporphyrin Macrocycle on the Photovoltaic Cell Performance

Zn porphyrin is the most widely used metalloporphyrin in different types of SCs. Because of different operating conditions and the demand of high efficiency of SCs, the porphyrin macrocycle is modified in many different ways. These include substituting with different peripheral groups, such as alkyl or phenyl groups, aromatic heterocycles, other porphyrins, or even fusing porphyrins with other aromatic molecules, or forming porphyrin oligomers. The effect of peripheral substituents of

porphyrin on SC efficiency is discussed below for three different types of SCs, i.e., DSSCs, BHJ SCs, and SMSCs.

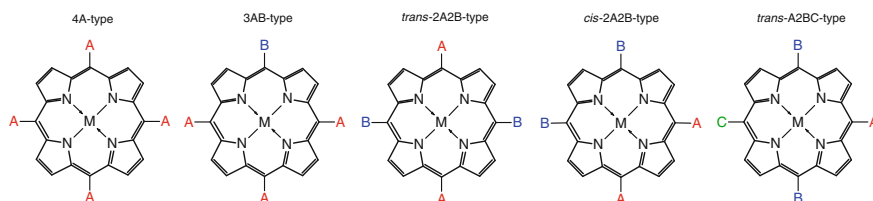
3.1 Porphyrins in Dye-Sensitized Solar Cells

For application in DSSCs, porphyrins should be attached to a semiconducting metal oxide (MO), e.g., TiO_2 . The most efficient attachment way involves introduction of an anchoring group (A in Scheme 7 and Table 1) allowing for binding the porphyrin molecule to the MO surface. In order to limit the scope of this broad topic, here we focus on *meso*-substituted porphyrins only (Scheme 7).

A large variety of porphyrin peripheral substituents was proposed in multiple efforts of increasing the DSSC efficiency, which resulted in an impressive progress over last decade. The PCE of the latest top-performing DSSCs with the porphyrin dyes is $\sim 12\%$ and, in some cases, as high as 13% for the SM315 porphyrin (Scheme 8) [9].

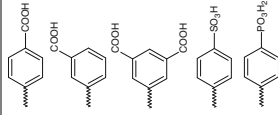
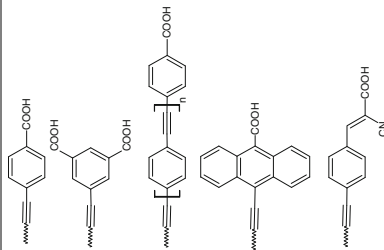
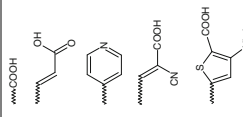
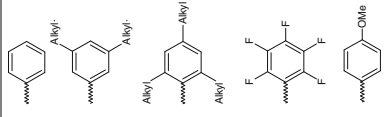
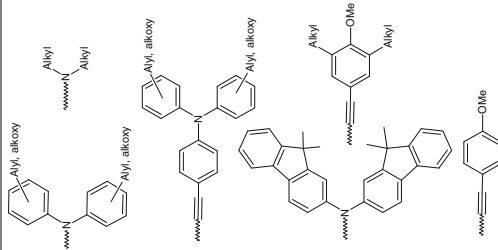
3.1.1 The Effect of Position, Nature, and Number of Porphyrin Anchoring Peripheral Substituents on Performance of a Dye-Sensitized Solar Cell

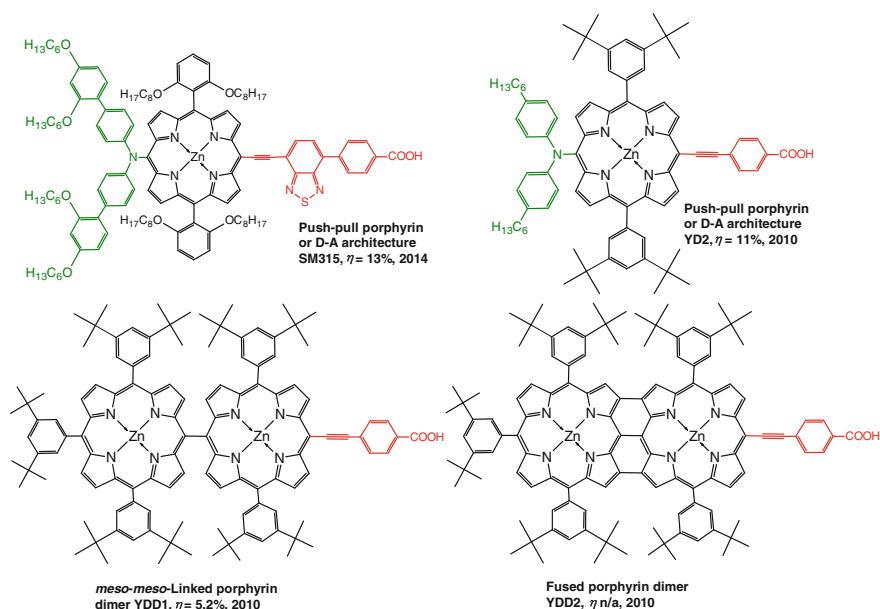
The long-lasting and efficient performance of a DSSC requires chemical binding of an MP to the TiO_2 surface with an anchoring group in at least one point [12]. There should be one or more such groups on the MP molecule. Chronologically, the first and still the most commonly used anchoring group is the carboxylic group (Scheme 9). Six major types of possible anchoring modes of this group have been identified, vis., a monodentate ester, bidentate chelating, bidentate bridging, monodentate, and bidentate hydrogen bonding, as well as a monodentate coordinating mode through a C=O group. Usually, bidentate chelating or bridging modes are the most stable [13]. Alternately, phosphate (Scheme 10) or pyridine (a in Scheme 11)



Scheme 7 Structural formulas of 4A-, 3AB-, *trans*-2A2B-, *cis*-2A2B-, and *trans*-A2BC types of *meso*-substituted porphyrins. *M* stands for a metal or H_2 , *A* is an anchoring and electron-accepting/withdrawing group, *B* and *C* are different substituents. Table 1 shows examples of the *A*, *B*, and *C* peripheral substituents

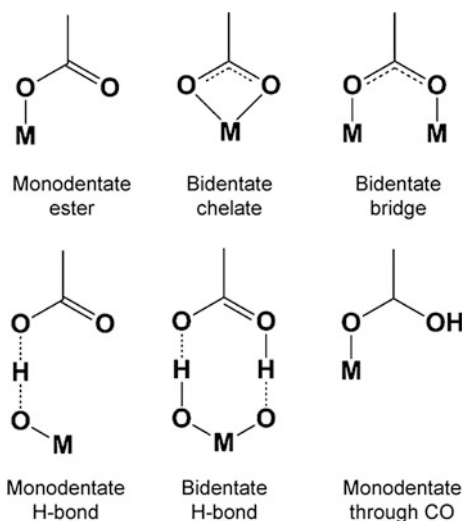
Table 1 Selected peripheral substituents of the porphyrin macrocycle, shown in Scheme 7, serving different purposes

A Anchoring group		B and/or C		
Aryl-	Ethynyl-	Other	Disaggregating/solubilizing groups	Electron-donating groups
				



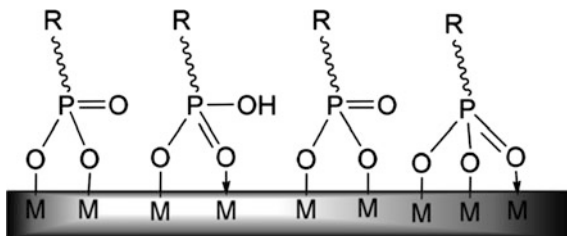
Scheme 8 Structural formulas of examples of porphyrin dyes high-performing in DSSCs along with their PCE and year of invention, vis., SM315, [9] YD-2, [10] YDD1 a *meso-meso* porphyrin dimer, and YDD2-fused porphyrin [11]

Scheme 9 Binding modes of the carboxylic group to a metal oxide ($M = \text{Ti, Zn, Al, etc.}$). Reprinted from Linkers for anchoring sensitizers to semiconductor nanoparticles, 248 (13–14), 1283–1297, Galoppini E, Coord Chem Rev, Copyright (2004), with permission from Elsevier

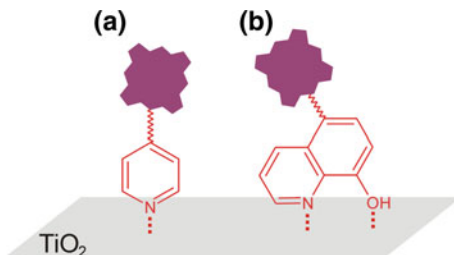


[14, 15] catechol, [16] rhodamine [17], azo-bridged salicylic acid [18], *gem*-silanediols [19], tetrazole [20], and a range of other groups [13, 21, 22] can serve that purpose. As an alternative to the carboxylic anchoring group, 8-hydroxyquinoline

Scheme 10 Binding of phosphonic acids to the MO (M = Ti, Zn, Al, etc.) surface via its Lewis and Brønsted acidic sites. Adapted from Ref. [24] with permission of The Royal Society of Chemistry



Scheme 11 Binding modes of **a** pyridyl and **b** 8-hydroxyquinoline groups to the TiO₂ surface



was proposed because it withstands acidic conditions (b in Scheme 11) [23]. The PCE of the ZnP reported, TPPZn-OQ, was nearly equal to that of the dye with carboxylic anchoring group, TPPZn-COOH, being 1.56 and 1.82 %, respectively.

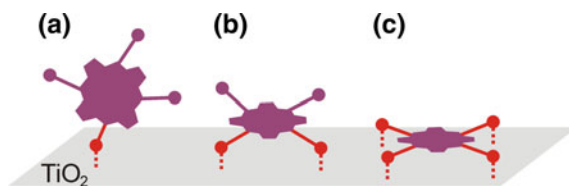
Advantageously, the anchoring groups are simultaneously withdrawing electrons from the porphyrin macrocycle, thus enhancing the electron transfer from the photoexcited dye molecule to the CB of the MO, respectively.

The carboxylic group is the far most commonly used metalloporphyrin (MO) linker because of MP binding stronger than that of alternative anchoring groups. Despite a high efficiency of the carboxylic group in dye binding to an MO, there are important reasons of searching for alternative anchoring groups. For instance, a small amount of water present in the electrolyte solution of an organic solvent results in hydrolysis and dissociation of this dye–MO binding, thus degrading long-term performance of the DSSC.

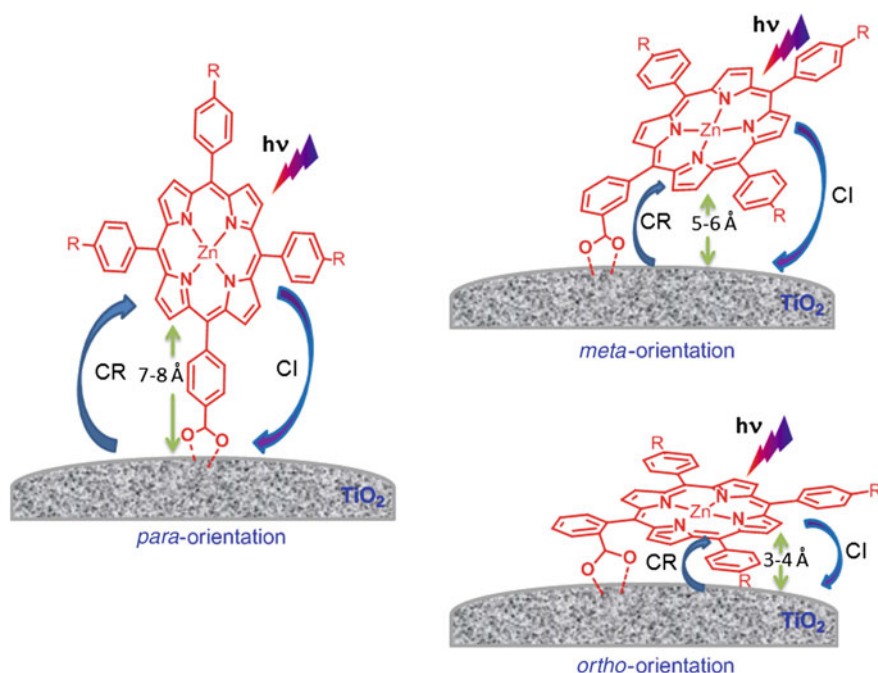
Computational studies predict that application of anchoring moieties with higher electron-accepting properties should result in DSSC performance higher than that of carboxylic-anchored MPs of the same structure [25]. This prediction found its experimental confirmation [26–28].

The position and number of anchoring carboxylic groups strongly influence the DSSC performance. This effect originates from different orientations of the MP macrocycle with respect to the MO substrate plane incurred by the nature of the MP–MO binding (Scheme 12). This position affects efficiency of the electron injection to metal oxide and the charge recombination rate.

This orientation highly influences the DSSC performance. Changing position of the carboxylic anchoring group within the carboxyphenyl anchoring moiety results in changing the tilt of the MP macrocycle with respect to the TiO₂ surface and, hence, changing efficiency of charge injection (CI) and charge recombination (CR)



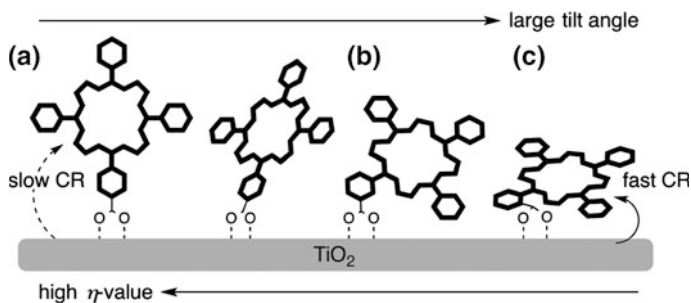
Scheme 12 The effect of the number of anchoring groups of the MP macrocycle on orientation of the MP macrocycle with respect to the TiO_2 substrate surface. **a** One, **b** two, or **c** four anchoring groups bind the MP molecule to the TiO_2 surface



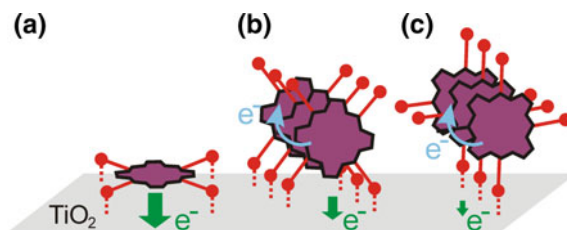
Scheme 13 The effect of the anchoring carboxylic group position on the charge injection (CI) and charge recombination (CR) and, hence, on the DSSC performance. Adapted from Ref. [28] with permission of The Royal Society of Chemistry

(Scheme 13) [28]. The DSSC performance, PCE = 4.17 %, and the MP surface concentration were the highest for the 1*m*-Zn dye with the carboxylic anchoring group in the *meta* position. The PCE was 3.13 % for the 1*p*-Zn dye with the anchoring group in the *para*-position, while the *ortho*-positioning of the anchoring group resulted in a low performance of the cell, PCE = 0.37 %.

In general, the PCE grows with the increase of the dye coverage of the TiO_2 surface (Scheme 14). At high surface density, however, porphyrins tend to form



Scheme 14 Orientation of a porphyrin molecule chemisorbed on the TiO_2 surface and its influence on the charge recombination (CR) rate. The anchoring group assumes the **a** *para*-, **b** *meta*-, and **c** *ortho*-position. Arrows indicate the direction of an increase of PCE of the DSSC and tilt angle of the macrocycle plane. Reproduced from Ref. [7] with permission of The Royal Society of Chemistry



Scheme 15 The effect of the MP- TiO_2 binding mode and surface concentration of the 4A-type porphyrin (see below) on the electron transfer. *Green* and *blue* arrows indicate direction of the electron injection to the conduction band of TiO_2 and undesired lateral electron transfer between the metalloporphyrin molecules, respectively. Adapted with permission from Rangan S, Coh S, Bartynski RA, Chitre KP, Galoppini E, Jaye C, Fischer D (2012) Energy alignment, molecular packing, and electronic pathways: zinc(II) tetraphenylporphyrin derivatives adsorbed on $\text{TiO}_2(110)$ and $\text{ZnO}(11\text{--}20)$ surfaces. *J Phys Chem C* 116(45):23921–23930. Copyright (2012) American Chemical Society

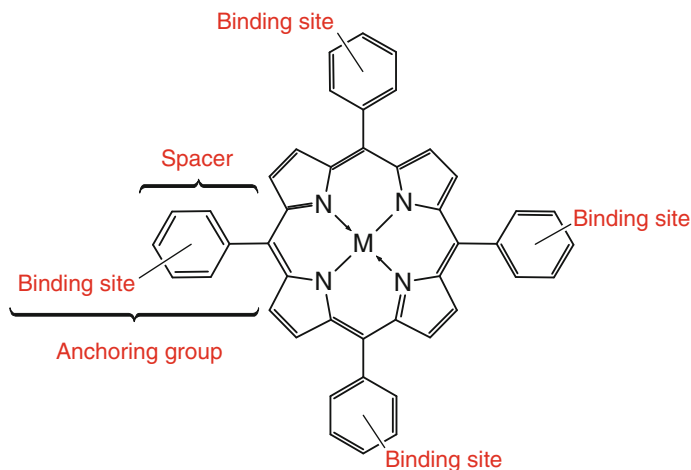
H-type aggregates. This aggregation may decrease performance of the DSSC, as discussed below. The presence of *meso*-substituted multiple binding anchor groups on the MP macrocycle allows for different tiltings of the MP macrocycle with respect to the TiO_2 surface depending on the preparation procedure, i.e., on the MP concentration in solution and the exposition time (Scheme 15). That is, peripheral groups compete for the TiO_2 surface molecules resulting in lower binding probability of all groups to the MO surface. The resulting binding mode directly influences the electron injection efficiency, charge recombination, and undesired lateral electron transfer between surface-confined MP molecules [29].

3.1.2 4A- and 3AB-Type *Meso*-Tetraphenyl Substituted Porphyrins

Symmetric with respect to the type of peripheral substituents *tetra*-substituted *meso*-porphyrins (Scheme 16) were widely used as dyes for DSSCs because of simplicity of their molecular design and synthesis according to the Lindsey or Adler-Longo procedures [30].

Properties of both free-base porphyrins and metalloporphyrins were intensively studied with respect to the nature of the central metal atom, length and nature of the extending part of anchoring groups as well as the nature of binding moieties of anchoring groups. DSSCs with Zn porphyrins are performing better than those with free-base porphyrins and other metalloporphyrins. This is because ZnPs fit well common TiO₂ (charge-mediating species) systems in terms of energy levels. This experimental observation was rationalized with the DFT calculations [31]. Moreover, designing of promising molecular architecture was attempted [32, 33]. The free-base and Zn tetrakis(carboxyphenyl)porphyrins have become reference standards for DSSCs. Consecutive steps in research aiming at enhancing efficiency of DSSCs with the 4A-type porphyrins involved relocation of the binding moiety of anchoring groups from the *ortho*- to *meta*-positions and/or increasing the number of the binding moieties on a single anchoring group. By the end of 2000, these improved dye applications to DSSCs were studied in detail and the topic is pretty much matured [34].

A more recent research on the 4A-type porphyrins focuses on investigation in detail the electron transfer between the MP dye and the TiO₂ semiconductor caused by different binding modes of the dye to the TiO₂ surface [29, 35]. In the parallel binding mode (a in Scheme 15), the dye reached unfavorably low surface coverage.



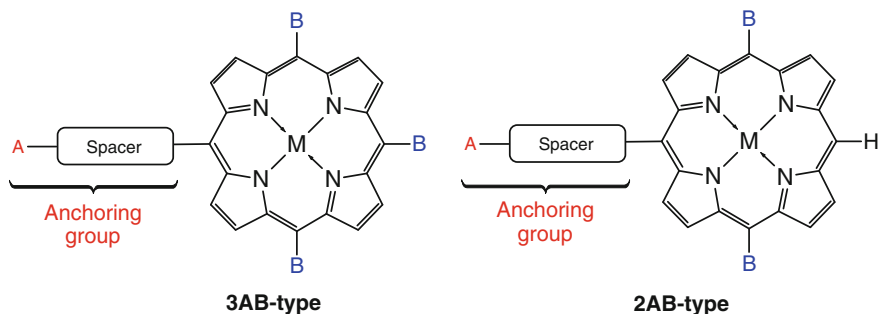
Scheme 16 General structural formula of a 4A-type tetrakis(phenyl)-*meso*-substituted porphyrin. The binding moiety of an anchoring group is $-\text{COOH}$, $-\text{SO}_3\text{H}$, $-\text{PO}_3\text{H}$, etc. $\text{M} = \text{H}_2$, Zn, or other metal. An aryl, ethylene, etc., spacer may be introduced between the anchoring group and the MP macrocycle

Advantageously, however, electron injection efficiency was high. The macrocycle-to-macrocycle planar stacking of the porphyrins on the TiO_2 surface in the edgewise binding mode resulted in a favorably higher surface coverage and, however, in a lower electron injection efficiency as well as undesired lateral electron transfer between the MP macrocycles (b and c in Scheme 15).

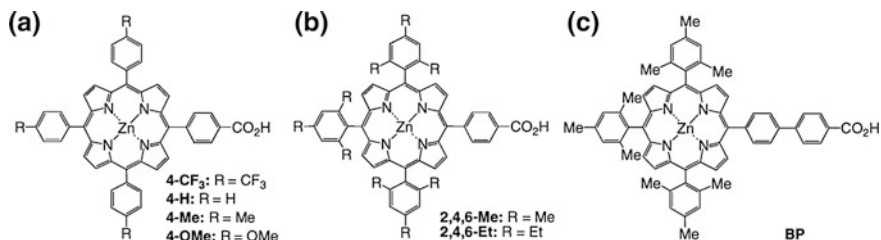
A relationship between the binding mode, orientation, and electron transfer of the 4A MPs with respect to the TiO_2 or ZnO surface was studied by both computational modeling and experimentally using several spectroscopic techniques. High MP concentration of the H-type MP aggregates on the MO surface resulted in unfavorable lateral electron transfer following the π - π stacking of MP macrocycles (green arrows in Scheme 15) [29]. However, planar binding of these macromolecules with multiple (up to four) anchoring groups resulting in lower surface concentration increased the electron injection efficiency (blue arrows in Scheme 15). Moreover, all the intermediate (between planar and vertical) binding modes and orientation, tilted with respect to the metal oxide surface forming J-type aggregates, were present at different MP surface concentrations.

3.1.3 3AB- and A3B-Type *Meso*-Tetraphenyl Substituted Porphyrins

The procedures of syntheses of the 3AB- and A3B-type MPs are the same as those of the 4A-type porphyrins. On the one hand, molecule symmetry breaking influences electronic properties of these MPs, thus allowing for the change of electron delocalization in the MP molecules. This change results in the increase of the electron injection efficiency into the TiO_2 conduction band, hence increasing the DSSC efficiency (Scheme 17). On the other hand, this symmetry breaking causes such disadvantages as complication of the synthesis as well as the separation and purification procedures.



Scheme 17 General structural formulas of the 3AB- and 2AB-type *meso*-substituted MPs. M is 2H, Zn, or other metal. A is the anchoring moiety ($-\text{COOH}$, $-\text{SO}_3\text{H}$, $-\text{PO}_3\text{H}$, or other) of an anchoring group. An aryl, ethylene, etc., spacer may be introduced between the anchoring group and the MP macrocycle. The most common B is the aryl substituent



Scheme 18 Structural formulas of carboxylated Zn porphyrins studied for unraveling the effect of conditions of MP adsorption on the TiO_2 surface on performance of the resulting DSSCs. BP stands for the best performing DSSC in this study. Adapted with permission from Imahori H, Hayashi S, Hayashi H, Oguro A, Eu S, Umeyama T, Matano Y (2009) Effects of porphyrin substituents and adsorption conditions on photovoltaic properties of porphyrin-sensitized TiO_2 cells. *J Phys Chem C* 113(42):18406–18413. Copyright (2009) American Chemical Society

An advantage of the 3AB- and 2AB-design is the possibility of introducing peripheral functional groups, different from anchoring groups, to serve for tuning the MP electronic properties, dissolving, preventing MP aggregation, and blocking undesired lateral electron transfer between surface-tethered MP molecules.

A series of *meso*-tetraphenyl ZnPs bearing substituents of different bulkiness was systematically studied (Scheme 18) [26]. The influence of conditions of MP adsorption on the TiO_2 surface on performance of the resulting DSSC was evaluated. This performance strongly depended upon the nature of the bridge linking the MP macrocycle and the TiO_2 surface, the bulkiness around the macrocycle, the nature of solvent, and time allowed for MP adsorption. In particular, the DSSC performance was high if a protic solvent (e.g., methanol) and short immersing time (0.5–1 h) were used for MP dye adsorption on TiO_2 , in sharp contrast to the Ru dye-based DSSCs. For the former, the DSSC performance was the highest for the 5-(4-carboxyphenyl)-10,15,20-tris(2,4,6-trimethylphenyl)porphyrinatozinc(II) sensitizer and methanol as the solvent with an immersing time of 1 h. Under these conditions and standard AM 1.5 sunlight illumination, the maximal incident photon-to-current efficiency was 76 %, the short-circuit photocurrent density was 9.4 mA cm^{-2} , the open-circuit voltage was 0.76 V, the fill factor was 0.64, and PCE was 4.6 %. These results provide valuable fundamental information on MP application resulting in DSSCs of higher performance (Table 2).

The effect of several parameters, including the free Gibbs energy change due to electron injection from D^* to the CB of TiO_2 , (ΔG_{inj}), the steric effect of peripheral substituents, and length of the anchoring group, on efficiency of the resulting DSSC was examined. In a series of the 4- CF_3 , 4-OMe, 4-H, and 4-Me dyes (a in Scheme 18), the increase in the electron-donating properties of substituents resulted in the increase of ΔG_{inj} in the order of -0.52 (4- CF_3) < -0.56 (4-OMe) < -0.57 (4-H) < -0.61 (4-Me) eV. PCE of the DSSC increased in the same order except of 4-H. Instead, it was 3.0, 3.5, 1.2, and 3.8 %, respectively. Aggregation of porphyrin molecules resulted in a lower PCE value for the 4-H.

Table 2 The highest performance of DSSCs achieved for A3B-type porphyrins in Ref. [26]

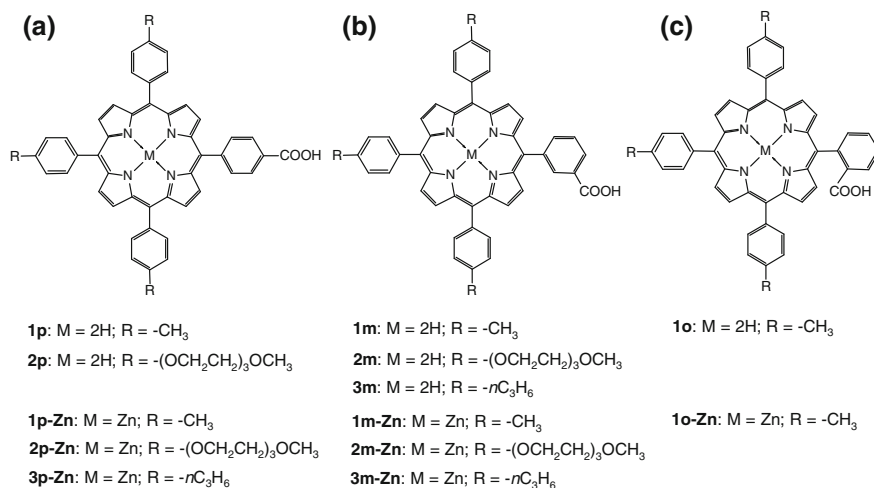
Dye	Adsorption time (h)	V_{oc} (V)	J_{sc} (mA cm ⁻²)	FF	η (%)
4-CF ₃	1	0.67	6.6	0.68	3.0
4-H	1	0.58	3.1	0.66	1.2
4-Me	0.5	0.68	8.3	0.68	3.8
4-OMe	1	0.66	8.3	0.63	3.5
2,4,6-Me	1	0.76	9.4	0.64	4.6
2,4,6-Et	0.5	0.69	8.6	0.63	3.7
BP	1	0.65	6.0	0.66	2.6

The steric effect of porphyrin *meso*-substituents on the DSSC performance was studied in the series of the 4-Me, 2,4,6-Me, and 2,4,6-Et ZnPs. That is, bulkiness of peripheral groups increased in this order. The increase of steric hindrance of ZnP macrocycles resulted in the decrease of the π - π interactions of neighboring ZnP macrocycles, that way decreasing the chance of lateral electron transfer between them. The PCE for the 2,4,6-Me ($\eta = 4.6\%$) was higher than that for the 4-Me ($\eta = 3.8\%$). However, PCE for the 2,4,6-Et ($\eta = 3.7\%$) was lower than that for the 2,4,6-Me under the same experimental conditions. This was because of lower TiO₂ surface coverage with the dye with bulkier peripheral substituents. The effect of the anchoring group length was evaluated by comparison of the PCE for the 2,4,6-Me (b in Scheme 18) and BP (c in Scheme 18) ZnPs. The only structural difference between these molecules consists in the presence of an extra phenyl ring in the anchoring group of BP. For the 2,4,6-Me ($\eta = 4.6\%$) the PCE was nearly twice that for the BP ($\eta = 2.6\%$). This result strengthened the importance of the length and electronic properties of the anchoring group.

The effect of carboxylic anchoring group position with respect to the *meso*-tetraphenyl-substituted A3B-type ZnPs on PCE of the DSSC was evaluated in the above-mentioned research (Schemes 13 and 19) [28]. Moreover, the effect of the Zn atom introduced into free-base porphyrin and the steric effect of peripheral substituents on PCE were evaluated as well.

The carboxylic group position in the peripheral phenyl substituents influences the tilt of the porphyrin macrocycle plane with respect to the TiO₂ surface (Scheme 13) and the macrocycle-to-TiO₂ distance. This distance is (7–8), (5–6), and (3–4) Å for the *para*-, *meta*-, and *ortho*-position, respectively. The lower the angle of the porphyrin macrocycle tilt with respect to the TiO₂ surface plane, the lower the surface concentration of porphyrin, i.e., 1*m*-Zn (219 nmol cm⁻²) > 1*p*-Zn (176 nmol cm⁻²) > 1*o*-Zn (132 nmol cm⁻²). The parameters determining performance of DSSCs were higher for the cells where ZnPs were used (Table 3) [28].

The charge separation and recombination rates for these dyes were determined with the femtosecond transient absorption spectral studies. The charge separation was ultrafast and similar for all three regioisomers, while the shorter time profile of the femtosecond transient absorption spectrum determined for the 1*o*-Zn indicated charge recombination faster than that for other studied MP isomers. The DSSCs

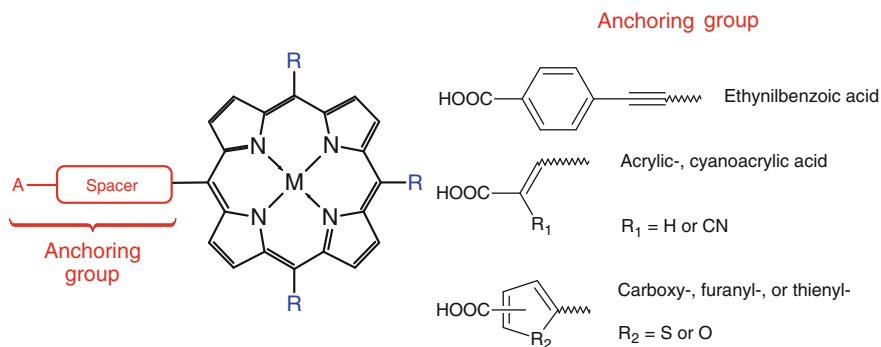


Scheme 19 Structural formulas of the A3B-type porphyrins used for examination of the effect of the position of the anchoring carboxylic group on the DSSC performance. The anchoring moiety located in the **a** *para*-, **b** *meta*-, and **c** *ortho*-position used in Ref. [28]

Table 3 The effect of the position of the anchoring carboxylic group in the A3B-type porphyrins on the DSSC performance in Ref. [28]

Dye	Γ (nmol cm ⁻²)	V_{oc} (V)	J_{sc} (mA cm ⁻²)	FF	η (%)
1p		0.45	1.26	0.75	0.42
2p		0.52	1.17	0.82	0.65
1p-Zn	176	0.59	6.67	0.79	3.13
2p-Zn		0.60	4.82	0.77	2.42
3p-Zn		0.57	4.88	0.76	2.09
1m		0.48	2.06	0.72	0.71
2m		0.55	1.61	0.74	0.65
3m		0.52	0.78	0.74	0.30
1m-Zn	219	0.65	8.42	0.82	4.17
2m-Zn		0.61	8.6	0.78	2.45
3m-Zn		0.56	8.6	0.73	1.99
1o		0.45	0.31	0.83	0.11
1o-Zn	132	0.51	1.01	0.71	0.37

with MPs with anchoring groups in the *meta*- (1m-Zn) and *para*- (1p-Zn) positions performed similarly, while the performance of cells with anchoring groups in the *ortho*-position (1o-Zn) was significantly lower. Therefore, the main factors responsible for low photovoltaic efficiency of 1o-Zn appeared the high charge recombination rate and lower as for the *meta*- and *para*-isomer surface concentration of such a ZnP [28]. Another research on the effect of length of the alkyl chain in the MP *meso*-substituents on the DSSC performance confirmed these conclusions [36].



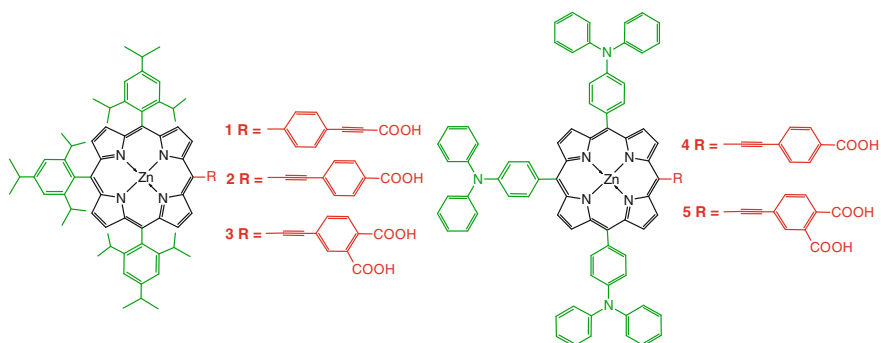
Scheme 20 Structural formulas of selected examples of different π -conjugated spacers in an anchoring group of a porphyrin ($M = H_2, Zn,$ or another metal)

One another way for increasing PCE of DSSC is to broaden wavelength range of the absorbance spectra of MPs by introducing appropriate peripheral substituents. Accordingly, introduction of a thiophene bridge into the anchoring group resulted in relatively high PCE, reaching 5.15 % for the P_{Zn} -hT dye [37].

Most of the 4A-, 3AB-, and A3B-MPs have phenyl peripheral substituents because of the ease of syntheses of these MPs. However, this molecular design has substantial disadvantage. Steric effects resulting from interactions of the *ortho*-carbon atoms of the *meso*-phenyl peripheral substituents and the β -pyrrolic carbon atoms of the porphyrin macrocycle hamper delocalization of electrons over the macrocycle and the phenyl spacer of peripheral groups. This effect limits efficiency of electron injection from the MP dye to the MO semiconductor and the electronic influence of peripheral substituents on the DSSC performance. In order to overcome this limitation, a new approach to attaching peripheral groups was proposed. In this approach, a π -conjugated spacer was introduced between the macrocycle and the anchoring group to enhance the electron transfer from an MP to a metal oxide and to broaden the absorption spectra of porphyrins (Scheme 20). Extensive computational studies were performed in order to evaluate preferential design of most promising dyes of that type [32, 33, 38, 39].

Two directions in designing π -conjugated spacers were explored: One focused on enhancing non-anchoring peripheral groups to broaden absorbance spectra of the porphyrin and the other on optimizing of anchoring groups with respect to their length and/or electron enrichment.

Examples of the former approach provide two *meso*-substituted ZnPs, i.e., those 2,4,6-triisopropylphenyl- and triphenylamine-substituted. They had different carboxyethylphenyl anchoring groups, examined with respect to their potential application in DSSCs (Scheme 21) [40]. However, these studies were limited to spectroscopic and electrochemical measurements. The HOMO–LUMO energy differences of the 2,4,6-triisopropylphenyl-substituted ZnPs appeared more promising than those of the triphenylamine-substituted for application in DSSCs.

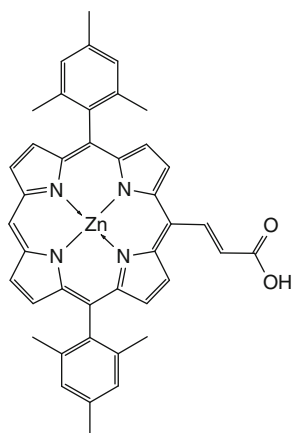


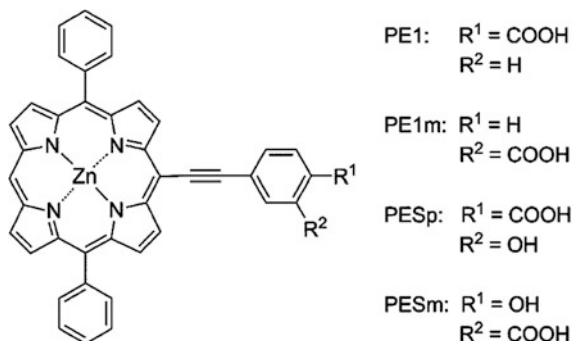
Scheme 21 The A3B *meso*-substituted ZnPs with **a** 2,4,6-triisopropylphenyl and **b** triphenylamine peripheral substituents, anchored with different carboxyethynylphenyl groups used in Ref. [40]

Examination of a large series of ZnPs with π -conjugated spacers in anchoring groups in the *meso*- or β -position were inconclusive with respect to the efficiency of the design because a co-adsorbent was used in the DSSC, which decreased aggregation and lateral electron transfer [41].

A simple design of the A2B-type ZnP with acrylic acid anchoring group, DMPZn-C₂COOH, featured quite reasonable PCE of 5.1 % (Scheme 22) [42]. Presumably, the high performance of the DSSC with this dye was because of a combination of two factors, i.e., (i) small ZnP–TiO₂ distance because the anchoring group was compact, and (ii) repulsion of peripheral methyl groups of phenyl rings in *meta*-positions resulted in disaggregating of ZnPs and blocking unfavorable electron transfers.

Scheme 22 The A2B-type ZnP with acrylic acid anchoring group, DMPZn-C₂COOH used in Ref. [42]





Scheme 23 Structural formulas of ZnPs with the ethynylbenzoic acid (PE1 and PE1m) and ethynylsalicylic acid (PESp and PESm) anchoring groups. Reprinted with permission from Gou F, Jiang X, Fang R, Jing H, Zhu Z (2014) Strategy to improve photovoltaic performance of DSSC sensitized by zinc porphyrin using salicylic acid as a tridentate anchoring group. *ACS Appl Mater Interfaces* 6(9):6697–6703. Copyright (2014) American Chemical Society

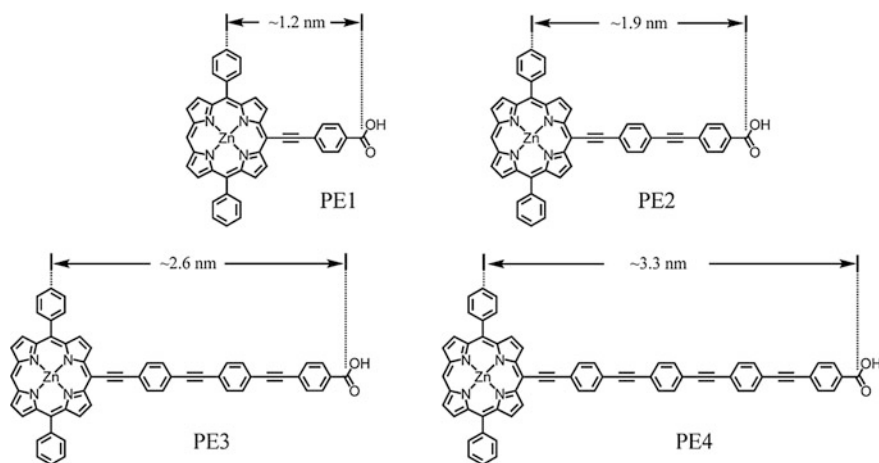
Further insight into the influence of the MP anchoring groups with an ethynyl spacer on PCE of DSSCs was gained by evaluating the advantage of tridentate anchoring via salicylic acid versus benzoic acid with *meta*- or *ortho*-location of the carboxylic group (Scheme 23) [43]. These ZnPs were very similar to those studied earlier (Scheme 19 and Table 3) [28]. Therefore, it was interesting to compare difference in PCE values incurred by introduction of π -conjugated anchoring groups. As expected, PCE values of the DSSCs using ZnPs with π -conjugated anchoring groups, especially those tridentate, were higher. Most likely, the reason of this higher PCE was the enhanced ZnP–TiO₂ electron communication and stronger attachment of the dyes to the TiO₂ surface.

It appeared that length of the phenylethynyl spacer in the anchoring groups of ZnPs affected performance of the resulting DSSCs [44]. For this study, four A2B-type porphyrins were synthesized with the number of phenylethynyl moieties ranging from one to four (Scheme 24).

Performance of DSSCs with these dyes was evaluated (Table 4) [44]. Despite the energy levels of these dyes were close one to the other and the UV–vis spectra were similar, the J_{sc} and η values of the cells were linearly decreasing with the anchoring group length from PE1 to PE4 and the IPCE for the PE4 was nearly an order of magnitude lower than that for PE1.

Absorbance of all four ZnPs was similar. Therefore, the determined decrease in the IPCE was ascribed to the decrease of the charge collection on the working electrode (η_c value) in the series of PE1 to PE4.

Theoretical study of these and similar dyes showed that efficiency of the electron injection and dye regeneration was lower the longer was the π -conjugated spacer, thus resulting in lower PCE [45]. Both computational and experimental studies confirmed the critical influence of the nature of a π -conjugated spacer on DSSC performance.



Scheme 24 Structural formulas of ZnPs with anchoring groups of different lengths involving one to four phenylethynyl chain members. Reprinted with permission from Lin C-Y, Lo C-F, Luo L, Lu H-P, Hung C-S, Diao EW-G (2009) Design and characterization of novel porphyrins with oligo (phenylethynyl) links of varied length for dye-sensitized solar cells: synthesis and optical, electrochemical, and photovoltaic investigation. *J Phys Chem C* 113(2):755–764. Copyright (2009) American Chemical Society

Table 4 The influence of the number of phenylethynyl moieties in the anchoring group (Scheme 24) on the performance of the DSSC under the AM 1.5G light irradiation

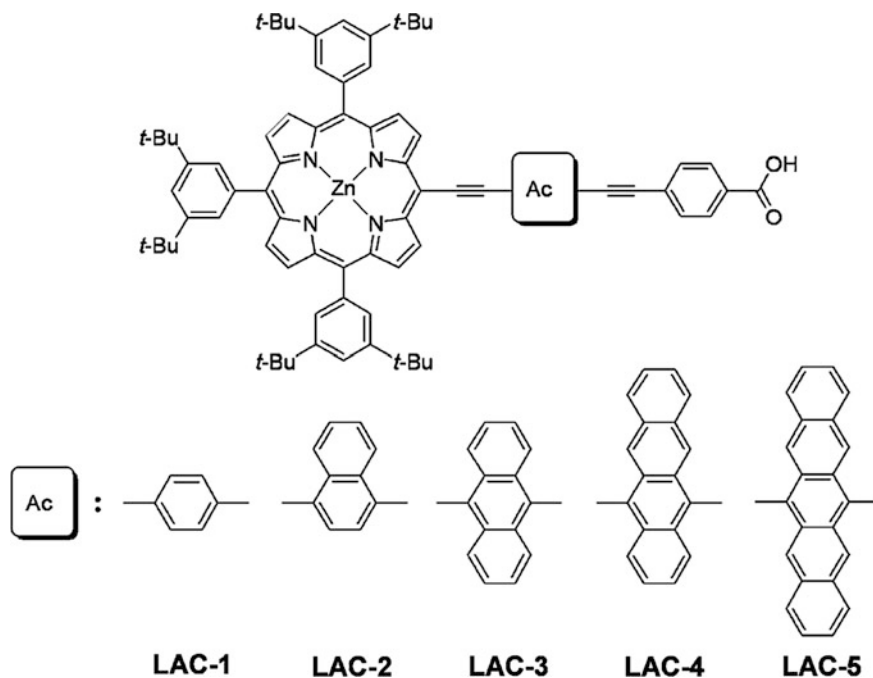
Dye	V_{oc} (V)	J_{sc} (mA cm^{-2})	FF	η (%)
PE1	0.56 ± 0.1	6.6 ± 0.7	0.67 ± 2	2.5 ± 0.2
PE2	0.57 ± 0.2	5.5 ± 0.1	0.64 ± 2	2.0 ± 0.1
PE3	0.56 ± 0.1	2.0 ± 0.3	0.70 ± 2	0.78 ± 0.09
PE4	0.51 ± 0.2	0.7 ± 0.03	0.69 ± 4	0.25 ± 0.2

Average values for three different cells [44]

In a subsequent study, a complementary strategy was developed involving a π -conjugated spacer enlarged in a lateral plane at the length of the anchor kept constant [46]. For this, acene-type spacers, vis., benzene to pentacene, LAC-1 to LAC-5, respectively, were introduced (Scheme 25).

In contrast to the previous research, the length of the anchoring group remained the same. Thus, no influence of the spacer nature on the electron injection or collection efficiency was expected. Instead, light absorbance should be increased. The increase of absorbance efficiency was postulated because of broadening the absorbance spectra in the series of LAC-1 to LAC-5, accompanied by the red shift of both the Soret and Q-bands of the porphyrins. In fact, PCE increased from LAC-1 to LAC-3 (Table 5). However, an increase of the spacer conjugation from LAC-3 to LAC-5 led to a rapid decrease of PCE almost to zero (Table 5).

The DFT computation with the B3LYP/LanL2 basis set indicated localization of the HOMO and LUMO levels on the porphyrin macrocycle for LAC-1 and LAC-2,



Scheme 25 Structural formulas of ZnPs with acene-modified π -conjugated spacer. Reprinted with permission from Lin C-Y, Wang Y-C, Hsu S-J, Lo C-F, Diao EW-G (2010) Preparation and spectral, electrochemical, and photovoltaic properties of acene-modified zinc porphyrins. *J Phys Chem C* 114(1):687–693. Copyright (2010) American Chemical Society

Table 5 The influence of the anchoring group conjugation extent on the performance of DSSC under AM 1.5G light irradiation [46]

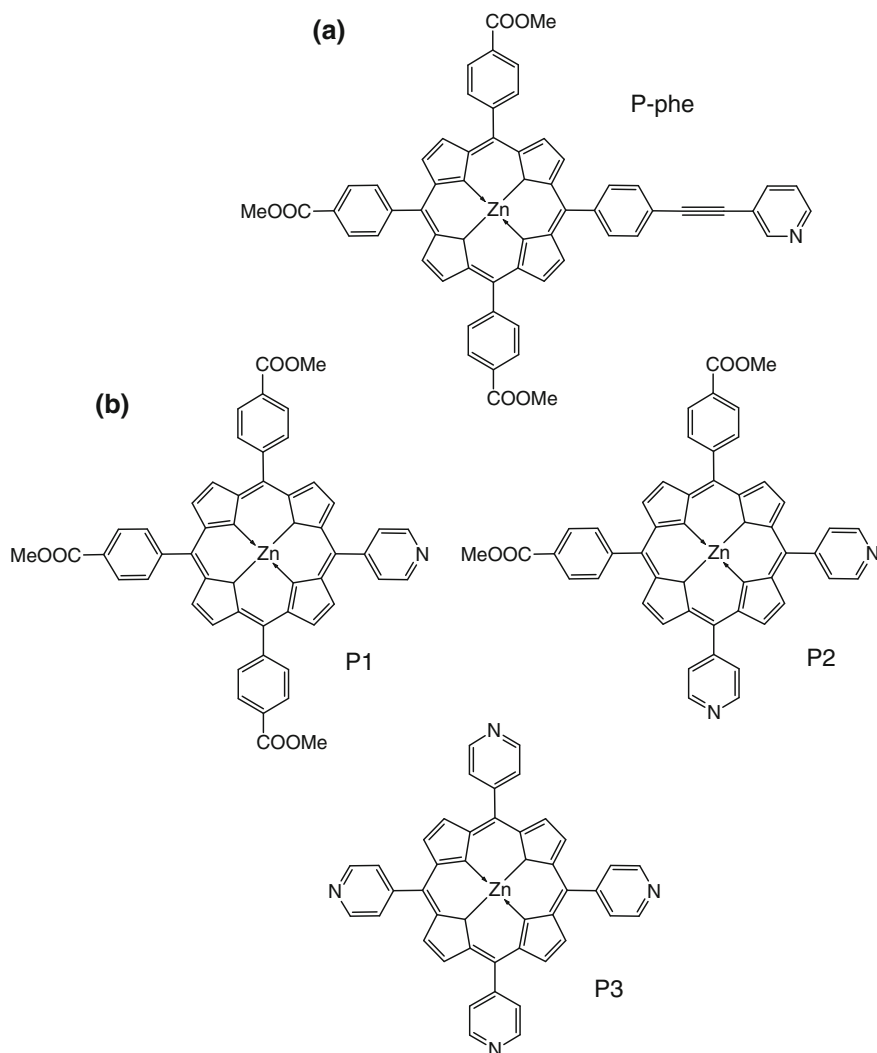
Dye	V_{oc} (V)	J_{sc} (mA cm^{-2})	FF	η (%)
LAC-1	0.67	6.13	0.72	2.95 ± 0.02
LAC-2	0.65	7.27	0.70	3.31 ± 0.06
LAC-3	0.67	12.67	0.64	5.44 ± 0.06
LAC-4	0.61	6.68	0.68	2.82 ± 0.14
LAC-5	0.49	0.33	0.62	0.10 ± 0.02

The performance under optimized conditions is shown (average values for three different cells)

strong delocalization over macrocycle and the anthracene spacer for LAC-3, and localization on the spacer for LAC-4 and LAC-5. Results of fluorescence measurement well corresponded to the computational results. Therefore, the PCE decrease in the series of LAC-3 to LAC-5 can be ascribed to intramolecular charge recombination in the dyes with the tetracene or pentacene spacers in the anchoring groups.

3.1.4 3AB-Type Porphyrins with Heteroatomic Anchoring Groups

Initially, heteroatomic anchoring groups were introduced for non-porphyrin dyes [14]. Only afterwards, these groups were introduced for porphyrins. A series of ZnPs with different numbers of anchoring groups at *meso*-positions [47] and one with the phenyl spacer in the A group [48] were synthesized and applied to DSSC (Scheme 26).



Scheme 26 Structural formulas of **a** pyridylethynyl-anchored ZnP, P-phe, and **b** a series of pyridyl-anchored P1–P3 ZnPs used in Refs. [48] and [47], respectively

Table 6 Performance of DSSCs with ZnPs anchored with a pyridyl group [47, 48]

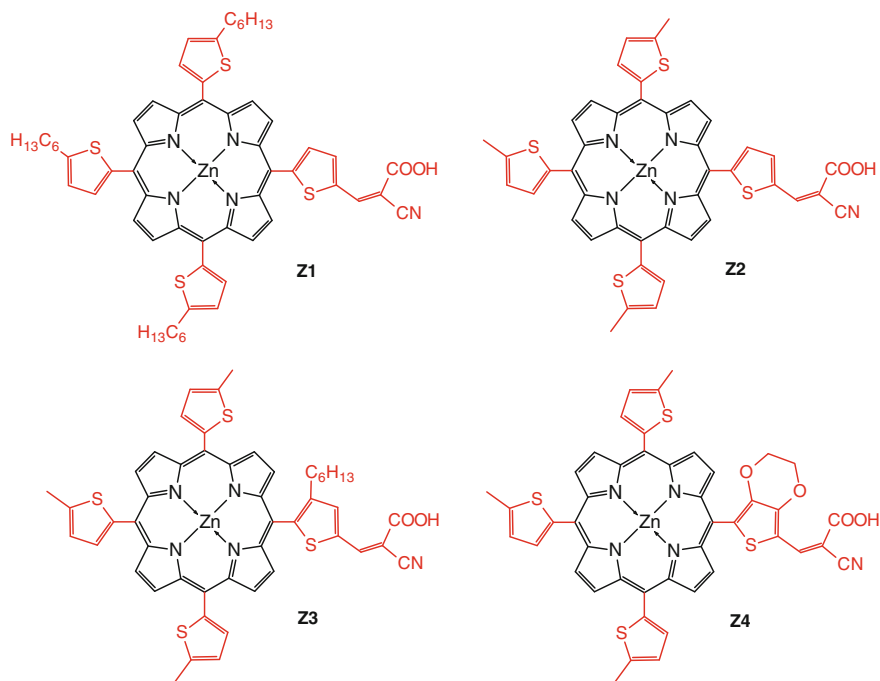
Dye	V_{oc} (V)	J_{sc} (mA cm ⁻²)	FF	η (%)	Ref.
P-phe	0.64	9.38	0.56	3.36	[48]
P1	0.60	9.2	0.56	3.10	[47]
P2	0.64	10.56	0.60	3.90	
P3	0.6	7.6	0.54	2.46	

Consecutive introduction of a co-adsorbent and then Ag nanoparticles to the DSSC with the P-phe dye allowed increasing performance of the photovoltaic cell by increasing PCE to 4.48 and 5.66 %, respectively (Table 6) [48]. Performance (Table 6) of DSSCs with the P1 to P3 dyes with different numbers and positions of anchoring group is discussed in Sect. 3.1.5, below.

Another example of the use of heteroaromatic anchoring groups involves five-member rings, including thienyl and furanyl substituents. Electronic properties of ZnPs with these substituents appeared different from those of phenyl-substituted ZnP because of two reasons. First, the presence of this relatively small-size five-member ring in the *meso*-position results in low steric hindrance and weaker interaction with β -pyrrolic atoms of porphyrin. Second, the angle between bonds is different from that with phenyl substituents. The resulting relative orientation of the porphyrin plane and the five-member ring plane is less orthogonal than for phenyl substituents. Moreover, a tilt of the five-member ring, because of the angled bonds, results in partial overlapping of π orbitals of the macrocycle and that of the anchoring group. Particularly, this electronic property difference results in a longer fluorescent lifetime, broader absorbance range, and red-shifted absorbance bands of thienyl-substituted porphyrins with respect to their phenyl-substituted analogs [49].

Toward that, 2-cyanoacrylic acid was used as the electron acceptor in studies of a series of multi-alkylthienyl appended porphyrins with anchoring moieties containing different π -conjugated spacers (Scheme 27) [50]. Electronic spectra of all Z1 to Z4 ZnPs were red-shifted and broadened with respect to those of the phenyl-substituted analogs. Introduction of thienyl groups at the *meso*-positions resulted in a significant positive shift of oxidation potentials of excited states compared to that of the reference phenyl-substituted ZnP. This shift indicated a decrease of the HOMO–LUMO energy gap. Out of the DSSCs based on four dyes Z1 to Z4, the highest PCE of 5.71 % was reached for that based on Z2 under the AM 1.5G irradiation conditions (Table 7).

Performance of the DSSC with Z1 lower than that with Z2 was because of bulkiness of the alkyl peripheral substituents of Z1 and the resulting lower surface concentration of the dye. Structures of the Z3 and Z4 differ by a spacer of the anchoring group. However, this difference has no influence on the cell performance.



Scheme 27 Structural formulas of a series of multi-alkylthienyl appended porphyrins, Z1–Z4, used in Ref. [50]

Table 7 Photovoltaic performance of DSSCs with multi-alkylthienyl appended porphyrins, Z1–Z4 (Scheme 27) [50]

Dye	V_{oc} (V)	J_{sc} (mA cm^{-2})	FF	η (%)
Z1	0.56 ± 0.1	12.13 ± 0.10	0.65 ± 1	4.44 ± 0.10
Z2	0.59 ± 0.1	14.18 ± 0.13	0.68 ± 1	5.71 ± 0.05
Z3	0.57 ± 0.1	11.37 ± 0.18	0.70 ± 1	4.54 ± 0.05
Z4	0.56 ± 0.1	11.56 ± 0.18	0.70 ± 2	4.54 ± 0.10

3.1.5 2A2B-Type Porphyrins

Porphyrins of the 2A2B type can combine advantages of both 4A- and 3AB-type porphyrins, allowing introduction of two anchoring substituents for stronger tethering the dye to the metal oxide surface. Two other substituents serve easier dissolution and disaggregation of the porphyrin as well as preventing lateral D*⁻-to-D electron transfer. There are two, *cis*- and *trans*-, isomers of 2A2B-type porphyrins. While the *cis*-isomer contributes to all above-mentioned advantages, the *trans*-isomer is not favorable for DSSCs operation. This is because of opposite position of anchoring groups. In effect, porphyrin molecule is planary orientated on the TiO₂ surface if two anchoring groups are engaged in dye surface binding or configuration of this molecule is energetically unfavorable if only one group is involved in it.

Table 8 Comparison of photovoltaic performance of the ZnPCA 3AB-type porphyrin and the ZnPCA *trans*-2A2B-type porphyrin in DSSCs in Ref. [53]

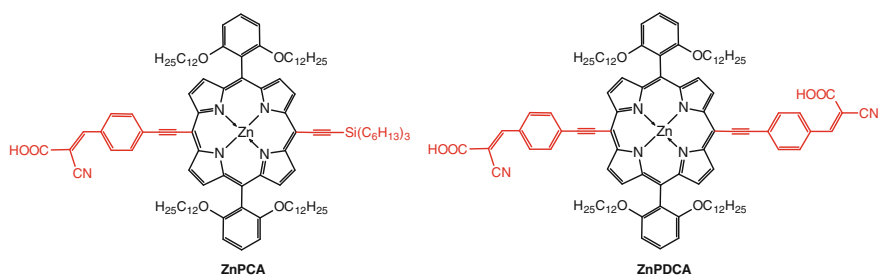
Dye	V_{oc} (V)	J_{sc} (mA cm ⁻²)	FF	η (%)
ZnPCA	0.68	7.5	0.69	3.5
ZnPDCA	0.66	11.3	0.70	5.5

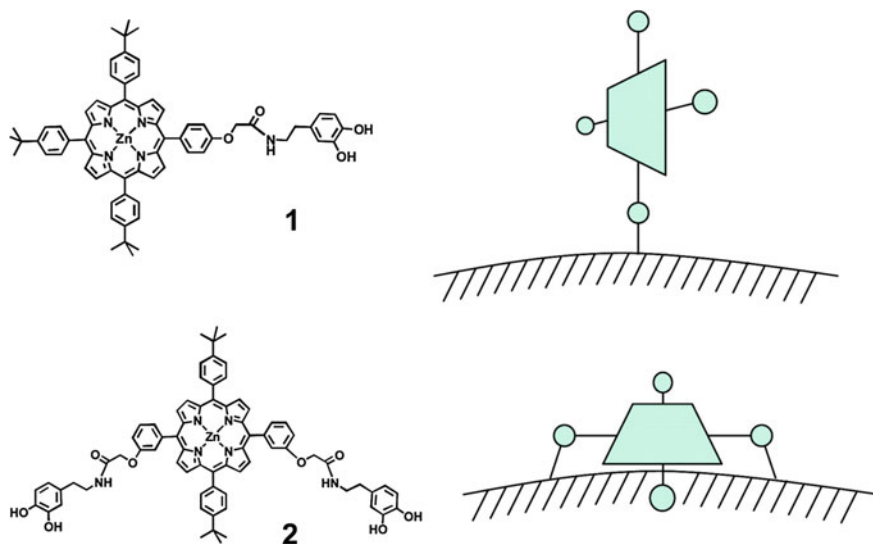
Then, the second anchoring group would decrease efficiency of electron injection into the CB of TiO₂. Synthesis of *cis*- and *trans*-2A2B-type porphyrins is typical as for porphyrins; however, yield of *cis*-isomer is low [30]. Despite progress in development of synthetic procedures selective with respect to one type of isomers, they tend to be complicated. Purification and separation of *cis*- and *trans*-2A2B-type porphyrins is time-consuming and requires the use of HPLC [51]. Complexity of synthesis and purification of these types of porphyrins made them not very popular in the DSSC research.

Properties of the 3AB- and *trans*-2A2B-type porphyrins were compared in several works [52–54]; *trans*-2A2B-type porphyrins are not very promising for DSSCs; nevertheless, significant PCE values were achieved. For instance, application of the ZnPDCA porphyrin resulted in the PCE as high as 5.5 % (Table 8) [53]. This high PCE was ascribed to efficient charge injection due to proximity of the ZnP macrocycle and TiO₂ planes (Scheme 28).

A vast 3AB- and *trans*-2A2B-type porphyrin research focused on the charge transfer in the porphyrins orientated parallel or perpendicularly with respect to an MO surface (M = Ti, Zn, or Al) (Scheme 29) [54].

Orientation of porphyrin molecules has not much influence on efficiency of the DSSCs. The PCE of the 3-AB-type porphyrin was higher than that of the *trans*-2A2B-type porphyrin and the ZnO semiconductor was superior to TiO₂. However, the PCE values of all cells were similar, and rather low, being 0.27 and 0.23 % for the cell 1 and 2, respectively (Scheme 29). This difference might originate from different surface concentrations of dyes on the MO surface. The 1:2 dye surface concentrations ratio was ~ 1.25 .

**Scheme 28** Structural formulas of the ZnPCA 3AB-type porphyrin, and the ZnPDCA *trans*-2A2B-type porphyrin used in Ref. [53]

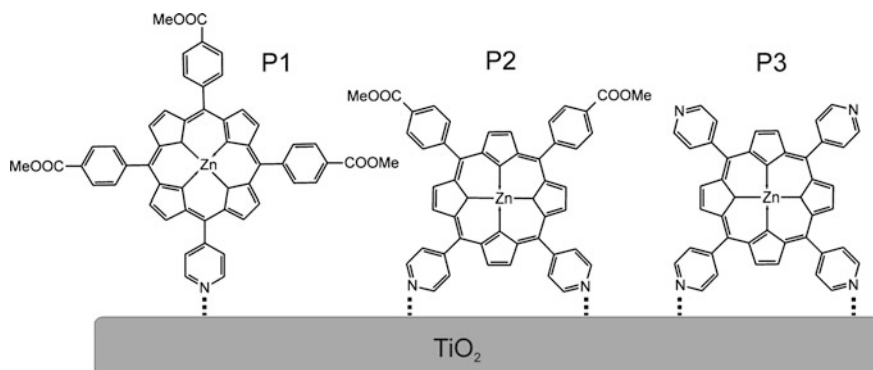


Scheme 29 Structural formulas and corresponding schematic orientations of (1) 3AB- and (2) *trans*-2A2B-type ZnPs on the MO surface (M = Ti, Zn, or Al). Adapted with permission from Werner F, Gnichwitz J-F, Marczak R, Palomares E, Peukert W, Hirsch A, Guldi DM (2010) Grafting porphyrins (face-to-edge/orthogonal versus face-to-face/parallel) to ZnO en route toward dye-sensitized solar cells. *J Phys Chem B* 114(45):14671–14678. Copyright (2010) American Chemical Society

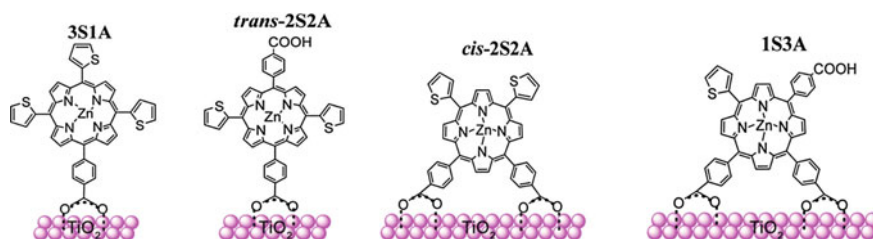
More conclusion on the influence of the type of an isomer and corresponding binding mode of MPs on the PCE of DSSC was drawn from the above-mentioned series of the pyridyl-anchored P1–P3 ZnPs (Scheme 26) [47]. Application of *cis*-2A2B-type MP in DSSC resulted in higher performance of this cell than that with the 3AB-type MP (P3 and P1 in Scheme 30, respectively, and Table 6). Unexpectedly, low surface concentration of P3 compared to that of P1 and a remarkable increase of the DSSC performance upon treating the cells with an acidic solution (or introduction of a co-adsorbent) suggested strong unfavorable coordination of peripheral pyridyl substituents with the Zn central atom of porphyrins in the ZnP deposited on the TiO₂ surface.

An extensive research comparing properties of *cis*- and *trans*-2A2B-type ZnPs as well as 3AB- and A3B-type ZnPs (one-anchor-three-thienyl and its “photo negative” three-anchor-one-thienyl group) was performed using *meso*-substituted ZnPs with the thienyl and anchoring *p*-carboxyphenyl groups (Scheme 31) [52].

Common for thienyl-substituted MPs, the more thienyl substituents were introduced into ZnP, the more red-shifted were the Soret and Q-bands, both in the absorption and emission spectra [50]. The number and position of *p*-carboxyphenyl groups strongly affected performance of DSSCs with these ZnPs. The ATR-FTIR measurements indicated a single-arm binding of 3S1A to TiO₂, and surprisingly *trans*-2S2A ZnPs. The double-arm binding, determined for 1S3A and *cis*-2S2A



Scheme 30 Surface orientation of P1 3AB-, P2 *cis*-2A2B-, and P3 4A-type Zn porphyrins used in Ref. [47]



Scheme 31 Structural formulas of a series of *meso*-substituted ZnPs appended with *p*-carboxyphenyl and thienyl substituents. Adapted with permission from Ambre R, Chen K-B, Yao C-F, Luo L, Diao EW-G, Hung C-H (2012) Effects of porphyrinic *meso*-substituents on the photovoltaic performance of dye-sensitized solar cells: number and position of *p*-carboxyphenyl and thienyl groups on zinc porphyrins. *J Phys Chem C* 2012 116(22):11907–11916. Copyright (2012) American Chemical Society

Table 9 Photovoltaic performance of DSSCs with the *cis-trans*-2A2B- and 3AB-A3B-type porphyrins [52]

Dye	Γ (nmol cm ⁻²)	V_{oc} (V)	J_{sc} (mA cm ⁻²)	FF	η (%)
1S3A	117	0.593	6.59	0.77	3.2
<i>cis</i> -2S2A	126	0.546	6.08	0.75	2.5
<i>trans</i> -2S2A	110	0.545	4.34	0.74	1.8
3S1A	83	0.455	0.907	0.48	0.2

isomers, allowed for stronger attachment of these ZnPs. An increased surface concentration of 1S3A and *cis*-2S2A was ascribed to H-type aggregation of ZnP molecules on the TiO₂ surface and, hence, denser packing. PCE of the DSSCs using these ZnPs increased in the 3S1A \ll *trans*-2S2A < *cis*-2S2A < 1S3A order (Table 9). These differences in PCE mostly originated from the difference in surface

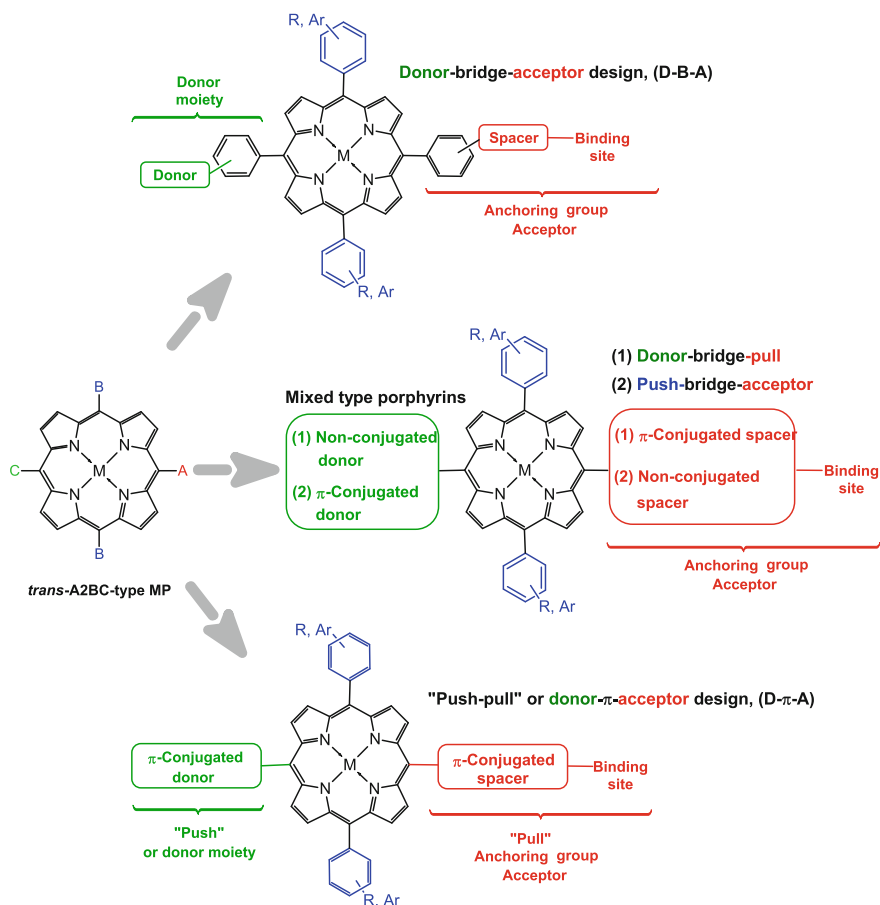
concentration of ZnPs because of different binding modes of dyes. A rapid decrease of performance for the 3S1A dye was ascribed to the peripheral thienyl substituent influence, which was believed to decrease V_{oc} .

3.1.6 *Trans*-A2BC-Type Porphyrins: Strategies for Improvement of the Porphyrin Design

The *trans*-A2BC-type porphyrins are similar to those of the 2A2B type in terms of isomerism as well as synthetic and purification complexity. However, they reveal several advantages because of more freedom of the peripheral substituent functionality. Nearly all of the A2BC-type porphyrins are *trans*-isomers; however, synthesis of the *cis*-isomer was also reported. An impressive performance of DSSCs with *trans*-A2BC-type porphyrins was reached. This was because of unique flexibility of these molecular structures, e.g., a multi-donor system with the D in an opposite position with respect to that of D resulting in common designs as the donor-bridge-acceptor (D-B-A) and donor-(π -bridged chromophore)-acceptor, (D- π -A) schemes. For clarity, the “push-pull” name is reserved for systems where the D, porphyrin macrocycle, and A moieties are electronically coupled, i.e., π orbitals of these moieties are overlapping, unlike the phenyl-bridged porphyrins. In addition, there is an intermediate scheme, where either the D or A moiety is coupled to the macrocycle. This is a “mixed type” class of porphyrins. That is, the design is “push-bridge-acceptor” if the D and the MP macrocycle are coupled, and it is the “donor-bridge-pull” if the A and the MP macrocycle are coupled. Scheme 32 presents common designs of the *trans*-A2BC-type porphyrins.

Decoupled Donor-(Bridge)-Acceptor (D-B-A) Systems

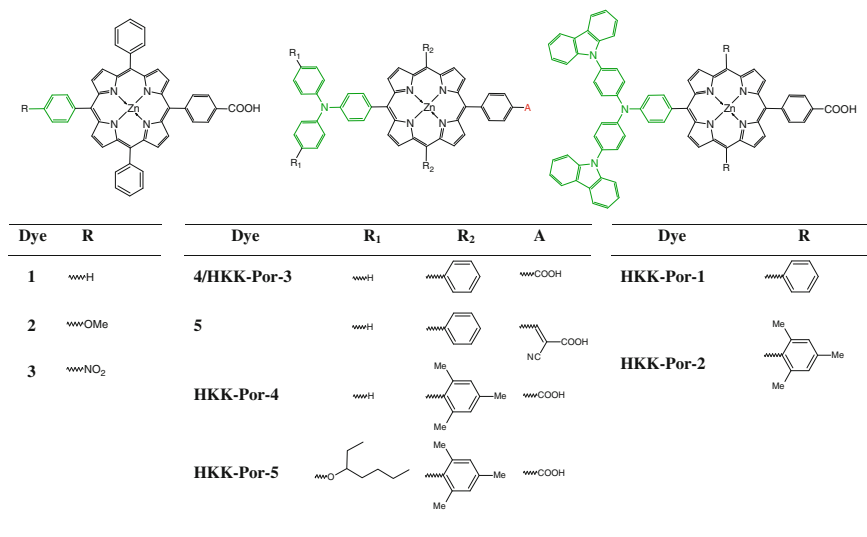
Several *trans*-A2BC porphyrins of the D-B-A fashion were proposed for DSSCs in a series of works [55–57]. First, D-B-A porphyrins with different phenyl- or phenylamino-D groups were synthesized (1–5 in Scheme 33) [55]. The DSSC performance was the highest for ZnPs with triphenylamine-based D moieties (4 and 5 in Scheme 33, Table 10) which are widely used as efficient electron donors. Application in DSSC of the porphyrin 5, with triphenylamine group, results in 3.6-fold PCE increase with respect to that of the porphyrin 1 with the phenyl group in this position (1 and 5 in Table 10). Further improvement of this ZnP design by introducing either alkoxy- or methyl-substituted phenyl groups for preventing aggregation of these porphyrins [57] and, further, by introducing an additional dye, carbazole, to the triphenylamine substituent [56] resulted in substantial increase of PCE of SCs (Table 10). Introduction of a spacious dye in the 10-*meso*-position resulted in both the decrease of unfavorable charge recombination and enhancement of light absorbance by the porphyrin while methylated phenyl groups in 5,15-*meso*-positions served disaggregation of porphyrins. The PCE of HKK-Por-1 and HKK-Por-2 dyes reached 5.01 and 4.70 %, respectively. That is, ZnPs with



Scheme 32 A common design of *trans*-A2BC-type metalloporphyrins. R is the alkyl- or alkoxy substituent and Ar the aryl substituent. The binding site is the carboxyl, pyridyl, etc., substituent

dicarbazole-triphenylamine substituent in the 10-*meso*-position resulted in remarkably higher PCE than that for ZnP with the triphenylamine group. Interestingly, photovoltaic performance of the DSSC with ZnP with methylated phenyl substituents in the 5,15-*meso*-positions was lower than that with phenyl groups. However, the difference was small. It could originate from lower surface concentration of HKK-Por-2.

Natural limitation of light energy conversion for porphyrins is their narrow absorbance bands. Porphyrins cannot absorb light in two energy-reach regions of solar spectrum, namely 450–550 (green) and 600–900 nm [red and near-infrared (NIR)]. Therefore, one of the most attractive ways of improving efficiency of porphyrin-sensitized SCs is to broaden light absorbance spectra of the porphyrins by introducing appropriate peripheral substituents in *meso*- or β -positions. Two

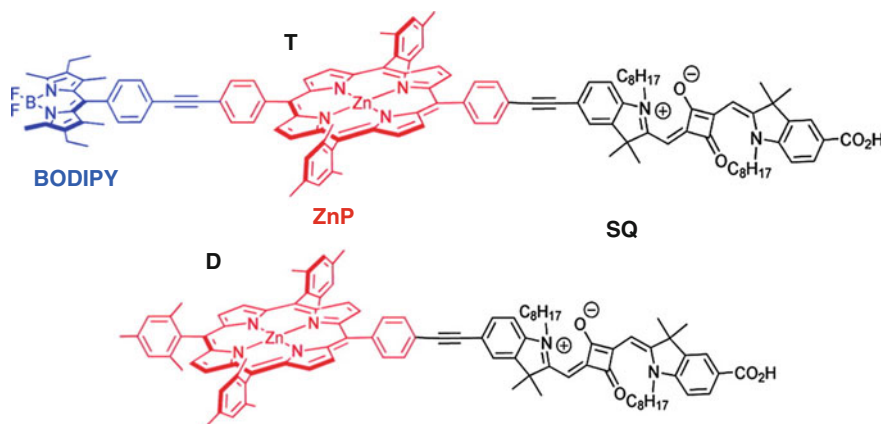


Scheme 33 General structural formulas of the *trans*-A₂BC *meso*-substituted ZnPs, the peripheral substituents R, R₁, R₂, and anchoring groups A, of D-B-A ZnPs studied in Refs. [55–57]

Table 10 Photovoltaic performance of D-B-A porphyrins shown in Scheme 33 and reported in Refs. [55–57]

Dye	V _{oc} (V)	J _{sc} (mA cm ⁻²)	FF	η (%)	Ref.
1	0.542	2.23	0.549	0.66	[55]
2	0.553	2.90	0.555	0.89	[55]
3	0.563	4.66	0.549	1.44	[55]
4 (as well HKK-Por-3)	0.605	4.95	0.508	1.52	[55]
5	0.613	7.63	0.510	2.38	[55]
HKK-Por-1	0.670	10.7	0.70	5.01	[56]
HKK-Por-2	0.640	10.9	0.68	4.70	[56]
HKK-Por-3 (as well 4)	0.590	5.38	0.66	2.09	[57]
HKK-Por-4	0.540	7.57	0.67	2.74	[57]
HKK-Por-5	0.570	9.04	0.66	3.36	[57]

efficient dyes were introduced into opposite *meso*-positions of the ZnP in order to explore this idea, namely, boradiaindacene (BODYPY) and squaraine (SQ), to result in trichromophoric dye (Scheme 34) [58]. In this molecule, the ZnP moiety absorbs light in the ranges of ~400–450 and 550–600 nm while the BODYPY and SQ moiety at ~500 and ~600–700 nm, respectively. Apparently, such conjugations largely enrich the absorption spectrum of the resulting multichromatic dye [59].



Scheme 34 Structural formula of trichromatic dye T and dichromatic dye D as well as their boradiazaindacene (BODIPY), ZnP, and squaraine (SQ) moieties. Adapted with permission from Warnan J, Buchet F, Pellegrin Y, Blart E, Odobel F (2011) Panchromatic trichromophoric sensitizer for dye-sensitized solar cells using antenna effect. *Org Lett* 13(15):3944–3947. Copyright (2011) American Chemical Society

Table 11 Photovoltaic performance of monochromatic, dichromatic, and trichromatic dyes studied in Ref. [58]

Dye	V_{oc} (V)	J_{sc} (mA cm^{-2})	FF	η (%)
SQI	0.615	6.6	0.73	3.0
D	0.635	8.0	0.72	3.6
T	0.625	8.7	0.71	3.9

The energies of the excitation and absorption spectra of the T dye components are complementary resulting in the 98 % intramolecular charge transfer efficiency from any component to the SQ moiety. The latter operated as both the light-harvesting and electron-withdrawing moiety. The use in DSSC of the dye T resulted in performance of DSSC superior with respect to that of the dye D and single squaraine dye SQ (Table 11).

Mixed-Type Donor-Bridge-Acceptor Systems Bearing Coupled with Metalloporphyrin Donor or Acceptor Moiety: “Push-Bridge-Acceptor” and “Donor-Bridge-Pull” Systems

Further increase of the DSSC performance required more efficient electron communication between the MP macrocycle and the D moiety in the 10-*meso*-position of the macrocycle. Introduction of the D moiety coupled with the porphyrin macrocycle allowed improving photovoltaic performance of dyes with respect to that of the D-B-A design (Table 12) [60–62]. Removal of the phenyl substituent

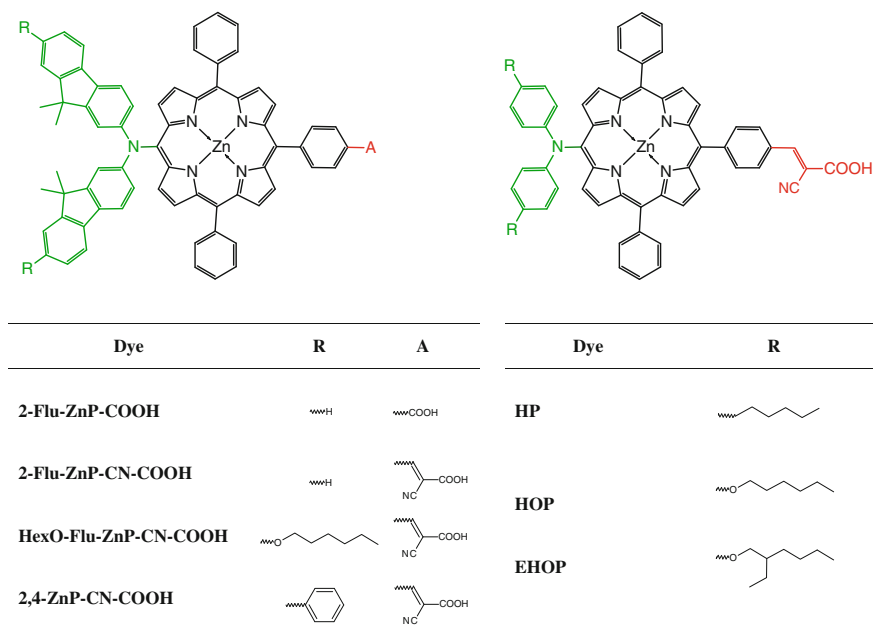
Table 12 Photovoltaic performance of D-B-A porphyrins shown in Scheme 35 and reported in Refs. [60–62] without co-adsorbents

Dye	V_{oc} (V)	J_{sc} (mA cm ⁻²)	FF	η (%)	Ref.
2-Flu-ZnP-COOH	0.558	7.31	0.77	3.16	[60]
2-Flu-ZnP-CN-COOH	0.579	10.0	0.75	4.37	[60]
HexO-Flu-ZnP-CN-COOH	0.602	10.4	0.73	4.53	[62]
2,4-ZnP-CN-COOH	0.629	10.9	0.71	4.88	[62]
HP	0.546	4.9	0.743	2.00	[61]
HOP	0.617	11.8	0.651	4.70	[61]
EHOP	0.548	9.6	0.689	3.60	[61]

present between the nitrogen atom of the triphenylamine moiety and the porphyrin macrocycle allowed more efficient electron transferring from the diphenylamine donor moiety to the ZnP. This structural change resulted in the PCE increase to 4.37 %. Moreover, PCE exceeded 7 % if a co-adsorbent for the 2-Flu-ZnP-CN-COOH was used (Scheme 35). This co-adsorbent effect prompted to interpret this behavior as if peripheral phenyl substituents in the 5- and 15-*meso*-positions did not prevent lateral electron transfer and porphyrin aggregation. Therefore, this series of porphyrins was enriched with those alkyl chain terminated [61]. Termination of the D moiety with the alkyl substituent resulted in PCE of DSSC with the DSSC higher than that of the former, being 4.7 and 4.37 %, respectively. Application of other co-adsorbent effectively increased PCE of DSSCs with these dyes even to 7.6 %. Further development of the strategy exploiting the use of ZnP with a co-adsorbent resulted in PCE of DSSC as high as 8.41 % [62].

Other studies confirmed the assumption on higher performance of DSSCs with porphyrins in the presence of a co-adsorbent [60–62]. For this purpose, a series of A3B-, A2BC, and *cis*-2A2B-type ZnPs, bearing single or double diarylamine substituents in the 10-*meso*-, 5,15-*meso*-, or 5,10-*meso*-position, respectively, was studied. Structure of the mono-ZnP dye [63] is similar to that of the HP [61] or 2-Flu-ZnP-COOH [60] dye. However, the mono-ZnP has trimethyl-substituted phenyl groups in 5,15-*meso*-positions. The presence of bulkier substituents resulted in disaggregation of ZnP molecules on the TiO₂ surface and higher PCE of the resulting DSSC. For instance, it was 6.5 % for mono-ZnP versus 2.00 and 3.16 % for the HP and 2-Flu-ZnP-COOH, respectively.

Interestingly, PCE of the DSSC with mono-ZnP and *trans*-ZnP of the same *trans*-A2BC-type porphyrins with one and two diarylamine peripheral substituents, respectively, was substantially different, being 6.5 and 3.8 %, respectively [63]. Several reasons accounted for this difference including lower efficiency of electron injection to CB of TiO₂ and lower surface concentration of *trans*-ZnP, despite of light-harvesting efficiency higher for the higher number of diarylamine substituents. That is, adsorbed photon-to-current conversion efficiency (APCE) for the mono-ZnP was higher than that for its analogs [63].

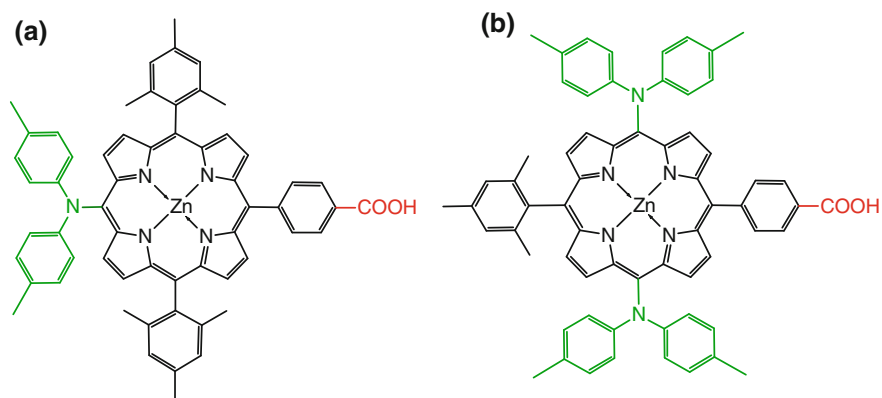


Scheme 35 General structural formulas of *trans*-A2BC *meso*-substituted ZnPs, the peripheral substituents, and anchoring groups of “push-bridge-acceptor” (P-B-A) ZnPs studied in Refs. [60–62]

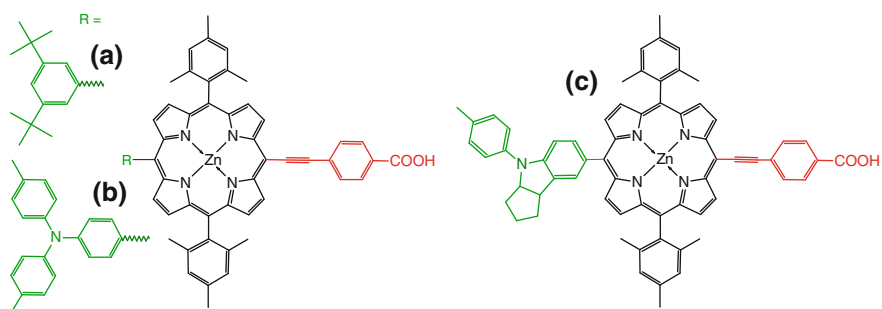
There are fewer examples of the opposite approach to the PCE increase of porphyrin-sensitized SCs. These include the use of the donor-bridge-pull (D-B-P) design where the acceptor moiety has a π -conjugated spacer (Scheme 32).

The PCE of DSSCs with phenyl-, diphenylamine-, and triphenylamine-substituted ZnPs with ethynyl carboxyphenyl anchoring group, YD0 to YD8, was evaluated [64]. The YD6 porphyrin was of the D-B-P design, while the other used more advanced “push–pull” porphyrin architecture (discussed below). PCE of the DSSC with the YD6 (b in Scheme 37) bearing triphenylamine D moiety in 10-*meso*-position was remarkably high, reaching 5.13 % [64]. However, this value was lower than that for its “turned inside out” analog (Scheme 36), “push-B-A” mono-ZnP (6.5 %) [63]. Nevertheless, PCE of the DSSC with the YD6 was higher than that of the YD0 ($\eta = 4.34$ %), bearing phenyl group in the 10-*meso*-position (a in Scheme 37) [64].

Another ZnP of the D-B-P design, namely VC-70, similar to YD6 but with a different D moiety performed in DSSC slightly better (c in Scheme 37) [65]. The indoline-based D moiety led to 5.59 % PCE of the cell (Table 13). Interestingly, PCE of the VC-70 sensitized SC substantially increased upon 90 min operation



Scheme 36 The **a** mono-ZnP and **b** *trans*-ZnP, both of *trans*-A2BC type used in Ref. [63]

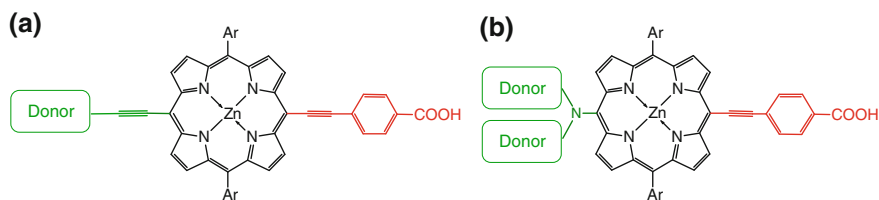


Scheme 37 The A2BC-type donor-bridge-pull design of ZnPs. **a** YD0 benchmark, **b** YD6 [64], **c** VC-70 porphyrin [65]

Table 13 Photovoltaic performance of D-B-pull porphyrins shown in Scheme 37 and reported in Refs. [64, 65]

Dye	V_{oc} (V)	J_{sc} (mA cm^{-2})	FF	η (%)	Ref.
YD0	0.675	9.45	0.68	4.34	[64]
YD6	0.708	10.81	0.67	5.13	[64]
VC-70, 0 min illumination time	0.674	12.20	0.67	5.59	[65]
VC-70, 90 min illumination time	0.699	14.47	0.72	7.31	[65]

under AM 1.5G illumination reaching PCE of 7.31 %. This performance increase under illumination was ascribed to migration of the electrolyte ions toward the TiO_2 surface and a resulting shift of CB of TiO_2 [65]. This effect was observed and discussed in other studies as well [66, 67].



Scheme 38 General structural formula of push–pull ZnPs with the **a** ethyne- and **b** amino-linked donors and the ethyne-carboxyphenyl linked anchor acceptor

Trans-A2BC-Type Porphyrin π -Conjugated with Both Donor and Acceptor Moieties: “Push–Pull” Porphyrins

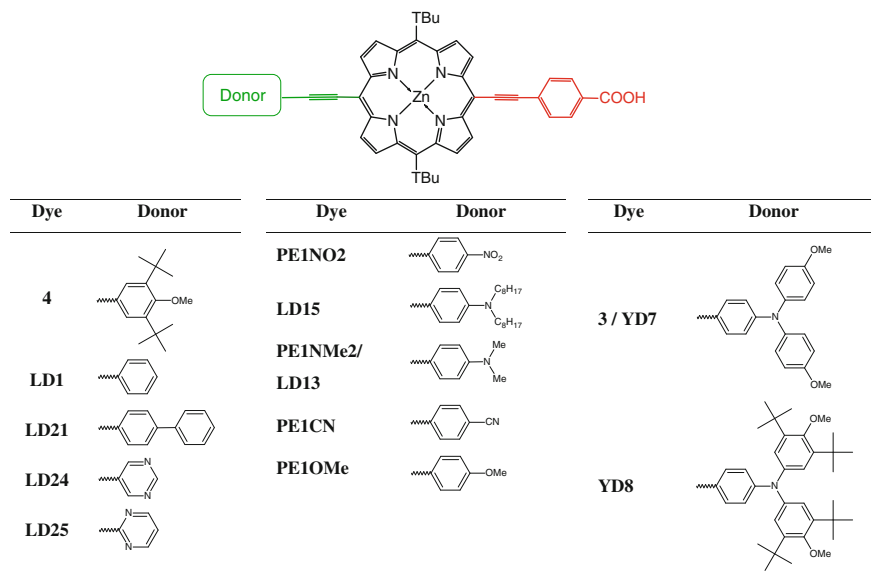
Porphyrins π -conjugated with both D and A moieties are so-called “push–pull” porphyrins. The *trans*-A2BC type of these MPs is on the cutting edge of the MP dye design for DSSCs. Typical modern high-performing MP of this design has ethyne- or amino-linked D and A moieties (Scheme 38), ethynyl carboxyphenyl anchoring group, and side bulky groups, such as alkylaryl. This design was proposed in 2009 [41], and as a result of consecutive progress, PCE of DSSCs with that type of porphyrins reached a relatively high performance.

The 3,5-di-*tert*butylphenyl substituent of the MP macrocycle is known for effective disaggregation of MPs on the MO surface. Since 2009, intensive studies have been performed on a series of *trans*-A2BC MPs with this substituent in the 5,15-*meso*-positions of the macrocycle with aryl- (Scheme 39), diphenylamine-, or triphenylamine-based (Scheme 40) or other 10-*meso*-substituents [10, 68–75].

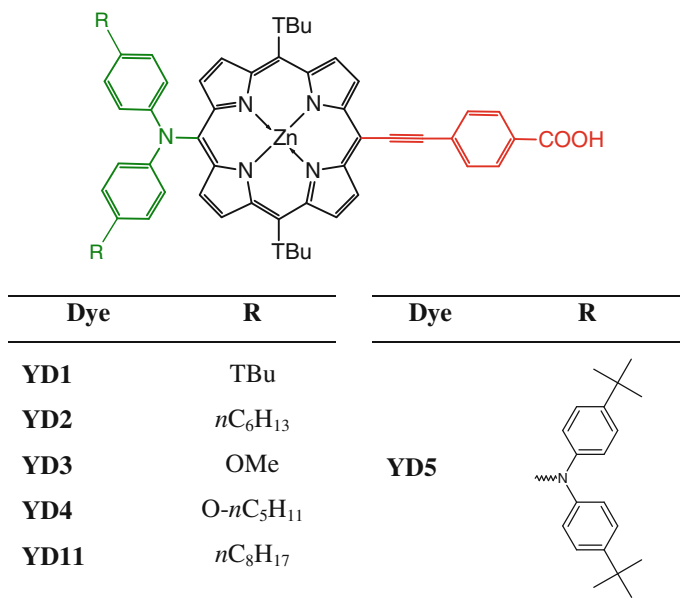
Admittedly, the presence of electron-withdrawing groups in the D moiety of the MP, such as NO₂, results in a rapid decrease of the performance of DSSCs with such a dye (PE1NO₂ in Table 14), while the presence of even simple donors results in an appreciable performance of DSSCs with MPs of the “push–pull” design (LD1 in Table 14). Application of MPs with an aryl group bearing long aliphatic chains resulted in a remarkably high PCE of DSSCs. That is, the PCE for the LD15 porphyrin (Scheme 39) reached $\sim 9\%$ (LD15 in Table 14) [72]. A series of MPs with a diphenylamine-based donor moiety (Scheme 40) performed comparably to Ru dyes in DSSCs (the YD series of MPs in Table 14). This behavior arose from overlapping of π orbitals of the donor moiety and MP macrocycle resulting in effective delocalization of electrons. Moreover, as efficient electron donors, diphenylamine derivatives allowed electron delocalizing over the entire MP macrocycle.

Consecutive cell optimization led to improvement of DSSCs with the YD2 porphyrin from PCE of 6.56 to 10.9%. These optimizations aimed at tuning thickness of the TiO₂ layer, selecting solvents for deposition of the dye, or applying co-adsorbent [10, 73–75].

Following successful “push–pull” porphyrin design for application in DSSCs, a study focused on enhancement of the “pull” properties of the anchoring moiety of



Scheme 39 General structural formula of 10-*meso* aryl- and 5,15-*meso* 3,5-di-tertbutylphenyl-substituted ZnPs used in Refs. [41, 64, 68–72]. TBu stands for 3,5-di-tertbutylphenyl



Scheme 40 General structural formula of 10-*meso* diphenylamine-derivative- and 5,15-*meso* 3,5-di-tertbutylphenyl-substituted ZnPs used in Refs. [10, 41, 64, 72–75]. TBu stands for 3,5-di-tertbutylphenyl

Table 14 Photovoltaic performance of “push–pull” ZnPs shown in Schemes 39 and 40 [10, 41, 64, 68–75]

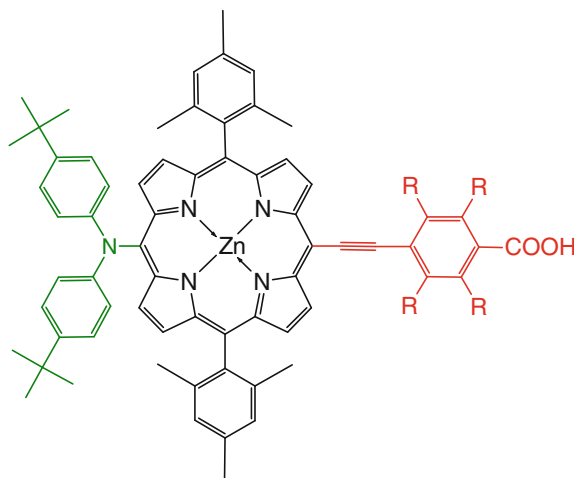
Dye	V_{oc} (V)	J_{sc} (mA cm ⁻²)	FF	η (%)	Ref.
LD1	0.660	10.56	0.733	5.11	[69]
LD21	0.682	12.92	0.717	6.30	[70]
LD24	0.644	11.78	0.708	5.40	[70]
LD25	0.624	9.07	0.727	4.10	[70]
YD7	0.650	10.05	0.670	4.38	[64]
YD8	0.651	9.94	0.660	4.27	[64]
3 (YD7)	0.546	3.76	0.672	1.40	[41]
4	0.544	3.17	0.680	1.20	[41]
PE1NMe2	0.680	13.08	0.680	6.12	[71]
PE1NO2	0.570	2.53	0.740	1.09	[71]
PE1CN	0.650	8.59	0.720	4.05	[71]
PE1OMe	0.560	10.13	0.690	4.76	[71]
LD13	0.697	18.44	0.727	9.34	[68]
LD13	0.676	17.43	0.710	8.37	[72]
LD15	0.676	17.87	0.726	8.77	[72]
LD15	0.669	18.56	0.718	8.92	[72]
YD1 ^a	0.686	12.20	0.645	5.40	[41]
YD1 ^b	0.708	13.20	0.640	6.00	[41]
YD0 ^b (benchmark)	0.675	9.45	0.680	4.34	[64]
YD1 ^b	0.710	12.73	0.680	6.15	[64]
YD2 ^b	0.710	13.40	0.690	6.56	[64]
YD3 ^b	0.713	10.85	0.690	5.34	[64]
YD4 ^b	0.711	11.68	0.680	5.65	[64]
YD5 ^b	0.651	5.05	0.640	2.10	[64]
YD11	0.714	13.43	0.690	6.62	[73]
YD11 ^b	0.721	13.17	0.690	6.55	[73]
YD2	0.660	15.40	0.620	6.36	[75]
YD2 ^{b,c}				5.6–10.9	[10]

^aYD1 was called “5” in the Ref. [41]

^bThe MP was used with the co-adsorbent, chenodeoxycholic acid, in the of 1 : 2 (mole : mole) MP: co-adsorbent ratio

^cDifferent values depending on the active layer modification procedure

these ZnPs. An enhanced electron withdrawing from the D and MP macrocycle toward the A moiety and, consequently, to the MO may increase PCE of the DSSC. According to this idea, two identical “push–pull” porphyrins with different anchoring groups were synthesized (Scheme 41) [76]. A higher performing π -conjugated D moiety in the 10-*meso*-position in both porphyrins allowed for efficient electron injecting into the ZnP macrocycle upon photoexcitation of the D moiety. The 4-carboxyphenylethynyl anchoring moiety served as the “regular” electron-withdrawing group and the 4-carboxy-2,3,5,6-tetrafluorophenylethynyl



Scheme 41 Structural formula of ZnPH (R = H) and ZnPF (R = F) porphyrins used in Ref. [76]

Table 15 Comparison of photovoltaic performance of “push–pull” ZnPs with regular (ZnPH) and enhanced (ZnPF) “electron pull” properties of the A moiety Ref. [76]

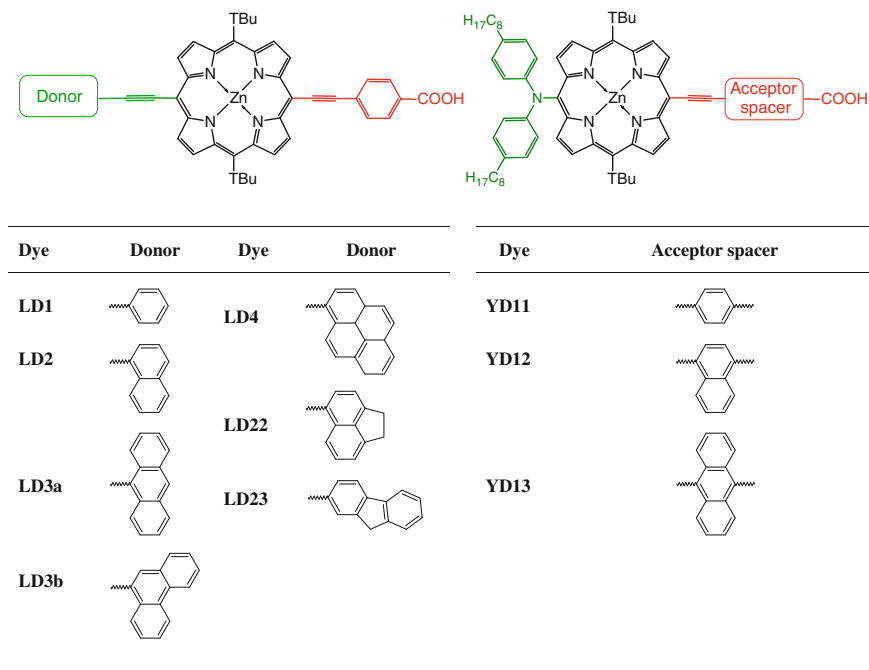
Dye	$\Gamma \times 10^{11}$ (mol cm ⁻²)	V_{oc} (V)	J_{sc} (mA cm ⁻²)	FF	η (%)	Ref.
ZnPH ^a	15	0.660	16.2	0.65	6.9	[76]
ZnPF ^a	6.2	0.650	10.6	0.66	4.6	[76]

^aCDCA co-adsorbent was used; the ZnP-to-CDCA mole ratio was 1 : 2. The DSSC preparation procedure resulting in the highest possible PCE was used

group as that with enhanced electron-accepting properties. The fluorine atoms present incurred these properties.

Surprisingly, PCE of the DSSC with the “regular” anchoring moiety, ZnPH, was higher than that of the cell using the fluorinated phenyl group, ZnPF (Table 15). Surface concentration of ZnPH was higher than that of ZnPF because of different binding modes of these ZnPs. This difference resulted from interactions of the F atoms of the anchoring group and the carboxylic group with the TiO₂ surface. The resulted lower dihedral angle of the macrocycle plane against the TiO₂ surface plane caused lower PCE of the DSSC with the ZnPF. Nevertheless, V_{oc} and FF were nearly the same for DSSCs utilizing both ZnPs (Table 15). From fluorescence measurements, it followed that the electron injection efficiency was nearly equal for both porphyrins. Hence, introduction of electron-withdrawing atoms or molecules did not enhance efficiency of electron injection to the MO conduction band.

Similar to the acene-modified anchoring moiety (Scheme 25) for π -conjugated D moieties [46], the effect of polycyclic aromatic spacer of the D or A moiety on the absorbance of ZnP dyes and the DSSC performance with these MPs were extensively studied (Scheme 42) [69, 70, 72, 77].



Scheme 42 Structural formulas of “push–pull” ZnPs with polycyclic aromatic D and spacer of A used in Refs. [69, 70, 73, 77]

Compared to porphyrins with nonconjugated D (the LAC series, Scheme 25, Table 5), the effect of π -extended spacer in the A moiety was similar, however, stronger. That is, the PCE of DSSC slightly increased from YD11 to YD12, and then the PCE rapidly dropped for the YD14 (Table 16). More promising with respect to the SC performance increase appeared to be incorporation of a π -conjugated efficient electron donor. The PCE increased with the increase of the number of conjugated phenyl rings in the D moiety starting from 5.11 % for the single phenyl group (LD1) and exceeding 10 % for the four conjugated phenyl rings (LD4).

Successful application of flexible bulky groups in the 10-*meso*-position of a porphyrin macrocycle resulted in isolating the MP macrocycle from undesired MP-to-“electron mediator in solution” electron transfer, thus prompting further development of the MP molecule design, i.e., introduction of flexible peripheral groups into 2- and 15-*meso*-positions of the macrocycle. This approach along with improvement of the electron mediator properties resulted in improvement of the performance of DSSCs. Application of Co(II)/Co(III) complexes allowed increasing V_{oc} [78–80]. Synthesis and application in DSSC of a Zn porphyrin similar to YD2 (Scheme 42), but with two 2,6-dioctyloxyphenyl groups instead of TBu, resulted in outstanding PCE of DSSC compared to that for the YD2 (Table 17). This design is called “alkoxy-wrapped” (YD2-*o*-C8 in Scheme 43) [77, 81, 82].

Table 16 Photovoltaic performance of “push–pull” porphyrins with the polycyclic aromatic D and a spacer of A

Dye	V_{oc} (V)	J_{sc} (mA cm ⁻²)	FF	η (%)	Ref.
YD11	0.715	12.99	0.710	6.56	[73]
YD12 ^a	0.714	13.77	0.680	6.69	[73]
YD13 ^a	0.618	3.97	0.720	1.76	[73]
N719 ^a (benchmark)	0.769	10.97	0.730	6.16	[73]
YD11 ^b	0.719	14.01	0.680	6.79	[73]
YD12 ^b	0.717	14.23	0.680	6.91	[73]
YD13 ^b	0.630	4.12	0.720	1.86	[73]
N719 ^b (benchmark)	0.786	13.08	0.710	7.27	[73]
LD1	0.660	10.56	0.733	5.11	[69]
LD2	0.682	15.92	0.721	7.83	[69]
LD3a	0.654	14.04	0.731	6.62	[69]
LD3b	0.678	17.02	0.716	8.26	[69]
LD4	0.711	19.63	0.721	10.06	[69]
N719 (benchmark)	–	–	–	9.27	[69]
LD22	0.689	17.26	0.681	8.1	[70]
LD23	0.685	15.51	0.700	7.4	[70]
N719 (benchmark)	0.836	14.79	0.746	9.2	[70]

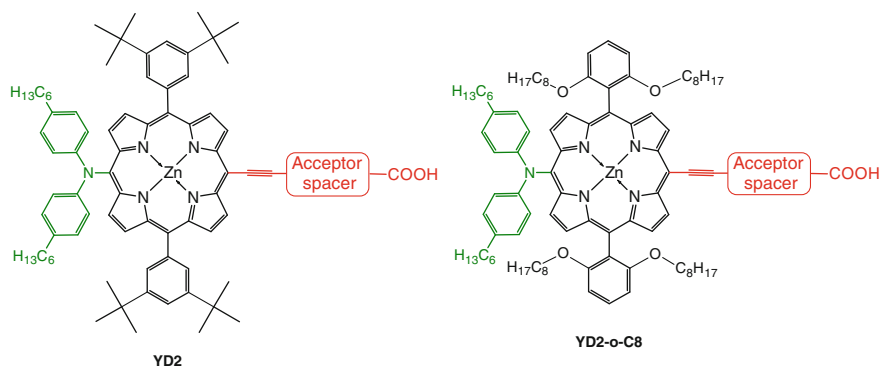
^aFilm thickness was 10 μm without scattering layer

^bFilm thickness was 10 μm ; additionally, a 4- μm scattering layer was deposited

Table 17 Comparison of the YD2 and YD2-*o*-C8 ZnPs in DSSCs with the Co-based electron mediator at different light intensities

Dye	P_{in} (mW cm ²)	V_{oc} (V)	J_{sc} (mA cm ⁻²)	FF	η (%)	Ref.
YD2	9.4	0.745	1.50	0.82	9.5	[78]
	51.3	0.805	8.00	0.76	9.5	[78]
	99.8	0.825	14.90	0.69	8.4	[78]
YD2- <i>o</i> -C8	9.4	0.875	1.70	0.77	12.5	[78]
	51.2	0.940	9.30	0.74	12.7	[78]
	99.5	0.965	17.30	0.71	11.9	[78]
YD2- <i>o</i> -C8 and Y123	9.4	0.840	1.83	0.79	13.0	[78]
	50.8	0.910	9.72	0.76	13.1	[78]
	99.5	0.935	17.66	0.74	12.3	[78]

Peripheral alkoxy groups play a dual role in this PCE increase. On the one hand, they prevent aggregation of porphyrins on the TiO₂ surface, thus preventing lateral electron transfer from the excited to non-excited ZnP. On the other hand, these groups are bulky and flexible. Therefore, they sterically hinder the Zn central atom and hamper unfavorable recombination of charge to the electron mediator. Moreover, the presence of alkoxy groups in *ortho*-positions of *meso*-substituents



Scheme 43 Structural formulas of “push–pull” zinc porphyrins with 3,5-tertbutylphenyl (YD2) and 2,6-dioctyloxyphenyl (YD2-*o*-C8) 5,15-*meso*-substituents

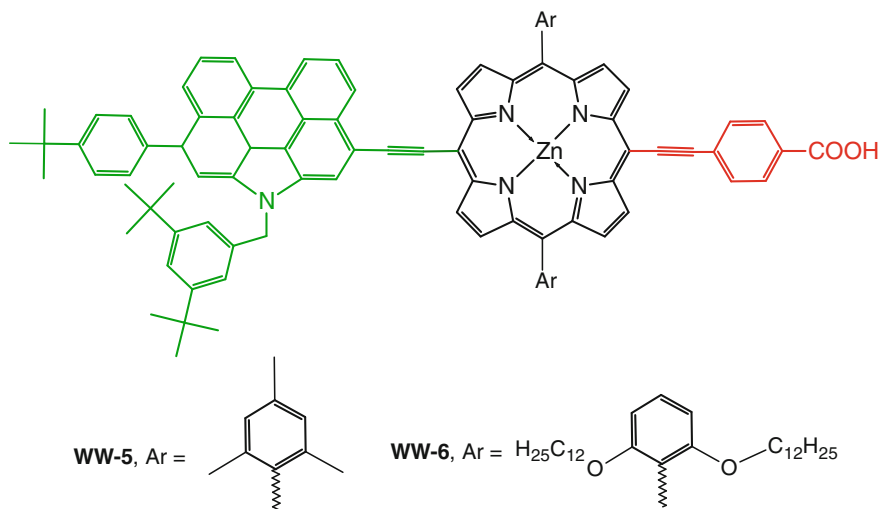
increases the substituent electron-donating properties. All these factors contribute to a higher performance of this dye design for DSSCs.

Extensive studies of the YD2-*o*-C8 ZnP revealed that the origin of high PCE of this dye comes from hampering charge recombination from the excited ZnP to the Co-based charge mediator. This mediator complex, advantageously, is bulky. Therefore, favorably, it is not entrapped in the MP layer on the TiO₂ surface.

Improvement of the YD2 and YD-*o*-C8 Zinc Porphyrin Design by Broadening Absorbance Wavelength Range for “Push–Pull” Porphyrins Through Modification of Their Donor and Acceptor Moieties

Despite initial disappointing results of attempts to broaden the absorbance wavelength range of MPs through modification of the porphyrin core by fusing porphyrins or porphyrins and other aromatic molecules [83–85], the idea of broadening the MP absorbance spectrum attracts continuous attention. So far, this idea was not much successful because of several reasons. First, large planar aromatic molecules tend to aggregate because of π – π interactions. This aggregation drastically decreases the dye performance in DSSCs. Second, this wavelength range extension for the MPs influences their HOMO–LUMO energy gaps and, particularly, decreases the LUMO energy. This effect decreases the ΔG gain because of injection of electrons from the dye molecular orbitals to the MO conduction band, thus decreasing performance of the DSSCs.

Another promising strategy to widen this spectral range, resulting in higher PCE of DSSCs, involved the use of light-harvesting antennas as peripheral substituents of the porphyrin macrocycle. A pioneer work involved synthesis of trichromatic ZnP by attaching effective dyes to the ZnP macrocycle, such as the BODIPY and SQ, at the D and A positions, respectively. However, PCE of DSSCs with those dyes did not exceed 3.9 % [58]. Progress in designing ZnP molecules for effective



Scheme 44 Structural formulas of panchromatic “push–pull” porphyrins (WW-5 and WW-6) based on the YD2-*o*-C8 molecular design and *N*-annulated perylene used in Ref. [86]

operation in DSSCs led to development of such efficient molecules as YD2 and YD-*o*-C8. The pattern of these molecules was taken as a backbone in multiple attempts of further increase of PCE of the porphyrin-sensitized SC. These involved broadening the absorbance wavelength range of MPs by taking advantage of the 5,15-*meso*-substituents. These substituents allowed simultaneous blocking the aggregation of ZnP molecules and lateral electron transfer. Adapting ZnP dyes of a complex structure, i.e., introducing complex dyes as the D and A moieties, appeared unsuccessful in increasing the DSSCs performance [58]. However, incorporating aromatic polycyclic hydrocarbon moieties in donor and/or acceptor/anchoring groups and/or thiophene derivatives as spacers of the anchoring group seemed to be more promising.

Application of the YD-*o*-C8-style design of porphyrins for broadening the absorbance spectra allowed for making a progress in efficiency of DSSCs for this type of dyes. Functionalization of ZnP with *N*-annulated perylene (NP) resulted in ZnPs of a “push–pull” type with absorbance spectra extended to the near-infrared (NIR) region (Scheme 44) [86]. Additionally, a Co(II/III)-based charge mediator was used. This modification of the porphyrin macrocycle resulted in a red shift of ca. 60–90 nm, compared to that of the YD2-*o*-C8 benchmark molecule. The resulting j_{sc} was high and the devices displayed correspondingly high PCE for the WW-5 and WW-6 dye (Table 18).

These values are close to that of the YD2-*o*-C8 cell under the same conditions. However, direct connection of the D moiety with the porphyrin macrocycle or fusing the D moiety with the macrocycle resulted in a drastic drop of the DSSC performance. That is, PCE of the WW-3 (directly connected D moiety) and WW-4

Table 18 Photovoltaic parameters of DSSCs with ZnPs modified with *N*-annulated perylene and with the Co-based electron mediator [86]

Dye	V_{oc} (V)	J_{sc} (mA cm ⁻²)	FF	η (%)
WW-3	0.744	9.81	0.767	5.6
WW-4	0.500	3.00	0.299	0.3
WW-5	0.766	18.43	0.733	10.3
WW-6	0.809	17.69	0.735	10.5
YD2- <i>o</i> -C8 (benchmark)	0.868	16.33	0.743	10.5

(fused D moiety) dye was 5.6 % and nearly zero, respectively. Inefficient π -conjugation with the directly connected D as well as the low-lying LUMO energy level and highly separated HOMO–LUMO levels of the NP-fused dye (WW-4) caused this lower PCE of DSSCs with those MPs. The higher j_{sc} of the WW-6 resulted from the absorbance spectrum broader than that of the YD2-*o*-C8 and the lower V_{oc} originating from the less-efficient electron injection from the excited donor to the TiO₂ conduction band. A lower energy of the LUMO level caused this effect. Thus, a fine-tuning of the D moiety structure to increase the LUMO level of the porphyrin dye was an effective way to improve the structure of MPs for an efficient DSSC.

A series of ZnPs with the D moiety composed of two or more ethyne-linked components resulting in DSSCs with high efficiency were developed [87, 88].

An anthracene unit was introduced as a spacer in the D moiety in order to enrich the ZnP dye with a broader absorbance wavelength range in the NIR region (Scheme 45) [88]. The DSSCs using the LD14 and LD31 dye reached PCE of 9.3 and 10.0 %, respectively, whereas an improved overall efficiency of the co-sensitized cells of LD31 and AN-4 was 10.3 % (Table 19).

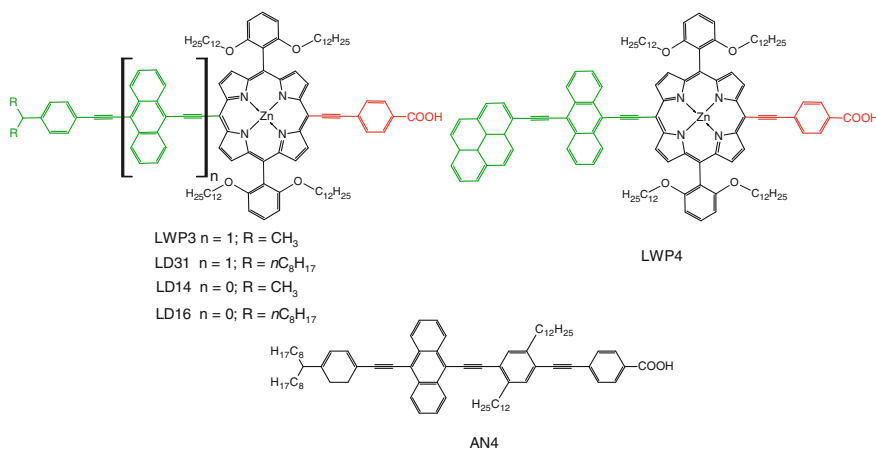
**Scheme 45** Structural formulas of “push–pull” Zn porphyrins with polycyclic aromatic D composed of ethyne-linked moieties and the AN4 co-adsorbent used in Refs. [87, 88]

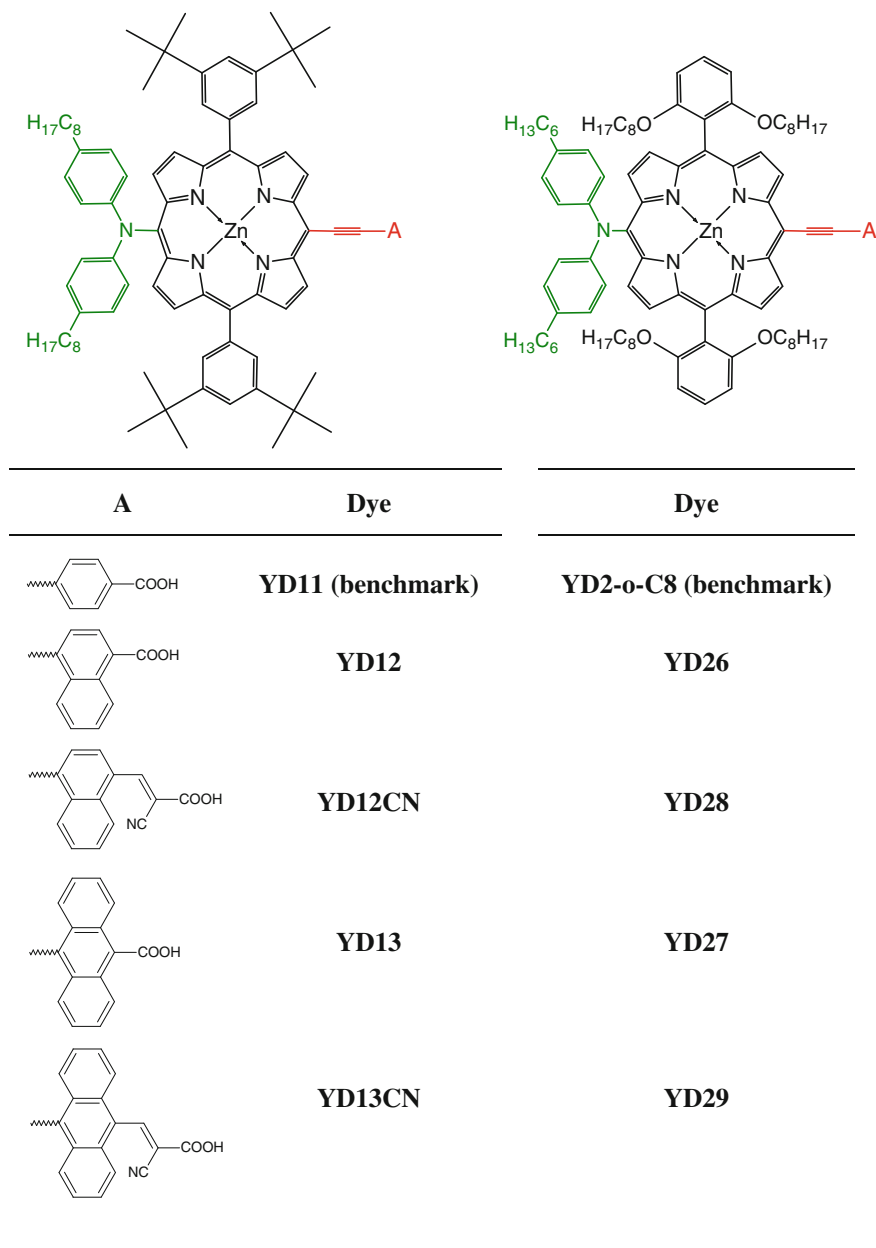
Table 19 Photovoltaic performance of DSSCs with ZnPs bearing the pyrene or 4-dimethylaminophenyl group modified D moiety

Dye	V_{oc} (V)	J_{sc} (mA cm ⁻²)	FF	η (%)	Ref.
LD31 ^a	0.699	20.02	0.711	9.95 ± 0.04	[88]
AN-4 ^a	0.692	8.85	0.726	4.44 ± 0.01	[88]
LD31 + AN-4 ^a	0.704	20.27	0.718	10.26 ± 0.07	[88]
LD14 ^a	0.738	17.50	0.723	9.34 ± 0.06	[88]
LWP3 ^a	0.720	17.76	0.74	9.51 ± 0.11	[87]
LWP4 ^a	0.680	14.20	0.69	6.70 ± 0.07	[87]
LD14 ^a	0.720	18.82	0.74	10.03 ± 0.02	[87]
N719 ^a (benchmark)	0.730	16.74	0.73	8.96 ± 0.10	[87]
LD4	0.711	19.63	0.721	10.06	[69]
LD13	0.697	18.44	0.727	9.34	[68]
LD14	0.736	19.17	0.721	10.17	[68]
LD13	0.676	17.43	0.710	8.37	[72]
LD14	0.710	20.40	0.694	10.05	[72]
LD16	0.707	20.59	0.704	10.24	[72]

^aThree independent cells were measured to obtain the average values

A series of ZnPs, LWP1-4, with the pyrene or 4-dimethylaminophenyl group was prepared (LWP3 and LWP4, respectively, in Scheme 45) [87] and their performance in DSSCs was compared with that of the previously reported ZnPs of a similar structure, i.e., LAC-3 [46], LD4, and LD14 [69]. Moreover, the anthracene spacer of the A moiety was used in addition to expansion of the D moiety to broaden the absorbance spectrum into an NIR range even more. Structure of the LWP3 and LWP4 porphyrins is similar to that previously reported. The DSSCs adopting the LWP1 dye exhibited energy conversion up to 800 nm without compromising the overall efficiency of the SC (Table 19). The DSSC with the best performing dyes of this series had comparable PCE slightly exceeding 10 %.

More attention with respect to panchromatic properties of “push–pull” ZnPs was focused on modification of the ethynyl-linked A spacer of the dyes [82, 89, 90]. “Push–pull” porphyrins with aromatic polycyclic or thiophene-derivative spacers introduced into the anchoring group with carboxylic or cyanoacrylic anchoring moieties were extensively studied (Scheme 46) taking advantage of alkoxy-wrapped or tBu-derivatized ZnP macrocycle design. Application of the cyanoacrylic anchoring group allowed for significant broadening and red shifting the ZnP absorption spectra. This effect originated from a strong electronic coupling between the porphyrin and the anchoring group due to the ethynyl linkage. However, the highest PCE for this series was for YD26 with the carboxylic acid anchor, being 8.04 %. Despite favorably broad absorbance spectra, ZnPs anchored through the cyanoacrylic group, namely YD28 and YD29, performed in DSSCs not as well as their analog anchored with the carboxylic group (Table 20). Apparently, this lower performance was because of insufficient rigidity of the cyanoacrylic acid (CAA) anchor and the resulted lower order of the dye layer, surface concentration,



Scheme 46 Structural formulas of the “push–pull” YD2 and YD2-*o*-C8-type Zn porphyrins with the modified anchoring moiety A used in Ref. [90]

Table 20 Comparison of photovoltaic performance of DSSCs sensitized with ZnPs of the YD2 and YD2-*o*-C8 type, bearing the carboxylic or cyanoacrylic anchoring group [90]

Dye	Anchoring moiety	V_{oc} (V)	J_{sc} (mA cm ⁻²)	FF	η (%)
3,5-Di-tertbutylphenyl peripheral substituents of the ZnP macrocycle					
YD12	COOH	0.713	14.06	0.721	7.23
YD12CN	CAA	0.651	8.79	0.748	4.28
YD13	COOH	0.679	5.09	0.743	2.57
YD13CN	CAA	0.632	6.03	0.752	2.86
2,6-Dioctyloxyphenyl peripheral substituents of the ZnP macrocycle					
YD26	COOH	0.745	15.37	0.702	8.04
YD28	CAA	0.696	11.30	0.737	5.80
YD27	COOH	0.720	11.59	0.723	6.03
YD29	CAA	0.673	7.17	0.755	3.64

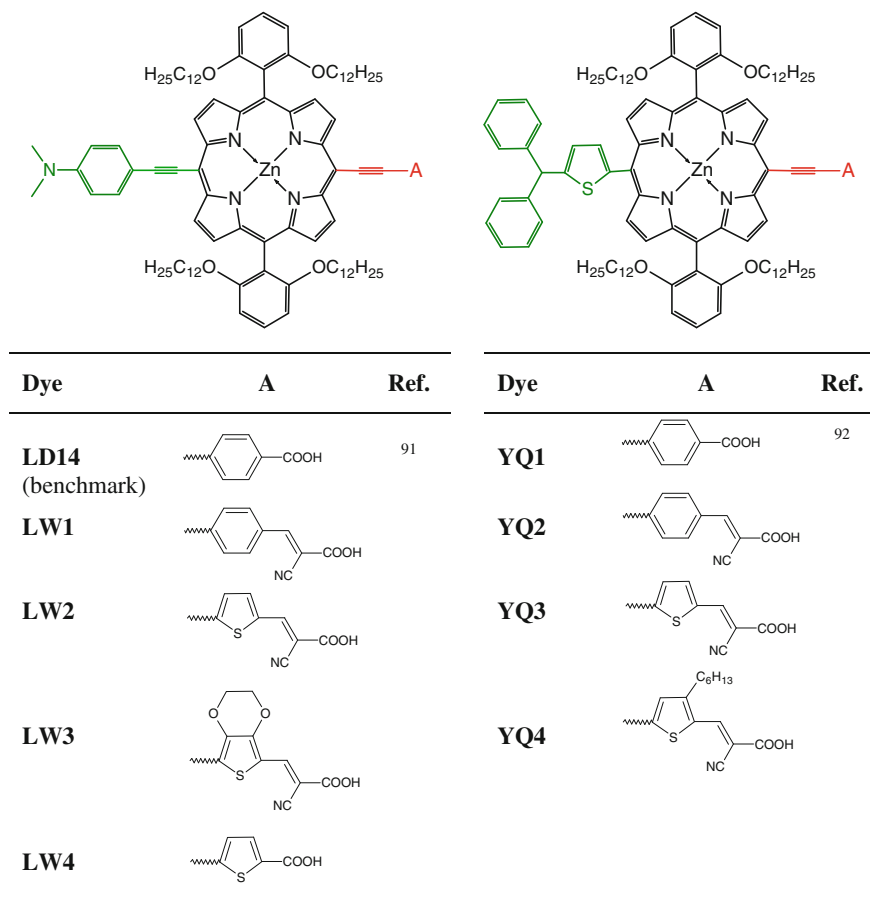
and an undesired lower tilt of ZnP molecules with respect to the TiO₂ surface plane, which caused an increase of the charge recombination rate.

Moreover, ZnPs synthesized according to alkoxy-wrapped design resulted in DSSCs of higher performance than that of those using ZnPs with TBu peripheral substituents (Table 20). Introducing a polycyclic carbon aromatic spacer, e.g., anthracene, into the anchoring moiety spacer decreased performance of the resulting DSSCs, while substitution of the phenyl spacer with the naphthalene enhanced performance of the resulting ZnPs in DSSCs.

Another research confirmed advantage of the carboxylic anchoring moiety presence in MPs over that cyanoacrylic. For this, two series of alkoxy-wrapped porphyrins with two 2,6-didodecyloxyphenyl side groups were synthesized. Ethynyl-*N,N*-dimethylaniline (LW series) [91] or 2-diphenylaminothiophene (YQ series) [92] were used as D moieties, while different anchoring groups were examined. The PCE of DSSCs was higher if the carboxylic binding site was used, while PCE of the DSSC with its analog bearing cyanoacrylic binding site was lower (LW4 and LW2 in Scheme 47 and Table 21). Remarkably, the best performing dye in the series, LW4, used the thioethynyl A spacer and the carboxylic group as the binding site. The thiophene spacer introduced some tilt (lower than 90°) of the MP plane with respect to that of the TiO₂ surface. However, this tilt did not compromise performance of the DSSC.

Modifying both D and A moieties may further broaden absorbance spectra of ZnPs toward NIR region. The 2-diphenylaminothiophene D moiety served this purpose (YQ series in Scheme 47 and Table 21) [92]. However, despite broadened absorbance spectra incurred by the D moiety, application of the cyanoacrylic binding site limited performance of DSSCs with these dyes.

Further improvement of alkoxy-wrapped design of ZnPs for superior performance led to developing of a “fully wrapped” ZnP where alkoxy chains were not only on the sides of the ZnP macrocycle, but, e.g., in 10-*meso*-position as well (Scheme 48, Table 22) [9].



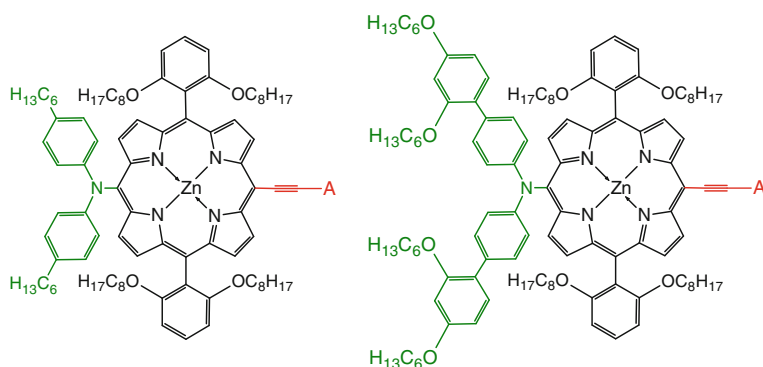
Scheme 47 Structural formulas of the “push–pull” porphyrins with the extended absorbance wavelength range into the NIR region by modification of A or D moieties used in Refs. [91, 92]

The application of such modified dyes to DSSCs with the Co(II)/Co(III) complex redox shuttle resulted in the up to now best performing cells with PCE reaching 12 and 13 % for SM371 and SM315, respectively (Table 22).

Introduction of the bis(2',4'-bis(hexyloxy)-[1,1'-biphenyl]-4-yl)amino group in the D moiety of the alkoxy-wrapped ZnP designs along with the (Co complex)-based electrolyte resulted in the highest performance of DSSCs with the SM series of dyes. The SM315 differs from SM371 by its A moiety where the benzothiadiazole spacer is used in order to broaden absorbance spectra of the dye by splitting the Soret band of the porphyrin as well as broadening and red shifting the Q-band. Broadened absorbance spectra and high electronic communication between the D, ZnP macrocycle, and A moieties resulted in higher IPCE of the DSSC with the SM315 dye. The benzothiadiazole spacer drastically influences the intramolecular

Table 21 The photovoltaic performance of DSSCs with “push–pull” porphyrins with extended absorbance wavelength range into the NIR region by modification of A or D moieties [91, 92]

Dye	V_{oc} (V)	J_{sc} (mA cm ⁻²)	FF	η (%)	Ref.
LW1	0.648	15.70	0.70	7.12	[91]
LW2	0.685	15.36	0.70	7.37	[91]
LW3	0.657	16.35	0.71	7.63	[91]
LW4	0.750	17.65	0.72	9.53	[91]
LD14 (benchmark)	0.730	17.38	0.71	9.01	[91]
YQ1	0.680	14.27	0.62	6.01	[92]
YQ2	0.630	12.51	0.54	4.23	[92]
YQ3	0.580	12.76	0.59	4.38	[92]
YQ4	0.600	13.61	0.62	5.00	[92]



A	Dye	Ref.	Dye	Ref.
	YD2-<i>o</i>-C8	78	SM371	9
	GY21	93		
	GY50	93	SM315	9

Scheme 48 The best performing dyes based on alkoxy-wrapped “push–pull” ZnPsZinc porphyrin

and dye-to-TiO₂ electron transfer increasing its rate in both directions [94]. The intensity-modulated photoinduced absorption experiment showed that the electron recombination rate of the SM315 is ~6 times faster than that of the SM371 dye. This effect results in lower V_{oc} for the SM315 compared to that of the SM371.

Table 22 The best performing dyes based on alkoxy-wrapped “push–pull” ZnPs

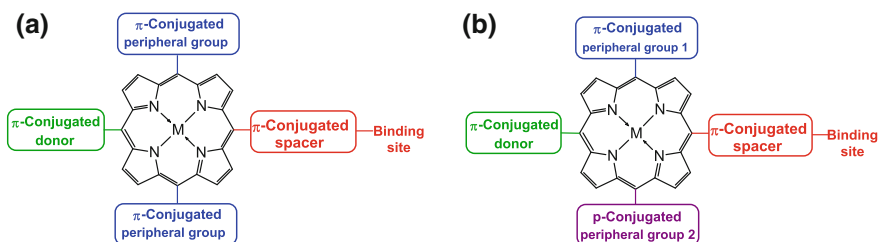
Dye	Redox shuttle	V_{oc} (V)	J_{sc} (mA cm ⁻²)	FF	η (%)	Ref.
SM315	Co(II)/Co(III)	0.910	18.10	0.780	13.0	[9]
SM371	Co(II)/Co(III)	0.960	15.90	0.790	12.0	[9]
GY21	Co(II)/Co(III)	0.615	5.03	0.798	2.52	[93]
	I ₃ ⁻ /I ⁻	0.552	11.50	0.751	4.84	[93]
GY50	Co(II)/Co(III)	0.885	18.53	0.773	12.75	[93]
	I ₃ ⁻ /I ⁻	0.732	18.45	0.657	8.90	[93]
YD2-o-C8	Co(II)/Co(III)	0.965	17.30	0.71	11.9	[78]
	I ₃ ⁻ /I ⁻	0.772	15.00	0.66	7.6	[78]
	I ₃ ⁻ /I ^{-a}	0.832	15.80	0.71	9.4	[78]

^aMeasured in different electrolytes

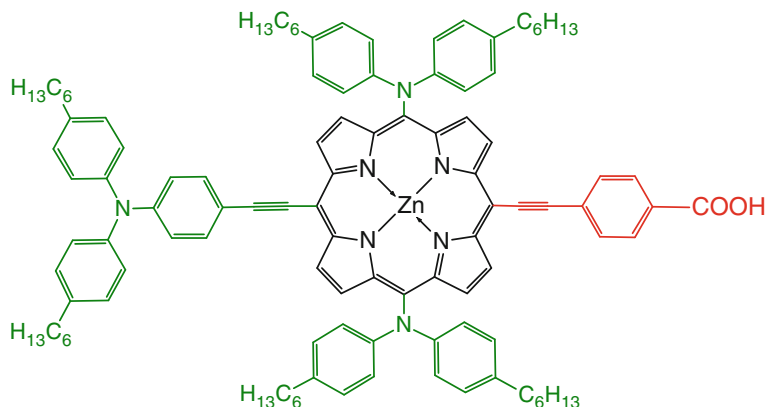
A similar idea was used in the GY dye series dyes to isolate the ZnP macrocycle with long aliphatic groups of the D moiety (Scheme 48) [93]. The influence of fine-tuning of the intramolecular charge transfer by modifying the A spacer of a ZnP is illustrated by comparison of GY21 and GY50 dyes (Table 22). That is, introduction of a terminal phenyl spacer into the A group of GY21 resulted in the pronounced increase of PCE of the DSSC (Table 22).

Fully Conjugated *Cis*-, *Trans*-A2BCD-, and ABCD-Type Porphyrins

Despite the success of the A2BCD design of MPs, systems that are even more complex were studied in an attempt to improve efficiency of DSSCs (Scheme 49). The 5,15-*meso*-positions of the MP macrocycle were used mostly for moieties serving as disaggregating or/and isolating from unfavorable charge transfer pathways rather than those electron donating. Nevertheless, potentially, introduction of additional donors into these positions can raise efficiency of light harvesting by the dye and increase performance of DSSCs with these dyes. There are early examples of fully conjugated MPs, e.g., YD15 (Scheme 50) [74].



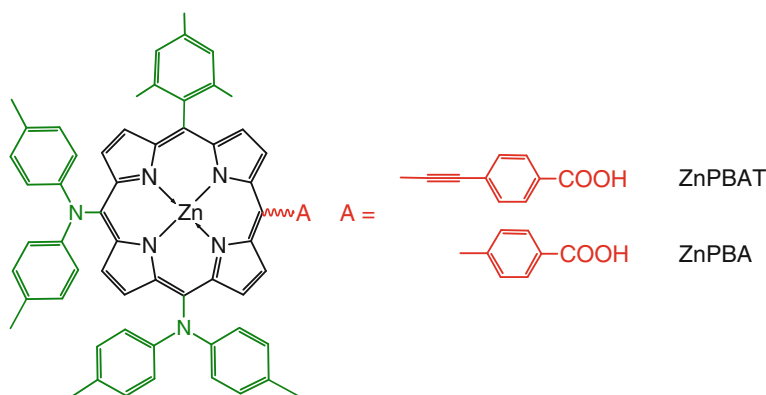
Scheme 49 General structural formula of **a** *trans*-A2BCD “fully-conjugated” MP and **b** ABCD-type asymmetric MP



Scheme 50 General structural formula of the multi-donor fully conjugated YD15 dye of the A2BCD type used in Ref. [74]

The YD15 dye was synthesized within the series of other A2BCD-type dyes. However, it was the only fully conjugated dye with three D moieties in the series. The DSSC with the YD15 dye performed moderately, showing V_{oc} of 0.623 V, j_{sc} of 9.42 mA cm^{-2} , and PCE of 4.2 %. These values were the lowest in the series of these dyes. In view of other less-conjugated ZnPs, the symmetric fully conjugated design for MPs in DSSCs was not promising. Apparent reason for low performance is strong aggregation of planary shaped molecules by π - π stacking. This suggestion is confirmed by higher performance of similar dyes with disaggregating substituents in 5,15-*meso*-positions [74].

In an attempt to increase performance of these dyes, not typical asymmetric fully conjugated ZnPs were synthesized, i.e., those of the *cis*-A2BCD type (Scheme 51).



Scheme 51 Structural formula of asymmetric *cis*-A2BCD-type porphyrins, ZnPBAT and ZnPBA, used in Ref. [95]

Table 23 Photovoltaic performance of DSSCs with the *cis*-A2BCD-type MPs [95]

Dye	$\Gamma \times 10^{11}$ (mol cm ⁻²)	V_{oc} (V)	J_{sc} (mA cm ⁻²)	FF	η (%)
ZnPBAT	9.2	0.719	19.33	0.724	10.1
ZnPBA	8.7	0.713	16.26	0.719	8.3
YD2 (benchmark)	8.9	0.742	17.05	0.718	9.1

The two, 10- and 15-*meso*, positions were occupied by the D moiety and that of the 5-*meso*-position by a disaggregating moiety. Either conjugated A moiety with the macrocycle (ZnPBAT) or not (ZnPBA) was used. Surprisingly, performance of DSSCs with the ZnPBAT dye was even higher than that with a similar but symmetric YD2 dye (Table 23).

A series of spectroscopic measurements showed that the origin of high performance of DSSC with the ZnPBAT was its high IPCE, while dye aggregation and the unfavorable disexcitation rate were higher compared to those of the YD2 benchmark.

3.1.7 Conclusions on Progress and Perspectives of Porphyrin-Sensitized Solar Cells

Over past 5 years, extensive research on porphyrin dyes for DSSCs resulted in impressive progress of the DSSC efficiency. The design of dyes molecules was optimized resulting in 13 % PCE for the cell with the “push–pull” type of ZnPs. Along with broadening the absorbance wavelength range, the progress in developing new charge-mediating species, including the Co(II)/Co(III) complexes and supporting electrolyte composition, allowed increasing V_{oc} of DSSCs to reach merely 1.0 V. Application of π -conjugated axial D- π -A architecture with side peripheral groups serving for disaggregation of MP molecules and isolation of the central metal atom allowed DSSCs performing efficiently. The best performing porphyrin dyes for DSSC appeared the *meso*-substituted Zn porphyrins featuring ethynyl-linked D and A moieties and two peripheral groups preventing ZnP aggregation on the TiO₂ surface and isolating the Zn atom from the charge-mediating species. The most commonly used peripheral groups in high-performing MP dyes are alkoxy-substituted phenyl rings. The best performing DSSCs devised up to now included SM315 and GY50 dyes and a Co(II)/Co(III) complex as the redox mediator.

3.2 Bulk Heterojunction Solar Cells

Porphyrins are key components of DSSC electrode materials. They are widely used in supramolecular SCs. However, their application for the BHJ SCs was so far

rather limited. Compared to DSSCs, MPs were merely noticed in BHJ SCs. Nevertheless, there are reports on designing polymeric electron-donor materials containing porphyrins.

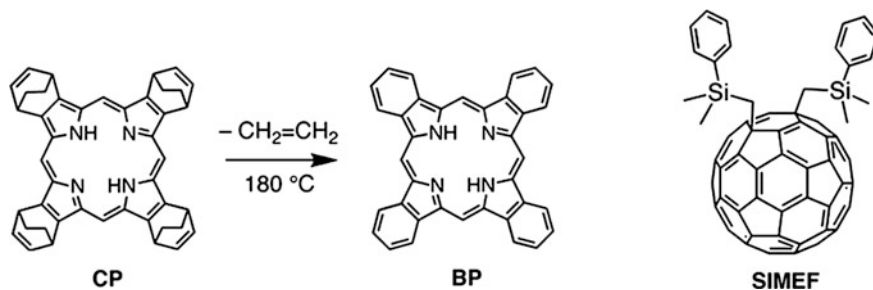
Typically, BHJ SC is constructed of two types of active materials, i.e., an electron donor and acceptor. Conjugated polymers, oligomers, or small molecules can serve as donors, while a molecular acceptor is most commonly used. More recently, π -bridged D–A conjugated polymers were designed for enhanced performance of BHJ SCs [96–99]. While the most popular electron-accepting materials are fullerene derivatives, several different electron-donating conjugated polymers are used. Typical examples of donor materials for BHJ SCs include polythiophenes, poly(phenylene vinylenes), and many other [99]. The PCE of the top-performing BHJ SC exceeds 10 % [100–102]. Moreover, BHJ SCs with molecular or oligomeric porphyrins were devised. Efficiency of these cells was enhanced by optimizing the MP design, D–A interface, and construction of the cell.

The PCE of BHJ SCs was improved by optimizing interfaces and the cell design. Consequently, the PCE of cells made of similar materials has grown from tiny fractions of a single percent to a few percents. Nevertheless, new materials had to be designed in order to make further progress in PCE. Accordingly, new semi-conducting polymers were extensively devised. These polymers can be divided into three consecutive generations, i.e., polyacetylenes (the first generation), polymers and copolymers of polyalkylthiophenes and poly(*p*-phenylene vinylenes) (the second generation), and, finally, those of more complex structure bearing higher number of repeatable monomer units [103]. Modern conjugated polymers containing porphyrins for the solar cell application can be referred as the third generation. In the top-performing BHJ SCs, porphyrins are used in a form of copolymers with more conventional molecules to produce electron-donating conjugated polymers with enhanced light-absorbing abilities. The copolymers of MPs with other monomers for BHJ SCs are usually synthesized via the Stille coupling reaction [104, 105]. The goal of the D polymer design for application in BHJ SCs is to make the lowest HOMO–LUMO energy difference because this difference linearly correlates with the V_{oc} of the resulting cell.

It is difficult to compare different BHJ SCs because their performance depends upon other active materials, electrodes, etc. Therefore, the data with respect to the details on the SC construction are given in headers of tables, below.

3.2.1 Monomeric and Oligomeric Porphyrins in Bulk Heterojunction Solar Cells

Application of monomeric porphyrins in BHJ SCs went a long way of development in a relatively short time by substantially rising efficiency of BHJ SCs with the “porphyrin D”–A. Porphyrins were applied in many different ways to BHJ SC and, among others, as a D [106], as an auxiliary D accompanying more traditional photoactive material [107], as a photoelectrode modification layer [108–110], or as a part of the synthetic D–A dyad with fullerene [111, 112], or even as an A [113].



Scheme 52 Structural formula of the 1,4,8,11,18:22,25-tetraethano-29H,31H-tetrabenzoporphyrin (CP), tetrabenzoporphyrin (BP), and bis(dimethylphenylsilylmethyl) [60]fullerene (SIMEF). Reprinted with permission from Matsuo Y, Sato Y, Niinomi T, Soga I, Tanaka H, Nakamura E (2009) Columnar structure in bulk heterojunction in solution-processable three-layered p-i-n organic photovoltaic devices using tetrabenzoporphyrin precursor and silylmethyl[60]fullerene. *J Am Chem Soc* 131(44):16048–16050. Copyright (2009) American Chemical Society

An impressive for that time PCE has been reported for BHJ SC with a benzo-porphyrin–fullerene active material (Scheme 52) [114]. A soluble precursor porphyrin in a mixture with a fullerene derivative, thermally converted into an insoluble terabenzoporphyrin (BP), was used to form an active layer (Scheme 52).

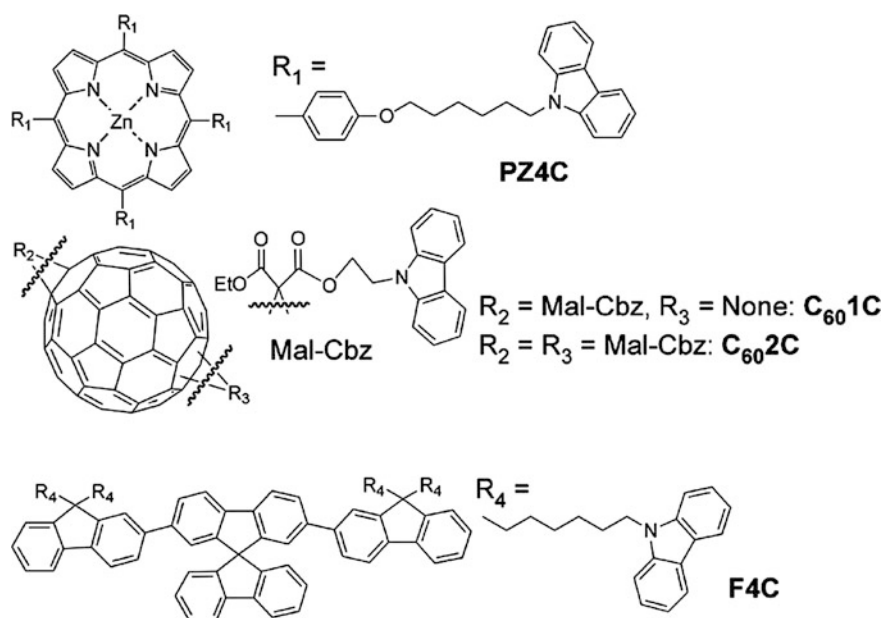
Upon heating the CP to 180 °C, this compound was converted into BP with a pillar type columnar morphology of the layer. An assembly of a photovoltaic cell of the ITO/PEDOT:PSS/BP/BP:SIMEF/SIMEF/Al structure revealed the 5.2 % PCE under the AM 1.5G illumination. A typical CP-to-SIMEF mass ratio was 3:7. A buffering layer material [phenanthroline derivatives; viz., bathocuproine (BCP) or 2,9-bis(naphthalen-2-yl)-4,7-diphenyl-1,10-phenanthroline (NBphen)] was used between the SIMEF and Al electrode. The highest PCE was obtained with the NBphen buffer. Then, BHJ SC with BP serving as the D moiety was reported [115]. This D moiety used a poly(propylene carbonate) sacrificial thermally degradable binder to form a nanostructured film with the morphology favorable for BHJ SCs. However, PCE of the resulted cells was lower than that obtained in the former research (Table 24).

A (porphyrin D)-(fullerene A) synthetic dyad was applied as an acceptor for a BHJ SC with advantageously high V_{oc} and j_{sc} compared to the benchmark SC with the PCBM acceptor [112]. However, PCE of this cell was lower than that of the cell with the PCBM acceptor because of the lower FF .

There was an attempt to construct a BHJ SC with controlled morphology of an active layer using a layer-by-layer assembling with consecutive electropolymerization of the resulting layers to form a covalently linked D–A active material of precisely controllable thickness [116]. Electropolymerization was performed under potentiodynamic conditions by coupling *N*-alkylcarbazole moieties of both D and A units. A photoactive layer was composed of three carbazol-derivatized components, i.e., [C₆₀]fullerene, ZnP, and oligofluorene derivatives (Scheme 53). The PCE of

Table 24 Photovoltaic performance of BHJ SCs of the BP:PCBNB with the ITO/PEDOT:PSS/Active layer/Al structure under the standard AM 1.5G light illumination [115]

Active layer	V_{oc} (V)	J_{sc} (mA cm ⁻²)	FF	η (%)
BP/BP':PCBNB	0.57	4.33	0.46	1.12
BP/BP':PCBNB	0.54	5.15	0.48	1.35
BP/BP'/BP:PCBNB	0.60	4.67	0.42	1.19
BP/BP'/BP:PCBNB	0.55	5.12	0.51	1.43
BP/BP:PCBNB	0.58	5.48	0.49	1.54
BP/BP:PCBNB/PCBNB	0.41	5.45	0.60	1.34

**Scheme 53** Structural formula of the porphyrin (PZ4C), benzopor (F4C), and the [60]fullerene derivative (C₆₀1C and C₆₀2C) used for layer-by-layer assembling, and then subsequent electropolymerization. Adapted with permission from Li M, Ishihara S, Akada M, Liao M, Sang, L, Hill JP, Krishnan V, Ma Y, Ariga K (2011) Electrochemical-coupling layer-by-layer (ECC-LbL) assembly. *J Am Chem Soc* 133(19):7348–7351. Copyright (2011) American Chemical Society

the BHJ SC with this active material was low ($\sim 0.001\%$). Apparently, this was because of traces of a supporting electrolyte left in the film, i.e., charge carriers were trapped.

A ZnP-bearing pyridinyl-ethynyl *meso*-substituent was synthesized and used as a D component of an active material of a BHJ SC [117]. Despite that the porphyrin was called “conjugated,” its conjugation was limited because the phenyl group was used to attach the substituent to the ZnP macrocycle, thus hampering intramolecular electron transfer between this substituent and the porphyrin ring. The V_{oc} of the

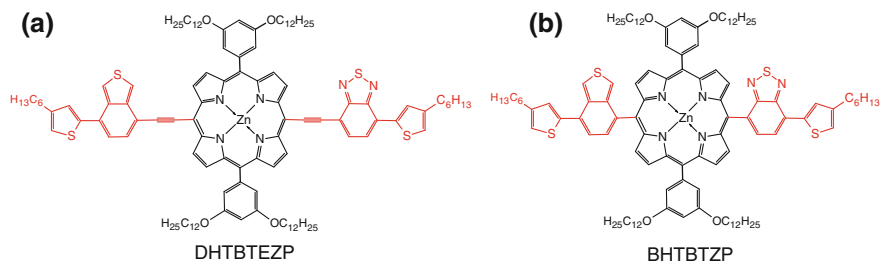
BHJ SC with this ZnP and fullerene derivative was high; however, PCE was moderate for this material, merely reaching 4 %.

Several mixed double-decker complexes of free-base porphyrin and phthalocyanine complexes of the rare-earth metal(III) cations were applied to BHJ SCs as donors for broadening the absorbance wavelength range to the NIR region [118]. Application of the rare-earth metal(III) complexes allowed devising materials with the light absorbance wavelength in the range of 300 nm to longer than 1100 nm. Devices of the ITO/PEDOT:PSS/(active layer)/LiF/Al structure were assembled and their photovoltaic performance was determined. The active layer was made of the bis(tetrapyrrole) complexes, serving as donors, blended with the PCBM or PDI in the TiO_x acceptor. The PCE of the top-performing cell of that type was 0.82 %. This low PCE value was because of low both the *FF* and *V*_{oc} of these cells.

Advantages of the “push–pull” MP design in the small-molecule BHJ SCs were evaluated using two similar *trans*-2B2C ZnPs. Two alkoxy *meso*-substituents were introduced to increase solubility of the porphyrins while others, vis., 3-hexylthienyl-terminated 2,1,3-benzothiadiazole, for enhancement of the intramolecular charge transfer (Scheme 54). Two compounds were synthesized, namely, 5,15-bis(7-(4-hexyl-thiophen-2-yl)-2,1,3-benzothiadiazole-4-yl-ethynyl)-10,20-bis(3,5-di(dodecyloxy)-phenyl) ZnP (DHTBTEZP) and 5,15-bis(7-(4-hexyl-thiophen-2-yl)-2,1,3-benzothiadiazole-4-yl)-10,20-bis(3,5-di(dodecyloxy)-phenyl) ZnP (DHTBTZP) with the ethynyl- and phenyl-linked acceptor moiety, respectively, (a and b, respectively, in Scheme 54) [119].

A drastic difference in PCE of these cells was because of efficient conjugation of the ZnP macrocycle with peripheral acceptor groups for the DHTBTEZP and lack of this conjugation in DHTBTZP, respectively (Table 25). This conjugation influenced absorbance spectra of the porphyrins. That is, the spectrum for the π -conjugated DHTBTEZP featured largely increased and red-shifted Q-band [119].

A moderate increase of PCE of the BHJ SCs with similar porphyrins was caused by the presence of heteroatomic ligands axially coordinated to the Zn central atom [120, 121]. Here, the DHTBTEZP and its analog with the diketopyrrolopyrrole-based electron-acceptor moieties were used to coordinate pyridine [121]. The



Scheme 54 General structural formula of the **a** D- π -A type ZnP, DHTBTEZP, and **b** its nonconjugated analog, DHTBTZP used in Ref. [119]

Table 25 Photovoltaic performance of BHJ SCs with the ITO/PEDOT:PSS/DHTBTEZP or DHTBTZP:PC₇₁BM/MoO₃/Al structure under the standard AM 1.5G light illumination [119]

Active layer	D:A mass ratio	V_{oc} (V)	J_{sc} (mA cm ⁻²)	FF	η (%)
DHTBTZP:PC ₇₁ BM	1:3	0.88	2.81	0.287	0.71
DHTBTEZP:PC ₇₁ BM	1:3	0.85	9.46	0.500	4.02

~1 % increase of the PCE of the BHJ SC resulting in 4.78 % was observed when the solvent for preparation of the active material was 3 % in pyridine.

Full peripheral *meso*-substituent conjugation with the porphyrin macrocycle affects PCE of the BHJ SC similar to DSSCs. That is, despite that, the nature of the interface between the D and A component in a BHJ SC greatly influenced photovoltaic performance of this cell. Clearly, conjugation of all four *meso*-substituents of *trans*-2B2C porphyrins hampered PCE of BHJ SCs with these D moieties (Scheme 55) [122, 123].

The BHJ SC with the 2-MgP donor bearing phenyl-conjugated “push” moieties revealed impressive V_{oc} of 0.92 V, the PCE being 2.5 %. Nevertheless, porphyrins terminated with other groups studied (neither “push” nor “pull”) did not provide more efficient D component for BHJ SCs.

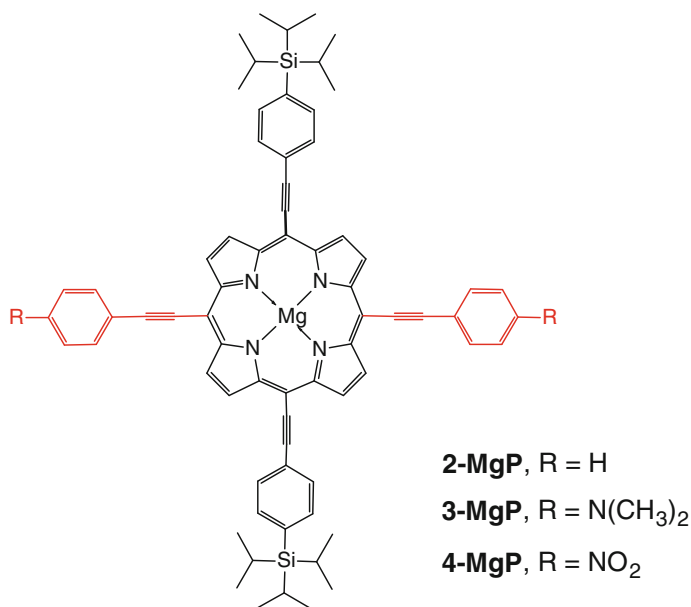
**Scheme 55** General structural formula of fully conjugated MgPs used in Ref. [122] (abbreviations introduced herein). In consecutive publications of these authors, 2-MgP was named TE-Por

Table 26 Photovoltaic performance of BHJ SCs with the ITO/PEDOT:PSS/Porphyrin D:fullerene A/Ca/Al structure under the standard AM 1.5G light illumination

Active layer	D:A mass ratio	V_{oc} (V)	J_{sc} (mA cm ⁻²)	FF	η (%)	Ref.
2-MgP:PC ₆₀ BM	(1:4) ^a	6.4	0.92	0.41	2.50	[122]
3-MgP:PC ₆₀ BM	(1:4) ^a	3.3	0.55	0.31	0.57	[122]
4-MgP:PC ₆₀ BM	(1:4) ^b	1.6	0.97	0.16	0.25	[122]
2-MgP:PCBM ^{c,d}	1:2	0.68	4.1	0.30	0.82	[123]
2-MgP:PCBM ^{c,d}	1:5	0.86	4.3	0.40	1.5	[123]
2-MgP:PCBM ^{c,d}	1:5	0.90	4.6	0.39	1.6	[123]

^aChlorobenzene was used as the solvent for preparing the BHJ layer

^bToluene/tetrahydrofuran (1:1, mass) was used as the solvent for preparing the BHJ layer

^cAn inverted BHJ SC of the PCBM:2-MgP ITO/ZnO/PEDOT:PSS/Au structure

^dThe TiO_x electron transporting layer was used instead of ZnO

An attempt of optimizing structure of the BHJ SC with fully conjugated 2-MgP [122] introduced to reach the highest performance did not result in higher PCE (Table 26) [123]. Similarly, synthesis of the *cis*-2B2C MgP did not improve performance of the resulting BHJ SC [124].

A series of porphyrin trimers linked into a star-shaped construct with triarylamine in the center was synthesized and applied to BHJ SCs [125–127]. These porphyrins were used as either donors or acceptors in the BHJ SCs. The PCE of these BHJ SCs was higher if these porphyrins served as D components of the active material. The PCE of these cells did not exceed 0.4 % [125, 126]. Recently, a similar triazine-bridged ZnP triad approached PCE of 4 % (Table 27, Scheme 56) [127]. Apparently, this improvement was due to symmetry breaking in the porphyrin triad. That is, two ZnPs with phenyl *meso*-substituents were linked with free-base porphyrin bearing one carboxyphenyl and two 2,4,6-trimethylphenyl substituents.

The X-ray diffraction measurement of active layers showed higher crystallinity of the active layer cast from the mixed solvent (Table 27). Hence, higher photovoltaic performance of the latter was due to a faster charge transport in the BHJ active layer [127].

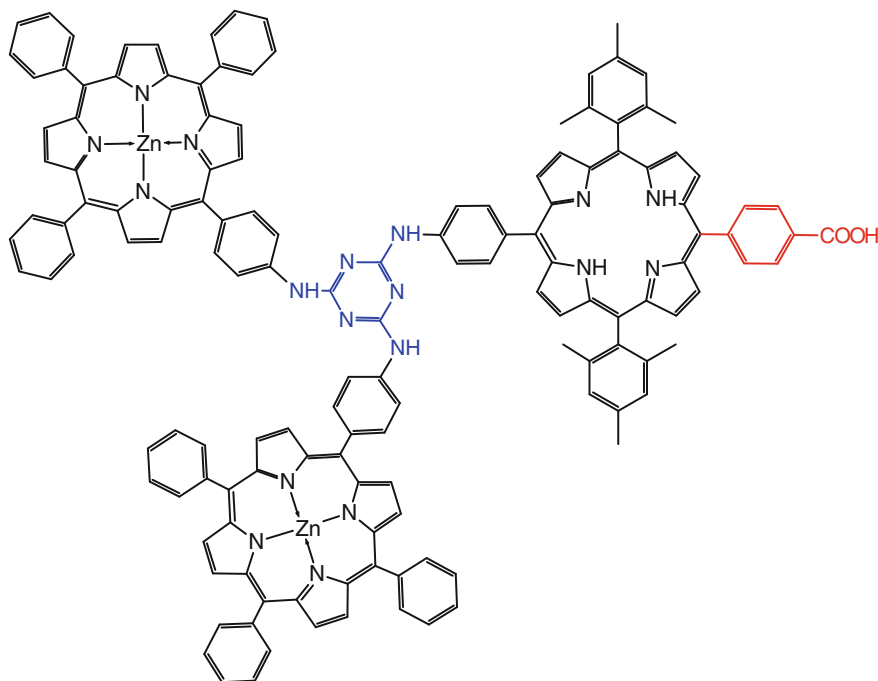
An interesting study on the influence of the porphyrin *meso*-substituents on parameters of BHJ SCs was performed [128]. These porphyrins served as auxiliary D components to broaden the absorbance wavelength range of the cell. Here, three

Table 27 Photovoltaic performance of BHJ SCs with the ITO/PEDOT:PSS/PPT:PC₇₀BM/Al structure under the standard AM 1.5G light illumination [127]

Active layer	D:A mass ratio	V_{oc} (V)	J_{sc} (mA cm ⁻²)	FF	η (%)
PPT:PC ₇₀ BM ^a	1:1	0.96	6.45	0.46	2.85
PPT:PC ₇₀ BM ^b	1:1	0.92	8.06	0.53	3.93

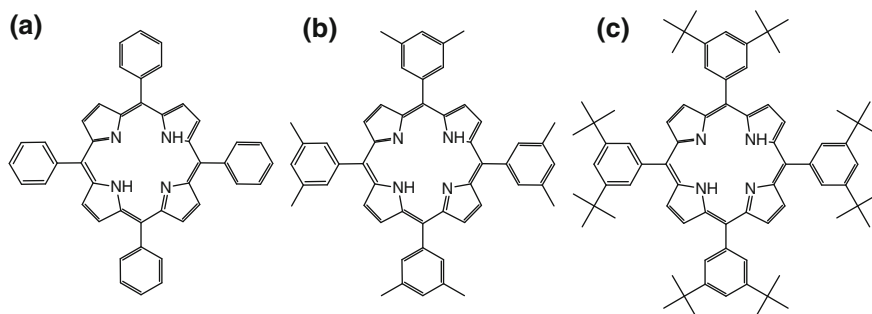
^aCast from tetrahydrofuran

^bCast from tetrahydrofuran, which was 5 % (vol.) in 1-chloronaphthalene



Scheme 56 Structural formula of the triad of the triazine-bridged ZnP and the free-base porphyrin (PPT) used in Ref. [127]

tetra-aryl free-base *meso*-porphyrins differing only in bulkiness of their peripheral substituents were synthesized (Scheme 57). These porphyrins were introduced, as the third component, into the D–A blend of poly[2-methoxy-5-(20-ethylhexyloxy)-1,4-phenylene-vinylene] (MEH-PPV) and [6,6]-phenyl C₆₁-butyric acid methyl ester (PCBM).



Scheme 57 Structural formulas of *tetra*-arylporphyrins **a** 5,10,15,20-*tetra*(*p*-tolyl)porphyrin (*p*TP), **b** 5,10,15,20-*tetra*(3,5-dimethylphenyl)porphyrin (XyP), and **c** 5,10,15,20-*tetra*(3,5-di-*t*-butylphenyl)porphyrin (*t*BuPP) used in Ref. [128]

Table 28 Photovoltaic performance of BHJ SCs with the ITO/PEDOT:PSS/MEH-PPV: Porphyrin:PCBM/Ca/Al structure under the standard AM 1.5G light illumination [128]

Active layer	V_{oc} (V)	J_{sc} (mA cm ⁻²)	FF	η (%)
MEH-PPV:PCBM (benchmark)	0.83 ± 0.01	5.34 ± 0.28	0.4 ± 0.01	1.77 ± 0.05
Equimass				
MEH-PPV: <i>p</i> TP:PCBM	0.45 ± 0.02	1.97 ± 0.10	0.31 ± 0.00	0.27 ± 0.00
MEH-PPV:XyP:PCBM	0.58 ± 0.02	2.64 ± 0.13	0.32 ± 0.00	0.48 ± 0.00
MEH-PPV:tBuPP:PCBM	0.64 ± 0.01	3.90 ± 0.30	0.33 ± 0.01	0.83 ± 0.00
Equimolar				
MEH-PPV: <i>p</i> TP:PCBM	0.50 ± 0.01	3.22 ± 0.21	0.31 ± 0.00	0.51 ± 0.00
MEH-PPV:XyP:PCBM	0.59 ± 0.01	3.68 ± 0.18	0.33 ± 0.00	0.70 ± 0.00
MEH-PPV:tBuPP:PCBM	0.64 ± 0.01	3.90 ± 0.30	0.33 ± 0.01	0.83 ± 0.00

Errors are mean standard deviations of measurement of eight independent OPV devices

The determined cyclic voltammetry and UV–vis spectroscopy energy of the HOMO, LUMO, and band gap were independent of the nature of peripheral substituents of the porphyrin.

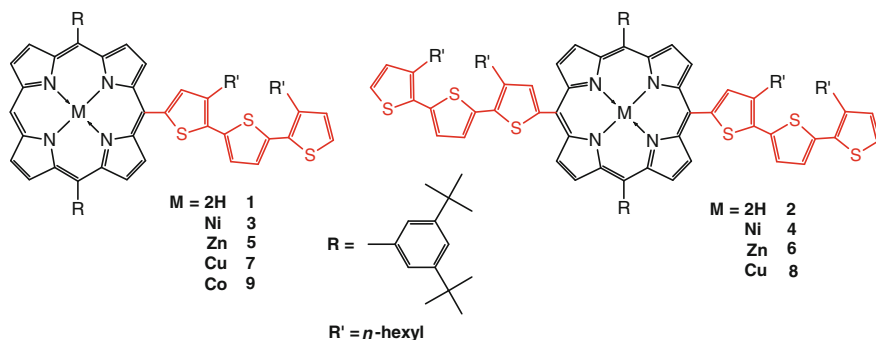
The porphyrin addition largely decreased the performance of BHJ SCs with limited enhancement in the absorbance spectra broadening (Table 28). The AFM imaging of the films showed that the porphyrin addition to the blend affected morphology of the resulting films. Moreover, electronic properties of the active materials were changed. The porphyrins acted as recombination sites for the excitons within the blend. However, the bulkier the molecule of the *meso*-peripheral substituent, the less pronounced was this effect [128].

A detailed study on improvement of the BHJ SC efficiency by applying porphyrins as auxiliary dyes in the active material showed an increase of the PCE for several porphyrins [129]. That is, a series of different MPs was synthesized, and then applied as components of the P3HT:PCBM blend active material of a BHJ SC (Scheme 58).

Addition of 1, 5, or 10 % of selected MP-oligothiophene conjugates to the blend allowed increasing the PCE of the SC compared to that of the P3HT:PCBM benchmark material not containing porphyrins (Table 29).

The PCE of the BHJ SC with an auxiliary MP donor increased in the order of free-base < Co < Zn < Ni < Cu. The addition of CuP resulted in the ~17 % increase of PCE of the BHJ SC with respect to that of the benchmark SC without porphyrin.

Recently, an example of an efficient BHJ SC was assembled of commercially available components by careful D–A interface optimization (Table 30) [108, 109]. Here, self-assembled porphyrins stacks were used as the charge mediators to assist effective exciton dissociation at the photocathode. This approach allowed constructing BHJ SC with the PCE as high as 7.13 %.



Scheme 58 General structural formulas of a series of MPs synthesized for application as auxiliary donors used in Ref. [129]

Table 29 Photovoltaic performance of BHJ SCs with the ITO/PEDOT:PSS/P3HT:PCBM/Ca/Al structure under the standard AM 1.5G light illumination [129]

Porphyrin addition	V_{oc} (V)	J_{sc} (mA cm^{-2})	FF	η (%)
None (benchmark)	0.59	7.6	0.62	2.77 ± 0.2
1 % 1	0.54	7.8	0.57	2.44 ± 0.1
1 % 2	0.56	7.4	0.60	2.50 ± 0.3
1 % 3	0.60	7.9	0.61	2.87 ± 0.2
1 % 4	0.58	7.8	0.62	2.83 ± 0.2
1 % 5	0.58	7.9	0.62	2.84 ± 0.3
1 % 6	0.58	7.8	0.60	2.71 ± 0.3
1 % 7	0.59	8.1	0.65	3.07 ± 0.2
5 % 7	0.60	8.1	0.63	3.07 ± 0.2
10 % 7	0.60	7.8	0.63	2.94 ± 0.3
1 % 8	0.59	8.1	0.62	2.94 ± 0.2
5 % 8	0.60	8.3	0.61	3.03 ± 0.2
10 % 8	0.60	7.8	0.63	2.96 ± 0.2
1 % 9	0.58	8.1	0.58	2.69 ± 0.3

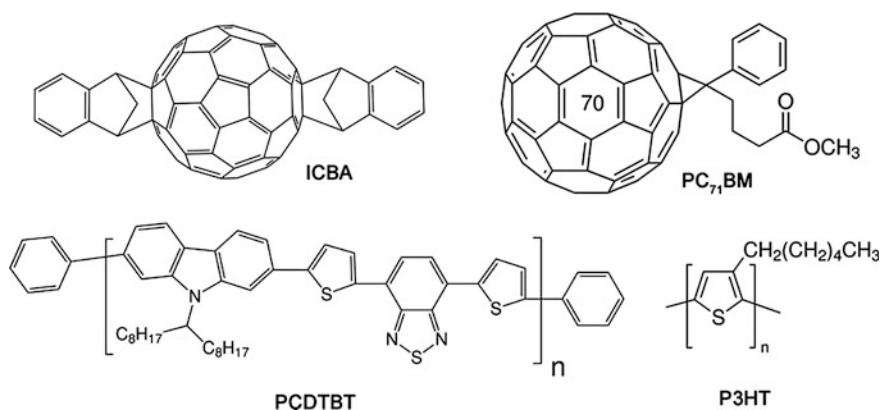
Average values determined for four BHJ SCs

The cell contained the PCDTBT:PC₇₁BM blend (Scheme 59) and its interface was modified with Porphyrin 1 (Scheme 60).

The photocathode modification with the *H*-aggregated Porphyrin 1 or *J*-aggregates of Porphyrin 2 allowed decreasing the work function of the electrode and easier exciton dissociating at the interface. This modification made the V_{oc} to increase to reach 0.92 V not hampering other parameters of the SC, thus increasing the BHJ SC performance.

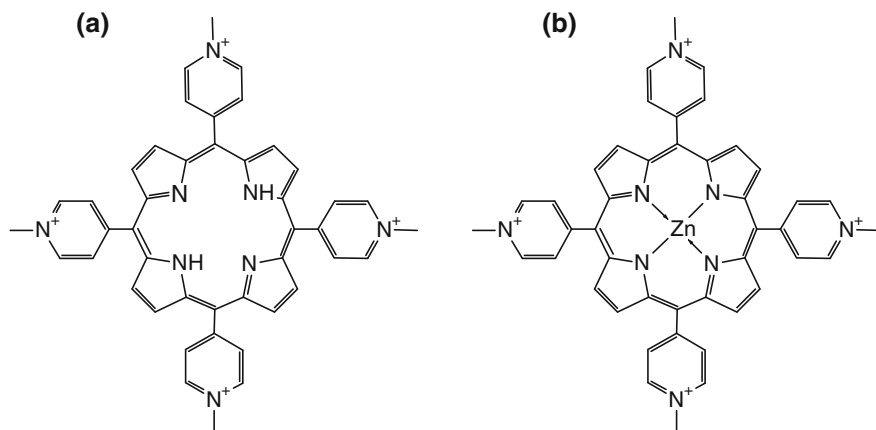
Table 30 Photovoltaic performance of inverted BHJ SCs with the ITO/MoO_x/Active material/Porphyrin/Al structure under the standard AM1.5G light illumination [108]

Active layer	V_{oc} (V)	J_{sc} (mA cm ⁻²)	FF	η (%)
P3HT:PC ₇₁ BM	0.55 ± 0.02	8.8 ± 0.16	0.53 ± 0.014	2.6 ± 0.13
P3HT:PC ₇₁ BM/MeOH	0.58 ± 0.01	9.2 ± 0.13	0.55 ± 0.011	2.9 ± 0.11
P3HT:PC ₇₁ BM/Porphyrin 1	0.69 ± 0.01	11.9 ± 0.11	0.59 ± 0.011	4.8 ± 0.10
P3HT:PC ₇₁ BM/Porphyrin 2	0.65 ± 0.01	10.5 ± 0.11	0.57 ± 0.011	3.9 ± 0.11
P3HT:ICBA	0.78 ± 0.02	8.60 ± 0.14	0.65 ± 0.013	4.3 ± 0.12
P3HT:ICBA/MeOH	0.80 ± 0.01	9.10 ± 0.12	0.67 ± 0.012	4.9 ± 0.10
P3HT:ICBA/Porphyrin 1	0.88 ± 0.01	11.00 ± 0.10	0.70 ± 0.011	6.8 ± 0.10
P3HT:ICBA/Porphyrin 2	0.84 ± 0.01	10.10 ± 0.10	0.69 ± 0.012	5.9 ± 0.10
PCDTBT:PC ₇₁ BM	0.79 ± 0.01	9.5 ± 0.17	0.57 ± 0.012	4.3 ± 0.14
PCDTBT:PC ₇₁ BM/MeOH	0.81 ± 0.01	9.8 ± 0.14	0.58 ± 0.011	4.6 ± 0.12
PCDTBT:PC ₇₁ BM/Porphyrin 1	0.92 ± 0.01	12.5 ± 0.13	0.62 ± 0.011	7.13 ± 0.11
PCDTBT:PC ₇₁ BM/Porphyrin 2	0.87 ± 0.01	11.5 ± 0.13	0.61 ± 0.011	6.1 ± 0.11

**Scheme 59** Structural formulas of selected commercially available donors: poly(3-hexylthiophene-2,5-diyl), (P3HT) and poly[*N*-9'-heptadecanyl-2,7-carbazole-alt-5,5'-(4',7'-di-2-thienyl-2',1',3'-benzothiadiazole)], (PCDTBT), and acceptor molecules for BHJ SCs: 1',1'',4',4''-tetrahydro-di[1,4]methanonaphthaleno[1,2:2',3',5,6,6':2'',3''] [5, 6] fullerene-C₆₀, (ICBA) and [6, 6]-phenyl-C₇₁ butyric acid methyl ester, (PC₇₁BM), used in Ref. [108]

3.2.2 Porphyrin Polymers in Bulk Heterojunction Solar Cells

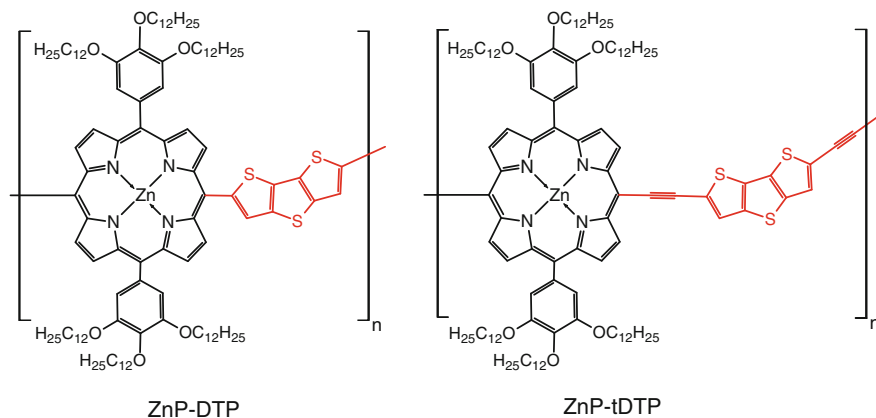
Porphyrin copolymers with other donor monomers synthesized for BHJ SC applications are relatively new. The successful application of porphyrins in DSSCs inspired their application in polymer donors for BHJ SCs. The first polymer of this



Scheme 60 **a** 5,10,15,20-Tetrakis(1-methyl-4-pyridinio) free-base porphyrin, Porphyrin 1, and **b** Zn porphyrin, Porphyrin 2, used for cathode modification in Refs. [108, 109]

kind was devised in 2008 [130]. This was the D–D-conjugated copolymer of alternating Zn porphyrin bearing peripheral alkoxy groups and dithienothiophene connected to the porphyrin macrocycle by either a single bond or the thienyl link (Scheme 61).

The average molecular weights of polymers for ZnP-DTP and ZnP-tDTP were 97.8 and ~ 26 kDa, respectively, (authors did not provide abbreviations for their polymers, and the abbreviations used were introduced herein). The UV–vis absorbance spectra of both polymers revealed pronounced Soret and Q-bands typical for porphyrins. Absorbance peaks of the polymers were red-shifted



Scheme 61 Structural formulas of the Zn-DTP and ZnP-tDTP porphyrin–dithienothiophene π -conjugated copolymers used in Ref. [130]

Table 31 Photovoltaic performance of ITO/PEDOT:PSS/Polymer:PCBM/Al cells under the standard AM 1.5G light illumination [130]

Active layer	ZnP polymer:PCBM mass ratio	V_{oc} (V)	J_{sc} (mA cm ⁻²)	FF	η (%)
Zn-DTP:PCBM	1:1	0.23	0.12	0.33	0.01
	1:2	0.46	1.29	0.26	0.15
	1:3	0.45	0.45	0.29	0.06
	1:4	0.52	0.62	0.29	0.09
Zn-tDTP:PCBM	1:1	0.53	0.88	0.33	0.15
	1:2	0.52	1.25	0.35	0.23
	1:3	0.58	1.52	0.34	0.30
	1:4	0.59	1.17	0.30	0.21

compared to those of the benchmark ZnP. This shift was even more pronounced for the thieryl-linked ZnP-tDTP. Unfortunately, performance of the BHJ SCs prepared with different ratios of the D to A components was below 1 % (Table 31).

The PCE of the BHJ SCs with thieryl-linked donor polymer (Zn-tDTP) was 0.3 %, being the highest reported value for the porphyrin-containing materials of that time. Similarly, Zn porphyrin copolymers with thiophene or furan of a simple structure were devised (Scheme 62) [131]. Despite strong fluorescence quenching of these polymers in the presence of an acceptor component (PCBM), indicative of the intermolecular charge transfer, performance of BHJ SCs with this rather simple donor ZnP polymers was low (Table 33).

Apparently, the reason of low PCE of these photoactive materials originated from the hindered electron transfer within the polymer donor–acceptor mixture (Table 32, Scheme 63).

Photovoltaic performance of BHJ SCs with these D-conjugated polymers do not differ much from those with the Zn-tDTP polymer reported earlier (Scheme 61 and Table 31). Molecular weights of the P-PTT and P-POT copolymer were 7.6 and 6.2 kDa, respectively.

Scheme 62 General structural formula of the porphyrin–furan and porphyrin–thiophene alternating copolymers (X = S or O) used in Ref. [131]

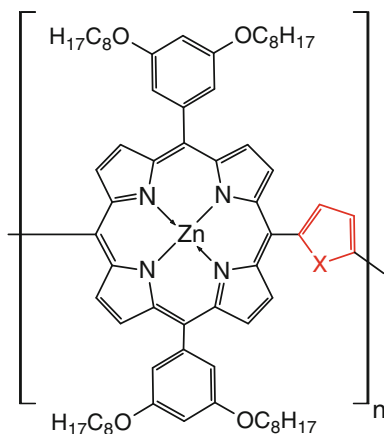
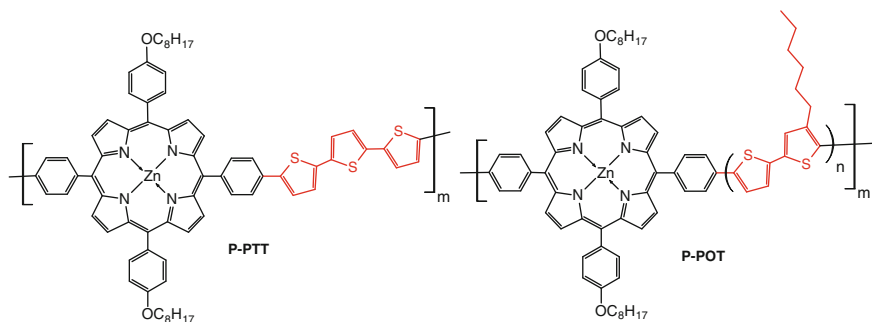


Table 32 Photovoltaic performance of the ITO/PEDOT:PSS/Polymer:PCBM/TiO_x/Al cells under the standard AM 1.5G light illumination [131]

Active layer	ZnP polymer:PCBM mass ratio	V_{oc} (V)	J_{sc} (mA cm ⁻²)	FF	η (%)
PZnPF:PCBM	n/a	0.58	0.34	0.24	0.048
PZnPT:PCBM	n/a	0.53	0.20	0.26	0.027

**Scheme 63** Structural formulas of Zn porphyrin copolymers with porphyrin-terthiophene (P-PTT), and oligothiophene (P-POT) used in Ref. [132]**Table 33** Photovoltaic performance of the ITO/PEDOT:PSS/Polymer:PCBM/Ca/Al cells under the standard AM 1.5G light illumination [132]

Active layer	Polymer:PCBM mass ratio	V_{oc} (V)	J_{sc} (mA cm ⁻²)	FF	η (%)
P-PTT	1:1	0.63	1.36	0.28	0.24
	1:2	0.58	1.49	0.30	0.26
	1:3	0.46	2.03	0.34	0.32
	1:4	0.49	1.69	0.27	0.22
P-POT	1:1	0.32	1.60	0.27	0.14
	1:2	0.50	1.12	0.27	0.15
	1:3	0.46	1.70	0.23	0.18
	1:4	0.48	1.07	0.25	0.13

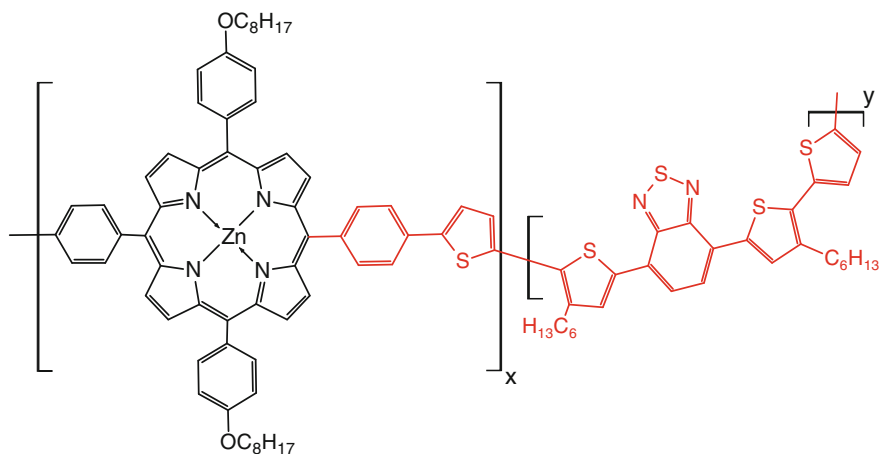
An interesting genuine-porphyrin linear polymer was prepared by electropolymerization [133]. However, its efficiency as D in BHJ SC was low, therefore, and this research was not developed further (Table 33).

In the range of 590–650 nm, light absorbance of the P-PTT polymer was higher than that of the P-POT. Furthermore, the electrochemically determined HOMO–LUMO energy bandgap of the P-PTT copolymer was larger than that of the P-POT copolymer. These differences resulted in the higher IPCE value and, consecutively, higher PCE for the SC using the P-PTT copolymer donor. Apparently, a lower

IPCE value for the P-POT resulted from a low electron transport efficiency of its longer oligothiophene chain.

Mutual comparison of photovoltaic performance of BHJ SCs, which use porphyrin copolymer donors with relatively simple structure, indicates that, prevalently, the absorbance spectra of these polymers are similar to those of monomeric porphyrins. That is, they do not cover completely the visible spectral range. Further progress in devising the D-conjugated polymers was made by complicating the polymer structure and broadening the absorbance wavelength range of these copolymers. That is, subsequent investigations more extensively developed the structure of the ZnP copolymer donors.

For widening, the absorbance spectra of the porphyrin copolymers, longer oligomers of thiophenes or their derivatives were used in early studies. However, these studies resulted in a limited PCE improvement. Even star-shaped porphyrin–polythiophene copolymers with all four *meso*-positions of the ZnP used for attaching polythiophene units, terminated with triphenylamine moieties, did not improve much PCE of the BHJ SCs [135]. Another way to synthesize a narrowband gap polymer is to introduce an electron-deficient building block, i.e., an electron acceptor, into the polymer backbone. By this way, the absorbance spectra of the polymer were successfully broadened in the range of 450–750 nm by introducing the 2,1,3-benzothiadiazole moiety, an electron acceptor (Scheme 64) [134]. The average molecular weight of the P1 copolymer was 11 kDa, while that of the P2 copolymer was 3.2 kDa. This structure refining directly influenced the PCE resulting in its doubling with respect to that of the porphyrin-containing materials reported earlier (Table 34). With the increase of the fraction of the A units in the copolymer, the red shift of the absorbance peaks increased, the wavelength range was broadened, and the optical band gap was narrowed to ~ 1.50 eV.



Scheme 64 General structural formula of the porphyrin, thiophene, and 2,1,3-benzothiadiazole copolymer. For the P1 copolymer, the $x : y$ ratio was 1 : 2, while it was 1:4 for the P2 copolymer used in Ref. [134]

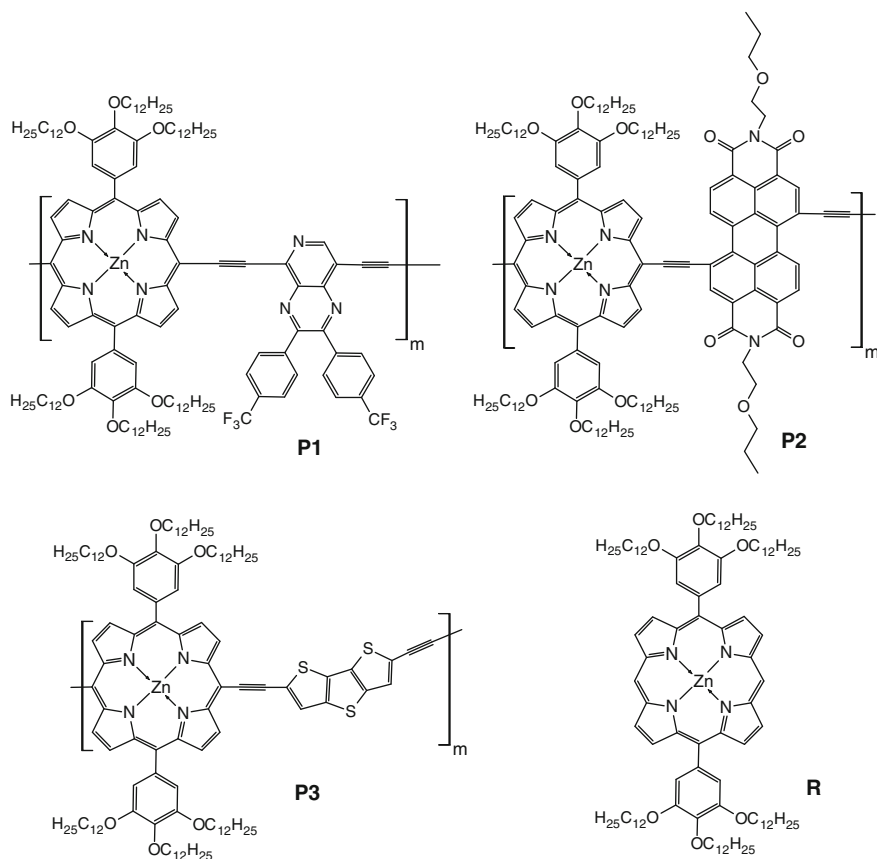
Table 34 Photovoltaic performance of the ITO/PEDOT:PSS/Polymer:PC₆₁BM/LiF/Al cells under the standard AM 1.5G light illumination [134]

Active layer	Polymer:PC ₆₁ BM mass ratio	V_{oc} (V)	J_{sc} (mA cm ⁻²)	FF	η (%)
P1	1:1	0.53	3.38	0.26	0.46
	1:2	0.55	3.13	0.26	0.45
	1:3	0.54	2.80	0.24	0.36
P2	1:1	0.57	4.10	0.36	0.84
	1:2	0.62	5.03	0.29	0.91
	1:3	0.57	3.99	0.36	0.83

An interesting series of the D- π -A copolymers of Zn porphyrin for the BHJ SC application was synthesized and electronic properties of these copolymers were compared with those of the D- π -D copolymer of the same ZnP and dithienothiophene as well as a molecular ZnP with the similar structure as the D ZnP unit of the copolymer (Scheme 65). Compared to the benchmark D- π -D polymer with the dithienothiophene block, the D- π -A copolymers P1 and P2 exhibited lower HOMO and LUMO energy levels, significantly red-shifted absorption spectra, and narrower band gaps. Absorption of these copolymers was stronger in the region of 820–950 nm and the band gap was as narrow as 1.15 eV. Molecular weights for the polymers made of P1, P2, and P3 were 30, 98, and 26.9 kDa, respectively. The ability of two-photon absorption by these copolymers was investigated. A typical for MPs light absorption minimum appeared at \sim 600 nm. Unfortunately, construction and examination of SCs was not reported for these copolymers. A more complex conjugated system was reported by the same group in a year later [136].

A higher PCE for the BHJ SC was achieved with a platinum polyynone copolymers with zinc(II) porphyrin [138]. Incorporation of Pt in the conjugated polymer enhanced overlapping of the d -orbitals of the Pt atom with the p -orbital of the alkyne unit allowing for mutual interaction of the two alkyne units through the d_{xy} and d_{yz} orbitals of the Pt atom [139]. Potentially, these electronic interactions could drastically improve π conjugation along the polymer backbone. Thiophene units in this backbone served for filling the gap in the absorbance spectrum between the Soret and Q-bands, and increasing the extent of conjugation. Despite a narrow optical band gap of the polymer series of P1–Pt to P3–Pt ranging from 1.93 to 2.02 eV, the j_{sc} value was low being 3.43 mA cm², while the V_{oc} was 0.78 and 0.77 V for the best performing cell with the latter two polymers (Table 35). All three isomers (Scheme 66) were simultaneously obtained in the same synthesis, and then separated.

Along with a low FF , a low j_{sc} indicates a high internal resistance of these photoactive polymer materials. Apparently, the porphyrin aryl link to the polymer backbone was responsible for a limited performance of this polymer in the BHJ SC. Nevertheless, crossing the 1 % PCE border for the BHJ SC with the porphyrin-based polymer donor was a remarkable step forward in development of the polymer chemistry.

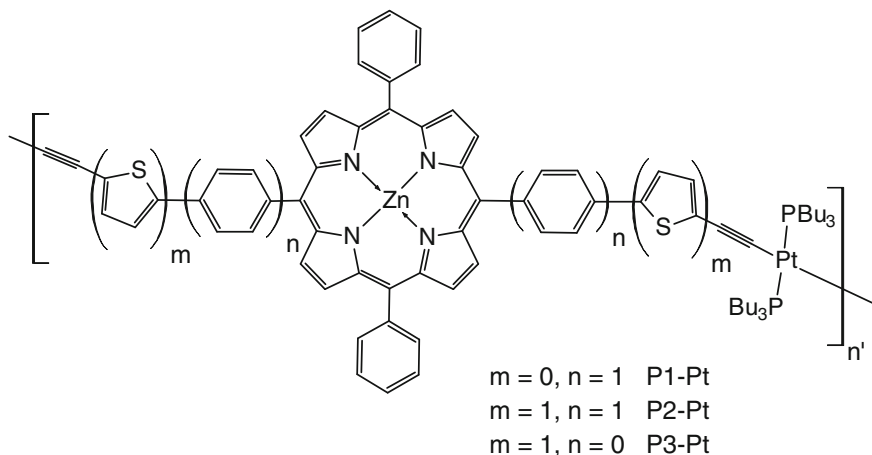


Scheme 65 Structural formulas of the D- π -A copolymers of ZnP with 2,3-bis(4-(trifluoromethyl)phenyl)pyrido[3,4-b]pyrazine, P1, and perylene diimide, P2, as well as the D- π -D copolymer of ZnP with dithienothiophene, P3, and the benchmark ZnP, R, used in Ref [137]

Table 35 Photovoltaic performance of the ITO/PEDOT:PSS/Polymer:PCBM/Al cells under the standard AM 1.5G light illumination [134]

Active layer	Polymer:PCBM mass ratio	V_{oc} (V)	J_{sc} (mA cm ⁻²)	FF	η (%)
P1-Pt	1:4	0.72	2.74	0.34	0.68
P2-Pt	1:4	0.78	3.02	0.30	0.71
P2-Pt	1:4	0.77	3.42	0.39	1.04

Devising copolymers of the porphyrin and thiophene or phenyl units with the porphyrin in the polymer backbone linked through phenyl groups in *meso*-position did not result in high-performing BHJ SCs; the PCE of the cells with these polymer donors remained on the level $\sim 1\%$ [140–142].



Scheme 66 General structural formula of metalloporphyrin-containing polyplatinyne polymers used in Ref. [138]

An elegant way to increase electron delocalization in the polymer backbone, thus decreasing the band gap, is to make this polymer more planar. However, the porphyrin-aryl *meso*-linkage introduces large dihedral angles in polymers and results in a low extent of conjugation. In order to avoid this effect, a new copolymer unit serving as a light-harvesting antenna for a porphyrin was introduced [143, 144]. The first porphyrin copolymer of this type, PCTTQP, revealed high absorbance in the entire visible wavelength range. Devising an SC with this copolymer allowed reaching the highest PCE of the BHJ SC, which exceeded 2.5 % (Table 36) [143]. In this copolymer, porphyrin units were mutually connected in an edge-fused fashion to form a quinoxalino[2,3-*b*]porphyrin moiety. By this way, two targets of the molecular design were reached. First, the HOMO–LUMO energy gap of the polymer was narrowed because of the presence of the pyrazine ring preserving conjugation. Next, an excessive dihedral twist of the planes of porphyrin macrocycles and neighboring units was avoided. For decreasing steric hindrance even more, a thiophene extender was introduced (Scheme 67).

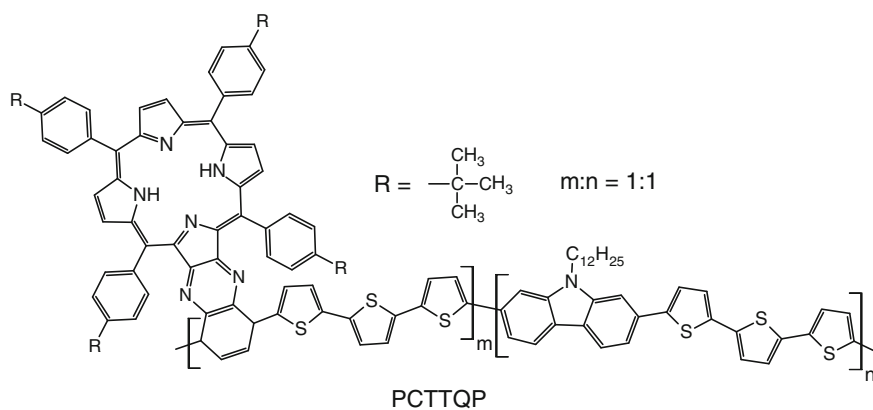
In subsequent studies, a series of similar copolymers was synthesized (Scheme 68) [144].

Here, thiophene extenders with different lengths were used. The highest PCE was reached for the BHJ SC with the copolymer of the free-base porphyrin with three thiophene units in the extending moiety of the polymer backbone (Table 36). Molecular weight of the P(C-T-QP), P(C-BT-QP), P(C-TT-QP), and P(C-TT-QP-Zn) copolymer was 5.2, 73.2, 130.3, and 138.1 kDa, respectively.

Moreover, this copolymer design was explored in another research. In this research, a quinoxalino[2,3-*b*]porphyrin polymer with the optimal three-thiophene unit spacer and electron-donating units served as the light-harvesting antenna,

Table 36 Photovoltaic performance of BHJ SCs with the quinoxalino[2,3-*b*]porphyrin polymer of the ITO/PEDOT:PSS/Polymer:A/Ca/Al structure under the standard AM 1.5G light illumination

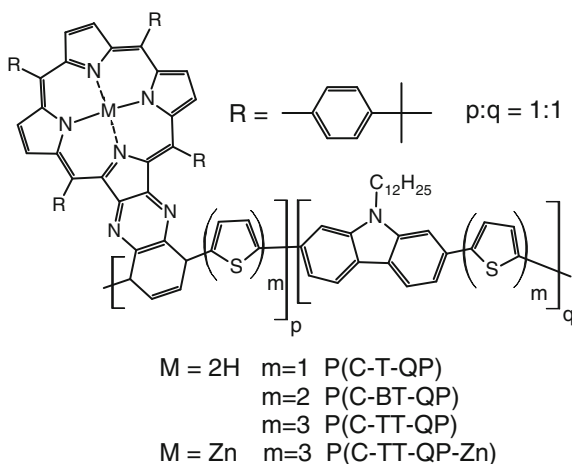
Active layer	Polymer:A mass ratio	V_{oc} (V)	J_{sc} (mA cm ⁻²)	FF	η (%)	Ref.
PCTTQP:PC ₇₁ BM	1:2	0.66	6.02	0.440	1.75	[143]
PCTTQP:PC ₇₁ BM	1:3	0.67	7.43	0.422	2.10	
PCTTQP:PC ₇₁ BM	1:3	0.68	8.32	0.446	2.53	
PCTTQP:PC ₇₁ BM	1:3	0.67	5.78	0.466	1.80	
P(C-T-QP):PC ₇₁ BM	1:2	0.69	4.15	0.34	0.97	[144]
P(C-BT-QP):PC ₇₁ BM	1:3	0.68	6.80	0.43	1.97	
P(C-TT-QP):PC ₇₁ BM	1:3	0.68	8.32	0.45	2.53	
P(C-TT-QP-Zn):PC ₇₁ BM	1:3	0.7	5.79	0.36	1.45	
PFTTQP:PC ₇₀ BM	1:3	0.81	7.39	0.4	2.39	[145]
PBDTTTQP:PC ₇₀ BM	1:3	0.63	6.13	0.4	1.53	

**Scheme 67** General structural formula of the polymer based on the quinoxalino[2,3-*b*]porphyrin unit with the oligothiophene π bridge used in Ref. [143]

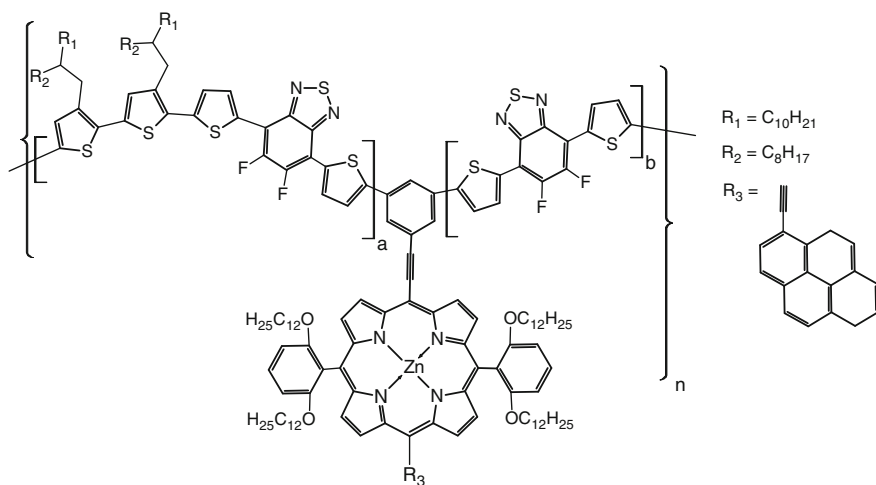
namely, fluorene and benzo[1,2-*b*:4,5-*b'*]dithiophene for the PBDTTQP and PFTTQP copolymer, respectively (Scheme 65). Unfortunately, higher PCE was not reached [145]. However, these investigations directed the porphyrin designing toward expelling the highly conjugated porphyrin unit out of the polymer backbone.

Several limitations of the state-of-art design of the D–A porphyrin polymers for BHJ SCs hamper further increase of PCE of these cells. Increasing all three main parameters influencing PCE of a SC by molecular design faces apparent contradiction. That is, (i) narrowing the HOMO–LUMO energy gap of the polymer

Scheme 68 General structural formula of D–A copolymers based on carbazole (C), quinoxalinoporphyrim (QP), thiophene (T), and 2,1,3-benzothiadiazole (BT) used in Ref. [144]



allows reaching higher j_{sc} ; however, it often hampers V_{oc} , (ii) a low-lying HOMO energy level promotes high V_{oc} ; however, it decreases j_{sc} , and (iii) keeping both the V_{oc} and j_{sc} high by virtue of the electronic structure of the polymer affects efficiency of the charge transfer between the polymer and the [60]fullerene derivative acceptor. Moreover, constructing polymers of a developed structure may be challenging with respect to formation of a favorable interface between the D and A components of the blend inside an active cell material (Scheme 69).



Scheme 69 General structural formula of the PPor-1 and PPor-2 polymer in Ref. [146]. The a:b molar ratio for PPor-1 and PPor-2 was 3:2 and 6:5, respectively, and for the PTh₄FBT benchmark polymer without the porphyrin moiety, it was 1:1

Table 37 Photovoltaic performance of inverted BHJ SCs with porphyrin-incorporated D–A polymers of the ITO/[ZnO or (ZnO/C-PCBSD)]/Polymer:PC₇₁BM/MoO₃/Ag structure under the standard AM 1.5G light irradiation [146]

Active layer	Polymer:A mass ratio	V_{oc} (V)	J_{sc} (mA cm ⁻²)	FF	η (%)
PTh ₄ FBT (benchmark) ^{a,b}	1:2	0.77	13.5	0.66	6.8
PPor-2:PC ₇₁ BM ^{a,d}	1:2	0.78	14.9	0.67	8.0
PPor-2:PC ₇₁ BM ^{a,d,e}	1:2	0.77	15.2	0.68	8.2
PPor-2:PC ₇₁ BM ^{c,d,e}	1:2	0.77	16.1	0.70	8.6

^aITO/ZnO/Polymer:PC₇₁BM/MoO₃/Ag cell

^b96 nm polymer blend thickness

^cITO/ZnO/C-PCBSD/PPor-2:PC₇₁BM/MoO₃/Ag cell

^d110 nm polymer blend thickness

^e5 vol. % of 1-chloronaphthalene was used as the processing additive in preparation of the photoactive material

These limitations were recently lifted resulting in the stunning increase of PCE from 2.5 to 8.6 % for the best performing BHJ SC with the porphyrin polymer [146]. Here, ZnP was moved out of the copolymer backbone. However, it was connected with this backbone through the ethynyl link, thus affording efficient conjugation. Moreover, two 2,6-bis(dodecyloxy)phenyl substituents on the porphyrin moiety prevented strong molecule aggregation. In order to evaluate contribution of the ZnP to the PCE of the resulting BHJ SC, a control polymer backbone without ZnP was synthesized (PTh₄FBT). Molecular weights of the PPor-1 and PPor-2 were 29.9 and 38.9 kDa, respectively. The UV–vis absorbance of these copolymers in the range of 500–750 nm was as high as that at the Soret band of porphyrins.

Advantageously, the optical HOMO–LUMO energy gap for the PPor-1 and PPor-2 copolymers was small, being 1.65 and 1.63 eV, respectively. Photovoltaic properties of PPor-2 were measured using an inverted SC (Table 37). In another research, the porphyrin moiety was moved out of the copolymer backbone and connected to this backbone through the phenyl spacer in the *meso*-position of the porphyrin. In contrast, this design resulted in no pronounced PCE increase, apparently because of lack of conjugation of the porphyrin macrocycle with the polymer backbone [147]. The PCE of the BHJ SC was the highest for the cell where surface of both the anode and the cathode was modified. That is, the silver anode was modified with MoO₃, while the ITO cathode with ZnO and cross-linked with [6,6]-phenyl-C₆₁-butyric styryl dendron ester (C-PCBSD). This careful electrode surface modification (Ag vacuum deposition on an extensively cleaned and heat-treated glass slide) contributed to an impressive result emphasizing an extreme importance of interfaces in the cell assembly.

3.2.3 Conclusions on the Progress of Porphyrin-Containing Bulk Heterojunction Solar Cells

Porphyrins were applied in BHJ SCs as the small-molecule, dimer, trimer, or polymer donors, auxiliary donors or electrode-modifying layers. Progress in PCE of BHJ SCs with porphyrin has been made in all these fields. The D–A interface modification as well as molecular design leading to higher performing SCs is still under work. Application of porphyrins in polymer donors for BHJ SCs is a relatively new field, which has been developed since 2008. Inspired by the success of porphyrin application in DSSCs, the PCE of BHJ SCs increased over these years from small fraction of a single percent to 8.6 % [130, 146]. This progress was possible because of adopting ideas generated during molecular designing of porphyrins applied in DSSCs to the BHJ SCs. However, the PCE of porphyrin-containing BHJ SCs is still lower than that of top-performing BHJ SCs with other efficient donor materials. Selected best performing BHJ SCs containing porphyrins are summarized in Table 38.

3.3 *Supramolecular Assemblies Based on Organic Donor–Acceptor Constructs*

Designing and devising supramolecular molecular assemblies of porphyrin donors with organic electron acceptors are attractive for photovoltaics because the convincing example of an effective solar light-harvesting system of that kind is provided by nature. There are continuous search for new efficient materials for organic photovoltaics. Photoinduced charge transfer in these D–A materials is a key step in operation of these materials as photoactive components of SCs. Toward that, there are numerous studies of photoinduced charge separation in (porphyrin D)-(nanocarbon material A) [148–152].

Porphyrin donors were organized into dyads with organic acceptors in different ways, including covalent linking, metal–ligand coordinating, π – π stacking, and H-bonding, while the active materials were self-assembled [153], adsorbed, chemisorbed, or electropolymerized [154] on the working electrode, etc. Chronologically, the most popular carbon acceptor materials used for constructing D–A dyads with porphyrin donors were fullerenes, carbon nanotubes, and graphene. However, advantageously, long lifetime of the charge separation state in D–A dyads is not directly transferrable into a considerably high overall PCE of the assembled cells. Most of the cells assembled using these materials reveals PCE in the order of decimal fraction of a single percent. Therefore, potential applicability of these materials in SCs and ways of improvement are evaluated by measuring duration of the photoinduced charge separation state and IPCE, while PCE under the standard AM 1.5G light illumination is not reported, as being very low. Therefore, only highly performing in SCs materials are discussed, below.

Table 38 Selected BHJ SCs cells of the best photovoltaic performance under the standard AM 1.5G light illumination conditions

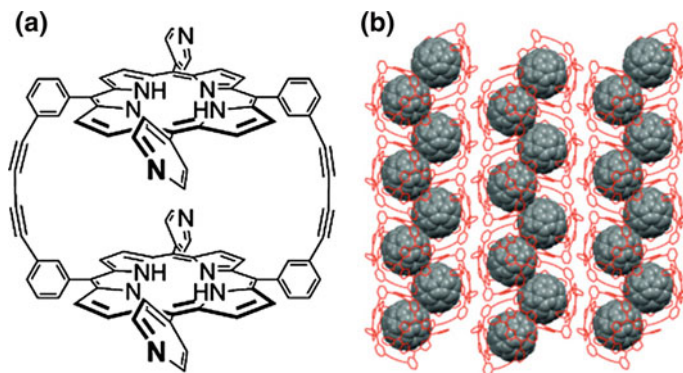
Cell structure	D:A mass ratio	V_{oc} (V)	J_{sc} (mA cm ⁻²)	FF	η (%)	Ref.
SCs with monomeric porphyrins						
ITO/PEDOT:PSS/BP/BP: SIMEF/SIMEF/Al	3:7	0.75	10.5	0.65	5.20	[114]
ITO/PEDOT:PSS/DHTBTEZP: PC ₇₁ BM/MoO ₃ /Al	1:3	0.85	9.46	0.50	4.02	[119]
ITO/PEDOT:PSS/PPT:PC ₇₀ BM/Al ^a	1:1	0.92	8.06	0.53	3.93	[127]
ITO/PEDOT:PSS/P3HT: PCBM/Ca/Al	1 % Por-7	0.59	8.10	0.65	3.07	[129]
ITO/MoO _x /PCDTBT: PC ₇₁ BM/Porphyrin/Al	–	0.92	12.5	0.62	7.13	[108]
SCs with polymeric porphyrins						
ITO/PEDOT:PSS/Zn-tDTP: PCBM/Al	1:3	0.58	1.52	0.34	0.30	[130]
ITO/PEDOT:PSS/PZnPF: PCBM/TiO _x /Al	n/a	0.58	0.34	0.24	0.048	[131]
ITO/PEDOT:PSS/P-PTT: PCBM/Ca/Al	1:3	0.46	2.03	0.34	0.32	[132]
ITO/PEDOT:PSS/P1:PC ₆₁ BM/LiF/Al	1:2	0.62	5.03	0.29	0.91	[134]
ITO/PEDOT:PSS/P2-Pt/Al	1:4	0.77	3.42	0.39	1.04	[134]
ITO/PEDOT:PSS/PCTTQP: PC ₇₁ BM/Ca/Al	1:3	8.32	0.68	0.45	2.53	[143]
ITO/PEDOT:PSS/P(C-TT-QP): PC ₇₁ BM/Ca/Al	1:3	0.68	8.32	0.45	2.53	[144]
ITO/ZnO/PPor-2:PC ₇₁ BM/MoO ₃ /Ag	1:2	0.78	14.9	0.67	8.0	[146]
ITO/ZnO/PPor-2:PC ₇₁ BM/MoO ₃ /Ag ^b	1:2	0.77	15.2	0.68	8.2	[146]
ITO/ZnO/C-PCBSD/PPor-2: PC ₇₁ BM/MoO ₃ /Ag	1:2	0.77	16.1	0.70	8.6	[146]

^aCast from 1-chloronaphthalene, which was 5 % (vol.) in tetrahydrofuran

^b5 % (vol.) of 1-chloronaphthalene was used for processing the additive in the course of preparation of the photoactive material

3.3.1 Porphyrin–Fullerene Donor–Acceptor Constructs

Having the longest “test together” history, the research involving porphyrin–fullerene dyads for photovoltaic application resulted in a gigantic number of publications. Unfortunately, performance of supramolecular SCs with these active materials is low. The pioneering 2007 report of composites of porphyrins and fullerenes organized by a polypeptide structure had a record of 56 % maximal ICPE and ~1.6 % PCE for the longest (16 units) polypeptide chain complex [155]. The charge separation lifetime was studied for a similar complex and, advantageously,



Scheme 70 **a** Structural formula of the free-base porphyrin dimer and the porphyrin ($H_4\text{-CPD}_{Py}$), and **b** a single crystal structure of its inclusion complex with C_{60} , determined by X-ray crystallography ($C_{60}@H_4\text{-CPD}_{Py}$). Reprinted from Nobukuni H, Shimazaki Y, Uno H, Naruta Y, Ohkubo K, Kojima T, Fukuzumi S, Seki S, Sakai H, Hasobe T, Tani F (2010) Supramolecular structures and photoelectronic properties of the inclusion complex of a cyclic free-base porphyrin dimer and C_{60} . *Chem Eur J* 16(38):11611–11623, Copyright (2010), with permission from Elsevier

it was long, being 0.84 ms [156]. However, the latter material was not tested in a photoelectrochemical cell.

An original supramolecular assembly of a cyclic free-base porphyrin dimer linked by butadiyne moieties bearing four pyridyl groups and C_{60} was constructed (Scheme 70) [157]. First, a 2B2C-type *trans*-porphyrin was synthesized, and then dimerized. An inclusion complex with the C_{60} molecule, fitting the cavity of the dimeric porphyrin, was prepared in solution. Next, this complex was deposited onto a nanostructured SnO_2 film on the surface of ITO for assembling a photoelectrochemical cell. The IPCE of this cell reached 17 % at ~ 530 nm and the IPCE spectrum was advantageously broad, while the charge separation lifetime was 470 ps. Metalation of the free-base porphyrin with Ni resulted in a lower IPCE and PCE of the cell.

Encapsulation of the Li^+ ion in the C_{60} cage to form an endohedral $\text{Li}^+@C_{60}$ increased ability of C_{60} to act as the electron acceptor [159]. The longest lifetime of charge separation for a non-covalent (porphyrin D)-(fullerene A) dyad of 0.67 ms was reported for the inclusion complex of a similar porphyrin dimer and $\text{Li}^+@C_{60}$ [160]. This porphyrin dimer featured Ni metal centers and alkoxy groups on the connecting links. With a simple dyad of sulfonated ZnP, an electrostatic D–A conjugate was prepared by taking advantage of better electron-accepting properties of the Li^+ -encapsulated fullerene [158]. Advantageously, this dyad had a long-lasting charge separation state of 0.3 ms. The maximal IPCE in the Soret and Q-band regions was 77 and 50 %, respectively. These values are very high as for this type of SCs. The PCE of the resulting SC was 2.1 %, which was by two orders of magnitude higher than that for a similar cell with pristine C_{60} (Table 39).

Table 39 Photovoltaic performance of a photoelectrochemical cell of the OTE/SnO₂/(Active material) structure

Active layer	V_{oc} (V)	J_{sc} (mA cm ⁻²)	FF	η (%)	Ref.
^a (C ₆₀ @H ₄ -CPD _{Py}) _n	0.30	1.10	0.40	0.33	[157]
^a (C ₆₀ @Ni-CPD _{Py}) _n	0.16	0.148	0.34	0.02	[157]
^b (ZnTPPS ⁴⁻ -Li ⁺ @C ₆₀) _n	0.46	3.4	0.37	2.1	[158]

Electrolyte: acetonitrile solution of 0.5 M LiI and 0.05 M I₂

^aUnder the 40 mW cm⁻² power of illumination

^bUnder the 28 mW cm⁻² power of illumination

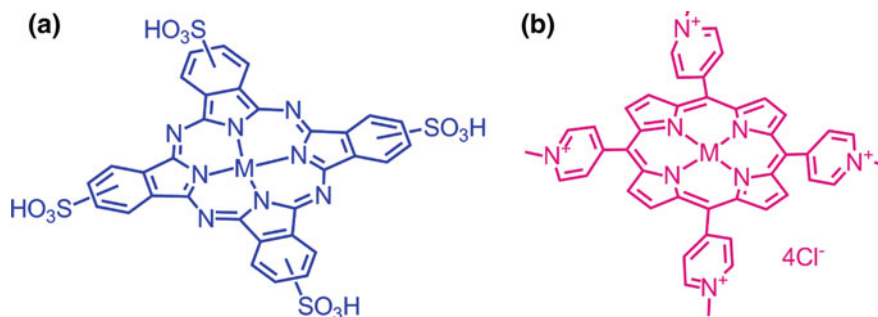
3.3.2 Porphyrin and Porphyrin–Phthalocyanine Constructs

Self-assembling of cations by exploiting electrostatic interactions is an elegant and simple way of semiconductor modification. By this way, cationic porphyrin was self-assembled on the surface of SnO₂ nanoparticles and photovoltaic properties of the resulting cell with the OTE/SnO₂/(cationic porphyrin) anode were investigated [161]. A water-soluble Zn(TMPPyP) dye was used. The use of this simple photoanode resulted in PCE of the cell of 0.31 % (Table 40). However, a dye with a broader UV–vis absorbance wavelength range is required to increase the j_{sc} of the SC. To meet this requirement, a mixed porphyrin–phthalocyanine dyad was assembled for a panchromatic supramolecular SC (Scheme 71) [162]. This water-soluble dyad was self-assembled on the surface of SnO₂ nanoparticles. The selected porphyrin and phthalocyanine had complementary light-absorbing and electronic properties, resulting in panchromatic absorbance and higher IPCE in the wavelength range of 400–750 nm. The IPCE spectrum had two maxima of the ~80 % corresponding to the Soret bands of these dyes. Moreover, the gap of the wavelength range in the absorbance spectra between the two Soret bands was filled by the Q-band of the porphyrin, thus increasing efficiency of the SC (Table 40).

Table 40 Photovoltaic performance of a photoelectrochemical cell of the OTE/SnO₂/(Active material) structure

Active layer	V_{oc} (V)	J_{sc} (mA cm ⁻²)	FF	η (%)	Ref.
Zn(TMPPyP)	0.18	4.7	0.38	0.31	[161]
H ₂ (TMPPyP)	0.13	3.7	0.31	0.15	[161]
Zn(PcS)	0.18	3.2	0.34	0.19	[162]
H ₂ (PcS)	0.17	3.1	0.33	0.17	[162]
Zn(PcS):Zn(TMPPyP)	0.19	7.0	0.31	0.50	[162]
Zn(PcS):H ₂ (TMPPyP)	0.19	5.7	0.31	0.34	[162]
H ₂ (PcS):Zn(TMPPyP)	0.15	5.4	0.29	0.23	[162]
H ₂ (PcS):H ₂ (TMPPyP)	0.17	5.4	0.31	0.29	[162]

Electrolyte: acetonitrile solution of 0.5 M (TBA)I and 0.05 M I₂



Scheme 71 Structural formula of **a** phthalocyanine **b** porphyrin ($M = \text{Zn}$ or 2H) used for the porphyrin–phthalocyanine dyad assembly on the surface of SnO_2 nanoparticles. Reproduced from Ref. [161] with permission of The Royal Society of Chemistry

The top-performing SC in this series had the $\text{Zn}(\text{PcS})\text{:Zn}(\text{TMPyP})$ active material and its PCE was 0.5 % (Table 40).

In search for new organic materials for SCs, conjugates of MPs with semiconducting SWCNTs and [60]fullerene were studied [163–165]. The SWCNTs (6,5) and (7,6), and MPs were self-assembled via π – π interaction of the SWCNTs and pyrene substituents of the ZnP [163], or long alkyl chain peripheral substituents of ZnP [164], or through combination of π – π interactions of SWCNTs with the pyrene followed by cation–dipole binding of the MP’s crown-ether substituents (Scheme 72) [165]. Three-layer conjugate was produced by applying the metal–ligand axial binding of the C_{60} imidazole adduct to the central Zn atom of the porphyrin–SWCNTs assembled [164].

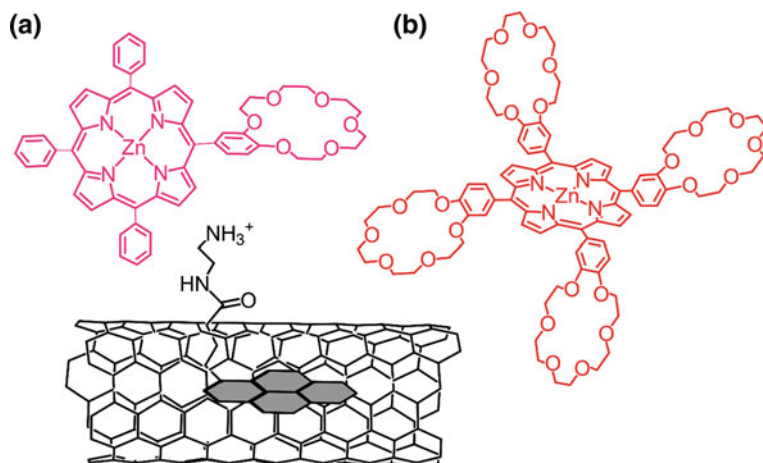
For the SWCNTs–ZnP construct, the recorded ICPE spectrum resembled the UV–vis spectrum of the corresponding ZnP. A maximum of 12 % in the IPCE spectrum was observed in the Soret band wavelength region of the ZnP at the ~ 430 nm.

Interestingly, application of semiconducting SWCNTs modified with the C_{60} imidazole adduct with porphyrin resulted in a lower IPCE with ~ 1 % conversion at ~ 430 nm [164].

3.3.3 Porphyrin–Graphene Donor–Acceptor Constructs

Since functionalization of the graphene with a porphyrin was reported for the first time [166], photovoltaic properties of this type constructs have intensively been studied. Photovoltaic properties of an assembly of the covalently linked free-base *meso*-tetraphenyl porphyrin with graphene oxide were evaluated [167]. The IPCE spectrum of this conjugate resembled the UV–vis absorbance spectrum of the porphyrin used reaching merely 1.5 % at the Soret band wavelength.

A differently synthesized “forest” of porphyrins was prepared on the graphene surface and its photovoltaic properties were evaluated [168, 169]. The maximum of



Scheme 72 Structural formulas of **a** single crown-ether modified ZnP, **b** tetra crown-ether modified ZnP, and **c** semiconducting SWCNT with π - π stacked alkyl-ammonium-functionalized pyrene. Adapted by permission of John Wiley & Sons, Inc from Sandanayaka ASD, Subbaiyan NK, Das SK, Chitta R, Maligaspe E, Hasobe T, Ito O, D'Souza F (2011) Diameter-sorted SWCNT-porphyrin and SWCNT-phthalocyanine conjugates for light energy harvesting *ChemPhysChem* 12(12):2266–2273, Copyright (2011) by John Wiley Sons, Inc.

the IPCE spectrum of the composite of chemically converted graphene with covalently connected porphyrin reached 3 % at 400 nm [169]. In order to increase performance of the graphene-containing materials, a ternary composite of a ZnP, reduced graphene oxide, and ZnO nanoparticles was devised [170]. This composite was sequentially assembled on the FTO photoanode of a supramolecular SC and the photovoltaic performance of the cell was evaluated. The SC of the FTO/SnO₂/(RGO/ZnO/ZnP composite) structure was tested using an acetonitrile solution of 0.5 M LiI and 0.01 M I₂ as the electrolyte under the applied constant potential of 0.05 V versus SCE. The recorded IPCE spectrum of the cell resembled that of the porphyrin UV–vis absorbance spectrum reaching maximal value of 70 % at the Soret band wavelength.

3.3.4 Conclusions on Porphyrin-Containing Supramolecular Solar Cells

The porphyrin-containing supramolecular SCs serve as test grounds for new donor–acceptor dyads or composites of potential application in SCs. Constructing of these dyads and photoelectrochemical cells, followed by the charge separation studies in D–A dyads, is an indispensable step in devising new organic photovoltaic materials. Therefore, it should be kept in mind when evaluating results of performance of these cells that they present rather proofs of concepts. The graphene-containing

photoactive materials performing in SCs comparably to the high-performing DSSCs or polymer BHJ SCs are yet to be designed, while application of $\text{Li}^+@\text{C}_{60}$ as the electron acceptor in SCs is promising.

4 Conclusion

In conclusion, the present chapter provides the up-to-date review on the utility of molecularly engineered porphyrins for DSSC, BHJ-OPV, and SSC applications. Among the different porphyrin systems developed for DSSC applications, the *meso*-substituted, donor- π -bridged ‘push-pull’ (A2BC) type chromophore-acceptor porphyrins have revealed the highest performance. In the design of A2BC-type porphyrins bearing an ethynylcarboxyphenyl anchoring group (B position) tailored with a strong donor group at the opposite site (C position) have been very promising. The remaining *meso*-positions (‘A’ positions) consisted of alkoxy-substituted phenyl ring playing an active role in reducing dye aggregation and charge recombination process. The SM315- and GY50-sensitized solar cells have exhibited a η -value of 13 %, a light energy conversion efficiency better than those of ruthenium polypyridyl sensitizer-based DSSCs. Further improvements are needed to realize porphyrin-based DSSCs for generating large-scale solar-electricity production. These include (i) extending the light-harvesting ability of porphyrins into the near-IR region (700–900 nm range), and providing the needed photostability under continuous illumination conditions; (ii) avoiding porphyrin aggregation on semiconductor surface to block unnecessary quenching of the excited singlet state; (iii) promoting electron injection while inhibiting charge recombination at the interface by controlling the structure and orientation of the sensitizer immobilized on the semiconductor surface; and (iv) exploring novel redox couples capable of increasing V_{OC} and fill factors.

For the BHJ-OPV success, further engineering of porphyrin systems are needed to seek advantage in increasing its competitiveness. Inventive design of porphyrins by talented synthetic chemists is perhaps an essential part to realize a higher success leading to commercial products. Other factors, such as efficiency, durability, and scalability, will also be contributing factors.

Research in the area of SSC is still emerging. If successful in terms of performance, this ‘self-healing’ capable methodology could be used in paintbrush technology to reduce the cost of solar panels. Consequently, much could be anticipated in the coming years from different research groups across the globe on this timely research topic.

Acknowledgements The authors are thankful to the Polish National Science Centre for financial support through the Grant No. NCN 2014/15/B/N27/01011 to W.K, and the US-National Science Foundation, through Grant Nos. 1110942 and 1401188 to F.D.

References

1. Darling SB, You F (2013) The case for organic photovoltaics. *RSC Adv* 3(39):17633–17648
2. Green MA, Emery K, Hishikawa Y et al (2015) Solar cell efficiency tables (Version 45). *Prog Photovolt Res Appl* 23(1):1–9
3. Cohen ER, Cvitas T, Frey JG et al (eds) (2008) Quantities, units and symbols in physical chemistry, IUPAC Green Book, 3rd edn. IUPAC & RSC Publishing, Cambridge
4. Tang CW (1986) Two-layer organic photovoltaic cell. *Appl Phys Lett* 48(2):183–185
5. Schlenker CW, Thompson ME (2011) The molecular nature of photovoltage losses in organic solar cells. *Chem Commun* 47(13):3702–3716
6. O'Regan B, Grätzel M (1991) Low-cost, high-efficiency solar cell based on dye-sensitized colloidal TiO₂ films. *Nature* 353(6346):737–740
7. Higashino T, Imahori H (2015) Porphyrins as excellent dyes for dye-sensitized solar cells: recent developments and insights. *Dalton Trans* 44(2):448–463
8. Robson KCD, Bomben PG, Berlinguette CP (2012) Cycloruthenated sensitizers: improving the dye-sensitized solar cell with classical inorganic chemistry principles. *Dalton Trans* 41(26):7814–7829
9. Mathew S, Yella A, Gao P et al (2014) Dye-sensitized solar cells with 13 % efficiency achieved through the molecular engineering of porphyrin sensitizers. *Nat Chem* 6(3):242–247
10. Bessho T, Zakeeruddin SM, Yeh C-Y et al (2010) Highly efficient mesoscopic dye-sensitized solar cells based on donor-acceptor-substituted porphyrins. *Angew Chem Int Ed* 49(37):6646–6649
11. Mai C-L, Huang W-K, Lu H-P et al (2010) Synthesis and characterization of diporphyrin sensitizers for dye-sensitized solar cells. *Chem Commun* 46(5):809–811
12. Ladomenou K, Kitsopoulos TN, Sharma GD et al (2014) The importance of various anchoring groups attached on porphyrins as potential dyes for DSSC applications. *RSC Adv* 4(41):21379–21404
13. Zhang L, Cole JM (2015) Anchoring groups for dye-sensitized solar cells. *ACS Appl Mater Interfaces* 7(6):3427–3455
14. Ooyama Y, Nagano T, Inoue S et al (2011) Dye-sensitized solar cells based on donor- π -acceptor fluorescent dyes with a pyridine ring as an electron-withdrawing-injecting anchoring group. *Chem Eur J* 17(52):14837–14843
15. Ooyama Y, Inoue S, Nagano T et al (2011) Dye-sensitized solar cells based on donor-acceptor π -conjugated fluorescent dyes with a pyridine ring as an electron-withdrawing anchoring group. *Angew Chem Int Ed* 50(32):7429–7433
16. Ooyama Y, Yamada T, Fujita T et al (2014) Development of D- π -Cat fluorescent dyes with a catechol group for dye-sensitized solar cells based on dye-to-TiO₂ charge transfer. *J Mater Chem A* 2(22):8500–8511
17. Mao J, He N, Ning Z et al (2012) Stable dyes containing double acceptors without COOH as anchors for highly efficient dye-sensitized solar cells. *Angew Chem Int Ed* 51(39):9873–9876
18. Gou F, Jiang X, Li B et al (2013) Salicylic acid as a tridentate anchoring group for azo-bridged zinc porphyrin in dye-sensitized solar cells. *ACS Appl Mater Interfaces* 5(23):12631–12637
19. Barozzino Consiglio G, Pedna F, Fornaciari C et al (2013) Assessment of new gem-silanediods as suitable sensitizers for dye-sensitized solar cells. *J Organomet Chem* 723:198–206
20. Massin J, Ducasse L, Toupance T et al (2014) Tetrazole as a new anchoring group for the functionalization of TiO₂ nanoparticles: a joint experimental and theoretical study. *J Phys Chem C* 118(20):10677–10685

21. Brennan BJ, Llansola Portoles MJ, Liddell PA et al (2013) Comparison of silatrane, phosphonic acid, and carboxylic acid functional groups for attachment of porphyrin sensitizers to TiO₂ in photoelectrochemical cells. *Phys Chem Chem Phys* 15(39):16605–16614
22. Galoppini E (2004) Linkers for anchoring sensitizers to semiconductor nanoparticles. *Coord Chem Rev* 248(13–14):1283–1297
23. He H, Gurung A, Si L (2012) 8-Hydroxylquinoline as a strong alternative anchoring group for porphyrin-sensitized solar cells. *Chem Commun* 48(47):5910–5912
24. Guerrero G, Alauzun JG, Granier M et al (2013) Phosphonate coupling molecules for the control of surface/interface properties and the synthesis of nanomaterials. *Dalton Trans* 42(35):12569–12585
25. Namuangruk S, Sirithip K, Rattanatwan R et al (2014) Theoretical investigation of the charge-transfer properties in different *meso*-linked zinc porphyrins for highly efficient dye-sensitized solar cells. *Dalton Trans* 43(24):9166–9176
26. Imahori H, Hayashi S, Hayashi H et al (2009) Effects of porphyrin substituents and adsorption conditions on photovoltaic properties of porphyrin-sensitized TiO₂ cells. *J Phys Chem C* 113(42):18406–18413
27. Griffith MJ, Sunahara K, Wagner P et al (2012) Porphyrins for dye-sensitized solar cells: new insights into efficiency-determining electron transfer steps. *Chem Commun* 48(35):4145–4162
28. Hart AS, Kc CB, Gobeze HB et al (2013) Porphyrin-sensitized solar cells: effect of carboxyl anchor group orientation on the cell performance. *ACS Appl Mater Interfaces* 5(11):5314–5323
29. Rangan S, Coh S, Bartynski RA et al (2012) Energy alignment, molecular packing, and electronic pathways: zinc(II) tetraphenylporphyrin derivatives adsorbed on TiO₂(110) and ZnO(11–20) surfaces. *J Phys Chem C* 116(45):23921–23930
30. Lindsey JS (2010) Synthetic routes to *meso*-patterned porphyrins. *Acc Chem Res* 43(2):300–311
31. Ju M-G, Liang W (2013) Computational insight on the working principles of zinc porphyrin dye-sensitized solar cells. *J Phys Chem C* 117(29):14899–14911
32. Y-c Li, Y-q Feng, Y-t Wang et al (2014) Design of high-performance chlorine type dyes for dye-sensitized solar cells. *Int J Quantum Chem* 114(3):222–232
33. Guo M, He R, Dai Y et al (2012) Electron-deficient pyrimidine adopted in porphyrin sensitizers: a theoretical interpretation of π -spacers leading to highly efficient photo-to-electric conversion performances in dye-sensitized solar cells. *J Phys Chem C* 116(16):9166–9179
34. Urbani M, Grätzel M, Nazeeruddin MK et al (2014) *meso*-Substituted porphyrins for dye-sensitized solar cells. *Chem Rev* 114(24):12330–12396
35. de Tacconi NR, Chanmanee W, Rajeshwar K et al (2009) Photoelectrochemical behavior of polychelate porphyrin chromophores and titanium dioxide nanotube arrays for dye-sensitized solar cells. *J Phys Chem C* 113(7):2996–3006
36. Xue X, Zhang W, Zhang N et al (2014) Effect of the length of the alkyl chains in porphyrin *meso*-substituents on the performance of dye-sensitized solar cells. *RSC Adv* 4(17):8894–8900
37. Liu Y, Xiang N, Feng X et al (2009) Thiophene-linked porphyrin derivatives for dye-sensitized solar cells. *Chem Commun* 18:2499–2501
38. Santhanamoorthi N, Lo C-M, Jiang J-C (2013) Molecular design of porphyrins for dye-sensitized solar cells: a DFT/TDDFT study. *J Phys Chem Lett* 4(3):524–530
39. Zhang X, Chen Q, Sun H et al (2014) Theoretical design and screening of alkyne bridged triphenyl zinc porphyrins as sensitizer candidates for dye-sensitized solar cells. *Spectrochim Acta Mol Biomol Spectrosc* 118:564–571
40. Ragoussi M-E, de la Torre G (2013) Torres T (2013) Tuning the electronic properties of porphyrin dyes: effects of *meso* substitution on their optical and electrochemical behaviour. *Eur J Org Chem* 14:2832–2840

41. Lee C-W, Lu H-P, Lan C-M et al (2009) Novel zinc porphyrin sensitizers for dye-sensitized solar cells: synthesis and spectral, electrochemical, and photovoltaic properties. *Chem Eur J* 15(6):1403–1412
42. He H, Gurung A, Si L et al (2012) A simple acrylic acid functionalized zinc porphyrin for cost-effective dye-sensitized solar cells. *Chem Commun* 48(61):7619–7621
43. Gou F, Jiang X, Fang R et al (2014) Strategy to improve photovoltaic performance of dssc sensitized by zinc porphyrin using salicylic acid as a tridentate anchoring group. *ACS Appl Mater Interfaces* 6(9):6697–6703
44. Lin C-Y, Lo C-F, Luo L et al (2009) Design and characterization of novel porphyrins with oligo(phenylethynyl) links of varied length for dye-sensitized solar cells: synthesis and optical, electrochemical, and photovoltaic investigation. *J Phys Chem C* 113(2):755–764
45. Guo M, Li M, Dai Y et al (2013) Exploring the role of varied-length spacers in charge transfer: a theoretical investigation on pyrimidine-bridged porphyrin dyes. *RSC Adv* 3(38):17515–17526
46. Lin C-Y, Wang Y-C, Hsu S-J et al (2010) Preparation and spectral, electrochemical, and photovoltaic properties of acene-modified zinc porphyrins. *J Phys Chem C* 114(1):687–693
47. Daphnomili D, Sharma GD, Biswas S et al (2013) A new porphyrin bearing a pyridinylethynyl group as sensitizer for dye sensitized solar cells. *J Photochem Photobiol A* 253:88–96
48. Daphnomili D, Landrou G, Prakash Singh S et al (2012) Photophysical, electrochemical and photovoltaic properties of dye sensitized solar cells using a series of pyridyl functionalized porphyrin dyes. *RSC Adv* 2(33):12899–12908
49. Boyle NM, Rochford J, Pryce MT (2010) Thienyl-appended porphyrins: synthesis, photophysical and electrochemical properties, and their applications. *Coord Chem Rev* 254(1–2):77–102
50. Zhou W, Zhao B, Shen P et al (2011) Multi-alkylthienyl appended porphyrins for efficient dye-sensitized solar cells. *Dyes Pigm* 91(3):404–412
51. Rao PD, Dhanalekshmi S, Littler BJ et al (2000) Rational syntheses of porphyrins bearing up to four different *meso* substituents. *J Org Chem* 65(22):7323–7344
52. Panda MK, Sharma GD, Justin Thomas KR et al (2012) A new family of A2B2 type porphyrin derivatives: synthesis, physicochemical characterization and their application in dye-sensitized solar cells. *J Mater Chem* 22(16):8092–8102
53. Lee CY, She C, Jeong NC et al (2010) Porphyrin sensitized solar cells: TiO₂ sensitization with a π -extended porphyrin possessing two anchoring groups. *Chem Commun* 46(33):6090–6092
54. Werner F, Gnichwitz J-F, Marczak R et al (2010) Grafting porphyrins (face-to-edge/orthogonal versus face-to-face/parallel) to ZnO en route toward dye-sensitized solar cells. *J Phys Chem B* 114(45):14671–14678
55. Pasunooti KK, Song J-L, Chai H et al (2011) Synthesis, characterization and application of *trans*-D-B-A-porphyrin based dyes in dye-sensitized solar cells. *J Photochem Photobiol A* 218(2–3):219–225
56. Lee MJ, Seo KD, Song HM et al (2011) Novel D- π -A system based on zinc-porphyrin derivatives for highly efficient dye-sensitized solar cells. *Tetrahedron Lett* 52(30):3879–3882
57. Seo KD, Lee MJ, Song HM et al (2012) Novel D- π -A system based on zinc porphyrin dyes for dye-sensitized solar cells: synthesis, electrochemical, and photovoltaic properties. *Dyes Pigm* 94(1):143–149
58. Warman J, Buchet F, Pellegrin Y et al (2011) Panchromatic trichromophoric sensitizer for dye-sensitized solar cells using antenna effect. *Org Lett* 13(15):3944–3947
59. Khan TK, Bröring M, Mathur S et al (2013) Boron dipyrin-porphyrin conjugates. *Coord Chem Rev* 257(15–16):2348–2387
60. Kang MS, Kang SH, Kim SG et al (2012) Novel D- π -A structured Zn(II)-porphyrin dyes containing a bis(3,3-dimethylfluorenyl)amine moiety for dye-sensitized solar cells. *Chem Commun* 48(75):9349–9351

61. Kang SH, Choi IT, Kang MS et al (2013) Novel D- π -A structured porphyrin dyes with diphenylamine derived electron-donating substituents for highly efficient dye-sensitized solar cells. *J Mater Chem A* 1(12):3977–3982
62. Kang MS, Choi IT, Kim YW et al (2013) Novel D- π -A structured Zn(II)-porphyrin dyes with bulky fluorenyl substituted electron donor moieties for dye-sensitized solar cells. *J Mater Chem A* 1(34):9848–9852
63. Imahori H, Matsubara Y, Iijima H et al (2010) Effects of *meso*-diarylamino group of porphyrins as sensitizers in dye-sensitized solar cells on optical, electrochemical, and photovoltaic properties. *J Phys Chem C* 114(23):10656–10665
64. Hsieh C-P, Lu H-P, Chiu C-L et al (2010) Synthesis and characterization of porphyrin sensitizers with various electron-donating substituents for highly efficient dye-sensitized solar cells. *J Mater Chem* 20(6):1127–1134
65. Pelleja L, Kumar CV, Clifford JN et al (2014) D- π -A porphyrin employing an indoline donor group for high efficiency dye-sensitized solar cells. *J Phys Chem C* 118(30):16504–16509
66. Wagner K, Griffith MJ, James M et al (2011) Significant performance improvement of porphyrin-sensitized TiO₂ solar cells under white light illumination. *J Phys Chem C* 115(1):317–326
67. Wagner P, Ewels CP, Adjizian J-J et al (2013) Band gap engineering via edge-functionalization of graphene nanoribbons. *J Phys Chem C* 117(50):26790–26796
68. Chang Y-C, Wang C-L, Pan T-Y et al (2011) A strategy to design highly efficient porphyrin sensitizers for dye-sensitized solar cells. *Chem Commun* 47(31):8910–8912
69. Wang C-L, Chang Y-C, Lan C-M et al (2011) Enhanced light harvesting with π -conjugated cyclic aromatic hydrocarbons for porphyrin-sensitized solar cells. *Energy Environ Sci* 4(5):1788–1795
70. Wu C-H, Pan T-Y, Hong S-H et al (2012) A fluorene-modified porphyrin for efficient dye-sensitized solar cells. *Chem Commun* 48(36):4329–4331
71. Lo C-F, Hsu S-J, Wang C-L et al (2010) Tuning spectral and electrochemical properties of porphyrin-sensitized solar cells. *J Phys Chem C* 114(27):12018–12023
72. Wang C-L, Lan C-M, Hong S-H et al (2012) Enveloping porphyrins for efficient dye-sensitized solar cells. *Energy Environ Sci* 5(5):6933–6940
73. Lu H-P, Mai C-L, Tsia C-Y et al (2009) Design and characterization of highly efficient porphyrin sensitizers for green see-through dye-sensitized solar cells. *Phys Chem Chem Phys* 11(44):10270–10274
74. Wu S-L, Lu H-P, Yu H-T et al (2010) Design and characterization of porphyrin sensitizers with a push-pull framework for highly efficient dye-sensitized solar cells. *Energy Environ Sci* 3(7):949–955
75. Barea EM, González-Pedro V, Ripollés-Sanchis T et al (2011) Porphyrin dyes with high injection and low recombination for highly efficient mesoscopic dye-sensitized solar cells. *J Phys Chem C* 115(21):10898–10902
76. Mathew S, Iijima H, Toude Y et al (2011) Optical, electrochemical, and photovoltaic effects of an electron-withdrawing tetrafluorophenylene bridge in a push-pull porphyrin sensitizer used for dye-sensitized solar cells. *J Phys Chem C* 115(29):14415–14424
77. Hsu H-Y, Chiang H-C, Hu J-Y et al (2013) Field-induced fluorescence quenching and enhancement of porphyrin sensitizers on TiO₂ films and in PMMA films. *J Phys Chem C* 117(47):24761–24766
78. Yella A, Lee H-W, Tsao HN et al (2011) Porphyrin-sensitized solar cells with cobalt (II/III)-based redox electrolyte exceed 12 percent efficiency. *Science* 334(6056):629–634
79. Yum J-H, Baranoff E, Kessler F et al (2012) A cobalt complex redox shuttle for dye-sensitized solar cells with high open-circuit potentials. *Nat Commun* 3:631
80. Feldt SM, Gibson EA, Gabrielsson E et al (2010) Design of organic dyes and cobalt polypyridine redox mediators for high-efficiency dye-sensitized solar cells. *J Am Chem Soc* 132(46):16714–16724

81. di Nunzio MR, Cohen B, Pandey S et al (2014) Spectroscopy and dynamics of YD2-o-C8 in solution and interacting with alumina nanoparticles electrode. *J Phys Chem C* 118(21): 11365–11376
82. Ripolles-Sanchis T, Guo B-C, Wu H-P et al (2012) Design and characterization of alkoxy-wrapped push-pull porphyrins for dye-sensitized solar cells. *Chem Commun* 48(36):4368–4370
83. Davis NKS, Thompson AL, Anderson HL (2010) *bis*-Anthracene fused porphyrins: synthesis, crystal structure, and near-IR absorption. *Org Lett* 12(9):2124–2127
84. Davis NKS, Thompson AL, Anderson HL (2011) A porphyrin fused to four anthracenes. *J Am Chem Soc* 133(1):30–31
85. Ball JM, Davis NKS, Wilkinson JD et al (2012) A panchromatic anthracene-fused porphyrin sensitizer for dye-sensitized solar cells. *RSC Adv* 2(17):6846–6853
86. Luo J, Xu M, Li R et al (2014) *N*-Annulated perylene as an efficient electron donor for porphyrin-based dyes: enhanced light-harvesting ability and high-efficiency Co(II/III)-based dye-sensitized solar cells. *J Am Chem Soc* 136(1):265–272
87. Wu C-H, Chen M-C, Su P-C et al (2014) Porphyrins for efficient dye-sensitized solar cells covering the near-IR region. *J Mater Chem A* 2(4):991–999
88. Wang C-L, Hu J-Y, Wu C-H et al (2014) Highly efficient porphyrin-sensitized solar cells with enhanced light harvesting ability beyond 800 nm and efficiency exceeding 10 %. *Energy Environ Sci* 7(4):1392–1396
89. Chang Y-C, Wu H-P, Reddy NM et al (2013) The influence of electron injection and charge recombination kinetics on the performance of porphyrin-sensitized solar cells: effects of the 4-*tert*-butylpyridine additive. *Phys Chem Chem Phys* 15(13):4651–4655
90. Masi Reddy N, Pan T-Y, Christu Rajan Y et al (2013) Porphyrin sensitizers with π -extended pull units for dye-sensitized solar cells. *Phys Chem Chem Phys* 15(21):8409–8415
91. Lu J, Xu X, Cao K et al (2013) D- π -A structured porphyrins for efficient dye-sensitized solar cells. *J Mater Chem A* 1(34):10008–10015
92. Wang Y, Xu L, Wei X et al (2014) 2-Diphenylaminothiophene as the donor of porphyrin sensitizers for dye-sensitized solar cells. *New J Chem* 38(7):3227–3235
93. Yella A, Mai C-L, Zakeeruddin SM et al (2014) Molecular engineering of push-pull porphyrin dyes for highly efficient dye-sensitized solar cells: the role of benzene spacers. *Angew Chem Int Ed* 53(11):2973–2977
94. Haid S, Marszalek M, Mishra A et al (2012) Significant improvement of dye-sensitized solar cell performance by small structural modification in π -conjugated donor-acceptor dyes. *Adv Funct Mater* 22(6):1291–1302
95. Kurotobi K, Toude Y, Kawamoto K et al (2013) Highly asymmetrical porphyrins with enhanced push-pull character for dye-sensitized solar cells. *Chem Eur J* 19(50):17075–17081
96. Hiramoto M, Fujiwara H, Yokoyama M (1991) Three-layered organic solar cell with a photoactive interlayer of codeposited pigments. *Appl Phys Lett* 58(10):1062–1064
97. Umeyama T, Imahori H (2014) Design and control of organic semiconductors and their nanostructures for polymer-fullerene-based photovoltaic devices. *J Mater Chem A* 2(30): 11545–11560
98. Hou J, Guo X (2013) Active layer materials for organic solar cells. Materials and device physics. In: Choy WCH (ed) *organic solar cells*. Springer, London, pp 17–42
99. Brabec C, Scherf U, Dyakonov V (eds) (2008) *Organic photovoltaics: materials, device physics, and manufacturing technologies*. Wiley VCH, Weinheim
100. He Z, Zhong C, Su S et al (2012) Enhanced power-conversion efficiency in polymer solar cells using an inverted device structure. *Nat Photon* 6(9):591–595
101. You J, Dou L, Yoshimura K et al (2013) A polymer tandem solar cell with 10.6 % power conversion efficiency. *Nat Commun* (4):1446
102. Green MA, Emery K, Hishikawa Y et al (2014) Solar cell efficiency tables (version 44). *Prog Photovolt: Res Appl* 22(7):701–710
103. Heeger AJ (2010) Semiconducting polymers: the third generation. *Chem Soc Rev* 39(7): 2354–2371

104. Stille JK (1986) Palladium-katalysierte kupplungsreaktionen organischer elektrophile mit organozinn-verbindungen. *Angew Chem* 98(6):504–519
105. Lunxiang Y, Liebscher J (2007) Carbon-carbon coupling reactions catalyzed by heterogeneous palladium catalysts. *Chem Rev* 107(1):133–173
106. Oku T, Noma T, Suzuki A et al (2010) Fabrication and characterization of fullerene/porphyrin bulk heterojunction solar cells. *J Phys Chem Solids* 71(4):551–555
107. Belcher WJ, Wagner KI, Dastoor PC (2007) The effect of porphyrin inclusion on the spectral response of ternary P3HT:porphyrin:PCBM bulk heterojunction solar cells. *Sol Energy Mater Sol Cells* 91(6):447–452
108. Vasilopoulou M, Georgiadou DG, Douvas AM et al (2014) Porphyrin oriented self-assembled nanostructures for efficient exciton dissociation in high-performing organic photovoltaics. *J Mater Chem A* 2(1):182–192
109. Vasilopoulou M, Douvas A, Georgiadou D et al (2014) Large work function shift of organic semiconductors inducing enhanced interfacial electron transfer in organic optoelectronics enabled by porphyrin aggregated nanostructures. *Nano Res* 7(5):679–693
110. Said AJ, Poize G, Martini C et al (2010) Hybrid bulk heterojunction solar cells based on P3HT and porphyrin-modified ZnO nanorods. *J Phys Chem C* 114(25):11273–11278
111. Kahnt A, Kärnbratt J, Esdaile LJ et al (2011) Temperature dependence of charge separation and recombination in porphyrin oligomer-fullerene donor-acceptor systems. *J Am Chem Soc* 133(25):9863–9871
112. Wang C-L, Zhang W-B, Van Horn RM et al (2011) A porphyrin-fullerene dyad with a supramolecular “double-cable” structure as a novel electron acceptor for bulk heterojunction polymer solar cells. *Adv Mater* 23(26):2951–2956
113. Rawson J, Stuart AC, You W et al (2014) Tailoring porphyrin-based electron accepting materials for organic photovoltaics. *J Am Chem Soc* 136(50):17561–17569
114. Matsuo Y, Sato Y, Niinomi T et al (2009) Columnar structure in bulk heterojunction in solution-processable three-layered p-i-n organic photovoltaic devices using tetrabenzoporphyrin precursor and silylmethyl[60]fullerene. *J Am Chem Soc* 131(44):16048–16050
115. Ku S-Y, Liman CD, Cochran JE et al (2011) Solution-processed nanostructured benzoporphyrin with polycarbonate binder for photovoltaics. *Adv Mater* 23(20):2289–2293
116. Li M, Ishihara S, Akada M et al (2011) Electrochemical-coupling layer-by-layer (ECC-LbL) assembly. *J Am Chem Soc* 133(19):7348–7351
117. Sharma GD, Daphnomili D, Biswas S et al (2013) New soluble porphyrin bearing a pyridinylethynyl group as donor for bulk heterojunction solar cells. *Org Electron* 14(7):1811–1819
118. Li Y, Bian Y, Yan M et al (2011) Mixed (porphyrinato)(phthalocyaninato) rare-earth(III) double-decker complexes for broadband light harvesting organic solar cells. *J Mater Chem* 21(30):11131–11141
119. Huang Y, Li L, Peng X et al (2012) Solution processed small molecule bulk heterojunction organic photovoltaics based on a conjugated donor-acceptor porphyrin. *J Mater Chem* 22(41):21841–21844
120. Li L, Huang Y, Peng J et al (2013) Enhancing the performance of porphyrin based solar cells by the bipy coordination. *Org Electron* 14(12):3430–3436
121. Li L, Huang Y, Peng J et al (2013) Enhanced performance of solution-processed solar cells based on porphyrin small molecules with a diketopyrrolopyrrole acceptor unit and a pyridine additive. *J Mater Chem A* 1(6):2144–2150
122. Hatano J, Obata N, Yamaguchi S et al (2012) Soluble porphyrin donors for small molecule bulk heterojunction solar cells. *J Mater Chem* 22(36):19258–19263
123. Yamamoto T, Hatano J, Nakagawa T et al (2013) Small molecule solution-processed bulk heterojunction solar cells with inverted structure using porphyrin donor. *Appl Phys Lett* 102(1):013305
124. Matsuo Y, Hatano J, Nakagawa T (2014) *cis*-Substituted tetraethynylporphyrin derivatives for small molecule organic solar cells. *J Phys Org Chem* 27(2):87–93

125. Kengthanomma T, Thamyongkit P, Gasiorowski J et al (2013) On the potential of porphyrin-spiked triarylamine stars for bulk heterojunction solar cells. *J Mater Chem A* 1(35):10524–10531
126. Luechai A, Gasiorowski J, Petsom A et al (2012) Photosensitizing porphyrin-triazine compound for bulk heterojunction solar cells. *J Mater Chem* 22(43):23030–23037
127. Sharma GD, Zervaki GE, Angaridis PA et al (2014) Triazine-bridged porphyrin triad as electron donor for solution-processed bulk hetero-junction organic solar cells. *J Phys Chem C* 118(11):5968–5977
128. Cooling N, Burke KB, Zhou X et al (2011) A study of the factors influencing the performance of ternary MEH-PPV:porphyrin:PCBM heterojunction devices: a steric approach to controlling charge recombination. *Sol Energy Mater Sol Cells* 95(7):1767–1774
129. Lyons DM, Kesters J, Maes W et al (2013) Improving efficiencies by modulating the central metal ion in porphyrin-oligothiophene-mediated P3HT/PCBM organic solar cells. *Synth Met* 178:56–61
130. Huang X, Zhu C, Zhang S et al (2008) Porphyrin-dithienothiophene-conjugated copolymers: synthesis and their applications in field-effect transistors and solar cells. *Macromolecules* 41(19):6895–6902
131. Umeyama T, Takamatsu T, Tezuka N et al (2009) Synthesis and photophysical and photovoltaic properties of porphyrin-furan and -thiophene alternating copolymers. *J Phys Chem C* 113(24):10798–10806
132. Xiang N, Liu Y, Zhou W et al (2010) Synthesis and characterization of porphyrin-terthiophene and oligothiophene π -conjugated copolymers for polymer solar cells. *Eur Polym J* 46(5):1084–1092
133. Walter MG, Wamser CC (2010) Synthesis and characterization of electropolymerized nanostructured aminophenylporphyrin films. *J Phys Chem C* 114(17):7563–7574
134. Zhou W, Shen P, Zhao B et al (2011) Low band gap copolymers consisting of porphyrins, thiophenes, and 2,1,3-benzothiadiazole moieties for bulk heterojunction solar cells. *J Polym Sci A Polym Chem* 49(12):2685–2692
135. Liu Y, Guo X, Xiang N et al (2010) Synthesis and photovoltaic properties of polythiophene stars with porphyrin core. *J Mater Chem* 20(6):1140–1146
136. Zhou W, Jin F, Huang X et al (2012) A low-bandgap conjugated copolymer based on porphyrin and dithienocoronene diimide with strong two-photon absorption. *Macromolecules* 45(19):7823–7828
137. Huang X, Shi Q, Chen W-Q et al (2010) Low-bandgap conjugated donor-acceptor copolymers based on porphyrin with strong two-photon absorption. *Macromolecules* 43(23):9620–9626
138. Zhan H, Lamare S, Ng A et al (2011) Synthesis and photovoltaic properties of new metalloporphyrin-containing polyplatinyne polymers. *Macromolecules* 44(13):5155–5167
139. Masai H, Sonogashira K, Hagihara N (1971) Electronic spectra of square-planar bis(tertiary phosphine)dialkynyl complexes of nickel(II), palladium(II), and platinum(II). *Bull Chem Soc Jpn* 44(8):2226–2230
140. Lee JY, Song HJ, Lee SM et al (2011) Synthesis and investigation of photovoltaic properties for polymer semiconductors based on porphyrin compounds as light-harvesting units. *Eur Polym J* 47(8):1686–1693
141. Deng L, Gu Z, Cao Z et al (2012) Synthesis and characterization of novel D-A porphyrin-containing copolymers for polymer solar cells. *Mater Sci Eng B* 177(18):1641–1648
142. Wu Y-C, Chao Y-H, Wang C-L et al (2012) Porphyrin-diindenothiophene[2,3-b]thiophene alternating copolymer-a blue-light harvester in ternary-blend polymer solar cells. *J Polym Sci A Polym Chem* 50(24):5032–5040
143. Shi S, Wang X, Sun Y et al (2012) Porphyrin-containing D- π -A conjugated polymer with absorption over the entire spectrum of visible light and its applications in solar cells. *J Mater Chem* 22(22):11006–11008

144. Shi S, Jiang P, Chen S et al (2012) Effect of oligothiophene-bridge length on the photovoltaic properties of D-A copolymers based on carbazole and quinoxalinoporphyrin. *Macromolecules* 45(19):7806–7814
145. Jiang P, Shi S, Chen S et al (2013) Synthesis and characterization of porphyrin-based D- π -A conjugated polymers for polymer solar cells. *J Polym Sci A Polym Chem* 51(10):2243–2251
146. Chao YH, Jheng J-F, Wu J-S et al (2014) Porphyrin-incorporated 2D D-A polymers with over 8.5 % polymer solar cell efficiency. *Adv Mater* 26(30):5205–5210
147. Angiolini L, Benelli T, Cocchi V et al (2013) Side chain porphyrin moiety linked to polymer-fullerene composite solar cell. *React Funct Polym* 73(9):1198–1206
148. D'Souza F, Ito O (2009) Supramolecular donor-acceptor hybrids of porphyrins/phthalocyanines with fullerenes/carbon nanotubes: electron transfer, sensing, switching, and catalytic applications. *Chem Commun* 33:4913–4928
149. Bottari G, Trukhina O, Ince M et al (2012) Towards artificial photosynthesis: supramolecular, donor-acceptor, porphyrin- and phthalocyanine/carbon nanostructure ensembles. *Coord Chem Rev* 256(21–22):2453–2477
150. Ito O, D'Souza F (2012) Recent advances in photoinduced electron transfer processes of fullerene-based molecular assemblies and nanocomposites. *Molecules* 17(5):5816
151. de la Torre G, Bottari G, Sekita M et al (2013) A voyage into the synthesis and photophysics of homo- and heterobinuclear ensembles of phthalocyanines and porphyrins. *Chem Soc Rev* 42(20):8049–8105
152. Ito O, D'Souza F (2013) Light harvesting, photosensitized electron transfer in nanocarbon-sensitizer hybrids. *ECS J Solid State Sci Technol* 2(10):M3063–M3073
153. Lee CY, Jang JK, Kim CH et al (2010) Remarkably efficient photocurrent generation based on a [60]fullerene-triosmium cluster/Zn-porphyrin/boron-dipyrrin triad SAM. *Chem Eur J* 16(19):5586–5599
154. Subbaiyan NK, Obraztsov I, Wijesinghe CA et al (2009) Supramolecular donor-acceptor hybrid of electropolymerized zinc porphyrin with axially coordinated fullerene: formation, characterization, and photoelectrochemical properties. *J Phys Chem C* 113(20):8982–8989
155. Hasobe T, Saito K, Kamat PV et al (2007) Organic solar cells. Supramolecular composites of porphyrins and fullerenes organized by polypeptide structures as light harvesters. *J Mater Chem* 17(39):4160–4170
156. Fukuzumi S, Saito K, Ohkubo K et al (2011) Multiple photosynthetic reaction centres using zinc porphyrinic oligopeptide-fulleropyrrolidine supramolecular complexes. *Phys Chem Chem Phys* 13(38):17019–17022
157. Nobukuni H, Shimazaki Y, Uno H et al (2010) Supramolecular structures and photoelectronic properties of the inclusion complex of a cyclic free-base porphyrin dimer and C₆₀. *Chem Eur J* 16(38):11611–11623
158. Ohkubo K, Kawashima Y, Sakai H et al (2013) Enhanced photoelectrochemical performance of composite photovoltaic cells of Li⁺@C₆₀-sulphonated porphyrin supramolecular nanoclusters. *Chem Commun* 49(40):4474–4476
159. Kawashima Y, Ohkubo K, Fukuzumi S (2012) Enhanced photoinduced electron-transfer reduction of Li⁺@C₆₀ in comparison with C₆₀. *J Phys Chem A* 116(36):8942–8948
160. Kamimura T, Ohkubo K, Kawashima Y et al (2013) Submillisecond-lived photoinduced charge separation in inclusion complexes composed of Li⁺@C₆₀ and cyclic porphyrin dimers. *Chem Sci* 4(4):1451–1461
161. Subbaiyan NK, Maligaspe E, D'Souza F (2011) Near unity photon-to-electron conversion efficiency of photoelectrochemical cells built on cationic water-soluble porphyrins electrostatically decorated onto thin-film nanocrystalline SnO₂ surface. *ACS Appl Mater Interfaces* 3(7):2368–2376
162. Subbaiyan NK, D'Souza F (2012) Light-to-electron converting panchromatic supramolecular solar cells of phthalocyanine-porphyrin heterodimers adsorbed onto nanocrystalline SnO₂ electrodes. *Chem Commun* 48(30):3641–3643

163. Maligaspe E, Sandanayaka ASD, Hasobe T et al (2010) Sensitive efficiency of photoinduced electron transfer to band gaps of semiconductive single-walled carbon nanotubes with supramolecularly attached zinc porphyrin bearing pyrene glues. *J Am Chem Soc* 132(23):8158–8164
164. D'Souza F, Das SK, Sandanayaka ASD et al (2012) Photoinduced charge separation in three-layer supramolecular nanohybrids: fullerene-porphyrin-SWCNT. *Phys Chem Chem Phys* 14(8):2940–2950
165. Sandanayaka ASD, Subbaiyan NK, Das SK et al (2011) Diameter-sorted SWCNT-porphyrin and SWCNT-phthalocyanine conjugates for light-energy harvesting. *ChemPhysChem* 12(12):2266–2273
166. Xu Y, Liu Z, Zhang X et al (2009) A graphene hybrid material covalently functionalized with porphyrin: synthesis and optical limiting property. *Adv Mater* 21(12):1275–1279
167. Karousis N, Sandanayaka ASD, Hasobe T et al (2011) Graphene oxide with covalently linked porphyrin antennae: synthesis, characterization and photophysical properties. *J Mater Chem* 21(1):109–117
168. Wang H-X, Zhou K-G, Xie Y-L et al (2011) Photoactive graphene sheets prepared by “click” chemistry. *Chem Commun* 47(20):5747–5749
169. Umeyama T, Mihara J, Tezuka N et al (2012) Preparation and photophysical and photoelectrochemical properties of a covalently fixed porphyrin-chemically converted graphene composite. *Chem Eur J* 18(14):4250–4257
170. Hayashi H, Lightcap IV, Tsujimoto M et al (2011) Electron transfer cascade by organic/inorganic ternary composites of porphyrin, zinc oxide nanoparticles, and reduced graphene oxide on a tin oxide electrode that exhibits efficient photocurrent generation. *J Am Chem Soc* 133(20):7684–7687

Photoelectrochemical Reactions at Phthalocyanine Electrodes

Derek Schlettwein

1 Introduction

One major driving force for the study of photoelectrochemically active electrode materials is the search for alternative solar cells. The concepts of photoelectrochemistry have been explored mainly between 1960 and 1980 and a number of strategies were developed that worked quite efficiently for single-crystalline inorganic semiconductors. Subsequent research explored new systems of acceptable efficiency and stability that could be established at a more affordable price. The use of amorphous inorganic semiconductors or materials grown as thin films was one strategy, the use of organic semiconductors another. In all cases, chemical stability in particular under photoelectrochemical working conditions turned out to be a major problem. Photogenerated high-energy electron vacancies (holes) that are supposed to be harvested externally often also led to irreversible oxidation reactions at the semiconductor surface. Electron vacancies in the valence band of the semiconductor electrodes, therefore, had to be avoided. This could be achieved by the use of *n*-doped semiconductors with a band gap large enough to not absorb the incident light. This latter main task, however, is crucial for a working solar cell. Organic dye molecules can serve to efficiently absorb light in the visible range of the spectrum. A concept of sensitization was developed that combined chemically stable inorganic *n*-type wide-bandgap semiconductors with adsorbed dye molecules. To provide a stable and efficiently working electrode, the excited state of the dye molecule has to inject an electron into the conduction band of the semiconductor. The remaining electron vacancy in the (then oxidized) dye has to be transferred to a redox electrolyte at a sufficiently high rate to avoid irreversible reactions at the dye molecule. Oxide electrodes like TiO₂, ZnO, etc., sensitized by

D. Schlettwein (✉)

Institute of Applied Physics, Justus-Liebig-University Gießen, Heinrich-Buff-Ring 16,
D-35392 Gießen, Germany
e-mail: schlettwein@uni-giessen.de

covalently attached dye molecules turned out to be suitable candidates for such reactions. To avoid nonradiative decay, dye aggregates have to be avoided in most cases, asking for monolayer coverage of the semiconductor electrodes. Even at the high absorption coefficients reached by organic dyes, porous semiconductor electrodes with high internal surface area accessible by dye molecules and redox electrolytes are needed to provide a high overall dye concentration in the film and maximize the active semiconductor/dye interface. Based on this concept, a good chance is seen to develop photoelectrochemical solar cells since semiconducting electrodes can be prepared that absorb visible light and still provide sufficient chemical stability to convert solar energy at attractive efficiencies [1–14].

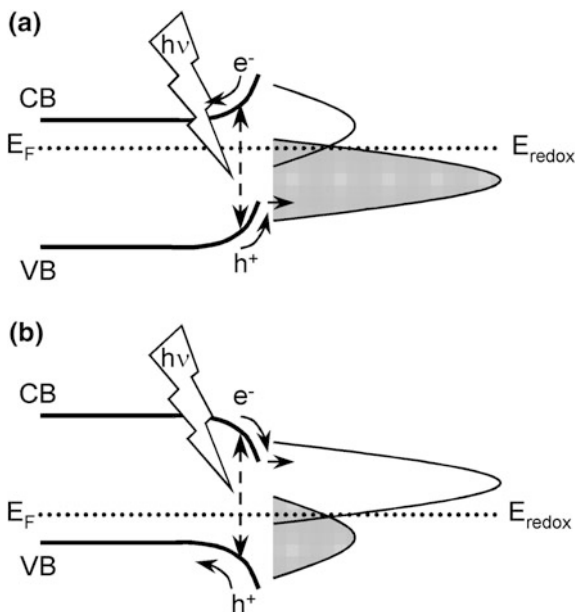
In photoelectrochemical studies on phthalocyanines the chromophore is either adsorbed as a dye to an inorganic oxide surface as outlined above or used in a pure pigment thin film, thereby also utilizing the semiconducting properties of solid phthalocyanines. The experiments with organic pigment thin films are performed to evaluate the feasibility of such an approach for solar energy conversion and also to investigate the role of dye aggregates at phthalocyanine-sensitized oxide electrodes. Such studies also provided quite fundamental insight. One major goal was to probe molecular materials in contact to electrolytes in order to establish aspects which are common and different, respectively, compared with classical semiconductors or insulators [15] on the one hand or in contact with a second solid on the other hand [16–20]. An important aspect in these studies was the use of photoelectrochemical reactions to characterize the electrical properties in thin films of molecular semiconductors and to analyze their surface properties. Mainly unsubstituted phthalocyanines Pc were studied as organic semiconductor photoelectrodes [21–55] or, with a chemical anchor group added, in the sensitization of oxide semiconductors [21, 56–60].

2 Essentials of Photoelectrochemical Reactions

Changes in the electrochemical currents or the established potentials as a consequence of illumination of an electrode/electrolyte interface can be observed if illumination leads to changes in the occupation of electronic levels that have a lifetime longer than the timescale of electrochemical reactions [1]. Such changes can occur either in the electrode or in the electrolyte. Electrodes in contact to dye solutions were studied with the goal to electrochemically harvest the energy of the absorbed light stored in the excitation energy of the molecules [61]. Much higher efficiencies, however, can be reached by electronic changes in an absorbing electrode. If a semiconductor electrode absorbs light of energy higher than its band gap, excess electrons are created in the conduction band and electron vacancies are created in the valence band of the semiconductor [1, 2, 62]. Both these changes can be detected in intrinsic semiconductors. In a doped semiconductor, only the concentration of the minority carriers is changed significantly because of the high concentration of majority carriers anyway present in a doped semiconductor.

n-doped electrodes are, therefore, characterized by anodic photocurrents, *p*-doped electrodes by cathodic photocurrents. To observe these currents, reduced redox species at energies in the range of the valence band of *n*-doped electrodes or oxidized redox species at energies in the range of the conduction band of *p*-doped electrodes are needed [1, 2]. Roughly speaking, to observe anodic photocurrents at *n*-doped electrodes a redox potential of the electrolyte below the semiconductor Fermi energy has to be chosen. To realize cathodic photocurrents at *p*-doped electrodes, a redox potential above the semiconductor Fermi energy is needed [1, 2]. In order to provide transportation of the photogenerated minority charge carriers from the site of light absorption inside the electrode to the interface with the electrolyte, the redox potential of the electrolyte has to be chosen appropriately. When brought into contact with an electrolyte, a semiconductor electrode will establish a contact similar to a semiconductor/metal contact because of the higher ionic concentration of charges in the electrolyte when compared with the charge density in a semiconductor. The space charge to compensate initial energy differences will be established mainly in the semiconductor electrode and will lead to a band bending as also known in semiconductor/metal contacts [1, 2, 62]. Optimum conditions are summarized in Fig. 1. A more detailed discussion, however, would have to include the quasi-Fermi levels of the light-induced minority carriers [2]. Changes in an applied external potential will lead to changes in the space charge region since this is the zone of the lowest charge density. In the context of this chapter it has to be pointed out that applicability of a semiconductor band model for the transport of charge carriers is not a prerequisite to establish a space charge region nor is it a necessary condition for the observation of photoelectrochemical currents (see below).

Fig. 1 Schematic representation of photoelectrochemically active **a** *n*-type semiconductors and **b** *p*-type semiconductors, each in contact to a redox electrolyte that allows facile transfer of the photogenerated minority carriers from the semiconductor electrode



3 Photoelectrochemical Experiments at Phthalocyanine Thin Films

3.1 Preparation of Thin Films

Film preparation plays a crucial role in determining the photoelectrochemical properties of phthalocyanine electrodes. Since the coupling of individual chromophores strongly depends on their relative orientation, the position of the absorption maximum and its width show a clear dependence on the structure of thin films. Also, charge transport within phthalocyanine films, a fundamental necessity for the films to work as electrodes, depends upon the overlap of the frontier orbital wave functions which is also dependent on intermolecular orientation. Beyond the microscopic structure of films the morphology of films plays an important role. In the case of crystalline films, the orientation of crystallites relative to the electrode surface will be relevant because of anisotropies in optical absorption and charge transport. The size of the observed photocurrent directly depends on the effective electrode surface area accessible by the electrolyte and this leads to a strong dependence on the porosity of the films.

In view of the high thermal stability of a number of phthalocyanines, *physical vapor deposition (PVD)* [20, 63–69] has become one of the major preparation routes for thin films. The method is based on sublimation under at least high vacuum conditions (HV, base pressures below 10^{-5} mbar) or, better, ultrahigh vacuum conditions (UHV, base pressures below 10^{-8} mbar). Thin film preparation by physical vapor deposition (PVD) is, compared to the methods from solutions, slightly more demanding with respect to the equipment involved in the laboratory because vacuum technology is needed. On the material side, however, PVD is a less demanding technique because a number of molecules are much easier accessible as a vacuum-compatible pigment than they are as a soluble dye. For film preparation by PVD, phthalocyanine powder is placed in a crucible, which can be heated resistively to temperatures typically between 200 and 400 °C. Substrates on which the films are deposited are mounted on a substrate holder which is placed approximately 10–50 cm above the source. This distance and the temperature of a given source serve to control the rate of deposition. Aside from the rate of deposition the substrate temperature is another important parameter for film growth. Since the parameters of film growth can be rather well controlled in a vacuum environment, the reproducibility of film deposition and, hence, film properties is also rather good relative to many other methods of film preparation. The films can be prepared in a wide thickness range from submonolayer coverage up to a few μm . Because of the vacuum environment which is needed for film preparation by PVD, the mechanism of film growth can be conveniently studied in situ. This is in particular the case for surface science methods like electron diffraction or electron spectroscopies, but also for more general methods like conductivity measurements, optical spectroscopy, or scanning probe techniques which can be performed in vacuum after proper installation. A general advantage of in situ studies as opposed

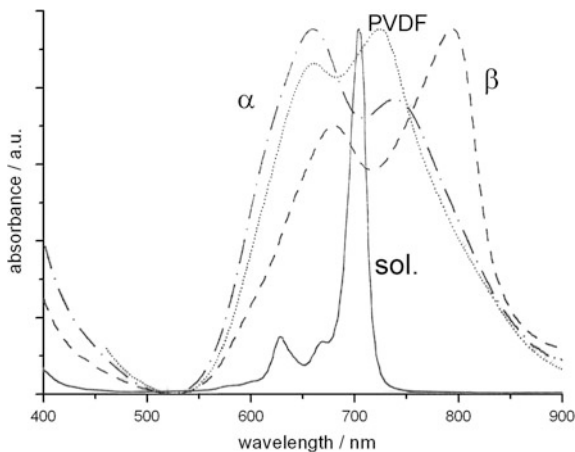
to studies at films which have been prepared by methods at ambient atmosphere or have been exposed to it is given by the good shielding of the in situ experiments from uncontrolled reactions of the films with ambient atmosphere prior to the measurements. For photoelectrochemical experiments at phthalocyanine surfaces this advantage is more difficult to use since a direct transfer of the thin film from a vacuum environment to an electrochemical cell through a controlled atmosphere of a load lock or a glove box is needed [70–75]. A special case of PVD can be seen in the technique of organic molecular beam epitaxy (OMBE). It makes use of the high purity of substrates which can be achieved in UHV and can lead to highly ordered, crystalline organic films of well-defined chromophore interactions [63–69].

The methods of *film preparation based on solutions of phthalocyanines* differ strongly in the kind of films that can be obtained, especially with respect to molecular order, choice of substrates, and achievable film thickness. Film preparation from solution further carries the attractive perspective of using continuous (“roll-to-roll”) processing technologies, a key toward affordable production of solar cells. Preparation of films consisting of phthalocyanine liquid crystals [76–79], self-assembled monolayers (SAM) [78, 80], or films prepared by the Langmuir–Blodgett (LB) technique [76, 77, 80–85] can produce highly ordered films. Spin coating and drop coating are examples of methods which aim at the deposition of bulk materials which typically are amorphous or polycrystalline. SAM and LB techniques on the other hand are restricted to the deposition of one or a few monolayers or at least yield optimum results for such thin films. Further, these deposition methods are restricted to specifically chosen molecules and substrates. Spin coating and drop coating, on the other hand, can be used to prepare films up to a few μm average thickness of a variety of soluble molecules on almost any substrate. Films of pure molecular compounds, molecules embedded in a polymer matrix and/or in a mixture with other components can be prepared. The matrix materials in general influence the formation of semiconductor aggregates, their structure and, hence, chromophore interaction. The matrix can also play an active role in the exciton dissociation and charge-carrier transport and, therefore, can be used to optimize the performance of electrodes [51]. Wetting of the substrate, the concentration of the components in the solution, and adjustment of the evaporation conditions are the main tuning knobs to control the film morphology and structure.

3.2 *Semiconductor Characteristics of Solid Phthalocyanine Films*

Since photoelectrochemical reactions discussed here heavily depend on the semi-conducting properties, some remarks about phthalocyanines as molecular semiconductor appear appropriate. One of the most characteristic properties of phthalocyanines is their intense blue–green color caused by strong absorption at wavelengths from 500–750 nm (Fig. 2) corresponding to about 1.6–2.5 eV. This

Fig. 2 Optical absorption spectra of a solution of PcZn in N,N-Dimethylacetamide (—) compared with thin films of PcZn drop coated from a mixed solution of PcZn and polyvinylidene fluoride (PVDF; ·····), and PcZn vapor deposited at room temperature (α -phase; - - -) or after annealing at 573 K for 3 h (β -phase; ———)



transition in the Q-band (HOMO \rightarrow LUMO) in a very simplified view leads to additional charge carriers in the HOMO (electron vacancies) and LUMO (excess electrons). Extended delocalization of the electrons in the excited state cannot be assumed in the films but the molecular excited state has to be looked at as a localized state. This corresponds to an exciton in the language of semiconductor physics. The dissociation of these excitons into electrons and electron vacancies (holes) that can separately contribute to charge transport in the films, needs an additional exciton dissociation (or -binding) energy. It was determined to be in the order of 0.5–1.5 eV [86–88], a significant energy when compared with the estimated difference of the transport level from the Fermi energy of 0.2–1.0 eV. Only from separated charge carriers we can expect photoelectrochemical activity for phthalocyanine films.

From a number of studies at thin films of unsubstituted phthalocyanines which have been reviewed earlier [18, 89–94], it has become clear that the films behave as semiconductors. The photoconductivity generally observed for films of phthalocyanines clearly showed the possibility to dissociate excitons into mobile carriers. Under most conditions films of unsubstituted phthalocyanines were found to be partly oxidized and hence showed *p*-type characteristics. This was seen from measurements of the electrical conduction, the thermopower established by a temperature gradient across a sample, and by the rectifying characteristics in junctions. A generally quite low mobility of about 10^{-4} – 10^{-1} cm² V⁻¹ s⁻¹ was found for the electron vacancies in phthalocyanines, barely allowing the applicability of a band model which dwells upon the assumption of delocalized electrons in a periodic potential of a solid. A rather localized character of the electronic system in phthalocyanines, however, is not at all surprising given the fact of rather loose bonds (van der Waals) among the molecules and very strong (covalent) bonds within the molecules as opposed to a three-dimensional covalent network of bonds in classical semiconductors. The materials are, therefore, generally referred to as molecular semiconductors considering the similarities but also the differences to

classical semiconductors. Models of charge-carrier transport based on hopping or tunneling of charge carriers from site to site are in most cases more appropriate than the band model of delocalized transport [68].

Such rather small coupling of the π -electrons of phthalocyanine molecules in solid state is directly seen in a comparison of the absorption spectra of solutions and thin films (Fig. 2). As opposed to a band edge and almost constant absorption at higher energies as characteristic for semiconductors, the well-defined molecular absorption bands detected in solutions of phthalocyanines are preserved also in the solid state, just split and broadened by the, albeit weak, coupling of the chromophores in the solid. Characteristically different spectra are obtained for different intermolecular arrangements in the solid state. This is seen in Fig. 2 for the two different crystalline modifications (α - and β -forms) of PcZn and for PcZn crystallized in a polymer matrix [51]. Such changes were reported for a number of different phthalocyanines and their different crystalline modifications, as reviewed earlier [65, 67, 68]. The differences in band splitting can be explained based on dipole–dipole interactions of the transition dipole characteristic for the optical transition.

Corresponding optical and electrical measurements at phthalocyanines with electron-withdrawing substituents in the ligand like octacyanophthalocyanines (CN)₈Pc, tetrapyrrodotetraazaporphyrins TPyTAP, tetrapyrazinotetraazaporphyrins TPzTAP, or hexadecafluorophthalocyanines F₁₆Pc showed quite comparable optical characteristics but the important difference is that *n*-type conduction was observed [68, 95–99], caused by the easy reduction of these molecules. Whereas the mobility in unsubstituted phthalocyanines was often found to be sufficiently high for a limited use of the band model, hopping transport had to be assumed in most cases for the substituted materials. Taking into account the observed conductivity in the dark and under illumination [68, 91], and comparing them to the observed photoelectrochemical currents (see below), it is seen that the conductivity is sufficiently high to provide transport of light-induced charge carriers to the electrode surface. The observed currents in photoelectrochemical experiments are typically limited by the kinetics of charge transfer at the electrode surface. This is also confirmed by higher photocurrents in organic/organic' heterojunctions compared with the photocurrents for identical films in photoelectrochemical cells [45].

3.3 Position of Frontier Energy Levels in Phthalocyanines

Since the rate and direction of light-induced charge transfer is governed by the relative position of occupied and unoccupied electronic states in the electrode and the electrolyte, this aspect of semiconductor characteristics of phthalocyanines is reviewed briefly. Knowledge of the position of the highest occupied molecular orbital (HOMO) and the lowest unoccupied molecular orbital (LUMO) of a given molecular electrode is crucial to discuss the photoelectrochemical characteristics. For the observed photoelectrochemical response of a semiconducting electrode the

polarity of the minority carrier (electron or hole) in an electrode material is of uttermost importance since it defines the observed direction of light-induced changes in the interfacial charge transfer. Depending on redox interactions of the semiconductor with dopant molecules either excess electrons in the LUMO or holes in the HOMO are formed.

The experimental methods to elucidate the position of the electronic energy levels in molecular materials aim at ionization of the sample and analysis of the energetic change involved. Two different sets of methods are frequently used, either based on redox electrochemistry as described in a number of chapters in this book or based on ionization in vacuum. Here, ultraviolet photoelectron spectroscopy (UPS) is a very direct method to determine occupied electronic states in a given material. The kinetic energy of photoelectrons following ionization by irradiation in the vacuum UV (e.g., He₁ 21.2 eV) or soft X-ray (e.g., synchrotron) is measured. Molecules can either be in the gas phase or in a thin film on a conductive substrate. Inverse photoelectron spectroscopy IPES (irradiation of the sample by an electron beam, spectral analysis of emitted photons) is an extension to the direct analysis of unoccupied electronic states. Electrochemical redox potentials reflect free enthalpies of reactions which involve ionization of the molecule of interest either in a solvent environment or as a thin film, then accompanied by intercalation of charge-balancing counter ions. In electrochemical experiments the accessible potential range of the electrolyte determines the experimental range. For a number of phthalocyanines, only the redox potential of reduction (characteristic for unoccupied levels) or oxidation (characteristic for occupied levels) can be obtained. To open a discussion about both, occupied and unoccupied frontier levels of a material despite these experimental limits, optical spectroscopy (absorption or emission) or electron energy loss spectroscopy (EELS) was frequently used to estimate the frontier orbital gap. A rather constant gap of about 1.6 eV for most Pc (with the exception perhaps of cofacially stacked polymorphs [100] was determined [52, 95, 101, 102]. In addition to this, however, an additional exciton binding energy (see above) has to be considered to estimate the energy needed to create mobile carriers.

UPS is also well suited to analyze details of the energetic alignment in heterojunctions beyond phenomenological observations [103]. The analysis of such heterojunctions [19, 20, 104–116] is of considerable interest in organic photovoltaic cells, in organic light-emitting diodes, and also for the characteristics of thin films in photoelectrochemically active junctions. The expected and in many cases desired establishment of a space charge in the films was analyzed in detail. Interface reactions, however, can also occur which can lead to surface defects, surface dipoles and, hence, shifts of the vacuum level across junctions.

3.4 Photocurrent Direction at Phthalocyanine Electrodes

Following absorption of a photon in a molecule, this molecule represents a stronger reducing agent due to an electron in a state of higher energy (LUMO in the case of

the Q band of phthalocyanines), but also a stronger oxidizing agent due to the electron vacancy in a state of lower electron energy (HOMO in the case of the Q band of phthalocyanines) when compared with the molecule in the ground state [117, 118]. From this point of view, an increased driving force for reduction reactions and oxidation reactions is expected for molecules in homogeneous solution. The same should then also be valid for reactions occurring at the surface of a solid electrode. At a closer look, however, it becomes clear that this principle can only be applied for intrinsic (or fully compensated [62]) electrode materials, since for doped (partially reduced or oxidized) materials the *relative* changes in the concentrations of excess electrons (LUMO) and holes (HOMO) will occur in an unsymmetrical way, leading to preferentially anodic photocurrents at *n*-type electrodes and cathodic photocurrents at *p*-type electrodes (see above).

In a comparison of the catalytic activity of thin films of PcH₂, PcCu, or PcFe in the dark and under illumination [42], it was found that the photocatalytic activity was barely correlated to the catalytic activity in the dark and this difference was discussed as arising from a photoconductivity effect in the bulk of the phthalocyanine films. A photocurrent and also photovoltage observed at H₂Pc [41] were discussed to be due to a photovoltaic effect at the phthalocyanine film. Phthalocyanine thin films used in early photogalvanic cells [40] were described as *p*-type semiconducting electrodes that established a region of space charge at the Pc/electrolyte interface. Nevertheless also small anodic photocurrents were observed and explained by light-induced changes in the concentration of both types of charge carriers in a weakly doped semiconductor [38, 39] or by a weak sensitization effect (see also below, Sect. 4) at the back electrode in the case of SnO₂ substrates [21, 37]. This reaction at the SnO₂ back contact was characterized in detail by the analysis of experiments at varied illumination conditions. It was concluded that a 35-nm-thick photoactive layer was formed on the electrolyte side [33], in agreement with potential-dependent impedance measurements at electrochemical contacts with films of PcH₂, PcNi, and PcZn [119]. It was noticed that partial oxidation by acceptor molecules in the volume of the films was crucial for the observed characteristics and that oxygen from air in most cases caused the observed *p*-doping and, hence, led to cathodic photocurrents. Controlled doping was achieved by reactions with halogen molecules like iodine, or organic molecules like ortho-chloranil, tetracyanoquinodimethane, tetrafluorenone, etc. Detailed investigations of the electrical properties in the solid state followed as sketched above and reviewed in great detail before [68, 91].

Utilization of the photoelectrochemical reactions purely based on the *p*-type character of phthalocyanine electrodes and optimization of the electrolyte led to photoelectrochemical cells with a power conversion efficiency of 0.07 % under illumination with 75 mW cm⁻² white light [34]. Electrodes consisting of phthalocyanines in polymer binders were used. A space charge region of 30 nm thickness and the presence of interfacial states at the electrolyte were detected in capacitance measurements. The interfacial states served as mediators of charge to the electrolyte, but it was also assumed that they limit the open-circuit photovoltage and lead to surface recombination of carriers (see below). Doping of phthalocyanine

films with organic electron acceptors was found to significantly increase the photoelectrochemical activity of evaporated phthalocyanine thin films and a quantum efficiency of 4.6 % was reached for doped PcH₂ corresponding, however, to only 0.04 % power conversion efficiency [33]. In a comparison of different methods of film preparation of divalent phthalocyanines, it was found that vapor-deposited films showed higher photocurrents when compared with drop-coated films [48]. This was explained by an increased trap density at the surface of grains in the drop-coated films leading to a decreased mobility across grain boundaries and an increased probability for the recombination of charge carriers. An electrophoretic deposition of PcH₂ from suspensions of the pigment by the use of surfactants was also used to obtain electrodes with an increased porosity, which led to an efficiency of 0.06 % under illumination with 6 mW cm⁻² white light [24].

The photoelectrochemical characteristics of thin films of phthalocyanines with higher valent central metals carrying additional electron-withdrawing axial ligands like PcAl(OH), PcAl(Cl), PcGa(F), PcGa(Cl), PcIn(Cl), PcTi(O), PcV(O) were also investigated in great detail [22, 27–29, 31, 35, 120–122]. For this group of materials, large differences in film characteristics were observed with either anodic or cathodic photocurrents dominating the photoelectrochemical behavior, despite the fact that all films had been prepared by vapor deposition. The role of oxygen as a dopant leading to *p*-type characteristics of phthalocyanines could be clearly elucidated in these studies [27, 120, 121]. The growth mode and morphology of films turned out to be crucial for interactions with the gas phase in vacuum as well as under ambient conditions and led to different levels of doping and trap sites [27, 28, 121]. An increased crystallinity and optimized orientation of crystals led to a larger exciton diffusion length and charge-carrier mobility as shown in an increased photoelectrochemical efficiency [122]. Films consisting of rather large crystallites with a small surface area provided conditions of almost defect-free surfaces as reflected in a proportionality between the observed photopotential and the electrolyte redox potential (no Fermi level pinning, see below) [31]. Photovoltaic efficiencies in the range of 0.1 % could be reached under illumination with 75 mW cm⁻² in the visible range (470–900 nm).

In the case of the aluminum complexes, the influence of different methods of film preparation and different chemical film treatment on the photoelectrochemical characteristics was clearly seen. By attachment of a surfactant chain to Al, electrophoretic deposition of very porous active thin films could be achieved which showed, however, a rather low efficiency of 0.01 % under illumination with white light of 0.5–100 mW cm⁻² due to an increased recombination of photogenerated carriers [32]. Spin coating of PcAl(OH) from DMSO was also used and gave active electrodes, however, with a low efficiency of only 0.006 % at 10 mW cm⁻² white light if a stable counter electrode was used [123]. Treatment of vapor-deposited thin films of PcAl(OH) in aqueous solutions of phthalic acid induced a structural transformation of the films and led to an increased efficiency of the films of 0.02 % under 10 mW cm⁻² white light [26]. Embedding of PcAl(OH) particles in a poly

(vinylpyridine) binder led to an efficiency of 0.04 % (10 mW cm⁻² white light). A detailed analytical investigation of different ways of chemical treatment of PcAl(Cl) as compared to PcGa(Cl) and PcIn(Cl) revealed the hydrolysis of the Al-Cl bond as the key step toward the formation of more efficient electrode materials [22].

Chemical substitution at the phthalocyanine ligand with electron-withdrawing substituents led to a dominance of anodic photocurrents as opposed to that of cathodic photocurrents observed at the unsubstituted materials. This was shown for (CN)₈PcZn [52, 124], TPyTAPZn [48, 52, 125], and TPzTAPZn [48, 52]. To restrict the observed differences in the photoelectrochemical characteristics to the influence of the different ligands, the central metal was kept constant in these studies. The films were prepared by vapor deposition if applicable and also by drop coating for comparison purposes. Figure 3 shows the dominance of cathodic photocurrents (high anodic dark currents) at PcZn and the dominance of anodic photocurrents (high cathodic dark currents) at electrodes of TPyTAPZn and TPzTAPZn, also seen for (CN)₈PcZn [52, 96]. Based on these results, *n*-type conductivity was assigned to these materials of molecules with electron-withdrawing substituents based on the argument outlined above [48, 52, 96, 124–128]. Electrodes of F₁₆PcZn showed photocurrents of almost identical significance in both photocurrent directions [128–130]. Since films of F₁₆PcZn investigated directly following the preparation still showed *n*-type characteristics, the photoelectrochemical behavior was explained by compensation of the dopants by air. The assignments were supported by studies of the electrical properties of the materials [47, 95–98, 125] and in solid heterojunctions [19, 20, 107]. A corresponding influence of an electron-withdrawing ligand was observed when electrodes of naphthalocyaninatozinc (cathodic photocurrents, *p*-conduction) were compared with electrodes of tetraquinoxalino-tetraazaporphyrinatozinc (anodic photocurrents, *n*-conduction) [126].

Thin films of TPyTAPZn have also been prepared by electrochemical deposition [131, 132]. The *n*-type character was preserved as shown by capacitance measurements. No clear preference of a photocurrent direction could be established, however, and the photocurrent action spectrum had no resemblance with the absorption spectrum of the material. It had to be assumed that the effect is caused by impurities in the film, which are incorporated during electrochemical film deposition.

Electrodes of two-dimensional sheet polymers of phthalocyanines prepared by in situ reaction of tetracyanobenzene with thin metal films were prepared and characterized in their photoelectrochemical characteristics [133]. Anodic photocurrents were detected, characterizing these films as *n*-type semiconducting materials. It was also found that such films could be reduced at more positive potentials than unsubstituted phthalocyanines. This change when compared to films of divalent unsubstituted phthalocyanines is caused by a smaller number of electron-donating benzene moieties and unreacted CN⁻ groups that were found in the films [134, 135]. Such films, therefore, can be looked at as substituted phthalocyanines with electron-withdrawing groups which explains the observed photoelectrochemical characteristics.

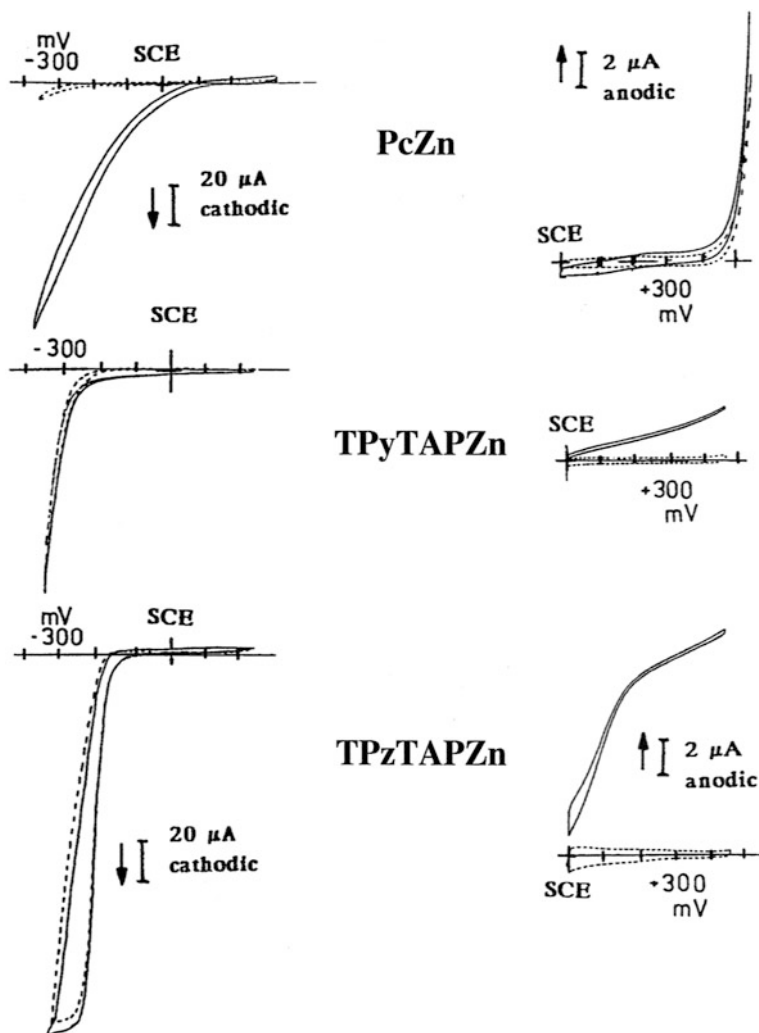


Fig. 3 Cyclic voltammograms measured at thin film electrodes of PcZn, TPyTAPZn, and TPzTAPZn in the reduction of $1.3 \cdot 10^{-3}$ M O_2 (left hand side) or in the oxidation of 0.1 M EDTA (right hand side). Experiments were performed in 0.5 M KNO_3 in the dark (.....) or under illumination with 400 mW cm^{-2} white light of a Xenon arc lamp (——). (Reproduced with permission from *J. Phys. Chem.* **1994**, *98*, 11771–11779. Copyright 1994 American Chemical Society)

3.5 Role of Higher Excited States

Caused by the possibility to separately absorb light in different absorption bands of a molecular semiconductor and by the remarkably distinct character of the resulting excited electronic states, phthalocyanine electrodes show the specific characteristics

of a switchable photocurrent direction which is demonstrated in this section [128]. Phthalocyanines show two absorption bands in the visible range, namely the Q band around 650–700 nm leading to the first excited singlet state S_1 and the B or Soret bands around 300–350 nm leading to the formation of S_2 . In the solid state these optical transitions of Pc molecules are preserved, just slightly shifted and broadened considerably [136]. Most of the light of a white light source that leads to the observed photocurrents described above will be absorbed in the Q bands. Excitation in the B band of PcZn ($\cong 340$ nm), however, led to strongly contrasting characteristics when compared to the situation described above for Q-band illumination. The origin of bands should therefore be introduced briefly.

MO calculations for Pc showed that the Q band basically corresponds to the excitation of an electron from the highest occupied molecular orbital (HOMO, $2a_{1u}$) to the lowest unoccupied molecular orbital (LUMO, $6e_g$) and the B band to the transition from the second highest occupied molecular orbital (SHOMO, $4a_{2u}$) to the LUMO, as is also the case for porphyrins [136–138]. The higher excited singlet state S_2 following B-band excitation is of sufficient lifetime to be transferred to reactants in the electrolyte despite the competing relaxation into S_1 or to the ground state S_0 . The assignment of the well-defined B and Q bands in the solid state to transitions between distinct molecular orbitals was proven to be of relevance also for the observed charge transfer in photoelectrochemical reactions at thin films. If a material of a suitable position of energy levels was chosen the direction of charge transfer could be switched by illumination with light of the two different wavelengths (Fig. 4). A rather small ratio of photocurrents to dark currents was seen for PcZn in contact with ethylenediaminetetraacetate EDTA (Fig. 4a) but larger changes were observed for PcZn in contact with O_2 as an oxidant in the cathodic direction (Fig. 4b). A considerable concentration of holes in the HOMO of PcZn is thereby indicated already in the dark stemming from partial ionization (doping) of the films. The polarity of the respective carrier confirms the characterization of PcZn as *p*-type material. Illumination in the Q band (620 nm) led to significant photocurrents in the reduction of O_2 (Fig. 4b, left side) by photogenerated electrons in the PcZn LUMO but no photocurrents were added to the dark currents in the oxidation of EDTA (Fig. 4a, left side) showing the absence of a significantly changed hole concentration in the PcZn HOMO, again consistent with the conduction type of the material.

Under B-band illumination of PcZn (340 nm) as opposed to the situation under Q-band illumination (620 nm), even anodic photocurrents could be observed (Fig. 4a, right side) aside from the still dominating cathodic photocurrents (Fig. 4b, right side). It is remarkable that the hole generated in the SHOMO obviously was stable enough to lead to considerable changes in the electrode characteristics despite a presumably high concentration of surface defects and a number of possible relaxation reactions of S_2 to S_1 or even recombination to S_0 . As also observed under Q-band illumination, the electron generated in the LUMO leads to the cathodic photocurrent in contact with O_2 (Fig. 4b, right side). The validity of the band assignment (Fig. 4c), the distinct reactivity of the different excited states as well as the partial oxidation of the PcZn HOMO (*p*-conductor) were clearly confirmed by

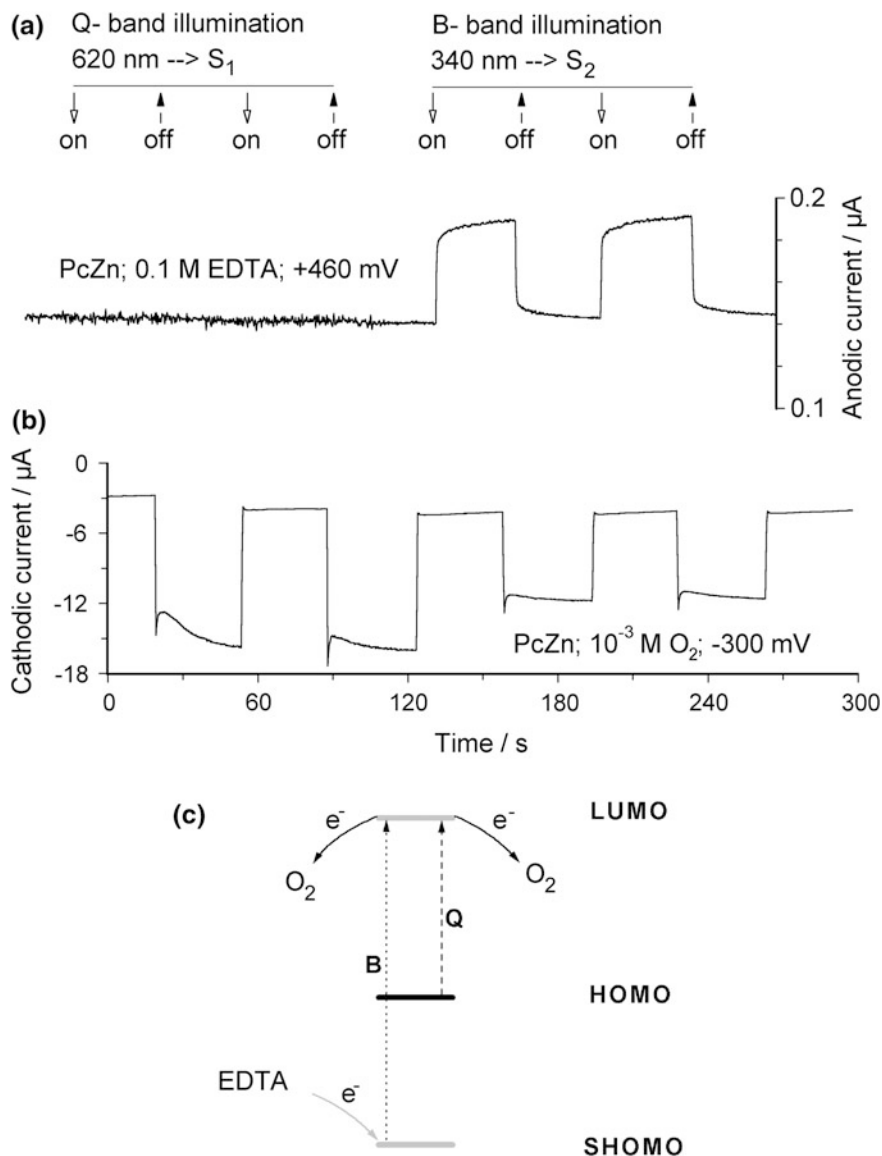


Fig. 4 Current at films of PcZn (100 nm) vapor deposited on ITO (1 cm^2) observed in contact to aqueous electrolytes during potentiostatic polarization. Illumination occurred either in the B band ($3 \times 10^{15} \text{ photons cm}^{-2} \text{ s}^{-1}$) or in the Q band ($7 \times 10^{15} \text{ photons cm}^{-2} \text{ s}^{-1}$). **a** In the presence of 0.1 M EDTA (+460 mV), **b** In the presence of 10^{-3} M O_2 (-300 mV vs. SCE). **c** Schematic representation of frontier energy levels and observed photocurrents. (adapted and in part reprinted from *Electrochim. Acta* **45**, D. Schlettwein, E. Karmann, T. Oekermann, and H. Yanagi: "Wavelength- Dependent Switching of the Photocurrent Direction at the Surface of Molecular Semiconductor Electrodes Based on Orbital- Confined Excitation and Transfer of Charge Carriers from Higher Excited States", p. 4697–4704, Copyright (2000), with permission from Elsevier Science)

this series of experiments demonstrating the possibility to switch the direction of interfacial charge transfer [128].

Anodic photocurrents dominated at electrodes of TPyTAPZn and F₁₆PcZn as described above, characterizing those materials as *n*-doped molecular semiconductors [128]. For these materials no such switching of the photocurrent direction as observed at PcZn could be observed. This is in good accordance with the assignment of the optical bands considering their conduction type because both holes in the HOMO (following Q-band excitation) or holes in the SHOMO (following B-band excitation) would represent minority carriers leading to significant photocurrents, but here in identical direction. The independence of the two paths of charge-carrier generation was also proven in these cases, however, by different quantum efficiencies of photocurrent generation [128]. For molecular electrodes it is appropriate to think of the transitions to higher excited states not only as contributors to an increased light absorption but also to consider charge transfer out of the higher excited states. This led to the observed switching in the direction of interfacial charge transfer by different illumination conditions [128], but also opens new reaction pathways utilizing the higher energy of the higher excited state as desired in the context of third generation solar cells [139].

3.6 Reactant Adsorption

In studies of electrochemical photocurrents obtained at molecular semiconductor thin films (PcZn, (CN)₈PcZn, TPyTAPZn, MePTCDI) and their dependence on the concentration of the reactant in the electrolyte (O₂, ethylthiolate (RS⁻), hydroquinone/benzoquinone (HQ/BQ), Fe(CN)₆^{3-/4-}, Ce^{3+/4+}), a saturation behavior of the photocurrents was found arising from reactant adsorption prior to charge transfer [45, 50, 124, 127]. Such adsorption of reactants could also explain fast interfacial charge transfer which can compete with relaxation reactions (see preceding section). Often functions according to Langmuir's adsorption isotherm based on the presence of only one kind of independent adsorption sites and a maximum coverage of a monolayer were found to give a reasonable fit to the observed photocurrent data. Assuming that only adsorbed species react, that the reaction products desorb quickly and that the photocurrent density *i* shows a first-order dependence on the concentration *c** of minority carriers at the surface and on the surface coverage *Γ* by the reactant *R*, the photocurrent is obtained as

$$i = n F k_f c^* \Gamma \quad (1)$$

where *n* is the number of charge carriers transferred to each molecule of reactant, *F* is the Faraday constant, and *k_f* is the rate constant of the electrochemical reaction. The value of *c** is assumed to be constant at a fixed potential and light intensity. At increasing light intensity the photocurrent increased corresponding to increased *c**

excluding diffusion limitation in the electrolyte to cause the observed saturation of i at increasing reactant concentration [50, 53, 130]. Assuming Langmuir adsorption equilibrium [140] for R leads to

$$d\Gamma/dt = k(\Gamma_{\max} - \Gamma)c_R - k'\Gamma - k_f c * \Gamma \quad (2)$$

where k is the rate constant of adsorption, k' is the rate constant of desorption, c_R is the reactant concentration in the electrolyte, and Γ_{\max} is the maximum coverage arising from the occupation of all available sites. For the initial photocurrent ($i = i_{\text{in}}$) for which an unperturbed adsorption equilibrium can be assumed and for the steady-state ($i = i_{\text{stead}}$) Eqs. 1 and 2 yield

$$c_R/i_{\text{in}} = c_R/i_{\max} + (k'/k)/i_{\max} \quad (3a)$$

$$c_R/i_{\text{stead}} = c_R/i_{\max} + [(k'/k) + (k_f c * / k)]/i_{\max} \quad (3b)$$

with i_{\max} as the photocurrent arising from Γ_{\max} [45, 50, 124, 127]. Assumption of a more complex adsorption equilibrium considering rather a distribution (Freundlich isotherm) of adsorption constants $k_a = k/k'$ than a fixed value (Langmuir isotherm) provided a better model [124]. In many cases, however, the Langmuir isotherm allowed a successful discussion of the observed data. The accommodation coefficients k_a can be discussed as a parameter characteristic for each pair of electrode material and reactant. Different tendencies of reactant adsorption were observed: a rather weak driving force was observed for adsorption of the anionic electron acceptor $\text{Fe}(\text{CN})_6^{3-}$ at PcZn, and an equilibrium clearly on the side of adsorbed reactants was seen for the anionic hole acceptor RS^- at $(\text{CN})_8\text{PcZn}$ but also for the cationic Ce^{3+} at F_{16}PcZn . No general trend was seen within the series of experiments but specific interactions seem to dominate the strength of adsorption.

The time dependence of photocurrents on the scale of seconds to minutes showed a decay which was caused by changes in the surface coverage of the reactant as a result of the electrochemical reaction (term $k_f c * / k$ in Eq. 3b) [50, 124, 127] and a monoexponential decrease was expected within the Langmuir model:

$$i(t) = i_{\text{stead}} + (i_{\text{in}} - i_{\text{stead}}) * \exp[-((k i_{\max} c_R)/i_{\text{stead}})t]. \quad (4)$$

Monoexponential decay functions were found to fit the transients in the light-induced reduction of O_2 at electrodes of PcZn showing the validity of the model [50]. Qualitatively similar transients were also observed in the light-induced oxidation of RS^- [124, 127], but its detailed analysis showed that a monoexponential decrease did not fit these data showing the limits of this approach. If again a Freundlich isotherm was assumed, however, a multiexponential behavior would be expected and already the assumption of just two adsorption sites (biexponential fit) gave a good fit to the experimental data [124].

3.7 Surface Defects

3.7.1 Fermi Level Pinning

For many electrode materials, surface defects were found to play an important role in the charge transfer to the electrolyte [4, 34, 141, 142]. On the other hand recombination of charge carriers at surface states can lead to significant losses and decreased conversion efficiencies [143–145]. Surface defects may be already present without electrolyte contact caused by crystal defects or can be introduced by adsorbed species from the electrolyte [146].

Surface defects can cause a potential drop across the electrode surface, which does not contribute to the photovoltage because it does not contribute to the space charge layer of the semiconductor. Such potential drop at the surface is also discussed as complete or partial Fermi level pinning (FLP) [147, 148]. The extent of FLP can be measured by the difference between the rest potential under illumination and in the dark (V_{ph}) of the electrode using electrolytes of different redox potentials. If the transfer occurs to adsorbed reactants, the redox potential of the adsorbed reactant would be the relevant entity. Since these, however, typically are not experimentally accessible, differences in the redox potential of the solutions were used as an approximation. For an ideal behavior (no pinning), V_{ph} should change directly with the redox potential, leading to a slope of -1 for a p -type semiconductor (1 for an n -type semiconductor) in a plot of V_{ph} against the rest potential in the dark [149]. Total FLP (no potential drop across the space charge region) is characterized by a slope of 0 , while slopes between -1 and 0 (p -type) and between 0 and 1 (n -type) indicate partial Fermi level pinning, a potential drop across both the space charge region and the layer of surface defects.

Illumination of electrodes of PcZn in contact with a variety of redox electrolytes under open-circuit conditions showed positive photovoltages as expected for a p -type electrode, when the rest potential in the dark was negative of the flat band potential. Measurements in KCl solutions containing various electroactive species led to rest potentials in the dark between 0 and 300 mV versus SCE [44]. The observed photovoltage V_{ph} was proportional to the rest potential in the dark. The more positive the equilibrium potential of the electrolyte, the smaller the potential drop in the space charge layer and, hence, the observed photovoltage. The quantitative comparison of the photovoltages observed at different equilibrium potentials indicated partial Fermi level pinning at PcZn electrodes with a proportionality coefficient clearly smaller than unity. These characteristics were quite independent of the redox pair, i.e., the surface defects were obviously not introduced by contact to the electrolytes but were a property of the electrode as prepared and transferred to the cell. The density of surface defects can be inferred from a plot of V_{ph} against the rest potential of the electrode in the dark from series of experiments in which the redox potential of the electrolyte is varied by changing the concentration ratio of the

redox pair (ferri/ferrocyanide) rather than the kind of redox pair and where the rate of hole transfer from the electrode HOMO (majority carriers of this electrode material) was held constant by a constant concentration of ferrocyanide [44]. A linear behavior was obtained for the plot of V_{ph} against the rest potential in the dark, with a slope of -0.35 for a series of experiments involving a PcZn electrode which was exposed to air for 5 days after preparation [44]. For an otherwise identical electrode, which had been exposed to air for 5 months a smaller slope of -0.21 was obtained [44]. The smaller slope after extensive exposure to air clearly showed a higher surface defect density. It was concluded that the surface defects at PcZn are caused by interaction with oxygen from air.

Under the assumption of a uniform energy distribution of the surface defects in the examined potential region, a semi quantitative model was introduced to interpret partial Fermi level pinning [149] according to equation

$$V_{\text{ph}} = a \cdot E_{\text{redox}} + b, \quad (5)$$

where b is the photovoltage observed at reference zero. A plot of V_{ph} against E_{redox} should therefore yield a linear dependence with a slope $-1 < a < 0$, as it was the case for PcZn. From a the surface defect density D_s can be calculated according to

$$D_s = \frac{-\varepsilon_0 \cdot \varepsilon_i \cdot (1 + a)}{e_0^2 \cdot \delta \cdot a}, \quad (6)$$

where ε_0 is the vacuum permittivity, ε_i the dielectric constant, e_0 the elementary charge, and δ the thickness of the interfacial layer in which the surface defects lead to the potential drop that causes the partial pinning of the Fermi level. The value of ε_i is assumed to be close to 1 since it relates to the spatial region where surface defects are exposed at the semiconductor phase boundary with the electrolyte. Assuming that only surface molecules can participate in the formation of surface defects, a value of 0.8 nm was estimated for δ in the case of PcZn, as the thickness of a monolayer of PcZn would vary from 0.36 to 1.2 nm, dependent on the orientation of the molecules. According to these geometrical assumptions a surface defect density $D_s = 4.2 \times 10^{13} \text{ cm}^{-2} \text{ eV}^{-1}$ was calculated from the slope of $a = -0.21$ obtained for an electrode stored in air for 5 months. For an electrode exposed to air for only 5 days prior to the experiments, a smaller $D_s = 2.1 \times 10^{13} \text{ cm}^{-2} \text{ eV}^{-1}$ was obtained from the slope of $a = -0.35$ [44].

Assuming, further, that D_s is constant over the whole range of the energy gap, (1.65 eV for PcZn), the overall number of surface defects was estimated to about $0.7 \times 10^{14} \text{ cm}^{-2}$ based on $a = -0.21$. This value is of a similar size as the calculated number of 0.6 to $2 \times 10^{14} \text{ cm}^{-2}$ molecules of PcZn present at the surface, if all possible orientations of the molecules are considered equally. According to this estimation a considerable part, if not all, of the surface molecules represent surface defects, which can act as electron traps.

3.7.2 Photoelectrochemical Electrode Kinetics

Photocurrent transient methods [44, 150–155] and intensity-modulated photocurrent spectroscopy (IMPS) [142, 151, 156–161] have been established as good techniques for the investigation of semiconductor surfaces [162]. By these methods the working electrode is illuminated with either a light pulse or with sinusoidal modulated light, respectively, and the resulting photocurrent is monitored. Both techniques have been used at phthalocyanine electrodes to analyze in detail the kinetics of the photoelectrochemical reactions.

Photocurrent Transients

In addition to the perturbations of the reactant adsorption equilibrium leading to a transient behavior of the photocurrent in the second-to-minute regime, charging and discharging photocurrents were observed in the millisecond regime, caused by trapping of light-induced minority carriers in surface defects and their subsequent recombination [151]. Currents dropping below the steady-state current in the dark shortly after the end of illumination indicated the discharge of such surface traps. Charging and discharging of surface traps were analyzed in detail for PcZn in contact to O_2 , BQ/HQ and $Fe(CN)_6^{3-/4-}$ and for $F_{16}PcZn$ in contact to $Ce^{3+/4+}$ and $Fe(CN)_6^{3-/4-}$ on a timescale of milliseconds [44, 129, 163].

A typical result for the example of PcZn electrodes after different times of exposure to air is displayed in Fig. 5 [44]. As expected for a *p*-type semiconductor,

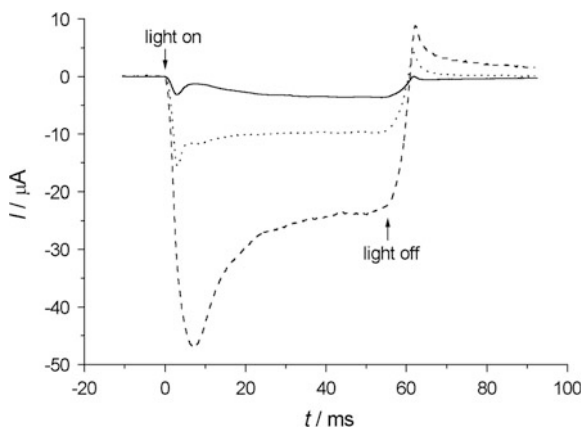


Fig. 5 Time-resolved photocurrent response of PcZn electrodes to a 50 ms flash of white light in an oxygen-saturated aqueous 1 mol l^{-1} KCl solution at 0 mV versus SCE. All electrodes were prepared in the same process and were exposed to air for 30 min (—), 1 day (.....) and 6 days (—) after preparation. (Reprinted from *J. Electroanal. Chem.* **462**, T. Oekermann, D. Schlettwein and N.I. Jaeger: “Role of surface defects and adsorbates in time-resolved photocurrent measurements and photovoltage generation at phthalocyaninatozinc(II)-photocathodes”, p. 222–234, Copyright (1999), with permission from Elsevier Science)

cathodic photocurrents were observed at PcZn electrodes as also seen earlier in steady-state photocurrent measurements [37, 44, 119, 164]. During the opening time of the photographic shutter used in these experiments (about 10 ms), the photocurrent increased beyond the value i_{in} (Eq. 3a) to a peak of the charging current (i_{peak}) and then decayed to i_{in} within about 30–40 ms. A reverse discharging current was observed upon closure of the shutter before the dark current was reestablished. The steady-state photocurrents as well as the charging- and discharging currents increased with the exposure time of the electrode to air. The increased steady-state photocurrent can be explained by the doping of the electrode bulk with oxygen from air. The increasing charging and discharging currents are consistent with the increasing surface defect density D_s found under exposure to oxygen.

Anodic photocurrents should be observed in the case of an n -type semiconductor like $F_{16}PcZn$. Figure 6, however, reveals both anodic and cathodic photocurrents in dependence on the electrode potential [125, 129]. The dark currents were generally quite small. The concentration of both electrons and holes was small in the dark and could be increased significantly under illumination. Such a behavior is characteristic for an intrinsic or compensated semiconductor electrode. A compensation of donor sites in films of $F_{16}PcZn$ by oxygen had been seen earlier in conductivity measurements in vacuum and under air [97].

The concentration dependence for i_{in} as discussed above was confirmed for these photocurrent transient measurements, and a Langmuir adsorption isotherm according to Eq. 3a was successfully used to fit the data for the photoreduction of benzoquinone at the surface of PcZn [44] and for the photooxidation of Ce^{3+} at the surface of $F_{16}PcZn$ [129]. In these studies quite remarkable differences were seen in the dependence or independence of charging and discharging currents on the

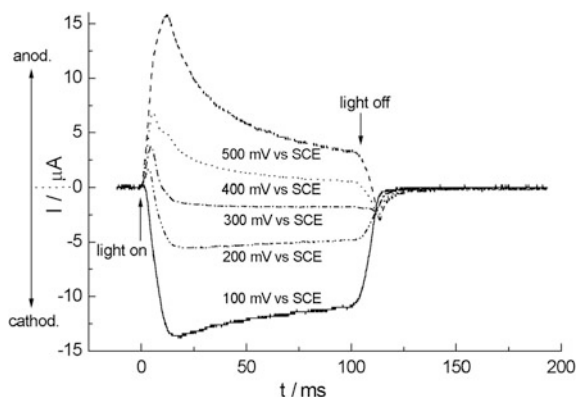


Fig. 6 Time-resolved photocurrent responses of $F_{16}PcZn$ electrodes to a 100 ms flash of white light at different electrode potentials between 100 and 500 mV versus SCE as indicated. The electrolyte was an aqueous KCl (1 mol l^{-1}) solution with $10^{-3} \text{ mol l}^{-1} Ce^{3+/4+}$. (*Journal of Porphyrins and Phthalocyanines* **3**, p. 444–452 (1999), T. Oekermann, D. Schlettwein, N.I. Jaeger and D. Wöhrle, copyright © John Wiley & Sons Limited. Reproduced with permission)

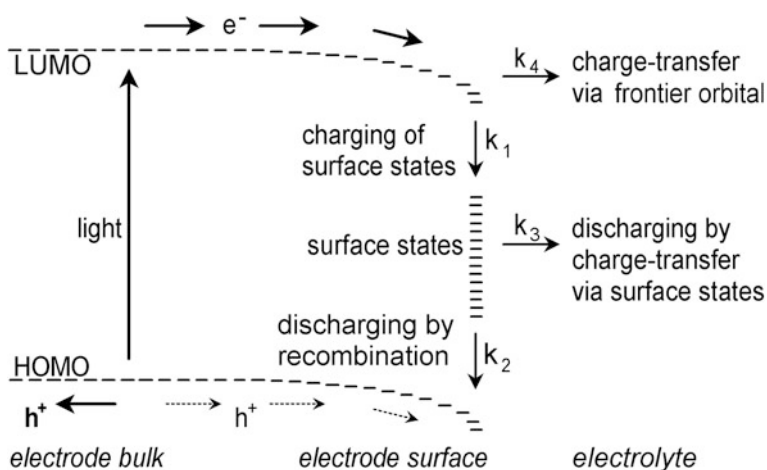


Fig. 7 Qualitative model showing the involvement of surface defects in the charging and discharging of electrode surfaces and in charge transfer. The k_i indicate rate constants, and the respective rates are referred to as r_i in the text. (Reproduced with permission from *J. Phys. Chem. B* **2001**, *105*, 9524–9532. Copyright 2001 American Chemical Society)

reactant concentration. In the case of the photoreduction of benzoquinone at the surface of PcZn a clear inverse dependence on the coverage of adsorbed reactants was observed for both, the charging and the discharging currents [44]. For the photooxidation of Ce^{3+} at F_{16}PcZn , however, charging and discharging currents were found to be independent on the Ce^{3+} concentration [129] despite the high similarity in the concentration dependence of i_{in} discussed above. A model (Fig. 7) involving the rate constants k_1 for surface trapping of light-induced minority carriers, k_2 for their recombination with majority carriers, k_3 for the transfer of trapped minority carriers to the electrolyte, and k_4 for the direct transfer of minority carriers to the electrolyte was used to discuss these differences [44, 129, 163].

The back reactions corresponding to the detrapping from surface defects (k_{-1}) and dissociation of electron–hole pairs to a trapped minority carrier and a majority carrier (k_{-2}) were energetically not favored at room temperature ($kT = 0.026$ eV as compared to a frontier orbital gap of about 1.65 eV) and were assumed to be negligible in first approximation. Electron injection from the electrolyte into the electrode (k_{-3} and k_{-4}) had also not been observed and hence all back reactions were assumed to be negligible. The charging and discharging of surface defects at molecular electrodes following the charging events but in a still unperturbed adsorption equilibrium could then be described by $r_1 = r_2 + r_3$ or, in more detail, by

$$k_1 \cdot c_{\text{min}} \cdot N_{\text{ss}} \cdot (1 - \Theta) = k_2 \cdot c_{\text{maj}} \cdot N_{\text{ss}} \cdot \Theta + k_3 \cdot c_{\text{redox,ad}} \cdot N_{\text{ss}} \cdot \Theta \quad (7)$$

where c_{min} and c_{maj} are the concentrations of light-induced minority carriers and majority carriers at the surface, $c_{\text{redox,ad}}$ is the concentration of the electroactive

species adsorbed at the electrode surface, N_{ss} is the overall number of chargeable surface defects, and Θ the occupation of these states ($0 \leq \Theta \leq 1$). Θ in this situation could be described by

$$\Theta = \frac{K}{1 + K} \quad (8)$$

with

$$K = \frac{k_1 \cdot c_{\min}}{k_2 \cdot c_{\text{maj}} + k_3 \cdot c_{\text{redox,ad}}} \quad (9)$$

Equations 8 and 9 predicted a decreasing Θ when $c_{\text{redox,ad}}$ is increased. Both, the amount of surface trapping upon opening of the shutter and detrapping upon closure of the shutter were expected to be proportional to Θ . As shown before, $c_{\text{redox,ad}}$ could be described by a Langmuir isotherm. Therefore K , Θ and also the charging and discharging currents should behave antipodal to i_{in} . This could clearly be seen for the photoreduction of BQ at PcZn in a decrease of the peak currents i_{peak} at increasing electrolyte concentration [44]. Consequently, i_{peak} of the charging and discharging reactions could be approximated by a modified Langmuir isotherm: [44]

$$i_{\text{peak}} = i_{\text{max,peak}} - \frac{i_{\text{max,peak}} - i_{\text{min,peak}}}{1 + \frac{1}{k'_a \cdot c_{\text{redox}}}} \quad (10)$$

where $i_{\text{max,peak}}$ and $i_{\text{min,peak}}$ at a given electrode potential were the maximum peak current for slow faradaic charge transfer (low values of c_{redox}) and the minimum peak current for fast faradaic charge transfer (high values of c_{redox}), respectively. The constant $k'_a = f \cdot k_a$ can be considered a corrected accommodation coefficient with f representing the strength of coupling between the coverage by adsorbed reactants and the size of charging and discharging currents. The accommodation coefficients and other constants according to Eqs. 3a and 10 are listed in Table 1 for PcZn and F₁₆PcZn electrodes for a variety of redox electrolytes. Despite a stronger interaction (higher k_a) of F₁₆PcZn with, e.g., Fe(CN)₆^{3-/4-} compared to that of PcZn a smaller i_{max} is reached at F₁₆PcZn under identical illumination conditions. A smaller concentration of light-induced charges at the surface or a smaller charge transfer rate is thereby indicated.

As mentioned above, the anodic charging currents and cathodic discharging currents at F₁₆PcZn in aqueous Ce^{3+/4+} solution were found to be independent on the electrolyte concentration and could not be analyzed by Eq. 10, although i_{in} did show a saturation behavior comparable to PcZn. This difference was discussed to arise from a missing pathway for minority carriers from the surface traps to the electrolyte leading to negligible k_3 . Traps seemed to be present in the surface region which were not, however, accessible, even by adsorbed electrolyte species. These were, therefore, referred to as “near-surface defects” [129].

Table 1 Values of accommodation coefficients and other constants [130, 163] according to Eqs. 3a, 3b, and 10 for PcZn and F₁₆PcZn electrodes in different electrolytes as indicated in parantheses

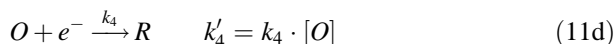
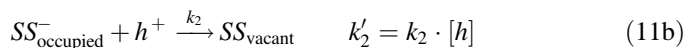
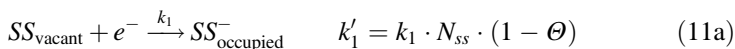
Measured photocurrent	Constant	PcZn	PcZn	F ₁₆ PcZn	F ₁₆ PcZn
		(Fe(CN) ₆ ^{3-/4-})	(O ₂)	(Ce ^{3+/4+})	(Fe(CN) ₆ ^{3-/4-})
<i>i</i> _{in}	<i>i</i> _{max,in} /μA	55.7	4.1	2.2	3.6
	<i>k</i> _a /l mmol ⁻¹	0.7	11.3	32.1	38.7
Charging current	<i>i</i> _{max,peak} ^{cath} /μA	17.6	13.6	4.5	8.3
	<i>i</i> _{min,peak} ^{cath} /μA	3.1	5.8	4.5	0.4
	<i>k</i> _a ^{cath} /l mmol ⁻¹	2.7	4.3	–	19.9
Discharging current	<i>i</i> _{max,peak} ^{an} /μA	8.3	5.2	2.6	1.7
	<i>i</i> _{min,peak} ^{an} /μA	3.3	0.9	2.6	0.2
	<i>k</i> _a ^{an} /l mmol ⁻¹	8.7	27.1	–	7.3

The indices ^{cath} and ^{an} are standing for the observed cathodic or anodic photocurrents, respectively

Since cathodic as well as anodic photocurrents were seen at F₁₆PcZn electrodes the question arose whether surface traps for electrons might also be detectable. Electrodes were also investigated at considerably more negative electrode potentials, using Fe(CN)₆^{3-/4-} in the electrolyte. Indeed, not only cathodic steady-state photocurrents, but also cathodic charging currents and anodic discharging currents could be found under these conditions [163]. The dependence on the electrolyte concentration was analyzed according to Eq. 10 with the accommodation coefficients and other constants shown in Table 1. Such behavior is opposite of that observed for the anodic charging and cathodic discharging currents [129] at F₁₆PcZn with Ce^{3+/4+} and resembled the characteristics found for cathodic charging and anodic discharging currents at PcZn [44, 50]. It was concluded that photo-generated electrons in F₁₆PcZn were trapped in states at the very surface and could be transferred to acceptors in the electrolyte, although holes were shown to be trapped in “near-surface defects” for which no charge transfer to the reactant in the electrolyte could be observed [163].

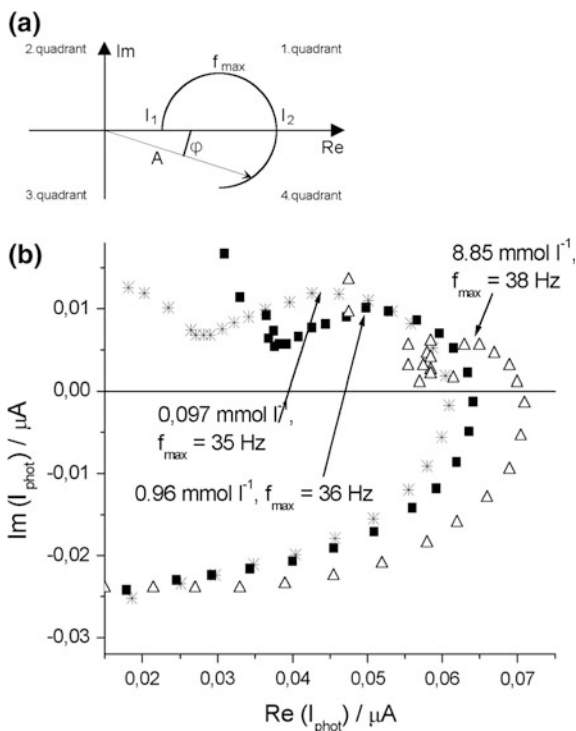
Intensity-Modulated Photocurrent Spectroscopy (IMPS)

To quantitatively determine the rate constants, IMPS measurements were performed at phthalocyanine electrodes in contact to different redox electrolytes. The Pc working electrode was illuminated by a modulated light-emitting diode as light source and the phase shift ϕ of the resulting photocurrent and its amplitude *A* were measured for different modulation frequencies ω . These served to calculate kinetic data of the photo-induced processes in a model of doped semiconductor electrodes, which considers surface recombination and charge transfer from the frontier orbital levels as well as from surface defects [151, 162, 165]. According to the following reactions for a *p*-type semiconductor, which are also shown in Fig. 7, pseudo first-order rate constants *k*_{*i*}' were used:



SS_{vacant} and SS_{occupied}^- represent vacant and occupied surface defects, respectively. O stands for the oxidized and R for the reduced form of the electroactive species in the electrolyte and k_i represent the rate constants. N_{SS} is the density of surface defects, Θ their occupation, $[h]$ is the concentration of electron vacancies (holes) in the HOMO at the surface and $[O]$ is the concentration of the oxidized form of the electroactive species in the electrolyte. The amplitudes A and phase shifts φ for different modulation frequencies $\omega = 2\pi f$ are presented in the complex plane as shown schematically in the first part of Fig. 8. Kinetic data of charge transfer and surface recombination can be extracted from the first quadrant in the complex plane plot by use of the intersections of the plot with the real axis I_1 and I_2 [165]. The low

Fig. 8 **a** Principal shape of an IMPS plot in the complex plane, as it is found in the presence of surface recombination. I_1 and I_2 are the intersections of the plot with the real axis. The modulation frequency with the highest imaginary value is f_{max} . **b** IMPS plots of a PcZn electrode using different $\text{Fe}(\text{CN})_6^{3-}$ concentrations in the electrolyte as indicated, measured at an electrode potential of 0 mV versus SCE. (Reproduced with permission from *J. Phys. Chem. B* **2001**, *105*, 9524–9532. Copyright 2001 American Chemical Society)



frequency limit I_1 represents the differential steady-state photocurrent increase due to a differential increase in the light intensity [162]. The high frequency intercept I_2 represents the amplitude of the Gärtner flux g , which is the flux of minority carriers to the electrode surface.

The values k_2' and k_3' can be calculated from the frequency of the highest imaginary part of the photocurrent (f_{\max}):

$$f_{\max} = \frac{k_2' + k_3'}{2 \cdot \pi}. \quad (12)$$

If no electroactive species are present in the electrolyte ($k_3' = 0$), k_2' can be directly calculated with this equation, given that photocorrosion can be neglected. This is normally the case for phthalocyanine electrodes even at very low electrolyte concentrations [45, 49]. After adding electroactive species, k_3' can be determined if k_2' is known. If both k_2' and k_3' are known, the ratio k_4'/k_1' can be calculated from I_1 and I_2 [165]:

$$\frac{k_4'}{k_1'} = -\frac{I_2}{I_1 - I_2} \cdot \frac{k_2'}{k_2' + k_3'} - 1. \quad (13)$$

At higher frequencies the effects of the $R_{el} \cdot C_{sc}$ time constant of the cell, where R_{el} is the resistance of the electrolyte and C_{sc} is the capacitance of the space charge layer, become evident and the photocurrent is attenuated. The frequency response then describes a semicircle in the fourth quadrant of the complex plain. For an n -type semiconductor the semicircle caused by surface recombination will appear in the third and the semicircle due to the $R_{el} \cdot C_{sc}$ time constant in the second quadrant.

IMPS at PcZn electrodes: Although the principle characteristics of IMPS were observed for electrodes of PcZn in contact with various electrolytes (Fig. 8) [163], flattened semicircles were observed in the first quadrant instead of true semicircles expected by the model [165]. A distribution of surface defects over a range of energies rather than at a single energy was thereby indicated since model calculations had shown that a Gaussian distribution of energies and the resulting Gaussian distribution of the rate constants k_i would lead to such characteristics [156, 166]. A kinetic limitation by diffusion in the electrolyte, however, may have an influence also especially in cases of rather large photocurrents and low concentrations of reactive species in the electrolyte.

Another deviation from the ideal behavior was found for PcZn and can also be seen in Fig. 8: for very low modulation frequencies, $\text{Im}(i_{\text{phot}})$ increased at 0 mV and -200 mV versus SCE instead of approaching zero as expected from the model. Another slow reaction at the electrode surface is thereby indicated [163]. In series of experiments with oxidized species in the electrolyte the increase in $\text{Im}(i_{\text{phot}})$ for very low frequencies was observed to much higher extent than without electroactive species added. Since the plots tend to new maxima at frequencies below 0.2 Hz (the lowest frequency applied in these studies), a slow process occurring in the second or minute regime was indicated. In this time regime, the adsorption equilibrium of

reactants at molecular semiconductor electrodes (see above) was found to change and establish a new equilibrium under illumination. Such change in the adsorption equilibrium could, therefore, also be detected in the IMPS plots at very low modulation frequencies.

Figure 8 depicts a typical series of IMPS experiments in which the concentration of an electroactive species has been changed, in this case the concentration of $\text{Fe}(\text{CN})_6^{3-}$. With increasing electrolyte concentration an increasing I_2 and a decreasing difference between I_2 and I_1 was observed, indicating a higher charge transfer rate from the LUMO (k'_4). On the other hand, an increasing f_{max} also showed a faster charge transfer from surface defects (k'_3). Similar measurements were also performed using different *p*-benzoquinone (BQ) concentrations and an oxygen-saturated solution. The results for $\text{Fe}(\text{CN})_6^{3-}$ and O_2 given in Table 2 show that charge transfer to $\text{Fe}(\text{CN})_6^{3-}$ mainly occurred from the PcZn LUMO, while charge transfer from surface defects also took place but only to a minor extent. Charge transfer to oxygen, however, mostly occurred via surface defects. This was explained by an additional introduction of surface defects by oxygen, which also could be observed in higher charging- and discharging currents, especially at freshly prepared PcZn electrodes, in oxygen-saturated as compared to nitrogen-saturated KCl solution [163]. The overall charge transfer to oxygen was less efficient compared with $\text{Fe}(\text{CN})_6^{3-}$ and *p*-benzoquinone, which was attributed to the low charge transfer rate from the LUMO to oxygen.

Table 2 also showed that k'_3 and k'_4 obviously did not depend linearly on the electrolyte concentration $[O]$, as it would have been expected from Eqs. 11c and 11d. This result confirmed that charge transfer from PcZn electrodes could only occur to adsorbed electroactive species (see above). If $[O]$ in Eqs. 11c and 11d is replaced by the concentration of adsorbed oxidized species $[O]_{\text{ad}}$, which should show a saturation behavior toward high values of $[O]$ when a Langmuir isotherm is assumed, the observed dependence of k'_3 and k'_4 on $[O]$ is explained.

IMPS at F_{16} PcZn electrodes: IMPS plots for F_{16} PcZn in different electrolytes are shown in Fig. 9 [163]. In aqueous KCl solution without electroactive species a

Table 2 Kinetic data for a PcZn electrode in different electrolytes of different concentrations at an electrode potential of 0 mV versus SCE

Electrolyte	$c/\text{mmol l}^{-1}$	k'_3/s^{-1}	k'_4/k'_1	Charge transfer via LUMO (%)	Charge transfer via surface defects (%)	Recombination (%)
$\text{Fe}(\text{CN})_6^{3-}$	0.097	6.3	0.975	49.4	1.4	49.2
	0.96	12.6	1.518	60.3	2.2	37.5
	8.85	25.1	3.538	78.0	2.3	19.7
O_2	1.2	75.4	0.086	7.9	24.0	68.1

The three columns on the right show the percentages of electrons that reach the surface (100 %) that will eventually recombine or undergo charge transfer to the electrolyte from either the LUMO or from surface defects [163]

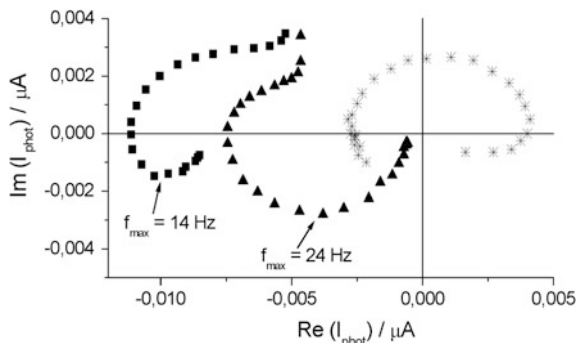


Fig. 9 IMPS plots of an $F_{16}PcZn$ electrode at 400 mV versus SCE. The electrolytes were 1 mol l^{-1} aqueous KCl solution (\blacktriangle), aqueous KCl with 1 mmol l^{-1} $Fe(CN)_6^{4-}$ ($*$) and aqueous KCl with 1 mmol l^{-1} $Fe(CN)_6^{3-}$ and 1 mmol l^{-1} $Fe(CN)_6^{4-}$ (\blacksquare). (Reproduced with permission from *J. Phys. Chem. B* **2001**, *105*, 9524–9532. Copyright 2001 American Chemical Society)

semicircle appeared in the third quadrant, indicating the recombination of photo-generated holes with electrons from the LUMO. It was mentioned before that photogenerated holes in $F_{16}PcZn$ are trapped in near-surface defects, which represent recombination centers [129]. With $Fe(CN)_6^{4-}$ added to the electrolyte, the IMPS plot appeared mainly in the first quadrant, indicating surface charging with photogenerated electrons and their recombination with holes from the HOMO (Fig. 9). The charging of the surface with photogenerated holes was also evident from a small cathodic charging current observed at the beginning of the illumination under these conditions [163].

Taking this into account, the IMPS plots at $F_{16}PcZn$ electrodes were discussed in a model shown in Fig. 10 [129, 163]. As already seen in the photocurrent transient measurements, the n -type behavior of $F_{16}PcZn$ is compensated by oxygen after storage in air. Both electrons and holes are photogenerated in significant amounts compared to their concentration in the dark. At +400 mV versus SCE, the transport of holes to the surface is favored as compared to the transport of electrons. Charging of surface defects with electrons may also occur, but to a smaller extent compared to the charging of near-surface defects with holes (Fig. 10a). Following the addition of $Fe(CN)_6^{4-}$, photogenerated holes from the HOMO can undergo charge transfer to the electrolyte, and the charging of near-surface defects is significantly reduced. The charging of surface defects with electrons and their recombination can, therefore, be observed in the photocurrent transients and in IMPS (Fig. 10b).

With both $Fe(CN)_6^{4-}$ and $Fe(CN)_6^{3-}$ added to the KCl solution in the same concentrations, the semicircle of the IMPS plot again appeared in the third quadrant (Fig. 9), since electrons now could also undergo charge transfer from the LUMO, so that anodic charging currents again became higher than the cathodic charging

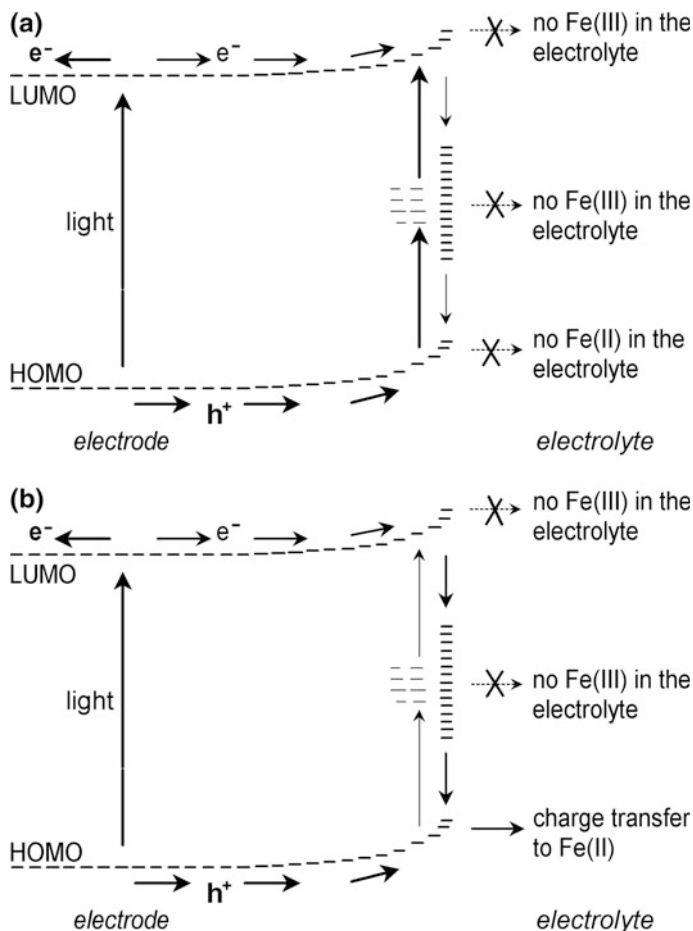


Fig. 10 Situation at the interface between the $F_{16}PcZn$ electrode and the electrolyte (1 mol l^{-1} KCl) at about +400 mV versus SCE (a) before and (b) after the addition of $1 \text{ mmol l}^{-1} Fe(CN)_6^{4-}$. (Reproduced with permission from *J. Phys. Chem. B* **2001**, 105, 9524–9532. Copyright 2001 American Chemical Society)

currents. The value of f_{max} (14 Hz) was now lower than it had been in KCl solution (24 Hz). The quantitative IMPS model presented above does not predict this change in f_{max} . This is due to the fact that the model applies to doped semiconductors only and that the concentration of majority carriers in a doped semiconductor is not significantly changed under illumination. The experimental results obtained at $F_{16}PcZn$ electrodes, on the contrary, clearly showed that $F_{16}PcZn$ is a compensated semiconductor after storage in air and that photocurrents involving both types of charge carriers have to be considered.

4 Sensitization of Oxide Semiconductors by Phthalocyanines

4.1 Sensitization of Nanoparticulate Semiconductors

Investigations of the photoelectrochemical properties of pure phthalocyanine thin films originated from studies in which phthalocyanines had been deposited on inorganic oxide electrodes to investigate their role as sensitizers and protecting layers against photocorrosion. Anodic sensitization could be achieved by vapor-deposited PcCu and by surface-bound tetrasulfonated copper phthalocyanine on *n*-SnO₂ conducting glass [56] and also by vapor-deposited thin films of PcH₂ on single-crystal electrodes of *n*-TiO₂, *n*-SrTiO₃, *n*-WO₃, *n*-ZnO, *n*-CdS, *n*-CdSe, *n*-Si, *n*-GaP, or slides of SnO₂ conducting glass [58]. The sensitization capability of the phthalocyanine layers could clearly be shown by anodic photocurrents that followed the absorption spectrum in their spectral dependence. The quantum efficiency of the sensitization was generally low and photocorrosion of the semiconductor substrate electrodes (evident for those materials of smaller band gap) could not be suppressed sufficiently. The same conclusion was drawn from an extended study in which also films of PcMg, PcZn, PcAl(Cl), PcTi(O), PcCo, and PcFe on single-crystalline *n*-TiO₂ or *n*-WO₃ were investigated [57]. In more recent studies it was found that although surface defects on TiO₂ quenched the photocurrent following light absorption in the oxide electrode, the (sensitized) photocurrents following light absorption in the phthalocyanine were left widely unchanged [59] and details of the energy level alignment were discussed. It was also shown that the film morphology of PcTi(O) or PcV(O) played a crucial role. Compact layers of the materials led to cathodic photocurrents originating from the phthalocyanine as active semiconductor material, whereas islands of the materials led to sensitized anodic photocurrents [167].

The photoelectrochemical properties of PcIn(Cl) thin films were investigated on single-crystalline layered semiconductor electrodes of SnS₂ or MoS₂ [168, 169]. These surfaces turned out to provide a suitable substrate to deposit highly ordered epitaxial phthalocyanine films by OMBE and to study such films as sensitizers for the *n*-type semiconductors. Very narrow absorption spectra and photocurrent action spectra were obtained speaking in favor of well-crystallized PcIn(Cl) on *n*-SnS₂ and injection of electrons from the excited state of the dyes into the crystallites of SnS₂. A quite constant quantum efficiency of about 10 % was found. Direct injection of electrons from excited molecules adjacent to SnS₂ was detected [169]. An increased quantum efficiency of up to 44 % was obtained on SnS₂ for drop-coated films of phthalocyanines carrying eight dodecylamide or dodecylester functions [170]. These films showed liquid-crystalline properties and small chromophore interaction. The high quantum efficiency was reached for films of submonolayer coverage and decreased for thicker films pointing toward efficient injection again from molecules close to the interface with SnS₂ only. Consequently, the incident

photon-to-current conversion efficiency (IPCE) for submonolayer or thicker films (up to 30 equivalent monolayers) was found quite constant at 0.8 % only.

Higher efficiencies of phthalocyanine-modified oxide semiconductor electrodes could be achieved if nanoparticulate oxide films were used since the electrode surface and, hence, the interface area of the phthalocyanine with the oxide could be increased significantly. In these cases a monolayer of phthalocyanine on the nanoparticles provided sufficient light absorption. A high quantum efficiency can be maintained if aggregation of the phthalocyanines can be suppressed. Vapor deposition of the phthalocyanines turned out to be not appropriate. The chromophores were typically adsorbed from solutions and preferably of phthalocyanines that carried a chemical substituent that provided good anchoring to the oxide surface. Tetrasulfonated metal-free phthalocyanine and the complexes of Zn, Ga(OH), Co, In(OH), and Ti(O) were adsorbed to nanocrystalline films of TiO₂ prepared by the sol-gel technique and their photoelectrochemical activity was measured under monochromatic illumination [171]. Among these, the zinc complex showed the highest IPCE at a sensitization quantum yield of 5.7 %. The aluminum complex of tricarboxymonoamidophthalocyanine adsorbed on commercial TiO₂ particles showed photocatalytic oxidations of organic molecules like phenols or hydroquinone [172]. A composite electrode of TiO₂/phthalocyanine could also be prepared by spray pyrolysis of a mixed solution of titanium-oxy-acetylacetonate and the Cu complex of a tetrasulfonated phthalocyanine. A sensitized photocurrent was obtained in the phthalocyanine Q-band absorption range. However, the photocurrents reached only a few $\mu\text{A cm}^{-2}$ under illumination with 100 mW cm^{-2} of white light [173]. Attempts have been made to prepare rather complex materials of TiO₂ particles modified by quantum-sized CdS on its surface and, further, by Ga(OH), Zn, In(OH), or V(O) complexes of tetrasulfonated phthalocyanines. Efficient sensitization by monomers of the Ga(OH) complex was claimed [174] at IPCE of up to 10 %, but photocorrosion will be a severe problem for such electrodes as reported earlier. Rather efficient electrodes sensitized by phthalocyanines used a Ru complex of octamethylphthalocyanine with two additional axial ligands of pyridine-bis-carboxylic acid to bind to the oxide surface which was grafted to nanoparticulate TiO₂, reaching an IPCE of 60 % and photocurrents of 10 mA cm^{-2} under illumination with white light under AM 1.5 conditions [175]. In a study using a number of differently carboxylated or sulfonated phthalocyanine complexes of Zn or Al (OH) similar values were reached with the zinc complexes of tetracarboxyphthalocyanine or tetrasulfophthalocyanine showing the best performance within this group of materials reaching an IPCE of 30–45 % and a conversion efficiency of about 1 % under AM 1.5 (100 mW cm^{-2}) conditions [60].

The work on phthalocyanines as sensitizer for TiO₂ revealed three conditions aside from an obviously needed positioning of the electron in the excited molecular state close above the conduction band edge of the semiconductor and good solubility for electrode preparation. Stable adsorption to the semiconductor surface typically achieved by covalent bonds through carboxylate or sulfonate anchoring groups allows fast electron injection within less than 1 ps which can easily compete with radiationless decay or direct injection into the electrolyte. Aggregation of the

adsorbed phthalocyanine sensitizers has to be avoided in order to maintain such fast injection also for larger dye coverage and avoid additional pathways for radiationless decay. Aggregated sensitizers, further, often allow rapid recombination of electrons already injected into the semiconductor to oxidized sensitizer molecules or back to the electrolyte. Aggregation of phthalocyanines is efficiently blocked by bulky substituents at the phthalocyanine ring or at additional axial ligands at the central metal atom. Even dyes fulfilling this requirement, like, e.g., octacarboxyphthalocyanines, provided low efficiencies only [176]. The influence of axial ligands at phthalocyanine central metal atoms on the properties as sensitizers was analyzed. It was shown that axial methylpyridine ligands at Ru phthalocyanines could suppress aggregation relative to identical complexes of Zn but efficiencies could not be lifted above 0.4 % [177]. Silicon phthalocyanines were synthesized which solely relied upon axial ligation and also the anchoring to TiO₂ was performed through carboxylate groups at the end of the axial ligands [178, 179]. Aggregation could again be efficiently blocked but efficiencies did not surpass a few tens of a percent. In the context of these different studies it was established that sensitizers leading to efficient dye-sensitized solar cells, further, should provide good overlap of the electron wave function in the excited state (often approximated by the lowest unoccupied molecular orbital of the dye in its ground state) with the Ti 3d orbitals of the TiO₂ conduction band to allow facile electron injection [180]. Such conditions are generally established by an asymmetric substitution pattern of electron-donating and electron-withdrawing substituents at the phthalocyanine ligands leading to an electronic “push-pull” configuration toward the anchoring group of the sensitizer and, hence, toward the semiconductor surface.

In consequence, good results of sensitized TiO₂ were reported for peripherally asymmetrically tetra-substituted zinc complexes with only one of the four substituents acting as carboxylate anchor to the semiconductor surface and with three bulky *tert*-butyl groups hindering aggregation [181–188]. The *tert*-butyl groups also increase the solubility of the sensitizers in organic solvents, allowing efficient impregnation of the electrodes. By the electron-donating capability of the *tert*-butyl groups toward the central Pc ring as opposed to the electron-withdrawing character of the carboxylic acid functionality, such unsymmetrical substitution adds the required “push-pull” characteristics to the molecular orbitals, helpful for electron injection to the semiconductor from the excited state, and, presumably, suppressing electron back transfer to the dye and to the electrolyte. Such influence of electronically unsymmetrical substitution had also been established earlier for Ru trisbipyridyl complexes serving as classical sensitizers for TiO₂ [189]. The validity of this approach was confirmed for porphyrins which turned out to serve as very efficient sensitizers of TiO₂ [190, 191]. In the latter case cells were reported reaching a record conversion efficiency of 12.3 % under simulated AM 1.5 conditions, based on a short-circuit photocurrent of 17.66 mA cm⁻², an open-circuit photovoltage of 0.935 V, and a fill factor of 75 %. A porphyrin was used in which the electronic directionality was increased beyond that of the established asymmetrically substituted phthalocyanines and porphyrins. An electron-deficient anchor substituent, two bulky hydrocarbon substituents at the two positions next to the

anchor, and a strong electron donor substituent at the position opposite to the anchor were used. Further, the standard iodine-based electrolyte was replaced by a Co-based redox electrolyte [191]. The success of this approach indicated the potential of technical application of appropriately substituted porphyrins and phthalocyanines as sensitizers in dye-sensitized solar cells. If such construction principle is followed, the above-mentioned approach of using Si complexes with additional bulky substituents further hindering aggregation can be a valuable additional ingredient to reach good sensitization of TiO₂ as demonstrated by an efficiency of 4.5 % reached by an NIR-absorbing phthalocyanine–naphthalocyanine hybrid complex of Si [192].

Despite their typically high extinction coefficients, the rather narrow absorption range of monomeric (nonaggregated) phthalocyanines can lead to incomplete absorption of visible light. To overcome this drawback for use as a sensitizer in technical dye-sensitized solar cells, a concept has been developed to use parallel absorption spreading over larger portions of the solar spectrum by more than one dye adsorbed to the TiO₂ surface (“dye cocktails”) [181]. A conversion efficiency of 7.74 % with $I_{sc} = 16.2 \text{ mA cm}^{-2}$, $V_{oc} = 0.666 \text{ V}$ and $FF = 72 \%$ was reached for sensitization by a mixture of a fluorine dye JK-2 and a zinc phthalocyanine substituted by one carboxylic acid anchor and three pushing and shielding (see above) tertiary butyl groups. This performance was improved beyond the conversion efficiency of 3.52 % in a cell sensitized by just the substituted phthalocyanine and beyond the conversion efficiency of 7.08 % reached in a cell just sensitized by JK-2. This is not the only example in which larger efficiencies were reached for dye cocktails than for the use of the corresponding single dyes, which is remarkable in view of the numerous additional recombination pathways that appear possible in mixtures of dyes [193, 194]. Rapid injection of electrons from the excited state of the sensitizers to the conduction band of TiO₂ represents a fundamental prerequisite. The efficiency could be increased even further by a cell with a separation of the sensitizers using an Al₂O₃ tunnel barrier, reaching a conversion efficiency of 8.65 % under simulated AM 1.5 conditions, based on $I_{sc} = 17.6 \text{ mA cm}^{-2}$, $V_{oc} = 0.696 \text{ V}$, and $FF = 70 \%$ [195]. Such optimization strategies could also increase further the efficiencies reached for Pcs as sensitizers of TiO₂.

4.2 Sensitization of Electrodeposited Semiconductor Thin Films

Aside from TiO₂, ZnO is one of the most promising semiconductor materials in dye-sensitized solar cells [196–199]. On the way toward both, improved electrode properties and more economically feasible cells, new ways of preparing semiconductor–dye composites are sought and ZnO offers new perspectives in this respect. Crystalline films can be obtained from solution, e.g., electrochemically on the cathode during electrolysis of aqueous Zn(NO₃)₂ or oxygen-containing ZnCl₂ solutions.

4.2.1 Electrodes Deposited in the Presence of Phthalocyanines

The successful preparation of dye-loaded porous but crystalline ZnO semiconductor thin films in the presence of water-soluble dyes [200] such as metal complexes of tetrasulfonated phthalocyanines (TSPcMt) [201, 202] was reported. This one-step preparation by dissolving the dye in the bath for the ZnO electrodeposition was found to allow *simultaneous self-assembly of ZnO and the adsorbed dye*, thus yielding homogeneously colored crystalline ZnO films with porous morphology. The dyes showed good compatibility with the aqueous deposition conditions and a suitable range of redox potentials to allow proper alignment of the energy levels in the contact to ZnO. Adsorption of dye molecules onto the growing surface of ZnO strongly affected the crystal growth of ZnO and led to a significantly higher surface area when compared to pure ZnO films formed without addition of the dyes, opening up a new synthetic route to photoactive materials for dye-sensitized semiconductor electrodes. Strongly differing crystal sizes, morphologies and porosities of the crystalline ZnO as well as different degrees of aggregation of the dye molecules could be obtained dependent upon the adsorbed dye molecules and proper choice of the deposition conditions [202, 203].

Examples of different film morphology are shown in Fig. 11. For a given phthalocyanine ligand the choice of the central metal allows to grow films of remarkably different morphology and relative orientation of the ZnO nanocrystals

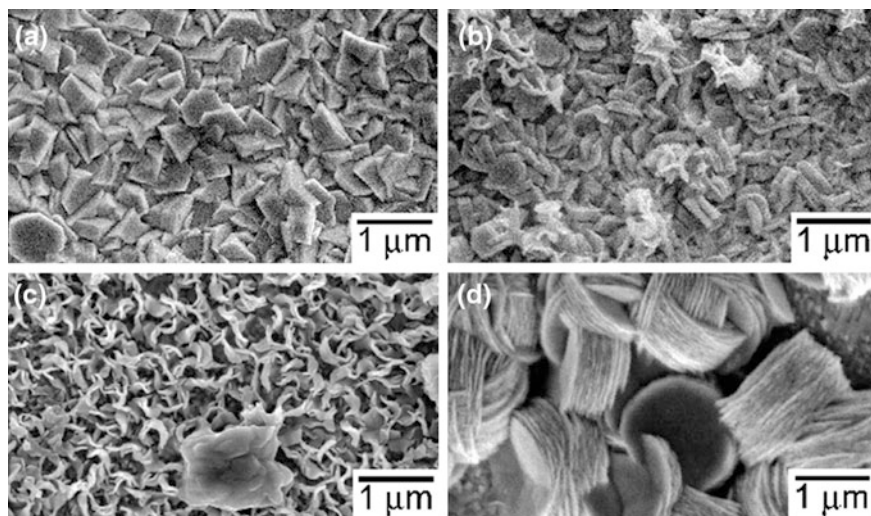


Fig. 11 Influence of the adsorbed dye molecules on the morphology of the films deposited at -0.9 V versus SCE from 0.1 M $\text{Zn}(\text{NO}_3)_2$ of **a** pure ZnO without dye and in the presence of **b** 50 μM TSPcZn, **c** 50 μM TSPcAl(OH), and **d** 50 μM TSPcSi(OH) $_2$ as revealed by scanning electron microscopy. (Reprinted from Z. H. Kafafi, (ed.): “Organic Photovoltaics II” Proceedings of SPIE, Volume 4465, Bellingham (WA), Copyright (2002), with permission from The International Society for Optical Engineering)

[202]. The formation of ester-like bonds through the sulfonic acid groups of a TSPcMt molecule to the surface of ZnO probably plays a decisive role in this assembly, since a formation of such bonds was also seen in TSPcCo/TiO₂ composites [204]. The adsorption of TSPcMt takes place preferentially onto the a/b-plane of ZnO, since crystal growth predominantly along the a and b axes was observed. The overall growth direction is defined vertical to the electrode. Therefore, ZnO crystallites with their a and b axes perpendicular to the substrate grew faster and represented the preferential crystal orientation of the final film [202]. Differences in the stability of TSPcMt adsorption to different crystallographic faces of ZnO led to the anisotropy of the crystal growth (Fig. 11).

Dye molecules at the interface not only react with ZnO but also form well-defined intermolecular structures. The intermolecular electronic interaction can be studied by measuring UV-vis absorption spectra, because the interaction of the chromophores in condensed dye assemblies leads to specific changes of the electronic structure [136, 205, 206]. This was discussed in detail for the electrodeposited ZnO/TSPcZn hybrid thin films [202, 207]. Films electrodeposited at -0.7 (slow growth) or -0.9 V versus SCE (faster growth) showed characteristic differences. Whereas both films were blue and less scattering than pure ZnO, the film deposited at -0.7 V obviously contained a higher amount of dye and showed absorption maxima at 337 nm, 639 nm, and a shoulder at around 680 nm. The film deposited at -0.9 V was pale blue and had a Q-band absorption peak at 690 nm and only a shoulder at around 630 nm. The absorption spectra of the ZnO/TSPcZn films deposited at -0.7 V indicated formation of π -stacking aggregates for the TSPcZn molecules in the ZnO/TSPcZn film. Formation of such ordered dye aggregates on inorganic surfaces was also reported for merocyanine dyes adsorbed on TiO₂, Al₂O₃, and ZrO₂, as a consequence of chemical interactions between the dye molecules and the ordered surface of inorganic materials as well as that among the neighboring dye molecules [208]. Films deposited at -0.9 V showed dye loading as monomers noticed from the dominance of the 690 nm Q-band absorption [206]. Washing the ZnO/TSPcZn hybrid thin film deposited at -0.7 V with a surfactant solution (CTAC) providing optimum solubility of TSPcZn led to partial desorption of TSPcZn molecules from the composite films and converted their absorption spectra resembling those of the hybrid thin film deposited at -0.9 V [202]. Such difference clearly indicated the formation of multilayers of dyes with strong dye/dye interaction in the films deposited at -0.7 V. At the bottom of such multilayers of dyes, however, TSPcZn molecules are present that are chemically attached to ZnO and that cannot be washed off by the CTAC treatment.

The *sensitization properties* of such films were studied by photocurrent spectra, time-resolved photocurrent measurements and by intensity-modulated photocurrent spectroscopy (IMPS) [207, 209]. Visible light absorbed in the dyes led to the sensitization of ZnO in contact to an organic I^-/I_3^- electrolyte as exemplary shown in Fig. 12. Many experiments were performed in a conventional three-electrode arrangement with the deposited hybrid thin films as working electrode, a Pt counter electrode and a Ag/AgNO₃ reference electrode. 0.5 M KI in acetonitrile/ethylenecarbonate (1: 4 by volume) was used as the electrolyte. Among TSPcMt

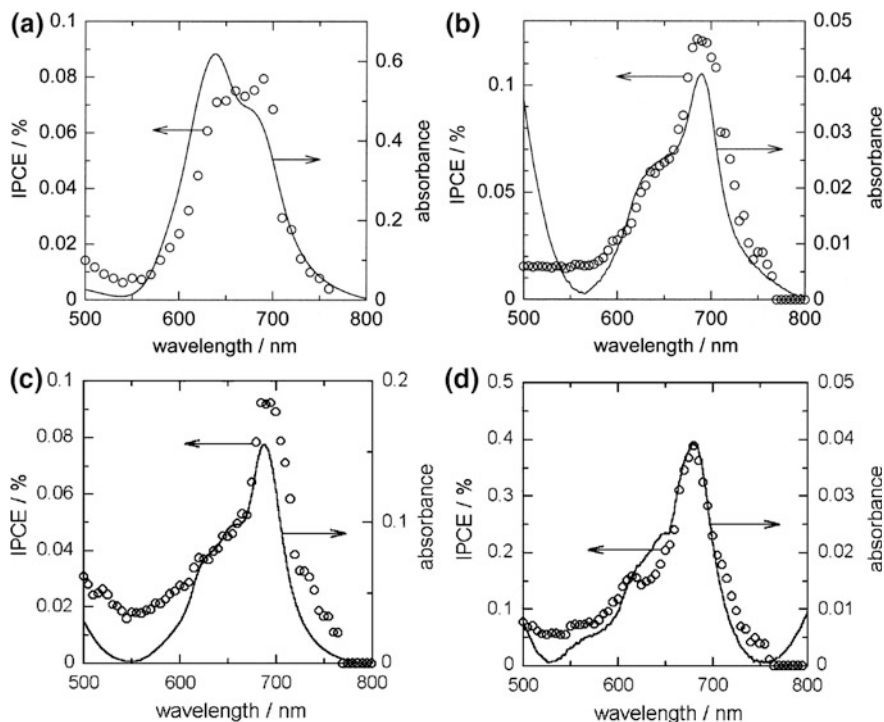


Fig. 12 Optical absorption spectra (*lines*) and photocurrent action spectra in the oxidation of iodide at -0.2 V versus Ag/AgNO_3 (*circles*) measured at films of TSPcZn/ZnO grown at -0.7 V versus SCE (a) and at -0.9 V versus SCE (b), $\text{TSPcAl}(\text{OH})/\text{ZnO}$ (c), and $\text{TSPcSi}(\text{OH})_2/\text{ZnO}$ (d), both grown at -0.9 V versus SCE. (Reprinted from Z. H. Kafafi, (ed.): “*Organic Photovoltaics II*” Proceedings of SPIE, Volume 4465, Bellingham (WA), Copyright (2002), with permission from The International Society for Optical Engineering.)

with different central metals, significantly higher conversion efficiencies were found for monomeric as compared to aggregated TSPcMt adsorbed on the ZnO surface [207, 209, 210]. This was also the case for electrodes having mostly aggregated TSPcZn, although these aggregates dominated the absorption spectra. A considerably higher quantum efficiency of monomeric dye when compared with aggregated dye was thereby shown. When the values of the IPCE are considered it has to be noted that the values reached by ZnO-TSPcMt hybrid thin films were generally low. Among the materials, however, clear differences could be detected showing the strong influence of the central metal. TSPcSi(OH)₂ proved to be the most efficient sensitizer since a peak IPCE of 0.4 % was reached at an absorbance of only 0.04. This indicated an internal quantum efficiency about a factor of 3 higher when compared to monomers of TSPcZn (0.12 % at similar absorbance) and about a factor of 17 higher when compared to TSPcAl(OH). The higher photocurrents in this comparison for TSPcSi(OH)₂ could be explained by quite efficient electron injection from the excited state of the dye to the conduction band of ZnO. A suitable

relative position of the electron energy levels combined with a strong chemical interaction of $\text{TSPcSi}(\text{OH})_2$ with ZnO was found to provide the basis for this increased efficiency when compared with other TSPcMt [209, 210]. In a direct comparison of the monomeric versus the aggregated zinc complex TSPcZn on ZnO (Fig. 12) the higher injection efficiency from monomers was confirmed by an increased quantum efficiency. Despite a smaller coverage by the monomers and, hence, decreased absorption, even the incident photon-to-current conversion efficiency (IPCE) was higher for the films with monomeric TSPcZn when compared to those with aggregated TSPcZn, in which photogenerated charge carriers mostly recombine within the aggregates [207, 209].

Time-resolved photocurrent measurements in the ms-regime were performed to discuss the efficiency of monomeric versus aggregated forms of TSPcMt and the role of the central group in TSPcMt (Fig. 13) [210]. Electrodes with monomers of TSPcZn on ZnO led to a more pronounced overshoot of the photocurrent above the stationary value when the light was switched on and significant cathodic currents when the beam was shut, whereas electrodes with aggregates of TSPcZn showed a more rectangular response consisting of anodic currents only. A more facile transfer of electrons from Γ^- to the aggregates compared with the monomers explained this behavior [207]. The slower regeneration of the neutral dye following electron transfer from the excited monomer to the conduction band of ZnO led to a significantly higher concentration of oxidized dye in the stationary state in this case with the consequence of the observed cathodic currents caused by transfer of electrons from the ZnO valence band, easily detected when the light beam was shut. The low efficiency of TSPcZn aggregates was not caused by slow regeneration kinetics but by fast radiationless decay within TSPcZn aggregates or by a slower electron injection rate into the conduction band of ZnO. Despite significantly faster

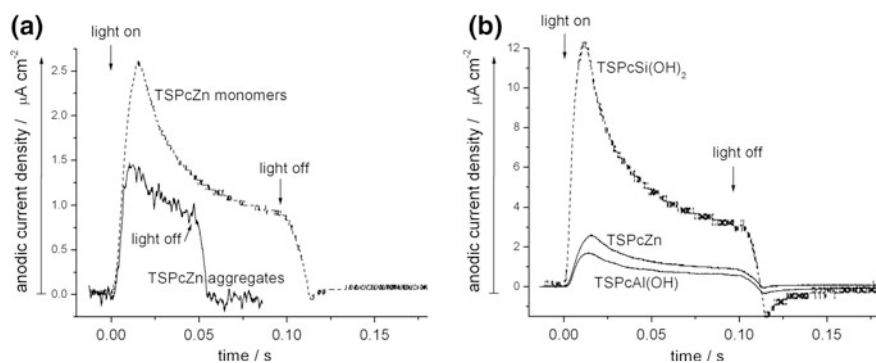


Fig. 13 Photocurrent transients observed at -200 mV versus Ag/AgNO_3 in contact to 0.5 M KI in acetonitrile/ethylenecarbonate (1:4 by volume). Comparison between aggregated and monomeric forms of TSPcZn (a), and of the influence of the central group in monomeric TSPc (b). (Reprinted from Z.H. Kafafi, (ed.): “*Organic Photovoltaics II*” Proceedings of SPIE, Volume 4465, Bellingham (WA), Copyright (2002), with permission from The International Society for Optical Engineering.)

electron transfer from I^- to the aggregates the electrodes were significantly less efficient.

Different TSPcMt monomers on ZnO showed transients of similar shape indicating similar relative rates of electron injection and regeneration. Compared with TSPcSi(OH)₂, however, smaller ratio of charging/steady-state and discharging/steady-state currents were observed for TSPcZn or TSPcAl(OH) (Fig. 13) [207, 209, 210]. A faster electron transfer from the electrolyte to TSPcZn or TSPcAl(OH) was thereby indicated relative to electron injection from the excited dyes into ZnO. Since lower steady-state values of the photocurrents were observed when compared with TSPcSi(OH)₂ it was concluded that TSPcSi(OH)₂ provided faster and more efficient electron injection into ZnO compared with TSPcZn or TSPcAl(OH).

The interplay of different dye molecules present during the electrodeposition reactions of dye-modified ZnO and also under photoelectrochemical working conditions were studied for zinc complexes of tetrasulfonated phthalocyanine (TSPcZn) and tetraphenylporphyrin (TSTPPZn). Both dyes were simultaneously adsorbed to ZnO during the deposition [211]. The typical absorption bands for both dyes were detected. Films of TSPcZn/ZnO consisted of larger particulate domains when compared with TSTPPZn/ZnO or (TSTPPZn + TSPcZn)/ZnO as also revealed by atomic force microscopy [211]. Composite films with both dyes present (TSTPPZn + TSPcZn)/ZnO absorbed 48 % of the light at 420 nm and 31 % at 680 nm. The presence of the porphyrin obviously stabilized the phthalocyanine on the ZnO since a higher amount of TSPcZn was adsorbed. It is relevant to note, however, that the aggregation tendency of TSPcZn was even increased in the films with both dyes present as seen in the increase of the aggregate absorption band (640 nm) relative to the monomer band (680 nm) of TSPcZn [211]. Both, TSPcZn and TSTPPZn worked in parallel and the contribution of each dye to the overall photocurrent was collected [212]. The presence of TSPcZn together with TSTPPZn improved the photoelectrochemical properties of TSTPPZn since a threefold increase of the photoelectrochemical quantum efficiency was found at 425 nm [212]. In this case the increased rate constant of the electron transfer to oxidized TSPcZn could be efficiently utilized to suppress recombination in TSTPPZn. TSPcZn took over a role as charge mediator in the electron transfer from I^- to oxidized TSTPPZn. Nevertheless, IPCE not larger than 0.1 % were observed for these electrodes in which TSPcZn was present during electrodeposition of ZnO leading to aggregates of TSPcZn and a small surface area of the hybrid material.

4.2.2 Sensitization by Subsequently Adsorbed Phthalocyanines

Clearly improved electrode characteristics were obtained when ZnO was prepared in a separate reaction step in the presence of a more favorable structure-directing agent before the phthalocyanine chromophores were adsorbed in a subsequent step [212–214]. Films of ZnO with a high porosity at preserved crystallinity were

obtained in the presence of Eosin Y [214–216]. Since Eosin Y can be desorbed from such films an efficient ZnO semiconductor matrix is provided that can subsequently be loaded with a variety of sensitizer molecules by adsorption from solution (“readsorption method”) [213, 214]. Using this method, TSPcZn was readsorbed on ZnO. By analysis of these films it was clearly observed that TSPcZn could perform at much better efficiency when compared with the films deposited in its presence. In the Q band an absorbance of about 0.7 above the scattering background was observed. This is about a factor of 5–10 higher than that in the films deposited in the presence of TSPcZn speaking in favor of an efficient adsorption of the sensitizer at such ZnO grown in the presence of EosinY. The shape of the band speaks for a widely monomeric adsorption of TSPcZn. The spectral dependence of the photocurrent (IPCE) basically follows the optical absorbance spectrum and shows the high efficiency of adsorbed monomers of TSPcZn. The IPCE reaches 30 % at the absorption maximum of 680 nm leading to a photocurrent density of 2.3 mA cm^{-2} calculated for the geometric surface area. When these values of the IPCE or the current density are compared to the values reached for the films deposited in the presence of TSPcZn, an increase by a factor of about 500–1500 was observed. By normalizing for the increased absorbance an internal quantum efficiency (absorbed photon-to-current conversion efficiency APCE) about 150 times higher can be estimated. The improvement of the photoelectrochemical properties for the TSPcZn/ZnO film can be understood by a mainly monomeric adsorption of the dye on the surface of ZnO, by the preserved crystallinity of ZnO and by the large overall surface area [212]. Despite such progress, however, efficiencies relevant for technical application could not be reported. Subsequent work focussed on the use of newly developed phthalocyanine sensitizers. Octacarboxyphthalocyanines with Zn, Al(OH) and Si(OH)₂ as central groups had shown very small aggregation tendency [217] and had performed well as photocatalysts [218]. These complexes were, therefore, employed as sensitizers on ZnO electrodeposited in the presence of EosinY [219]. Decent values of IPCE (31 %) and APCE (60 %) were reached in the absorption maximum but overall low currents and conversion efficiencies $\eta < 0.3 \%$ were obtained because of a limited achievable load by monomeric dye on the ZnO surface. Small improvements (IPCE = 51 %, APCE = 63 % and $\eta = 0.45 \%$) could be reached using the TiO complex of octacarboxyphthalocyanine [220]. Use of an asymmetrically substituted phthalocyanine with three naphthylxy and one carboxy-dioxyphenyl groups improved the performance only slightly (IPCE = 31 %, APCE = 35 % and $\eta = 0.48 \%$) [220]. It has to be stated that the attractive efficiencies reported for phthalocyanines in the sensitization of TiO₂ as referred to above could not be reached for ZnO yet. It still has to be found out if this is caused by the slightly higher energy of the ZnO conduction band edge or by details in the sensitizer design.

5 Technology Outlook

Photoelectrochemical properties of molecular semiconductors have recently regained new interest in view of their possible application in photovoltaic cells. Phthalocyanines are of interest for this application because of high absorption coefficients for visible light, high chemical and thermal stability, and good commercial availability. Originally, they had been tested successfully for applications in all-solid-state photovoltaic cells [16, 18, 221, 222], where the best results with molecular semiconductors were obtained for *p-n* cells containing a phthalocyanine as *p*-type semiconductor and perylenetetracarboxylic acid diimides (PTCDI) as *n*-type semiconductor in a configuration ITO/PTCDI/Pc/Au [18, 221]. Efficiencies of up to about $\eta = 2\%$ were found for such cells of PcZn and N,N'-dimethyl-3,4,9,10-perylenetetracarboxylic acid diimide (MePTCDI) [221]. The efficiency of such cells could be increased significantly in interpenetrating networks ("mixed layers") of the two electrode materials leading to an increased interfacial area [222]. Crystallographic strain can be expected in the interface of two crystalline molecular semiconductors, leading to a small interfacial contact area and efficiency losses due to chemical and physical defect centers. Such interfacial states have been directly observed as surface dipoles in photoelectron spectroscopy studies of organic/organic' heterojunctions [19, 20, 103, 107, 113, 116]. PcZn and MePTCDI were therefore also investigated in photoelectrochemical *p-n* cells to increase the effective surface area by an electrolyte between the two semiconductor thin films (e.g., ITO/PcZn/Fe(CN)₆^{3-/4-}(aq)/MePTCDI/ITO) [45]. However, although the semiconductor/electrolyte interface avoids the organic/organic' solid contact and should provide larger contact areas at the surfaces, ridiculous efficiencies ($\eta = 0.00032\%$) were found for these cells, caused by a very low photocurrent ($i_{SC} = 10.5 \mu\text{A cm}^{-2}$) which was explained by charge transfer limitation and mandatory reactant adsorption prior to the charge transfer step. Such limitation was generally found for electrodes of phthalocyanines [45, 50, 124], and also for thin films of perylene derivatives [45]. Further, surface defects observed at thin films of phthalocyanines and perylene derivatives [163] mainly act as recombination centers, since charge transfer from surface defects is slow. The rather small surface area of the Pc and PTCDI thin films (roughness factor only about 2) [45] could by far not compensate these limiting effects of reactant adsorption and surface recombination. Rather low efficiencies of only up to 0.08% were therefore also reported for photoelectrochemical solar cells with Pc electrodes and metal counter electrodes, corresponding to all-solid-state Schottky cells [121, 223].

In further developments of all-solid-state cells using phthalocyanines as a donor in a mixed layer with an acceptor, PcCu was very successfully used as donor with C₆₀ as acceptor. Efficiencies of up to 5.7% were reached in a tandem cell approach using such mixed layers [224]. The approach has been developed further to 12% efficient cells claimed by the company Heliatek without, however, mentioning specific composition of the cells [225], and 11.1% efficiency reported for a triple-junction solar cell of the same type using two layers of tetraphenyldibenzoperiflanthene

(DBP) as a donor blended with C₇₀ as acceptor and a layer of 2-((7-(5-(dip-tolylamino)thiophen-2-yl)benzo[c] [1, 2, 5] thiadiazol-4-yl)methylene)malononitrile (DTDCTB) as a donor blended with C₆₀ as acceptor [226]. Such cells are directly competing with solution-processed “plastic solar cells” consisting of at least one polymeric organic donor and, typically, a molecular organic acceptor, which have also reached similar efficiency levels of 6.1 % [227], 7.4 % [228], 8.7 % [229], and 9.4 % [230] for different material combinations in conventional single-cell device structures, 10.6 % in a tandem cell [231], and even 11.5 % [232] or 11.8 % [233] in triple-junction devices.

The problem of short diffusion lengths of excited states in organic absorbers compared with the thickness needed for efficient absorbance could alternatively be solved by the development of nanocrystalline dye-sensitized solar cells, using organic dyes as sensitizers for porous inorganic wide-bandgap semiconductors like TiO₂ or ZnO as reviewed above. When photoelectrochemical cells are considered, the concept of dye-sensitized oxide electrodes therefore provides the best perspective. Although good oxide–dye combinations have already been presented, further work will reveal new composite materials, prepared by different, preferably simpler, preparation techniques and phthalocyanines might very well play a role in this context. One should keep in mind, however, the mostly low efficiency of phthalocyanine aggregates as opposed to considerably more efficient monomers of phthalocyanines on the one hand and the high aggregation tendency of phthalocyanines on the other hand. A goal therefore will be to continue tailoring phthalocyanines with specifically designed anchoring groups to bring the chromophore π -system close toward the oxide surface, optimize the relative energetic and local orbital overlap with the oxide (electronic “push-pull”) and at the same time hinder the chromophores from aggregate formation even at a high coverage on the surface. The photoelectrochemical properties of phthalocyanine surfaces are also of interest in interactions with gas environments. Chemical reactions with redox-active gas molecules lead to similar changes of the surface trap distribution as discussed above for the reactions in contact to liquid redox-active electrolytes. Changes of the electrical conductivity as a consequence of redox interactions with gas molecules were therefore often used to test phthalocyanine thin films as sensitive layers in chemical sensors. Vapor-deposited phthalocyanine thin films and thin films prepared by the LB technique were extensively studied and discussed in review articles [68, 80, 92–94, 234, 235]. Photoelectrochemical experiments in contact to solutions of the analytes or their model compounds can be used to study the surface reactions at the electrodes in great detail and, hence, assist in deepening the insight of chemical sensing at phthalocyanine surfaces. Of particular interest in this context is the finding that the photoconductivity of phthalocyanine films showed a considerably higher sensitivity to the presence of redox-active gas molecules than the dark conductivity [236]. A clear relevance of surface defects as centers of charge-carrier dissociation and traps for charge carriers is thereby shown.

A close link of the photoelectrochemical research at phthalocyanine thin films and research toward their application as chemical sensors should therefore be maintained and used to further develop both fields, although they appear quite independent judged from their technological aspects.

Acknowledgments The author is grateful to T. Yoshida (Yamagata University, Japan) and to T. Nyokong (Rhodes University, South Africa) for numerous fruitful discussions in the course of recent joint work on dye-sensitized solar cells, to the German Academic Exchange Service (DAAD) for partial sponsorship of the work and to a number of students and visiting researchers in the author's group who performed parts of the experimental work reviewed in this chapter.

References

1. Gerischer H, Willig F (1976) Reactions of excited dye molecules at electrodes. In: Boschke FL (ed) Physical and chemical applications of dyestuffs (Topics in current chemistry, vol 61, Springer, Berlin-Heidelberg 1976) pp 31–84
2. Memming R (1996) Semiconductor electrochemistry. Wiley-VCH, Weinheim
3. Grätzel M (2001) Photoelectrochemical cells. *Nature* 414:338–344
4. Nozik AJ, Memming R (1996) Physical chemistry of semiconductor-liquid interfaces. *J Phys Chem* 100:13061–13078
5. Hannappel T, Burfeindt B, Storck W, Willig F (1997) Measurement of ultrafast photoinduced electron transfer from chemically anchored Ru-dye molecules into empty electronic states in a colloidal anatase TiO₂ film. *J Phys Chem B* 101:6799–6802
6. Grünwald R, Tributsch H (1997) Mechanisms of instability in Ru-based dye sensitization solar cells. *J Phys Chem B* 101:2564–2575
7. Dloczik L, Illeperuma O, Lauermann I, Peter LM, Ponomarev EA, Redmond G, Shaw NJ, Uhlendorf I (1997) Dynamic response of dye-sensitized nanocrystalline solar cells: Characterization by intensity-modulated photocurrent spectroscopy. *J Phys Chem B* 101:10281–10289
8. Huang SY, Schlichthörl G, Nozik AJ, Grätzel M, Frank AJ (1997) Charge recombination in dye-sensitized nanocrystalline TiO₂ solar cells. *J Phys Chem B* 101:2576–2582
9. de Jongh PE, Vanmaekelbergh D (1997) Investigation of the electronic transport properties of nanocrystalline particulate TiO₂ electrodes by intensity-modulated photocurrent spectroscopy. *J Phys Chem B* 101:2716–2722
10. Solbrand A, Lindström H, Rensmo H, Hagfeldt A, Lindquist S-E, Södergren S (1997) Electron transport in the nanostructured TiO₂-electrolyte system studied with time-resolved photocurrents. *J Phys Chem B* 101:2514–2518
11. Hlilgendorff M, Sundström V (1998) Dynamics of electron injection and recombination of dye-sensitized TiO₂ particles. *J Phys Chem B* 102:10505–10514
12. Ellingson RJ, Asbury JB, Ferrere S, Ghosh HN, Sprague JR, Lian T, Nozik AJ (1998) Dynamics of electron injection in nanocrystalline titanium dioxide films sensitized with [Ru(4,4'-dicarboxy-2,2'-bipyridine)(2)(NCS)(2)] by infrared transient absorption. *J Phys Chem B* 102:6455–6458
13. Ghosh HN, Asbury JB, Lian T (1998) Direct observation of ultrafast electron injection from coumarin 343 to TiO₂ nanoparticles by femtosecond infrared spectroscopy. *J Phys Chem B* 102:6482–6486
14. Haque SA, Tachibana Y, Klug DR, Durrant JR (1998) Charge recombination kinetics in dye-sensitized nanocrystalline titanium dioxide films under externally applied bias. *J Phys Chem B* 102:1745–1749

15. Willig F (1981) Electrochemistry at the organic molecular crystal/aqueous electrolyte interface. In: Gerischer H, Tobias CW (ed) *Advances in electrochemistry and electrochemical engineering*. Wiley, New York, pp 1–111
16. Wöhrle D, Meissner D (1991) *Organic Solar Cells*. *Adv Mater* 3:129–138
17. Wöhrle D, Elbe J, Kreienhoop L, Schnurpfeil G, Tennigkeit B, Hiller S, Schlettwein D (1995) Investigation of n/p junction photovoltaic cells of perylenetetracarboxylic acid diimides and phthalocyanines. *J Mater Chem* 5:1819–1829
18. Wöhrle D, Kreienhoop L, Schlettwein D (1996) Phthalocyanines and related macrocycles in organic photovoltaic junctions. In: Leznoff CC, Lever ABP (ed) *Phthalocyanines-properties and applications*, vol 4. VCH, New York, Weinheim, Cambridge, 1996, pp 219–284
19. Schlettwein D, Oekermann T, Jaeger NI, Armstrong NR, Wöhrle D (2003) Interfacial trap states in junctions of molecular semiconductors. *Chem Phys* 285:103–112
20. Schlettwein D, Hesse K, Gruhn N, Lee PA, Nebesny KW, Armstrong NR (2001) Electronic energy levels in individual molecules, thin films, and organic heterojunctions of substituted phthalocyanines. *J Phys Chem B* 105:4791–4800
21. Minami N, Watanabe T, Fujishima A, Honda K-I (1979) Photoelectrochemical study on copper phthalocyanine films. *Ber Bunsenges Phys Chem* 83:476–481
22. Santerre F, Cote R, Veilleux G, Saint-Jacques RG, Dodelet JP (1996) Highly photoactive molecular semiconductors: Determination of the essential parameters that lead to an improved photoactivity for modified chloroaluminum phthalocyanine thin films. *J Phys Chem* 100:7632–7645
23. Harima Y, Yamashita K (1989) Electrochemical characterization of phthalocyanine thin films prepared by the electrolytic micelle disruption method. *J Phys Chem* 93:4184–4188
24. Harima Y, Yamashita K (1988) Phthalocyanine photoelectrochemical cell prepared by a micelle disruption method. *Appl Phys Lett* 52:1542–1543
25. Schuhmann W, Josel H-P, Parlar H (1987) A new photosynthesis-like system for the light-induced reduction of water to molecular hydrogen. *Angew Chem Int Ed* 26:241–243
26. Perrier G, Dao LH (1987) Improvement of the performance of a hydroxyaluminum phthalocyanine photoelectrochemical cell by a phthalic acid treatment. *J Electrochem Soc* 134:1148–1152
27. Klofta TJ, Sims TD, Pankow JW, Danziger J, Nebesny KW, Armstrong NR (1987) Spectroscopic and photoelectrochemical studies of trivalent metal phthalocyanine thin films: the role of gaseous dopants (oxygen and hydrogen) in determining photoelectrochemical response. *J Phys Chem* 91:5651–5659
28. Klofta T, Rieke P, Linkous C, Buttner WJ, Nanthakumar A, Mewborn TD, Armstrong NR (1985) Tri- and tetravalent phthalocyanine thin film electrodes: comparison with other metal and demetallated phthalocyanine systems. *J Electrochem Soc* 132:2134–2143
29. Buttner WJ, Rieke PC, Armstrong NR (1985) The gold/GaPc-Cl/ferri, ferrocyanide/GaPc-Cl/platinum photoelectrochemical cell. *J Am Chem Soc* 107:3738–3739
30. Harima Y, Yamashita K (1985) Organic photoelectrodes based on p-p iso-type junctions. *J Phys Chem* 89:5325–5327
31. Rieke PC, Armstrong NR (1984) Light-assisted, aqueous redox reactions at chlorogallium phthalocyanine thin-film photoconductors: dependence of the photopotential on the formal potential of the redox couple and evidence for photoassisted hydrogen evolution. *J Am Chem Soc* 106:47–50
32. Belanger D, Dodelet JP, Dao LH, Lombos BA (1984) Photoelectrochemical characteristics and behavior of a surfactant aluminum phthalocyanine cell. *J Phys Chem* 88:4288–4295
33. Leempoel P, Fan F-RF, Bard AJ (1983) Semiconductor electrodes. 50. Effect of mode of illumination and doping on photochemical behavior of phthalocyanine films. *J Phys Chem* 87:2948–2955
34. Loutfy RO, McIntyre LF (1983) Phthalocyanines: electrolyte Schottky-Junction devices. *Can J Chem* 61:72–77
35. Mezza TM, Linkous CL, Shepard VR, Armstrong NR (1981) Improved photoelectrochemical efficiencies at methalocyanine-modified SnO₂ electrodes. *J Electroanal Chem* 124:311–320

36. Meier H, Albrecht W, Tschirwitz U, Geheeb N, Zimmerhackl E (1979) Organische Halbleiter in Photoelektroden. *Chem Ing Tech* 51:653–656
37. Tachikawa H, Faulkner LR (1978) Electrochemical and solid state studies of phthalocyanine thin film electrodes. *J Am Chem Soc* 100:4379–4385
38. Meshitsuka S, Tamaru K (1977) Photoelectrocatalysis by metal phthalocyanine evaporated films in the oxidation of oxalate ion. *J Chem Soc, Faraday Trans 1*(73):236–242
39. Meshitsuka S, Tamaru K (1977) Spectral distributions of photo-electrochemical reactions over metal phthalocyanine electrodes. *J Chem Soc, Faraday Trans 1*(73):760–767
40. Meier H, Albrecht W, Tschirwitz U, Zimmerhackl E, Geheeb N (1977) Zum photovoltaischen Effekt am System Organischer Halbleiter/Elektrolyt. *Ber Bunsenges Phys Chem* 81:592–597
41. Sevastyanov VI, Alferov GA, Asanov AN, Komissarov GG (1975) Photovoltaiv effect in the films of pigments contacting with electrolyte. *Biofizika* 20:1004–1009
42. Shumov YS, Heyrovsky M (1975) The relation between catalytic and photoelectro-chemical properties of phthalocyanine films. *J Electroanal Chem* 65:469–471
43. Schlettwein D, Graaf H, Meyer J-P, Oekermann T, Jaeger NI (1999) Molecular interactions in thin films of hexadecafluorophthalocyaninatozinc (F16PcZn) as compared to islands of N, N'-dimethylperylene-3,4,9,10-bicarboximide (MePTCDI). *J Phys Chem B* 103:3078–3086
44. Oekermann T, Schlettwein D, Jaeger NI (1999) Role of surface states and adsorbates in time-resolved photocurrent measurements and photovoltage generation at phthalocyaninatozinc(II)-photocathodes. *J Electroanal Chem* 462:222–234
45. Oekermann T, Schlettwein D, Wöhrle D (1997) Characterization of N, N'-dimethyl-3,4,9,10-perylenetetracarboxylic acid diimide and phthalocyaninatozinc(II) in electrochemical photovoltaic cells. *J Appl Electrochem* 27:1172–1178
46. Wöhrle D, Schlettwein D, Schnurpfeil G, Schneider G, Karmann E, Yoshida T, Kaneko M (1995) Phthalocyanines and related macrocycles for multi-electron transfer in catalysis, photochemistry and photoelectrochemistry. *Polym Adv Technol* 6:118–130
47. Schlettwein D, Wöhrle D, Karmann E, Melville U (1994) Conduction type of substituted tetraazaporphyrins and perylene tetracarboxylic acid diimides as detected by thermoelectric power measurements. *Chem Mater* 6:3–6
48. Yanagi H, Tsukatani K, Yamaguchi H, Ashida M, Schlettwein D, Wöhrle D (1993) Semiconducting behavior of substituted tetraazaporphyrin thin films in photoelectrochemical cells. *J Electrochem Soc* 140:1942–1948
49. Sobbi AK, Wöhrle D, Schlettwein D (1993) Stability of various porphyrins in solution and as thin film electrodes. *J Chem Soc Perkin Trans 2*:481–488
50. Schlettwein D, Jaeger NI (1993) Identification of the mechanism of the photoelectrochemical reduction of oxygen on the surface of a molecular semiconductor. *J Phys Chem* 97:3333–3337
51. Schlettwein D, Jaeger NI, Wöhrle D (1992) Influence of polymer matrices on the photoelectrochemical properties of a molecular semiconductor by structural modification. *Makromol Chem, Macromol Symp* 59:267–279
52. Schlettwein D, Jaeger NI, Wöhrle D (1991) Photoelectrochemical investigations of molecular semiconductors: characterization of the conduction type of various substituted porphyrins. *Ber Bunsenges Phys Chem* 95:1526–1530
53. Schlettwein D, Kaneko M, Yamada A, Wöhrle D, Jaeger NI (1991) Light-induced dioxygen reduction at thin film electrodes of various porphyrins. *J Phys Chem* 95:1748–1755
54. Wöhrle D, Schlettwein D, Kirschenmann M, Kaneko M, Yamada A (1990) The combination of phthalocyanines and polymers for electrochemically induced processes. *J Macromol Sci Chem A* 27:1239–1260
55. Kaneko M, Wöhrle D, Schlettwein D, Schmidt V (1988) Dioxygen sensitivity of a photoexcited thin film of phthalocyanine dispersed in poly(vinylcarbazole). *Makromol Chem* 189:2419–2425
56. Shepard VR, Armstrong NR (1979) Electrochemical and photoelectrochemical studies of copper and cobalt phthalocyanine-tin oxide electrodes. *J Phys Chem* 83:1268–1276

57. Giraudeau A, Fan F-RF, Bard AJ (1980) Semiconductor electrodes. 30. Spectral sensitization of the semiconductors titanium oxide (n-TiO₂) and tungsten oxide (n-WO₃) with metal phthalocyanines. *J Am Chem Soc* 102:5137–5142
58. Jaeger CD, Fan F-RF, Bard AJ (1980) Semiconductor electrodes. 26. Spectral sensitization of semiconductors with phthalocyanine. *J Am Chem Soc* 102:2592–2598
59. Yanagi H, Chen S, Lee PA, Nebesny KW, Armstrong NR, Fujishima A (1996) Dye-sensitizing effect of TiOPc thin film on n-TiO₂ (001) surface. *J Phys Chem* 100:5447–5451
60. Nazeeruddin MK, Humphry-Baker R, Grätzel M, Wöhrle D, Schnurpfeil G, Schneider G, Hirth A, Trombach N (1999) Efficient near-IR sensitization of nanocrystalline TiO₂ films by zinc and aluminum phthalocyanines. *J Porphyrins Phthalocyanines* 3:230–237
61. Gerischer H (1978) Electrochemistry of the excited electronic state. *J Electrochem Soc* 125:218C–226C
62. Sze SM (1981) *Physics of semiconductor devices*. Wiley, New York
63. Rompf C, Ammermann D, Kowalsky W (1995) Deposition and characterization of crystalline organic semiconductors for photonic devices. *Mater Sci Technol* 11:845–848
64. Koma A (1995) Molecular-beam epitaxial-growth of organic thin films. *Prog Crystal Growth Charact* 30:129–152
65. Schmidt A, Chau LK, Back A, Armstrong NR (1996) Epitaxial phthalocyanine ultrathin films grown by organic molecular beam epitaxy (OMBE). In: Leznoff CC, Lever ABP (eds) *Phthalocyanines: properties and applications*, vol 4. VCH, New York, Weinheim, Cambridge, pp 307–341
66. Yamashita A, Hayashi T (1996) Organic molecular beam deposition of metallophthalocyanines for opto-electronics applications. *Adv Mater* 8:791–799
67. Schlettwein D, Alloway D, Back A, Nebesny KW, Lee PA, Armstrong NR (2002) Organic molecular beam epitaxy (OMBE): creation of ordered organic thin films and organic/organic heterojunctions. In: Hubbard A (ed) *Encyclopedia of surface and colloid science*. Marcel Dekker, New York, pp 3842–3857
68. Schlettwein D (2001) Electronic properties of molecular organic semiconductor thin films. In: Nalwa H (ed) *Supramolecular photosensitive and electroactive materials*. Academic Press, San Diego, pp 211–338
69. Hooks DE, Fritz T, Ward MD (2001) Epitaxy and molecular organization on solid substrates. *Adv Mater* 13:227–241
70. Jaegermann W, Mayer T (1995) What do we learn from model experiments of semiconductor/electrolyte interfaces in UHV-coadsorption of Br₂ with Na and H₂O on WSe(0001)? *Surf Sci* 335:343–352
71. Svensson S, Forsell J-O, Siegbahn H, Ausmees A, Bray G, Södergren S, Sundin S, Osborne SJ, Aksela S, Nommiste E, Jauhiainen J, Jurvansuu M, Karvonen J, Barta P, Salaneck WR, Ewaldsson A, Lögdlund M, Fahlmann A (1996) New end station for the study of gases, liquids, and solid films at the MAX laboratory. *Rev Sci Instrum* 67:2149–2156
72. Lindström H, Rensmo H, Lindquist S-E, Hagfeldt A, Henningsson A, Södergren S, Siegbahn H (1998) Redox properties of nanoporous TiO₂ (anatase) surface modified with phosphotungstic acid. *Thin Solid Films* 323:141–145
73. Bansal A, Lewis NS (1998) Stabilization of Si photoanodes in aqueous electrolytes through surface alkylation. *J Phys Chem B* 102:4058–4060
74. Sturzenegger M, Prokopuk N, Kenyon CN, Royea WJ, Lewis NS (1999) Reactions of etched, single crystal (111)B-oriented InP to produce functionalized surfaces with low electrical defect densities. *J Phys Chem B* 103:10838–10849
75. Beerbom M, Henrion O, Klein A, Mayer T, Jaegermann W (2000) XPS analysis of wet chemical etching of GaAs(110) by Br₂-H₂O: comparison of emersion and model experiments. *Electrochim Acta* 45:4663–4672
76. Smolenyak PE, Peterson RA, Dunphy DR, Mendes S, Nebesny KW, O'Brien DF, Saavedra SS, Armstrong NR (1999) Formation and spectroelectrochemical characterization

- of multilayer and submonolayer thin films of 2,3,9,10,16,17,23,24-octa(2-benzyloxyethoxy) phthalocyaninato copper (CuPc(OC(2)OBz)(8)). *J Porphyrins Phthalocyanin* 3:620–633
77. Smolenyak PE, Peterson RA, Nebesny KW, Törker M, O'Brien DF, Armstrong NR (1999) Highly ordered thin films of octasubstituted phthalocyanines. *J Am Chem Soc* 121:8628–8636
 78. Fox M-A (1999) Fundamentals in the design of molecular electronic devices: Long-range charge carrier transport and electronic coupling. *Acc Chem Res* 32:201–207
 79. Eichhorn H, Bruce DW, Wöhrle D (1998) Amphitropic mesomorphic phthalocyanines—a new approach to highly ordered layers. *Adv Mater* 10:419–422
 80. Cook MJ (1999) Phthalocyanine thin films. *Pure Appl Chem* 71:2145–2151
 81. Wegner G (1991) Ultrathin films of polymers. *Ber Bunsenges Phys Chem* 95:1326–1333
 82. Wegner G (1992) Ultrathin films of polymers: architecture, characterization, properties, thin solid films 216:105–116
 83. Wu J, Lieser G, Wegner G (1996) Direct imaging of individual shape-persistent macromolecules and their interaction by TEM. *Adv Mater* 2:151–154
 84. Silerova(Back) R, Kalvoda L, Neher D, Ferencz A, Wu J, Wegner G (1998) Electrical conductivity of highly organized Langmuir-Blodgett films of phthalocyaninatopolysiloxane. *Chem Mater* 10:2284–2292
 85. Gattinger P, Rengel H, Neher D, Gurka M, Buck M, van de Craats AM, Warman JM (1999) Mechanism of charge transport in anisotropic layers of a phthalocyanine polymer. *J Phys Chem B* 103:3179–3186
 86. Sato N, Yoshida H, Tsutsumi K (2003) Unoccupied electronic states in phthalocyanine thin films studied by inverse photoemission spectroscopy. *Synth Metals* 133:673–674
 87. Hill IG, Kahn A, Soos ZG, Pascal RA Jr (2000) Charge-separation energy in films of pi-conjugated organic molecules. *Chem Phys Lett* 327:181–188
 88. Wu CI, Hirose Y, Sirringhaus H, Kahn A (1997) Electron-hole interaction energy in the organic molecular semiconductor PTCDA. *Chem Phys Lett* 272:43–47
 89. Meier H, Albrecht W (1965) Zum Problem der pn-Übergänge zwischen organischen und anorganischen Photoleitern. *Ber Bunsenges Phys Chem* 69:160–167
 90. Meier H (1974) Organic semiconductors. VCH, Weinheim
 91. Simon J, Andre J-J (1985) Molecular semiconductors: photoelectrical properties and solar cells. Springer, Berlin
 92. Wright JD (1989) Gas adsorption on phthalocyanines and its effects on electrical properties. *Prog Surf Sci* 31:1–60
 93. Snow AW, Barger WR (1989) Phthalocyanine Films in Chemical Sensors. In: Leznoff CC, Lever ABP (1989) Phthalocyanines: properties and applications, vol 1. VCH, New York, Weinheim, Cambridge 1989, pp 341–392
 94. Guillaud G, Simon J, Germain JP (1998) Metallophthalocyanines—Gas sensors, resistors and field effect transistors. *Coord Chem Rev* 178:1433–1484
 95. Schlettwein D, Armstrong NR, Lee PA, Nebesny KW (1994) Factors which control the n-type or p-type behavior of molecular semiconductor thin films. *Mol Cryst Liq Cryst* 253:161–171
 96. Schlettwein D, Armstrong NR (1994) Correlation of frontier orbital positions and conduction type of molecular semiconductors as derived from UPS in combination with electrical and photoelectrochemical experiments. *J Phys Chem* 98:11771–11779
 97. Meyer J-P, Schlettwein D, Wöhrle D, Jaeger NI (1995) Charge transport in thin films of molecular semiconductors as investigated by measurements of thermoelectric power and electrical conductivity. *Thin Solid Films* 258:317–324
 98. Meyer J-P, Schlettwein D (1996) Influence of central metal and ligand system on conduction type and charge carrier transport in phthalocyanine thin films, D. *Adv Mat Opt Electron* 6:239–244
 99. Schlettwein D, Meyer J-P, Jaeger NI (1999) Intermolecular interactions and electrical properties in thin films of tetrapyrrodotetraazaporphyrinatozinc(II). *J Porphyrins Phthalocyanin* 3:611–619

100. Schmidt A, Schlaf R, Louder D, Chau LK, Chen S-Y, Fritz T, Lawrence MF, Parkinson BA, Armstrong NR (1995) Epitaxial growth of the ionic polymer fluoroaluminum phthalocyanine on the basal plane of singlecrystal tin disulfide. *Chem Mater* 7:2127–2135
101. Chau LK, England CD, Chen S-Y, Armstrong NR (1993) Visible absorption and photocurrent spectra of epitaxially deposited phthalocyanine thin films: interpretation of exciton coupling effects. *J Phys Chem* 97:2699–2706
102. Buefler J (1993) Dissertation: Vergleichende elektrische, elektrochemische und oberflächenspektroskopische Untersuchungen an den radikalischen Phthalocyaninen LuPc₂ und LiPc. Universität Tübingen, Tübingen
103. Ishii H, Sugiyama K, Ito E, Seki K (1999) Energy level alignment and interfacial electronic structures at organic metal and organic interfaces. *Adv Mater* 11:605–625
104. Ishii H, Sugiyama K, Yoshimura D, Ito E, Ouchi Y, Seki K (1998) Energy-level alignment at model interfaces of organic electroluminescent devices studied by UV photoemission: Trend in the deviation from the traditional way of estimating the interfacial electronic structures. *IEEE J Selected Topics in Quantum Chemistry* 4:24–33
105. Tamoto N, Adachi C, Nagai K (1997) Electroluminescence of 1,3,4-oxadiazole and triphenylamine-containing molecules as an emitter in organic multilayer light emitting diodes. *Chem Mater* 9:1077–1085
106. Hung LS, Tang CW (1999) Interface engineering in preparation of organic surfaceemitting diodes. *Appl Phys Lett* 74:3209–3211
107. Hiller S, Schlettwein D, Armstrong NR, Wöhrle D (1998) Influence of surface reactions and ionization gradients on junction properties of F₁₆PcZn. *J Mater Chem* 8:945–954
108. Karl N, Sato N (1992) UV-photoelectron spectroscopy of one- and two-component organic crystals. *Mol Cryst Liq Cryst* 218:79–84
109. Sato N, Yoshikawa M (1996) Valence electronic structure at the interface of organic thin films. *J Electron Spectrosc Relat Phenom* 78:387–390
110. Schlaf R, Parkinson BA, Lee PA, Nebesny KW, Armstrong NR (1998) Determination of frontier orbital alignment and band bending at an organic semiconductor heterointerface by combined X-ray and ultraviolet photoemission measurements. *Appl Phys Lett* 73:1026–1028
111. Rajagopal A, Kahn A (1998) Molecular-level offset at the PTCDA/Alq(3) heterojunction. *Adv Mater* 10:140–144
112. Hill IG, Kahn A (1998) Energy level alignment at interfaces of organic semiconductor heterostructures. *J Appl Phys* 84:5583–5586
113. Rajagopal A, Wu CI, Kahn A (1998) Energy level offset at organic semiconductor heterojunctions. *J Appl Phys* 83:2649–2655
114. Hill IG, Kahn A (1999) Combined photoemission/in vacuo transport study of the indium tin oxide/copper phthalocyanine/N, N'-diphenyl-N, N'-bis(1-naphthyl)-1,1' biphenyl-4,4'' diamine molecular organic semiconductor system. *J Appl Phys* 86:2116–2122
115. Lee ST, Wang YM, Hou XY, Tang CW (1999) Interfacial electronic structures in an organic light-emitting diode. *Appl Phys Lett* 74:670–672
116. Schlaf R, Parkinson BA, Lee PA, Nebesny KW, Armstrong NR (1999) HOMO/LUMO alignment at PTCDA/ZnPc and PTCDA/ClInPc heterointerfaces determined by combined UPS and XPS measurements. *J Phys Chem B* 103:2984–2992
117. Darwent JR, Douglas P, Harriman A, Porter G, Richoux M-C (1982) Metal phthalocyanines and porphyrins as photosensitizers for reduction of water to hydrogen. *Coord Chem Rev* 44:83–126
118. Ferraudi G (1989) Photochemical properties of metallophthalocyanines in homogeneous solution. In: Leznoff CC, Lever ABP (ed) *Phthalocyanines, properties and applications*, vol 1. VCH, New York, Weinheim, Cambridge 1989, pp 291–340
119. Fan F-R, Faulkner LR (1979) Phthalocyanine thin films as semiconductor electrodes. *J Am Chem Soc* 101:4779–4787
120. Klofta T, Buttner WJ, Armstrong NR (1986) Effect of crystallite size and hydrogen and oxygen uptake in the photoelectrochemistries of thin films of chlorogallium phthalocyanine. *J Electrochem Soc* 133:1531–1532

121. Klofta TJ, Danziger J, Lee PA, Pankow J, Nebesny KW, Armstrong NR (1987) Photoelectrochemical and spectroscopic characterization of thin films of titanyl phthalocyanine: comparisons with vanadyl phthalocyanine. *J Phys Chem* 91:5646–5651
122. Yanagi H, Douko S, Ueda Y, Ashida M, Wöhrle D (1992) Improvement of photoelectrochemical properties of chloroaluminum phthalocyanine thin films by controlled crystallization and molecular orientation. *J Phys Chem* 96:1366–1372
123. Perrier G, Dao LH (1986) Cellules photoélectrochimiques de phthalocyanine d'hydroxyaluminium déposées par rotation. *Can J Chem* 64:2431–2439
124. Karmann E, Schlettwein D, Jaeger NI (1996) Photoelectrochemical oxidation of 2-mercaptoethanol at the surface of octacyanophthalocyanine thin film electrodes. *J Electroanal Chem* 405:149–158
125. Karmann E, Meyer J-P, Schlettwein D, Jaeger NI, Anderson M, Schmidt A, Armstrong NR (1996) Photoelectrochemical effects and (photo)conductivity of “n-type” phthalocyanines. *Mol Cryst Liq Cryst* 283:283–291
126. Yanagi H, Kanbayashi Y, Schlettwein D, Wöhrle D, Armstrong NR (1994) Photochemical investigations on naphthalocyanine derivatives in thin films. *J Phys Chem* 98:4760–4766
127. Karmann E (1996) Dissertation: Photoelektrochemische Untersuchungen an dünnen Filmen molekularer n-Halbleiter mit Porphyrinstruktur. Universität Bremen, Bremen
128. Schlettwein D, Karmann E, Oekermann T, Yanagi H (2000) Wavelength-dependent switching of the photocurrent direction at the surface of molecular semiconductor electrodes based on orbital-confined excitation and transfer of charge carriers from higher excited states. *Electrochim Acta* 45:4679–4704
129. Oekermann T, Schlettwein D, Jaeger NI, Wöhrle D (1999) Influence of electronwithdrawing substituents on photoelectrochemical surface phenomena at phthalocyanine thin film electrodes. *J Porphyrins Phthalocyanin* 3:444–452
130. Oekermann T (2000) Die Rolle von Oberflächenzuständen in der Kinetik photoelektrochemischer Reaktionen an Elektroden molekularer Halbleiter. Shaker Verlag, Aachen
131. van Vlierberge B, Yang MZ, Sauvage FX, de Backer M-G, Chapput A (1986) The photoreduction of zinc tetra-2,3-pyridino porphyrazine: a photochemical, electrochemical and spectroscopic study. *Spectrochim Acta* 42:1133–1139
132. Yang MZ, de Backer MG, Sauvage FX (1990) Electrochemical and photoelectrochemical characterizations of electrodes covered by zinc tetra 2,3 pyridinoporphyrazine layers. *New J Chem* 14:273–277
133. Wöhrle D, Bannehr R, Schumann B, Meyer G, Jaeger NI (1983) Synthesis, electrochemical and photoelectrochemical properties of polyphthalocyanine coated electrodes. *J Mol Cat* 21:255–262
134. Knothe G, Wöhrle D (1989) Polymeric phthalocyanines and their precursors, 16; a structure model for polymeric phthalocyanines. *Makromol Chem* 190:1573–1586
135. Knothe G (1993) Isomerism and symmetry of bridged polymeric phthalocyanines. *Macromol Theory Simul* 2:503–516
136. Stillman MJ, Nyokong T (1989) Absorption and magnetic circular dichroism spectral properties of phthalocyanines. In: Leznoff CC, Lever ABP (ed) *Phthalocyanines: properties and applications*, vol 1. VCH, New York, Weinheim, Cambridge 1989, pp 133–290
137. Gouterman M (1978) Optical spectra and atomic structure. In: Dolphin D (ed) *The porphyrins*, part A vol III. Academic Press, New York, pp 1–159
138. Kobayashi N, Konami H (1996) Molecular orbitals and electronic spectra of phthalocyanine analogues. In: Leznoff CC, Lever ABP (ed) *Phthalocyanines: properties and applications*, vol 4. VCH, New York, Weinheim, Cambridge, pp 343–404
139. Green MA (2003) *Third generation photovoltaics: advanced solar energy conversion*. Springer, Berlin
140. Bard AJ, Faulkner LR (1980) *Electrochemical methods*. Wiley, New York
141. Wilson RH (1977) A model for the current-voltage curve of photoexcited semiconductor electrodes. *J Appl Phys* 48:4292–4297

142. Chazalviel J-N (1982) Electrochemical transfer via surface states: a new formulation for the semiconductor/electrolyte interface. *J Electrochem Soc* 129:963–969
143. Abrantes LM, Peter LM (1983) Transient photocurrents at passive iron electrodes. *J Electroanal Chem* 150:593–601
144. Gerischer H (1991) Electron-transfer kinetics of redox reactions at the semiconductor/electrolyte contact. A new approach. *J Phys Chem* 95:1356–1359
145. Hagfeldt A, Grätzel M (1995) Light-induced redox reactions in nanocrystalline systems. *Chem Rev* 95:49–68
146. Batchelor RA, Hamnett A (1992) Surface states on semiconductors. In: Bockris JO, Conway BE, White RE (1992) *Modern aspects of electrochemistry*, vol 22. Kluwer Academic Publishers/Plenum Publishers, Boston, pp 265–415
147. Bard AJ, Bocarsly AB, Fan F-RF, Walton EG, Wrighton MS (1980) The concept of Fermi level pinning at semiconductor/liquid junctions. Consequences for energy conversion efficiency and selection of useful solution redox couples in solar devices. *J Am Chem Soc* 102:3671–3677
148. Bocarsly AB, Bookbinder DC, Dominey RN, Lewis NS, Wrighton MS (1980) Photoreduction at illuminated p-type semiconducting silicon photoelectrodes. Evidence for Fermi level pinning. *J Am Chem Soc* 102:3683–3688
149. Lewerenz HJ (1993) Surface states and fermi level pinning at semiconductor/electrolyte junctions. *J Electroanal Chem* 356:121–143
150. Albery WJ, Dias NL, Wilde CP (1987) The photoelectrochemical kinetics of n-type cadmium sulfide I. The hydroquinone system. *J Electrochem Soc* 134:601–609
151. Peter LM (1990) Dynamic aspects of semiconductor photoelectrochemistry. *Chem Rev* 90:753–769
152. Rajeshwar K (1992) Charge transfer in photoelectrochemical devices via interface states: unified model and comparison with experimental data. *J Electrochem Soc* 129:1003–1008
153. Kelly JJ, Memming R (1992) The influence of surface recombination and trapping on the cathodic photocurrent at p-type III-V-electrodes. *J Electrochem Soc* 129:730–738
154. Schwarzburg K, Willig F (1997) Modeling of electrical transients in the semiconductor/electrolyte cell for photogeneration of charge carriers in the bulk. *J Phys Chem B* 101:2451–2458
155. Smith BB, Nozik AJ (1997) Theoretical studies of electron transfer and electron localization at the semiconductor-liquid interface. *J Phys Chem B* 101:2459–2475
156. Albery WJ, Bartlett PN, Wilde CP (1987) Modulated light studies of the electrochemistry of semiconductors. Theory and experiment. *J Electrochem Soc* 134:2486–2490
157. Schefold J (1992) Impedance and intensity modulated photocurrent spectroscopy as complementary differential methods in photoelectrochemistry. *J Electroanal Chem* 341:111–136
158. Modestov AD, Zhou G-D, Ge H-H, Loo BH (1994) A study of copper electrode behavior in alkaline solutions containing benzotriazole-type inhibitors by the photocurrent response method and intensity-modulated photocurrent spectroscopy. *J Electroanal Chem* 375:293–299
159. Goossens A (1996) Intensity-modulated photocurrent spectroscopy of thin anodic films on titanium. *Surf Sci* 365:662–671
160. Oskam G, Schmidt JC, Searson PC (1996) Electrical properties of n-type (111)Si in aqueous K₄Fe(CN)₆ solution. 2. Intensity modulated photocurrent spectroscopy. *J Electrochem Soc* 143:2538–2543
161. Schlichthörl G, Park NG, Frank AJ (1999) Estimation of the charge-collection efficiency of dye-sensitized nanocrystalline TiO₂ solar cells. *Z Phys Chem* 212:45–50
162. Peter LM, Vanmaekelbergh D (1999) Time and frequency resolved studies of photoelectrochemical kinetics. In: Alkire RC, Kolb DM (ed) *Advances in electrochemical science and engineering*, vol 6. Wiley-VCH, Weinheim 1999, pp 77–163

163. Oekermann T, Schlettwein D, Jaeger NI (2001) Charge transfer and recombination kinetics at electrodes of molecular semiconductors investigated by intensity modulated photocurrent spectroscopy. *J Phys Chem B* 105:9524–9532
164. Meier H (1965) Organic dyes as photoelectric semiconductors. *Angew Chem Int Ed* 4:619–635
165. Peat R, Peter LM (1987) A study of the passive film on iron by intensity modulated photocurrent spectroscopy. *J Electroanal Chem* 228:351–364
166. Li J, Peter LM (1986) Surface recombination at semiconductor electrodes: part iv. Steady-state and intensity modulated photocurrents at n-GaAs electrodes. *J Electroanal Chem* 199:1–26
167. Taira S, Miki T, Yanagi H (1999) Dye-sensitization of n-TiO₂ single-crystal electrodes with vapor-deposited oxometal phthalocyanines. *Appl Surf Sci* 143:23–29
168. Armstrong NR, Nebesny KW, Collins CE, Lee PA, Chau LK, Arbour C, Parkinson BA (1991) O/I-MBE: formation of highly ordered phthalocyanine/semiconductor junctions by molecular-beam epitaxy: photoelectrochemical characterization. In: Lessard RA (ed) *Photopolymer device physics, chemistry, and applications II*. Proceedings of SPIE vol 1559, The International Society for Optical Engineering, Bellingham, WA, pp18–26
169. Chau LK, Arbour C, Collins GE, Nebesny KW, Lee PA, England CD, Armstrong NR, Parkinson BA (1993) Phthalocyanine aggregates on metal dichalcogenide surfaces: dye sensitization on tin disulfide semiconductor electrodes by ordered and disordered chloroindium phthalocyanine thin films. *J Phys Chem* 97:2690–2698
170. Chau LK, Osburn EJ, Armstrong NR, O'Brien DF, Parkinson BA (1994) Dye Sensitization with octasubstituted liquid crystalline phthalocyanines. *Langmuir* 10:351–353
171. Deng H, Mao H, Liang B, Shen Y, Lu Z, Xu H (1996) Aggregation and the photoelectric behavior of tetrasulfonated phthalocyanine adsorbed on a TiO₂ microporous electrode. *J Photochem Photobiol A* 99:71–74
172. Hodak J, Quinteros C, Litter MI, San Roman E (1996) Sensitization of TiO₂ with phthalocyanines. I. Photo-oxidations using hydroxoaluminium tricarboxymonoamidophthalocyanine adsorbed on TiO₂. *J Chem Soc, Faraday Trans* 92:5081–5088
173. Yanagi H, Ohoka Y, Hishiki T, Ajito K, Fujishima A (1997) Characterization of dyedoped TiO₂ films prepared by spray-pyrolysis. *Appl Surf Sci* 113:426–431
174. Fang J, Wu J, Zhang X, Mao H, Shen Y, Lu Z (1997) Fabrication, characterization and photovoltaic study of a GaTSPc-CdS/TiO₂ particulate film. *J Mater Chem* 7:737–740
175. Nazeeruddin MK, Humphry-Baker R, Grätzel M, Murrer BA (1998) Efficient near IR sensitization of nanocrystalline TiO₂ films by ruthenium phthalocyanines. *Chem Commun* 719–720
176. Diacon A, Fara L, Cincu C, Mitroi MR, Zaharia C, Rusen E, Boscornea C, Rosu C, Comaneci D (2010) New materials for hybrid dye-sensitized solar cells. *Optical Mat* 32:1583–1586
177. Yanagisawa M, Korodi F, Bergquist J, Holmberg A, Hagfeldt A, Akermark B, Sun L (2004) Synthesis of phthalocyanines with two carboxylic acid groups and their utilization in solar cells based on nano-structured TiO₂. *J Porphyrins Phthalocyanines* 8:1228–1235
178. Martin-Gomez L, Barea EM, Fernandez-Lazaro F, Bisquert J, Sastre-Santos A (2011) Dye sensitized solar cells using non-aggregated silicon phthalocyanines. *J Porphyrins Phthalocyanines* 15:1004–1010
179. Lin K-C, Doane T, Wang L, Li P, Pejic S, Kenney ME, Burda C (2014) Laser spectroscopic assessment of a phthalocyanine-sensitized solar cell as a function of dye loading. *Sol Energy Mater Sol Cells* 126:155–162
180. Barea EM, Ortiz J, Paya FJ, Fernandez-Lazaro F, Fabregat-Santiago F, Sastre-Santos A, Bisquert J (2010) Energetic factors governing injection, regeneration and recombination in dye solar cells with phthalocyanine sensitizers. *Energy Environ Sci* 3:1985–1994
181. Cid J-J, Yum J-H, Jang S-R, Nazeeruddin MdK, Martinez-Ferrero E, Palomares E, Ko J, Grätzel M, Torres T (2007) Molecular cosensitization for efficient panchromatic dye-sensitized solar cells. *Angew Chem Int Ed* 46:8358–8362

182. Yum J-H, Jang S-R, Humphry-Baker R, Grätzel M, Cid J-J, Torres T, Nazeeruddin MdK (2008) *Langmuir* 24:5636–5640
183. Listorti A, López-Duarte I, Martínez-Díaz MV, Torres T, DosSantos T, Barnes PR, Durrant JR (2010) Zn(II) versus Ru(II) phthalocyanine-sensitized solar cells. A comparison between singlet and triplet electron injectors. *Energy Environ Sci* 3:1573–1579
184. Lee J, Leventis HC, Haque SA, Torres T, Grätzel M, Nazeeruddin MdK (2011) Panchromatic response composed of hybrid visible-light absorbing polymers and near-IR absorbing dyes for nanocrystalline TiO₂-based solid-state solar cells. *J Power Source* 196:596–599
185. Cid J-J, Garía-Iglesias M, Yum J-H, Forneli A, Albero J, Martínez-Ferrero E, Vázquez P, Grätzel M, Nazeeruddin K, Palomares E, Torres T (2009) Structure–function relationships in unsymmetrical zinc phthalocyanines for dye-sensitized solar cells. *Chem Eur J* 15:5130–5137
186. Giribabu L, Kumar CV, Reddy PY, Yum J-H, Grätzel M, Nazeeruddin MdK (2009) Unsymmetrical extended π -conjugated zinc phthalocyanine for sensitization of nanocrystalline TiO₂ films. *J Chem Sci* 121:75–82
187. Reddy PY, Giribabu L, Lyness C, Snaith HJ, Vijaykumar C, Chandrasekharam M, Lakshmikantam M, Yum J-H, Kalyanasundaram K, Grätzel M, Nazeeruddin MdK (2007) Efficient sensitization of nanocrystalline TiO₂ films by a near-IR absorbing unsymmetrical zinc phthalocyanine. *Angew Chem Int Ed* 47:373–376
188. Giribabu L, Kumar CV, Raghavender M, Somaiah K, Reddy PY, Rao VP (2008) Durable unsymmetrical zinc phthalocyanine for near IR sensitization of nanocrystalline TiO₂ films with non-volatile redox electrolytes. *J Nano Res* 2:39–48
189. Hagfeldt A, Grätzel M (2000) Molecular photovoltaics. *Acc Chem Res* 33:269–277
190. Nazeeruddin MdK, Humphry-Baker R, Officer DL, Campbell WM, Burrell AK, Grätzel M (2004) Application of metalloporphyrins in nanocrystalline dye-sensitized solar cells for conversion of sunlight into electricity. *Langmuir* 20:6514–6517
191. Yella A, Lee H-W, Tsao HN, Yi C, Chandiran AK, Nazeeruddin MdK, Diao EW-G, Yeh C-Y, Zakeeruddin SM, Grätzel M (2011) Porphyrin-sensitized solar cells with cobalt (II/III)-based redox electrolyte exceed 12 percent efficiency. *Science* 334:629–634
192. Lim B, Margulis GY, Yum J-H, Unger EL, Hardin BE, Grätzel M, McGehee MD, Sellinger S (2013) Silicon-naphthalophthalocyanine-hybrid sensitizer for efficient red response in dye-sensitized solar cells. *Org Lett* 15:784–787
193. Holliman PJ, Davies ML, Connell A, Vaca Velasco B, Watson TM (2010) Ultra-fast dye sensitisation and co-sensitisation for dye sensitized solar cells. *Chem Commun*, 7256–7258
194. Kuang D, Walter P, Nüesch F, Kim S, Ko J, Comte P, Zakeeruddin SM, Nazeeruddin MdK, Grätzel M (2007) Co-sensitization of organic dyes for efficient ionic liquid electrolyte-based dye-sensitized solar cells. *Langmuir* 23:10906–10909
195. Yum JH, Jang SR, Walter P, Geiger T, Nüesch F, Kim S, Ko J, Grätzel M, Nazeeruddin Md K (2007) Efficient co-sensitization of nanocrystalline TiO₂ films by organic sensitizers. *Chem Commun* 4680–4682
196. Rensmo H, Keis K, Lindström H, Södergren S, Solbrand A, Hagfeldt A, Lindquist S-E, Wang LN, Muhammed M (1997) High light-to-energy conversion efficiencies for solar cells based on nanostructured ZnO electrodes. *J Phys Chem B* 101:2598–2601
197. Bedja I, Kamat PV, Hua X, Lappin AG, Hotchandani S (1997) Photosensitization of nanocrystalline ZnO films by bis(2,2'-bipyridine)(2,2'-bipyridine-4,4'-dicarboxylic acid) ruthenium(II). *Langmuir* 13:2398–2403
198. Rao TN, Bahadur L (1997) Photoelectrochemical studies on dye-sensitized particulate ZnO thin-film photoelectrodes in nonaqueous media. *J Electrochem Soc* 144:179–185
199. Fessenden RW, Kamat PV (1995) Rate constants for charge injection from excited sensitizer into SnO₂, ZnO, and TiO₂ semiconductor nanocrystallites. *J Phys Chem* 99:12902–12906
200. Yoshida T, Minoura H (2000) Electrochemical self-assembly of dye-modified zinc oxide thin films. *Adv Mater* 12:1219–1222

201. Yoshida T, Miyamoto K, Hibi N, Sugiura T, Minoura H, Schlettwein D, Oekermann T, Schneider G, Wöhrle D (1998) Self assembled growth of nano particulate porous ZnO thin film modified by 2,9,16,23-tetrakisulfophthalocyanatozinc(II) by one-step electrodeposition. *Chem Lett* 7:599–600
202. Yoshida T, Tochimoto M, Schlettwein D, Schneider G, Wöhrle D, Sugiura T, Minoura H (1999) Self-assembly of zinc oxide thin films modified with tetrasulfonated metallophthalocyanines by one-step electrodeposition. *Chem Mater* 11:2657–2667
203. Yoshida T, Terada K, Schlettwein D, Oekermann T, Sugiura T, Minoura H (2000) Electrochemical self-assembly of nanoporous ZnO/eosin Y thin films and their sensitized photoelectrochemical performance. *Adv Mater* 12:1214–1217
204. Schubert U, Lorenz A, Kundo N, Stuchinskaya T, Gogina L, Salanov A, Zaikonovskii V, Maizlish V, Shaposhnikov GP (1997) Cobalt phthalocyanine derivatives supported on TiO₂ by sol-gel processing.1. Preparation and microstructure. *Chem Ber/Recl* 130:1585–1589
205. Hunter CA, Sanders KM (1990) The nature of π - π interactions. *J Am Chem Soc* 112:5525–5534
206. Schneider G, Wöhrle D, Spiller W, Stark J, Schulz-Ekloff G (1998) Photooxidation of 2-Mercaptoethanol by various water soluble phthalocyanines in aqueous alkaline solution under irradiation with visible light. *Photochem Photobiol* 60:333–342
207. Schlettwein D, Oekermann T, Yoshida T, Tochimoto M, Minoura H (2000) Photoelectrochemical sensitisation of ZnO-tetrakisulfophthalocyaninatozinc composites prepared by electrochemical self-assembly. *J Electroanal Chem* 481:42–51
208. Nüesch F, Moser JE, Shklover V, Grätzel M (1996) Merocyanine aggregation in mesoporous networks. *J Am Chem Soc* 118:5420–5431
209. Oekermann T, Yoshida T, Schlettwein D, Sugiura T, Minoura H (2001) Photoelectrochemical properties of ZnO/tetrakisulfophthalocyanine hybrid thin films prepared by electrochemical self-assembly. *Phys Chem Chem Phys* 3:3387–3392
210. Schlettwein D, Oekermann T, Yoshida T, Sugiura T, Minoura H, Wöhrle D (2002) Electrochemically self-assembled ZnO/dye electrodes: preparation and time-resolved photoelectrochemical measurements. In: Kafafi ZH (ed) *Organic photovoltaics II*, Proceedings of SPIE vol 4465, The International Society for Optical Engineering, Bellingham, WA 2002, pp 113–122
211. Michaelis E, Nonomura K, Schlettwein D, Yoshida T, Minoura H, Wöhrle D (2004) Hybrid thin films of ZnO with porphyrins and phthalocyanines prepared by one-step electrodeposition. *J Porphyrins Phthalocyanin* 8:1366–1375
212. Nonomura K, Loewenstein T, Michaelis E, Wöhrle D, Oekermann T, Yoshida T, Minoura H, Schlettwein D (2006) Photoelectrochemical characterization of electrodeposited ZnO thin films sensitized by porphyrins and phthalocyanines. *Phys Chem Chem Phys* 8:3867–3875
213. Yoshida T, Iwaya M, Ando H, Oekermann T, Nonomura K, Schlettwein D, Wöhrle D, Minoura H (2004) Improved photoelectrochemical performance of electrodeposited ZnO/EosinY hybrid thin films by dye re-adsorption. *Chem Commun* 400–401
214. Yoshida T, Zhang JB, Komatsu D, Sawatani S, Minoura H, Pauporte T, Lincot D, Oekermann T, Schlettwein D, Tada H, Wöhrle D, Funabiki K, Matsui M, Miura H, Yanagi H (2009) Electrodeposition of inorganic/organic hybrid thin films. *Adv Funct Mater* 19:17–43
215. Yoshida T, Terada K, Schlettwein D, Oekermann T, Sugiura T, Minoura H (2000) Electrochemical self-assembly of nanoporous ZnO/eosin Y thin films and their sensitized photoelectrochemical performance. *Adv Mater* 12:1214–1217
216. Yoshida T, Oekermann T, Okabe K, Schlettwein D, Funabiki K, Minoura H (2002) Cathodic Electrodeposition of ZnO/eosinY hybrid thin films from dye added zinc nitrate bath and their photoelectrochemical characterizations. *Electrochemistry* 70:470–487
217. Ozoemena K, Kuznetsnova N, Nyokong T (2001) Photosensitized transformation of 4-chlorophenol in the presence of aggregated and non-aggregated metallophthalocyanines. *J Photochem Photobiol, A* 139:217–224

218. Agboola B, Ozoemena KI, Nyokong T (2006) Comparative efficiency of immobilized non-transition metal phthalocyanine photosensitizers for the visible light transformation of chlorophenols. *J Mol Catal A-Chem* 248:84–92
219. Idowu M, Loewenstein T, Hastall A, Nyokong T, Schlettwein D (2010) Photoelectrochemical characterization of electrodeposited ZnO thin films sensitized by octacarboxymetallaphthalocyanine derivatives. *J Porph Phthalocyanin* 14:142–149
220. Masilela N, Nombona N, Loewenstein T, Nyokong T, Schlettwein D (2010) Symmetrically and unsymmetrically substituted carboxy phthalocyanines as sensitizers for nanoporous ZnO films. *J Porph Phthalocyanin* 14:985–992
221. Rostalski J, Meissner D (2000) Photocurrent spectroscopy for the investigation of charge carrier generation and transport mechanisms in organic p/n-junction solar cells. *Sol Energy Mater Sol Cells* 63:37–47
222. Brabec CJ, Sariciftci NS, Hummelen JC (2001) Plastic solar cells. *Adv Mater* 13:15–26
223. Yanagi H, Ashida M, Harima Y, Yamashita K (1990) Photoelectrochemical Properties of orientation-controlled thin film for 5,10,15,20-tetraphenylporphyrin. *Chem Lett* 385–388
224. Xue J, Uchida S, Rand B, Forrest SR (2004) Asymmetric tandem organic photovoltaic cells with hybrid planar-mixed molecular heterojunctions. *Appl Phys Lett* 85:5757–5759
225. http://www.heliatek.com/wp-content/uploads/2013/01/130116_PR_Heliatek_achieves_record_cell_efficiency_for_OPV.pdf. Accessed 29 Apr 2015
226. Che X, Xiao X, Zimmerman JD, Fan D, Forrest SR (2014) High-efficiency, vacuum-deposited, small-molecule organic tandem and triple-junction photovoltaic cells. *Adv Energy Mater* 4:1400568
227. Park SH, Roy A, Beaupré S, Cho S, Coates NS, Moon JS, Moses D, Leclerc M, Lee K, Heeger AJ (2009) Bulk heterojunction solar cells with internal quantum efficiency approaching 100 %. *Nat Photonics* 3:297–302
228. Liang Y, Xu Z, Xia J, Tsai S-T, Wu Y, Li G, Ray C, Yu L (2010) For the bright future-bulk heterojunction polymer solar cells with power conversion efficiency of 7.4 %. *Adv Mater* 22: E135–E138
229. Susanna G, Salamandra L, Ciceroni C, Mura F, Brown TM, Reale A, Rossi M, Di Carlo A, Brunetti F (2015) 8.7 % power conversion efficiency polymer solar cell realized with non-chlorinated solvents. *Sol Energy Mater Sol Cells* 134:194–198
230. Nguyen TL, Choi H, Ko S-J, Uddin MA, Walker B, Yum S, Jeong J-E, Yun MH, Shin TJ, Hwang S, Kim JY, Woo HY (2014) Semi-crystalline photovoltaic polymers with efficiency exceeding 9 % in a 300 nm thick conventional single-cell device. *Energy Environ Sci* 7:3040–3051
231. You J, Dou L, Yoshimura K, Kato T, Ohya K, Moriarty T, Emery K, Chen C-C, Gao J, Li G, Yang Y (2012) A polymer tandem solar cell with 10.6 % power conversion efficiency. *Nat Commun* 4:1446
232. Chen C-C, Chang W-H, Yoshimura K, Ohya K, You J, Gao J, Hong Z, Yang Y (2014) An efficient triple-junction polymer solar cell having a power conversion efficiency exceeding 11 %. *Adv Mater* 26:5670–5677
233. Yusoff ARBM, Kim D, Kim HP, Shneider FK, da Silva WJ, Jang J (2015) A high efficiency solution processed polymer inverted triple-junction solar cell exhibiting a power conversion efficiency of 11.83 %. *Energy Environ Sci* 8:303–316
234. Zhou R, Josse F, Göpel W, Öztürk ZZ, Bekaroglu Ö (1996) Phthalocyanines as sensitive materials for chemical sensors. *Appl Organomet Chem* 10:557–577
235. Mabeck JT, Malliaras GG (2006) Chemical and biological sensors based on organic thin-film transistors. *Anal Bional Chem* 384:343–353
236. Waite S, Pankow J, Collins GE, Lee PA, Armstrong NR (1989) Interactions of ammonia and oxygen with the surfaces of chlorogallium phthalocyanine thin films: microcircuit photoconductivity and quartz-crystal microgravimetry studies. *Langmuir* 5:797–805

Index

A

Anchoring groups, 184, 185, 187–189, 191, 192, 194, 195, 198, 208, 217, 221
Attenuated total reflection Fourier transform infrared (spectroscopy), 201

B

Boradiazaindacene (BODIPY), 205, 206, 216
Broad-band capture, 181, 195
Bulk heterojunction, 171, 173, 176, 177, 226, 227, 236, 247

C

Carbon nano-network, 75, 82, 92
Charge injection, 184, 200
Charge recombination, 180, 184–186, 190, 216, 253
Chemistry gold electrode, 145–147
Conduction band, 178, 186, 188, 218
Cyanoacrylic acid, 219

D

Density functional theory, 22, 148
Donor-(porphyrin bridge)-acceptor, 203, 205–207
Durability, 70, 71
Dye-sensitized solar cells, 178, 180–184, 188–190, 193, 194, 198–200, 203, 207, 208, 210, 213, 214, 216, 219, 227, 253, 293, 294, 303

E

Electron-donor molecule, 199
Excited electron–donor molecule, 175, 177, 199

F

Fe–NX active ensembles, 79, 93
Fe–NX/C catalysts, 89, 92, 93

Fill factor of a photovoltaic cell, 175, 189, 253
Flat heterojunction, 176, 177
Fluorine-doped tin oxide, 252
Four electron pathway, 10, 11

G

Gold cluster, 150, 152, 156, 157

H

Highest occupied molecular orbital, 192, 195, 198, 216, 218, 227, 234, 239, 241, 243, 246
Hydrogen, 70, 78, 83, 89, 90

I

Incident photon-to-current efficiency, 174, 175, 194, 226, 239, 247, 249–251
Iron phthalocyanine, 76, 87

L

Langmuir–Blodgett, 267, 302
Lowest unoccupied molecular orbital, 192, 195, 198, 216, 218, 227, 234, 239, 241, 243, 244, 246

M

Macrocyclic modified graphene, 19, 20
Mechanism of ORR, 10
Mesoporous carbon, 75, 79, 83, 84, 86, 87, 92
Meso-porous silica, 76, 88
Metalloporphyrin, 173, 180, 184, 186, 187, 204, 243
Metal oxide, 176, 181, 183, 184, 188, 192, 199
Microporosity, 84, 85, 88, 92
M–N₄, 1, 2, 4
M–N₄ clusters between graphitic pores, 27
M–N₄ clusters embedded in graphene, 29
M–N₄ macrocyclic modified carbon nanotube, 19

- M-N₄ macrocyclic complex, 132, 133, 136
 catalytic properties of, 2, 4, 7, 13, 20
 electronic properties of, 2, 18
 heat treatment of, 2, 12
- Molecular electronic, 144, 159
- Molecular semiconductors, 264, 268, 277, 301
- N**
- Nanoscience, 144
- Nanotechnology, 144, 146
- Nanotube, 179, 247
- Near-infrared, 204
- Non-noble metal catalyst, 92
- Non-platinum group metal (non-PGM), 41, 42, 49, 52, 53, 60
- Normal hydrogen electrode, 176
- O**
- Oligomeric porphyrin, 227
- Organic photovoltaics, 173, 176, 247
- Oxygen adsorption, 23, 24
- Oxygen reduction, 44, 49, 59, 61, 117, 119–121, 126, 128, 129, 132–136
- Oxygen reduction reaction (ORR), 2, 41, 45, 47, 71, 148, 153, 154
- P**
- PEM fuel cells, 70
- Photoelectrochemistry, 263
- Photovoltaic cell, 180
- Photovoltaics, 173
- Phthalocyanine, 1, 8, 18
- Physicochemical testing
 Brunauer–Emmett–Teller (BET), 57
 Raman spectroscopy, 57
 X-ray absorption spectroscopy, 56
 X-ray photoelectron spectroscopy, 50
- Polyaniline, 43, 45, 63
- Polymer electrolyte fuel cells, 41, 60
- Polypyrrole, 43, 83, 84
- Porphyrin, 1, 8, 18, 173, 178, 181, 183, 184, 186, 187, 189–192, 194, 195, 198–208, 210, 213–219, 221–223, 225–235, 237–242, 250–253
- Porphyrin–fullerene, 248
- Porphyrin–graphene, 251
- Porphyrin–phthalocyanine, 230, 250, 251
- Power conversion efficiency (of a photovoltaic cell), 175, 183–186, 189, 190, 192–196, 198, 200–203, 207, 208, 210, 212–219, 221, 222, 224–228, 230–232, 234, 238, 240, 241, 243, 244, 246–249, 251
- Precursors
 nitrogen, 42, 43, 45, 62, 64
 transition metal, 42, 43, 45, 58
- Push–pull systems, 210, 216
- ”Push–pull”, donor-(π -bridged chromophore)-acceptor, 203
- Pyrolysis iron acetate, 74
- Pyrolyzed catalysts, 4, 13, 18
- R**
- Redox-conducting polymers, 173, 174
- Reduced graphene oxide, 75, 80, 92
- S**
- SBA15 silica, 76, 87
- Scanning electrochemical microscopy (SECM), 103, 116, 129
- Self-standing Fe–N_x–C catalyst, 93
- Single-wall carbon nanotube, 251, 252
- SnO₂, 249, 250, 252
- Solar cell, 174, 176, 181, 226, 227, 236, 247
- Squaraine, 205, 206
- Supramolecular, 143–149, 163
- Supramolecular solar cells, 178, 252
- T**
- Tetraphenyl porphyrin, 251
- Tetraphenyl zinc porphyrin, 184
- Thin films, 263, 264, 266, 268, 270, 272, 275, 277, 291, 295, 296, 301, 302
- Thin-layer solar cell, 179
- Thiocyanate oxidation, 148, 159–161
- Tin-doped indium oxide, 228–232, 242, 246, 249
- TiO₂, 176, 178–181, 185–190, 193, 199–202, 207, 209, 210, 213, 215, 216, 218, 221, 223, 226
- Transition metal phthalocyanines on gold, 144
- Transparent conductive oxide, 178, 179
- Tris(2-pyridyl)-s-triazine, 79
- Two electron pathway, 10, 11
- U**
- Ultraviolet–visible (light), 194, 234, 237, 246, 250–252
- V**
- van der Waals interaction, 152
- Y**
- Yeager, E., 11
- Z**
- Zinc porphyrin, 180, 184, 187, 189–195, 197, 198, 200–202, 205–208, 211–219, 221, 222, 224–226, 229, 230, 237–242, 251, 252